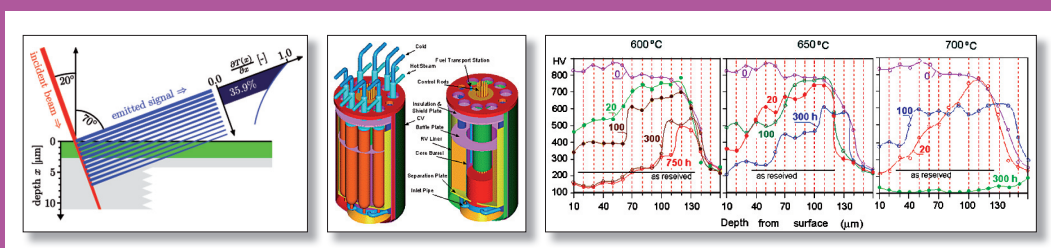


Structural Materials for Innovative Nuclear Systems (SMINS)

Workshop Proceedings
Karlsruhe, Germany
4-6 June 2007



Nuclear Science

ISBN 978-92-64-04806-5

Structural Materials for Innovative Nuclear Systems (SMINS)

**Workshop Proceedings
Karlsruhe, Germany
4-6 June 2007**

© OECD 2008
NEA No. 6260

NUCLEAR ENERGY AGENCY
ORGANISATION FOR ECONOMIC CO-OPERATION AND DEVELOPMENT

ORGANISATION FOR ECONOMIC CO-OPERATION AND DEVELOPMENT

The OECD is a unique forum where the governments of 30 democracies work together to address the economic, social and environmental challenges of globalisation. The OECD is also at the forefront of efforts to understand and to help governments respond to new developments and concerns, such as corporate governance, the information economy and the challenges of an ageing population. The Organisation provides a setting where governments can compare policy experiences, seek answers to common problems, identify good practice and work to co-ordinate domestic and international policies.

The OECD member countries are: Australia, Austria, Belgium, Canada, the Czech Republic, Denmark, Finland, France, Germany, Greece, Hungary, Iceland, Ireland, Italy, Japan, Korea, Luxembourg, Mexico, the Netherlands, New Zealand, Norway, Poland, Portugal, the Slovak Republic, Spain, Sweden, Switzerland, Turkey, the United Kingdom and the United States. The Commission of the European Communities takes part in the work of the OECD.

OECD Publishing disseminates widely the results of the Organisation's statistics gathering and research on economic, social and environmental issues, as well as the conventions, guidelines and standards agreed by its members.

* * *

This work is published on the responsibility of the Secretary-General of the OECD. The opinions expressed and arguments employed herein do not necessarily reflect the official views of the Organisation or of the governments of its member countries.

NUCLEAR ENERGY AGENCY

The OECD Nuclear Energy Agency (NEA) was established on 1st February 1958 under the name of the OEEC European Nuclear Energy Agency. It received its present designation on 20th April 1972, when Japan became its first non-European full member. NEA membership today consists of 28 OECD member countries: Australia, Austria, Belgium, Canada, the Czech Republic, Denmark, Finland, France, Germany, Greece, Hungary, Iceland, Ireland, Italy, Japan, Luxembourg, Mexico, the Netherlands, Norway, Portugal, Republic of Korea, the Slovak Republic, Spain, Sweden, Switzerland, Turkey, the United Kingdom and the United States. The Commission of the European Communities also takes part in the work of the Agency.

The mission of the NEA is:

- to assist its member countries in maintaining and further developing, through international co-operation, the scientific, technological and legal bases required for a safe, environmentally friendly and economical use of nuclear energy for peaceful purposes, as well as
- to provide authoritative assessments and to forge common understandings on key issues, as input to government decisions on nuclear energy policy and to broader OECD policy analyses in areas such as energy and sustainable development.

Specific areas of competence of the NEA include safety and regulation of nuclear activities, radioactive waste management, radiological protection, nuclear science, economic and technical analyses of the nuclear fuel cycle, nuclear law and liability, and public information. The NEA Data Bank provides nuclear data and computer program services for participating countries.

In these and related tasks, the NEA works in close collaboration with the International Atomic Energy Agency in Vienna, with which it has a Co-operation Agreement, as well as with other international organisations in the nuclear field.

© OECD 2008

OECD freely authorises the use, including the photocopy, of this material for private, non-commercial purposes. Permission to photocopy portions of this material for any public use or commercial purpose may be obtained from the Copyright Clearance Center (CCC) at info@copyright.com or the Centre français d'exploitation du droit de copie (CFC) contact@cfcopies.com. All copies must retain the copyright and other proprietary notices in their original forms. All requests for other public or commercial uses of this material or for translation rights should be submitted to rights@oecd.org.

FOREWORD

Structural materials research is a field of growing relevance in the nuclear sector, especially for the different innovative reactor systems being developed within the Generation IV International Forum (GIF), for critical and subcritical transmutation systems, and of interest to the Global Nuclear Energy Partnership (GNEP). Indeed, the goals defined for the GIF innovative nuclear systems – sustainability and waste minimisation; enhanced economics; safety and reliability; and enhanced proliferation resistance – call for demanding material-related operating conditions, such as high in-service and off-normal temperatures, high fuel burn-ups, long service lifetimes (~60 years) and compatibility with different coolants. All these conditions imply new challenges with respect to current nuclear industry experience on structural materials.

A common feature in developing the different nuclear systems is the widely recognised need for experimental programmes to select and characterise innovative structural materials. These materials may, however, vary from one system to another. For example, in the case of very-high-temperature reactors (VHTRs), research is expected to be needed on nuclear graphite for the core and on nickel-based alloys and ceramics for intermediate heat exchangers and turbines. In the case of gas-cooled fast reactors (GFRs), silicon-carbon materials are being considered for fuel encapsulation.

It is in this context that the NEA Nuclear Science Committee (NSC) organised the Workshop on Structural Materials for Innovative Nuclear Systems (SMINS) in collaboration with the *Forschungszentrum Karlsruhe* in Germany. The objectives of the workshop were to exchange information on structural materials research issues and ongoing programmes for the different types of reactor concepts, as well as to foster the development of synergies. The workshop took place on 4-6 June 2007 at the *Forschungszentrum Karlsruhe* in Germany and was attended by approximately 100 participants with contributions from Europe, the United States, Japan, Korea and the Russian Federation. On the basis of the positive feedback received, the SMINS Scientific Advisory Committee proposed that the NSC envisage further initiatives on information exchange and development of potential synergies in the areas of both experimental assessment and advanced modelling of structural materials. It was suggested that the establishment of an NSC expert group and/or a working party could be an appropriate tool to help co-ordinate future activities in this field.

Acknowledgements

A special mention and acknowledgement should be addressed to the members of the Scientific Advisory Committee (SAC) of the SMINS workshop. The SAC members were very active in shaping the programme, stimulating participation and reviewing abstracts. Some members acted as session chairs, and accepted to peer review the manuscripts of these proceedings.

Members of the Scientific Advisory Committee

Al Mazouzi, A.	SCK•CEN, Belgium
Allen, T.	University of Wisconsin, USA
Billot, Ph.	CEA, France
Bolt, H.	IPP, Germany
Burlet, H.	CEA, France
Corsi, F.	ENEA, Italy
Fazio, C. (<i>Chair</i>)	FZK, Germany
Gómez Briceño, D.	CIEMAT, Spain
Heikinheimo, L.	VTT, Finland
Hoffelner, W.	PSI, Switzerland
Horvath, A.	KFKI, Hungary
Inozemtsev, V.	IAEA
Kato, C.	JAEA, Japan
Maloy, S.	LANL, USA
Mansur, L.K.	ORNL, USA
Marsden, B.J.	University of Manchester, UK
Massoud, J-P.	EdF, France
Moeslang, A.	FZK, Germany
Mompean, Ff	OECD/NEA
Perlado, J-M.	University PM, Spain
Ryu, W-S.	KAERI, Republic of Korea
Tromm, W.	FZK, Germany
Van Goethem, G.	CEC
Wallenius, J.	KTH, Sweden
Yvon, P.	CEA, France

TABLE OF CONTENTS

Foreword.....	3
Executive summary	9
OVERVIEW	13
Chair: W. Tromm	
<i>G. Van Goethem</i>	
EURATOM RDDD in Innovative Reactor Systems and Fuel Cycles.....	15
SESSION I KEYNOTE LECTURES	37
Chairs: W. Tromm, G. Van Goethem	
<i>F. Carré, P. Yvon, P. Chaix</i>	
Innovative Reactor Systems and Requirements for Structural Materials	39
<i>N. Sekimura</i>	
Ageing Management and Knowledge Base for Safe Long-term Operation of Japanese Light Water Reactors.....	49
<i>T. Allen</i>	
Modelling, Microstructures, Radiation Damage and Understanding of Irradiation Data.....	57
SESSION II GAS-COOLED SYSTEMS	67
Chairs: W. Hoffelner, B.J. Marsden	
<i>W. Hoffelner</i>	
Material Research for VHTR Design Codes.....	69
<i>H. Burllet, J-M. Gentzbittel, C. Cabet, P. Lamagnère, M. Blat, D. Renaud, S. Dubiez-Le Goff, D. Pierron</i>	
Evaluation of Nickel-based Materials for VHTR Heat Exchanger.....	79
<i>D. Blanchet, K. Mikityuk, P. Coddington, R. Chawla</i>	
An Uncertainty Assessment Methodology for Materials Behaviour in Advanced Fast Reactors.....	91
SESSION III LIQUID-METAL-COOLED SYSTEMS	101
Chairs: P. Yvon, C. Kato	
<i>A. Kimura, H-S.Cho, N. Toda, R. Kasada, K. Yutani, H. Kishimoto, N. Iwata, S. Ukai, M. Fujiwara</i>	
High-Cr ODS Steels R&D for High Burn-up Fuel Cladding	103

	<i>S. Obara, T. Onizawa, T. Wakai, T. Asayama</i> Influence of Normalising Temperature on MX Precipitation Behaviour in High-chromium Steel.....	115
	<i>A.A. Nikitina, V.S. Ageev, M.V. Leontyeva-Smirnova, V.V. Sagaradze, B.V. Safronov, A.P. Chukanov, V.V. Tsvelev, M.M. Potapenko</i> Development of ODS Ferritic-martensitic Steels for Innovative Nuclear Fast Breeder Reactors.....	127
	<i>K.G.M. Nair, B.K. Panigrahi, J. Arunkumar, C. David, S. Balaji, R. Rajaraman, G. Amarendra, S. Abhaya, M.C. Valsakumar, C.S. Sundar, B. Raj</i> Void Swelling and Defect Processes in Ti-modified Steels Using Accelerator Irradiation	137
	<i>A. Weisenburger, A. Heinzl, G. Müller, A. Rousanov</i> First Results on T91 Claddings with and Without Modified FeCrAlY Coatings Exposed in PbBi Under Varying Conditions	147
SESSION IV	FUSION, HIGH-POWER ACCELERATOR TARGETS AND OTHER FISSION REACTOR SYSTEMS	159
	<i>Chairs: L. Heikinheimo, D. Gómez Briceño</i>	
	<i>S. Teyseyre, G.S. Was</i> Assessing SCC and IASCC of Austenitic Alloys for Application to the SCWR Concept.....	161
	<i>D. Gómez Briceño, L. Castro, F. Blázquez</i> Oxidation and Stress Corrosion Cracking of Stainless Steels in SCWRs.....	171
	<i>L. Tan, K. Sridharan, T.R. Allen</i> Microstructural Influence on the Corrosion Behaviour of Structural Materials for Nuclear Power Systems	183
	<i>X. Li, W. Van Renterghem, A. Al Mazouzi</i> Influence of Stacking Fault Energy (SFE) on the Deformation Mode of Stainless Steels	193
	<i>F. Tavassoli</i> Evolution of Structural Materials in Nuclear Reactors.....	201
SESSION V	FUNDAMENTAL RESEARCH.....	215
	<i>Chairs: A. Al Mazouzi, S. Maloy</i>	
	<i>W. Dietz, B-C. Friedrich</i> Qualification of Structural Materials for Reactor Systems: Synergies in Materials for Fusion/Fission Reactors and Advanced Fission Reactors.....	217
	<i>L. Malerba, A. Al Mazouzi, D. Terentyev, M. Matjasevic</i> Understanding Radiation Damage in FECD Alloys.....	229
	<i>A. Takahashi, N.M. Ghoniem</i> A New Computational Method for Studies of 3-D Dislocation-precipitate Interactions in Reactor Steels.....	241

<i>D. Gaude-Fugarolas, N. Régent, Y. De Carlan</i> On the Theoretical Development of New Creep Resistant Alloys and Their Empirical Validation	253
<i>C. Berre, G. Hall, B.J. Marsden, S.L. Fok, T.J. Marrow, P.M. Mummery</i> Modelling of Nuclear-grade Graphite Using X-ray Tomography Data.....	265
<i>M. Hernández-Mayoral, M.J. Caturla,</i> <i>D. Gómez-Briceño, J.M. Perlado, E. Martínez, J. Marian</i> Basic Experiments for Understanding Microstructure Evolution Under Irradiation: TEM and KMC Characterisation of Irradiated Pure Iron	275
<i>F. Bergner, A. Al Mazouzi, M. Hernandez-Mayoral, A. Ulbricht</i> Combined TEM, PAS and SANS Investigation of Neutron-irradiated Pure Iron	283
<i>M.A. Pouchon, A. Froideval, C. Degueldre, D. Gavillet, W. Hoffelner</i> Synchrotron Light Techniques for the Investigation of Advanced Nuclear Reactor Structural Materials.....	291
<i>P. Van Uffelen, E. Kotomin, E. Heifets, D. Gryaznov</i> First-principles Modelling of Advanced Nuclear Fuels: Problems and Prospects	303
POSTER SESSIONS	313
<i>C. Cabet, F. Rouillard, B. Duprey</i> High Temperature Corrosion Properties of Alloy 230 in the Environment of Gas-cooled Reactors	317
<i>W. Hoffelner, M. Samaras, B. Bako, R. Iglesias</i> Materials Modelling – A Possible Design Tool for Advanced Nuclear Applications	327
<i>C. Jang, D. Lee, D. Kim</i> Characterisation of Oxidation and Oxide Layers of Nickel-base Superalloys at High Temperature	335
<i>W.J. Kim, K.H. Park, C.H. Jung, J.Y. Park</i> An Experimental Survey on Mechanical Property Characterisations of Ion-irradiated Silicon Carbides.....	345
<i>H. Steiner, C. Schroer, Z. Voß, O. Wedemeyer, J. Konys</i> New Aspects of Oxygen Control in LBE Systems	353
<i>L. Soler Crespo, F.J. Martín Muñoz, D. Gómez Briceño</i> Corrosion Behaviour of Stainless Steels in Lead-bismuth Eutectic and Lead Existing Experience and Needs.....	363
<i>T.Y. Song, C.H. Cho, C.H. Cho, E.H. Kim</i> The Lead and LBE Corrosion Research at KAERI	371
<i>M. Takahashi, Abu R. Khalid, T. Kumagai</i> Performance of Oxygen Sensor and Corrosion of Surface-coated Steels, Ceramics and Refractory Metals in High Temperature LBE	381

<i>J-B. Vogt, A. Verleene, I. Serre, F. Balbaud-Célérier, L. Martinelli, A. Terlain</i> Liquid Metal-assisted Fracture of the T91 Martensitic Steel.....	391
<i>O. Yeliseyeva, V. Tsisar, Ya. Matychak, V. Fedirko, T. Muroga, Z. Yao</i> Conception of Operation of <i>In Situ</i> Oxide Coatings Concerning Liquid Metal Cooling Systems	401
<i>V. Di Marcello, L. Luzzi</i> Modelling of Pellet Cladding Interaction During Power Ramps in PWR Rods by Means of TRANSURANUS Fuel Rod Analysis Code	417
<i>R.E.H. Clark, G. Mank, N. Dytlewski, D. Humbert, A. Malaquias, A. Mengoni, F. Mulhauser, A.L. Nichols, A. Stanculescu</i> Materials Demand for Fusion Power Plants: IAEA Projects, Initiatives and Databases.....	429
<i>C. Kato, T. Motooka, M. Numata, S. Endo, M. Yamamoto</i> Effect of Neptunium Ions on Corrosion of Ultra Low Carbon Type 304 Stainless Steel in Nitric Acid Solution	439
<i>V. Kršjak, M. Mikloš</i> Non-destructive Techniques Study of the Fe-Cr Based Alloys	449
<i>M. Lambrecht, A. Al Mazouzi</i> The Influence of Different Chemical Elements in the Hardening/ Embrittlement of RPV Steels.....	457
<i>G. Bonny, R.C. Pasianot, P. Olsson, L. Malerba</i> Interatomic Potentials Consistent with Thermodynamics.....	467
<i>H.H. Over, W. Dietz</i> The Web-enabled Database of JRC-EC, a Useful Tool for Managing European Gen IV Materials Data.....	475
Other contributions: Abstracts.....	485
List of participants	531

EXECUTIVE SUMMARY

Introduction

Structural materials research is a field of growing relevance in the nuclear sector, especially for the different innovative reactor systems being developed within the Generation IV International Forum (GIF), for critical and subcritical transmutation systems, and of interest to the Global Nuclear Energy Partnership (GNEP).

Indeed, the goals defined for the GIF innovative nuclear systems – sustainability and waste minimisation; enhanced economics; safety and reliability; and enhanced proliferation resistance – call for demanding material-related operating conditions, such as high in-service and off-normal temperatures, high fuel burn-ups, long service lifetimes (~60 years) and compatibility with different coolants. All these conditions imply new challenges with respect to current nuclear industry experience on structural materials.

A common feature in developing the different nuclear systems is the widely recognised need for experimental programmes to select and characterise innovative structural materials. These materials may, however, vary from one system to another. For example, in the case of very-high-temperature reactors (VHTRs), research is expected to be needed on nuclear graphite for the core and on nickel-based alloys and ceramics for intermediate heat exchangers and turbines. In the case of gas-cooled fast reactors (GFRs), silicon-carbon materials are being considered for fuel encapsulation.

It is in this context that the NEA Nuclear Science Committee (NSC) organised the Workshop on Structural Materials for Innovative Nuclear Systems (SMINS) in collaboration with the Forschungszentrum Karlsruhe in Germany. The objectives of the workshop were to exchange information on structural materials research issues and ongoing programmes for the different types of reactor concepts, as well as to foster the development of synergies. The workshop took place on 4-6 June 2007 at the Forschungszentrum Karlsruhe in Germany and was attended by approximately 100 participants with contributions from Europe, the United States, Japan, Korea and the Russian Federation. On the basis of the positive feedback received, the SMINS Scientific Advisory Committee proposed that the NSC envisage further initiatives on information exchange and development of potential synergies in the areas of both experimental assessment and advanced modelling of structural materials. It was suggested that the establishment of an NSC expert group and/or a working party could be an appropriate tool to help co-ordinate future activities in this field.

Programme

According to the objectives of SMINS, the programme was structured as follows:

- Overview from the European Commission and the IAEA;
- Session I: Keynote lectures;
- Session II: Gas-cooled systems;
- Session III: Liquid-metal-cooled systems;
- Session IV: Fusion, high-power accelerator targets and other fission reactor systems (LWR, SCWR, MSR);
- Session V: Fundamental research;
- Summary session.

Five keynote lectures were given by leading scientists on topics related to: 1) materials for Gen IV reactors; 2) LWR and life extension; 3) synergies between fission and fusion; 4) modelling and experimental validation; 5) available irradiation facilities.

In the following sections, the contributions presented and discussed at the workshop are shortly summarised in terms of highlights by class of materials for the different nuclear systems and in terms of the importance of fundamental material science.

Highlights by class of materials

For fast neutron systems, cooled with liquid metals as SFR, LFR and ADS, the presentations and discussion on structural materials for the reactor components can be summarised as follows:

- *Claddings*
 - Past and present research is focused on the status of advanced austenitic steels.
 - For higher burn-ups, there is a wide convergence on the interest of 9-12Cr F/M steels. However, due to the upper operational temperature limit of this class of steel, ODS alloys are envisaged as alternative promising candidate. It is recognised that ODS alloys need an important development programme, as shown by the Japanese programme.
- *Primary loop for loop-type reactor*
 - A significant reduction in piping and elbows can be achieved by using 9Cr F/M steel (e.g. mod. 9Cr-1Mo) according to studies performed within the Japanese sodium-cooled fast reactor (JSFR) demonstrator project. This reduction would improve the compactness and the economy of the reactor system. A 9Cr F/M steel qualification programme for this application was discussed as well.
- *Highlights on fabrication and joining*
 - The availability, industrial fabrication and cost of innovative materials, e.g. ODS.

- Development and qualification of innovative technologies for the fabrication of protective corrosion barriers through specific surface alloying processes (e.g. GESA).
- Qualification of welding and joining processes for, in particular, ODS and F/M steels.
- *Experimental facilities*
 - Need of facilities and appropriate experimental techniques in order to understand the structural materials behaviour in representative conditions for the different reactor systems.
 - Use of accelerators and MTR for separate effect investigation.

Moreover, the same classes of materials (e.g. austenitic steels, F/M steels and ODS alloys) were discussed as concerns their application in SCWR. The resistance of these materials to oxidation, stress corrosion cracking (SCC) and irradiation-assisted stress corrosion cracking (IASCC), were the main topics of discussion.

As far as the gas-cooled systems, driving activities on structural materials research are performed in the frame of the very high temperature reactor (V/HTR) concept. However, the experimental results obtained for these systems are also important for the development of the gas-cooled fast reactors (GFR). Important items highlighted during the workshop can be summarised by considering the materials for the different reactor components:

- *IHX and vessel*
 - The performance of the V/HTR concept is limited by the thermo-mechanical properties of the structural materials selected for the intermediate heat exchanger (IHX) and the reactor vessel. For the short-term development of V/HTR, Ni-based alloys are pre-selected as reference structural materials for the IHX. Mod. 9Cr-1Mo steel is under consideration for the “hot” vessel option. Both classes of materials need a specific qualification programme.
- For long-term development of V/HTR, new materials with enhanced thermo-mechanical performances need to be developed.
- *Core*

The graphite selection and qualification include the following items:

- Dimensional change behaviour and changes of physical/mechanical properties with irradiation.
- Compatibility with the coolant in terms of its impurity levels and graphite oxidation characteristics.
- Manufacturing costs.

The main topics concerning the qualification of carbon fibre composites (CFC) and SiC/SiC composites (relevant for fusion and core components of GFR) were indicated as follows:

- The irradiated SiC/SiC shows mechanical stability but degradation of thermal conductivity.
- The irradiation of CFC materials (e.g. for application in control rods), shows that swelling can occur and the impact on mechanical degradation is still unknown.

Increased role of material science

Numerous contributions on this topic did underline the importance of fundamental science, physical models development and validation in the area of structural materials. The discussion was characterised by the evaluation of problems already known and by tackling them with new tools, i.e. looking at old problems with new eyes. The main points discussed were:

- *Role of advanced modelling*
 - Predictive multi-scale modelling from *ab initio* calculations to component analysis has been strongly underlined.
 - Use of advanced modelling with a science-based approach to improve the performance of structural materials.
 - Numerical experiments based on a robust theory should be used when no experimental data are available.
 - Use of modern materials science techniques is valuable to uncover new phenomena (e.g. ultra-high-strength alloys).

Moreover:

- Large databases from past experimental programmes (e.g. EFR) should be made available and can be used for the development of modern theory supplemented with focused new data.
- Co-operation to investigate phenomena and develop improved structural materials should be encouraged among fusion and the various innovative fission reactor programmes.
- Ageing problems of existing LWRs and material problems for future reactor systems should positively influence each other.

OVERVIEW

Chair: W. Tromm

EURATOM RDDD IN INNOVATIVE REACTOR SYSTEMS AND FUEL CYCLES

Georges Van Goethem
European Commission

Abstract

In this introductory overview paper, the following questions are addressed:

- 1) What are the innovation challenges in energy technologies, in particular, in nuclear fission, that the European industry and research organisations are faced with? In the short (today), medium (2015) and long term (2040)?
- 2) What kind of response do the EURATOM research, development, demonstration and deployment (RDDD) programmes offer as solution to the above challenges? And what has been achieved so far, using the Community instruments?

The history of nuclear fission power production is usually divided in four technological Generations (called I, II, III and IV), with timescales extending from 1950 to around 2040. This paper focuses on the future Generations III and IV, and on the solutions they plan to offer to some socio-economic challenges raised by the new *Energy Policy for Europe*:

- Generation III (2015): competitiveness (e.g. increased plant performances, like 60 years lifetime), and enhanced security and safety (e.g. “practical elimination” of severe accidents)
- Generation IV (2040): enhanced sustainability (e.g. full actinide recycling) and enhanced competitiveness (e.g. cogeneration of heat and power for process heat, syn-fuels and hydrogen).

Fuel and structural materials research, both at national and at European level, brings very important contributions to the innovative designs of Generations III and IV. This paper discusses the international framework that has been set up to address the innovation process from basic research to market uptake (in particular, EUR for Generation III, and GIF and INPRO for Generation IV). The role of EURATOM in nuclear fission innovation and the European added value of participating in Framework Programme activities are demonstrated by some examples taken from EURATOM RDDD, focusing on the synergy between research, innovation and education.

Finally, the role of the stakeholders in the success of international nuclear RDDD is recalled, i.e.:

- the research organisations (public and private);
- the systems suppliers (e.g. nuclear vendors, engineering companies, etc.);
- the energy providers (e.g. electric utilities, heat and/or hydrogen vendors, etc.);
- the regulatory bodies and associated technical safety organisations (TSO);
- the education and training institutions, and, in particular, the universities;
- the international institutional framework (IAEA and OECD/NEA) and the civil society.

Introduction/a holistic approach for EURATOM RDDD related to Generations III and IV

In the general debate about innovation in energy technologies in the EU-27, there are two types of challenges:

- Scientific and technological (S/T) *challenges* related to *research* and technological *development*: the main instrument provided by the EU is the research Framework Programme (FP).
- Economic and political (E/P) *challenges* related to engineering *demonstration* and industrial *deployment*: the main instruments provided by the EU are economic and regulatory incentives.

To facilitate the industrial deployment of modern energy infrastructures in Europe, the stakeholders (in particular, the systems suppliers and the energy providers) are looking for their national governments, together with the EU, to play a triple role:

- *Initiator* of ambitious *research and development* programmes: e.g. to orient public funding to visionary research programmes (basic and applied) on well targeted issues with potential breakthroughs and to cosponsor large infrastructures to be shared for research and training.
- *Financial investor*: e.g. to support and facilitate investments for *demonstration and deployment*, especially during the transition period between two technological steps (in particular, when going from the current traditional economy to the future “*clean, clever and competitive*” economy).
- *Regulator* to ensure that the *citizens’ interests* are defended and that the *industrial competition* is fair (level playing field at international level): e.g. establish a common European framework for the mutual recognition of best practices for safety culture, risk governance, codes and standards.

Together with research, one of the priorities of the current EU policy is to “*put knowledge into practice*”. This is done, in particular, through Community instruments aiming at supporting each phase of the RDDD process. For example, in the Commission Communication “*Putting knowledge into practice: A broad-based innovation strategy for the EU*” of September 2006, the emphasis was put on the contribution of standardisation to innovation, which is important for the deployment phase. The Presidency Conclusions of the European Council of 8-9 March 2007 highlighted, amongst others, the role of standardisation in research and new fields of technology and the integration of standardisation aspects in EU and national R&D projects. A new “*Communication on Standardisation and Innovation*” is planned for October 2007. For the nuclear fission community, in particular, it is worth recalling that the *Pressure Equipment Directive (PED) (97/23/EC)* places responsibility for safety on the manufacturer and is applicable to all pressure equipment put into service within the European Union. Pressure equipment with a maximum allowable pressure greater than 0.5 bars, such as boilers, vessels, piping and valves which can be dangerous if established rules have not been met prior to installation are, in most cases, pertinent to this Directive.

The above RDDD related issues (innovation in energy technologies, role of governments and EU, putting knowledge into practice) are also discussed in the *Strategic Energy Technology Plan (SET Plan)*, that the Commission will draft by the end of the year, as a follow-up action on the Green Paper “*An Energy Policy for Europe*” (EPE) issued in January 2007 (see next section). The aim is to provide an objective perspective on the different energy technologies which will or might become available

between now and 2050 to tackle the “energy supply issue” while respecting the environment (CO₂ and GHG free) and being competitive. The prospects for market penetration of a series of low carbon technologies will be analysed, be it for electricity/heat conversion or for transport technology. As a result one would have a better picture what are the real chances of the different technologies and what is needed to support their development. Nuclear energy will naturally be part of the SET Plan [1].

Besides examples of innovation in nuclear fission and the relevant EURATOM actions, this paper shows:

- To what extent are all components of EURATOM RDDD integrated in one coherent approach? That is: the setting up of a European framework for the production, integration and dissemination, and exploitation of knowledge and technologies related to nuclear fission (RDDD or RD3 for short = *Research, technological Development, engineering Demonstration, and industrial Deployment*).
- To what extent do the results of EURATOM RDDD in innovative reactor systems and fuel cycles respond to the technology goals proposed for the Generation IV systems and for the partitioning and transmutation (P&T) technologies? That is: (1) *sustainability*, (2) *economics*, (3) *safety*, (4) *proliferation resistance* (that are naturally in line with the new *Energy Policy for Europe*).

As far as EURATOM actions in fission and fusion energy are concerned, Table 1 outlines the amounts (million EUR) for the research framework programmes under FP4 till FP7. Roughly speaking, the budget between nuclear energy research (fission and fusion) and non-nuclear energy research has been equally shared (50% each) in the EU over the past 20 years. The 7th EURATOM Framework Programme (FP7) for the period 2007 to 2011 has a budget of 2 751 M EUR.

Table 1. EURATOM research Framework Programmes for fusion and fission (FP4 to FP7)

	FP4 (1994-98)	FP5 (1998-02)	FP6 (2003-06)	FP7 (2007-11)
Fusion energy	840	788	750	1 947
Nuclear fission and radiation protection	170	191	190	287
JRC’s EURATOM activities	271	281	290	517
Total	1 281	1 260	1 230	2 751

Energy policy for Europe: The “energy triangle” (security, sustainability, competitiveness)

In March 2006, the EC published a *Green Paper on Energy: “A European Strategy for Sustainable, Competitive and Secure Energy”* COM(2006)105 [2]. The European energy strategy is based on a balance between:

- increasing security of supply;
- ensuring the competitiveness of EU energy industry so as to provide energy at the best possible prices for citizens and companies and stimulate investments;
- promoting environmental sustainability (with emphasis on the objective to limit the rise in global temperatures to 2°C).

In January 2007, as a follow-up of this Green Paper on Energy, the EC published the Energy Package [3], that is:

- the EC Communication *An Energy Policy for Europe* (EPE) together with;
- the action document *Towards a European Strategic Energy Technology Plan* (SET).

The response of the Council of the EU (Energy Ministers) to the Energy Package tabled by the Commission is summarised in the conclusions of the Spring European Council of 8-9 March 2007 (document 7224/07 “*Europe – Succeeding Together*”). This new European policy proposal contains clear commitments on GHG emissions (clean fossil energies), on energy efficiency, on renewable energies, on biofuels and on fissile (nuclear) energy. An Action Plan is proposed in Annex I of this Council document, containing agreed upon quantitative targets (three 20% and one 10% target by 2020, out of which two are binding and two are not binding). This will contribute to stabilise the long-term framework that investors need for the deployment of new technologies. In the energy market, in particular, the business environment should be as much as possible *objective, consistent and predictable*. An excerpt of this Council document is copied below (in italic): the selected text focuses on the preamble (Lisbon 2000 strategy) and on the statements related to the role of nuclear fission in the desired energy mix and on the support that EURATOM research could bring to this policy.

Europe – Succeeding Together/Brussels European Council (8-9 March 2007): Excerpts of the Presidency Conclusions (document 7224/07) [4]

Building on the significant progress in implementing the aims of the renewed Lisbon Strategy for Growth and Jobs to date and in order to face the most pressing challenges, the European Council calls on Member States and EU institutions to pursue actions to:

- *strengthen the internal market and competitiveness, create better framework conditions for innovation and greater investment in research and development, boost quality employment and improve social cohesion,*
- *enhance the better regulation agenda to create a more dynamic business environment,*
- *develop a sustainable integrated European climate and energy policy.*

***ANNEX I/EUROPEAN COUNCIL ACTION PLAN (2007-2009)
ENERGY POLICY FOR EUROPE (EPE)***

V. Energy Technologies

11. Recalling that the EPE will fully respect Member States' choice of energy mix, the European Council:

- *notes the Commission's assessment of the contribution of nuclear energy in meeting the growing concerns about safety of energy supply and CO₂ emissions reductions while ensuring that nuclear safety and security are paramount in the decision-making process;*
- *confirms that it is for each and every Member State to decide whether or not to rely on nuclear energy and stresses that this has to be done while further improving nuclear safety and the management of radioactive waste, and to that effect it:*
 - * *supports R&D on waste management, particularly under the 7th Framework Programme;*
 - * *can envisage the creation of a high-level group on nuclear safety and waste management;*
- *suggests that broad discussion takes place among all relevant stakeholders on the opportunities and risks of nuclear energy.*

International framework for fission innovation (EUR for GEN III, GIF and INPRO for GEN IV)

As far as the European integration of nuclear innovation efforts is concerned, it is worth recalling the role of the EUR association (created in 1991) that aims at setting up common “*European Utility Requirements*”. The EUR group includes 12 major utilities: British Energy (UK), Tractebel-Suez (BE), Electricité de France (FR), NRG (NL), IBERDROLA (ES), VGB PowerTech (DE), SOGIN (IT), Vattenfall (SE), TVO and FORTUM (FI), Swissnuclear (CH) and Rosenergoatom (RF). These electricity producers fixed the technical specifications for Generation III (horizon 2015) in a series of documents aiming at harmonising design targets for evolutionary LWRs. Following a rather prescriptive approach, a total of approximately 4 000 individual requirements are fixed in the EUR documents, that deal with all the topics a utility has to address to have a LWR developed and built [5]. A benchmark comparison has been made with the US equivalent association EPRI/URD.

For Generation III, the following technological goals were agreed upon as selection criteria:

- standardised designs to accelerate licensing, reduce capital cost and construction time;
- more robust designs, making the plants easier to operate and maintain (on-line or outage);
- use modern man-machine interfaces (digital I&C, ergonomic control rooms, CAD);
- higher availability and longer operating life – typically 60 years (plant performance);
- enhanced safety (in particular, reduced probability of severe accidents) and security;
- minimal effect on the environment.

Building upon Generation III but with a world-wide longer term perspective (2040), a High Level Policy Group met in January 2000 to launch the Generation IV International Forum (GIF). The Office of Advanced Nuclear Research at the DOE Office of Nuclear Energy, Science and Technology (ONEST) organised a task force [6] with the aim to select a number of innovative nuclear reactor technologies or *systems* for deployment between 2030 and 2040. The Generation IV Roadmap exercise started in March 2001. A total of six systems were selected in July 2002 (four fast – SFR, GFR, LFR, SCWR – and two thermal – VHTR, MSR, listed below), following the evaluation of more than 100 different nuclear energy concepts by more than 100 scientists and engineers from a dozen countries.

The GIF Charter was signed in July 2001. The GIF members are primarily nuclear research organisations and systems suppliers. They were originally a group of nine countries: Argentina, Brazil, Canada, France, Japan, South Africa, South Korea, the UK, and the USA. Switzerland signed in February 2002, and the European Atomic Energy Community (EURATOM) in July 2003. The Russian Federation and the People’s Republic of China signed the GIF charter in November 2006, bringing the number of members of the organisation to 13. The scientific secretariat of GIF is with OECD/NEA, Paris. The legal and administrative structure of GIF consists of:

- one Framework Agreement (signed by 5 members in February 2005, later on by CH and EU);
- six System Arrangements (SFR signed by a first group of GIF countries in February 2006 and SFR, VHTR, GFR and SCWR by another group in November 2006);
- several Project Agreements per system (SFR “Advanced Fuel” signed in January 2007 and VHTR “Materials” planned to be signed by the middle of this year).

Here is the list of the six Generation IV systems, with some indications about the expected performances and about the national composition of each System Arrangement:

- *Sodium-cooled fast reactors (SFR):*
 - mainly electricity production (with high efficiency, close to 40%); maybe cogeneration; actinide management/reference power = modules of 50 MWe or large plant of 1 500 MWe;
 - GIF steering committee leader = Japan and USA/members = EURATOM, France, Korea and UK.
- *Very high-temperature gas reactors (VHTR):*
 - mainly cogeneration; maybe only electricity production (with high efficiency, in the order of 40-45%); no actinide management – once-through cycle/reference power = 600 MWth/300 MWe;
 - GIF steering committee leader = Japan and France/members = EURATOM, Canada, Korea, South Africa, Switzerland, UK and USA.
- *Gas-cooled fast reactors (GFR):*
 - mainly electricity production (with high efficiency, higher than 45%); maybe cogeneration; actinide management/reference power = 300-1 500 MWe;
 - GIF steering committee leader = France and USA/members = EURATOM, Japan, South Africa, Switzerland and UK.
- *Supercritical water-cooled reactors (SCWR):*
 - mainly electricity production (with high efficiency, close to 45%); maybe cogeneration; actinide management in the fast version/reference power = 1 700 MWe;
 - GIF steering committee leader = Canada and USA/members = EURATOM, Japan and Korea;
- *Lead-cooled fast reactors (LFR):*
 - mainly electricity production (with high efficiency, close to 45%); maybe cogeneration; actinide management/reference power = small modules of 20 MWe and moderated-size system of 600 MWe;
 - GIF steering committee under discussion: members = EURATOM, USA and Japan.
- *Molten salt reactors (MSR):*
 - electricity production; maybe cogeneration; full actinide management/reference power = 1 000 MWe;
 - GIF steering committee under discussion: members = EURATOM, France and USA.

Another international initiative, complementary to GIF, was launched by the IAEA also in 2000: the “*INternational PROject on Innovative Nuclear Reactors and Fuel Cycles*” (INPRO). It was proposed by the President of the Millennium Summit and confirmed by the UN General Assembly of 2001 [7]. As of February 2007, INPRO has 28 members: Argentina, Brazil, Bulgaria, Canada, Chile, China, Czech Republic, France, Germany, India, Indonesia, Republic of South Korea, Netherlands, Pakistan, Russian Federation, South Africa, Spain, Switzerland, Turkey + European Commission (EURATOM) + Armenia, Morocco and Ukraine in 2004 + United States, Slovakia and Japan + Belarus and Kazakhstan. Taking account of the Agency’s unique mandate in the field of nuclear technology, safety and safeguards, the IAEA General Conference has invited all interested member

states to consider jointly innovative actions in nuclear reactors and fuel cycles that use economically competitive technology that is based on systems with inherent safety features and minimises the risk of proliferation and the impact on the environment (time horizon = 2050).

The IAEA brings together primarily governmental bodies in charge of nuclear energy policy. INPRO takes the long-term view that nuclear energy should be considered in the broader perspective of future energy needs, and addresses the problems from the point of view of potential users (especially in developing countries, for example, with small grids and/or desalination needs) by identifying their specific needs in INS (“*Innovative Nuclear Systems*”). INPRO does not address any specific technology. They produce comprehensive catalogues of basic principles for assessment methodologies in six areas (*economics, environment, safety, waste management, proliferation resistance and research infrastructures*). They also publish “*User Requirements*”, reflecting, in particular, the specific needs of developing countries interested in nuclear cogeneration.

GIF technology goals for innovative systems and roadmap for their deployment by 2040

Technology goals for industry and society were identified within the GIF in four areas (see Table 2 below). Sustainability goals focus on fuel utilisation and waste management. Safety and reliability goals focus on safe and reliable operation and investment protection – essentially eliminating the need for emergency response. Economics goals focus on competitive life cycle and energy production costs. Proliferation resistance and physical protection focus on safeguarding nuclear material and nuclear facilities.

In 2002, when the GIF members selected the six reactor systems, they also agreed upon individual roadmaps [8] consisting in three phases extending over a period of several decades, namely:

- The *viability* phase (basic concepts, technologies and processes are proven out under relevant conditions, with all potential show-stoppers identified and resolved – pre-conceptual design). Between 5 and 15 years needed.
- The *performance* phase (engineering scale processes, phenomena, and materials capabilities are verified and optimised under prototypical conditions – conceptual design). Between 5 and 10 years needed.
- The *demonstration* phase (preliminary design – in view of the commercialisation phase). Between 3 and 6 years needed.

It should be noted that only the above phases 1 and 2 are covered by the GIF collaboration agreements: the execution of the last *demonstration* phase will be left to the individual GIF members.

At the time being, the research activities, carried out by the GIF members for each of the above phases, aim at supporting the pre-conceptual design (*viability phase*). Later on, the GIF members will focus on the conceptual design (*performance phase*), following in fact the chronological sequence that is applied to most large scale industrial projects, that is:

- pre-conceptual design (*viability phase*);
- conceptual design (*performance phase*);
- preliminary design (*demonstration phase*);

- engineering design (*industrial phase*);
- reference design;
- final project.

The GIF members have agreed on the following milestones or “endpoints” in their roadmap for the *viability* and *performance* phases:

- *Viability phase:*
 1. pre-conceptual design of the entire system, with nominal interface requirements between subsystems and established pathways for disposal of all waste streams;
 2. basic fuel cycle and energy conversion (if applicable) process flow-sheets established through testing at appropriate scale;
 3. cost analysis based on pre-conceptual design;
 4. *simplified PRA for the system;*
 5. *definition of analytical tools;*
 6. *pre-conceptual design and analysis of safety features;*
 7. *simplified preliminary environmental impact statement for the system;*
 8. *preliminary safeguards and physical protection strategy;*
 9. *consultation(s) with regulatory agency on safety approach and framework issues.*
- *Performance phase:*
 1. conceptual design of the entire system, sufficient for procurement specifications for construction of a prototype or demonstration plant, and with validated acceptability of disposal of all waste streams;
 2. processes validated at scale sufficient for demonstration plant;
 3. detailed cost evaluation for the system;
 4. *PRA for the system;*
 5. *validation of analytical tools;*
 6. *demonstration of safety features through testing, analysis, or relevant experience;*
 7. *environmental impact statement for the system;*
 8. *safeguards and physical protection strategy for system, including cost estimate for extrinsic features;*
 9. *pre-application meeting(s) with regulatory agency.*

Safety considerations, implying, in particular, materials and fuel behaviour, are naturally important in all milestones of the above viability and performance phases, but particularly in the milestones n° 4 to 9 (*listed in italic*).

Research and development programmes to meet the GIF technology goals (sustainability, economics, safety and reliability, and proliferation resistance and physical protection)

For each of the above technology goals, a number of research activities are conducted by the GIF members in their national and international programmes (in particular, EURATOM) – see Table 2.

Table 2. Research challenges: translation of the four GIF goals and planning over three phases

GIF technological goals (2002)	Technological implementation	Industrial solution	Research challenges	Viability perform. demo.
Sustainability	<i>Promote effective fuel utilisation</i>	Fast neutron reactors (SFR, GFR, LFR)	Used fuel contains 97% of re-usable fuel	t.b.c.
	<i>Minimise and manage their nuclear waste</i>	Full (major and minor) actinide recycling (breeder versus burner)	MA fuel: e.g. oxide, metal, nitride, carbide, dispersion	t.b.c.
	<i>Reduce the long term maintenance burden in the future</i>	Optimal life cycle strategy (fuel and reactor): “clean waste”	➤ Single stratum (homogeneous) ➤ Double strata (heterogeneous)	t.b.c.
Economics	<i>Level of financial risk comparable to other energies (capital cost, kWe installed)</i>	➤ Constructability (O&M, ISI & R) (SCWR) ➤ Operating lifetime of 60 years	➤ Plant simplification ➤ Materials: e.g. FMS, 15/15Ti, T91 and ODS	t.b.c.
	<i>Life-cycle cost advantage (externalities, production of MWh)</i>	➤ Enhanced system performance ➤ Cogeneration of heat & power (VHTR)	➤ High T outlet ➤ Efficient coupling (high T process heat, syn-fuels, hydrogen)	t.b.c.
Safety and reliability	<i>Very low likelihood and degree of reactor core damage</i>	“Practical elimination” of some severe accident sequences (defense in depth DiD)	Robust “safety demonstration”: using active and passive systems	t.b.c.
	<i>Eliminate the need for offsite emergency response</i>	Prevention and mitigation measures	<i>Ad hoc</i> instrumentation and control (I&C)	t.b.c.
Proliferation resistance	<i>Unattractive route for diversion</i>	“Dirty fuel” and “clean waste” (MSR)	Homog. reprocessing (no separation of Pu)	t.b.c.
Physical protection	<i>Physical protection against acts of terrorism</i>	Set up security barriers, similar to safety in DiD	➤ Evaluation of PP and PR threats ➤ Integral design	t.b.c.

Demonstration and deployment policies related to innovation in energy technologies

In addition to the S/T instruments (such as the research Framework Programmes), the Commission proposes a number of E/P instruments to support all phases of the RDDD, such as:

- Economic: e.g. risk-sharing finance facility in FP7, fiscal incentives, *European Economic Interest Grouping* (EEIG), loans from the European Investment Bank [9], Regional Funds [10].
- Political: e.g. Barcelona 2002 target of “3% – 2/3” aiming at “*an increase of the overall R&D in the EU up to 3% of the GDP by 2010*” (up from 1.9% in 2000), that is: 2% should come private sector (up from 1.7 in 2000) + 1% from public sector.

- Legal: e.g. regulatory framework (Community legislation, proposed “Nuclear Package”), co-operation agreements with third countries, Joint Undertakings, *open method of co-ordination* (OMC), co-ordination of national programmes (ERA-net), IPR conventions, EU patent.
- Incentives for education and emulation amongst universities across Europe: e.g. training and mobility (e.g. Bologna 1999 mutual accreditation methodology, *European Credit Transfer System* – more than 1.2 million Erasmus students across 2 200 establishments in 31 countries as of 2004).

Of particular interest are also the “*private-public partnerships*” (PPP): this is a form of co-operation between the public authorities and economic operators. The primary aims of this type of co-operation are to fund, construct, renovate or operate an infrastructure or the provision of a service. PPPs are present in sectors such as public health, education, national security, waste management, and energy distribution (see *PPP Green Paper*, COM(2004) 327). In this way, Community policies contribute also to the demonstration and/or the deployment of new energy infrastructures, that is: the last two phases of the RDDD cycle (*research, development, demonstration, deployment*). The sharing of large “*Research Infrastructures*” [11] is also supported by an *ad hoc* Community instrument.

As far as innovation in nuclear fission is concerned, the organisation of the *European Fast Reactor* programme (EFR), which lasted from 1988 until 1995, can be considered as a kind of precursor of the above instruments (PPP and sharing of infrastructures). This was a collaboration between research/development institutions (public) and engineering/manufacturing organisations (private), aimed at satisfying the requirements of a clearly identified customer interested in operating an EFR (a group of European energy providers). A small-scale adaptation of this approach has been used in the organisation of the FP5 project PDS-XADS and in the follow-up FP6 project EUROTRANS [12]. This approach could be applied *mutatis mutandis* in the European research programme that supports the pre-conceptual and conceptual designs of Generation IV.

Examples of research and development related to the four GIF Technology Goals

At the time being, the international collaborative research in the GIF context aims at contributing to the pre-conceptual design (viability phase), focusing on the technological implementation of the four GIF Technology Goals (extension of Table 2). Therefore strategy studies are conducted in areas such as those mentioned below. Some laboratories, however, – in particular, those close to the industry – work already on the next phase, namely: the conceptual design (performance phase).

*** GIF Goal n° 1: Safety and reliability (GIF Methodology Working Group RSWG)**

- “Robust” safety architecture (set up principally by a deterministic approach):
 - mastering of the associated uncertainties and consideration of sufficient margins (support of PSA);
 - integration of all four GIF technological goals in the design (“built-in” features, not “added”);
 - numerical modelling: code scaling, applicability and uncertainties methods;
 - defence-in-depth strategy including the fourth level (CDA), internal and external events;
 - design of reactors with negative total reactivity coefficients (Doppler, temperature, void, etc.) for all accidental transient conditions (in particular, when coolant is lost from the core).

- “Robust” safety demonstration, in particular, regarding “dealt with” and “excluded” CDA initiators:
 - “dealt with” postulated single initiating events (design basis and extension conditions)
 - design and sizing of provisions to address their prevention and nevertheless management of their consequences: e.g. unprotected accidents ULOF, ULOHS, UTOP for FRs;
 - mitigation of hypothetical severe accident consequences (core melt progression, retention, air or coolant ingress): oxidation/thermo-hydraulics models;
 - passive decay heat removal if appropriate (as a step beyond the last defence against fuel melting): e.g. core catcher for mitigation of some core disruptive accidents (CDA);
 - provide sufficiently large grace period for implementing corrective actions;
 - passive and active safety system assessment (limited experience feedback makes it difficult).
 - “excluded” postulated single initiating events (physically impossible or to be “practically eliminated” by design): e.g. failure of the core support structure, excessive core compaction:
 - “practical elimination” of a limited number of events and phenomena which could lead to unacceptable core damage and/or uncontrolled large early releases of fission products;
 - demonstrate that sufficient provisions are foreseen to make these events practically impossible to happen (e.g. events where the consequences cannot be realistically managed);
 - the consequences of such extremely rare events will not be addressed by the design.

- Reactor design and plant management (primary and secondary circuit):
 - high requirements that go beyond the *European Utility Requirements* and the current engineering practices, aimed at achieving thermal, neutronic, mechanical and chemical equilibrium (EUR);
 - man – technology – organisation (MTO) interface, human factor;
 - in-service inspection (RPV integrity, surveillance programme, NDT);
 - radiological impact (radiation dose limits, ALARP principle/as low as reasonably practicable);
 - instrumentation and control (detection/protection systems, shutdown and decay heat removal);
 - impact on systems design (including balance of plant) under normal and abnormal situations.

- Integration in and dissemination through the GIF WG on *Risk and Safety* (RSWG). The objective is to “*assure an harmonised approach to long-term safety, risk, and regulatory issues in the development of next generation systems*”. Therefore an evaluation methodology is defined for safety goals, reliability of passive safety systems, approach to severe accidents and quality assurance standards. Technology neutral risk and safety criteria are investigated.

*** GIF Goal n° 2: Sustainability (Environmental impact – is Pu an asset or a waste?)**

- Full closure of the fuel cycle along one of the two following long-term routes:
 - *single stratum* (Generation IV scenario: infinite recycling of Pu and minor actinides in fast reactors): the actinides are not separated (homogeneous reprocessing), but returned as “dirty fuel” to the reactors where they are recycled, thereby generating a kind of “clean wastes”.
 - *double strata* (NPP and transmutation): the major actinides are recycled through MOX either in a PWR (Pu single recycling) or in a fast reactor (Pu infinite recycling), whereas the minor actinides (separation in heterogeneous reprocessing) are burnt in a subcritical/critical facility.
- Development of minor actinide (MA) bearing fuels: innovative fabrication technologies.
- Workers doses and in-site impact; population doses and off-site impact (release to biosphere, etc.).
- Plant decommissioning, for example immediate or deferred dismantling (safe enclosure for 30-100 years).

*** GIF Goal n° 3: Economics (Economical Impact GIF Methodology Working Group EMWG)**

- Constructability (less than 48 months), high burn-up (up to 150 GWd/tHM), life time of 60 years.
- Development of high-performance turbines for efficient generation of electricity, using high temperature Brayton cycles with He or supercritical CO₂ (e.g. VHTR and GFR).
- Digital systems (instrumentation and control); ISI, maintenance and repair.
- Economics (versus costing) of non-electricity energy products and modular plants.
- Nuclear fuel cycle model: fabrication procedures, (re)processing possibilities and limitations, waste, minor actinide recycling, infrastructures necessary for materials and fuel fabrication.
- Integration and dissemination in the GIF WG “*Economics Modelling*” (EMWG) [13].

*** GIF Goal n° 4: Proliferation Resistance and Physical Protection (GIF Group PR&PP)**

- Developing a closed fuel cycle, applicable also to weapons-grade plutonium:
 - higher concentrations of ²³⁸Pu (after long term n-irradiation) make Pu useless for weapons;
 - contamination of MAs increases fuel activity and makes Pu less attractive for weapons.
- Fabricating the fuel so that it is difficult to extract fissile material from spent fuel (but this may complicate material accounting in the international safeguards system).
- Evaluate PR threat elements (e.g. overt diversion or misuse, clandestine dedicated facilities).

- Evaluate PP threat elements (e.g. setting up “security” barriers, similar to safety in the DiD).
- Integration in and dissemination through the GIF WG “*Proliferation Resistance and Physical Protection*” (PR&PPWG) [14].

Examples of research and development specific to innovative materials, fuels and coolants

In parallel with the above mentioned strategic studies, the international collaborative research in the GIF context pursues their efforts in the investigation and development of innovative materials, fuels and coolants, as it is described in the next three sub-sections (extension of Table 2).

*** *Materials research in Generation IV systems: challenges for claddings, reactor vessel, internals (primary components), heat exchangers and balance of plant***

- Analysis: identify the system dependent key criteria for materials selection (in particular, to cope with the safety and reliability requirements and with the challenge of 60 years lifetime).
- Examples of innovative materials for fuel claddings and core internal components (control rod, wrapper, vessel, primary or secondary structures) in Generation IV, ADS and fusion systems:
 - 15Cr-15Ni austenitic stainless steel (15/15 Ti, French standard, Na-cooled LMFBR);
 - 9-12 Cr ferritic-martensitic steel (FMS, standard for LMFR), in particular, 9Cr1MoVNb ferritic-martensitic steel (T91, proposed for LFR and ITER) – use up to 600°C;
 - Oxide Dispersed Strengthened (ODS) ferritic or martensitic steels (proposed for SFR) and ODS Fe-Cr alloys (proposed for fusion) – use between 600 and 850°C;
 - Ceramics (e.g. silicon carbide SiC, proposed for high coolant temperatures, VHTR and GCFR).
- Research (including development of predictive numerical tools, validated against experiments:
 - elevated temperatures (up to 1 600°C for VHTR) compared to existing LWRs and elevated pressures (complex thermo-mechanical loading; oxidation and corrosion; creep and fatigue);
 - elevated irradiation (fast neutron fluence up to 200 *displacements per atom* /DPA/ for SFR; embrittlement; irradiation assisted cracking; void swelling);
 - coolant chemistry: interaction with environment (sodium; lead and lead-bismuth eutectics; high temperature gas) under elevated service parameters (environmentally-assisted corrosion).
- Materials characterisation during normal and off-normal conditions (PIE including NDT, etc.):
 - evolution of mechanical and thermo-mechanical properties (elasticity, plasticity, creep and damage models, thermal conductivity, cracking);
 - thermo-physical properties: embrittlement (irradiation and thermal aging); corrosion (waterside/gas side); environmental compatibility (chemistry).
- Materials qualification for design and manufacturing (nuclear standards, inspection requirements):
 - manufacture: fabrication (powder metallurgy for ODS steels);
 - joining/welding for ODS and FMS, special coatings for cor-/e-rosion protection against high T;

- qualification of fracture properties at manufacture (e.g. ASME/RCC-M);
- qualification of manufacturer may be required (e.g. for RPV);
- manufacturing costs (e.g. difficulties in supply).
- Integration and dissemination:
 - transfer of basic knowledge to designers (e.g. basic properties and constitutive equations for “design by analysis” methods) and to applied scientists (e.g. input data for predictive multi-scale multi-physics numerical tools as a support to scaling up from laboratory to reactor conditions);
 - education and training in innovative materials developed for Generation IV and ADS.

*** Fuels research in Generation IV systems: challenges for minor actinide bearing fuel (fast reactor systems) and for high operational temperatures**

- Analysis: identify the system dependent key criteria for fuel selection (in particular, to cope with the sustainability requirements/full closure of the fuel cycle).
- Examples of innovative fuels in Generation IV and transmutation systems: oxide, metal, nitride, carbide, dispersion fuel.
- Research (including development of predictive numerical tools, validated against experiments):
 - fuel performance/thermal, mechanical, chemical and thermodynamic challenges:
 - in-service performance: robust and refractory fuel with high level of fission products (fuel rod dimensional changes; high burn-up; fission product diffusion/krypton and xenon);
 - accident situations: reactivity insertion and loss of coolant accidents.
 - fuel fabrication (up to 5% of Am and/or Np in minor actinides /MA/bearing fuel):
 - pellet versus particle fuel (fuel microspheres for HTRs and inert matrices for actinide transmutation, also for specific LWR and FR systems);
 - co-precipitation for carbides, sol-gel process for MA bearing oxides and nitrides;
 - GFR specific fuel: (U-Pu)C/SiC or (U-Tru)N or (U-Pu)N/TiN for fissile compound with SiC or ZrC for matrix/cladding (FUTURIX concept);
 - SFR specific fuel: proposed fuel composition in the *Global Actinide Cycle International Demonstration (GACID)/Monju research under GIF* = $U_{0.674} Pu_{0.25} Np_{0.03} Am_{0.04} Cm_{0.006}$.
- Fuel characterisation during normal and off-normal conditions (PIE including NDT, etc.):
 - evolution of thermo-mechanical properties: elasticity, plasticity, creep and damage models, thermal conductivity, cracking;
 - evolution of thermo-dynamic properties: phase diagram of fuels containing Pu and MAs;
 - evolution of thermo-chemical properties (internal and external interactions of the fuel) and thermo-physical properties (thermal transport and microstructure evolution).
- Fuel and fuel/cladding system modelling:
 - evaluate the impact of various fuel types (fuel cladding mechanical interaction; fuel cladding chemical interaction; high burn-up potential; actinide recycling potential).

- Fuel cycle back-end (reprocessing or spent fuel):
 - characterisation of waste and scaling up of reprocessing techniques: homogeneous recycling of Pu and MA (no individual separation) or heterogeneous recycling (separation of Pu and MA);
 - optimisation of the waste form in terms of long term radiotoxicity and thermal load impact on the required volume for the geological repository.
- Fuel qualification for design and manufacturing (nuclear standards, inspection requirements).
- Integration and dissemination:
 - transfer of basic knowledge to designers (e.g. physical properties) and to applied scientists (e.g. input data for predictive numerical tools related to transport and microstructure, thermodynamic stability and chemical interactions, and thermo-mechanics behaviour);
 - education and training in innovative fuels developed for Generation IV and ADS.

Coolant research

- Analysis: identify the system dependent key criteria for coolant selection (in particular, to cope with the safety and reliability requirements).
- Research (including development of predictive numerical tools, validated against experiments):
 - water: e.g. in- or ex-vessel molten core retention strategies, hydrogen management;
 - gas: e.g. core melting exclusion strategies, operation at very high temperatures, fluences;
 - liquid metal: e.g. core melting management strategies (minimisation of risk from hypothetical core disruptive accidents, recriticality free concepts for sodium systems).
- Coolant characterisation during normal and off-normal conditions:
 - advanced coolants open the way to high temperatures, chemical inertness, optical transparency: no phase changes (e.g. very high boiling point), increased thermal capacity (important for the “grace period” for starting up the decay heat removal/DHR/ system), no cliff edge effects.
- Integration and dissemination:
 - transfer of basic knowledge to designers and applied scientists;
 - education and training in innovative coolants developed for Generation IV and ADS.

Examples of demonstration and deployment: challenges and roadmap for GIF demo projects

Here is a non-exhaustive list of the main challenges that the six GEN IV systems will face during their respective demonstration and deployment phases. Information is also given about the currently agreed upon roadmaps and about the relevant EURATOM research actions (FP6/2003-2006).

- *Sodium-cooled fast reactors* (SFR)/best case deployment year = 2020:
 - best experienced system in France, USA and Japan/GEN IV priority n° 1 in those countries;
 - power per unit of core volume > 200 MWth/m³/efficient management of U resources;
 - demonstration reactors (pool- or loop-type designs) = prototype of fourth-generation reactor of 250-600 MWe (announced by President Chirac – start-up of operations by 2020), Advanced Burner Reactor (ABR in the USA – deployment by 2022), Japanese Sodium Fast Reactor (JSFR), Chinese Experimental Fast Reactor (CEFR);

- EURATOM FP6 project = “EISO FAR”: Roadmap for a European Innovative Sodium Cooled Fast Reactor/Specific Support Action funded for 1 year with a total budget of 0.5 M including 0.25 M from EC, initiated in February 2007, co-ordinated by CEA Cadarache (research organisation);
- European roadmap: confirmation of key technologies and design options in 2012.
- Very high-temperature gas reactors (VHTR)/best case deployment year = 2020:
 - decay heat removed by conduction (no need for DHR/emergency core cooling system);
 - fuel can resist fast neutron fluences $> 10^{21}$ n/cm², with specific burn-ups reaching 200 GWd/ton of fuel (i.e. FIMA of 20%, about four times that of PWRs) and temperatures of 1 600°C in accident conditions;
 - power per unit of core volume = 5-10 MWth/m³/high degree of passive safety;
 - demonstration reactors for nuclear cogeneration = Next Generation Nuclear Plant (NGNP) planned in the USA by 2021 and European demo planned by 2015-2020;
 - EURATOM FP6 project = “RAPHAEL”: ReActor for Process heat, Hydrogen And ELectricity generation/Integrated Project funded for four years with a total budget of 20 M EUR including 9 M from EC, initiated in April 2005, co-ordinated by AREVA NP Paris/Erlangen (industry);
 - European roadmap: confirmation of design options (including cogeneration) in 2012.
- Gas-cooled fast reactors (GFR)/best case deployment year = 2020:
 - power per unit of core volume = 50-100 MWth/m³/efficient management of U resources/chemically inert and optically transparent coolant (but poor cooling capacity);
 - demonstration reactor (if selected as second type of FR system in Europe) = Experimental Technology Demonstration Reactor (ETDR in Europe, 50-100 MWth) – start-up by 2020;
 - EURATOM FP6 project = “GCFR”: Gas-cooled Fast Reactor/Specific Targeted Research Project funded for four years with a total budget of 3.6 M EUR including 2 M EUR from EC, initiated in March 2005, co-ordinated by AMEC-NNC Knutsford (industry);
 - European roadmap: confirmation of design options in 2012 (back-up solution after SFR).
- Supercritical water-cooled reactors (SCWR)/best case deployment year = 2025:
 - excellent economy (no steam generator, no recirculation pump, no steam separator)/existing technology in commercial supercritical-water-cooled fossil-fired power plants;
 - passive safety systems similar to the boiling water reactor SWR-1000 (Generation III);
 - EURATOM FP6 project = “HPLWR”: High Performance Light Water Reactor/Specific Targeted Research Project funded for 3.5 years with a total budget of 4.65 M including 2.5 M from EC, initiated in Sept. 2006, co-ordinated by FZK Karlsruhe (research organisation).
 - European roadmap: confirmation of design options (viability) in 2012.
- Lead-cooled fast reactors (LFR)/best case deployment year = 2020:
 - experience from Russian NIKIET development of the lead-cooled 300 MWe reactor BREST (Beloyarsk, with an on-site fuel cycle, completion of the project by 2020), passive DHR;
 - proliferation resistance due to core design and long refuelling intervals (up to 20 years);
 - demonstration reactor (if selected as second type of FR system in Europe) – start-up by 2020;
 - EURATOM FP6 project = “ELSY”: European *Lead-cooled/Specific Targeted Research Project* funded for three years with a total budget of 6.5 M including 2.95 M from EC, initiated in October 2006, co-ordinated by Ansaldo Nucleare Genova (industry);
 - European roadmap: confirmation of design options in 2012 (back-up solution, after SFR).

- Molten salt reactors (MSR)/best case deployment year = 2030:
 - non-conventional technology closely linked to P&T (quasi-continuous recycling of fuel in a *closed fuel cycle* with *continuous extraction of fission products*):
 - breeder in thermal/fast spectrum (thorium cycle possible), or burner for spent fuel recycling;
 - EURATOM FP6 project = “ALISIA”: *Assessment of liquid salts for innovative applications*/ Specific Support Action funded for one year with a total budget of 0.5 M including 0.25 M from EC, initiated in February 2007, co-ordinated by CEA Saclay (research organisation).

As far as the development of MA bearing fuels and the advanced recycling processes are concerned, it is worth mentioning the (very preliminary) planning proposed in Europe (2012-2017):

- a fuel manufacturing workshop;
- a micropilot for MA recycling (separation and MA bearing fuel manufacturing).

EURATOM training strategy: modular approach with common qualification, mutual recognition, mobility of students and teachers across the EU

Keeping the nuclear option open means also maintaining an adequate skills base to ensure sufficient personnel in research organisations as well as in nuclear installations. This is especially true when considering the development of the future Generations III and IV of fission reactors – not to mention fusion. This concern is naturally shared by all nuclear stakeholders and, in particular, by the international organisations (IAEA, OECD/NEA and EURATOM). Since 2000, EURATOM has decided to strengthen their efforts in nuclear education and training in all sectors of nuclear fission, that is: nuclear engineering and design, radioactive waste management and radiation protection.

For the sake of clarification, education and training (E&T) are defined as follows:

- Education is a basic or life-long learning process: education is broader than training and encompasses the need to maintain completeness and continuity of competences across generations (it is essentially a knowledge-driven process, involving academic institutions as suppliers, and students as customers).
- Training is learning a particular skill required to deliver a particular outcome: training is about schooling activities other than regular academic education schemes (it is essentially an application-driven process, involving industrial training organisations as suppliers, and professionals as customers).

In the specific area of EURATOM, the goal of the E&T programme is to offer to the EU nuclear community a number of instruments, enabling them to produce high-quality teaching modules that can be assembled into Euomaster programmes or higher level training packages that are jointly qualified and mutually recognised across the EU. The mutual recognition instruments are inspired by the EU programme in the field of higher education Socrates/Erasmus. The Erasmus Mundus programme is of particular interest [15]. This programme comprises, in particular, the *Erasmus Mundus Masters Courses*, that is: top-quality Masters Courses offered by a group of higher education institutions, leading to a master degree – selected Masters Courses must be attended by European graduate students as well as by a specific number of third-country graduate students and scholars.

In this context, EURATOM proposes a nuclear E&T strategy with the following objectives:

- MODULAR APPROACH AND COMMON QUALIFICATION CRITERIA
(with the aim to offer a coherent E&T framework with a wide variety of modules)
- ONE MUTUAL RECOGNITION SYSTEM ACROSS THE EUROPEAN UNION
(using the European Credit Transfer and accumulation System of Erasmus /ECTS/)
- FACILITATION OF MOBILITY FOR TEACHERS AND STUDENTS
(in particular, through support from “private-public partnerships” or “PPP”).

In order to achieve the above objectives, a non-profit making association (*under French law of 1901*) was formed in September 2003: this is the “*European Nuclear Education Network*” (ENEN), a spin-off of the homonymous FP5 project. The ENEN Association consists nowadays in 35 universities (effective members) and 6 research centres (associated members). Supported by FP5 and FP6, the ENEN Association established the delivery of the *European Master of Science in Nuclear Engineering* certificate (EMSNE). The ENEN association can be considered as a step towards the creation of *European Nuclear Education and Training Networks* that will ultimately harmonise governmental and industrial activities aimed at increasing the skills base in view of the possible “nuclear Renaissance”. More details about the ENEN Association and the modalities for members registration are provided in the website [16].

Besides a number of EURATOM FP6 projects devoted exclusively to education (academia), it is worth mentioning the training activities proposed as work packages in some of the large FP6 projects.

In the previously mentioned FP6 integrated project *EUROTRANS (EUROpean Research Programme for the TRANsmutation of High Level Nuclear Waste in an Accelerator Driven System/ADS*, co-ordinated by FZK), there are 17 universities, represented by the ENEN Association. A doctoral school on P&T is organised by the ENEN association under this project. The proposed training scheme is open to young students as well as professionals.

In the FP6 integrated project *PERFECT (Prediction of Irradiation Damage Effects on Reactor Components*, co-ordinated by EDF, <https://www.FP-6perfect.net/site/index.htm>), resources are also assigned for training. The simulation tools developed in this project will reduce the need for dedicated irradiation campaigns and address most of the irradiated material-related issues: (i) help design experimental programmes; (ii) explore conditions outside existing experimental databases; (iii) evaluate the individual or combined influence of material and service conditions that may exceed the capacity of any experimental programme; (iv) help understand the phenomena leading to degradations; (v) optimise the design and interpretation of irradiation surveillance programmes; (vi) verify the consistency of existing databases; (vii) predict long-term projections for NPP life management. It is foreseen that these benefits could extend, in time, from fission reactors to fusion reactors. The proposed numerical tools allow students and professionals to perform “virtual irradiations” on “virtual reactors”, with the aim to analyse the resulting evolution of mechanical properties and microstructure.

In the previously mentioned FP6 integrated project *RAPHAEL* (co-ordinated by AREVA NP, <http://www.raphael-project.org/index.html>), a number of major industrial issues are discussed in training courses related to future energy technologies and energy policies (e.g. high temperature heat and electricity supply, natural resource preservation). Special attention is paid to education in innovative nuclear hydrogen production technologies and in communication with the public at large.

Finally, “*EURATOM Fission Training Schemes*” of direct industrial interest are planned. It is well known that the nuclear industry (systems suppliers as well as energy providers) organises, usually at corporate (national) level, training activities related to CPD (Continuing Professional Development), in particular in the areas of human and organisational performances and safety regulations. In this context, an interesting initiative at European level was taken, as a follow up action after the workshop “*Towards European Nuclear Training Networks*” (ENTN/36 participants from industry and research organisations/AREVA TA Cadarache, 12-13 October 2006). Three industrial organisations (namely AREVA, Nexia Solutions, Empresarios Agrupados) agreed to produce a preliminary programme for a Eurocourse on “*Safety Culture*” under the ENEN umbrella, using the SAT approach proposed by the IAEA (“*Systematic Approach to Training*”). If successful, later on, other training activities of the same kind could touch upon the following subjects: basic nuclear training for newcomers; waste management (including geological disposal); decommissioning; ALARP wherever ionising radiations are used, design of Generation III, fuels and structural materials of Generation IV, depending on the needs expressed by the end-users (private and/or public). This new action – “*EURATOM Fission Training Schemes*” – was announced in the work programme 2007 [17] of EURATOM FP7.

Conclusion

Whatever the nuclear technological and political challenges are, the public needs to be assured that the *highest standards of safety, security and environmental protection* will continue to be applied. This is achieved a.o. through the *research, development, demonstration and deployment (RDDD) programmes of the EU*. This overview paper discusses some preliminary results of the EURATOM RDDD programmes in nuclear fission innovation. All EURATOM projects in this area are also reported in the proceedings of the FISA-2006 conference (Luxembourg, 13-16 March 2006, EUR 21231) [18].

It has been shown, in particular, that fuel and structural materials research, both at national and at European level, brings important contributions to the innovative future designs. The international framework was also presented (in particular, EUR for GEN III, and GIF and INPRO for GEN IV).

Moreover this paper illustrates the unique synergy between *research, innovation and education* actions in the EURATOM programme. It should be recalled, however, that the success of the Community RDDD actions depends not only on Framework Programme funding but also on the scientific co-operation and the financial involvement of all the stakeholders. In the particular area of nuclear fission, the stakeholders are:

- research organisations (public and private);
- systems suppliers (e.g. nuclear vendors, engineering companies, etc.);
- energy providers (e.g. electric utilities, heat and/or hydrogen vendors, etc.);
- regulatory bodies and associated technical safety organisations (TSO);
- education and training institutions, and, in particular, the universities;
- international institutional framework (IAEA and OECD/NEA) and the civil society.

Finally a number of strategic questions are left open, such as:

- To what extent will nuclear fission energy (Generations III and IV) significantly impact the new environmental, energy-security and competitiveness policies of the EU?
- What is the realistic timescale for the development of the innovative reactor systems and fuel cycles (roadmap for the viability, performance and demonstration phases)?
- What are the technology developments needed for the transition period (from GEN III to GEN IV) and what will then be needed for the full market uptake of GEN IV systems?
- What are the social and political issues that could slow technology implementation?

Some of these issues are dealt with in the new *Nuclear Fission Technology Platform* that takes advantage of the results obtained in the current FP6 strategy studies *Sustainable Nuclear Fission* (SNF-TP) and *Partitioning and Transmutation European Roadmap for Sustainable nuclear energy* (PATEROS). The aim of this new platform is to develop later on into a *Joint Technology Initiative*, that is: an ambitious industry driven private-public consortium, committed to carry out the long term actions of the agreed upon European Research Agenda in view of the Industrial Deployment.

REFERENCES

- [1] http://ec.europa.eu/energy/energy_policy/doc/19_strategic_energy_technolgy_plan_en.pdf
- [2] http://ec.europa.eu/comm/energy/green-paper-energy/index_en.htm
- [3] http://ec.europa.eu:8082/research/energy/index_en.htm
- [4] www.consilium.europa.eu/ueDocs/cms_Data/docs/pressData/en/ec/93135.pdf
- [5] <http://www.europeanutilityrequirements.org/>
- [6] <http://nuclear.energy.gov/genIV/neGenIV1.html>
- [7] http://www.iaea.org/worldatom/Programmes/Nuclear_Energy/NENP/NPTDS/Projects/inpro.html
- [8] <http://www.gen-4.org/Technology/roadmap.htm>
- [9] <http://www.eib.europa.eu/>
- [10] http://ec.europa.eu/regional_policy/funds/prord/sf_en.htm
- [11] http://cordis.europa.eu/infrastructures/survey2_introduction.htm

- [12] <http://nuklear-server.ka.fzk.de/eurotrans/>
- [13] www.gen-4.org/Technology/horizontal/EMWG_Guidelines.pdf
- [14] <http://nuclear.energy.gov/pdfFiles/PRPP.pdf>
- [15] http://ec.europa.eu/comm/education/programmes/mundus/index_en.html
- [16] www.enen-assoc.org.
- [17] http://cordis.europa.eu/fp7/dc/index.cfm?fuseaction=UserSite.EURATOMDetailsCallPage&call_id=9
- [18] http://cordis.europa.eu/FP-6-euratom/ev_fisa2006_proceedings_en.htm

SESSION I

Keynote Lectures

Chairs: W. Tromm, G. Van Goethem

INNOVATIVE REACTOR SYSTEMS AND REQUIREMENTS FOR STRUCTURAL MATERIALS

Frank Carré, Pascal Yvon, Pascal Chaix
Nuclear Energy Division, CEA Saclay
F-91191 Gif-sur-Yvette, France

Abstract

The fast growing energy demand requires nuclear energy to play a role among other energy sources to satisfy future energy needs of mankind. Generation III light water reactors (LWRs) are anticipated to be built in large numbers to replace existing nuclear power plants or to augment the nuclear production capacity. Beyond the commercialisation of best available light water reactor technologies, it is essential to start now the development of breakthrough technologies that will be needed to prepare the longer term future for nuclear power. These innovative systems include fast neutron reactors with a closed fuel cycle, high temperature reactors which could be used for process heat applications, accelerator driven systems or fusion reactors.

Key technologies for such nuclear systems encompass high temperature structural materials, fast neutron resistant fuels and core materials, advanced fuel recycle processes with co-management of actinides, possibly including minor actinides, and specific reactor and power conversion technologies (intermediate heat-exchanger, turbo-machinery, high temperature electrolytic or thermo-chemical water splitting processes...).

The paper will give a brief overview of various materials that are essential for above nuclear systems' feasibility and performance, such as ferritic/martensitic steels (9-12% Cr), nickel-based alloys (Haynes 230, Inconel 617...), oxide dispersion strengthened ferritic/martensitic steels, and ceramics.

The paper will also give an insight into the various natures of R&D needed on advanced materials, including fundamental research to investigate basic physical and chemical phenomena occurring in normal and accidental operating conditions, multi-scale modelling to predict macroscopic materials properties and to direct innovative research for improvements, lab-scale tests to characterise candidate materials mechanical properties and corrosion resistance, as well as component mock-up tests on technology loops to validate potential applications while accounting for mechanical design rules and manufacturing processes.

Finally, the paper will stress the benefit of prospects of multilateral collaboration to join skills and share efforts of R&D to achieve in the nuclear field breakthroughs on materials that have already been achieved over the past decades in other industry sectors (aeronautics, metallurgy, chemistry...).

Introduction

The fast growing energy demand driven by the increasing world population and the development of China and India, along with recognised assets of nuclear energy in terms of energy security and limitation of greenhouse gas emission have led to acknowledge the role that nuclear energy ought to play among other energy sources to satisfy future energy needs of mankind. Generation III light water reactors (LWRs), which materialise optimised versions of current nuclear generating facilities, are anticipated to develop actively in both the large populated countries mentioned above as well as to replace or augment existing nuclear power plants in already equipped countries. Beyond the commercialisation of best available light water reactor technologies, it is essential to start developing breakthrough technologies that will be needed to prepare the longer term future for nuclear power to represent a significant share of energy production in the second half of the 21st century and beyond:

- Fast neutron reactors with a closed fuel cycle which afford making an efficient use of uranium resource (more than 80% instead of 1% at most by light water reactors which essentially consume ²³⁵U) and minimising long-lived radioactive waste, thus making nuclear energy more sustainable.
- High temperature reactors that may drive more efficient processes to generate other energy products than electricity such as hydrogen, synthetic hydrocarbon fuels from coal or biomass, or process heat for the industry, thus contributing to enlarge the range of applications of nuclear energy.
- Accelerator-driven systems (ADS) which may contribute to transmute minor actinides in dedicated systems, in addition to transmutation that could be achieved through advanced recycling modes in fast reactor systems.
- Fusion reactors, which use elements abundant in nature, lithium and deuterium as fuel, and do not produce long lived radioactive waste.

Several initiatives today such as the Generation IV International Forum [1] and the IAEA International Project on Innovative Nuclear Reactor (INPRO) aim at revisiting the technologies that led to early prototypes of fast neutron and high temperature reactors, and to search for innovations that could make them progress significantly in competitiveness, safety and operability so as to prepare the development of attractive commercial nuclear systems. Fast reactors are expected to be needed around 2040 if, as anticipated today, the installed capacity of LWRs reaches 1 300-1 500 GWe by 2050, and uranium prices escalate because most of the estimated resource below 130 \$/kg (i.e. ~15 Mtonnes) is pre-empted by fuelling needs of these reactors over a 60-year lifetime. Moreover, if their technical maturity and competitiveness arise earlier, fast neutron reactors could support the industrial implementation around 2030 of the Global Nuclear Energy Partnership's strategy that is proposed by the US-DOE to safely develop nuclear power worldwide with an adequate control of proliferation risks. This strategy is based on a practice of nuclear fuel leasing and take-back services assured by "fuel cycle states" that would operate such fast neutron reactors to recycle nuclear materials recovered from retrieved LWR spent fuel. For either of both above applications, fast neutron reactors are being revisited along basically three tracks: innovative sodium-cooled fast reactors (SFRs) that are likely to lead to prototypes around 2020-25 and be ready for industrial deployment by 2040 or earlier, and alternative technologies, gas- or lead-alloy-cooled fast reactors (GFRs and LFRs), that call for experimental technology demonstrators around 2020 prior to considering prototypes around 2030-35, and industrial deployment after 2050. Besides, high temperature reactor (V/HTR) energy products

might become marketable as early as 2025, especially to oil and refinery companies that need high temperature process heat and hydrogen already today and possibly synthetic hydrocarbon fuels from coal or biomass to complement fuels from fossil origin.

Key technologies for such innovative nuclear systems encompass high temperature structural materials, fast neutron resistant fuels and core materials, advanced fuel recycle processes with co-management of actinides, possibly including minor actinides, and specific reactor and power conversion technologies (intermediate heat-exchanger, turbo-machinery, high temperature electrolytic or thermo-chemical water splitting processes...).

Materials requirements for the innovative reactor systems

The main requirements for the materials to be used in these reactor systems are the following:

- The in-core materials need to exhibit dimensional stability under irradiation, whether under stress (irradiation creep or relaxation) or under no stress (swelling, growth).
- The mechanical properties of all structural materials (tensile strength, ductility, creep resistance, fracture toughness, resilience) have to remain acceptable after ageing.
- The materials have to retain their properties in corrosive environments (reactor coolant or process fluid).

Other criteria for the materials are their cost to fabricate and to assemble, and their composition could be optimised in order for instance to present low-activation (or rapid desactivation) features which facilitate maintenance and disposal. These requirements have to be met under normal operating conditions, as well as in incidental and accidental conditions. These demands are similar in their nature to those required for the current operating commercial reactors, but are actually much more demanding, due to the specifications of the innovative systems. The general characteristics of these systems are summarised in Table 1 along with some of the candidate materials. It can be noted that, when the operating temperature of commercial light water reactors does not exceed 350°C, the levels of temperature required here are much higher, which represents a major challenge. Another tough challenge is the high irradiation doses sustained by the in-core materials. Also, it can be difficult to find materials compatible with some of the coolant or process fluids considered. The combination of high temperature, high neutron dose and environment could prove to be a major obstacle for the viability of some of the systems. Finally, the toughest demand is the lifetime expectancy, which is 60 years, where the maximum design life of reactor materials is more in the range of 30 years [2].

To meet these specifications, existing commercial or near commercial materials have to be assessed and qualified. They may require optimisation and in some instances new materials have to be developed. This means extensive experimental programmes have to be carried out in order to characterise the ageing capacity, the corrosion resistance and the mechanical behaviour before and after irradiation of base materials as well as welds. The behaviour under irradiation of a wide range of structural materials such as graphite (VHTR and MSR), austenitic and ferritic steels (VHTR, SFR, GFR, LFR), Ni-based alloys (SCWR), ceramics (GFR) has to be assessed... Experimental irradiations have to be carried out in order to study microstructural and dimensional evolution, but also the behaviour under stress. Corrosion tests have also to be performed in representative environments. These characterisation programmes are lengthy and costly. A good basic understanding of the mechanisms controlling material performance will allow an optimisation of these tests, with the extraction of maximum information. Furthermore it is of high interest to look for commonalities in

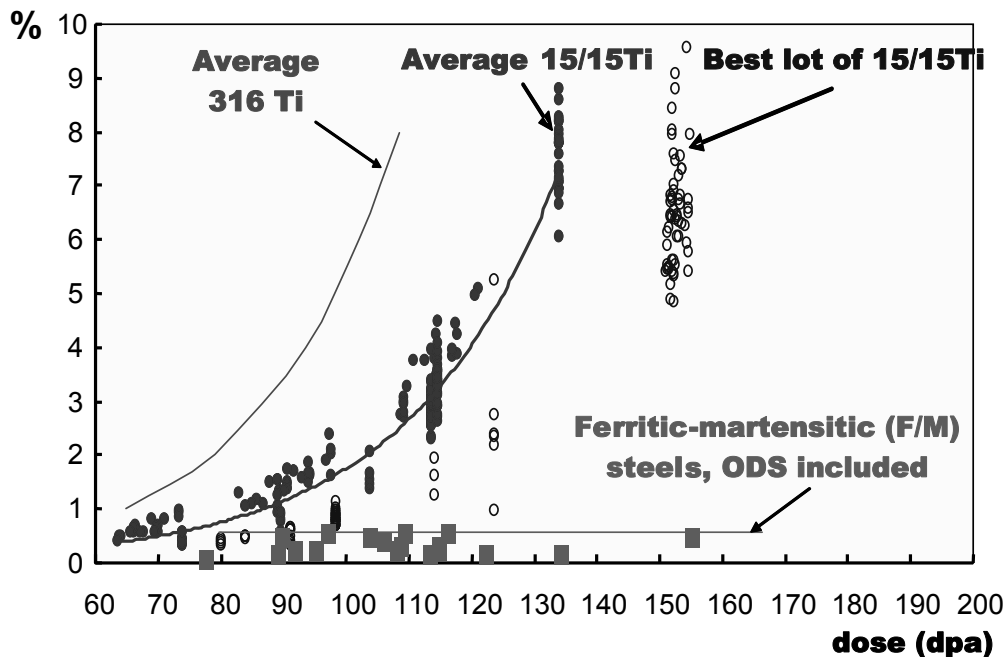
service conditions for different systems. For instance, LFR materials have benefited from research done in the frame of ADS programmes and fusion materials (F/M steels, ODS, SiC/SiC) are also widely considered for Generation IV systems.

In the following section, several promising candidate materials will be described in more detail with an emphasis on the benefits of crosscutting research programmes. Also, the need to develop predictive modelling tools will be addressed.

Candidate materials for innovative reactor systems

Ferritic/martensitic steels (9-12% Cr) are promising candidate materials for sodium or lead-cooled reactors with a high temperature (<600°C) and compact primary system, as well as for the pressure vessel of high temperature gas-cooled reactors. They are also considered for core structure materials of fusion reactors. First, there is a strong push to reach high burn ups to optimise the use of resources and to minimise the waste, and the swelling of alloys currently used for fuel cladding in fast neutron reactors limits the burn-up, because of geometrical constraints and also the loss of mechanical strength. This limitation could be overcome with improved materials such as ferritic/martensitic steels which exhibit a much lower swelling as shown in Figure 1. This also shows the need to be thorough in the material characterisation, since no problem seems to exist until the dose reaches ~70 dpa – at that dose, a swelling mechanism gets triggered for some grades of austenitic alloys. Also, implementing low swelling materials may allow reducing coolant channels thickness, which is one of the paths to cope with coolant void reactivity coefficient, a major safety issue.

Figure 1. Hoop deformation of different grades of austenitic Phénix claddings and ferrito-martensitic materials versus dose



Structural reactor materials and fuel cladding materials have to be identified to withstand the combined effects of high temperatures, harsh irradiation conditions and the rather corrosive/erosive operating conditions of lead or lead alloys coolant. A careful selection of steels meeting these

conditions from the present nuclear materials database is required. Austenitic steels like AISI 316L that are used in water cooled reactors are not only susceptible to irradiation induced swelling and creep, but also show limited corrosion resistance in Pb-alloys at high temperature. Ferritic-martensitic steels have better corrosion behaviour in liquid Pb-alloys than austenitic steels. They also present a better behaviour under irradiation and thus appear to be candidate materials for fuel cladding and structures in high flux zones.

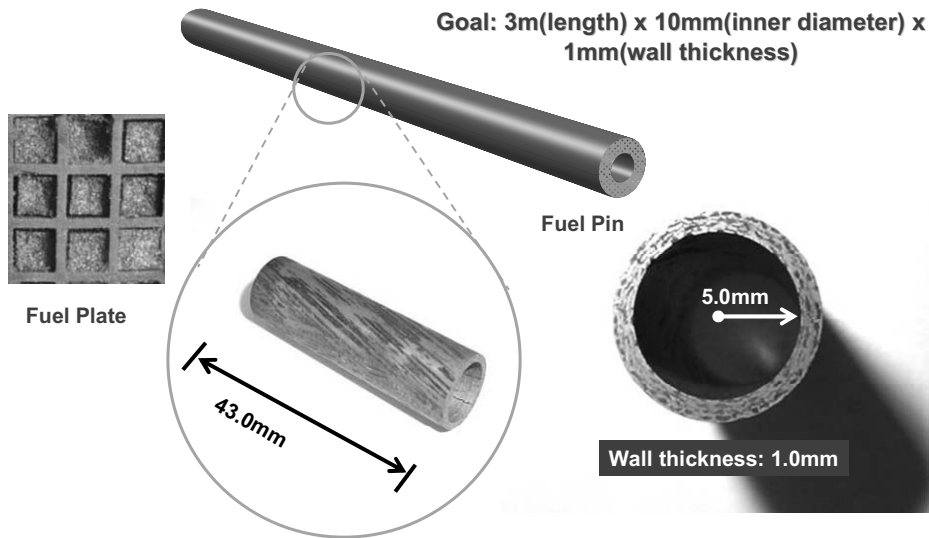
The 9% Cr martensitic steels with their low activation (LA) variants for fusion are foreseen for operating temperatures up to 550°C. A large set of data issued from the various fast neutron reactor programmes exist for the classical 9-12% Cr martensitic steels for doses ~100 dpa in the range 400-550°C. The resistance to swelling is excellent due to the bcc crystalline structure and the high density of sinks of the martensitic microstructure. The hardening and embrittlement are negligible when irradiation occurs in the range 400 to 550°C. Finally, these alloys exhibit better mechanical properties, lower thermal dilation and are cheaper than alloys used previously in the intermediary circuit of sodium-cooled fast reactors, which would help design a much more compact circuit and make the system more competitive economically.

Oxide dispersion strengthened (ODS) ferritic/martensitic steels are promising candidates as cladding materials for high burn-up fast neutron reactor fuels. Figure 1 shows the benefits of a ferritic/martensitic matrix with respect to swelling problems. The nanoscale dispersion of yttrium oxide precipitates will give these alloys a good creep resistance at high temperatures. The ODS grades currently developed in the frame of the SFR or fusion contain 9 to 12% Cr. However, these alloys could show some limitations in terms of internal corrosion (oxide clad reaction) and temperature (phase transition around 800°C). Therefore, ferritic steels with ~14% Cr and more could be used up to 900°C. Although irradiation data are scarce, the bcc crystalline structure should present an excellent resistance to swelling. The main in-service issues, in the low temperature range, remain the effect of the α/α' unmixing on the mechanical properties and, in the high operating temperature domain, the required stability of the oxide dispersion to maintain the improved creep resistance of this type of material and the absence of heavy intermetallic phase precipitation that could degrade the toughness of the cladding. Preliminary results under mixed and fast neutron spectrum show that α/α' demixing should allow this type of materials to keep reasonable ductility and fracture toughness. The under irradiation stability of the oxide dispersion is an open issue to be settled. The action of the oxide dispersion on the in-reactor creep, where climb phenomena are predominant, remains to be understood. Other types of strengthening precipitates may also be considered (e.g. carbides and nitrides).

Ceramic materials are needed for very high temperature components (> 1 000°C) such as heat exchangers and thermal insulations in the primary system, as well as core components such as control rod sheath (V/HTR and GFR) and fuel constituents (GFR as shown in Figure 2). A major effort of research is being invested in developing less brittle ceramics forms such as composite ceramics, or nano-structured plastic ceramics. SiC ceramics, that have been extensively investigated for fusion applications, are the major focus of R&D today but other carbides (TiC, ZrC) or nitride (TiN, ZrN...) are also currently considered in screening tests. Ceramics are also needed for parts of power conversion systems such as very high temperature gas turbine blades or intermediate heat exchangers to decompose sulphuric acid (> 850°C) as high temperature step of several thermo-chemical water splitting processes (iodine-sulphur, Westinghouse hybrid...).

C/C composites are planned to be used for control rod cladding (start-up/shutdown control rods and operating control rods) and core support plates because of their high specific resistance and their good mechanical behaviour at temperatures above 1 100°C. Unfortunately these materials are sensitive to oxidation at such temperatures and their behaviour under irradiation is badly known that is

Figure 2. 2-D SiC/SiC fuel pin or fuel plate for GFR



particularly critical for operating control rods. Some industrial solutions exist to improve the oxidation resistance (protective coating, SiC final or full impregnation, self-healing matrix, SiC/SiC) but irradiation behaviour might be a real problem (risk of swelling, drop of thermal conductivity and mechanical properties, damage, failure).

The fibre architecture is generally specific of the component in order the fibres to bear the thermal-mechanical loading, and the grades used for fusion might not fit VHTR applications. Indeed, the fibre nature, the fibre architecture (2-D, 3-D...), the matrix nature, the heat treatment and the geometry of the components have to be adjusted to meet the specific requirements of control rods. At last, composite materials are inhomogeneous and most of the time anisotropic. Moreover, there is a wide dispersion during mechanical characterisation, which necessitates a large quantity of tests to qualify a composite material. Acceptable values of fracture toughness $\sim 25 \text{ MPa}\cdot\text{m}^{1/2}$ are obtained via tailored inter-phase between the fibres and the matrix. The tensile property and dimension stability of this type of composite, cubic and stoichiometric, has been proven satisfactory only up to moderate doses around 10 dpa under mixed neutron spectrum. The main issues are: (i) long-term stability of dimension and physical properties; (ii) irradiation detrimental effect on the inter-phase and its capability of deviating cracks and thus providing reasonable fracture toughness; (iii) required higher creep strength of the fibre to bear the thermal-mechanical loading in long-term service under high temperature and neutron flux; (iv) type of mechanical damage under irradiation and creep. The behaviour of these materials under coupled irradiation and mechanical stress needs to be assessed. This is a major challenge for fuel development where containment high performance and evolution under irradiation have to be demonstrated.

This rapid survey is pointing out that there is a real need for irradiation data (on composite materials and on fibres themselves) for better dimensioning the composite materials. The oxidation behaviour has to be evaluated too to ensure the integrity of the control rods in case of accidental air ingress. These two points appear to be the most important ones. Data on thermo-mechanical properties are also needed on each grade selected to feed data bases. Testing components as representative as possible of the final structure is necessary too. Indeed, results obtained on flat samples might be different from results obtained on tubes. The problem of tested sample representativity will be of real importance for irradiation experiments where the size and the number of samples are limited. At last, modelling of the composite behaviour will be essential for assessing components lifetime.

Nickel-based alloys (Haynes 230, Inconel 617...) are promising candidate materials for high temperature gas-cooled primary system components such as the intermediate heat exchanger, and oxide dispersion strengthened grades are considered to match requirements for higher temperature service conditions (intermediate heat exchanger, gas turbine blades...).

New concepts of nuclear reactors, based on gas coolant systems at very high temperature (VHTR) with a gas turbine are theoretically able to deliver higher efficiency than conventional steam cycle, by means of using very high efficiency components, as helium/helium recuperator heat exchangers or helium/gas mixture intermediate heat exchangers. These components should work under very harsh conditions (very high temperature, 800-1 000°C; and high pressure, 50-80 bars). According to a recent investigation, no proven industrial technology could be directly used. The main topic of these heat exchangers concerns the use of nickel-base high temperature materials and more precisely the coupling between ideal geometries coming from the optimised design, and the ability of the material to be formed and assembled according to this requirement.

The most critical components of the turbomachinery in a VHTR direct cycle are the first stages of the turbine disks. In order to achieve a high efficiency, it is recommended to limit the cooling of the turbine. For the blades, materials such as directionally solidified superalloys or single crystals should meet the specifications. The only investigations launched so far are related to corrosion. For the disk, no commercial materials satisfy the specifications of this gas turbine (maintenance intervals of 60 000 h unusual impure helium environment, maximum temperature of the disk expected between 700 to 750°C, disk size of 1.5 m). Among the materials issued from the aircraft and the land-based gas turbine industries, the Ni-based superalloy Udimet 720 constitutes the best candidate. This alloy is elaborated either through a cast and wrought (C&W) process route either through a powder metallurgy one. For the latter, the powder is first consolidated in a Hot Isostatic Pressure (HIP) facility, optionally followed by a forging operation. The C&W process leads to a high creep resistant grade, but the maximum size of a forged disk ever manufactured is less than 1 meter. The developments required to manufacture larger disk have to be investigated. The HIP process allows for manufacturing of large disk but usually leads to intermediate creep resistance due to the small grain size generated by this process.

The material for the primary circuit must exhibit very good thermal stability for long operating time, moderate creep strength, well established metal working and welding techniques. The candidates will thus be selected within the class of Ni-base solid solution strengthened superalloys. During the past, exhaustive work has been performed on Inconel 617 which was the candidate material of the German team and on Hastelloy XR (it is an adapted grade of Hastelloy X for VHTR application) which was the chosen material for the Japanese team. Many results have been reported in the literature on both materials. Inconel 617 exhibits the best creep properties, but suffers from a quite poor corrosion resistance (non-protective oxide film leading to internal oxidation and decarburisation). Moreover its high Co content may give rise to potential radioactive contamination problem. Hastelloy XR exhibits very good stability in VHTR environment, but is not so good in terms of creep resistance. CEA has selected alloy 230 as a very promising candidate material for this application. Indeed, this material has been developed to withstand aggressive environment, and should exhibit good creep properties. Experimental programmes have been launched to qualify alloy 230 for this specific application. It includes long-term thermal exposure treatments, mechanical characterisation (tensile, impact toughness, creep under air and vacuum) and corrosion studies (static exposure tests and creep tests under impure atmosphere). Both the bulk material and relevant welds are investigated.

The evolution of the microstructure under thermal ageing is accurately investigated in order to be able to predict the behaviour of the material under very long service period. The first results obtained at 850°C have revealed the formation of carbides either close to the grain boundaries (with a typical lamellar structure) either close to the former coarse W-rich carbides. This change in the microstructure

leads to a limited drop of the mechanical properties of the material. It seems that after 1 000 h at 850°C the material has reached a stable structure. Similar investigations at 950°C are underway. First results of the creep tests under air and vacuum have indicated a creep resistance similar to that of Inconel 617.

Different ageing treatments have been characterised to highlight the influence of the microstructure on the creep resistance of the material. Indeed, it has been established that at high stresses, the intra-granular microstructure (i.e. the γ' populations) is responsible for the creep strength whereas at low stress and high temperature, the grain size is the controlling factor. It is thus recommended to coarsen the grain size to increase the creep resistance. However, during super-solvus ageing treatment, the grain boundaries are pinned by the small precipitates decorating the prior particles such that the austenitic grain size is limited to the powder granulometry. To overcome this limitation, coarser grain size material ($\sim 100 \mu\text{m}$), for which the austenitic grain is larger than the former powder particles, can be developed.

Modelling

As mentioned above, the selection, assessment and validation of materials necessitate a large number of experiments, involving rare and expensive facilities such as research reactors, hot laboratories or corrosion loops. The modelling and the codification of the behaviour of materials will always involve the use of such technological experiments, but it is of utmost importance to develop a predictive material science: in most cases the experimental database does not cover the whole range of conditions needed (temperature, time, neutron spectrum) and it is essential to develop robust physical models in order to extrapolate with confidence outside the experimentally known domain. Furthermore, modelling and simulation can give access to basic information hardly obtainable by global experiments; standard irradiation tests with their post-irradiation examinations, e.g. on the dynamics of impurities and defects under irradiation. This understanding of the mechanisms underlying the material behaviour is critical to identify and control the most relevant parameters (for instance very little is known on the actual structure of oxide nano-clusters in ODS steels, their coherence with the iron matrix, the mechanisms responsible for their impact on the overall potential behaviour in service conditions). This will also prove a powerful tool to optimise existing materials or develop new materials.

Modelling must make the best use of the continuously increasing computing capabilities, but must also be supported by dedicated experiments. Our understanding of radiation damage at the atomic scale now allows simulating radiation induced microstructures and dislocation dynamics in volumes that are of the same order of magnitude as those that can be irradiated (with ion beams of a few MeV), characterised physically and chemically (by transition electron microscopy, X-rays, atom probes, ion beam analysis...), and characterised mechanically (nano-indentation, TEM testing...). For example, coupling multi-ion beams irradiation with modern characterisation like in the JANNUS facility currently under development by CEA and CNRS, will provide a unique way to validate the atomic scale modelling and build predictive tools for radiation effects up to high dose and content of transmutation products. These experimental and theoretical tools will be the basis for developing materials more resistant to radiation effects, designing optimised test programmes in dedicated neutron sources (material testing reactors, IFMIF), extrapolating their results to the wider range of in-service conditions of the innovative reactor systems (both GenIV and fusion), and finally giving higher confidence in the data involved in the licensing processes.

The physical modelling based on the theory and computation of atomic cohesive forces that control thermodynamics, kinetics and mechanics has already been undertaken for LWR structural materials for instance in the frame of the integrated project PERFECT of the 6th Framework

Programme of the EU, and it is important to capitalise on such experience. There is a certain maturity of the modelling in the field of thermodynamics and kinetics in metals and alloys, and it is possible for instance to predict with some confidence the evolution of microstructure under irradiation. This level of physical robustness has now to be extended to mechanical modelling by coupling microstructure and mechanics (plasticity – creep – fracture), and to other materials (such as nano-structured alloys, ceramics and composite materials).

Conclusions

The development of innovative nuclear systems requires extensive research to find, qualify and codify materials able to withstand the extreme demands in terms of temperature, high neutron flux, corrosive environment and lifetime expectancy. In most cases, the viability of these concepts relies on the capacity of obtaining such materials.

The development and implementation of advanced metallic alloys and ceramic composites will need breakthroughs in material science, from process development (material fabrication, assembling...) to performance assessment (behaviour under coupled temperature, mechanical stress and irradiation). These challenges require comprehensive tests and in-depth investigations of structural materials

The extensive characterisation of candidate materials will require a joint effort from the international community, and these efforts have to be mutualised between the different systems as synergies have already proven to be helpful. Finally, beside the experimental testing, a strong emphasis should be placed on developing a predictive material science and robust modelling, based on the physics of materials at the atomic and grain scale.

REFERENCES

- [1] <http://geniv.ne.doe.gov>
- [2] Corwin, W.R., *Nucl. Eng. Technol.*, 38, 591 (2006).

Table 1. Main characteristics of innovative nuclear systems to direct materials selection

	Sodium fast reactor	Gas fast reactor	Lead fast reactor & ADS	High temperature reactor	Supercritical water reactor	Molten salt reactor	Fusion	
Coolant	Liquid Na few bars	He, 70 bars 480-850°C	Lead alloys 550-800°C	He, 70 bars 600-1 000°C	Water	Molten salt	He, 80 bars 300-480°C	Pb-17Li, ~ bar 480-700°C
Core structures	Wrapper: martensitic steels; clad. tubes: ODS	SiCf-SiC composite	Target structure: martensitic steels; window & clad: martensitic, ODS	Graphite (structures), composites C/C, SiC/SiC for control rods	Ni-based alloys F/M steels	Graphite	Martensitic steels ODS ferritic steel SiCf-SiC therm. & elect. insulator	
Temperature	390-700°C	600-1 200°C	350-480°C	600-1 600°C	350-620°C	700-800°C	FW: Tmax: 625°C → ODS Channel: Tmax: 500°C (SiC)	
Dose	Cladding: 200 dpa	60/90 dpa	Clad: ~100 dpa ADS/target: ~100 dpa + He	7/25 dpa			~ 100 dpa + He (10 appm/dpa) and H (45 appm/dpa)	
Other components		IHX or turbine: Ni-based alloys		IHX or turbine: Ni-based alloys				

AGEING MANAGEMENT AND KNOWLEDGE BASE FOR SAFE LONG-TERM OPERATION OF JAPANESE LIGHT WATER REACTORS

Naoto Sekimura

Department of Quantum Engineering and Systems Science
Department of Nuclear Engineering and Management
University of Tokyo, Japan

Abstract

There are 55 operating commercial light water reactor plants (32 BWRs and 23 PWRs) in Japan. Twelve (12) plants have been operating for more than 30 years. Utility companies are required to perform an “Ageing Management Technical Assessment” before the end of 30 years operation of each plant. The assessments for each plant have been evaluated by the Nuclear and Industry Safety Agency (NISA) of the Ministry of Economy Trade and Industry (METI) for these 12 plants. The Japan Nuclear Energy Safety Organisation (JNES) has compiled Technical Review Manuals for six major degradation phenomena for the evaluation of Ageing Management Technical Assessment.

A “Roadmap for Ageing and Plant Life Management” was established in 2005 by the Special Committee in the Atomic Energy Society of Japan under the commission from the JNES. Within the framework of the roadmap, the major research and development fields are divided into the following four categories: 1) engineering information systems; 2) research and development of technologies for inspection, evaluation and repair of the components and materials; 3) development of codes and standards; 4) synthesised maintenance engineering.

Continuous revision of the “Strategy Maps for Ageing Management and Safe Long-term Operation” has been performed under the Co-ordinating Committee of Ageing Management to promote research and development activities by industries, government and academia, effectively and efficiently. Systematic development of the information basis for database and knowledge-base has been undertaken in addition to the development of codes and standards by academic societies through intensive domestic safety research collaborations and international collaboration.

Introduction

Light water reactors (LWRs) which have become an important infrastructure element in Japan are required to provide safety and public acceptance in addition to achieving their major function of stable energy supply. Complicated engineering products made of a huge number of components tend to have weaker correlation between the function of the system and each component and material. Engineering data and knowledge increase rapidly within each subdivided field of engineering but tend to be enclosed within the narrow field.

There are 55 commercial LWR plants in Japan and 12 LWRs which have been operating for more than 30 years, as shown in Figure 1. The number of aged LWRs which have been operating for more than 30 years will exceed 20 in 2010 and 30 in 2015. Utilities are required to conduct an ageing management technical assessment before the 30th year of commercial operation, as a regulatory requirement, to ensure safe operation and integrity of the plant for long-term operation. The regulating agency, the Nuclear and Industrial Safety Agency (NISA) of the Ministry of Economy, Trade and Industry (METI) reviews the report of the ageing management assessments.

After the Mihama-3 accident on 8 August 2004, a Committee for Ageing Management was established in NISA. The Committee reviewed and discussed the basic policy, guidance documents, and the technical base for ageing management. By the end of August 2005, the Committee confirmed the NISA report on improved ageing management. Based on this report, the Nuclear Power Plant Ageing Management Office (AMO) and Nuclear Power Plant Ageing Evaluation Office were established in NISA and the Japan Nuclear Safety Organisation (JNES), respectively.

In the Report on Improved Ageing Management of NISA approved on 31 August 2005, the following issues were considered to be necessary for maintenance and regulatory activities for ageing management of nuclear power plants:

- 1) to assure transparency and effectiveness;
- 2) to provide a technical information basis;
- 3) to prevent non-physical degradation;
- 4) to offer clear accountability to the public.

The need for various types of safety research is also emphasised in the report. “R&D Roadmaps for Ageing Management and Safe Long-term Operation” developed by the Atomic Energy Society of Japan is an excellent reference for this wide collection of safety research. Industries, government and research organisations, including universities, must collaborate and share their roles effectively.

Ageing Management Technical Assessment and its review processes by NISA and JNES

Figure 2 shows the evaluation procedures of the Ageing Management Technical Assessment report for the light water reactor plant submitted by utility companies. Each plant is assumed to operate for 60 years in order to estimate the integrity and safety of structures, systems and components. Utilities will classify and select the components and structures depending on the importance of safe long-term operation of the plant. They will evaluate the integrity of the component or the structure reflecting the latest database and technological knowledge reviewing operational experiences and possible ageing phenomena in SSC, followed by the preparation of long-term maintenance programmes for the next 10 years including further research activities, if necessary.

The review procedures by NISA and JNES are clearly defined by the Guideline and Standard Review Plan documents, which were issued in December 2005. Figure 3 shows the details of the standard review procedures. The major left part of this figure shows the procedures for each ageing or degradation phenomena. The right portion of Figure 3 shows the seismic safety evaluation processes considering degradation of materials or ageing phenomena under earthquake induced extra-stress. For the technical evaluation of the ageing management, JNES compiled the Series of Technical Evaluation Manuals for the following six major degradation phenomena:

- 1) neutron irradiation embrittlement of reactor pressure vessel;
- 2) stress corrosion cracking including IGSCC, PWSCC and IASCC;
- 3) fatigue;
- 4) thinning of piping by flow-accelerated corrosion and erosion;
- 5) insulation degradation of electrical cables;
- 6) degradation of concrete properties for strength and shielding.

A seismic Safety Evaluation manual has also been prepared. Another manual prepared by JNES is for the Prevention for Organisation Culture Degradation.

Figure 4 shows the review processes for the technical evaluation of irradiation embrittlement, in which the current version of Japan Electric Association (JEA) codes prepared by the Nuclear Standard Committee of JEA are utilised. JEAC 4201-2004 is a code for surveillance test methods of structural materials for nuclear power plants including a set of prediction formulae of the irradiation embrittlement from a large database of surveillance tests results. In addition to utilising these JEA codes, introduction of the latest knowledge of radiation embrittlement is also encouraged as an optional evaluation method. The Central Research Institute of the Electrical Power Industries (CRIEPI) has been developing a new method of irradiation embrittlement correlation based on a mechanistically guided model to predict embrittlement behaviour of low alloy steels, which can be effectively used, for example, to verify the possible observed scatter of surveillance data especially for BWRs with variations in neutron irradiation flux.

Technical information basis and research roadmaps for ageing management

To make these technical evaluation manuals and to make reports of the technical assessment, we need an information basis for ageing management. Industries and utilities have their own databases on fabrication of the components, inspection results for degradation of the materials during the operation of LWR plants and resultant failures or accidents. Technical information and knowledge bases for the design, construction, operation and maintenance of nuclear power plants should be utilised comprehensively not only for utilities and industries but also regulation. Mechanistic understandings of degradation of materials, and new inspection technologies for crack propagation, property changes and other abnormal operation modes have been the major topics of research institutes and universities. From these synthetic databases and knowledge bases, we can also define the issues to be solved by future research.

A Co-ordinating Committee with members from industries, utilities, research organisation and regulatory institutes on ageing management has been established in Japan to establish the technical

information basis for ageing management. One of the major roles of the Co-ordinating Committee is the improvement of the “R&D Roadmaps for Ageing Management and Safe Long-term Operation” issued at the end of March 2005 by the Atomic Energy Society of Japan.

In the original Roadmap 2005, we picked up many research items for the future 20 years through an intensive discussion by experts from industries, utilities, regulatory institutes, research organisations and universities. We defined 70 research topics and then categorised them into 4 major research fields:

- 1) information basis for ageing management;
- 2) development for evaluation methodologies of ageing phenomena, inspection techniques and repair or replacement technologies;
- 3) development of codes and standards;
- 4) systematic maintenance engineering to apply this information and technology to operating and future plants.

Figure 5 shows the structure of the R&D items in the Roadmap 2005. The systematic maintenance engineering field includes methodologies for optimum combination for inspection, maintenance actions and cost, definition of importance of components for maintenance, and performance index of power plant systems. To keep leading engineers and to improve regulatory systems, studying and learning these systematic approaches is considered to be one of the important issues for collaboration of industries, regulatory bodies and universities.

We have selected 26 important topics out of the 70 research items listed, and drawn the roadmaps for the next 20 years. Figure 6 shows schematically the example of the roadmaps for radiation embrittlement of pressure vessels.

In the Safety Research Sub-committee of the Co-ordinating Committee of Ageing Management, we decided to continuously improve and revise the Roadmap 2005 to the strategy maps for ageing management. The current activities of the Safety Research Sub-committee for the new strategy maps are shown in Figure 6. We have also been discussing the roles of industries, government and academia in role-sharing and effective and efficient budgeting for ageing management for safe long-term operation of LWRs. The scenario for ageing management of LWRs is closely related to the introduction scenario of the next generation reactors. We have come to understand that we should communicate with a greater variety of fields. Academic societies like the Atomic Energy Society of Japan, Japan Society for Mechanical Engineers and the Japan Electric Association will also play important roles in establishing codes and standards, utilising databases and knowledge-bases from R&D and experts. The updated version of the Strategy Maps 2007 will be issued in July 2007.

Figure 7 shows the structure of the Strategy Maps for Ageing Management from the viewpoints of knowledge and its management. There are three different categories of activities to utilise engineering knowledge for stable, safe and economical operation of the plants. As is pointed out in the original Roadmap 2005, the information base for ageing management is the most important issue not only for safe long-term operation of current light water reactors but also for future advanced reactors. Technical information on operation and maintenance engineering should be collected as database. In order to put knowledge to practical use, systematic information systems including codes and standards should be established. This information system should also be put into practice for operation and maintenance at each plant site. It should also be emphasised that leading engineers who have

synthesised knowledge are an important requirement for the safe and stable operation of nuclear power plants. This new field frontier can be referred as “system maintenology” to synthesise engineering for the safe and reliable operation of current and next generation LWRs.

Development of technologies can be achieved not only in each field of engineering, but also by synthesis of different approaches in many fields especially for one of the most complicated engineering assemblies like nuclear reactors. Under the current situation of subdivided engineering and a huge quantity of knowledge, systematic approaches to synthesise the complicated systems such as nuclear power plants are also required for superior regulation and inspection.

Summary

- The current status of ageing management and technical evaluation procedures of safe long-term operation of Japanese light water reactors is briefly stated.
- Continuous revision of Strategy Maps for Ageing Management and Safe Long-term Operation by all the stakeholders has been performed under the Co-ordinating Committee of Ageing Management.
- Intensive safety research collaborations have been performed according to the following activities:
 - systematic development of information basis for database and knowledge base;
 - development of codes and standards by academic societies;
 - international contribution and collaboration;
 - effective sharing and collaboration between industries, government and academia.

Figure 1. Nuclear power plants in Japan

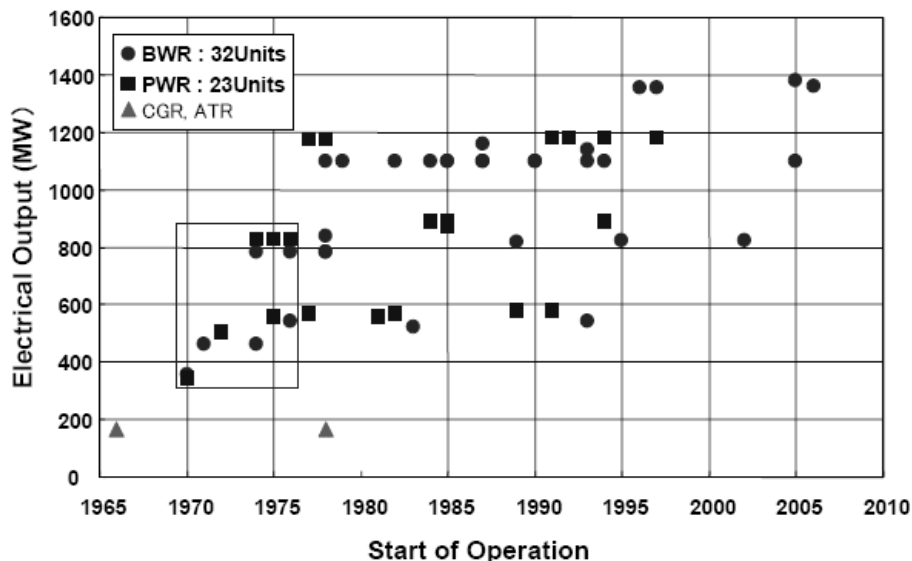


Figure 2. Evaluation procedures of the report on Ageing Management Technical Assessment of each plant by utilities

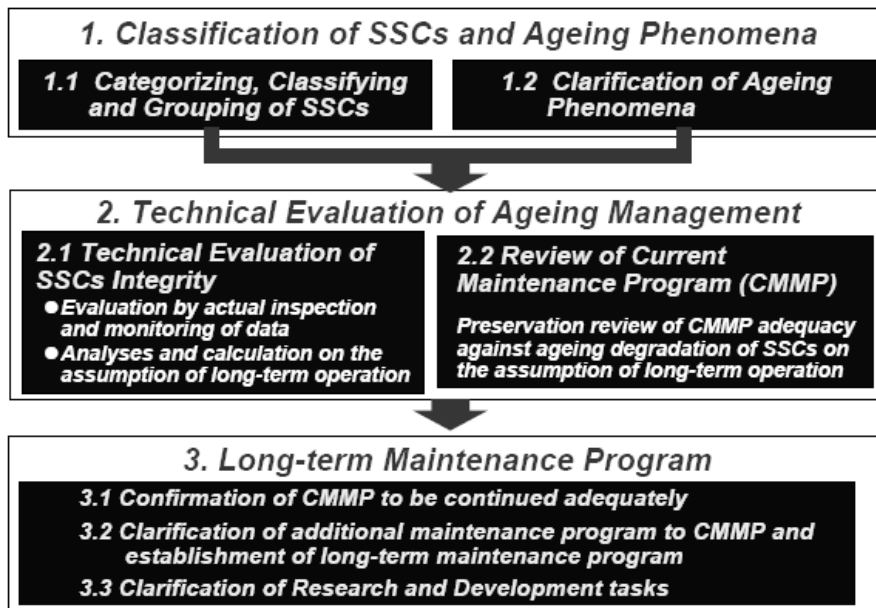


Figure 3. Standard review procedures of Ageing Management Technical Assessment

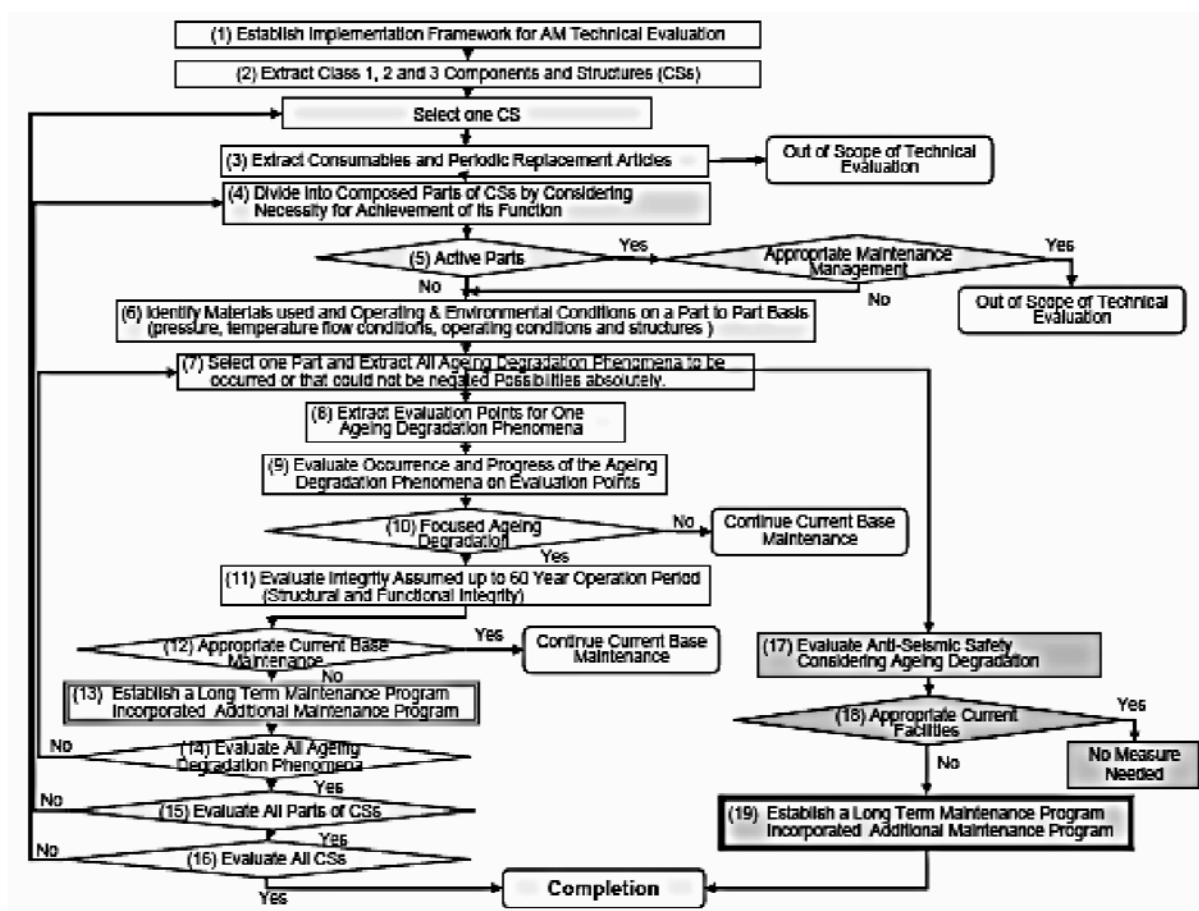


Figure 4. R&D Roadmaps for Ageing Management and Safe Long-term Operation developed by the Atomic Energy Society of Japan in 2005

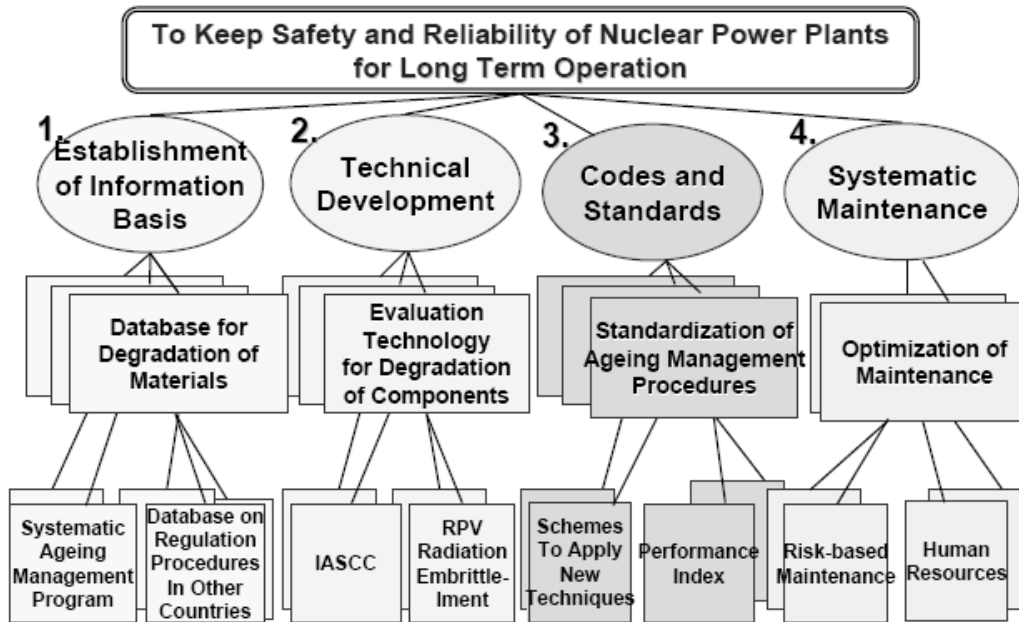


Figure 5. Example of individual roadmap on important research item (improvement of prediction methods for embrittlement of reactor pressure vessel steels)

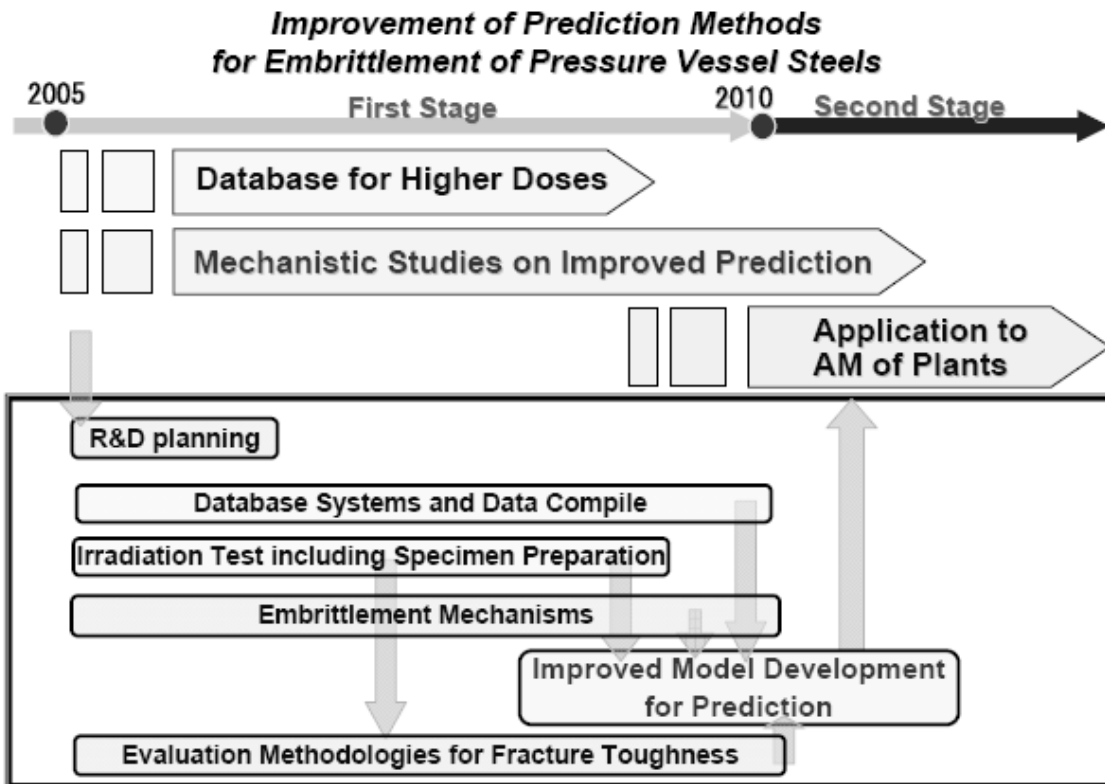


Figure 6. Continuous revision of strategy maps for ageing management by all the stakeholders in the Safety Research Subcommittee in the Co-ordinating Committee on Ageing Management

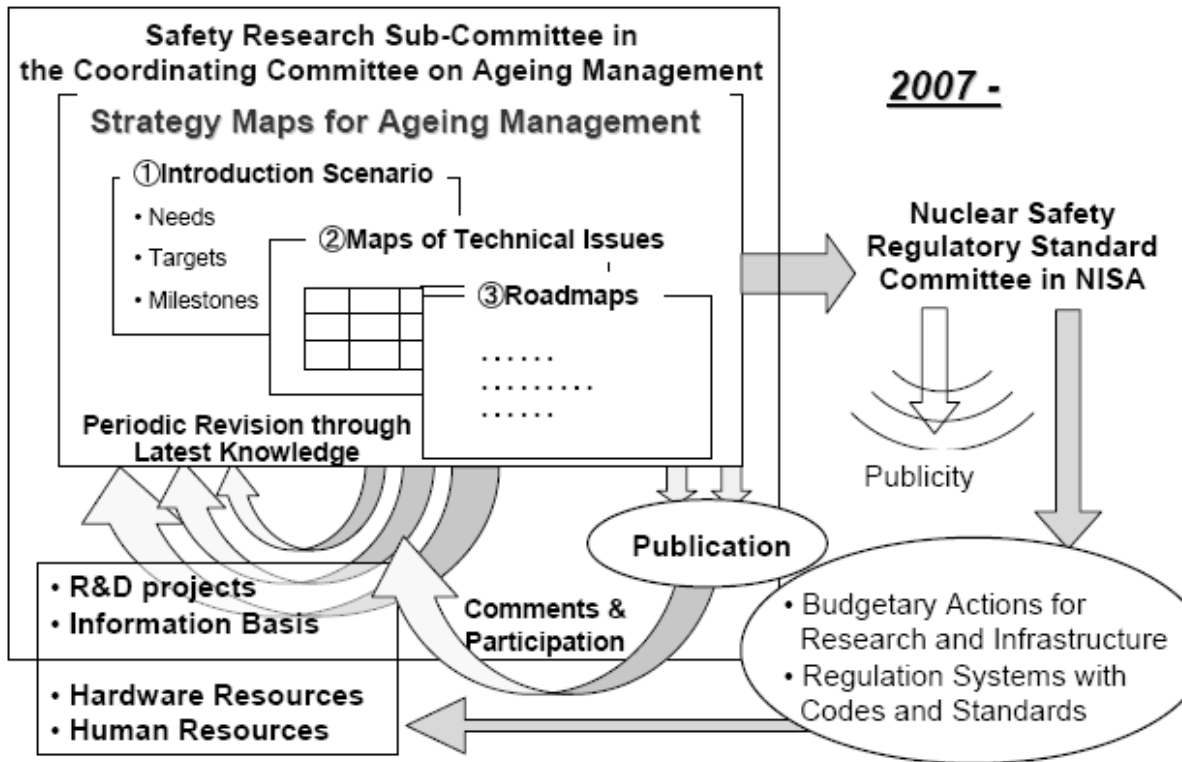
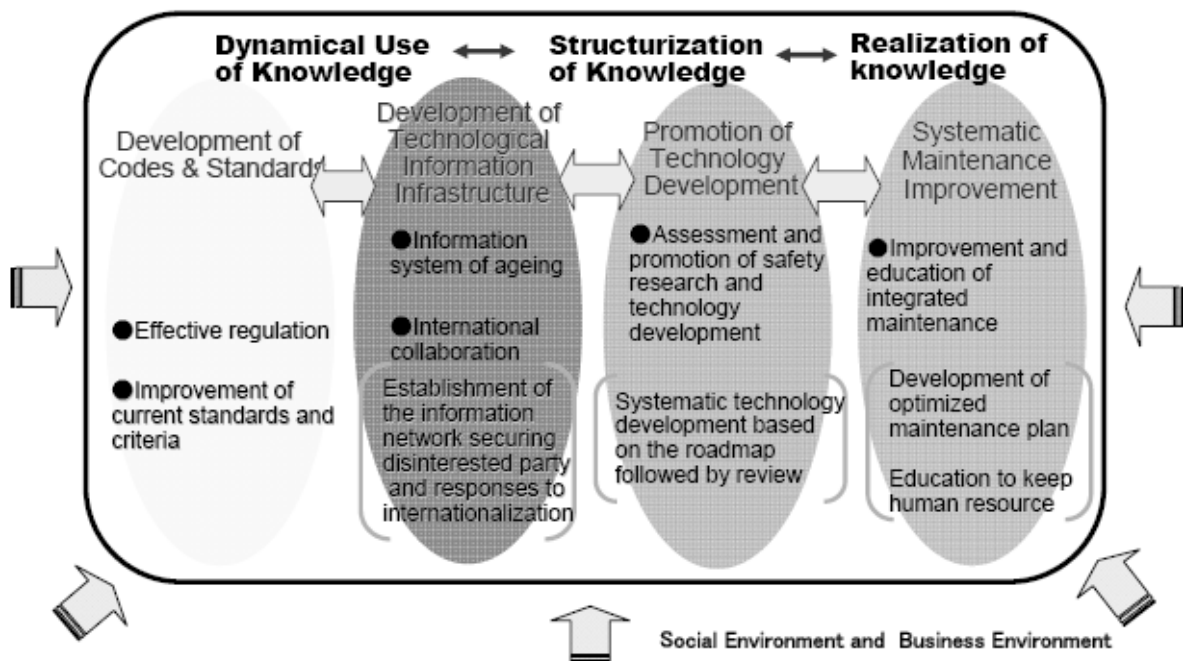


Figure 7. Basic structure of the Strategy Maps for Ageing Management and Safe Long-term Operation of nuclear power plants



MODELLING, MICROSTRUCTURES, RADIATION DAMAGE AND UNDERSTANDING OF IRRADIATION DATA

Todd Allen

University of Wisconsin, Madison, Wisconsin, USA

Abstract

The mechanical properties and dimensional stability of reactor structural materials are critical to nuclear system performance. These bulk properties are controlled by the microstructural developments that occur due to radiation, with the microstructural development being a function of temperature, radiation dose and dose rate. Past ability to model these changes in microstructure was limited by three significant factors: limitations and approximations associated with having to extrapolate diffusion data from high temperature to reactor operating temperature, the inability to describe interstitial diffusion for multi-component alloys and the inability to describe the complex interactions at surfaces and interfaces that exist in a multi-component system. Advances in computational materials need to develop the ability to address these three issues. Void swelling and the associated radiation-induced segregation in an austenitic alloy is used to describe why the ability to model diffusion in complex alloys is needed to properly predict materials performance. Radiation damage and segregation in a ferritic system and oxide stability in an oxide dispersion strengthened steel are also described as two areas where modelling radiation damage in complex materials is also required. Finally, examples of ongoing research where modelling is starting to be applied to complex materials are described. These modelling efforts are critical to developing computation modelling into the primary modern theory and analysis tool.

Introduction

Deleterious property changes in reactor materials are all linked to underlying changes in the microstructure. Developing the ability to understand and predict radiation-induced microstructural changes is important to both understanding component lifetime and the development of new, improved materials. The development of modern computational tools, combined with experimental measurements are allowing for a deeper understanding of the effect of radiation on materials properties, especially the complex materials used in nuclear systems. Although past computational programs have helped to understand radiation effects in simple model alloys, tools are now becoming available to understand more complex alloys. Properly describing changes in complex materials, composed of many atoms, is a critical direction to which advanced computational techniques need to be applied.

In this short paper, the synergy between radiation-induced segregation and the development of microstructural features in austenitic alloys will be used to demonstrate the need to better understand complex materials. The similarity of complex microstructural development under irradiation in ferritic-martensitic steels, including oxide dispersion strengthened steels is briefly described. Finally, examples of the use of modern computational tools towards understanding radiation damage in complex alloys are highlighted.

Void swelling and associated microstructures in austenitic steels

Void swelling in austenitic alloys can cause unacceptable dimensional changes in reactor structural materials. After void swelling was discovered in irradiated austenitic stainless steels [1], many studies were undertaken to determine not only the magnitude of the swelling problem but also the variables that influenced swelling. A comprehensive review of void swelling data is contained in Ref. [2]. Studies in the 1960s and 1970s determined that void swelling arose because the bias at interstitial loops for interstitials was greater than the bias for vacancies. This net bias left excess vacancies available to form voids. The net positive volume difference of the interstitial loop and void formation leads to bulk volumetric swelling. Wolfer predicted that elemental radiation-induced segregation to the surface of loops and voids would change the net bias, leading to changes in swelling behaviour [3-5]. The segregation was predicted to change the lattice parameter and shear modulus near the loop or void surface, leading to a change in bias for absorbing point defects.

During the fast reactor cladding and duct development programme, the discovery that increasing bulk nickel content in austenitic steel decreased the amount of bulk swelling was made. This trend holds up in neutron, proton and ion irradiations (Figure 1). Recent studies have found that, as bulk nickel concentration increases in austenitic alloys, the rate at which radiation-induced segregation (chromium depletion and nickel enrichment) develops decreases (Figure 2 shows chromium segregation data). Alloys with slowly developing segregation incur the greatest void swelling. Consistent with Wolfer's predictions, the change in lattice parameter due to segregation at the defect surface decreases with increasing bulk nickel (Figure 3). This relationship between compositional changes via segregation, microstructural development, and the affected bulk property (void swelling) typifies the challenge in developing long-life components in nuclear systems. To properly predict the radiation-induced microstructure requires a fundamental ability to model radiation-induced segregation, as well as all diffusion and phase stability under radiation.

Figure 1. The effect of bulk nickel concentration on swelling

Ni^+ ion irradiation data from [6], proton irradiation data from [7], neutron irradiation data from [8]

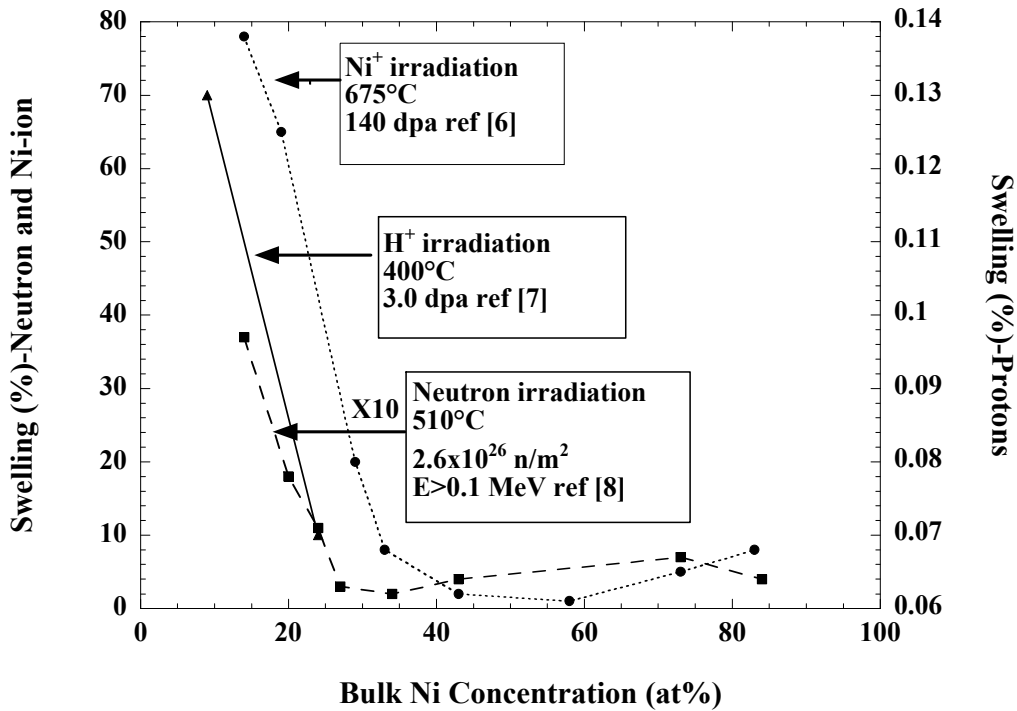


Figure 2. Grain boundary segregation as a function of alloy composition; alloys with less bulk nickel develop segregation at a slower rate [10]

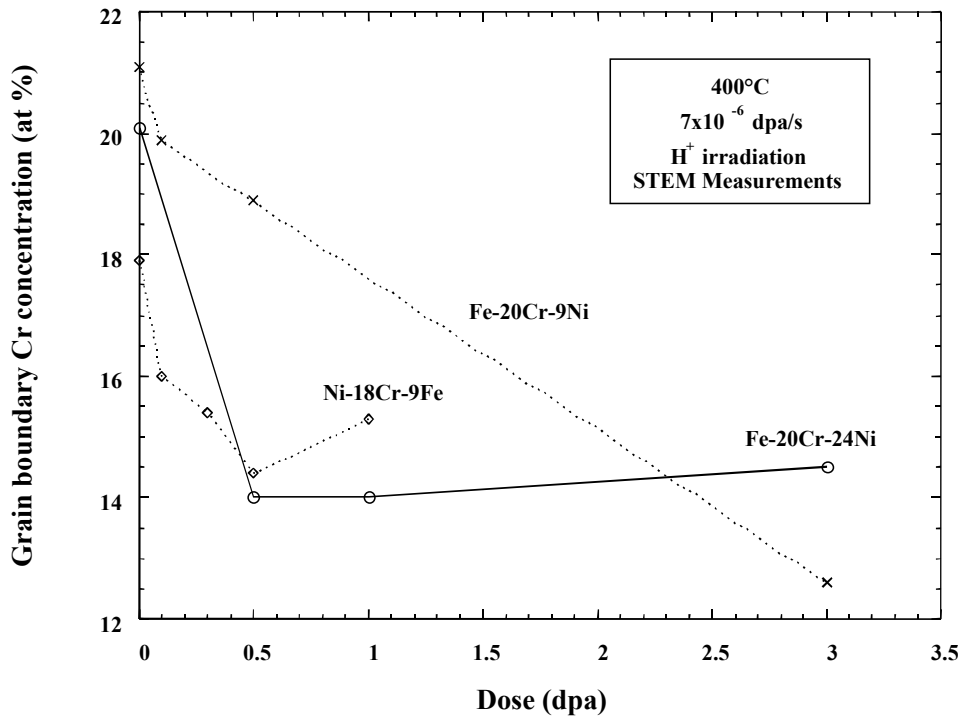
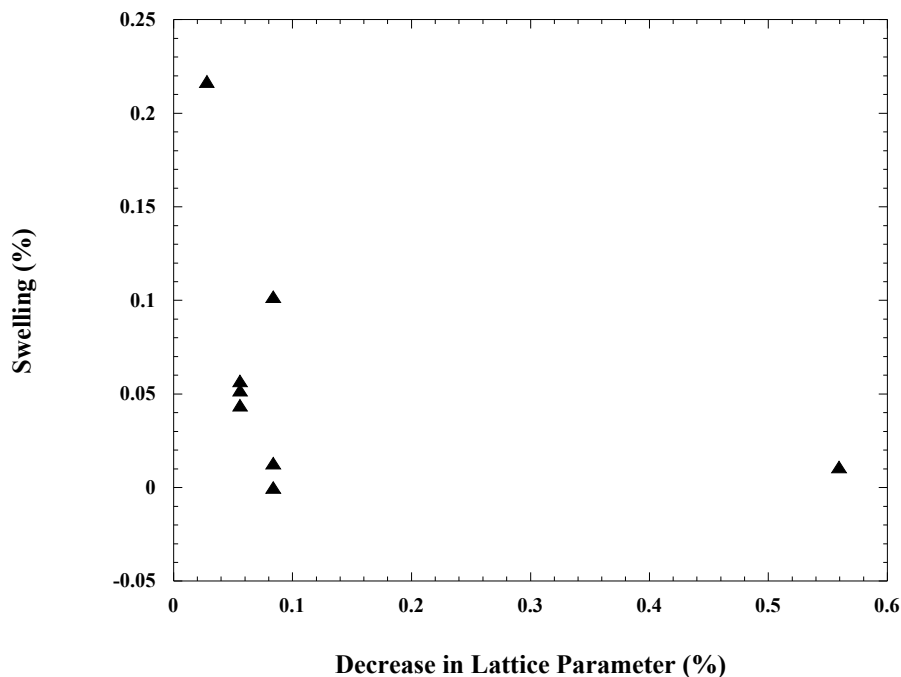


Figure 3. Decrease in swelling as a function of changing lattice parameter caused by radiation-induced segregation. A decrease in the lattice parameter indicates smaller lattice parameter at the boundary surface [11].



Modelling radiation-induced segregation

Radiation-induced segregation is a non-equilibrium process that occurs at grain boundaries and other defect sinks such as dislocation loops and voids during irradiation of an alloy at high temperature (30 to 50% of the melting temperature) [12]. Radiation produces quantities of point defects far in excess of equilibrium concentrations. At high temperatures, these defects are mobile and travel to low energy sites such as surfaces, grain boundaries, dislocations and other defect sinks. Segregation occurs when a given alloying component has a preferential association with the defect flux. Enrichment or depletion of each element occurs according to the relative participation of each element in the defect flux. The segregation profiles have typical widths of 5-10 nm.

In general, preferential interaction with vacancies and/or interstitials can contribute to RIS. Two different mechanisms have been proposed to describe RIS in austenitic Fe-Cr-Ni alloys. One segregation mechanism is inverse Kirkendall behaviour, where preferential association with a defect gradient (either a vacancy gradient or an interstitial gradient) causes a solute flux. A second segregation mechanism is the formation of mobile defect-solute complexes (interstitial-solute or vacancy-solute), where the solute is dragged with the defect flux. If a solute binds with a defect to form a complex, and the complex undergoes significant diffusion before dissociating, then the solute can be dragged to the boundary. The diffusion of defect-solute complexes will enrich the solute near the sink. Mobile defect-solute complexes have been shown to be important in segregation in dilute alloys [6] but the concept of a defect-solute complex becomes ill-defined in the case where the nearest neighbours to a defect change significantly as the defect migrates. Although defect-solute complexes are not expected to form in concentrated alloys, the possibility has been raised that undersized elements may be more likely to exist as interstitials [13]. Greater participation in the interstitial flux would lead to an enrichment of an undersized element at the grain boundary.

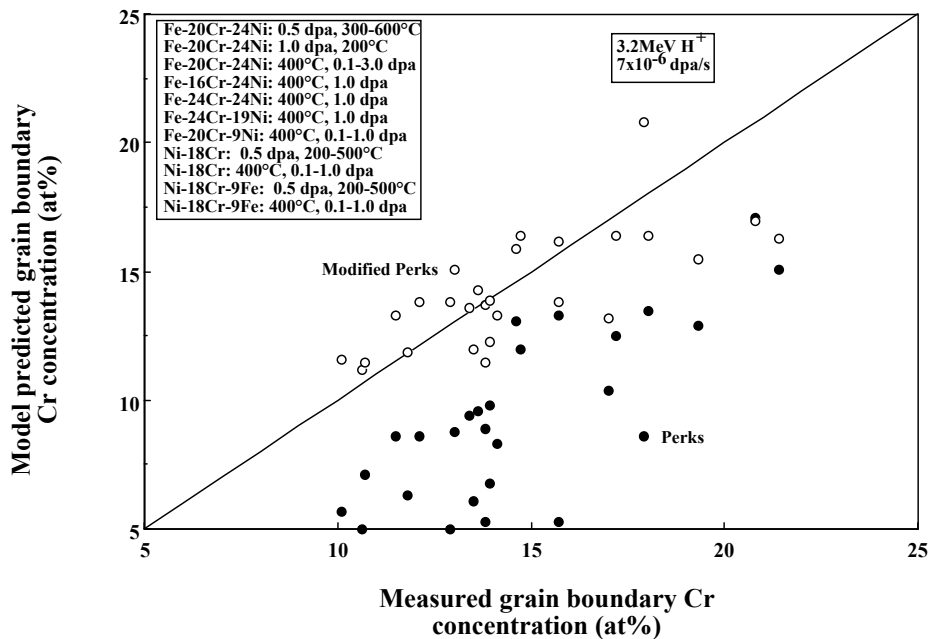
For Fe-Cr-Ni alloys, comparisons of model calculations to a large database of RIS measurements lead to the following conclusions [14]:

- The segregation can be explained primarily using an inverse Kirkendall mechanism, driven by interactions of atoms with the vacancy flux.
- The diffusivity parameters used in the models must be functions of alloy composition.
- Short range order effects should be included in models.

Figure 4 shows the improvement in RIS modelling that is possible when incorporating the three above factors into RIS models [14]. The figure compares model calculations using constant diffusion coefficient (Perks model) with those that calculate atom-vacancy diffusion coefficients based on a nearest neighbour model. Even though this approach is an improvement over the simple Perks model, it has the following limitations:

- Vacancy diffusion information is extrapolated across a wide temperature difference and possibly regions of different stable phase.
- Interstitial effects were not included as there are no measurements for the migration energy of specific atoms as interstitials.
- Compositional effects are treated to only the first nearest neighbour.

Figure 4. Improvement in the ability to model RIS in Fe-Cr-Ni austenitic alloys by including local composition



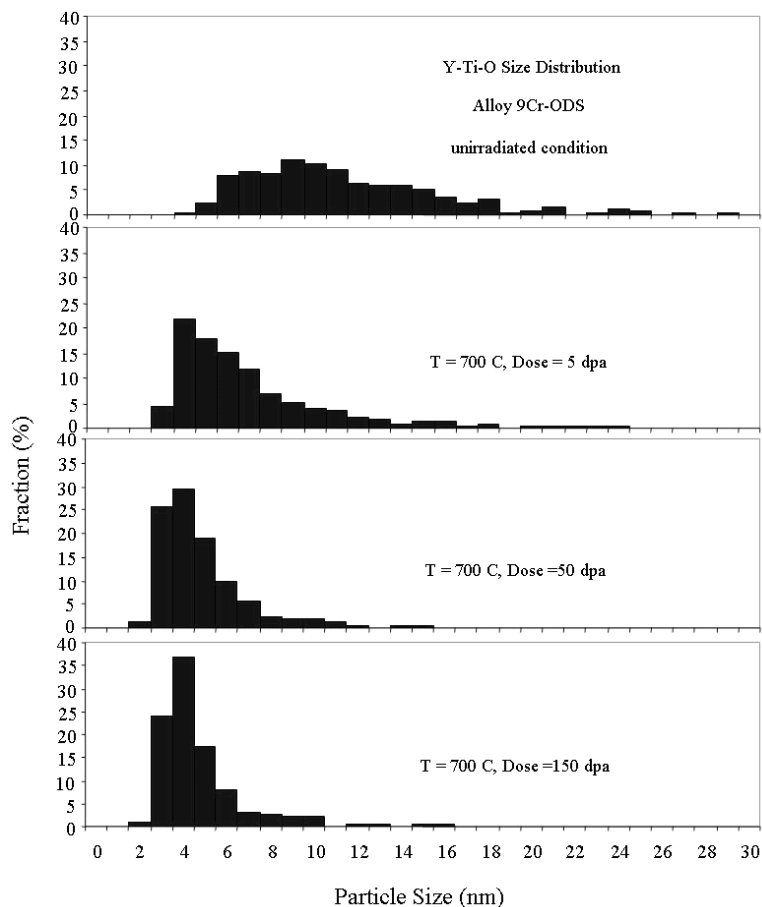
The ability to explain RIS in ferritic and martensitic steels is even less developed. The database of segregation is far smaller and measurements for similar alloys coming from different experimenters do not even agree in the trend of the segregation (e.g. enrichment or depletion of chromium). Nonetheless, the relationship between segregation and the development of microstructural features that

has been shown in austenitic alloys is likely to be just as important in ferritic-martensitic steels. Therefore, since the physical information (e.g. diffusion barriers and hopping rates) needed to properly model segregation and associated microstructural changes is so far impossible to access experimentally, computational modelling becomes a critical tool in understanding radiation damage.

Stability of nanoclusters in oxide dispersion strengthened steels

To improve the high temperature strength of ferritic-martensitic steels being considered for cladding in advanced fast spectrum reactors, oxide dispersion strengthened steels are currently being developed [15,16]. The stability under radiation of the Y-Ti-O nanoclusters that provide the high temperature strength is an important question relative to their long-term performance. A large number of studies report the nanoclusters to be stable under radiation while a smaller number show decreasing size with increasing radiation dose. For those studies that show a decreasing size under radiation, the decrease occurs faster at higher temperature (an example for a 9Cr ODS alloy irradiated at 700°C with 5 MeV Ni ions is shown in Figure 5.). Understanding the stability of these nanoclusters, as a function of temperature and radiation dose, will be greatly assisted by the use of modern computational techniques including molecular dynamics to understand the effect of collision cascades on nanoclusters as well as *ab initio* to understand migration barriers relevant to radiation-induced diffusion and segregation to the nanocluster surface.

Figure 5. Particle size (diameter) distribution for 9Cr ODS samples irradiated at 700°C to doses of 0, 5 and 150 dpa

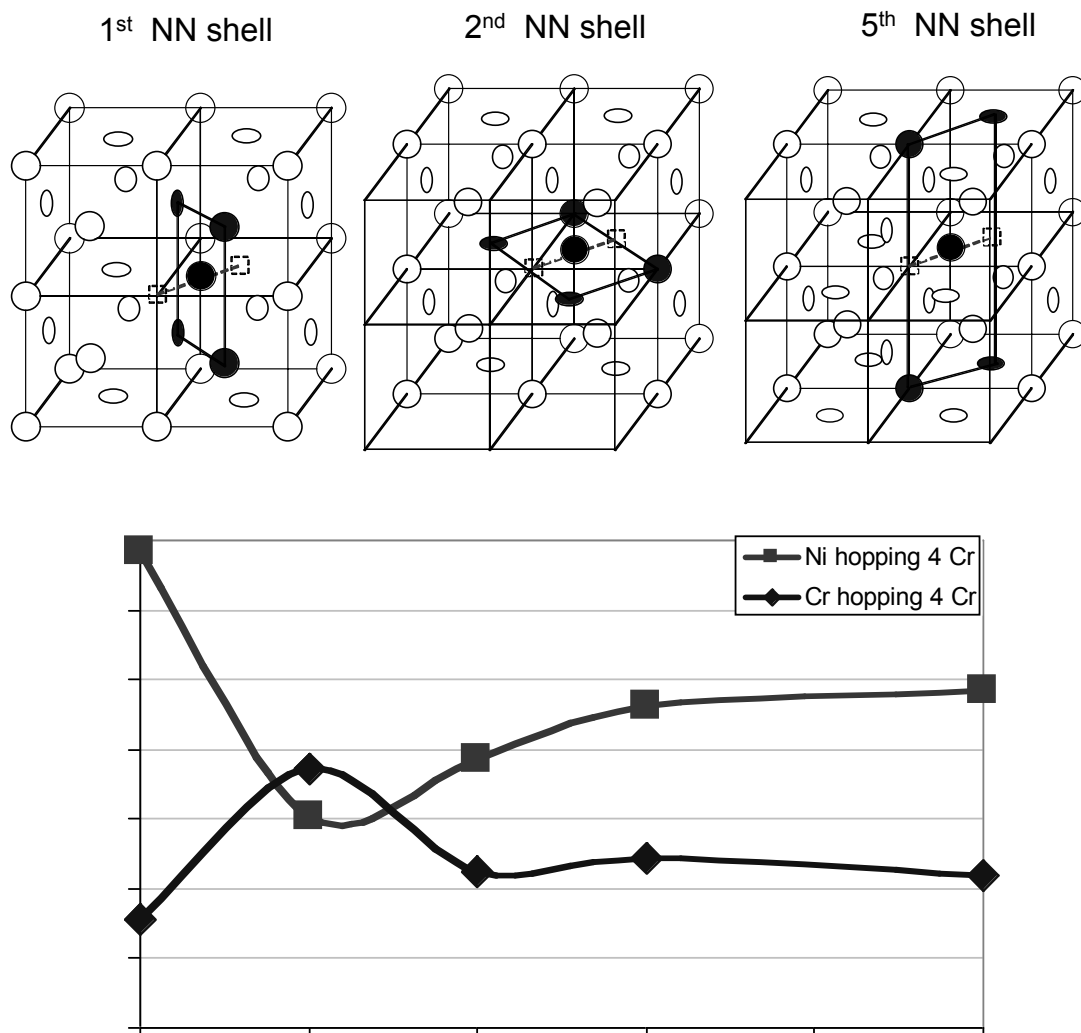


Modelling complex alloys

While the use of multi-scale (time and position) models as a means of bridging from radiation cascades to the ultimate changes in bulk physical properties has been proposed as the basis for understanding radiation damage, until recently, limited work has been done to apply these tools to the complex alloys used in real nuclear systems. The examples presented earlier in this paper indicate that modelling of these complex alloys is necessary to truly understand reactor materials. A few examples are given of recent attempts to include the required complexity in radiation damage modelling.

As mentioned earlier, modelling RIS in austenitic alloys requires knowledge of diffusion information as a function of local composition. Work at the University of Wisconsin using density functional theory to calculate migration barriers, combined with cluster expansion formalism, is being used to establish a basis for diffusion constants in austenitic Fe-Cr-Ni alloys. Figure 6 shows an example of the effect of local chromium atom location on the migration barrier for a chromium and nickel atoms diffusing in a nickel matrix [17].

Figure 6. Influence of the location of Cr atoms on the migration energy of a Cr or Ni atom in a nickel matrix [17]



Similar work is being performed at the University of California on ferritic-martensitic alloys [18]. Wirth and colleagues have done *ab initio* calculations indicating Cr is a faster vacancy diffuser than Fe in a Fe-10Cr alloy. If vacancy effects primarily drove RIS in this alloy, Cr would deplete at boundaries. Since the preponderance of the RIS measurements are pointing toward Cr enrichment, Wirth's calculations point toward preferential interaction with the interstitial flux as being important. Wirth has also shown, using molecular dynamics calculations that during cascade collisions, Cr preferentially locates in interstitial dumbbell configurations. Similar collision cascade results were also produced by Terentyev, *et al.* [19].

Clustering and precipitation in Fe-10Cr alloys have been modelled by Olsson and colleagues [20]. These detailed studies included *ab initio* calculations to understand migration barrier energetics, magnetic moments, heat of mixing and clustering tendencies. They also performed molecular dynamics studies to understand cascade sequences. Their calculations, in a similar manner to those of Wirth, *et al.*, indicate Cr atoms have preferential interactions with interstitials and these interactions may be critical to the development of microstructures under radiation.

The importance of the studies listed above is that they are at the forefront of adding the complexity of alloy systems to the understanding of radiation damage. They use modern computational techniques to provide critical data and understanding and probe where experimental techniques currently cannot provide data. These modern analytical techniques are the basis for understanding radiation damage experiments and guiding the development of new radiation-resistant alloys.

REFERENCES

- [1] Cawthorne, C., J.E. Fulton, *Nature*, Vol. 216, p. 515 (1967).
- [2] Garner, F.A., "Irradiation Performance of Cladding and Structural Steels in Liquid Metal Reactors", in *Materials Science and Technology, A Comprehensive Treatment*, Vol. 10A Nuclear Materials, R.W. Cahn, P. Haasen, E.J. Kramer (Eds.), VCH Weinheim (1994).
- [3] Si-Ahmed, A., W.G. Wolfer, *Effects of Radiation on Materials: 11th Conference*, ASTM STP 782, H.R. Brager, J.S. Perrin (Eds.), American Society for Testing and Materials, p. 1008 (1982).
- [4] Wolfer, W.G., L.K. Mansur, *J. Nucl. Mater.*, 91, 265 (1980).
- [5] Sniegowski, J.J., W.G. Wolfer, *Proc. of Topical Conference on Ferritic Alloys for Use in Nuclear Energy Technologies*, Snowbird, Utah, 19-23 June 1983.
- [6] Johnston, W.G., J.H. Rosolowski, A.M. Turkalo, T. Lauritzen, *J. Nucl. Mater.*, Vol. 54, p. 24 (1974).
- [7] Busby, J.T., T.R. Allen, J. Gan, E.A. Kenik, G.S. Was, *Proceedings of the 8th International Symposium on Environmental Degradation of Materials in Nuclear Power Systems-water Reactors*, Amelia Island, FL, 10-14 August 1997.

- [8] Bates, J.F., W.G. Johnston, *Proc. Int. Conf. Radiation Effects in Breeder Reactor Structural Materials*, Scottsdale, New York, The Metallurgical Society of AIME, pp. 625-644 (1977).
- [9] Allen, T.R., J.I. Cole, J. Gan, G.S. Was, R. Dropek, E.A. Kenik, *J. Nucl. Mater.*, 342, 90 (2005).
- [10] Allen, T.R., J.T. Busby, G.S. Was, E.A. Kenik, "On the Mechanism of Radiation-induced Segregation in Austenitic Fe-Cr-Ni Alloys", *J. Nucl. Mater.* 255, 44 (1998).
- [11] Allen, T.R., J.I. Cole, J. Gan, G.S. Was, R. Dropek, E.A. Kenik, "Swelling and Radiation-induced Segregation in Austenitic Alloys", *J. Nucl. Mater.*, 342, 90 (2005).
- [12] Okamoto, P.R., L.E. Rehn, *J. Nucl. Mater.*, Vol. 83, p. 2 (1979).
- [13] Okamoto, P.R., H. Wiedersich, *J. Nucl. Mater.*, 53, 336 (1974).
- [14] Allen, T.R., G.S. Was, *Acta Met.*, 46, 3679-3692 (1998).
- [15] Yamashita, S., K. Oka, S. Ohnuki, N. Akasaka, S. Ukai, *J. Nucl. Mater.*, 307-311, 283 (2002).
- [16] Ohtuska, S., S. Ukai, M. Fujiwara, T. Kaito, T. Narita, *Materials Transactions*, 46 (3), 1 (2005).
- [17] Tucker, J., private communication.
- [18] Wirth, B.D., H.J. Lee, B. Sadigh, J-H. Shim, K. Wong, submitted to the Materials Research Society, Fall Meeting 2006, Boston, MA, 28 November 2006.
- [19] Terentyev, D.A., L. Malerba, R. Chakarova, K. Nordlund, P. Olsson, M. Rieth, J. Wallenius, *Journal of Nuclear Materials*, 349, 119-132 (2006).
- [20] Olsson, Pär, Christophe Domain, Janne Wallenius, *Physical Review B*, 75, 014110 (2007).

SESSION II

Gas-cooled Systems

Chairs: W. Hoffelner, B.J. Marsden

MATERIAL RESEARCH FOR VHTR DESIGN CODES

Wolfgang Hoffelner

Senior Lecturer at Swiss Federal Institute of Technology Zürich

Abstract

Design codes and standards are the backbone for construction of power plants, particularly of nuclear power plants. Advanced high-temperature reactor projects like the US-NGNP clearly demonstrated lacking code information for the envisaged operation conditions. Questions concerning criteria for negligible creep of advanced RPV materials, extension of temperature limits for materials already in use, creep-fatigue interactions, design criteria for graphite and ceramics and design of intermediate heat exchangers are – amongst other problems – highly relevant for future VHTRs. Answering these questions is not possible with existing data alone but it needs additional materials research particularly in the fields of long-term damage and damage interactions. Such investigations are therefore not only performed within the GIF VHTR materials project but they are also followed up by an ASME task sponsored by the US DOE. The paper will provide an overview about these activities with particular emphasis on materials research.

Introduction

Advanced nuclear plants are expected to exceed demands on materials compared with current installations. This means, however, that design reaches a regime where essential design bases like materials data and/or applicable design codes and design rules are insufficient or simply missing. There are a number of advanced reactor concepts which are summarised in the road map of the international Generation IV (GIF) initiative [1]. Currently, sodium fast reactor (SFR) and very high-temperature reactor (VHTR) are considered internationally with priority. They could be deployed in relatively short time. For the VHTR – which we shall consider in more detail here – US DOE recently contracted a pre-conceptual design phase to the companies Westinghouse, General Atomics and AREVA [2]. This new generation nuclear plant (NGNP) is aimed at providing co-generation of electricity and high-temperature process heat, e.g. for hydrogen production. This means that basic design parameters, design rules and codes must soon be available. This is one of the reasons why the US DOE is also sponsoring an ASME project aimed at providing a basis for design and safety considerations [3]. Several tasks which were considered as essential for the design and safe operation of the NGNP are listed in Table 1.

Table 1. Tasks defined in the ASME NGNP support project after [3]

- **TASK 1** – Alloy 800H and Grade 91 allowables
- **TASK 2** – VHTR regulatory issues
- **TASK 3** – Grade 91 creep rules
- **TASK 4** – Code Case N-201
- **TASK 5** – Grade 91 and Hastelloy XR creep-fatigue data
- **TASK 6** – Graphite and ceramic materials
- **TASK 7** – NH evaluation and simplified rules
- **TASK 8** – Elevated temperature design testing needs
- **TASK 9** – Neutron fluence effects
- **TASK 10** – Intermediate heat exchanger (IHx) rules
- **TASK 11** – Flaw assessment and leak before break (LBB)
- **TASK 12** – Improved NDE methods

The current ASME Section III, Subsection NH criteria and material coverage originate largely from the liquid-metal reactor programme of the late 1960s, 70s and early 80s. Hence, the design rules of Subsection NH for Class 1 elevated-temperature components are limited to temperatures typical for such reactors, i.e. significantly lower than the VHTR. Materials are also limited to two stainless steels (304S and 316S), two ferritic steels (2¼Cr-1Mo and modified 9Cr-1Mo), and the superalloys 800H and 718. Code cases will be required for more materials, higher temperatures and longer allowable times. Inconel 617, Haynes 230, Hastelloy XR and modified 9Cr-1Mo are the primary candidate materials for piping, IHx and the RPV. Other candidate materials will require development of entirely new code cases, e.g. ODS alloys, ferritic-martensitic steels and additional superalloys.

The ASME Section III Code, specifically Subsection NH for elevated temperature design, has historically not allowed design of components at the very high temperatures indicative of a VHTR.

ASME code considerations

Temperatures and materials are summarised in Table 2 and they certainly do not cover VHTR and NGNP needs. Hence, new design guidelines must be developed for extending the time and temperature use of existing NH materials and new NH materials. For an extended description of these code-related questions see e.g. [4] and [5]. Design guidelines must include new or modified simplified design methods to predict stresses and deformation, creep-fatigue, de-rating of welds (or equivalent methods), as well as failure criterion and safety assessment methods. Subsection NH, and the ASME code in general, have typically not addressed the effects of environment (e.g. impure helium) and irradiation. Efforts should be taken to assess the significance of such effects.

Task 4 is devoted to an updating of ASME Nuclear Code Case N-201 to accommodate the needs of high-temperature gas-cooled reactors currently in development. The scope of the code case needs to be expanded to include the materials with higher allowable temperatures or extend the temperature limits of current materials and to confirm that the design methodology used is acceptable for design of core support structure components at the appropriate elevated temperatures. In this task operating parameters, temperature, pressure, environment, etc. for VHTRs are to be defined and reviewed by potential vendors of such reactors.

Table 2. Current subsection NH materials and maximum temperatures

Material	Maximum allowable metal temperature °C (300 000 hours max.)
304 SS	816
316 SS	816
Alloy 800H	760
2.25Cr-1Mo	593
Alloy 718	566

Task 2, regulatory safety issues in structural design criteria of ASME Section III Subsection NH and for very high temperatures for VHTR & GEN IV shall identify the safety issues relevant to this section of the code that must be resolved for licensing purposes. This task includes developing a description of how Subsection NH of the ASME code addresses these issues and the further needs to add criteria to cover unresolved safety concerns for very-high-temperature service criteria and stress/strain limits. The task should therefore be performed in close collaboration with the NRC.

Structural metallic materials

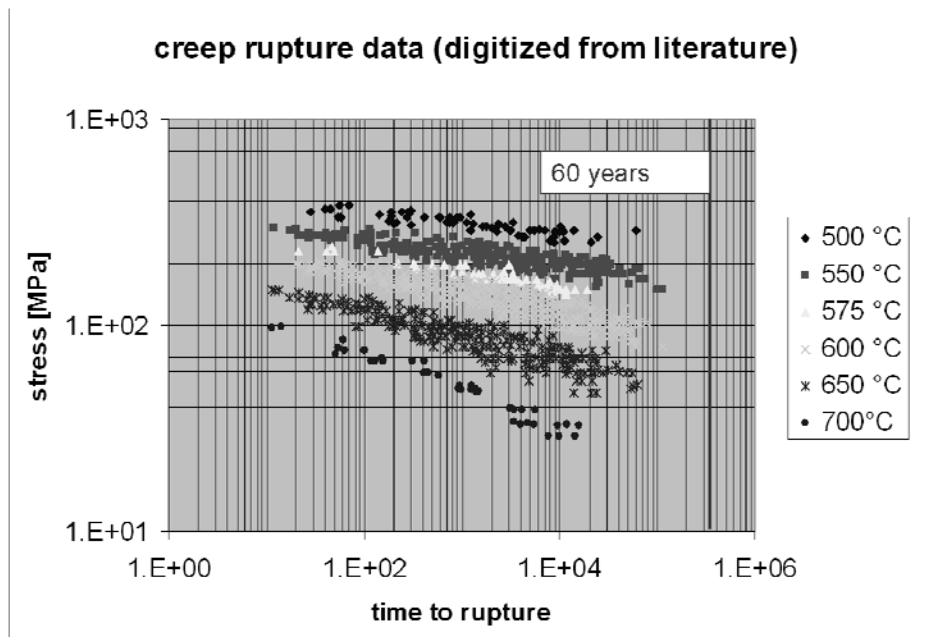
The DOE/ASME project started mid-2006 with the first five tasks which were considered of highest priority. They mainly deal with the following metallic structural materials: nickel-iron-based alloys (Alloy 800H, Hastelloy XR, IN-617) and the advanced ferritic/martensitic mod 9Cr1Mo steel, Grade 91. Alloy 800H is considered as a candidate for the VHTR control rod. Hastelloy XR is mainly a Japanese development of the well known Hastelloy X with the aim to improve the corrosion behaviour ranges of chemical in high-temperature gas-cooled reactor environments. This was essentially achieved by better specifying composition and by lowering the contents of Al and Ti [6]. Hastelloy XR is an interesting material for VHTR piping applications. Grade 91 steel is a well known structural high-temperature material for conventional power and coal gasification plants. It was developed as highly creep resistant martensitic steel which should allow the use of this class of materials up to temperatures of 650°C to avoid the necessity to use much more expensive nickel-based

superalloys. Modified 9% Cr steels were also adopted by the fusion society in low activation versions and finally by the VHTR society as a highly creep resistant candidate alloy for reactor pressure vessel and/or core internals. Materials data exist in international databases like the Japanese NIMS [7] or the European ODIN [8]. But there are still data lacking to cover several VHTR needs. For the future it is planned to establish a Generation IV materials handbook on the web [9]. Damage assessments in existing design codes, however, also need to be modified or enlarged to cover VHTR applications.

Typical damage mechanisms

Key elements of a VHTR must be designed for a lifetime of 60 years corresponding to about 500 000 hours of service. Even for a well-established set of data this needs considerable extrapolation, as shown in Figure 1.

Figure 1. Creep rupture data for Grade 91 steel (digitised from literature [10])



From this set of data it can be seen that above 70 000 hours only very limited amount of data exists and that the scatter can reach two orders of magnitude in rupture time (not only for the digitised, but also for the original data). Extrapolation to 500 000 hours and lower bound scatterband considerations are necessary. The set of data is surprisingly robust concerning extrapolation.

Table 3 lists four different 200 000 hour stress rupture extrapolations. The values for MRM, LM and MC were taken from the original paper [10] whereas “this paper” was obtained with the digitised set of data from Figure 1 according to the formula:

$$\log_{10}(t_R) = T.(A.\log_{10}(\sigma) + B.\sigma + C) + D \quad (1)$$

with t_R being stress rupture time, σ being the applied stress and A, B, C, D being constants. The data are quite close together and even the predictions from Eq. (1) fit surprisingly well taking into consideration that no original data were available for this fit. The high amount of scatter of the data reflects the different microstructures which can be present in huge forgings due to forgeability and

Table 3. Grade 91 creep rupture extrapolations for 200 000 hours at three different temperatures

*MRM – Mendelson, Roberts, Manson, LM – Larson Miller MC – minimum commitment
This paper – according to Eq. (1) with data digitised from [10]*

550°C	MRM	141 MPa
	LM	147 MPa
	MC	137 Mpa
	This paper	132 MPa
600°C	MRM	77 MPa
	LM	86 MPa
	MC	76 Mpa
	This paper	74 MPa
650°C	MRM	38 MPa
	LM	46 MPa
	MC	39 Mpa
	This paper	35 MPa

local effects of heat treatment. It has also to be stated that the data were measured with virgin material. Thermal ageing, weldments and eventual environmental effects need separate considerations. According to nuclear design criteria, the reactor pressure vessel is not allowed to operate in the creep regime, meaning that conditions for negligible creep must be established. Extrapolations of creep strains and stress rupture data thus correspond to low temperatures (425-500°C).

Other critical design issues are fatigue and creep-fatigue interactions. A high portion of fatigue at high alternating strains (low cycle fatigue, LCF) is a crack growth phenomenon for cracks starting from stress raisers like inclusions and/or persistent slip bands. With increasing number of cycles the stage of crack initiation becomes the dominant part. In contrast to the LCF type of damage, creep damage occurs very often in the bulk and along grain boundaries. Creep type of damage can also occur during cyclic load with low strain rates at elevated temperatures. Environment must also often be considered. All these facts make it very complicated to find appropriate creep-fatigue interaction rules and even the results of experiments depend on the definition of failure of the specimen. We would like to illustrate this with a simple example: taking number of cycles to failure in a fatigue test as failure criterion might not be an appropriate choice because there is much experimental evidence showing that at about 50-80% of LCF life the sample contains propagating fatigue cracks. If this sample is then exposed to creep testing it will most probably fail prematurely. This is certainly not a result of a creep-fatigue interaction in the bulk. Similar considerations can be made for other types of interactions, too. These examples demonstrate the importance of the choice of a proper failure criterion. The usual way of treating creep-fatigue interactions in codes or for design purpose is the assumption of a linear life fraction rule linking the actual number of cycles at a given strain range, n , the number of cycles to initiation or failure N_f (endurance value, not necessarily fracture), the time maintained over a certain creep period t and the time to creep failure (not necessarily fracture) at the same stress t_f by a simple linear life fraction rule:

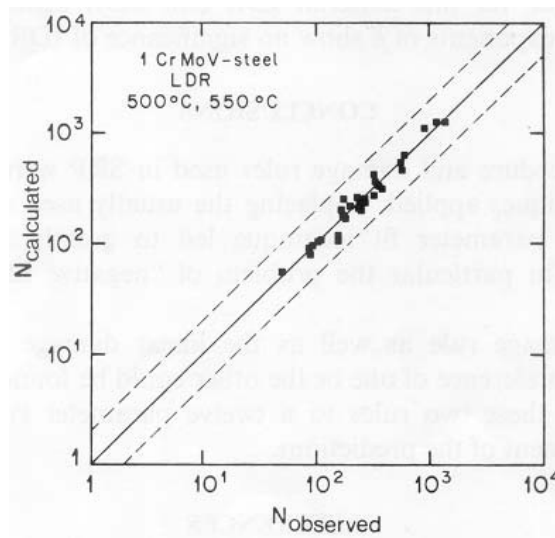
$$N/N_f + t/t_f = D \quad (2)$$

D depends on the material and can take almost each value between 0.1 and 1. Although this is a very simple approach containing no physics at all it is still in use for design purpose. The main reason is that it is difficult with currently available tools to take cyclic softening, shake down of mean stress and the other facts mentioned above properly into consideration. As an improvement we propose to use the number of cycles to crack initiation instead of the number of cycles to failure and a strain or ductility

related measure for creep failure (e.g. ductility exhaustion). This all requires further data which must be produced under well-defined conditions with well-defined damage criteria. It should be mentioned that a huge amount of literature exists offering alternative damage interaction assessments (e.g. [16,13]).

Although they can lead to very good correlations of creep-fatigue experiments (e.g. Figure 2 [11]) they are not easy to apply to a real component because of many uncertainties concerning response of materials under complex service loads. It is therefore often necessary to treat situations relevant to component life with additional considerations like e.g. crack growth or specific environmental assessments [12]. Improvements of the current approach for creep-fatigue interactions are certainly necessary, but they are not easy to establish. For the far future chances exist to employ advanced materials modelling tools to assist in lifetime assessments under complex creep-fatigue loading.

Figure 2. Creep fatigue life for CrMoV steel using the strain range partitioning approach (after [11])



Besides damage due to mechanical load also environmental effects play an important role for damage in VHTRs. The reactor coolant helium contains CO, CO₂, H₂O, O₂ as impurities which can lead to corrosion effects at the high operation temperatures. For core applications radiation effects must also be considered.

Related ASME tasks

It is clear that the issues mentioned above need specific consideration in design particularly when new designs or enhanced operation conditions occur, like in a VHTR. Their importance can be seen from the fact that they play a central role in more than only one task. Task 1 is aimed at a verification of allowable stresses in ASME Section III, Subsection NH with emphasis on the materials 800H and Grade 91 steel base materials and weldments. Review of Alloy 800H and Grade 91 stress allowables and extension of time-dependent allowable stresses to 900°C are performed. The work is based on reviews of international databases and currently employed methods. Using these assessments supplementary testing to address the needs to provide a sound design code for VHTR is identified. Task 3 is aimed at an improvement of ASME Subsection NH Rules for Grade 91 steel concerning negligible creep and creep-fatigue. Negligible creep is a very important issue for the reactor pressure vessel which has to be designed without creep. In addition to task 1, task 3 is also concerned with

creep-fatigue interactions. As another output of this work an identification of tests required to support the definition of negligible creep conditions and the creep-fatigue procedures for Grade 91 steel is expected. Within task 5 available creep-fatigue data are collected and existing creep-fatigue evaluation procedures for Grade 91 steel and Hastelloy XR are studied, mainly based on Japanese experience. Data on cyclic inelastic behaviour are also collected. Creep-fatigue is of importance in task 7 on NH evaluation and simplified methods. In this task different current design methods of different codes and standards are to be reviewed and compared. Creep-fatigue methodologies, crack growth, damage-based and strain-based methods are to be studied including aging, crack initiation, surface and environmental effects on relevant materials. Life prediction models, extrapolation of data, test data and techniques shall be included. A specific task 9 will analyse environmental and neutron fluence effects in structural design criteria of ASME Section III Subsection NH and for VHTR and GenIV designs. Needs for inclusion of environmental and neutron fluence effects in design criteria for VHTR core support structures are to be evaluated including the role of environmental degradation and neutron fluence degradation in the design for metallic core internal structures of high-temperature gas-cooled reactors. Obtaining VHTR conceptual design information is essential to the development of supplemental design criteria. This information will include materials of construction, expected range of temperatures, expected range of gas compositions, expected neutron fluence, capabilities for component replacement, and the like. Task 8 asks for a proposal of identifying future test needs to validate elevated temperature design of VHTR.

Other topics

Graphite and structural components

The graphite components of the reactor are the permanent inside and outside reflectors, the core blocks (in the case of a block-type core reactor) and the core supports. Procurement of new graphite grades will be undertaken for meeting the VHTR in-service conditions. New fine-grained isotropic graphite types with high strength and low irradiation damage will be required to achieve high outlet gas temperature, long life and continuity of supply. Extensive irradiation and properties test data are needed to qualify the new materials. Establishing a mechanical and thermal property database is necessary for core design. Material performance modelling will help to assess irradiation and oxidation damage, and predict graphite components lifetime.

Carbon fibre reinforced carbon (CFRC) composites with allowable temperatures up to 1 800°C and other ceramic composite materials (for example, SiC/C and SiC/SiC) have been proposed for several subcomponents in the control rod assembly. The CFRC and SiC/SiC composite and ceramic materials are relatively new reactor materials for which considerable irradiation and other material properties data are needed. Standardisation and codification of materials are major issues that will need to be resolved for use of these materials in reactor safety-related systems. For example, in a typical SiC/SiC composite tube, the continuous SiC fibres are bound together inside a SiC matrix using a chemical vapour infiltration and matrix densification technique. This SiC matrix material coats and surrounds the continuous fibres, producing a solid SiC matrix with embedded SiC fibres. Mechanical and thermal property, fracture behaviour, and other tests, including oxidation effects and post-irradiation tests are required to establish design guidelines and a design database. The modelling of the material behaviour and stress analyses in these codes will need to consider the anisotropic nature of these materials. Obtaining non-destructive testing data and fracture toughness data is necessary to establish acceptance guidelines. Task 6 was therefore created for graphite and ceramic code development. This task will support development of design rules and code requirements for qualification of non-metallic components, including carbon-carbon composites and ceramics such as SiC/SiC composites for advanced VHTR plant designs.

Intermediate heat exchanger

The intermediate heat exchanger (IHX) plays a central role concerning heat applications. It is used to transfer the heat from the primary cycle to secondary loops. Currently there is no IHX specific code available. It should therefore be developed as addressed in task 10. The intent of this task is to determine how and where within ASME codes and standards the IHX, safety valve, etc. would be addressed. In order to answer this question, many technical questions need to be tackled to determine how the function of such components affects the plants safety. Aspects of materials, design, fabrication, testing, overpressure protection and in-service inspections must be considered amongst others. Working fluid temperatures at the upper end of the creep regime of the materials employed must be considered. Cyclic life, qualification of materials and fabrication techniques must be included.

Leak before break and improved non-destructive evaluation (NDE) methods for metals

Leak-before-break (LBB) refers to a methodology that means that a leak will be discovered prior to a fracture occurring in service. LBB also has several technical definitions. LBB can occur under stress controlled conditions for an axial flaw in a pipe where the penetration of the wall thickness will result in a stable axial through crack. For instance can thermal expansion stresses become an LBB case under displacement control for a circumferential crack in a pipe. A comprehensive discussion of LBB can be found in the literature [14]. LBB analyses are deterministic, but they could be extended to probabilistic evaluations as well. LBB combines crack detection and fracture mechanics assessments and is closely related to NDE methods for metals. Although in-service inspections and advanced ultrasonic methods are well established in the nuclear field there are specific items to be considered for VHTRs. The temperatures are much higher than in conventional LWRs and main piping materials are austenitic (eventually even coarse grained). High damping of ultrasound and high noise levels need to be taken into consideration for flaw detectability limits and flaw sizing. LBB and NDE are addressed by tasks 11 (flaw assessment and LBB approaches) and 12 (improved NDE methods for metals). Within the LBB task fracture mechanics methods with respect to crack growth and stability should also be studied. For NDE specific emphasis should be given to a reliability-based load and resistance factor design (LRF) [15] development.

Conclusions

Design of advanced plants or components need a code work containing design curves and design rules which allow manufacturing and safe operation throughout the envisaged operation time. If key parameters like temperature, operating conditions, expected lifetime or materials change, existing codes must be adapted or even new codes must be established. We tried to highlight such an approach for the GENIV VHTR design based on an ASME procedure for the NGNP. Besides code modifications and early consideration of regulatory concerns relevant materials data like long-term creep data, negligible creep, fatigue, creep-fatigue interactions, environment and irradiation must be considered for metals and – where necessary – also for ceramics. Codes for specific components (IHX) must be established and plant safety considerations in terms of fracture mechanics and non-destructive evaluation must be taken into consideration. Although demonstrated here for VHTR the basic elements of this approach also apply to other types of advanced plants.

Acknowledgements

Work was partly done within the DOE/ASME Materials Project in collaboration with ASME Standards Technology, LLC. The support is greatly acknowledged.

REFERENCES

- [1] http://www.ne.doe.gov/genIV/documents/gen_iv_roadmap.pdf, visited May 2007.
- [2] <http://www.neimagazine.com/story.asp?storyCode=2039562>, visited May 2007.
- [3] <http://files.asme.org/STLLC/9274.pdf>, visited May 2007.
- [4] Stoller, R.E., T. McGreevy, “Examples from US High Temperature Design Strategy”, *IEA Workshop Symposium on Fusion Reactor Materials Development*, Tokyo International Exchange Center Tokyo, Japan, 10-12 July 2006, <http://insdell.tokai-sc.jaea.go.jp/IEA-FM-symp/presentation/2nd/18.pdf>, visited May 2007.
- [5] Shah, V.N., S. Majumdar, K. Natesan, *Review and Assessment of Codes and Procedures for HTGR Components*, NUREG/CR-6816 ANL-02/36.
- [6] Shindo, M., T. Kondo, “Studies on Improving Compatibility of Nickel-base Alloys with a High-temperature Helium-cooled Reactor Environment”, *Proc. Int. Conf. on Gas-cooled Reactors Today*, Bristol, British Nuclear Energy Society, Vol. 2, 96-119 (1982).
- [7] http://mits.nims.go.jp/db_top_eng.htm.
- [8] https://odin.jrc.nl/eng_welcome.html.
- [9] http://nuclear.inl.gov/deliverables/docs/geniv_handbook_imp_plan.pdf.
- [10] Cipolla, L., F. Cirilli, *New Creep Rupture Assessment of Grade 91*, <http://www.msm.cam.ac.uk/phase-trans/2005/LINK/162.pdf>, 2005, visited May 2007.
- [11] Hoffelner, W., K.N. Melton, C. Wuethrich, “On Lifetime Predictions with the Strain Range Partitioning Method”, *Fatigue of Eng. Mat. Struct.*, Vol. 6, No. 1, 77-87 (1983).
- [12] Hoffelner, W., “Lifetime Analysis of Highly Loaded Hot Section Components in Industrial Gas Turbines”, *Conf. on Life Assessment and Repair Technology from Combustion Turbine Hot Section Components*, Phoenix, Arizona, 17-19 April 1990, Conf Proc. ASM 1990, 35-39.
- [13] Rémy, L., F. Rezai-Aria, R. Danzer, W. Hoffelner, *Evaluation of Life Prediction Methods in High Temperature Fatigue*, ASTM STP 942, 1988, 1115-1132.
- [14] Wilkowski, G., “Leak-before-break: What does it Really Mean?” *Journal of Pressure Vessel Technology*, Volume 122, Issue 3, pp. 267-272 (August 2000).
- [15] Load and Resistance Factor Design Specification for Safety-related Steel Structures for Nuclear Facilities, December 2003.
- [16] *Fatigue at Elevated Temperatures*, A.E. Carden, *et al.* (Eds.), ASTM STP 520 (1973).

EVALUATION OF NICKEL-BASED MATERIALS FOR VHTR HEAT EXCHANGER

**H. Burlet¹, J-M. Gentzbittel¹, C. Cabet², P. Lamagnère³,
M. Blat⁴, D. Renaud⁴, S. Dubiez-Le Goff⁵, D. Pierron⁶**

¹DRT/LITEN, CEA Grenoble

²DEN/DPC, CEA Saclay

³DEN/DTEC, CEA Valrhô

⁴EDF Les Renardières

⁵AREVA-NP Lyon

⁶AREVA-NP Saint-Marcel

Abstract

Two available conventional nickel-based alloys (617 and 230) have been selected as structural materials for the advanced gas-cooled reactors, especially for the heat exchanger. An extensive research programme has been launched in France within the framework of the ANTARES programme to evaluate the performances of these materials in VHTR service environment. The experimental work is focused on mechanical properties, thermal stability and corrosion resistance in the temperature range (700-1 000°C) over long time. Thus the experimental work includes creep and fatigue tests on as-received materials, short- and medium-term thermal exposure tests followed by tensile and impact toughness tests, short- and medium-term corrosion exposure tests under impure He environment. The status of the results obtained up to now is given in this paper. Additional tests such as long-term thermal ageing and long-term corrosion tests are required to conclude on the selection of the material.

Introduction

The selection of the commercial materials for the intermediate heat exchanger has been performed considering mainly creep strength and corrosion resistance at high temperature. Two candidate materials have been selected. The nickel-based alloy NiCr22Co12Mo (Alloy 617) was widely studied in the early 80s for HTR application, particularly by the German team [1-2]. It has been shown that the mechanical performances of this alloy meet the HTR requirements, but also exhibits rather poor corrosion resistance under impure helium leading to significant internal oxidation. Moreover, carburisation or decarburisation may occur depending on the exposure temperature and on the helium coolant chemistry (carbon activity). Additional tests are thus required before assessing this material performance. Over the last twenty years, alloys manufacturers have developed several alloys with improved corrosion resistance to high temperatures. Among them, Alloy 230 (NiCr22W14) exhibits the best corrosion resistance to high-temperature and long-term thermal stability. This material has thus been selected as a second candidate material in the ANTARES programme.

Various product forms have been ordered: bars, thick hot rolled plates and 2 mm cold rolled sheets. Tests are dispatched between CEA, EDF and AREVA laboratories in a joint research programme. All the data are then collected in a database for further design studies. The programme addresses the following issues:

- baseline mechanical property data under air environment;
- long-term thermal stability;
- effect of helium coolant chemistry on materials degradation;
- corrosion effects on mechanical properties.

This programme began in 2003 and is still under way. This paper is a review of the results obtained up to now.

Selected commercial alloys

The composition of the heats used for the bars and sheets are reported in Table 1. The mechanical tests and the metallurgical examinations have been conducted on the bars, whereas the corrosion tests and creep tests under impure helium environment have been carried out on the sheets.

Table 1. Composition of the studied heats

Alloys	Ni	Cr	Fe	C	Si	Co	Mo	Al	Ti	W	Others
617 sheet	b.	21.55	0.95	0.06	0.18	12.1	9.21	1.01	0.42	–	Cu:0.1
230 sheet	b.	22.02	1.33	0.1	0.35	0.2	1.30	0.38	0.01	14.28	Mn:0.53
617 bar	b.	21.3	0.29	0.06	0.08	12.1	9.1	0.9	0.41	–	Cu:0.01
230 bar	b.	22	1.8	0.1	0.4	0.2	1.5	0.3	0.01	14.1	Mn:0.5

Typical microstructures of Alloys 617 and 230 are given in Figures 1 and 2. The grain size of Alloy 617 is larger than that of Alloy 230. Both materials contain several carbides. Alloy 230 contains quite large carbides rich in W inside the grains and small Cr-rich carbides along the grain boundaries. Alloy 617 contains some TiC along the grain boundaries and several $M_{23}C_6$ and M_6C (Cr and Mo rich) precipitates inside the grains.

Figure 1. Microstructure of Alloy 230

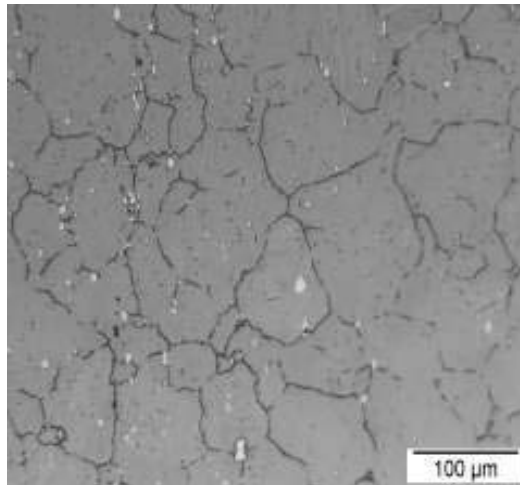
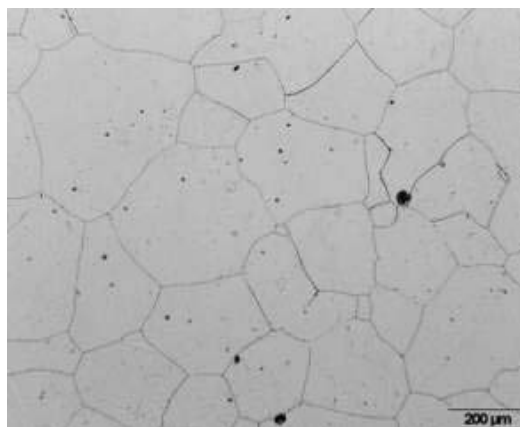


Figure 2. Microstructure of Alloy 617



The tensile properties of both materials have been determined up to 1 000°C. Alloy 230 exhibits higher strength than Alloy 617 up to 750°C. At 850°C and 950°C, the strengths of both materials become similar. The ductility of Alloy 617 is higher than that of Alloy 230 up to 750°C, for higher temperatures ductilities of both materials become similar. Moreover, yield and maximum tensile strengths are very close beyond 850°C which leads to difficulties to define design criteria at such temperatures.

Ageing mechanisms

Thermal ageing tests have been performed on both materials up to 5 000 h under several temperatures (700°C, 750°C, 850°C and 950°C) to provide information on the residual strength and ductility after service exposure. Microstructural examinations and short-term mechanical tests (tensile at room temperature and exposure temperature test, impact toughness at room temperature) have been conducted on the aged materials.

Tensile properties and impact toughness of aged 617 and 230

The results of tensile tests at exposure temperatures in Figures 3 and 4 show that for Alloy 617 and above 800°C the strength remains unchanged between un-aged and 5 000 h aged, whereas at lower temperatures both hardening and loss of ductility are observed. For Alloy 230, no hardening effect occurs in the range [700°C-850°C], and a slight softening is observed at 950°C. A loss of ductility is observed for all ageing temperatures, but it is less pronounced at 850°C. Similar results have been obtained after 1 000 h of thermal exposure tests.

Impact energy values measured at room temperature for both materials after thermal exposure up to 5 000 h at temperatures from 700°C to 950°C are plotted in Figures 5 and 6. A drastic drop is observed especially for Alloy 617. The minimum values obtained at 950°C close to 30J are similar to the values obtained by Schubert [1] and Breitling [2]. According to these authors, longer exposure tests do not lead to additional decrease of the impact energies. Moreover, they consider that RT-impact strengths are of minor importance for the design rule. Concerning Alloy 230, the impact values are lower than those of Alloy 617 for intermediate ageing temperatures [700-850°C], but the values slightly increased for higher temperatures. Since no other data are available for Alloy 230, it is clear that longer tests are required to reach stable values that will allow to conclude on the degradation of the mechanical performance of this material.

Figure 3. UTS after thermal ageing 5 000 h

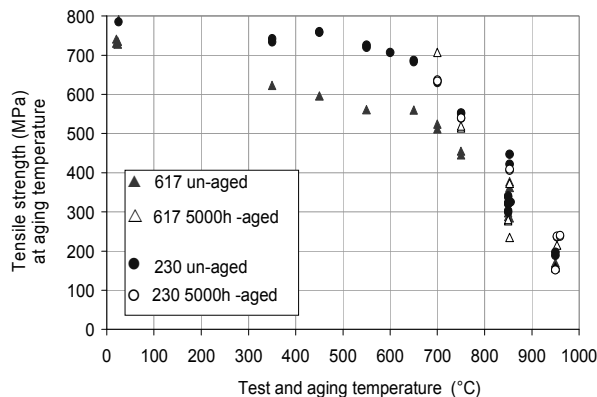


Figure 4. Elongation after thermal ageing 5 000 h

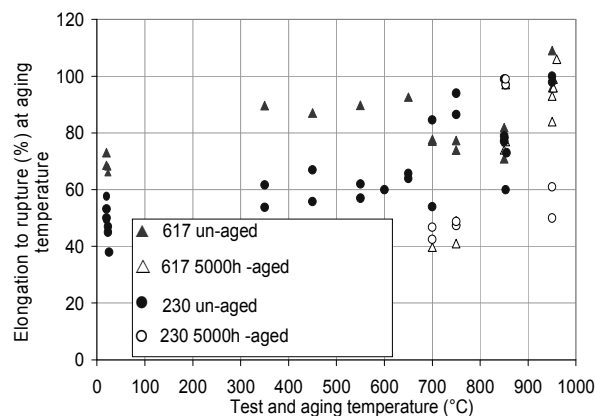


Figure 5. RT-impact energy of aged 617

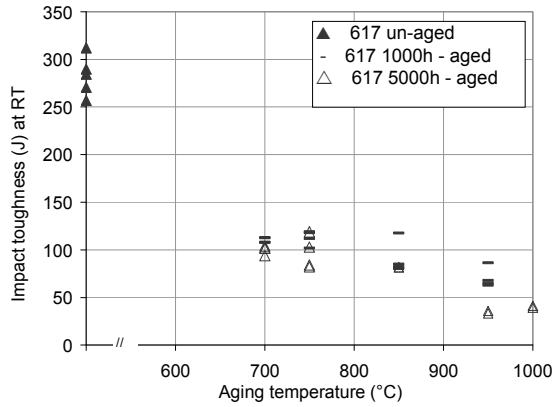
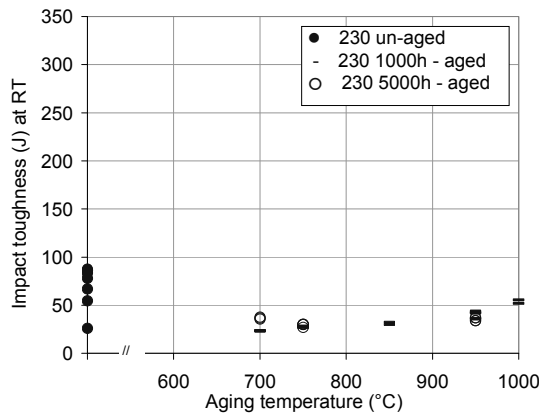


Figure 6. RT-impact values of aged 230



Microstructure of aged 617 and 230

Fine microstructural examinations have been performed at both SEM and TEM scales. For both alloys, the grain size remains unchanged with exposure temperature and time, though many precipitates are formed. Microstructural ageing of Alloy 617 is characterised by a very dense intragranular precipitation of $M_{23}C_6$ carbides especially along dislocations (Figure 7). The size of the carbides increases with the ageing temperature. Mixed $M_{23}C_6$ and TiC precipitates are formed at 950°C. For Alloy 230, precipitation of $M_{23}C_6$ carbides occurred mainly at the grain boundaries. The shape of the carbides varies with the temperature: lamellar or faceted for temperatures up to 850°C and globular for higher temperatures (Figure 8). The carbide precipitation is responsible for the embrittlement observed for both materials at room temperature; however, these changes of microstructure lead only to limited modifications of the high-temperature mechanical properties.

Fatigue properties

Low cycle fatigue tests have been conducted in air on both materials at 850°C. The results are plotted in Figure 9, in which average values extracted from KTA [3] on Alloy 617 are also reported. It can be seen that our test results are slightly lower than the average German data. Alloy 230 exhibits better fatigue performance than Alloy 617 due to its smaller grain size.

Figure 7. TEM observation of Alloy 617 aged 1 000 h at 700°C

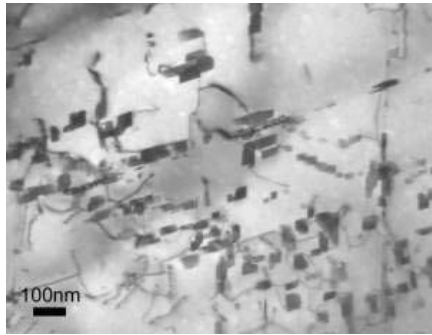


Figure 8. TEM observations of Alloy 230 aged a) 1 000 h at 850°C, b) 1 000 h at 950°C

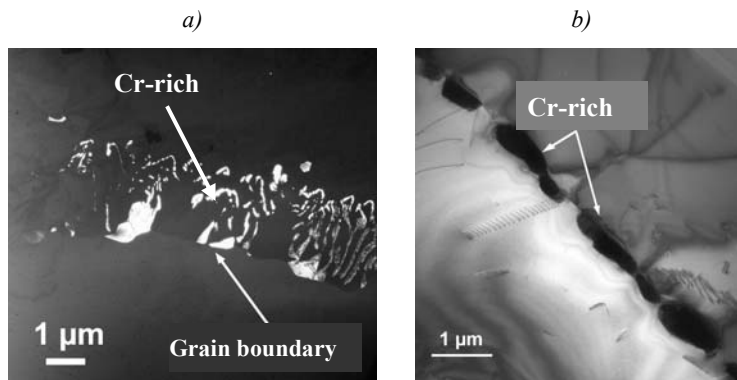
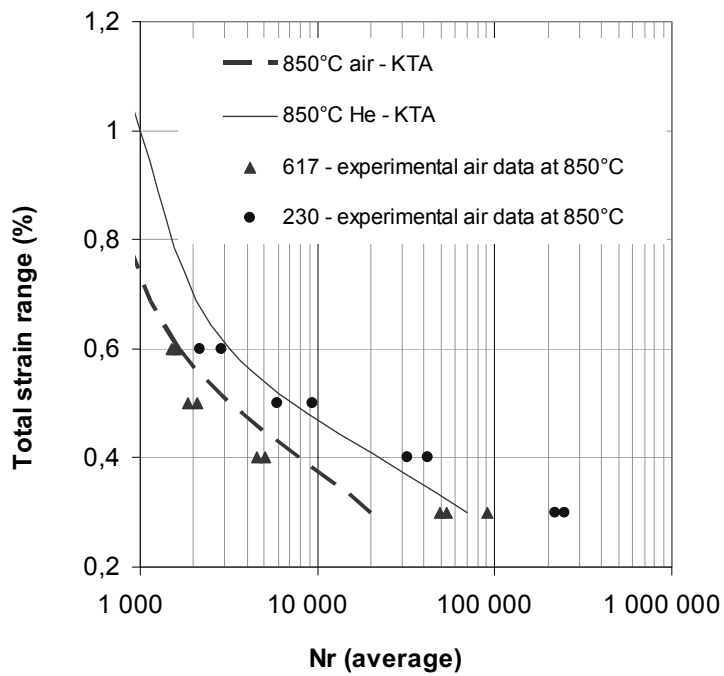


Figure 9. Low cycle fatigue results



High-temperature corrosion behaviour under impure He

Design of the experiments

Operative experience from experimental HTRs [4,6] indicates that helium contains residual contaminants. Impurities mainly result from degassing of adsorbed species out of permanent components such as H₂, CO (and CO₂), CH₄, N₂ ranging from few microbar to hundred μ bar or so and water vapour in the microbar range. It is worth noting that oxygen potential is extremely low in HTR atmosphere. Although at very low levels in helium, impurities are reactive toward hot metallic materials. Generally speaking, high-temperature corrosion resistance of chromia former alloys relies on the formation of a surface chromium-rich oxide scale that must be adherent, dense and slow-growing and so may prevent any gas from accessing to the metal. This regime is called passive oxidation. For long-term integrity of IHX material, the VHTR environment must thus definitely allow oxidation. According to the thermodynamics and the kinetics of the impurity/metal reactions this implies that for a given material:

- P(H₂O)/P(H₂) ratio, related to the oxygen potential, must be oxidising with regard to chromium;
- partial pressures of carbon-carrying species (methane and carbon monoxide) relatively balance the partial pressure of water vapour;
- P(CO) is higher than a critical level that mainly depends on temperature [7,8]; in another work [9,10], the variation of critical P(CO) vs. temperature has been established for Alloy 230.

These criteria delineate the borderlines of a “benign atmosphere” domain in which passive oxidation can occur. If gas conditions fall out of the benign domain, impurities have access to the surface and exchange carbon with the metal. This carbon transfer can rapidly cause in-depth changes in the alloy microstructure, carburisation or decarburisation, both detrimental to the mechanical properties at ambient temperature and elevated temperature.

For long-term resistance of IHX materials, VHTR normal operating conditions must obviously fall within the benign atmosphere domain and knowledge on the metallic surface reactivity should allow designing an appropriate set of specifications on impurities contents. The question is whether one of the two IHX candidate materials performs better in such a benign environment. Thus we carried out short-term corrosion tests under a benign test helium at 950°C in order to describe the corrosion behaviour of Alloys 617 and 230 and to compare their resistance. In another paper, we discuss the damaging consequences of out-of-specification situations [11].

Experimental

Materials

Coupons of 5 cm² were machined in the as-received alloys sheets. The specimen surfaces were mechanically ground to 1 200-grit emery paper, and then cleaned ultrasonically in an acetone/alcohol mixture.

Test conditions

Corrosion tests were performed in the CORALLINE facility (described in [12]) that allows exposing specimens to impure flowing helium. They ran for up to 1 000 hours at 950°C. The gas flow

rate was $10 \text{ ml}\cdot\text{min}^{-1}$ per cm^2 of specimen surface. Considering our previous work [8-10] on the high-temperature reactivity of Alloy 230, we designed a benign test gas mixture that contains about 200 μbar H_2 , 50 μbar CO and 20 μbar CH_4 . No water was deliberately added but the residual amount of water vapour was around 2 ppm. Table 2 gives the experimental concentration ranges and the corresponding oxygen and carbon potential with the assumption by Quadackers in Ref. [7].

Table 2. Composition, oxygen partial pressure and carbon activity of the test gas at 950°C

H_2 (μbar)	CH_4 (μbar)	CO (μbar)	H_2O (μbar)	N_2 (μbar)	O_2 (μbar)	P_{O_2} [Pa]	a_{C}
189±6	20.1±0.5	50.6 ±1.4	~2.1	<8	<0.1	$10^{-19.8}$	$10^{-3.8}$

Post-exposure observations

After exposure the specimens were weighted and evaluated metallographically. Microstructure of the corroded alloy was observed and analysed using optical microscope, SEM equipped with an EDS-probe and XRD.

Results

Mass gains

Table 3 displays the mass changes after exposure. Every specimen gains weight. Mass gains globally increase with time and are significantly higher for Alloy 617.

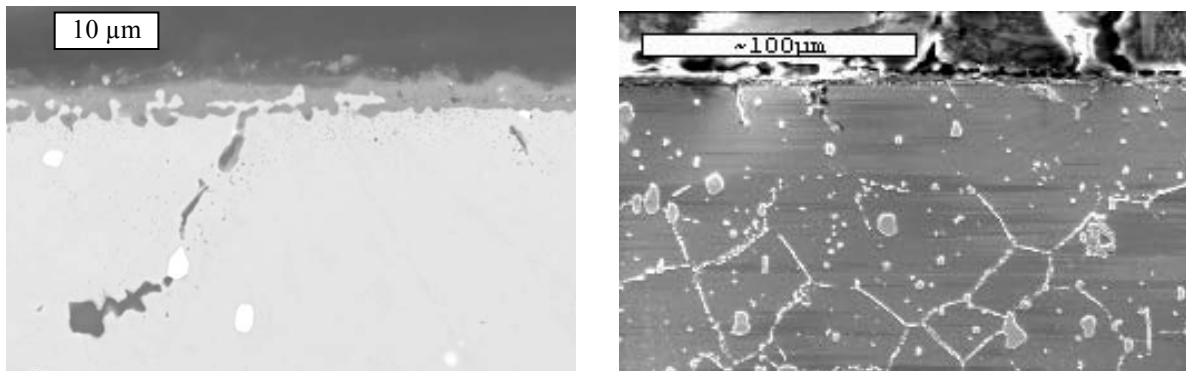
Table 3. Mass gain, average thickness of the oxide scale, mean depth of the carbide-free zone for Alloys 230 and 617 exposure to impure helium

	Time [h]	Mass gain [$\text{mg}\cdot\text{cm}^{-2}$]	Surface scale [μm]	Carbide-free zone [μm]
Alloy 230	226	0.29	1.5	
	239	0.38	2	30
	498	0.46	2	
	518	0.43	2	30
	813	0.66	3	55
	1 027	0.63	3	
Alloy 617	239	0.45	1	35
	518	0.70	2	45
	813	1.19	5	65

Oxidation of Alloy 230

Figure 10 shows cross-sections of the 813-hour coupon. A duplex surface oxide scale has formed with a Cr-Mn spinel at the outside and an inner Cr-rich oxide. Table 3 gives the scale mean thickness. Besides the formation of surface corrosion products, the exposure in He has also induced a change in the alloy microstructure. Beneath the surface layer, Al has oxidised at the grain boundaries up to 40 μm deep in the bulk alloy. Moreover a sub-surface zone free of secondary carbides precipitation due to thermal ageing is observed.

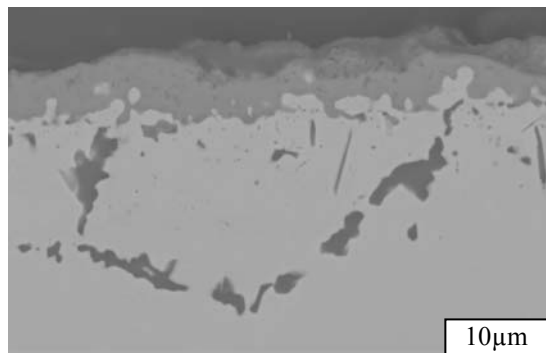
Figure 10. SEM pictures of Alloy 230 specimen exposed 813 h in test He at 950°C



Oxidation of Alloy 617

Figure 11 shows a cross-section of Alloy 617 after 813 hours in test He at 950°C. An irregular, rather thick, chromia-scale significantly doped in Ti has grown on its surface (see Table 3). Besides, Alloy 617 has suffered from an intense internal oxidation that contributes for about one half to the mass gain. Al oxidised at all grain boundaries as well as within the grains.

Figure 11. SEM picture of Alloy 617 specimen exposed 813 h in test He at 950°C



Comparison of Alloys 230 and 617

In the previous sections, we identified changes in the alloy microstructure that characterise the corrosion behaviour in VHTR “benign atmosphere”. The set of data, given in Table 3, is used to compare the oxidation resistance of both candidates at 950°C. Mass gains and microscopic observations pointed out that Alloy 617 oxidised more than Alloy 230 in terms of total corrosion rate as well as internal oxidation.

Creep properties under impure He

Experimental

A specific creep facility named CORSAIRE has been developed to conduct creep tests under controlled atmosphere. Impure helium is provided by gas cylinder of controlled impurity levels. The moisture level is measured at CORSAIRE outlet using a dew point hygrometer with a capacitive

probe. The gas flow rate over the specimens is around 10 NI/h.cm². CORSAIRE is equipped with a 2 kN tensile device allowing creep tests on 1- or 2-mm thick plate specimens. The typical size of the uniform-gage test section is 25 × 5 mm². A reference unstressed sample can be tested at the same time and in the same operating conditions as the creep specimen. All specimen surfaces were mechanically ground to 1 200-grit emery paper before testing.

Two different helium chemistries have been tested: a “pure” helium and a chemistry close to the benign composition used in the CORALLINE facility. The definition of the atmospheres and the comparison to CORALLINE atmosphere are reported in Table 4. In fact the moisture level decreased during the tests due to furnace and circuit degassing, reaching a few 40 μbars after a few tens of hours. Compared to CORALLINE atmosphere, the content of hydrogen is higher in order to partially compensate for the higher water content. Therefore, this composition also corresponds to the “Cr₂O₃” domain in the modified stability diagram for chromium proposed by Quadackers in Ref. [7], which is the domain that promotes the growth of a protective oxide layer.

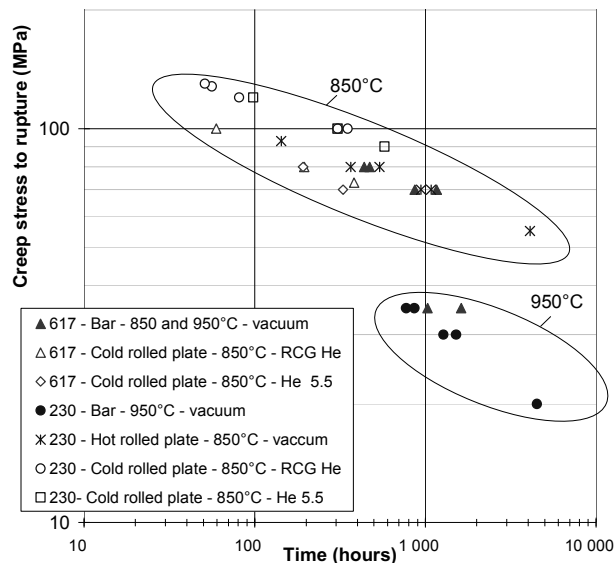
Table 4. Impurity contents in the helium of CORSAIRE tests

Atmosphere	H ₂ (μbar)	CH ₄ (μbar)	CO (μbar)	H ₂ O (μbar)
CORALLINE	189±6	20.1±0.5	50.6±1.4	~2.1
CORSAIRE He-GCR	500	20	50	<0.5
CORSAIRE He 5,5	<0.1	<0.1	<0.1	<2

Results

Figure 12 shows the creep rupture properties of Alloys 230 and 617 at 850°C in GCR helium and “pure” helium atmospheres. Some additional data obtained in vacuum at 850°C and 950°C are also plotted in Figure 12. In the conditions studied, i.e. “benign” atmosphere and medium-term creep tests, no significant effect of the atmosphere has been found on the time to rupture of candidate alloys. The scatter observed are related to the product form (vacuum data are obtained on bars) rather than on atmospheres.

Figure 12. Creep rupture properties of 617 and 230



Creep properties of the Alloy 230 sheet seem to be better at 850°C than those of Alloy 617 in terms of both creep rupture strength and minimum creep rates, according to the relatively short-term tests already performed. According to the first results obtained on bars at 950°C, the trend seems the opposite. Fractographic examinations revealed that creep damage occurred mainly by formation of cavities along the grain boundaries. Numerous intergranular cracks related to near-surface oxidation of aluminium have also been observed, mainly on Alloy 617. However, these cracks do not seem to play a significant detrimental role on the creep life of the alloys. No significant difference in the damage mechanisms has been found between tests performed in GCR helium and in “pure” helium.

Conclusions

An extensive programme has been launched in France in the framework of the ANTARES project on Alloys 617 and 230. Data generated in AREVA, EDF and CEA are gathered in a joint evaluation. The goal of this programme is to select the best material for the heat exchanger, and to collect data for design purpose. The programme is still under way but the first results lead to the following features:

Both alloys exhibit material evolutions for temperatures higher than 700°C, characterised mainly by carbide precipitation. These precipitates either inside the grain or along the grain boundaries lead to an embrittlement of the room temperature material properties (drop of impact energy values). However, the high temperature properties even if they withdraw some decrease compared to the as-received values, remain acceptable. After 5 000 h of exposure tests, neither material is stable, and longer tests are required to extrapolate the values for longer service operation life.

Both alloys behave quite similarly with regard to their mechanical properties in terms of fatigue and creep. The main behavioural difference is related to the variation in grain size between the alloys. Creep-fatigue tests under vacuum or impure helium environment are required to compare the mechanical performances of these two alloys.

Regarding corrosion resistance, the results obtained under a slightly oxidising atmosphere show a better resistance for Alloy 230 compared to Alloy 617. However, some inner oxidation has been detected along the grain boundaries in Alloy 230. It is expected that the use of a low Al cast of Alloy 230 might further improve its oxidation resistance in inhibiting the intergranular oxidation. Longer exposure tests and tests under various helium chemistries must be conducted before concluding upon the corrosion resistance of these alloys for VHTR application.

Manufacturing parameters are furthermore examined in order to perform a global analysis needed to choose the most convenient alloy for the IHX application.

REFERENCES

- [1] Schubert, F., *Proc. of a Symposium on Heat Exchanging Components of Gas-cooled Reactors*, Dusseldorf, IWGGCR-9, 309 (1984).
- [2] Breitling, H., *et al.*, *Proc. of a Symposium on High Temperature Metallic Materials for Gas-cooled Reactors*, Cracow, IWGGCR-18, 91 (1988).
- [3] *Metallic HTR Components*, Part 1, KTA 3221.1, draft version December 1992.
- [4] Graham, L.W., *et al.*, *Proc. of a Symposium on Gas-cooled Reactors with Emphasis on Advanced Systems*, Vol. I, International Atomic Energy Agency, Vienna, Austria, 319 (1976).
- [5] Sabaka, N., *et al.*, *Proc. GLOBAL 2005*, p. 263, Tsukuba, Japan, 9-13 October (2005).
- [6] Yao, M.S., *et al.*, *Nucl. Eng. Des.* 218, 163 (2002).
- [7] Quadackers, W.J., *Werkstoffe und Korrosion*, 36, 141 and 335 (1985).
- [8] Cabet, C. *et al.*, *Proc. HTR 2006 Conf.*, Sandton, SA, 1-4 Oct. (2006) E00000143.
- [9] Rouillard, F., *et al.*, *Proc. EUROCORR 2005*, p. 358, Lisbon, Portugal, 4-8 Sept. (2005).
- [10] Rouillard, F., *et al.*, *JNM* (2007), in press.
- [11] Cabet, C., *et al.*, these proceedings.
- [12] Cabet, C., *et al.*, *Mat. Corr.*, 57, N°2, 147 (2006).

AN UNCERTAINTY ASSESSMENT METHODOLOGY FOR MATERIALS BEHAVIOUR IN ADVANCED FAST REACTORS

D. Blanchet, K. Mikityuk, P. Coddington, R. Chawla
Paul Scherrer Institut, Switzerland

Abstract

The current study represents a first important step towards the extension of the FAST code system to perform a statistically-based uncertainty analysis of fast reactor fuel behaviour under base-irradiation conditions. The principal input parameters related to the physical models and to the system description (geometry, material properties, etc.) are characterised by their uncertainty ranges and probability distributions based on state-of-the-art knowledge. These input parameters are then randomly sampled with the use of a Monte Carlo method. The basic procedure has currently been implemented in the context of a statistical analysis of the thermal-mechanical behaviour of ETDR helium-cooled fast reactor fuel (MOX pins in stainless steel cladding) under base-irradiation conditions.

Introduction

The FAST code system [1], under development at the Paul Scherrer Institut, is devoted to the steady-state and transient analysis of advanced fast-spectrum reactor concepts in multiple domains, e.g. different coolants, fuel types, structural materials, reactor designs, etc. Stand-alone neutron kinetics, thermal-hydraulics and fuel behaviour codes are coupled together and are being qualified for analysis of different advanced fast-spectrum reactor systems. In particular, the FRED code [2] is used in the framework of the FAST code system for simulating fuel element thermal-mechanics under both base-irradiation and transient conditions, allowing for the evolution of fuel and cladding temperatures, fuel-clad gap heat conductance, inner gas content and pressure, fuel and clad stress-strain conditions (considering thermal-elastic-viscous-plastic deformation), fission gas release (FGR), fuel swelling, etc.

The current study represents a first important step towards the extension of the FAST code system to perform a statistically based uncertainty analysis of fast reactor fuel behaviour under base-irradiation conditions. The principal input parameters related to the physical models and to the system description (geometry, material properties, etc.) are characterised by their uncertainty ranges and probability distributions based on state-of-the-art knowledge. These input parameters are then randomly sampled with the use of a Monte Carlo method. The basic procedure has currently been implemented in the context of a statistical analysis of the thermal-mechanical behaviour of the ETDR helium-cooled fast reactor fuel [3] (MOX pins in stainless steel cladding) under base-irradiation conditions.

The assessment of uncertainties in the calculational results of the FAST code system is based on the statistical approach originally proposed at Los Alamos by McKay, *et al.* [4], and further developed and expanded at the Gesellschaft für Reaktor Sicherheit (GRS) in Germany [5] with the use of the Wilks' formula [6] and the quantification of uncertainty by means of tolerance limits. This methodology has already been successfully applied at PSI in the context of the BEMUSE project [7], and also for the objective quantification of prediction uncertainty for specific code physical models [7].

Main parameters of the ETDR start-up core

The European Technological Demonstration Reactor (ETDR) [3] aims at providing a vehicle for the demonstration of gas-cooled fast reactor (GFR) technology. It will provide a “first-of-a-kind” demonstration of this new technology and provide qualification of the innovative GFR fuel concepts and materials under prototypic fast neutron spectrum irradiation. The evolutionary approach of two successive core configurations will be considered, through a “start-up core”, based on conventional LMFBR pin bundle subassembly containing (U,Pu)O₂ fuel in stainless steel cladding, with inlet/outlet He temperature of 260/560°C and a “demonstration core”, based on GFR plate type subassembly (U,Pu)C-SiC, with inlet/outlet He temperature of 480/850°C. Although the ETDR MOX fuel pin design relies on existing technology, questions still remain on material structures for clad that will be submitted to fast neutron fluence and relatively high temperatures. The main characteristics of ETDR start-up core are summarised in Table 1. A fuel pin with an average linear heating rate of 85 W/cm is used for the analysis.

Sources of uncertainties considered

The effects of uncertainties on the most important input parameters, such as material properties, initial and boundary conditions related to the system description and physical models are considered as part of this analysis. Uncertainty ranges and distributions assumed in this study for the different variables under consideration are given in Table 2 as multipliers for the corresponding values. The following sections address, in more detail, the justification of the choice of these uncertainties.

Table 1. Main characteristics of the ETDR start-up core

Core thermal power (MW)	50
Cycle length (EFPD)	1 705
Fuel pellet material	(U,Pu)O ₂ (+A.M.)
Fuel cladding material	AIM1 austenitic stainless steel alloy
Fissile length (mm)	860
Pellet diameter (mm)	5.42
Clad inner diameter (mm)	5.65
Clad outer diameter (mm)	6.65
Operating coolant (He) pressure (bar)	70
Coolant flow rate (kg/s)	32
Core inlet temperature (°C)	260
Core outlet temperature (°C)	560

Table 2. Input uncertainty ranges and distributions for the parameters considered

Variable	Law	Min	Max	Mean	Std dev
Initial gap width	Uniform	0.88	1.12	–	–
Fission gas release	Normal	0.0	–	1.0	0.3
Fuel swelling	Uniform	0.6	1.0	–	–
Fuel thermal conductivity	Normal	0.0	–	1.0	0.1
Inner gas conductivity	Normal	0.0	–	1.0	0.11

Uncertainties in the initial gap width

The uncertainty in the initial fuel-clad gap width is relatively small because the fabrication tolerances for fuel pellet and cladding are very low (~0.1%). However, during the initial stages of irradiation (burn-up lower than 5 MWd/kgHM), there is a number of effects which significantly increase the uncertainty in the gas gap size. These effects include, first of all, fuel pellet cracking and relocation caused by thermal stresses as well as fuel densification as a result of a sintering process. Analytical examination of uncertainties in prediction of these effects with simple engineering models used in the FRED code showed that they could result in uncertainty in the fuel outer radius of up to 0.5%. Therefore, to take into account the uncertainties introduced by the relocation and densification models, we consider a uniform variation of $\pm 0.5\%$ of the initial fuel outer radius, which approximately corresponds to a uniform conservative variation of $\pm 12\%$ in the initial fuel-clad gap size. This uncertainty appears to be consistent with the specifications given in [9].

Uncertainties in fission gas release model

The fission gas atoms produced in the fuel either remain in the pellets and contribute to the swelling, or are released from the pellets and increase the rod inner gas pressure while reducing the heat transfer in the gap by degradation of the inner gas thermal conductivity (fission gases have a much lower conductivity than helium). The fission gas release model implemented in FRED is an empirical function of local fuel temperature, burn-up and linear heat generation rate, which is a modification of the engineering zone fission gas release model [10].

If one considers the wide spread of measured values and predictions of available models for FGR (see for example FUMEX-II code benchmark results in Figure 19 in [11] which show that FGR predictions by the different codes vary in the range from 5 to 35%), it appears that there is a rather large uncertainty in this important parameter. We assumed that the predicted gas release fractions are normally distributed with an approximate relative standard deviation of 30%. This assumption seems quite reasonable with regard to the FRAPCON-3 [12] recommendations on the modified Massih-Forsberg model ($\sigma \sim 100\%$ for $FGR < 1\%$, $\sigma \sim 50\%$ for $FGR < 0.1$, and $\sigma \sim 15\%$ for $FGR > 0.3$).

Uncertainties in the fuel swelling model

The fuel swelling, resulting from the progressive build-up of fission products, has two components:

- the solid fission product swelling which is linearly dependent on burn-up and has an averaged rate ranging from 0.6% to 1.0% ($\Delta V/V$) per 10 MWd/kgHM (according to [12]);
- the gaseous fission product swelling which occurs at high temperature and is related to the gas pressure in fuel pores.

The fuel swelling is assumed to be isotropic. Due to a relatively low linear heat generation rate in the ETDR core, a low temperature ($< 1000^\circ\text{C}$) swelling, i.e. mainly due to the solid fission products, dominates under ETDR conditions. In this case, the linear swelling rate is assumed to be uniformly distributed from 0.6% to 1.0% ($\Delta V/V$) per 10 MWd/kgHM.

Uncertainties in the fuel thermal conductivity

The degradation of fuel thermal conductivity with irradiation was predicted by Philipponeau's model [13], which has been implemented in FRED. This model correlates a range of experimental data and accounts for the effects of temperature, fuel burn-up, stoichiometry and porosity. On the basis of examining the spread of the test data which were used for deriving the correlation [13], we assumed a normal distribution for the predicted values of conductivity with a relative standard deviation of 10%. This value is consistent with the FRAPCON code recommendation [12] to use a relative standard deviation of 7% for burn-ups lower than 40 MWd/kgHM and 10% for burn-ups in the range from 40 to 60 MWd/kgHM [14].

Uncertainties in the inner gas thermal conductivity

The uncertainty in the gas-gap conductance depends on uncertainties in both the gas conductivity and gap width (in particular in case of swelling and cracking); as the initial gap size uncertainty is already taken into account, only the gas conductivity uncertainty is considered here.

In the open gap regime (ETDR conditions), the gap conductance due to the inner gas conductivity is calculated in FRED according to the classical Ross and Stoute model [15]:

$$h_{gas} = \frac{k_{gas}}{\Delta r_{gap} + \delta r}$$

where Δr_{gap} is the fuel-cladding radial gas-gap (m), δr the temperature jump distance to account for the imperfect heat transport across the solid-gas interface (m), and k_{gas} the thermal conductivity of the gas mixture (W/mK) which is calculated in FRED by the following equation:

$$k_{gas} = \prod_i k_i^{w_i}$$

where w_i stands for the gas component mass fractions (He, Ar, Kr, and Xe) and k_i are the individual gas conductivities given by the general temperature-dependent correlation: $k_i = k_0 * T^n$, using the fixed parameter k_0 and n given in Table 3 [16].

Table 3. Gas conductivity correlations

	k_0	n	Std dev on k at T = 900°C
He	2.639E-3	0.7085	6.6%
Ar	2.986E-4	0.7224	5.4%
Kr	8.247E-5	0.8363	4.8%
Xe	4.351E-5	0.8616	4.9%

These uncertainties were averaged to estimate the uncertainty on k_{gas} as equal to 11% (1σ). As different gases have similar uncertainties in their conductivities, the resulting standard deviation is assumed independent of the gas composition (and therefore of the burn-up).

Propagation of uncertainties

The statistical analysis has been performed using the GRS (Gesellschaft für Anlagen und Reaktorsicherheit) methodology, implemented in the code package SUSA [7]. A Monte Carlo method is used to generate N random samples of the input parameters, taking into account their ranges and probability distributions. These inputs are then processed by N code executions. The analysis of the output samples allows a determination of statistical tolerance intervals for the output parameters, with a certain probability content and a certain confidence level. The determination of this two-sided tolerance interval, including for example a fraction of at least $\beta = 95\%$ of the output population with a confidence level of $\gamma = 95\%$, requires a minimum number of $N = 93$ samples, with regard to the application of the Wilks formula [6]. However, to improve the statistical output results 500 samples were used.

The main statistical results concerning the fission gas release, gap size, inner gas pressure and peak fuel temperature are presented in Table 4 and in Figures 1-4. For each output variable, the table shows the mean and standard deviation, minimum and maximum values, as well as the confidence intervals including 95% of the population with a 95% confidence level.

Table 4. Uncertainty results at EOC

Values	Fission gas release, %	Gap size, μm	Peak fuel temperature, °C	Inner gas pressure, bar
Mean $\pm 1 \sigma$	11 \pm 4	19 \pm 8	872 \pm 38	28 \pm 2
Minimum – maximum	2 – 23	1 – 36	780 – 989	23 – 35
Lower – upper limit for $\beta = 0.95, \gamma = 0.95$	4 – 18	3 – 34	798 – 952	24 – 32

Figure 1. Fission gas release

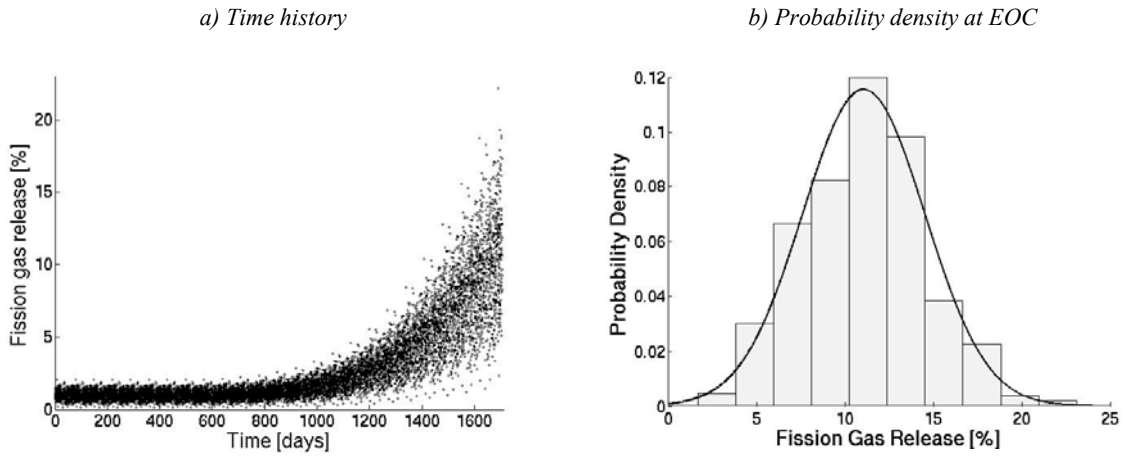


Figure 2. Inner gas pressure

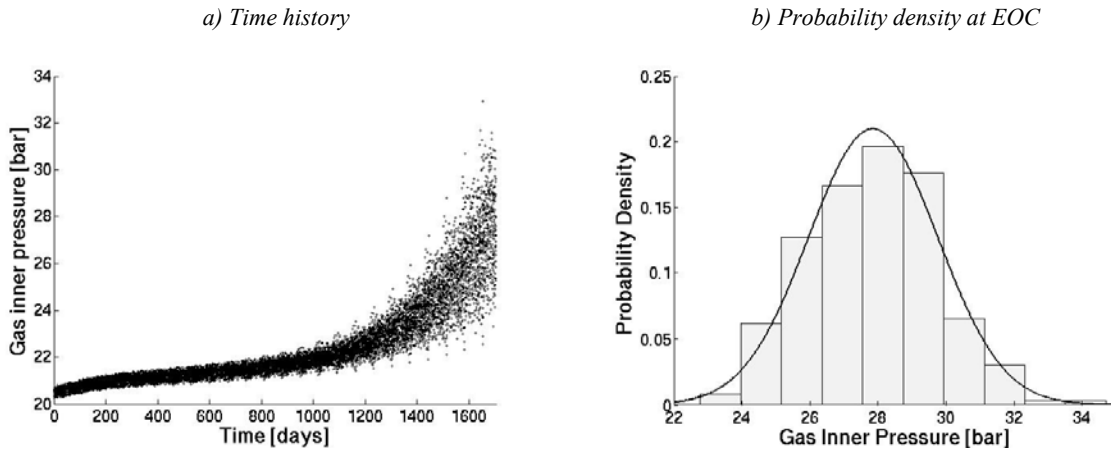


Figure 3. Gas gap size

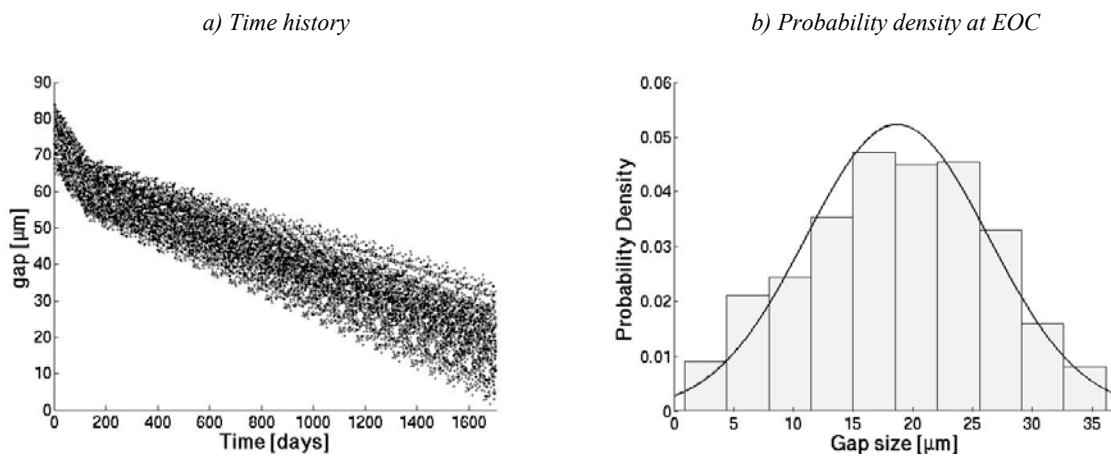
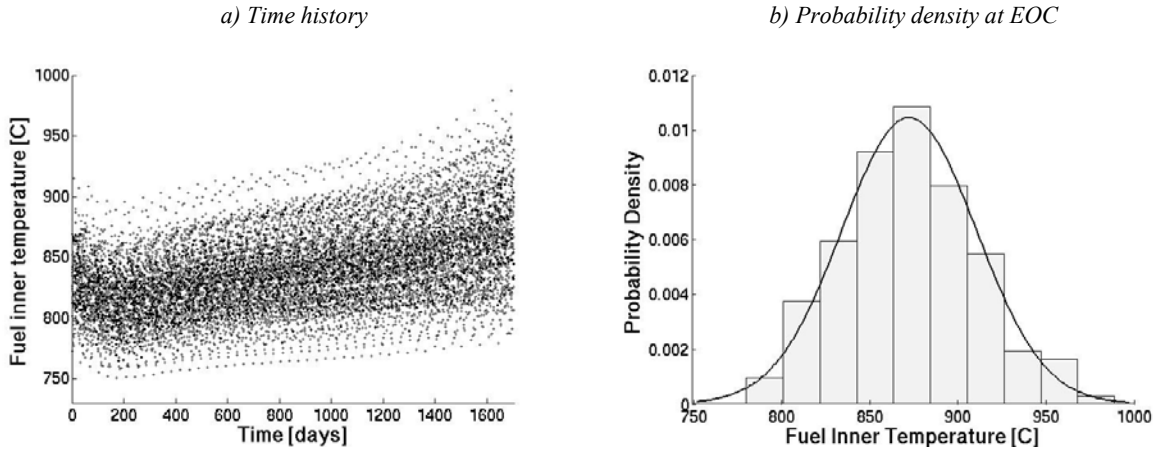
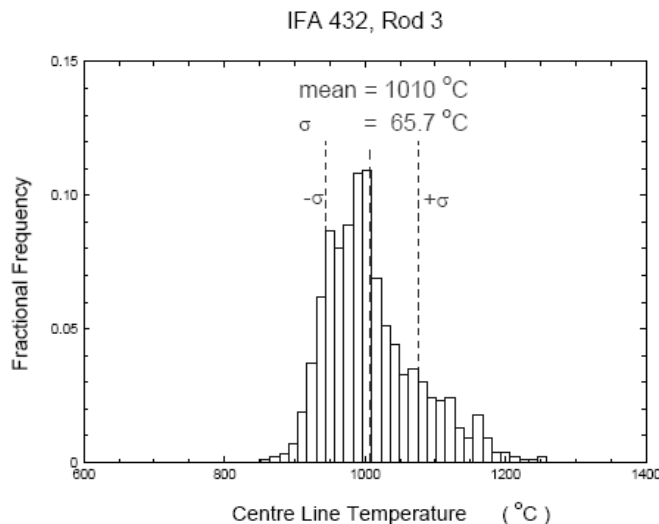


Figure 4. Peak fuel temperature



The Lilliefors's test of normality is passed successfully (with a significance level of 5%) for the different predictions: the histograms can indeed be fitted by normal distributions [Figures 1(b)-4(b)]. The fission gas release (Figure 1) is in fact one of the input parameters, so that the close-to-normal distribution obtained at EOC in this case [Figure 1(b)] serves to demonstrate the validity of the procedure for random sampling of the input parameters. The inner gas pressure increases due to the fission gas release (Figure 2), but remains lower than the coolant pressure. Therefore, the cladding hoop stress remains negative and the cladding undergoes no plastic deformation. Among the relatively small number of input variables currently considered for the propagation of uncertainties, the gap size at EOC (Figure 3) has the largest uncertainty (~41%). The tolerance limits obtained for the gap size reveal that, under the used assumptions, no pellet-clad mechanical interaction occurs during the entire base irradiation. The peak fuel temperature has a standard deviation of 4.4%, which is comparable with other analyses, e.g. the corresponding value presented in [11], and reproduced in Figure 5, is close to 6.5%. The difference may be explained by the fact that we did not take into account the uncertainty in the linear heat generation rate taken into account in [11].

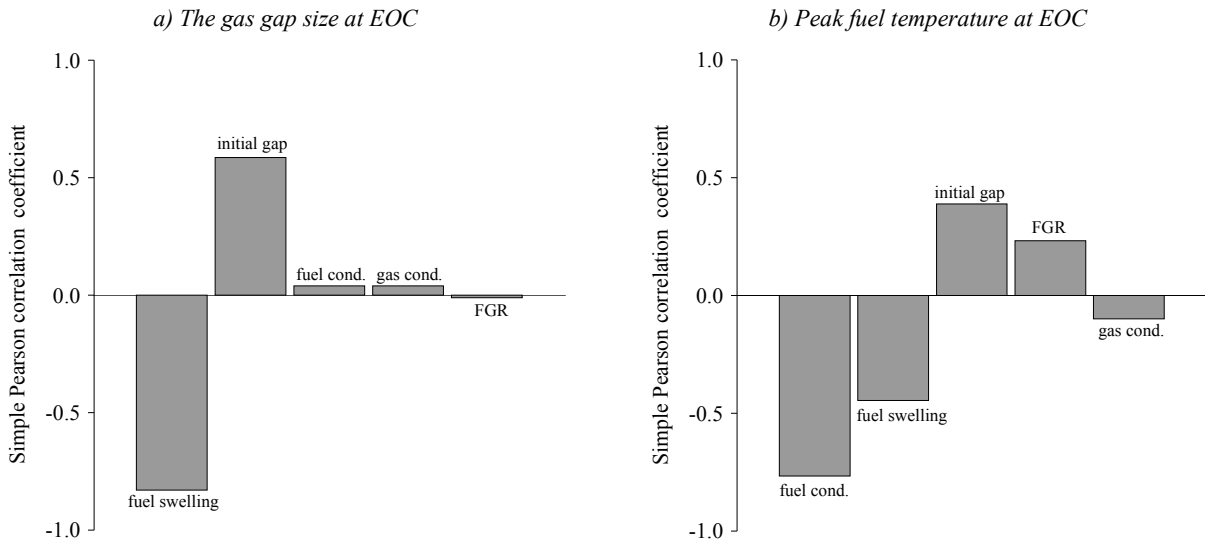
Figure 5. Fractional frequency of centreline temperature predictions when varying only three input parameters (q' , h_{gap} , λ) (figure from [12])



Sensitivity studies

The Monte Carlo uncertainty propagation method determines the tolerance limits for the output, as a global measure of the output variability with respect to the uncertainties in the inputs. However, it is also possible to supplement this uncertainty information by performing a sensitivity study, which is based on a regression analysis of the input and output samples, so as to separate and quantify the contribution of individual input parameters to the global output variability. Indeed, a regression coefficient such as the simple correlation coefficient of Pearson provides a good measure of the strength and direction of a linear relationship between two random variables, which is of particular interest in our case to measure the linear sensitivity of the output to an input variable. A better measure of the linear association, between two variables from a set of variables, would be the partial correlation coefficient of Pearson. One can also obtain sensitivity coefficients from the least square solution of a multi-linear regression. Finally, the partial rank correlation coefficient of Spearman offers the possibility of measuring a non-linear, but monotonic, relation between two variables. These various sensitivity measures provide statistical criteria to select and rank the input variables by importance, with respect to their respective contributions to the output uncertainty. For example, Figure 7 shows the ranking of relative sensitivity of the gas gap size at EOC, and of the peak fuel temperature at EOC, to the considered input variables. The final gap size is evidently most sensitive to fuel swelling and initial gap size uncertainties (with different sign). Increases in fuel conductivity, fuel swelling and gas conductance result in better cooling of the fuel and hence to the reduction of the peak fuel temperature [Figure 7(b)], while increases in values of the fission gas release and initial gap have reverse effects.

Figure 6. Sensitivity to considered input variables



Conclusions

This study initiates the development and application of a robust uncertainty and sensitivity calculation methodology in the context of the FAST code system, which couples the neutronic, thermal-hydraulic and thermal-mechanical calculations for a wide range of Generation IV reactors concepts. A working framework has been developed and successfully tested for the application of the statistical methodology, which propagates uncertainties in input and physical model variables to output results. As a demonstration, the thermal-mechanical behaviour of the pin-type MOX fuel foreseen for the ETDR gas-cooled fast reactor has been investigated during base irradiation. Within

the limitations of the present study (small number of input variables considered), it has been shown that the fuel rod design yields an open-gap regime during the entire cycle. Further variables need to be included in the analysis, and work is under way to investigate the possibility of considering the effects of other types of uncertainty, e.g. in the coupled neutronic (cross-sections, kinetic parameters, etc.) and thermal-hydraulic (heat transfer correlations, physical properties, etc.) calculations. This is clearly a major challenge, a key aspect being the identification of reliable uncertainty information on the different parameters and models involved.

REFERENCES

- [1] Mikityuk, K., *et al.*, “FAST: An Advanced Code System for Fast Reactor Transient Analysis”, *Annals of Nuclear Energy*, 32, pp. 1613-1631 (2005).
- [2] Mikityuk, K., P. Fomitchenko, “FRED: Computational Model of Fuel Rod Behavior Under Accident Conditions Coupled with RELAP5/MOD3”, *Proceedings of the 8th Int. Conf. on Nuclear Engineering (ICONE8)*, Baltimore, MD, USA.
- [3] Poette, C., *et al.*, “Status of ETDR Design”, forthcoming in ICAPP 2007.
- [4] McKay, M.D., “Sensitivity and Uncertainty Analysis using a Statistical Sample of Input Values”, Ch. 4 in *Uncertainty Analysis*, Y. Ronen (Ed.), CRC Press, FL (1988).
- [5] Glaeser, H., T. Skorek, E. Hofer, M. Kloos, *Uncertainty Methods Study for Advanced Best Estimate Thermal-hydraulic Code Applications*, Vol. 2, Report from the Uncertainty Analysis Group, CSNI (1998).
- [6] Conover, W.J., “Practical Non-parametric Statistics”, Ch.4, Wiley & Sons, NY, USA (1980).
- [7] Macian, R., *PSI Contribution to BEMUSE Phase III Report: Uncertainty and Sensitivity Analysis of the LOFT L2-5 Test*, August 2006.
- [8] Vinai, P., R. Macian, R. Chawla, “A Statistical Methodology for Quantification of Uncertainty in Best Estimate Code Physical Models”, *Annals of Nuclear Energy* (2007), in press.
- [9] Wulff, W., *et al.*, “Quantifying Reactor Safety Margins. Part 3: Assessment and Ranging of Parameters”, *Nuclear Engineering and Design*, 119, 33-65 (1990).
- [10] Olander, D.R., *Fundamental Aspects of Nuclear Reactor Fuel Elements*, Division of Reactor Development and Demonstration. Energy Research and Development Administration: Berkeley (1976).
- [11] Van Uffelen, Paul, *Modelling of Nuclear Fuel Behaviour*, EUR 22321 EN.
- [12] Lanning, D.D., C.E. Beyer, C.L. Painter, *FRAPCON-3: Modifications to Fuel Rod Material Properties and Performance Models for High-burnup Application*, Vol. 1, NUREG/CR-6534, October 1997.

- [13] Philipponneau, Y., "Thermal Conductivity of (U,Pu)O_{2-x} Mixed Oxide Fuel", *J. Nuclear Materials*, 188, 194-197 (1992).
- [14] Lucuta, P.G., H.S. Matzke, I.J. Hastings, "A Pragmatic Approach to Modeling Thermal Conductivity of Irradiated UO₂ Fuel: Review and Recommendations", *Journal of Nuclear Materials*, Vol. 232, pp. 166-180 (1996).
- [15] Ross, A.M., R.L. Stoute, *Heat Transfer Coefficient Between UO₂ and Zircaloy-2*, AECL-1552 (1962).
- [16] *SCDAP/RELAP5-3D Code Manual: Vol. 4: MATPRO – A Library of Materials Properties for Light-water-reactor Accident Analysis*, INEEL/EXT-02-00589, Rev. 2.2, October 2003.
- [17] Kloos, M., E. Hofer, *SUSA Version 3.5. User's Guide and Tutorial* (2002).

SESSION III

Liquid-metal-cooled Systems

Chairs: P. Yvon, C. Kato

HIGH-Cr ODS STEELS R&D FOR HIGH BURN-UP FUEL CLADDING

**Akihiko Kimura¹, Han-Sik Cho², Naoki Toda², Ryuta Kasada¹, Kentaro Yutani²,
Hirotatsu Kishimoto¹, Noriyuki Iwata¹, Shigeharu Ukai³, Masayuki Fujiwara⁴**

¹Institute of Advanced Energy, Kyoto University
Gokasho, Uji, Kyoto 611-0011, Japan

²Graduate School of Energy Science, Kyoto University
Yoshida-honmachi, Sakyo-ku, Kyoto 606-8501, Japan

³OEC, Japan Nuclear Cycle Development Institute
Narita Oarai, Higashi-ibaraki-gun, Ibaraki-ken 311-1393, Japan

⁴Kobelco, Ltd
Takatsukadai, Nishi-ku, Kobe 651-2271, Japan

Abstract

High-performance cladding materials are essential to realise highly efficient and high burn-up operation over 150 GWd/t of so-called Generation IV nuclear energy systems, such as supercritical water-cooled reactor (SCWR) and lead-cooled fast reactor (LFR). Oxide dispersion strengthening (ODS) ferritic/martensitic steels, which contain 9-12%Cr, show rather high resistance to neutron irradiation embrittlement and high strength at elevated temperatures. However, their corrosion resistance is not good enough in SCW and in lead at high temperatures. High-Cr ODS steels have been developed to improve corrosion resistance. An increase in Cr content resulted in a drastic improvement of corrosion resistance in SCW and in lead. However, high-Cr steels often show increased aging and irradiation embrittlement. Anisotropy in tensile properties is another issue. In order to address these issues, surveillance tests of the material performance have been performed for high-Cr ODS steels produced by new processing technologies. It is demonstrated that the dispersion of nano-sized oxide particles in high density is effective to attain high-performance and high-Cr ODS steels having a good potential as fuel cladding materials for SCWR and LFR with high efficiency and high burn-up.

Introduction

High-performance cladding material is essential to realise high burn-up operation over 150 GWd/t of supercritical water-cooled reactors (SCWR) and lead-cooled fast reactor (LFR) with high efficiency. The materials performance required for the fuel claddings include: 1) high resistance to irradiation embrittlement and swelling; 2) corrosion resistance in the relevant environment; 3) high strength at elevated temperatures and so on.

Oxide dispersion strengthening (ODS) ferritic/martensitic steels, which contain chromium at most 12%, have been developed for the application to fuel cladding material of sodium-cooled fast reactor (SFR) [1,2]. Recent irradiation experiments clearly showed that the ODS steels were rather highly resistant to neutron irradiation embrittlement at temperatures between 573 and 773 K up to 15 dpa [3,4]. They never showed irradiation-induced loss of elongation that was generally observed in metallic materials. That is, the ODS steels showed irradiation hardening accompanied by no loss of ductility. The mechanism of irradiation hardening with no loss of elongation should be made clear for further development of radiation-resistant materials.

A remarkable improvement was attained in the high-temperature strength of ferritic steels by dispersing nano-scale oxide particles. However, it is well known that the corrosion resistance in high-temperature water is reduced significantly by decreasing chromium concentration below 12%. Thus, for 9-12%Cr-ODS ferritic steels, the most critical issue for the application to SCWR and LFR is to improve their corrosion resistance. A project to develop corrosion-resistant ODS steels was undertaken at Kyoto University [4,5].

In our previous researches [4-9], it was reported that the addition of chromium (>13 wt.%) and aluminium (4.5 wt.%) to the ODS steels is very effective to suppress the corrosion in a SCPW (783 K, 25 MPa) environment. Recent corrosion experiment in lead-bismuth clearly showed that the Al-added ODS steel is much more resistant than without addition of Al. The addition of Al also improves the Charpy impact property of the high-Cr ODS steels, while it reduces high-temperature strength. In general, however, an increase in the Cr concentration of the steels often results in an increase in the susceptibility to thermal aging embrittlement. This dilemma could be resolved for high-Cr ODS steels.

In this report, it is demonstrated that high-Cr ODS steels are very promising for fuel cladding material for high burn-up operation of SCWR and LFR based on the recent works on irradiation effects, corrosion resistance and SCC susceptibility as well as the previous database.

Materials

The materials used were reduced-activation oxide dispersion strengthening ferritic steels, a ferritic/martensitic steel, an austenitic steel and nickel super alloys for comparison. The chemical compositions are shown in Table 1 for six high-chromium ODS steels in which the titanium and yttrium concentrations were changed. The details of the fabrication process of the ODS steels are provided in Refs. [1,2,10].

Experimental and results

Corrosion in SCPW

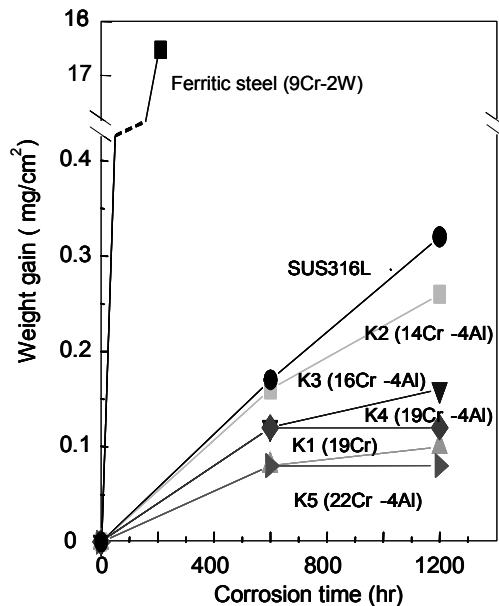
To evaluate corrosion resistance of the K series ODS high-Cr ODS steels, corrosion tests in a SCPW (783 K, 25 MPa) were carried out by means of weight loss and/or gain measurement. After the

Table 1. Chemical compositions of materials

Materials	Cr	W	Al	Ti	N	Y	Y ₂ O ₃
19Cr (K1)	18.37	0.29	<0.01	0.28	0.014	0.29	0.368
13Cr-4Al (K2)	13.64	1.65	4.12	0.28	0.009	0.30	0.381
19Cr-4Al (K3)	16.00	1.82	4.59	0.28	0.006	0.29	0.368
16Cr-4Al (K4)	18.85	1.83	4.61	0.28	0.005	0.29	0.368
22Cr-4Al (K5)	22.05	1.80	4.55	0.27	0.005	0.28	0.356
19Cr-4Al-1.8Si (K6)	19.02	1.85	4.69	0.28	0.005	0.29	0.368

elapsed corrosion times of 600 and 1 200 hours, the weight of the specimens was measured. Figure 1 shows the dependence of weight gain on the corrosion test period for each of the steel. The weight gain of all the high-Cr ODS steels is smaller than that of an austenitic stainless steel (SUS316L). It is of note that even the 14Cr-ODS steel shows higher resistance to corrosion than SUS316L that contains 17%Cr and 10%Ni. The corrosion resistance increases with chromium concentration. The mechanism of high resistance to corrosion of the ODS steels are not yet clear, although it is expected that the yttria particles play a role in the production of homogeneous chromia on the steel surface. The detail of the mechanism is under investigation. As for the corrosion of 9Cr martensitic steel, the weight gain is much larger than SUS316L, as expected. An EDS analysis revealed that a thick Fe₃O₄ oxide film was formed in the 9Cr martensitic steel but not detected in the ODS steels.

Figure 1. Weight gains of the high-Cr ODS ferritic steels as well as those of a 9Cr martensitic steel (JLF-1LN) and an austenitic stainless steel (SUS316L) in a supercritical pressurised water (783 K, 25 MPa). The ODS steels shows a better corrosion resistance than SUS316L.

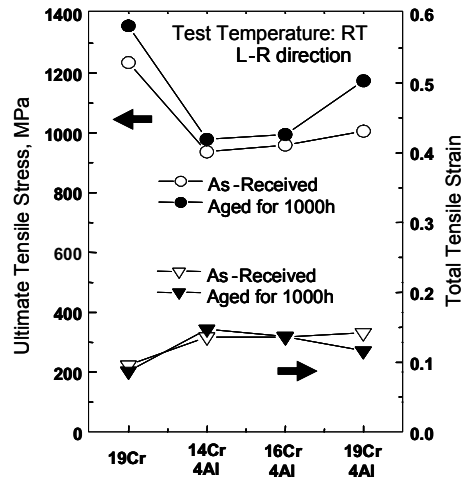


A trade-off issue: thermal aging embrittlement

Although an increase in Cr concentration results in an improvement of corrosion properties, it also often causes an enhancement of aging embrittlement due to the formation of Cr-rich secondary phases. A trade-off between corrosion resistance and aging embrittlement caused by increasing Cr content is one of the critical issues for high-Cr ODS steels.

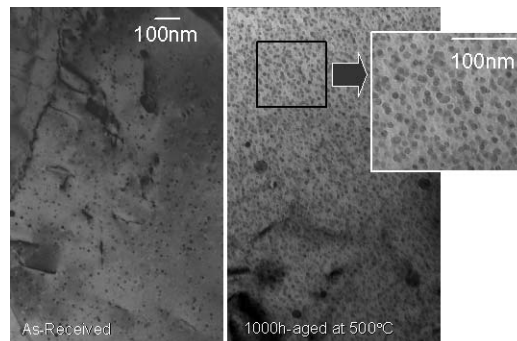
The effects of aging on tensile properties were investigated after aging at 500°C for 1 000 hrs. The test temperature was RT and the deformation rate was 0.5 mm/min. Ultimate tensile stress and total strain of each steels are shown in Figure 2 before and after the aging. Although the aging caused an increase in yield stress, almost no effect was observed for total strain in all the steels. The hardening was larger in higher-Cr content ODS steels. The ductile-to-brittle transition temperature (DBTT) shifted to high temperature by about 40 K and 70 K in the 19Cr-4Al-ODS and 19Cr-ODS steels, respectively. In contrast, the 16Cr-4Al ODS steel never showed the DBTT shift even after the aging at 500°C for 1 000 hrs. It should be noted that in 19Cr-ODS steels, the aging caused hardening and DBTT shift, while they were accompanied by no loss of ductility.

Figure 2. The effects of aging at 500°C for 1 000 hrs on the tensile properties at RT in each high-Cr ODS steel. Sampling direction is L-R, meaning that the tensile axis is parallel with the extrusion direction.



To make clear the mechanism of this behaviour, the microstructure was observed by transmission electron microscope (TEM) before and after aging. Figure 3 shows TEM micrographs of 19Cr-ODS steel observed before and after aging at 500°C for 1 000 hr. At as-received condition, fine oxide particles were observed in the matrix, while many larger structures as well as oxide particles were observed after aging. Since the diffraction patterns of the aged sample did not show any extra spots besides oxide particles, the structures were estimated to be Cr-rich phases which had BCC structure with a lattice parameter somewhat similar to that of iron. The hardening observed for the aged specimen is interpreted in terms of precipitation hardening by Cr-rich phases.

Figure 3. TEM micrographs of 19Cr-ODS steel observed before and after aging at 500°C for 1 000 hrs



The effects of aging on the 19Cr-ODS steel are summarised in Table 2, indicating that 14Cr and 16Cr-ODS steels suffer no aging embrittlement after the aging at 500°C for 1 000 hrs, while 19Cr-ODS showed a remarkable embrittlement. It is interesting that Cr-rich α' phases were observed in 16Cr-ODS steel that did not suffer any aging embrittlement. A more precise correlation study is necessary to understand the role of Cr-rich α' phases in the aging embrittlement, while it is expected that a fine Cr-rich phase only causes hardening, but no reduction of fracture stress.

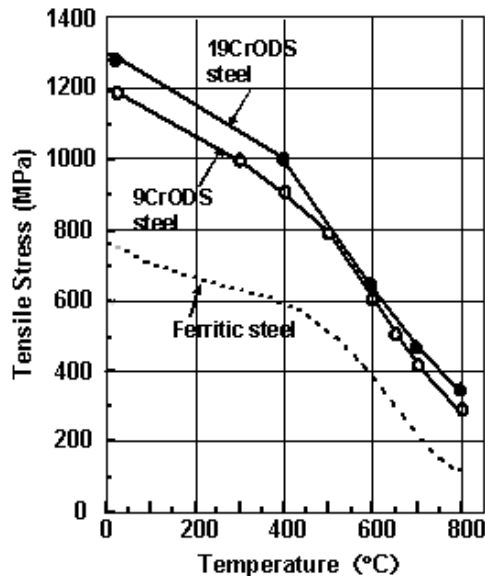
Table 2. Summary of aging effects on 19Cr-ODS steel

	$\Delta \sigma_{UTS}$	$\Delta \epsilon$	$\Delta DBTT$	TEM
14Cr-4Al	42.1	No change	~ 0	–
16Cr-4Al	34.6	No change	~ 0	α' -phase
19Cr-4Al	168	Small	70 K	α' -phase

Improvement of high-temperature strength

A dispersion of oxide particles increased the strength of ferritic steels. Figure 4 clearly shows the tensile strength of 9Cr-ODS and 19Cr-ODS steels is much higher than ferritic steel that contains 10%Cr. The hardening mechanism in the ODS steels are considered to be interpreted in terms of dispersion barrier model against moving dislocations, in which the number density and size of the particles are the controlling factors of the strengthening.

Figure 4. The dependence of tensile stress on test temperature in ferritic steel, 9Cr-ODS steel and 19Cr-ODS steel



An increase in the Cr content increased tensile stress. This can be explained by solid solution hardening by Cr. The tensile stress was larger than 9Cr-ODS about 100 MPa at temperatures between RT and 400°C, and about 50 MPa at 800°C. Since the potential hardening by oxide dispersion is much larger than that by solid solution of Cr, the difference in the tensile stress by increasing Cr is rather smaller than the difference in the tensile stress between ferritic steel and 9Cr-ODS steel in which the only difference is the existence of nano-sized (less than 4 nm in diameter) oxide particles in high density in 9Cr-ODS steel.

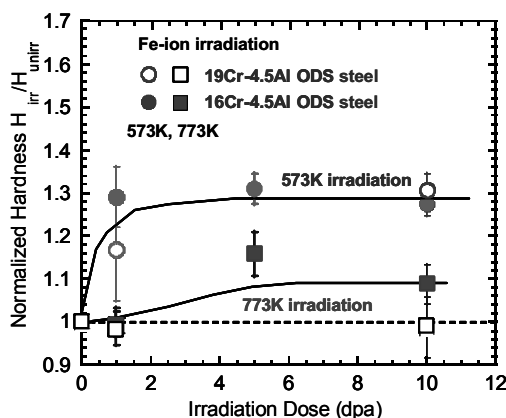
Ion irradiation effects

For the application of the ODS steels to nuclear power plant as a structural material, the phase stability of the oxide particles under irradiation is essential. The ion irradiation experiments were performed at temperatures of 573, 773 and 973 K up to 20 dpa (56 hrs) for the 19Cr-4.5Al ODS steel as a reference of high-Cr ODS steels.

Microstructure observations revealed that a number of small dislocation loops were observed after the irradiation at 573 K, although no significant change was observed for the other structures such as voids and precipitates. Furthermore, at 773 K, any significant effects such as formation of dislocation loops and voids, and precipitation of secondary phases were not observed. Fine precipitates in grains did not grow up significantly during ion irradiation. At 973 K, however, the irradiation caused a change in the precipitation behaviour, showing that carbides precipitated both in grains and along grain boundaries. The size of larger precipitates reached several hundred nm, and the precipitation occurred in both the irradiated and un-irradiated region. The TEM-EDX analysis of matrix, grain boundaries and precipitates in grains were performed. The normalised atomic ratio of chromium on grain boundaries was higher than the others, the carbides were considered to be chromium-rich phase. In contrast, the normalised atomic ratio of aluminium was almost uniform in the matrix and along grain boundaries. It is expected that the segregation of aluminium at grain boundaries would not occur under the irradiation at 973 K.

Irradiation hardening was measured for the specimens irradiated at 573 and 773 K up to 10 dpa. The normalised irradiation hardening of H_{irr}/H_{unirr} was measured using nano-indenter, and the results are shown in Figure 5. H_{irr} and H_{unirr} was the hardness of 19Cr-4.5Al ODS steel before and after ion irradiation, respectively. The irradiation hardening increased with increasing irradiation dose at 573 K. On the other hand, no hardening was observed at 773 K for 19Cr ODS steel. This trend is similar to the 9Cr ferritic steels.

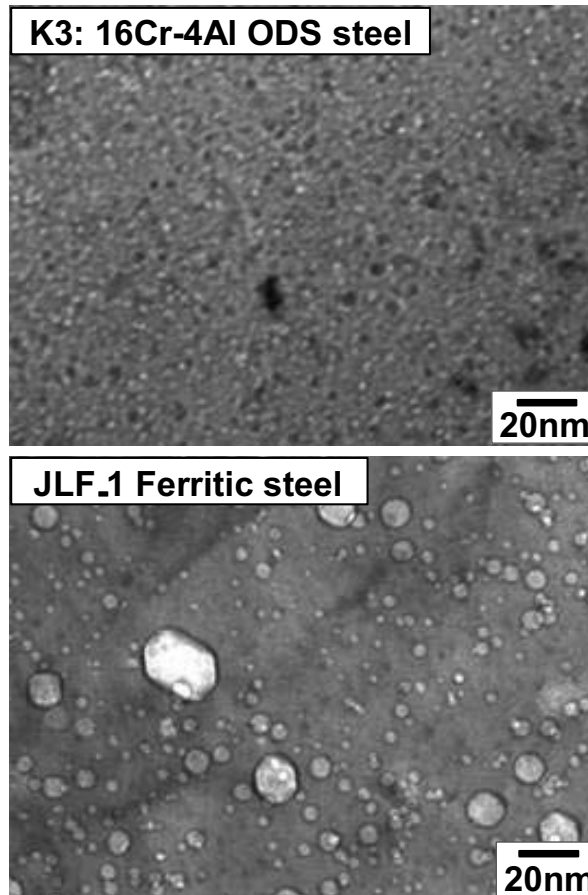
Figure 5. The dependence of the irradiation hardening on the ion dose in the 16, 19Cr-4.5Al-ODS steel irradiated at 573 K and 773 K



It was reported that high-Cr ODS steels often suffer irradiation embrittlement caused by the phase decomposition of Fe/Cr. In previous work, the Cr-rich α' phases were observed in the 12Cr ferritic steel after neutron irradiation at 653 K to 15 dpa (about one year) being accompanied by a large irradiation hardening. In this work, the ion irradiation hardening at 573 K is considered to be due to the irradiation-induced dislocation loops but not the Cr-rich α' phases, as no such phase was observed after the irradiation. It should be noted that even at 573 K the Cr-rich α' phases were not formed up to 10 dpa in 19Cr-4.5Al ODS steel.

Neutron irradiation often generates helium through nuclear transmutation reaction. The generated helium causes so-called helium embrittlement by forming helium bubbles. Figure 6 shows the microstructure of a ODS steel and martensitic steel (JLF-1). Large voids were formed in the JLF-1 steel but no such void was observed in the ODS steels. This is because the oxide particles trapped helium and prevent helium from gathering to form large bubbles.

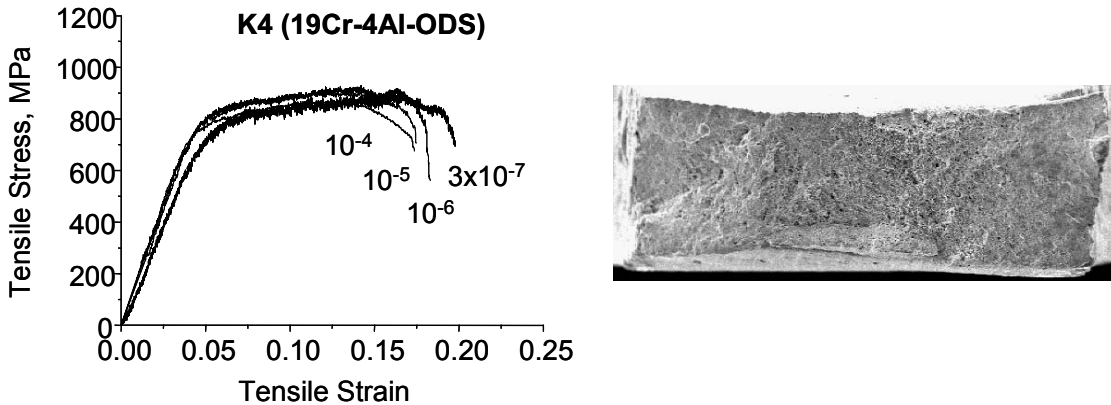
Figure 6. Much higher resistance to formation of helium bubbles in ODS steel than in ferritic steel (JLF-1)



Stress corrosion cracking (SCC) susceptibility

The susceptibility to SCC was evaluated by means of slow strain rate tests (SSRT) in the loop system of hot pressurised water at 288°C at the pressure of 7.8 MPa. Dissolved oxygen (DO) was controlled to be 8 ppm, which is larger than BWR condition. The strain rate was changed from 10^{-4} to $3 \times 10^{-7} \text{ sec}^{-1}$. For comparison, similar tests were carried out for sensitised SUS316L; the sensitisation at 700°C for 100 hrs caused a remarkable reduction of the total strain that indicated the occurrence of the SCC. In ODS steels, as shown in Figure 7, the ductility did not depend on the strain rate between 10^{-4} to $3 \times 10^{-7} \text{ s}^{-1}$, indicating that the 19Cr-ODS steel and 19Cr-4.5Al-ODS steel show very low SCC susceptibility. The fracture surface observation by SEM revealed that the entire fracture surface showed ductile mode with many dimples as shown in the bottom of Figure 7. The reduction in area was also large at all the strain rate conditions.

Figure 7. Stress-strain behaviour and fracture surface of 19Cr-4.5Al-ODS steel tested in a hot water at a strain rate of $3 \times 10^{-7} \text{ sec}^{-1}$



Compatibility with lead

As the solubility value of nickel in lead is very high, it has been considered that austenitic stainless steels and nickel base alloys are inadequate for Pb-17Li systems with regard to corrosion resistance.

Several corrosion tests were carried out on ferritic and austenitic steels in liquid Pb-17Li. It was confirmed that the corrosion rate of the ferritic-martensitic steels was five times slower than that of the SUS316 steel [11]. Although the test periods were limited to 6 000 hrs at most in the temperature range from 723 to 823 K, the evaluated corrosion rate of ferritic-martensitic steels is less than 100 $\mu\text{m}/\text{year}$ below 755 K. It should be noted that the corrosion rate significantly increases with increasing test temperature: 370 $\mu\text{m}/\text{year}$ at 873 K [12]. As for the flow rate effect, high flow rates resulted in a high corrosion rate, indicating that the flow rate could be small to reduce the corrosion rate as well as the influence of the magneto-hydrodynamic (MHD) pressure drop.

The stress corrosion cracking in liquid metals or liquid metal embrittlement (LME) is another critical issue. Sample, *et al.* investigated the tensile deformation and fracture behaviour of ferritic-martensitic steels in Lb-17Li at temperatures ranging from 523 to 723 K [13-17]. The results showed that almost no indication of LME was present in the tensile behaviour of the ferritic-martensitic steels, although a serrated flow was observed in a slow strain rate test at $2.8 \times 10^{-7}/\text{sec}$ [14]. However, the weld metals that did not undergo post-weld heat treatment (PWHT) suffered from LME, showing the reduction of total elongation [15,16]. It was reported that the PWHT at an adequate temperature was inevitable to avoid the LME, and that the investigation is necessary to assess the potential of the LME for the irradiation-hardened ferritic-martensitic steels. It is also considered that a synergistic effect of liquid metal, irradiation and hydrogen/helium may appear in the fracture behaviour of the stressed metallic materials.

Discussion

Requirements of performance and processing

A scenario of high burn-up operation over 150 GWd/t of a water-cooling nuclear system imposes a number of requirements for cladding materials, which include: 1) resistance to neutron irradiation embrittlement; 2) dimensional stability under irradiation; 3) corrosion resistance; 4) low susceptibility to SCC and hydrogen and/or helium embrittlement; 5) high-temperature strength; 6) long creep life.

Among these, the irradiation embrittlement is most critical for the cladding of light water reactors, because in many metallic materials, the irradiation induces the embrittlement accompanied by hardening below 673 K [18], and with decreasing irradiation temperature, the embrittlement becomes more significant. When the claddings is highly susceptible to hydrogen and/or helium embrittlement, synergistic degradation by irradiation embrittlement and H/He embrittlement becomes crucial for determining the lifetime of the cladding. SCC often determines the lifetime of the claddings.

High-temperature properties are essential for the application to SCPWR, such as tensile strength, creep, swelling and corrosion at high temperatures. When the irradiation temperature is higher than 673 K, the irradiation induces no hardening but embrittlement that is due to irradiation-induced phase changes, such as precipitation [18] and phase transformation in the materials. The phase changes often increase the susceptibility to irradiation embrittlement, H/He embrittlement, swelling and even corrosion. Thus, the phase stability is most critical for high-temperature usage. According to the preliminary irradiation experiments, the ODS steels did not show irradiation-induced softening that was due to reduction of dislocation. This indicates that the dispersed oxide particles played a role in stabilising microstructure.

For practical applications, not only materials performance under irradiation but also basic engineering technologies, such as productivity, weldability and workability, are demanded for the material. As for the ODS steels, those technologies have been successfully developed by JNC and KOBELCO [10]. A one-tonne ball mill for mechanical alloying is available to produce more than 200 fuel pins with 3-m length. A frictional bonding technique was developed to fabricate a creep tube end-capped. It was shown that the crept tube broke at the centre of the tube far from the bonding.

Material selection

According to the report on corrosion behaviour [19] of the candidate cladding materials for SCPWR, which includes ferritic steels (Mod. 9Cr-1Mo, 12Cr-1Mo), austenitic stainless steels (SUS316, SUS310), Ni-based alloys (Alloy690, Alloy718) and Ti alloys (Ti-3Al-2.5V, Ti-15V-3Al-3Sn-3C), Ni-based alloys were selected as the most promising material based on the experimental results of corrosion tests in a SCPW (839 K, 25 MPa) and mechanical tests before irradiations. However, the most critical issue for Ni-based alloys is strain-age cracking [20] that is significantly influenced by residual stress produced by welding. Because the temperature range of the occurrence of strain-age cracking is from 813 K to 923 K for mother alloy and probably goes down to 698 K for weld metal, difficulties would arise for the cladding at these temperatures.

As for the irradiation effects on the mechanical properties of Ni-based alloys [21], Inconel X750 suffered a significant embrittlement after neutron irradiation at 653-683 K up to 1.2 dpa, showing almost two times larger yield stress and half of the uniform elongation in comparison to those before irradiation. For high burn-up applications, a much higher neutron dose will be imposed and transmutation helium and hydrogen might accelerate the embrittlement, and finally a tremendous irradiation embrittlement is considered to occur in Ni-based alloys.

Austenitic stainless steels are one of the candidates, though they are susceptible to SCC, helium embrittlement and high-temperature creep rupture. An effort to develop fine-grain-size austenitic steels has been made, although recent studies revealed that the ultra-fine-grain formation at the steel surface increased the SCC susceptibility.

Based on the surveillance test for the high-Cr ODS steels thus far, it is considered that the ODS steels are most promising as high burn-up fuel cladding material. They have rather high resistance to

neutron irradiation at temperatures between 573 and 773 K up to 15 dpa, and the investigation of irradiation effects beyond the above conditions is now under way. A high tensile stress was achieved for the 9 to 19Cr-ODS steel, which ranged from 300 to 350 MPa at 1 073 K. Creep strength of the 9Cr-ODS steel was measured to be 120 MPa at 973 K for 10⁴ hrs. The authors concluded that the ODS steels were neither highly susceptible to hydrogen [8,9] nor to helium embrittlement [22,23]. The most promising materials performance of the ODS steels is considered to be due to dispersion of very fine yttria oxides of which the diameter ranges from 1 to 5 nm [24,25].

Summary

Surveillance tests have been carried out for high-Cr ODS steels to evaluate their basic properties. The results of short-term experiments indicate better total performance than the other materials. It is considered that the nano-sized oxide dispersion resulted in an increase in the phase stability that is essential for good material performance under irradiations. It is demonstrated that high-Cr ODS steels have a high potential as fuel cladding materials for SCWR and LFR. Long-term experiments such as neutron irradiation experiments, creep tests and long-period corrosion and aging tests, are necessary to assess the performance of high-Cr ODS steels as cladding material of advanced nuclear systems with high efficiency and high burn-up. After the evaluation of baseline properties of high-Cr ODS steels, a joint technology development is necessary to move toward a practical application to nuclear systems.

Acknowledgements

This work was partly supported by a 21st Century Centre of Excellence (COE) Programme Grant from the Ministry of Education, Culture, and Sports, Science and Technology (MEXT) of Japan and the Ministry of Economy, Trade and Industry (METI) of Japan.

REFERENCES

- [1] Ukai, S., T. Nishida, H. Okada, T. Okuda, M. Fujiwara, K. Asabe, “Development of Oxide Dispersion Strengthened Ferritic Steels for FBR Core Application (I) Improvement of Mechanical Properties by Recrystallization Processing”, *J. Nucl. Sci. Technol.*, 34 [3], 256 (1997).
- [2] Ukai, S., T. Nishida, T. Okuda, T. Yoshitake, “Development of Oxide Dispersion Strengthened Ferritic Steels for FBR Core Application (II) Morphology Improvement by Martensite Transformation”, *J. Nucl. Sci. Technol.*, 35 [4], 294 (1998).
- [3] Yoshitake, T., T. Ohmori, S. Miyakawa, “Burst Properties of Irradiated Oxide Dispersion Strengthened Ferritic Steel Claddings”, *J. Nucl. Mater.*, 307-311, 788 (2002).
- [4] Kimura, A., S. Ukai, M. Fujiwara, “R&D of Oxide Dispersion Strengthening Steels for High Burn-up Fuel Claddings”, *Proc. Int. Cong. Advances in Nuclear Power Plants (ICAPP-2004)* ISBN 0-89448-680-2, CD-ROM file, paper 2070-2076 (2004).

- [5] Kimura, A., S. Ukai, M. Fujiwara, "Development of Fuel Clad Materials for High Burn-up Operation of LWR", *Proc. Int. Conf. of Global Environment and Advanced Nuclear Power Plants, (GENES4/ANP2003)*, ISBN 4-901332-01-5, CD-ROM file, paper 1198 (2003).
- [6] Cho, H.S., A. Kimura, S. Ukai, M. Fujiwara, "Corrosion Properties of Oxide Dispersion Strengthened Steels in Super-critical Water Environment", *J. Nucl. Mater.*, 329-333, 387-391 (2004).
- [7] Cho, H.S., A. Kimura, S. Ukai, M. Fujiwara, "Development of Fuel Clad Materials for High Burn-up Operation of LWR", *Journal of ASTM International*, 2 [7], 194-205 (2005).
- [8] Lee, J.S., A. Kimura, S. Ukai, M. Fujiwara, "Effects of Hydrogen on the Mechanical Properties of Oxide Dispersion Strengthening Steels", *J. Nucl. Mater.*, 329-333, 1122-1126 (2004).
- [9] Lee, J.S., A. Kimura, S. Ukai, M. Fujiwara, I.S. Kim, "Hydrogen Embrittlement of Oxide Dispersion Strengthening Steels Under *In-situ* Cathodic Charging", *ICAPP-2004*, ISBN 0-89448-680-2, CD-ROM file, paper 2016.
- [10] Ukai, S., S. Mizuta, T. Yoshitake, T. Okuda, S. Hagi, M. Fujiwara, T. Kobayashi, "Tube Manufacturing and Characterization of Oxide Dispersion Strengthened Ferritic Steels", *J. Nucl. Mater.*, 283-287, 702-706 (2000).
- [11] Borgstedt, H.U., G. Drechsler, G. Frees, Z. Peric, "Corrosion Testing of Steel X 18 CrMoVNb 12 1 (1.4914) in a Pb---17Li Pumped Loop", *J. Nucl. Mater.*, 155-157, 728-731 (1988).
- [12] Broc, M., T. Flament, P. Fauvet, J. Sannier, "Corrosion of Austenitic and Martensitic Stainless Steels in Flowing 17Li---83Pb Alloy", *J. Nucl. Mater.*, 155-157, 710-714 (1988).
- [13] Coen, V., H. Kolbe, L. Orecchia, "Effects of Pb---17Li on the Tensile Properties of Steels", *J. Nucl. Mater.*, 155-157, 740-743 (1988).
- [14] Sample, T., V. Coen, H. Kolbe, L. Orecchia, "The Effects of Hydrogen and Pb---17Li on the Tensile Properties of 1.4914 Martensitic Steel", *J. Nucl. Mater.*, 191-194, 960-964 (1992).
- [15] Sample, T., P. Fenici, H. Kolbe, "Liquid Metal Embrittlement Susceptibility of Welded MANET II (DIN 1.4914) in Liquid Pb---17Li", *J. Nucl. Mater.*, 233-237, 244-247 (1996).
- [16] Sample, T., H. Kolbe, "Liquid Metal Embrittlement (LME) Susceptibility of the 8-9% Cr Martensitic Steels F82H-mod., OPTIFER IVb and Their Simulated Welded Structures in Liquid Pb-17Li", *J. Nucl. Mater.*, 283-287, 1336-1340 (2000).
- [17] Benamati, G., C. Fazio, I. Ricapito, "Mechanical and Corrosion Behaviour of EUROFER 97 Steel Exposed to Pb-17Li", *J. Nucl. Mater.*, 307-311, 1391-1395 (2002).
- [18] Kimura, A., T. Morimura, M. Narui, H. Matsui, "Irradiation Hardening of Reduced Activation Martensitic Steels", *J. Nucl. Mater.*, 233-237, 701-706 (1996).
- [19] Harada, M., O. Kubota, H. Anada, "Fuel Cladding Materials for Supercritical-water Cooled Power Reactor", *Kobe Steel Engineering Reports*, 53 [3], 92-97 (2003).

- [20] James, M.R., S.A. Maloy, F.D. Gac, W.F. Sommer, J. Chen, H. Ullmaier, "The Mechanical Properties of an Alloy 718 Window After Irradiation in a Spallation Environment", *J. Nucl. Mater.*, 296, 139-144 (2001).
- [21] Allen, T.R., C.L. Trybus, J.I. Cole, "The Effects of Low Dose Rate Irradiation and Thermal Aging on Reactor Structural Alloys", *J. Nucl. Mater.*, 270, 290-300 (1999).
- [22] Kimura, A., R. Kasada, R. Sugano, A. Hasegawa, H. Matsui, "Annealing Behavior of Irradiation Hardening and Microstructure in Helium-implanted Reduced Activation Martensitic Steel", *J. Nucl. Mater.*, 283-287, 827-831 (2000).
- [23] Kimura, A., R. Kasada, K. Morishita, R. Sugano, A. Hasegawa, K. Abe, T. Yamamoto, H. Matsui, N. Yoshida, B.D. Wirth, T.D. Rubia, "High Resistance to Helium Embrittlement in Reduced Activation Martensitic Steels", *J. Nucl. Mater.*, 307-311, 521-526 (2002).
- [24] Miller, M.K., D.T. Hoelzer, E.A. Kenik, K.F. Russel, "Stability of Ferritic MA/ODS Alloys at High Temperatures", *Intermetallics*, in press.
- [25] Ohtsuka, S., S. Ukai, M. Fujiwara, T. Kaito, T. Narita, "Improvement of 9Cr-ODS Martensitic Steel Properties by Controlling Excess Oxygen and Titanium Contents", *J. Nucl. Mater.*, Vol. 329-333, Part 1, 372-376 (2004).

INFLUENCE OF NORMALISING TEMPERATURE ON MX PRECIPITATION BEHAVIOUR IN HIGH-CHROMIUM STEEL

Satoshi Obara, Takashi Onizawa, Takashi Wakai, Tai Asayama
Japan Atomic Energy Agency, Japan

Abstract

This paper describes the influence of normalising temperature on metal carbonitride (MX) precipitation behaviour and mechanical property of high chromium (Cr) ferritic steel for fast breeder reactor (FBR) structures. Generally, vanadium (V) and niobium (Nb) play a role of precipitation strengthening elements as MX particles in high Cr ferritic steels. Precipitation behaviour of MX particles depends not only on the amounts of V and Nb but also on heat treatment conditions. In order to obtain fine and dense MX precipitations and superior mechanical properties, optimal heat treatment conditions were investigated. The microstructures were observed using optical and electron microscopy. Extracted residue analysis was conducted to identify the precipitated elements. It was clarified that fine and dense MX precipitations and superior strength were obtained by normalising at higher temperatures. This mainly resulted from Nb which had dissolved in matrices in normalising at higher temperature and then precipitated as fine MX particles in tempering process. In addition, M_2X precipitations were also found to be fine and dense by normalising at higher temperatures. This might contribute to improve the strength of the steel. It can be concluded that the normalising process at high temperature enables MX precipitations to be fine and dense because Nb can be dissolved as much as possible in matrices by the process. Further, since FBR components are used at elevated temperatures for very long periods, the long-term stability and efficiency of strengthening mechanism brought about with such MX particles needs to be investigated.

Introduction

For the commercialisation of the fast breeder reactor (FBR), it is essential to reduce construction costs by employing high chromium (Cr) ferritic steels as the main structural materials. Conventional high Cr ferritic steels which have been developed as the materials for thermal power boilers have both excellent high-temperature strength and thermal properties, such as thermal conductivity and thermal expansion rate. However, the ductility and toughness of the steels tend to degrade with long-term ageing at elevated temperatures because of microstructure evolution. Since long-life plant design is required for future FBR plants, long-term microstructure stability is one of the most important characteristics for the structural materials of FBR.

Generally, high-temperature strength of the high Cr ferritic steels is achieved through several strengthening mechanisms [1]. The precipitation strengthening mechanism using fine metal carbonitride (MX) particles which consist of vanadium (V) and/or niobium (Nb) is the most important. Vanadium carbonitride (VX) and niobium carbonitride (NbX) contribute to strengthening by becoming obstacles to dislocation motions. However, the long-term stability at elevated temperatures of the MX particles in the steels has not yet been verified. The number of fine MX particles may be decreased with long time creep and long time creep strength may degrade obviously. Such degradations resulted from precipitation and growth of Z phase which consists of V and Nb, as reported by Suzuki, *et al.* [2,3].

Therefore, optimum contents of V and Nb for FBR structural materials should be investigated. For this purpose, several kinds of high Cr steels which have various V and Nb contents had been produced and a series of mechanical tests and metallurgical examinations had been conducted [4,5]. However, precipitation behavior depends not only on the amount of V and Nb but also on the heat treatment conditions [6-11]. In this study, in order to investigate the optimum heat treatment conditions for FBR structural materials, several kinds of high Cr steels with different heat treatments were produced and a series of mechanical tests and metallurgical examinations were conducted.

Materials

Chemical compositions

In order to investigate the effects of V and Nb on the mechanical properties and microstructure evolutions, 11 kinds of steels were prepared [4]. Chemical compositions are shown in Table 1 [5]. These steels were melted as 150 kg ingots using a vacuum induction furnace and hot rolled at 1 523 K to 30 mm plates. All the steels were normalised at 1 333 K for 1 hour then cooled in air and tempered at 1 033 K for 1 hour then cooled in air.

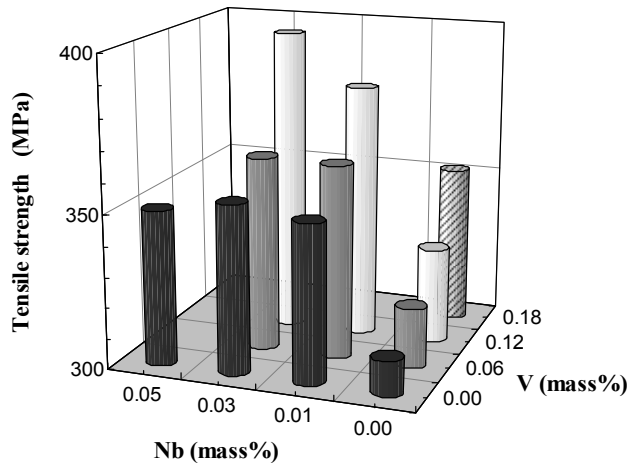
Table 1. Chemical compositions of the trial steels (mass%) [5]

	C	Si	Mn	P	S	Ni	Cr	Mo	W	N	V	Nb
VN00	0.106	<0.002	0.69	0.002	0.0022	<0.002	10.19	1.21	<0.002	0.050	<0.002	0.003
VN01	0.109	<0.002	0.68	0.002	0.0023	<0.002	10.15	1.16	<0.002	0.052	<0.002	0.012
VN02	0.108	0.003	0.68	0.002	0.0023	<0.002	10.11	1.18	<0.002	0.048	<0.002	0.031
VN03	0.108	0.003	0.68	0.002	0.0023	<0.002	10.16	1.18	<0.002	0.049	<0.002	0.051
VN10	0.108	<0.002	0.68	0.002	0.0023	<0.002	10.18	1.21	<0.002	0.051	0.06	0.003
VN11	0.107	<0.002	0.69	0.002	0.0022	<0.002	10.21	1.20	<0.002	0.048	0.06	0.012
VN12	0.107	<0.002	0.69	0.002	0.0022	<0.002	10.18	1.20	<0.002	0.049	0.06	0.031
VN20	0.108	<0.002	0.69	0.002	0.0019	<0.002	10.19	1.19	<0.002	0.049	0.12	0.003
VN21	0.106	<0.002	0.69	0.002	0.0022	<0.002	10.12	1.20	<0.002	0.048	0.12	0.012
VN22	0.105	<0.002	0.69	0.002	0.0023	<0.002	10.10	1.21	<0.002	0.047	0.12	0.032
VN30	0.108	<0.002	0.69	0.002	0.0019	<0.002	10.16	1.20	<0.002	0.049	0.18	0.003

Mechanical properties

Figure 1 shows the tensile strength of the steels at 873 K [5]. Higher tensile strength was obtained with an increase of V content. The tensile strength of the Nb-added steels was superior to that of Nb-free ones, but the effect of Nb on the strength was not obvious in the steels to which Nb was added more than 0.01 mass%. This was caused because dissolved temperature of V was lower than that of Nb. Although the normalised temperature, 1 333 K, was high enough to dissolve all added V in the matrices, only approximately 0.01 mass% Nb could dissolve in the matrices at that temperature [6].

Figure 1. Influence of V and Nb on the tensile strength at 873 K [5]



Observed MX particles

Precipitation behaviour of MX under normalised and tempered conditions was observed using a field emission transmission electron microscope (FE-TEM). The observation results are summarised in Table 2 [5]. VX particles were observed in the steels of which V content was more than 0.12 mass%. NbX particles were observed in Nb-added steels. Only in the steels VN21 and VN22, both VX and NbX precipitated under the normalised and tempered conditions.

Table 2. The analysis result of the deposit by TEM-EDX [5]

	V (mass%)	Nb (mass%)	$M_{23}C_6$	M_2X	MX	
					NbX	VX
VN00	0.00	0.00	◇	◇	×	×
VN01	0.00	0.01	◇	◇	◇	×
VN02	0.00	0.03	◇	◇	◇	×
VN03	0.00	0.05	◇	◇	◇	×
VN10	0.06	0.00	◇	◇	×	×
VN11	0.06	0.01	◇	◇	◇	×
VN12	0.06	0.03	◇	◇	◇	×
VN20	0.12	0.00	◇	◇	×	◇
VN21	0.12	0.01	◇	◇	◇	◇
VN22	0.12	0.03	◇	◇	◇	◇
VN30	0.18	0.00	◇	◇	×	◇

◇ – Observed, × – Not observed

In this study, the relationship between the precipitation behaviour of MX, which includes VX and NbX, and the mechanical properties is discussed based on the results of mechanical tests and metallurgical examinations of VN22 steel.

Experiments and analyses

As mentioned in the section “*Mechanical properties*”, a normalising process at 1 333 K is not high enough to dissolve Nb more than 0.01 mass%. It is supposed that the unsolved Nb precipitates as coarse NbX and such coarse NbX particles do not contribute to strengthening of the steel. Therefore, a normalising process at higher than 1 333 K is required to dissolve Nb and to make Nb precipitate as fine NbX particles in the tempering process for heat resistant steels.

In this study, the effect of heat treatment conditions is also investigated, as are as the effects of V and Nb contents on the mechanical properties and microstructure evolutions. Some specimens of VN22 steels normalised at several temperatures were prepared (Table 3). The normalising conditions were determined to increase the amount of dissolved Nb in the matrices accounting for precipitation of δ ferrite phase. Prior to the normalising process, these specimens were subjected to solution treatment at the same temperature as the hot rolled process, i.e. 1 523 K, to erase the effects of the prior heat treatment processes. After the normalising process, the specimens were tempered at 1 033 K. After the tempering, it was confirmed using an optical microscope that all specimens showed typical full martensitic microstructures and that little δ ferrite phase precipitated.

Table 3. Heat treatment conditions of the steels

	Solution	Normalise	Temp.	Condition
	×1h A.C. /K			
N1	1 523	1 333	—	As normalised
T1	1 523	1 333	1 033	Tempered
N2	1 523	1 373	—	As normalised
T2	1 523	1 373	1 033	Tempered
N3	1 523	1 423	—	As normalised
T3	1 523	1 423	1 033	Tempered

To investigate the influence of normalising temperature on the precipitation behaviours of MX, the extracted replica observations were conducted using a FE-TEM. The replicas were produced using 10% acetyl acetone, 1% tetramethyl ammonium chloride and methanol electrolyte. The chemical compositions of the precipitations were analysed using energy dispersion X-ray spectrometry (EDX) attached to the FE-TEM equipment. Radii of the precipitations were measured and the number densities of the precipitations were also calculated based on the FE-TEM images.

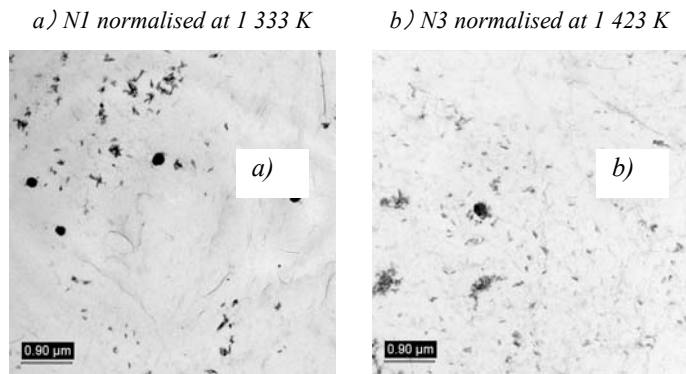
Tensile tests at 873 K and Vickers hardness tests were conducted to measure the mechanical properties of the VN22 steels normalised at several temperatures.

Results

Precipitates observed in the normalised specimens (before tempering)

Figure 2 shows the TEM images of carbon extracted replicas from the specimens normalised at 1 333 K and 1 423 K. Coarse round shape precipitations and fine rod shape ones were observed. The diameter of former precipitations was approximately 0.5 μm and the length of the latter ones was

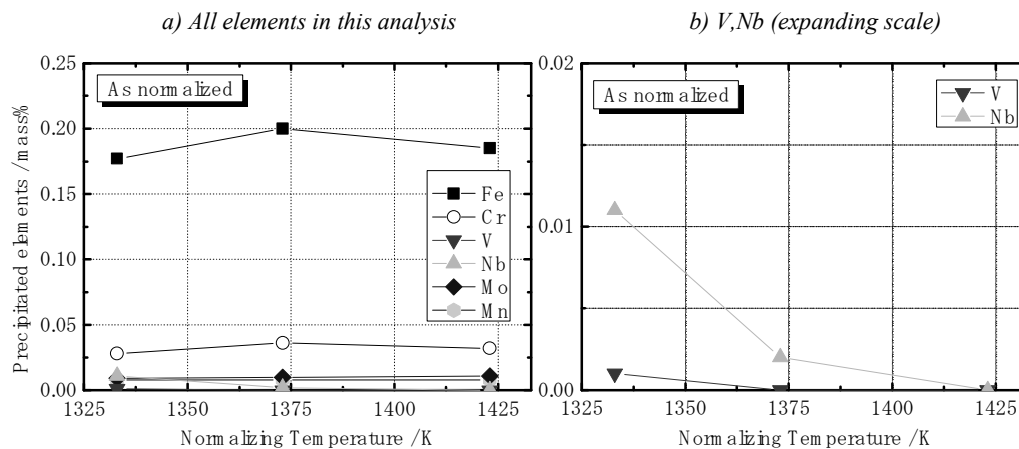
Figure 2. Transmission electron micrographs after normalising heat treatment



approximately 0.1 μm . The former was identified as MnS and MX, and the latter was identified as Fe_3C by TEM-EDX analyses. Although the coarse MX was not observed in the specimen normalising at 1 423 K, MnS and Fe_3C were observed even in the specimen normalised at 1 423 K. The coarse MX is supposed to be unsolved MX [6,10].

Figure 3 shows extracted residue analysis results for the normalised specimens. Most of the V dissolved even in the specimen normalised at 1 333 K. In contrast, the amount of precipitated Nb decreased with increase of normalising temperature and Nb completely dissolved in the matrices by normalising at 1 423 K. This extracted residue analysis result agrees with the observation that the number of coarse precipitations decreases with normalising at high temperature.

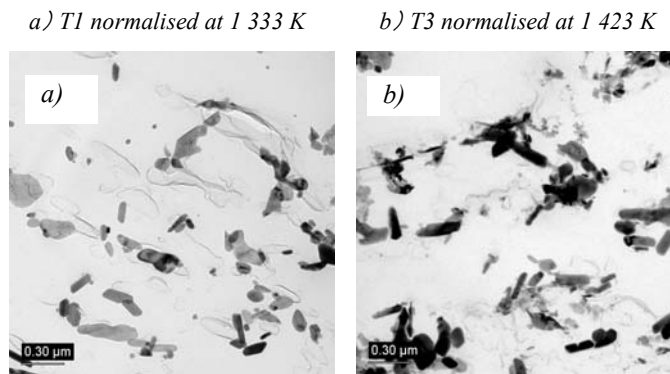
Figure 3. Relationship between amount of precipitated elements and normalising temperature in as-normalised specimen



Precipitates observed in the tempered specimens

Figure 4 shows TEM images of carbon extracted replicas from the specimens tempered at 1 033 K. On the martensite lath boundaries, coarse precipitations were observed. The size of the precipitations is approximately 0.5 μm at maximum. In contrast, in the martensite laths, fine rod shape and film-like precipitations were observed. Based on the TEM-EDX analysis results, three types of precipitations were observed in the tempered specimens, namely M_{23}C_6 , M_2X and MX. Although the MX particles observed in the tempered specimen consist of NbX and VX, most of the MX particles were not identified.

Figure 4. Transmission electron micrographs after tempered heat treatment



As some literature reported that fine precipitations such as MX were observed at in the martensite laths [12,13], the observations in this study were mainly conducted in the martensite laths.

Figure 5 shows the relationship between the normalising temperature and mean diameter of the precipitations. The observed areas were mainly selected in the martensite laths. The number of analysed precipitations was approximately 200, 50 and 30 for M_2X , $M_{23}C_6$ and MX, respectively. MX is the smallest precipitation in all precipitations observed in the tempered specimens. Although the mean diameter of MX was approximately 30 nm in the specimen normalised at 1 333 K, the smaller particles were observed with increase of normalising temperature. The mean diameters of $M_{23}C_6$ and M_2X also decreased with increase of normalising temperature.

Figure 5. Relationship between mean diameter of precipitations and normalising temperature

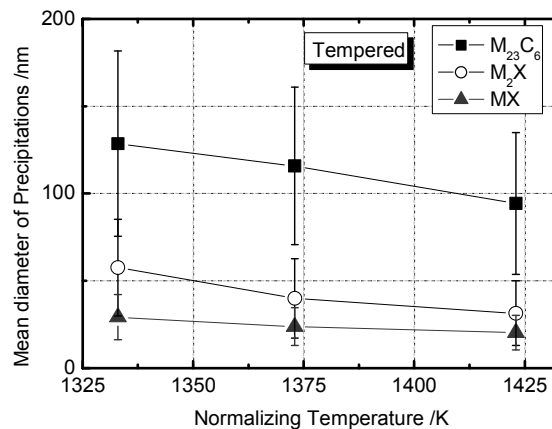


Figure 6 shows the relationship between the normalising temperature and number density of the precipitations observed in martensite laths. The number density of M_2X in martensite laths was obviously larger than that of the other precipitations. Excluding M_2X , the number density of the precipitations becomes larger with normalising in high temperatures.

Figure 7 shows the extracted residue analysis results of the tempered specimens. Amounts of precipitated elements do not depend upon the normalising temperature, as far as this study analysed. Thus, the increase of number density with increase of normalising temperature resulted from fine dispersion of the precipitations.

Figure 6. Relationship between number density of precipitations and normalising temperature

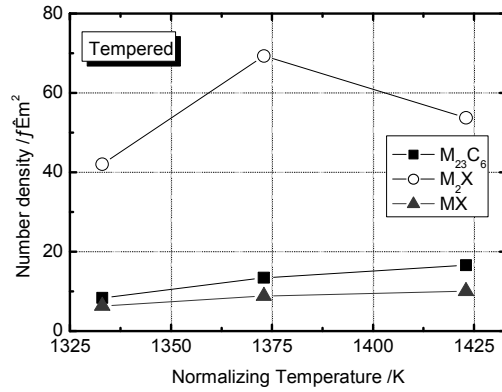
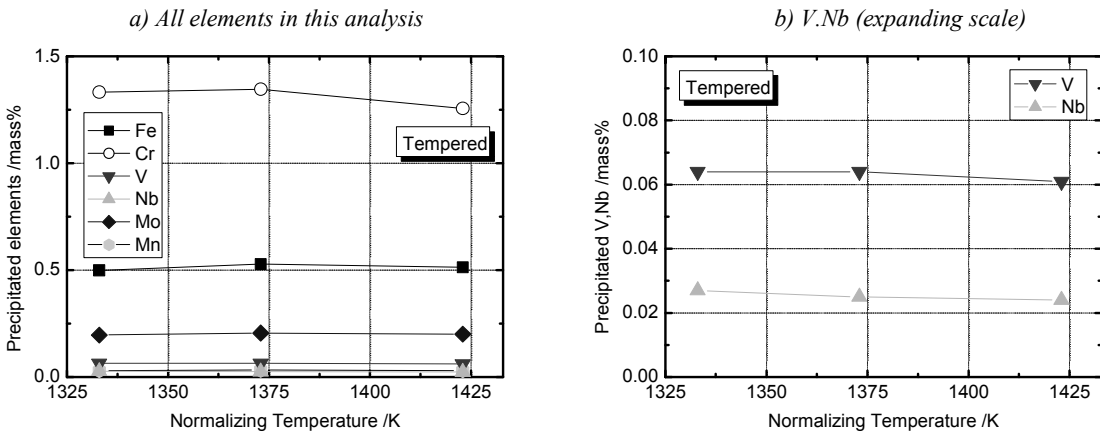


Figure 7. Relationship between amount of precipitated elements and normalising temperature in as-tempered specimen



Discussions

Influence of normalising temperature on prior austenite grain size

Figure 8 shows influence of normalising temperature on prior austenite grain size. The higher the temperature at which the steels were normalised, the coarser prior austenite grain sizes were observed.

Influence of normalising temperature on precipitation behaviour of MX

It was clarified based on microstructure observation using a FE-TEM that fine and dense MX precipitation was obtained by normalising at high temperature. The reason for this was supposed to be that fact that the amount of dissolved Nb in the matrices increased and the coarse unsolved MX particles decreased. Dissolved Nb could precipitate as fine MX particles in the tempering process.

Therefore, the total amounts of precipitated V and Nb in the tempering process were calculated based on the results of the extracted residue analyses for the steels. The relationship between normalising temperature and the total amount of precipitated V and Nb in the tempering process is shown in Figure 9. The amount of $\Delta[V + Nb]$ increased with the increase of normalising temperature at a temperature range below 1373 K. Saturation occurred at higher temperature.

Figure 8. Effect of normalising temperature on prior austenite grain size

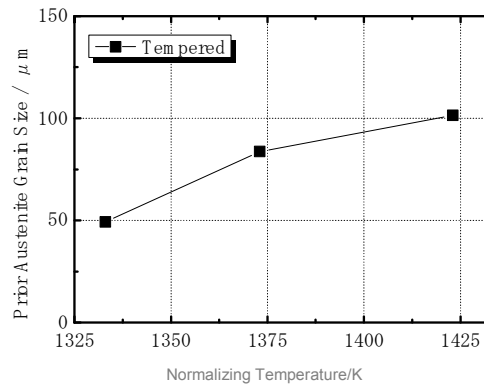
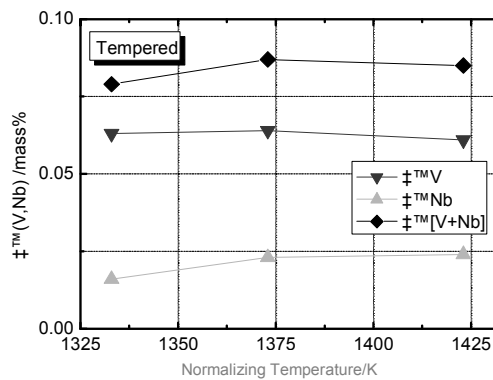


Figure 9. Relationship between amount of V and Nb precipitated in tempering process and normalising temperature



Based on the TEM observation results, fine and dense MX precipitation delivered by increase of normalising temperature from 1 333 to 1 373 K resulted from an increase in the amount of dissolved Nb in the matrices. However, because few coarse MX particles were observed in the specimens normalised at 1 373 K, it could be presume that some different mechanisms might contribute to produce the fine and dense MX precipitation by normalising in temperature higher than 1 373 K. Since M_{23}C_6 and M_2X particles were not observed in the specimen before tempering, these particles were supposed to precipitate in the tempering process. Although the tempering conditions were completely the same for all specimens, the obvious difference was observed in the precipitation behaviour of these particles. Therefore, the precipitation behaviour of such particles in the tempering process was supposed to be strongly affected by microstructure evolution of the steels in the normalising process.

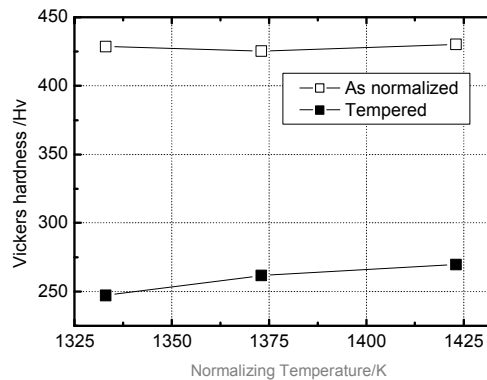
In general, prior austenite grain boundary is supposed to be one of the preferential nucleation sites of precipitations [14-16]. As shown in Figure 8, the prior austenite grain size became coarser with an increase of normalising temperature. The region of grain per unit volume is decreased by coarsening grain size.

Takaki, *et al.* and Okaguchi, *et al.* mentioned that dislocations and surrounding areas of the precipitated second phase can also be preferential nucleation sites [14,15], in addition to prior austenite grain boundary. All the specimens in this study have a typical tempered martensite microstructure with high dislocation density. For such a microstructure, when the number of preferential nucleation sites (prior austenitic grain boundaries) decrease due to coarsening of prior austenite grains, it can be presumed that precipitation newly occurred at dislocations inside the prior austenite grains.

Influence of normalising temperature on mechanical properties

Figure 10 shows Vickers hardness test results for the specimens normalised at several temperatures. The hardness before tempering does not depend upon normalising temperature. After tempering, the hardness increases with increase of normalising temperature.

Figure 10. Relationship between hardness and normalising temperature

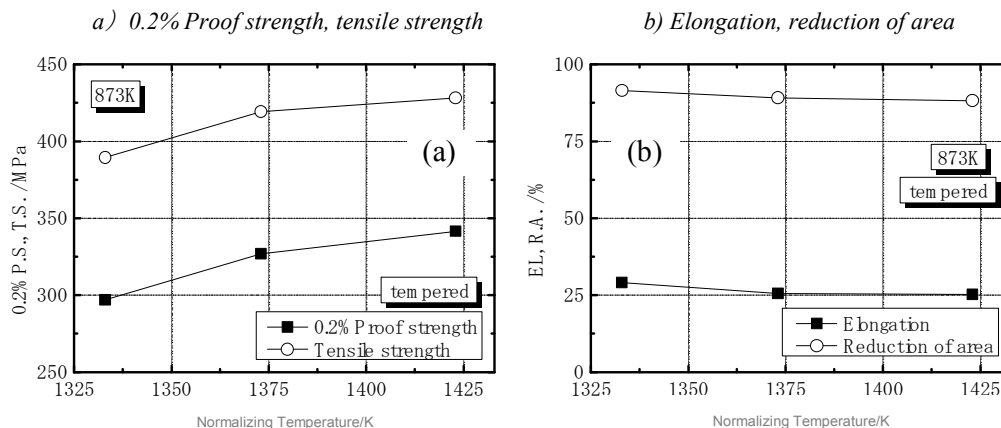


In general, V and Nb are expected to contribute to strengthening as solid solution strengthening elements [6]. The total amount of dissolved V and Nb was calculated based on the extracted residue analysis results for the steels. The difference in the amounts of dissolved V and Nb between the specimen normalised at 1 333 K and that normalised at 1 423 K was 0.012 mass%. Nakazawa, *et al.* shows that Vickers hardness increases about 20 Hv with 0.1 mass% increase of total amount of dissolved V and Nb [6]. Because the 0.012 mass% difference is very small, the influence of normalising temperature on hardness before tempering is small.

In contrast, the hardness increases with increase of normalising temperature after tempering. This was mainly caused by fine and dense precipitations which contributed to precipitation strengthening, based on the TEM observation results.

Figure 11 shows the results of tensile tests at 873 K. Both 0.2% proof stress and ultimate tensile strength increased with increase of normalising temperature as shown in Figure 11(a). This was caused by precipitation strengthening by fine and dense particles precipitated in the tempering process. As shown in Figure 11(b), the ductility of the steel slightly degraded.

Figure 11. Relationship between tensile properties at 873 K and normalising temperature



Performing creep tests and/or thermal aging tests is necessary, and the long-term microstructure stability and efficiency of strengthening mechanisms brought with such MX particles should be investigated. Nakazawa, *et al.* showed that the short- and middle-term creep strength could be improved with an increase of the normalising temperature [6]. Creep endurance in the short- and middle-term region of the steels in this study is expected to be improved by normalising at higher temperatures, but it is essential to improve the long-term creep endurance for the structural materials of the long-life FBR plants.

Whilst, coarsening of prior austenite grain size may make the steel brittle. The ductility of the steels does not degrade remarkably by normalising at higher temperature in the tensile test at 873 K as shown in Figure 11(b). However, the degradation of long-term ductility and toughness must be studied.

Conclusions

The influence of normalising temperature on MX precipitation behaviour has been investigated in high Cr steel. The following results were obtained:

- 1) $M_{23}C_6$, M_2X and MX (NbX, VX) were observed in the tempered specimens. The mean diameter of these precipitations which were observed in martensite laths decreased with increasing normalising temperature. The number density of $M_{23}C_6$ and MX became larger with increasing normalising temperature.
- 2) The fine and dense MX precipitation was obtained presumably because the amount of dissolved Nb in the matrices increased and the coarse unsolved MX particles decreased. In addition, since preferential nucleation site which is as prior grain boundary was decreased with increasing normalising temperature, as the results, new precipitation occurred at dislocation inside the prior austenite grains.
- 3) Hardness and tensile properties as tempered condition increased with increase of normalising temperature. This was mainly caused by fine and dense precipitations which contributed to precipitation strengthening.
- 4) It was clarified that a high normalising temperature is the best heat treatment to produce fine and dense MX particles in normalised-tempering condition. However, since FBR components are used at elevated temperatures for very long periods, it is essential to improve the long-term creep endurance for structural materials of the long-time FBR plants. The effects of heat treatment on long-term ductility and toughness should also be investigated.

REFERENCES

- [1] Takahashi, N., T. Fujita, “Effect of Individual Addition of Alloying Element on the Creep-Rupture Strength and Microstructure of 12% Cr Steel”, *Tetsu-to-Hagane*, Vol. 60, No. 10, pp. 1506-1518 (1974).
- [2] Suzuki, K., S. Kumai, H. Kushima, K. Kimura, F. Abe, “Heterogeneous Recovery and Precipitation of Z Phase During Long Term Creep Deformation of Modified 9Cr-1Mo Steel”, *Tetsu-to-Hagane*, Vol. 86, No. 8, pp. 550-557 (2000).
- [3] Suzuki, K., S. Kumai, H. Kushima, K. Kimura, F. Ab, “Precipitation of Z-phase and Precipitation Sequence During Creep Deformation on Mod.9Cr-1Mo Steel”, *Tetsu-to-Hagane*, Vol. 89, No. 6, pp. 691-698 (2003).
- [4] Wakai, T., M. Ando, K. Aoto, *Development of the High Chromium Ferritic Steel FBR Grade (1) Fabrications and Mechanical Properties of some Trial Products Controlling V and Nb Contents*, JNC TN9400 2004-010.
- [5] Onizawa, T., M. Ando, T. Wakai, S. Kato, K. Aoto, *Development of the High Chromium Ferritic Steel FBR Grade (2) Mechanical Properties and Observations of As-received and Aged some Trial Products Controlling V and Nb Contents*, JNC TN9400 2005-012.
- [6] Nakazawa, T., Y. Yamada, T. Takahashi, M. Yamazaki, H. Hongo, “Relation Between Mechanical Properties and Microstructures of 9Cr-W-Mo Steel”, *JHPI*, Vol. 40, No. 6, pp. 340-347 (2002).
- [7] Iseda, A., H. Teranishi, F. Masuyama, “Effects of Chemical Compositions and Heat Treatments on Creep Rupture Strength of 12wt%Cr Heat Resistant Steels for Boiler”, *Tetsu-to-Hagane*, Vol. 76, No. 7, pp. 1076-1083 (1990).
- [8] Ishii, R., Y. Tsuda, M. Yamada, K. Kimura, “Fine Precipitates in High Chromium Heat Resisting Steels”, *Tetsu-to-Hagane*, Vol. 88, No. 2, pp. 36-43 (2002).
- [9] Tsuchida, Y., T. Takeda, Y. Tokunaga, “Effect of Rolling and Normalizing Conditions on the Creep Rupture Strength of 9Cr-1Mo-VNbN Steel and the Pole of V,Nb Carbo-nitride”, *Tetsu-to-Hagane*, Vol. 80, No. 9, pp. 723-728 (1994).
- [10] Yoshino, M., Y. Mishima, Y. Toda, H. Kushima, K. Sawada, K. Kimura, “Phase Equilibrium Between Austenite and MX Carbonitride in a 9Cr-1Mo-V-Nb Steel”, *ISIJ International*, Vol. 45, No. 1, pp. 107-115 (2005).
- [11] Tokuno, K., K. Hamada, T. Takeda, “Dispersion Strengthening High-Cr Steels by Forming ‘V-Wings’”, *JOM*, pp. 25-28, April (1992).

- [12] Taneike, M., M. Kondo, T. Morimoto, “Accelerated Coarsening of MX Carbonitrides in 12%Cr Steels During Creep Deformation”, *ISIJ International*, Vol. 41, Supplement, pp. S111-115 (2001).
- [13] Yamada, K., M. Igarashi, S. Munei, F. Abe, “Effect of Heat Treatment on Precipitation Kinetics in High-Cr Ferritic Steels”, *ISIJ International*, Vol. 42, No. 7, pp. 779-784 (2002).
- [14] Takaki, S., K. Tsuzaki, “Material Engineering Series 2 Physical Metallurgy”, Asakura Publishing Co., Ltd., p.102 (2000).
- [15] Okaguchi, S., T. Hashimoto, “Computer Model for Prediction of Carbonitride Precipitation During Hot Working in Nb-Ti Bearing HSLA Steels”, *ISIJ International*, Vol. 32, No. 3, pp. 283-290 (1992).
- [16] Qiu, P. M. Nagumo, “Effect of Austenitizing Temperature on Intergranular Proeutectoid Ferrite Nucleation in a V-N Steel”, *Tetsu-to-Hagane*, Vol. 85, No. 1, pp. 45-51 (1999).

**DEVELOPMENT OF ODS FERRITIC-MARTENSITIC STEELS
FOR INNOVATIVE NUCLEAR FAST BREEDER REACTORS**

**A.A. Nikitina¹, V.S. Ageev¹, M.V. Leontyeva-Smirnova¹, V.V. Sagaradze²,
B.V. Safronov¹, A.P. Chukanov¹, V.V. Tsvelev¹, M.M. Potapenko¹**

¹A.A. Bochvar All-Russian Research Institute of Inorganic Materials, Moscow, Russia

²Institute of Metal Physics, Russian Academy of Sciences, Yekaterinburg, Russia

Abstract

The present paper outlines the first research results of elaboration and investigation of oxide dispersion strengthened (ODS) steel on the basis of ferritic-martensitic steel Fe-13Cr-2Mo-Nb-V-B-0,12C. The results of works concerning the creation of ODS ferritic-martensitic steels and further prospects of their development in Russia are reviewed.

Introduction

The energetic strategy of Russia during the period up to 2020 proposes the gradual input of a new nuclear energy technology on fast breeder reactors (FBR) with closed fuel cycle using MOX fuel. Further development of atomic energy will demand the inclusion of fast breeder reactors in the structure of APP powers.

Of all types of fast breeder reactors, those with liquid sodium coolant (SFR) are the most industrially developed today. The most striking example of such reactors is BN-600, working on Beloyarskaya APP from 1980.

The Federal Special Program “Development of Atomic Power-industrial Complex of Russia on 2007-2010 Years and on Prospect Up to 2015” provides construction and putting in operation in 2012 the fourth block of Beloyarskaya APP with reactor BN-800, creation of MOX fuel production and realisation of closed fuel cycle on the base of this reactor.

Today the use of austenitic steel Fe-16Cr-15Ni-2Mo-0,06C cw for fuel pin claddings and ferritic-martensitic steel Fe-13Cr-2Mo-Nb-V-B-0,12C for wrapper tubes had assured the working capacity of fuel assemblies in reactor BN-600 up to damage dose ~ 83 dpa and fuel burn-up $\sim 11\%$, but achieved fuel burn-up does not assure the effective techno-economic factors of the BN fuel cycle. At present the limitation of maximum fuel burn-up is connected with relatively low radiation resistance of structural materials for fuel pin claddings and low heat resistance of wrappers of fuel assemblies.

The main factors which determine the radiation resistance of structural materials for BN are: void swelling, radiation creep, high- and low-temperature radiation embrittlement and also the radiation stability of structure and properties of material in the field of neutron irradiation.

The heat resistance of high-strength aging steels is determined by the stability of steel matrix, reinforced by particles, at increased temperatures and loadings. Usually particles of intermetallic phases and disperse carbides, applied for the purpose of strengthening, begin to coagulate and to dissolve at temperatures superior to 700°C .

Currently, steels of almost all classes – austenitic, ferritic and ferritic-martensitic – are being taking up as perspective structural materials for step-by-step increase of fuel burn-up in BN reactors.

Work concerning the creation of oxide dispersion strengthened (ODS) steels began at the end of 2004 at the Institute of Inorganic Materials. These steels combine high radiation resistance of ferritic-martensitic steels and high heat resistance due to the presence in the structure of thermally stable oxides of 3-5 nm [1-12].

As is well known, work concerning the development of such steels for fast breeder and fusion-type reactors are now actively in place in Japan, USA, Europe, China and other countries.

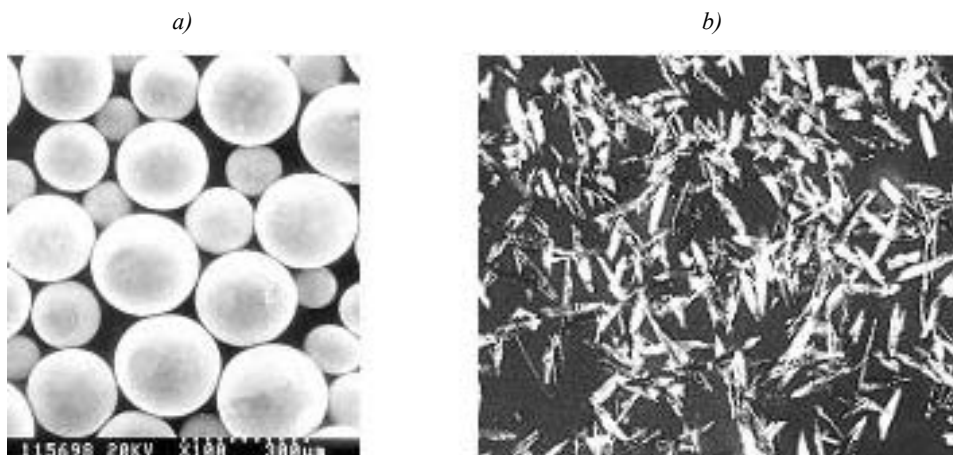
ODS steels are being considered as prospective structural materials, which will be able to work in the core of BN in high flows of fast neutrons ($E > 0.1$ MeV) up to damage dose ~ 200 dpa at temperatures $370-710^{\circ}\text{C}$.

Results of works over creating ODS ferritic-martensitic steels

On the basis of world-wide and Institute of Inorganic Materials experience in powder metallurgy we have tested the following technological scheme of receiving the ODS ferritic-martensitic steels on the base of Fe-13Cr-2Mo-Nb-V-B-0,12C steel:

- receiving of matrix steel powder (Fe-13Cr-2Mo-Nb-V-B-0,12C) with spherical or scaly shape of particles by the centrifugal atomisation of melt from revolving crucible in inert gas atmosphere [Figures 1(a) and 1(b)];
- mechanical alloying of received powder by nanoparticles of Y_2O_3 in vibration high-energy mill;
- vibro-infill of steel cans by received powder blend, decontamination and sealing of cans;
- hot extrusion at 1 150°C of cans with powder blend in hot-extruded bar with drawing no more than 10-12 and subsequent mechanical treatment.

Figure 1. Outward of spherical (a) and scaly (b) powder of steel Fe-13Cr-2Mo-Nb-V-B-0,12C

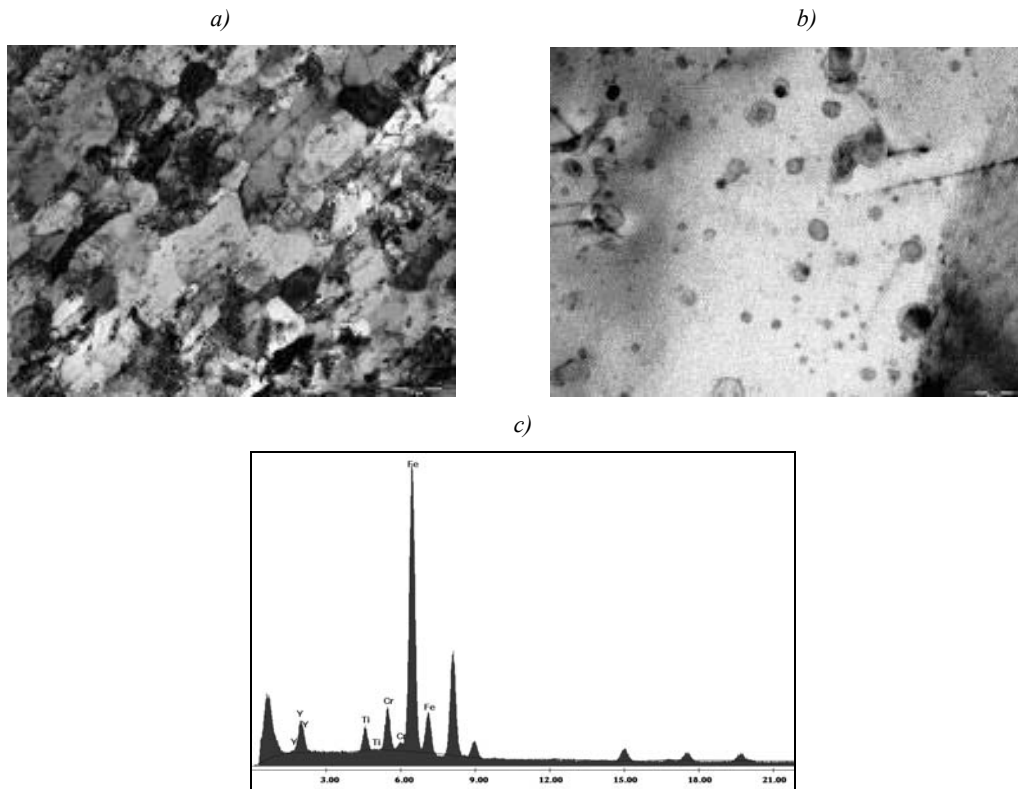


On the spherical powder of steel Fe-13Cr-2Mo-Nb-V-B-0,12C complex investigations over optimisation of mechanical alloying parameters (time, mass ratio of milling balls and powder, size of initial powders, etc.) were carried out. Methods used included X-ray and neutron diffraction analysis, electron microscopy and Mössbauer spectroscopy on initial and mechanically-alloyed powders and on compacted materials.

In the last experiment the scaly powder of matrix steel Fe-13Cr-2Mo-Nb-V-B-0,12C was used. Mechanical alloying of steel Fe-13Cr-2Mo-Nb-V-B-0,12C by 0.25 wt.% of yttrium oxide was carried out in a high-energy vibration mill during 30 h without intermediate openings of the mill. In addition to the Y_2O_3 , 0.3 wt.% of Ti powder was introduced in charge before mechanical alloying with the purpose of ensuring the oxygen balance and receiving more disperse and stable particles of double oxides during subsequent thermo-mechanical treatment of powders in the process of receiving the compact material [13,14].

The structure of a bar, received by hot extrusion, is shown in Figures 2(a) and 2(b). In the specimen the oblong shape of the grains along the extrusion direction is observed. The structure consists mainly of ferritic grains with sizes ranging from 0.3 to 3 μm . The use of powder metallurgy leads to the very

Figure 2. Microstructure of a bar from steel (Fe-13Cr-2Mo-Nb-V-B-0,12C) ODS (a,b) and X-ray spectrum from oxide particles (c)



strong refinement of grains in comparison with structure of matrix steel Fe-13Cr-2Mo-Nb-V-B-0,12C. The mean size of grains in this steel is about 20 μm . Oxides are situated on the boundaries and inside the grains. Oxide sizes on the boundaries range from 5 to 100 nm and inside the grains from 2 to 10 nm. The largest volume fraction consists of oxides with mean size 4-6 nm. According to X-ray spectrum microanalysis it was detected that all particles consist of combined oxides of yttrium and titanium [see Figure 2(c)].

A portion of a bar from steel (Fe-13Cr-2Mo-Nb-V-B-0,12C) ODS, received after hot extrusion, was hot rolled in the longitudinal direction in a 2-mm thick plate. Hot rolling was carried out at 1100°C up to 2 mm thickness at three passes with intermediate annealing 1150°C, 30 minutes after each pass. Later on plate specimens of 50 × 10 × 2 mm sizes from steels Fe-13Cr-2Mo-Nb-V-B-0,12C (cut out from the wrapper tube of reactor BN-600) and (Fe-13Cr-2Mo-Nb-V-B-0,12C) ODS (cut out from the hot-rolled plate) the comparative tests on thermal creep were carried out. Tests were carried out at temperatures 650 and 700°C and stresses 140 and 120 MPa, respectively (Figure 3).

The test results (Table 1) show that the thermal creep rate in steel (Fe-13Cr-2Mo-Nb-V-B-0,12C) ODS is two orders of magnitude less than thermal creep rate in steel Fe-13Cr-2Mo-Nb-V-B-0,12C.

An estimation of the deformative ability of received material was carried out to determine the manufacturing route for the thin-walled tubes from steel (Fe-13Cr-2Mo-Nb-V-B-0,12C) ODS. To that purpose the hot-rolled plates from steel (Fe-13Cr-2Mo-Nb-V-B-0,12C) ODS were cold-rolled up to 0.4 mm thickness with different deformation ratios. Standard test specimens (width of specimen – 3 mm, length of test portion – 12 mm) were cut out from the plates. Tests on short-term mechanical properties were carried out on these specimens.

Figure 3. Thermal creep curves of the plated specimens from Fe-13Cr-2Mo-Nb-V-B-0,12C and (Fe-13Cr-2Mo-Nb-V-B-0,12C) ODS steels at temperatures 650°C (a) and 700°C (b)

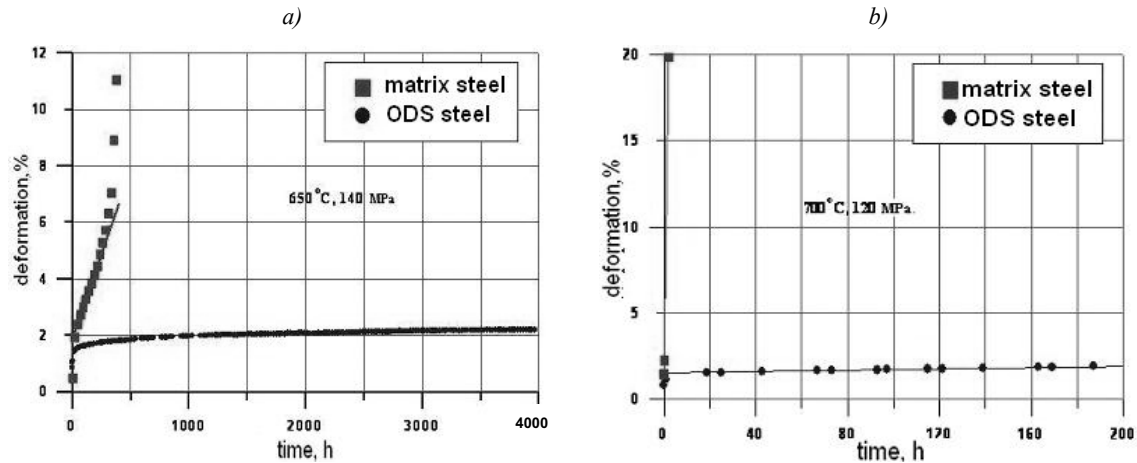


Table 1. Results of thermal creep tests of the plated specimens 50 × 10 × 2 mm from Fe-13Cr-2Mo-Nb-V-B-0,12C and (Fe-13Cr-2Mo-Nb-V-B-0,12C) ODS steels at temperatures 650°C and 700°C

Material	Test temperature, °C	Stress, MPa	Creep rate, %/h
Fe-13Cr-2Mo-Nb-V-B-0,12C	650	140	$1.18 \cdot 10^{-2}$
(Fe-13Cr-2Mo-Nb-V-B-0,12C) ODS	650	140	$2.38 \cdot 10^{-4}$
Fe-13Cr-2Mo-Nb-V-B-0,12C	700	120	9.1
(Fe-13Cr-2Mo-Nb-V-B-0,12C) ODS	700	120	$1.82 \cdot 10^{-3}$

Table 2 performs the values of per cent elongation, yield strength and ultimate tensile strength for specimens with different deformation ratios. It can be seen from the table that ultra disperse steel (Fe-13Cr-2Mo-Nb-V-B-0,12C) ODS retains rather high residual elongation after cold rolling with deformation ratios up to 60%. This has allowed forming a conclusion as to the possibility of application of existing manufacturing route for thin-walled tubes from standard steel Fe-13Cr-2Mo-Nb-V-B-0,12C for receiving tubes from (Fe-13Cr-2Mo-Nb-V-B-0,12C) ODS steel.

Table 2. Mechanical properties of the plates from (Fe-13Cr-2Mo-Nb-V-B-0,12C) ODS steel with different deformation ratio

Def. ratio, %	Elongation, %	YS, MPa	UTS, MPa
20	7.1	839	885
30	6.6	868	909
40	6.2	881	922
50	5.0	893	945
60	4.6	912	960
70	3.8	1 086	1 169

On a specimen of a plate, cold-rolled with a deformation ratio of 40%, a heat treatment at 1 150°C, was carried out for 1 h. Standard test specimens were cut out from a plate and tests on short-term mechanical properties were carried out. The test results of tests are displayed in Table 3 in comparison with the results of test specimens from steel Fe-13Cr-2Mo-Nb-V-B-0,12C after standard heat treatment.

Table 3. Mechanical properties of a plate from steel (Fe-13Cr-2Mo-Nb-V-B-0,12C) ODS of 0.4 mm thickness (40% c.w.) after heat treatment 1 150°C, 1 h in comparison with mechanical properties of steel Fe-13Cr-2Mo-Nb-V-B-0,12C after standard heat treatment

Material	UTS, MPa	YS, MPa	Elongation, %
(Fe-13Cr-2Mo-Nb-V-B-0,12C) ODS	822±13	667±9	15±2
Fe-13Cr-2Mo-Nb-V-B-0,12C (standard heat treatment)	650	580	16

As can be seen from Table 3, this heat treatment leads to a significant increase in material ductility. The ductility level of steel (Fe-13Cr-2Mo-Nb-V-B-0,12C) ODS is on the ductility level of steel Fe-13Cr-2Mo-Nb-V-B-0,12C after standard heat treatment. The strength of steel (Fe-13Cr-2Mo-Nb-V-B-0,12C) ODS is higher than the strength of steel Fe-13Cr-2Mo-Nb-V-B-0,12C.

At the end of 2006 the first experimental batch of thin-walled tubes of 6.9×0.4 mm size from steel (Fe-13Cr-2Mo-Nb-V-B-0,12C) ODS was received at the Institute of Inorganic Materials.

The structure of received tubes after final heat treatment – 1 150°C, 1.5 h – consists of equiaxed subgrains with sizes ranging from 0.1 to 3 μm [Figure 4(a)]. Such structure does not seem to lead to anisotropy of properties in the longitudinal and transverse directions. Inside subgrains the uniformly distributed oxides are observed [Figure 4(b)]. The distribution of oxides by size is performed on Figure 5. The mean size of oxide particles is about 7 nm, concentration is about 10^{16} cm^{-3} .

It might be supposed that small particles of 1-6 nm in size are the complex oxides of titanium and yttrium, which precipitate from the lattice of matrix steel in the hot extrusion process after deformative dissolution of yttrium oxide during mechanical alloying [15]. Particles larger in size are present in the structure due to incomplete dissolution of yttrium oxide during mechanical alloying.

Figure 4. Structure of a cladding tube from steel (Fe-13Cr-2Mo-Nb-V-B-0,12C) ODS after heat treatment 1 150°C, 1.5 h

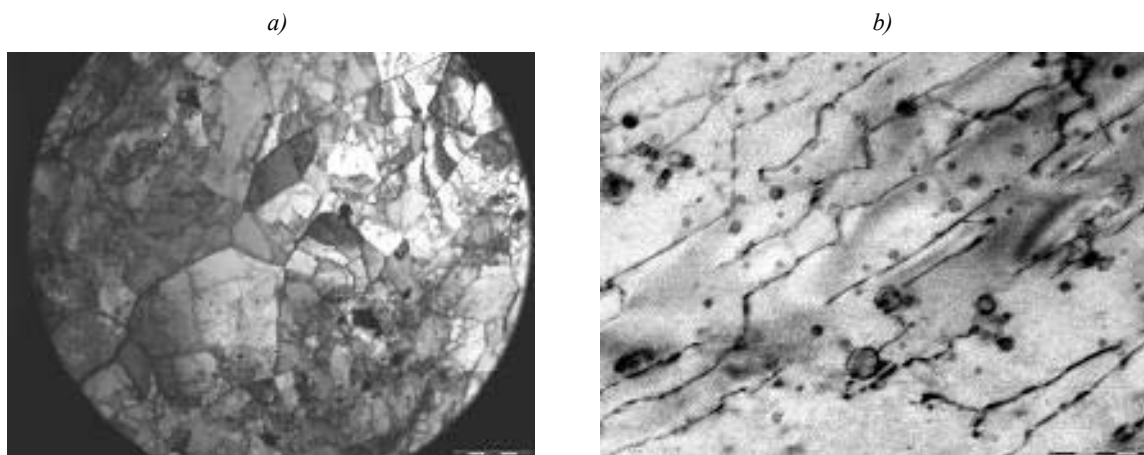
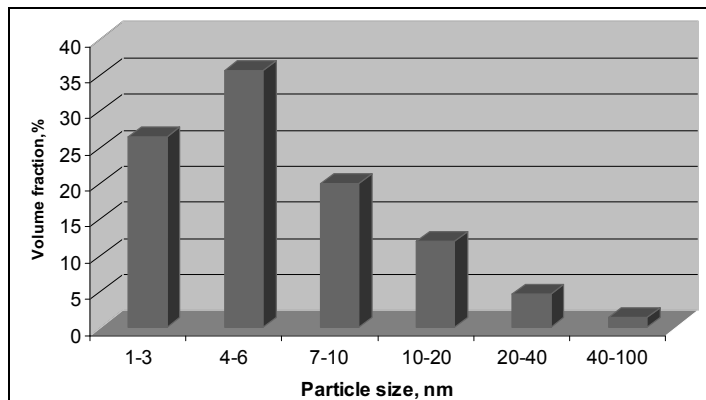


Figure 5. Oxide sizes distribution in specimen of a cladding tube from (Fe-13Cr-2Mo-Nb-V-B-0,12C) ODS steel



Prospects of development of works over ODS ferritic-martensitic steels

In 2007 we plan the following investigations of experimental specimens of thin-walled tubes from steel (Fe-13Cr-2Mo-Nb-V-B-0,12C) ODS:

- tests on short- and long-term mechanical properties on longitudinal and transverse specimens (including determination of impact toughness);
- choice of sealing conditions (working out different methods of welding and brazing);
- investigation of corrosion properties (corrosion in liquid sodium, in water, stress corrosion and corrosion during interaction with fuel).

At present, works over receiving the ODS steel on the base of reduced-activation martensitic steel 12Cr-2W-V-Ta-B-0,16C are being carried out.

At the end of 2007, beginning of 2008 we plan to put tubes on irradiation as specimens in material authority fuel assembly in reactor BN-600 and as fuel pin claddings in reactor BOR-60.

To increase the corrosion properties, the reception of ODS ferritic steel with increased (14-18%) Cr content is planned.

To further increase the heat resistance (up to 850°C) the optimisation of technological parameters of receiving the ODS ferritic steels with oxide sizes 1-2 nm and concentration $\sim 10^{18} \text{ cm}^{-3}$ is provided.

Conclusion

The present work presents the first research results concerning the elaboration and investigation of oxide dispersion strengthened (ODS) steel on the base of ferritic-martensitic steel Fe-13Cr-2Mo-Nb-V-B-0,12C.

The experimental batch of powder of steel Fe-13Cr-2Mo-Nb-V-B-0,12C was attained through the atomisation of a liquid melt in an inert gas atmosphere. The mechanical alloying of the steel

Fe-13Cr-2Mo-Nb-V-B-0,12C by yttrium oxide and titanium was carried out. Complex investigations of initial and mechanical alloyed powders were undertaken using methods such as electron microscopy, X-ray and Mössbauer researches.

Methods of compacting of the powders from heat-resistant steel (Fe-13Cr-2Mo-Nb-V-B-0,12C) ODS by hot extrusion were worked out and tested.

The investigation of structure and phase composition of the bar from steel (Fe-13Cr-2Mo-Nb-V-B-0,12C) ODS was carried out using electron microscopy and X-ray microanalysis. Information about the composition and distribution of oxide particles present in the material was received.

Thermal creep tests were carried out on the plate specimens of matrix steel Fe-13Cr-2Mo-Nb-V-B-0,12C and on steel (Fe-13Cr-2Mo-Nb-V-B-0,12C) ODS. It was determined that presence of double yttrium and titanium oxides of 2-5 nm size in the structure of the steel leads to a decrease in the thermal creep rate at 700°C of about two orders of magnitude.

Estimations concerning the deformative ability of steel (Fe-13Cr-2Mo-Nb-V-B-0,12C) ODS has shown that nanostructured steel (Fe-13Cr-2Mo-Nb-V-B-0,12C) ODS retains a rather high level of residual elongation after cold deformation up to 60%.

In light of this, the manufacturing route for tubes 6.9 × 0.4 mm size with intermediate heat treatments was chosen.

The experimental batch of thin-walled tubes 6.9 × 0.4 mm from steel (Fe-13Cr-2Mo-Nb-V-B-0,12C) ODS was received and complex investigations of their structure were carried out.

Further prospects of development of works concerning ODS steels in Russia are in review.

REFERENCES

- [1] Huetj, J.J., "Sintered Metal-ceramic Composites", Elsevier Science Publishers B V, Amsterdam, pp. 197-212 (1984).
- [2] Dewilde, L., J. Gedopt, A. Delbrassine, C. Driesen, B. Kazimierzak, *Proc. of the Int. Conf. of Materials for Nuclear Reactor Core Application*, Bristol, pp. 271-276 (1987).
- [3] Tian Yun, Shan Binguan, Pan Qingchun, Sun Jiguang, "Studies on ODS Ferritic Alloy for Advanced LMFBR Cladding Application in CISRI", *Proc. Mater. for Advanced Energy Systems & Fission and Fusion Engineering*, Southwestern Institute of Physics, Chengdu, China, pp. 110-115 (1995).
- [4] Tian Yun, Shan Binguan, Liu Guangzu, *et al.*, "An Overview of Several Iron Base Oxide Dispersion Strengthened Alloys for Nuclear Application", *Mater. for Advanced Energy Systems & Fission and Fusion Engineering*, A. Kohuama, *et al.* (Eds.) Japan. Soc. Mater. Advanced Energy Systems, pp. 307-312 (1994).

- [5] Ukai, S., M. Harada, H. Okada, *et al.*, “Alloying Design of Oxide Dispersion Strengthened Ferritic Steel for Long Life FBRs Core Materials”, *J. Nucl. Mater.*, Vol. 204, pp. 65-73 (1993).
- [6] Ukai, S., M. Harada, H. Okada, *et al.*, “Tube Manufacturing and Mechanical Properties of Oxide Dispersion Strengthened Ferritic Steel”, *J. Nucl. Mater.*, Vol. 204, pp. 74-82 (1993).
- [7] Wilson A.M., M.C. Clayden, J. Standing, *Proc. of the Int. Conf. of Materials for Nuclear Reactor Core Application*, Bristol, pp.25-30 (1987).
- [8] Asano K., Y. Kohno, A. Kohyama, T. Suzuki, H. Kusanagi, “Microstructural Evolution of an Oxide Dispersion Strengthened Steel Under Charged Particles Irradiation”, *J. Nucl. Mat.*, Vol. 155-157, pp. 928-934 (1988).
- [9] Mukhopadhyay, D.K.H., F. Froes, D.S. Gelles, “Development of Oxide Dispersion Strengthened Ferritic Steel for Fusion”, *J. Nucl. Mat.*, Vol. 258-263, pp. 1209-1215 (1998).
- [10] Klueh, R.L., D.S. Gelles, S. Jitsukawa, A. Kimura, G.R. Odette, B. Van der Schaaf, M. Victoria, “Ferritic/Martensitic Steels – Overview of Recent Results”, *J. Nucl. Mat.*, Vol. 307-311, pp. 455-465 (2002).
- [11] Ukai, S., T. Nishida, K. Kaneda, T. Okuda, M. Fujiwara, K. Asabe, S. Hagi, “Development of Oxide Dispersion Strengthened Ferritic Steel for Fast Reactor Core Application”, *The 4th Japan – China symposium on Materials for Advanced Energy Systems & Fission and Fusion Engineering* (1996).
- [12] Klueh, R.L., P.J. Maziasz, I.S. Kim, L. Heatherly, D.T. Hoelzer, N. Hashimoto, *et al.*, “Tensile and Creep Properties of an Oxide Dispersion-strengthened Ferritic Steel”, *J. Nucl. Mat.*, Vol. 307-311, pp. 773-777 (2002).
- [13] Miller, M.K., D.T. Hoelzer, S.S. Babu, E.A. Kenik, K.F. Russell, “High Temperature Microstructural Stability of a MA/ODS Ferritic Alloy. High Temperature Alloys: Processing for Properties”, G.E. Fuchs, J.B. Wahl (Eds.), *The Minerals, Metals & Materials Society (TMS)* (2003).
- [14] Ohtsuka, S., S. Ukai, M. Fujiwara, T. Kaito, T. Narita, “Improvement of 9Cr-ODS Martensitic Steel Properties by Controlling Excess Oxygen and Titanium Contents”, *J. Nucl. Mat.*, Vol. 329-333, pp. 372-376 (2004).
- [15] Sagaradze, V.V., V.I. Shalaev, V.L. Arbuzov, B.N. Goshchitskii, Yun Tian, Wan Qun, Sun Jiguang, “Radiation Resistance and Thermal Creep of ODS Ferritic Steels”, *J. of Nuclear Materials*, 295, pp. 265-272 (2001).

VOID SWELLING AND DEFECT PROCESSES IN Ti-MODIFIED STEELS USING ACCELERATOR IRRADIATION

**K.G.M. Nair, B.K. Panigrahi, J. Arunkumar, C. David, S. Balaji, R. Rajaraman,
G. Amarendra, S. Abhaya, M.C. Valsakumar, C.S. Sundar, B. Raj**
Indira Gandhi Centre for Atomic Research, Kalpakkam 603 102, India

Abstract

The void swelling behaviour of (15Ni-14Cr)-0.25Ti and (15Ni-14Cr)-0.15Ti steels are studied using heavy ion irradiation for understanding the influence of titanium in the void swelling resistance of these D9 alloys. The cold worked samples have been pre-implanted with a uniform helium concentration of 30 appm spanning a width of about 640 nm. This was followed by a 5-MeV nickel ion irradiation to create a peak damage of ~100 dpa at a damage rate of 7×10^{-3} dpa/s at various irradiation temperatures between 700 and 970 K. The gross swelling in the implanted range is measured by step height measurements. It is found that the peak swelling temperatures and the magnitude of swelling for the alloys are different. The difference in void swelling behaviour with variation in titanium concentration in these two alloys is discussed on the basis of the role of titanium on the vacancy migration and TiC precipitate formation. Isochronal annealing study of the positron lifetime in the un-irradiated alloys reveals different TiC precipitates formation behaviour in the two alloys. *Ab initio* calculations of positron lifetime, using large supercells, show that C vacancies at the TiC/austenite interface are the predominant positron trapping centres in these alloys.

Introduction

One of the most important property changes caused by irradiation in neutron environment is void swelling, which introduces dimensional changes and thereby limits the lifetime of structural components used in a reactor. Therefore, resistance to void swelling is a major consideration in the choice of materials for the core components. Efforts have been made to improve resistance to void swelling by adjusting the minor alloying elements (P, Si, Ti) and thermo-mechanical treatments to introduce efficient traps for vacancies and helium such as dislocations and precipitate-matrix interfaces [1,2]. The titanium-modified steels exhibited greatly improved swelling resistance under breeder reactor conditions [3] and consequently, have become prime candidates for structural applications. In the cold worked Ti-modified austenitic stainless steels, formation of fine stable precipitates of TiC have been reported to enhance resistance against void swelling, helium embrittlement and in-pile creep during irradiation [4-8].

For the development of better swelling-resistant alloys, one needs to optimise composition of minor alloying elements like P, Si, Ti, etc., which have a major influence on the swelling [9]. Therefore the alloy development programme is in need of a test bed where one can study the effect of minor elements on swelling of the model alloys, which are exposed to high displacement damage levels. Accelerated heavy ions, which possess an inherent advantage of producing high displacement rates, have been used for evaluating the effect of minor alloying elements on swelling and for basic studies in radiation damage [6,10]. Titanium-modified (15Ni, 14Cr) steel D9, and its modified version with phosphorous addition (designated as D9I) are envisaged as fuel cladding and wrapper materials in the Indian Fast Breeder Reactor (FBR) programme. In the FBR, the fuel clad tubes would experience temperatures in the range 673-973 K under steady-state condition and the maximum neutron dose for target burn-up of 100 000 MWd/t is 85 dpa.

In this paper we compare the void swelling behaviour of two titanium-modified austenitic steels with 0.25 and 0.15 wt.% Ti. The alloys are pre-injected with 30 appm of helium followed by a 5-MeV irradiation to a damage level of 100 dpa in the temperature range of 700-970 K. The swelling in these alloys are measured by surface profilometry. Positron lifetime measurements are carried out on the un-irradiated alloys to monitor the defect recovery during isochronal annealing. Positron annihilation spectroscopy (PAS) is an established technique for studies concerning vacancy clustering and helium bubbles [11] as well as studies on the early stages of solute atom clustering and precipitation [12]. The ability of PAS to monitor the TiC precipitation process in D9 alloy has been reported earlier [13]. The difference in void swelling behaviour in the alloys under study is discussed on the basis of the role of titanium on the vacancy migration and TiC precipitate formation.

While positron annihilation spectroscopy provides valuable insight into defect evolution at atomic scales, it is imperative to complement the experimental results with computed annihilation parameters for an unambiguous understanding. In view of the very small supercell sizes, the earlier computational studies focused on an ordered array of interacting vacancies rather than on isolated monovacancies. They also suffered from a lack of self-consistent structural relaxation around the vacancy. With the recent developments in *ab initio* electronic structure calculations and availability of parallel computing facilities, it is now feasible to make more realistic computation of monovacancies and their interactions with impurities. One of the aims of the present study is to use *ab initio* calculations identify the vacancy that acts as a trapping centre for positrons.

Experimental details

Specimen preparation

D9 alloy samples, of size 15 mm × 15 mm × 1.5 mm and 5 mm × 12 mm × 1.5 mm are spark cut from 20% cold-worked D9 hexagonal wrappers supplied by M/s. Valinox, France (designated as Sample A) and 20% cold-worked D9 wrapper tubes obtained from NFC, Hyderabad (designated as Sample B). The samples were further mechanically polished and finished with a diamond-lapping compound to a smooth surface. The chemical compositions of Samples A and B are given in Table 1.

Table 1. Composition of Samples A and B

Element	Sample A	Sample B
	Conc. in wt.%	Conc. in wt.%
Carbon	0.037 ± 0.005	0.037 ± 0.005
Chromium	15.0 ± 0.5	15.0 ± 0.5
Nickel	14.0 ± 0.5	14.0 ± 0.5
Manganese	1.90 ± 0.05	1.42 ± 0.05
Molybdenum	2.20 ± 0.05	2.10 ± 0.5
Phosphorous	<0.014	<0.014
Silicon	0.75 ± 0.05	0.88 ± 0.05
Cobalt	0.020 ± 0.005	0.020 ± 0.005
Titanium	0.250 ± 0.005	0.150 ± 0.005
Vanadium	0.045 ± 0.003	0.045 ± 0.

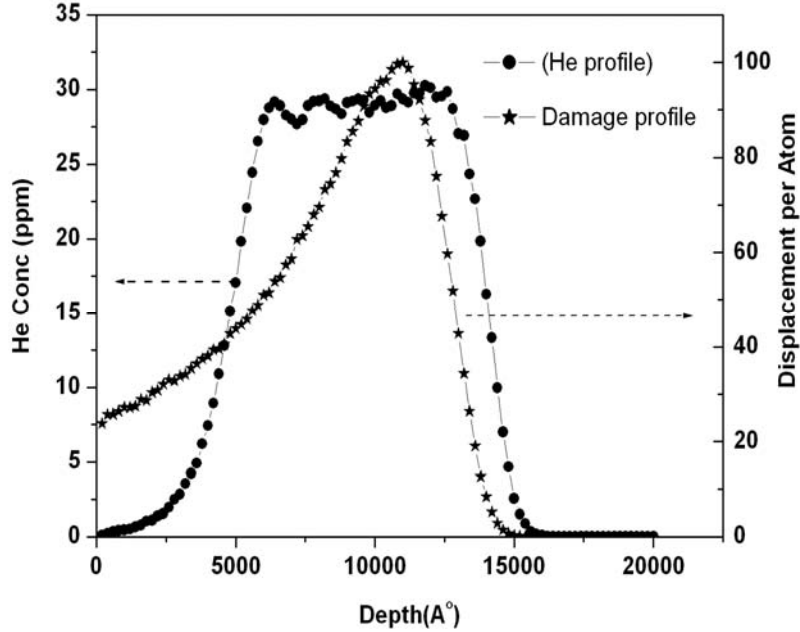
Irradiation procedure

The pre-injection of helium was carried out at room temperature at different energies from 200 keV to 700 keV in order to obtain a uniform concentration of 30 appm helium around the peak damage region of 5.0-MeV Ni²⁺ ions. These pre-injected specimens were sequentially implanted with 5.0-MeV Ni²⁺ ions, using a 1.7-MV Tandetron accelerator (M/s HVEE, Europa, The Netherlands), to a dose of about 9.0×10^{16} ions/cm² which corresponds to ~100 dpa at the damage peak as calculated by the TRIM program [14] invoking modified Kinchin-Pease analytic solution for the calculation of damage. The range and straggling of 5.0-MeV Ni²⁺ in stainless steels as calculated from TRIM program are 140 nm and 118 nm respectively as shown in Figure 1. The nickel ion irradiation was carried out at temperatures ranging from 700 to 970 K. The temperature stability during irradiation was ±2 K. The irradiations were carried out in a UHV irradiation chamber, which was maintained at a vacuum of 4×10^{-7} mbar. During irradiation, the sample was mounted on a UHV manipulator (M/s Vacuum Generator, UK) equipped with a high-temperature heating attachment. After the high-temperature irradiation, the sample was quenched to the ambient temperature using a jet of helium gas cooled by liquid nitrogen.

Step height measurements

For carrying out the step height measurements, the specimen was partially masked with a stainless steel mask with a knife edge during ion irradiation, so that only the unmasked region was irradiated. As the bombarded region swells, the surface becomes elevated and a step forms at the

Figure 1. Implantation scheme showing helium concentration profile and 5-MeV nickel damage profile simulated using TRIM program



interface between the masked and unmasked regions. Measurement of this step height provides the total integrated swelling that has occurred along the path of the bombarding ion [15]. The step height was measured using a surface profilometer (model Dektak 6M). In order to arrive at the quantitative estimate of volumetric swelling, suitable corrections were made for the changes in step height due to injected nickel ions and for the sputtering of the sample by the nickel ions. The one-dimensional step height measurement gives the volumetric swelling. As the range of the 5-MeV nickel ions is much less than 1% of the specimen thickness, the swelling in this thin layer is laterally constrained by the bulk of the material underneath. Thus the entire volume change is accommodated by a movement of the mass perpendicular to the sample surface. An estimate of the height h of the plateau elevated from the initial surface could be as [16]:

$$h = \frac{S_A}{1 + S_A} \Delta R$$

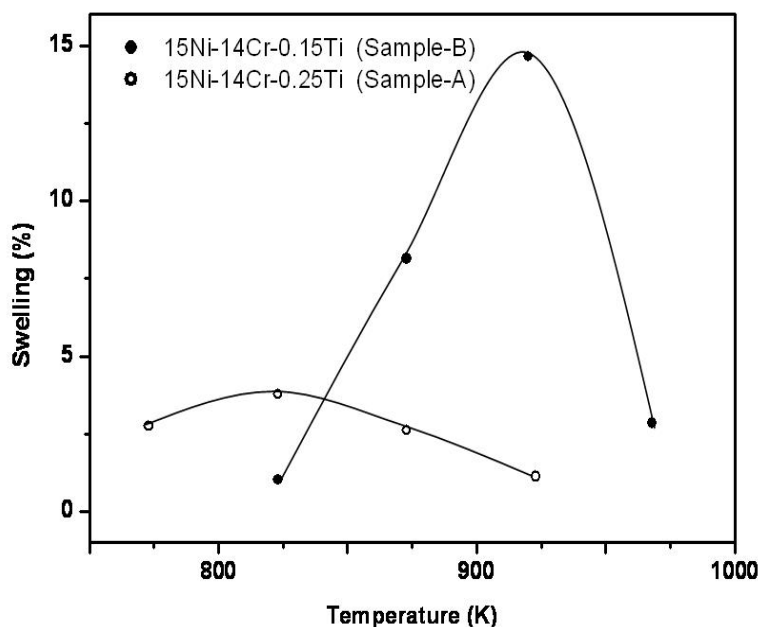
where h is the step height (\AA), ΔR is the visible void spreading width (\AA), S_A is the average void swelling and ΔR was assumed to be $R_p + \frac{\Delta R_p}{2}$, where R_p and ΔR_p are the range (\AA) and straggling (\AA) of the nickel ions. From the measurements of h , we have estimated the void swelling S_A .

Results and discussion

Figure 2 shows the variation of void swelling as a function of irradiation temperature for Samples A and B. For either alloy the swelling increases as a function of temperature to a peak and thereafter decreases at higher temperature. At low temperatures, the swelling is low because the defect migration is slow and hence results in high steady-state concentrations of interstitials and vacancies. This leads to an enhanced recombination and only few defects migrate to biased sinks to cause swelling. As the

temperature is increased, recombination is no longer a dominant process as the vacancies become mobile and the defects migrate to sinks. At such temperatures, void growth takes place in the presence of a dislocation bias (i.e. the dislocations absorb more interstitials compared to vacancies). The drop in swelling at temperatures beyond the peak swelling temperatures is due to the thermal emission of vacancies from the voids. The temperature-swelling relationship of both the alloys shown in Figure 2 is in agreement with the physical picture of void formation. However, the peak swelling temperature and the magnitude of swelling at that temperature are different in the irradiated alloys. As can be seen in Figure 2, the alloy with 0.15% Ti displayed a swelling of ~15% at the peak swelling temperature of 923 K, whereas the alloy with 0.25% Ti has a swelling maximum of ~4% at 823 K. In view of the similar thermo-mechanical treatment on both the samples and the irradiation conditions, the observed difference in void swelling behaviour can be attributed to the differences in the chemical composition.

Figure 2. Temperature dependence of void swelling measured by surface profilometry for the D9 alloys with different titanium concentration



From Table 1, which compares the chemical composition of both the alloys, one can see that there is a difference in titanium concentration. Herschbach, *et al.* [19] carried out a study of in-pile creep and swelling behaviour of a series Fe-15Cr-15 Ni steels containing 0.1 wt.% C and found the swelling to be a minimum for Ti content of 0.25% at temperatures of 773-873 K when the Ti content was varied between 0.25% and 0.15% [19]. This complex behaviour of swelling is due to the synergetic effect between C and Ti. Absence of Ti is expected to result in trapping of vacancies by freely migrating carbon, thereby lowering the super-saturation of vacancies leading to lowering of swelling. However, in the absence of Ti carbon moves to grain boundaries and therefore enhances swelling. Stability of the TiC precipitates plays an important role in retaining C in the matrix. In the case of finely dispersed and under-stabilised TiC precipitates, the precipitates are dynamically redissolved during irradiation thus freeing C for trapping vacancies, which results in reduced swelling. Over-stabilisation, on the other hand, is deleterious in the sense that all the free carbon atoms are bound by the Ti and hence results in enhanced swelling. Ti in titanium-modified steels influences the swelling behaviour in several ways: (a) The residual gases are strongly gettered and are thus unavailable for stabilisation of void nuclei. (b) The cold-work dislocation structure is stabilised. (c) The interaction between helium atoms and the metal-carbon particle-matrix interface strongly modifies the helium bubble distribution [3].

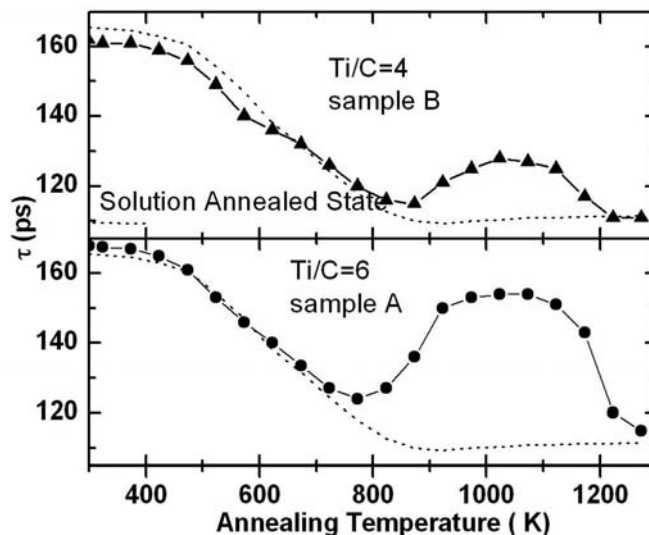
Besides, fine precipitates of TiC are strong neutral sinks for vacancies and interstitials, and hence act as sites for increased recombination of vacancies and interstitials which reduces the swelling in these alloys. Void swelling studies on proton-irradiated Japanese PCA alloy steels (Fe-16.2 Ni-14.6 Cr-2.37 Mo-1.79 Mn-0.53 Si-0.24 Ti-0.06 C) have shown a decrease in swelling with increased formation of TiC precipitates [20]. Thus TiC precipitates play a crucial role in reducing swelling in titanium-modified steels. Hence a comparison of TiC precipitate formation in the two titanium-modified steels under study was carried out to obtain insight into the difference in their swelling behaviour.

Positron lifetime measurements

In order to monitor the evolution of the TiC precipitation process, isochronal annealing treatments were carried out from 300 to 1273 K in steps of 50 K on un-irradiated samples in a vacuum of 10^{-6} mbar. The annealing time for each temperature was fixed at 30 min. The positron lifetime measurements were carried out at room temperature after each isochronal annealing step using a spectrometer having a time resolution (FWHM) of 260 ps. The measured lifetime spectra were analysed into different lifetime components and their intensities using the programs RESOLUTION and POSITRONFIT [17].

Figure 3 shows the variation of positron lifetime τ , with annealing temperature for Samples A and B. The positron annihilation of the samples in the solution annealed state is also shown. The observed variation of lifetime displays distinct stages *viz*, a monotonic decrease in τ from the initial cold-worked state up to ~ 900 K in Sample B and ~ 800 K in Sample A. This is followed by a stage where there is an increase in lifetime to saturation, followed by a decrease.

Figure 3. Variation of positron lifetime τ with annealing temperature for the cold-worked D9 alloys with different Ti concentration, Sample A (Ti/C = 6) and Sample B (Ti/C = 4). The dashed lines in both the graphs correspond to the recovery curve for cold-worked Ti-free steel samples.



The first stage corresponds to point defect recovery. This is explained by the migration of vacancies to sinks such as cold-worked dislocations resulting in the annihilation of dislocations. The subsequent stage where there is an increase in lifetime is the result of positron trapping at the TiC precipitate-austenitic matrix interface. TEM studies reported [2,23] the formation of TiC precipitates in cold-worked titanium-modified stainless steels in the temperature range of 923 to 1073 K. These

precipitates have a face-centred cubic lattice structure with extremely high lattice parameter mismatch of 19-21% with the austenitic matrix. The large strains arising from this lattice mismatch results in generation of misfit dislocations at the precipitate-matrix interface region. These misfit dislocations are effective traps for positrons [13]. The increase in the average lifetime of positrons trapped in Sample A in comparison to Sample B is due to the increase in the number density of TiC precipitates formed in the former. It is observed that there is no increase in lifetime in the 800-1 200 K regime in the samples without titanium.

The decrease in lifetime beyond $\sim 1\ 200$ K in either alloys is ascribed to the decrease in the number density of TiC precipitates due to coarsening of the TiC precipitates [13]. In addition, one finds that in Sample A, the onset of TiC precipitate formation has occurred at slightly lower temperatures compared to Sample B. This may be due to the difference in kinetics of formation and growth of TiC precipitates as a result of varying titanium concentration.

Calculation of positron lifetime parameters

As mentioned in the introduction, the earlier computational studies suffered from the usage of a small supercell size, as well as a lack of incorporation of self-consistent structural relaxation around the vacancy. With the recent developments in *ab initio* electronic structure calculations, and the availability of parallel computing facilities, it is now feasible to make more realistic computations of monovacancies and their interactions with impurities. The positron annihilation results discussed in this paper revolve around the nanometer-sized TiC precipitates formed in titanium modified steels. We have, therefore, modelled possible positron trapping centres as vacancies inside precipitates as well as at the interface of TiC and the matrix. For simplicity, we have taken the matrix to be Fe in the face-centred structure. The computed positron lifetimes were compared to experiments. We have also made self-consistent electronic structure calculations using PAW pseudopotentials [24], as implemented in VASP [25], to address the carbon and titanium vacancies in TiC. The vacancy structure was relaxed and resultant electron density and relaxed structure were used to compute positron annihilation parameters. Similar calculations were done for carbon, titanium and iron vacancies at the interface between TiC and the matrix.

We now discuss the results of the *ab initio* calculations. In the case of C vacancies, our *ab initio* calculations show a strong outward relaxation of 0.0098 nm for the first nearest neighbour Ti atoms, which is essentially brought about by the TiC binding. On the other hand, the outward relaxation of first nearest neighbour C atoms of the Ti vacancies is lower due to the strong C-C interaction partially nullifying the outward relaxation. An isosurface view of 50% positron density computed with a C vacancy in the TiC precipitate as well as TiC/Fe interface are shown in Figure 4. The positron lifetime computed with C vacancy, Ti vacancy and Fe vacancy are given in Table 2.

It is interesting to note that the defect-free lifetimes in TiC and Fe are almost same, and such very small differences cannot be distinguished in the experiments. In case of vacancies in TiC, one can clearly see from Table 2 the effect of supercell size on the deduced positron lifetime. It is important that supercells be sufficiently big so as to reduce the artificial vacancy ordering effect. Experimental positron lifetime in vacancy-rich TiC is 160 ps [21]. Earlier computations on vacancies in TiC assigned Ti vacancies as positron trapping centres [22]. The size of the supercell employed in that calculation is too small to avoid a vacancy ordering effect; moreover, the structure was not relaxed to around vacancies. Our refined calculation using VASP clearly shows that the positron lifetime at the relaxed C vacancy in TiC matches the experimental observations. Since the unrelaxed vacancy lifetimes are nearly the same for a vacancy inside TiC and at the TiC/Fe interface, it is logical to expect similar behaviour for relaxed vacancies too.

Figure 4. (a) Shows the isosurface view of 50% positron density computed with a C vacancy at the centre of a relaxed $3 \times 3 \times 3$ TiC supercell. (b) Shows similar positron density profile for C vacancy at the interface of the un-relaxed TiC/Fe(fcc).

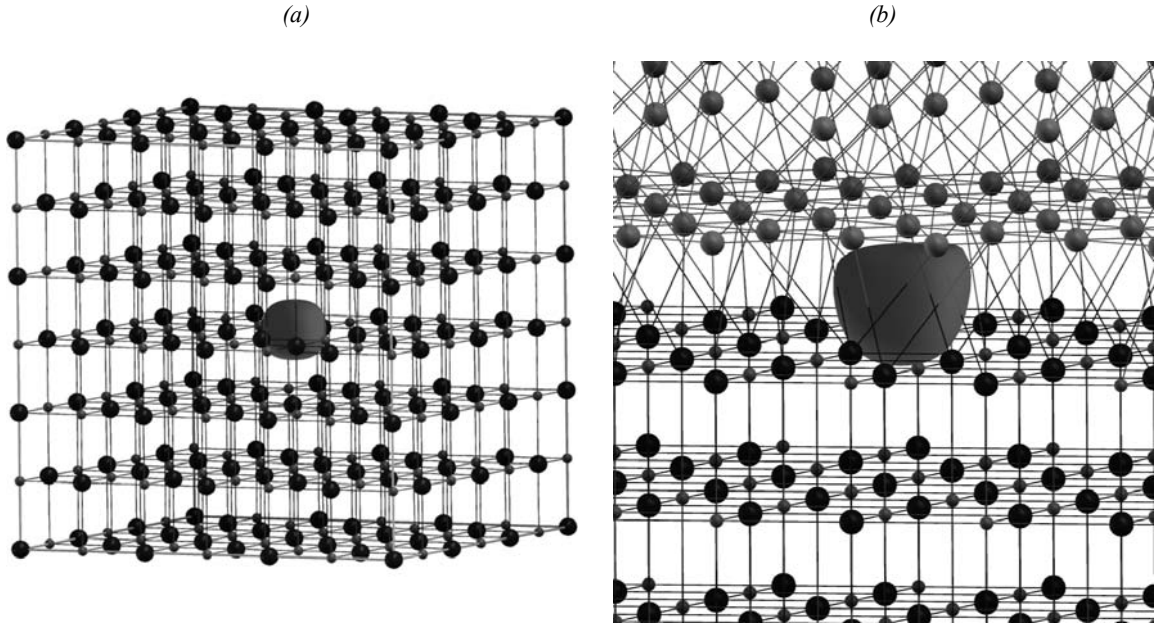


Table 2. The computed positron lifetimes for various vacancies in TiC and TiC/Fe interface

	Calculated lifetime (ps)					
	TiC ($1 \times 1 \times 1$) 4.327 Å (exp) (unrelaxed)	TiC ($3 \times 3 \times 3$) 4.327 Å (exp) (unrelaxed)	TiC ($5 \times 5 \times 5$) 4.327 Å (exp) (unrelaxed)	TiC ($3 \times 3 \times 3$) 4.342275 Å		TiC ($5 \times 5 \times 5$):Fe ($6 \times 6 \times 6$) 4.327 Å (exp) (unrelaxed)
				Unrelaxed	Relaxed	
Bulk	112	112	112	113	113	108
V_{Ti}	165	180	181	182	188	180
V_C	137	136	139	137	162	130
V_{Fe}	–	–	–	–	–	188

Thus our computations reveal that carbon vacancies are those which correlate with the experimentally measured lifetime. This is also naturally expected due to carbon off-stoichiometry during preparation of metal carbides. We assign C vacancy at TiC/austenite interface as positron trapping centre for all our positron observations in D9 alloys. Further work is in progress to study the relaxed vacancies at TiC/Fe interfaces and their interaction with helium atoms and free vacancies.

While evaluating the effect of titanium additions on swelling it should be mentioned that titanium, being an oversized atom compared to the major constituents, interacts with the vacancies and diffuses via a vacancy migration mechanism. Titanium is a fast-diffusing species, diffusing faster in γ -iron by a factor of 7.6 times or more than Fe [23]. Therefore, the effective diffusion coefficient of vacancy migration will be elevated by the addition of titanium.

The effective diffusion coefficient of vacancies is given by [23]:

$$D_v^{eff} = \frac{(D_v + KC_s D_s)}{(1 + KC_s)}$$

where D_v is the diffusion coefficient for vacancy migration in the pure host, and D_s is the diffusion coefficient of the solute. K is the mass action constant for the solute-vacancy dissociation in an fcc lattice. Recently, Okita, *et al.* [23] have compared the swelling behaviour in Fe-Cr-Ni ternary alloy, and Fe-Cr-Ni with titanium additions. They have observed that peak swelling temperature of the ternary alloy is greater than that of ternary alloy with 0.25% titanium addition by ~ 100 K. This effect of titanium in solution is consistent with our results (see Figure 2) where the alloy with higher titanium concentration has a peak swelling temperature lower than the other. In Sample A the recombination dominated regime is shortened and void growth regime reached at lower temperature due to increase in the effective vacancy diffusion coefficient. Also, the increased production of TiC precipitates in Sample A has resulted in a decrease in vacancy supersaturation at temperatures higher than the peak swelling temperatures. This decrease in supersaturation should occur at lower temperatures in Sample A than in Sample B. Also, the increased concentration of titanium has lowered the onset of TiC precipitate formation by ~ 100 K in Sample A (as observed in Figure 3). This effect has resulted in reduction in swelling at temperatures lower than Sample B. Thus the increased titanium concentration in D9 alloy has provided a beneficial effect in reducing the swelling at the peak swelling temperature.

Conclusion

Void swelling behaviour has been investigated by step height measurements in Ni ion-irradiated Ti-modified stainless steels with varying titanium concentrations. The swelling at the peak swelling temperature of the alloys with 0.25% of titanium and 0.15% of titanium are found to be $\sim 4\%$ and $\sim 15\%$ respectively. The TiC precipitate formation in these two alloys was studied by positron lifetime measurements of the un-irradiated alloys which are annealed at various temperatures. The reduced swelling in the alloy with 0.25% titanium is due to the greater number density of TiC precipitates formed. The difference in peak swelling temperatures between the two alloys is due to the effect of titanium in solution in increasing the effective vacancy diffusion coefficient. *Ab initio* calculations of positron lifetime, using large supercells, show that C vacancies at the TiC/austenite interface are the predominant positron trapping centres in these alloys.

REFERENCES

- [1] Mansur, L.K., E.H. Lee, P.J. Maziasz, A.P. Rowcliffe, *J. Nucl. Mater.*, 141, 633 (1986).
- [2] Kesternich, W., *J. Nucl. Mater.*, 127, 153 (1985).
- [3] Rowcliffe, A.F., M.L. Grossbeck, *J. Nucl. Mater.*, 122 & 123, 181 (1984).
- [4] Maziasz, P.J., in *Optimization of Processing, Properties and Service Performance Through Microstructural Control* (3rd Ed.), ASTM-STP 979, B.L. Bramfitt, R.L. Benn, C.R. Brinkman, G.F. Vander (Eds.), ASTM, Philadelphia, PA, 116 (1988).
- [5] Maziasz, P.J., *J. Nucl. Mater.*, 205, 118 (1993).

- [6] Tateishi, Y., *J. Nucl. Sci. Tech.*, 26, 132 (1989).
- [7] Gilbon, D., L. Le Naour, C. Rivera, H. Lorant, *Proc. 12th Int. Symp. on Effects of Radiation on Materials*, F.A. Garner, J.S. Perrin (Eds.), ASTM, Philadelphia, PA, 115 (1985).
- [8] Suzuki, M., S. Hamada, P.J. Maziasz, M.P. Tanaka, A. Hishinuma, *Proc. 14th Int. Symp. on Effects of Radiation on Materials*, H. Packan, R.E. Stoller, A.S. Kumar (Eds.) (3rd Ed.), ASTM-STP 1045 Vol. I, ASTM, Philadelphia, PA, 160 (1989).
- [9] Raj, B., S.C. Chetal, S.L. Mannan, *Selection of Materials for Prototype Fast Breeder Reactor*, Transactions of Indian Institute of Metals, 56, 2, pp. 155-178 (2003).
- [10] Mazey, D.J., *J. Nucl. Mater.*, 174, 196 (1990).
- [11] Peterson, K., in *Positron Solid State Physics*, W. Brandt, A. Dupasquier (Eds.), North Holland, Amsterdam, 298 (1983); Sundar, C.S., *et al.*, *Phil. Mag.*, 50A, 635 (1984); Amarendra, G., *et al.*, *Phys. Rev.*, B 45, 10231 (1992).
- [12] Bharathi, A., C.S. Sundar, *Mater. Sci. Forum*, 105, 905 (1992).
- [13] Rajaraman, R., P. Gopalan, B. Viswanathan, S. Venkadesan, *J. Nucl. Mater.*, 217, 325 (1994).
- [14] Biersack, J.P., L.G. Haggmark, *Nucl. Instrum. Methods*, 174, 257 (1980).
- [15] Johnston, W.G., J.H. Rosolowski, A.M. Turkalo, T. Lauritzen, *J. Nucl. Mater.*, 46, 273 (1973).
- [16] Wang, Z.G., K.Q. Chen, L.W. Li, C.H. Zhang, J.M. Quan, M.D. Hou, R.H. Xu, F. Ma, Y.F. Jin, C.L. Li, Y.M. Sun, *J. Nucl. Mater.*, 271 & 272, 306 (1999).
- [17] Kirkegaard, P., M. Eldrup, O.E. Mogensen, N.J. Pedersen, *Comput. Phys. Commun.*, 68, 307 (1981).
- [18] Herschbach, K., W. Schneider, K. Ehrlich, *J. Nucl. Mater.*, 203, 233 (1993).
- [19] Kimoto, T., H. Shiraishi, *J. Nucl. Mater.*, 132, 266 (1985).
- [20] Kesternich, W., D. Meertens, *Acta Metall.*, 34, 1071 (1986).
- [21] Rempel, A.A., M. Forster, H.E. Schaefer, *J. Phys: Condens. Matter*, 5, 261 (1993).
- [22] Puska, M.J., M. Sob, G. Brauer, T. Korhonen, *Phys. Rev.*, B 49, 10947 (1994).
- [23] Okita, T., W.G. Wolfer, F.A. Garner, N. Sekimura, *Phil. Mag.*, 85, 2033 (2005).
- [24] Kresse, G., J. Joubert, *Phys. Rev.*, B 59, 1758 (1999).
- [25] Kresse, G., J. Hafner, *Phys. Rev.*, B 47, R558 (1993); Kresse, G., J. Furthmüller, *Phys. Rev.*, B 54, 11169 (1994).

FIRST RESULTS ON T91 CLADDINGS WITH AND WITHOUT MODIFIED FeCrAlY COATINGS EXPOSED IN PbBi UNDER VARYING CONDITIONS

A. Weisenburger¹, A. Heinzel¹, G. Müller¹, A. Rousanov²

¹Forschungszentrum Karlsruhe GmbH, IHM, P.O. Box 3640, D-76021 Karlsruhe, Germany

²IPPE, Bondarenko Square 1, Kalugia Region, 249020 Obninsk, Russia

Abstract

It is well known that at temperatures above 500°C low activation austenitic steels suffer from severe corrosion in lead or lead-bismuth. Low activation martensitic steels instead form under similar conditions concerning temperature and oxygen content thick oxide scales that periodically may spall off. Both groups of materials are therefore restricted to areas having lower temperature load.

For parts that are intended to be used in high-temperature regions, like claddings, surface protection has to be applied. From gas turbines the role of elements forming thin stable oxide scales is well understood. The concept chosen here for thermally high loaded parts, the claddings, is the deposition of a FeCrAlY coating of about 30 µm thickness that is afterwards re-melted applying a pulsed electron beam (GESA). The beam energy is adjusted in a way to melt the entire coating together with a few µm thin region of the bulk to create a perfect intermixing at the boundary. This results in a new surface area of the cladding with an aluminium content of the order of 5 wt.% that will be sufficiently high to grow thin stable oxide scales. This concept is proven for austenitic cladding materials like 1.4970 as well as for martensitic ones like T91. In long-term corrosion tests the compatibility to Pb or PbBi, the resistance against corrosion and severe oxidation, was clearly demonstrated. No negative response of such a modified coating on the mechanical properties and the stability under irradiation has been observed as of yet.

This paper will focus on the surface modification process, the corrosion results thus far obtained and on the evaluation of some mechanical properties. For example, the swelling of the fuel by irradiation will lead during operation to an increase of the internal pressure. This is simulated in experiments where an internal pressure of defined value was applied on T91 cladding tubes. The influence of flow velocity between 1 to 3 m/s on the oxidation behaviour of T91 with and without surface modification was also investigated. Specimens with GESA-modified coating do not show any influence on the oxidation behaviour, in contrast to the non-modified ones.

Introduction

It is known from literature [1-3] that low activation austenitic steels suffer from severe corrosion attack in lead or lead-bismuth eutectic (LBE) melt at temperatures above 500°C. Low activation martensitic steels, however, form thick oxide scales that periodically may spall off. Both materials are therefore restricted to temperatures below 500°C.

Structure parts that are exposed to temperatures above 500°C have to be protected by a suitable surface modification. Surface alloying of strong oxide formers like Al has shown potential to protect steel surfaces against corrosion and severe oxidation in contact with lead alloys [2,4,5].

This paper will focus on the influence of different temperatures, LBE flow rates and mechanical stresses on the corrosion behaviour. The influence of the surface coating, modified by GESA, is examined for the highest temperature of 600°C and in the experiments with different LBE flow rates. Examination of the influence of mechanical stresses is necessary because swelling of the fuel by irradiation will lead during operation to an increase of the internal pressure. This is simulated in experiments where an internal pressure of defined value is applied to a T91 cladding tube.

Materials and test specimens

The steel tested in the loops is T91. Part of the test tube surface is in as-received condition (original), other tube specimens are coated at the surface with FeCrAlY. The composition of both materials is displayed in Table 1.

Table 1. Measured composition of T91 steel and of the coating FeCrAlY

	C	Si	Mn	Cr	Al	Y	Mo	Fe	Ni	V	Nb
T91 [wt.%]	0.105	0.43	0.38	8.26			0.95	rest	0.13	0.20	0.075
FeCrAlY coating [wt.%]				15.89	5.95	0.64		rest	<0.03		
FeCrAlY coating + GESA [wt.%]				15.2	4-5	<0.5		rest			

For the first time cladding tube specimens with dimensions relevant for reactor loops have been produced by the Institute for Power Physics and Engineering (IPPE) in Obninsk, Russia, for conducting the corrosion experiments. Mechanical properties and thermal treatment are provided in Table 2.

Table 2. Mechanical properties and thermal treatment of the T91 tube specimens

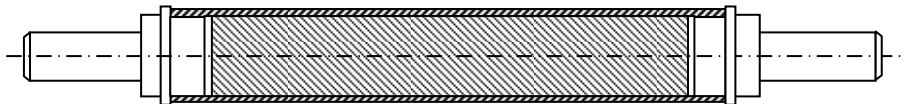
Grain size (μm)	6-9	Normalisation: 1 040°C, 15 min
Ultimate tensile strength σ_{uts} (MPa)	744	
Yield strength $\sigma_{\text{p}0.2}$ (MPa)	607	Tempering: 710°C, 40 min
Total elongation ε_{t} (%)	22	
Uniform elongation ε_{u} (%)	10	

It is known that alloys containing Al in a concentration range of 4-15 wt.% have a very good oxidation resistance, as the alumina scale that forms in the presence of oxygen is thin and stable [2]. Therefore a FeCrAlY coating of about 30 μm thickness was precipitated by Sulzer, Wohlen, Switzerland onto the surface of some of the specimens to improve the corrosion resistance against the lead-bismuth eutectic melt (LBE) containing oxygen. This coating, however, is relatively porous and

of varying thickness because the coating is not much thicker than the size of the melt drops in the low-pressure plasma spray (LPPS) process applied. The GESA pulse power process [6] was employed to modify the coated surface layer, a process that allows large area surface melting of materials to a depth of several 10 μm in some 10 μs without influencing the material structure of the bulk material. In this way the coating becomes homogeneous and, moreover, the bonding of the coating to the steel surface improves because the melting depth is slightly deeper than the thickness of the coating.

Figure 1 shows the scheme of the test specimens which consists of the test tube plugged at the ends by connection pins that are welded into the tube. The tubes have a diameter of 8.5×0.5 mm and are of 100 mm and 49 mm length for the original and coated tubes, respectively. Inside each tube there is a displacer that fits in with a 0.1 mm gap.

Figure 1. Scheme of the test specimen used in tests without internal pressure



The scheme of the specimen used for testing with internal pressure is drawn in Figure 2. In this case the displacer is a tube to allow easy expansion of the gas inside the tube. One end plug has an axial bore hole for the gas inlet. The tube diameter is again 8.5×0.5 mm and the length 150 mm.

Figure 2. Scheme of the test specimen used in tests with internal pressure



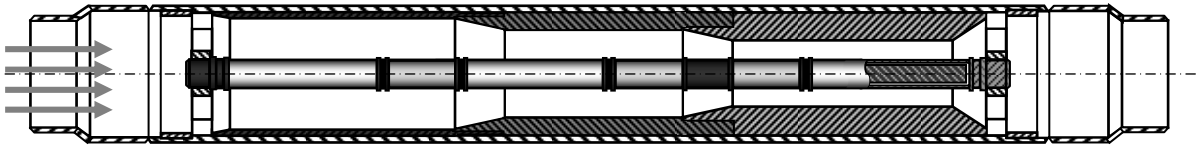
Test equipment and experimental conditions

Two loops are employed in the examination of the steel specimen tubes, the loops Tsu-2M and SM-1, both in the Institute for Physics and Power Engineering (IPPE) in Obninsk, Russia [7]. They are non-isothermal loops driven by an impeller pump with a capacity of 5 m^3/h at 1.5 MPa. The loop capacity is 80 litres. After passing the test section the LBE is cooled to 270°C and then heated up to the desired temperature by direct electrical heating before entering the test section. An electromagnetic flow meter is used to measure the velocity of the liquid metal flow.

Loop Tsu-2M is used to examine the behaviour of the test tubes at 480, 550 and 600°C with a LBE flow velocity of 1-1.2 m/s. The lower temperatures are applied to the original tubes, the high temperature of 600°C to the coated ones only. The second loop, SM-1, which works at 550°C , is in a condition to allow exposure of tubes at liquid metal velocities of 1, 2 and 3 m/s by employing a special test section. Another test section is used to pressurise the tubes for examination of the influence of mechanical stresses on steel corrosion and oxidation, respectively.

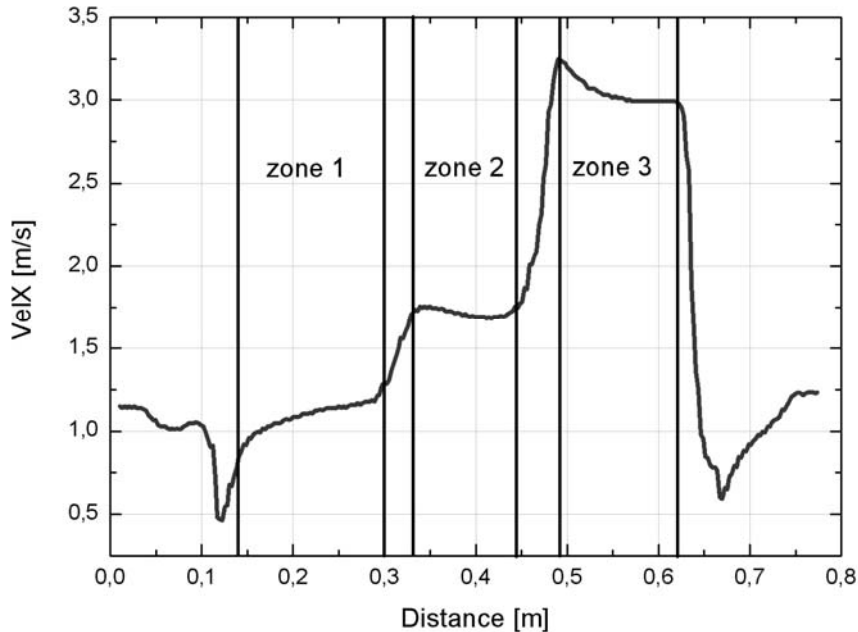
The test section for different LBE velocities consists of a tube with 48 mm outer diameter that in its interior has three areas of different diameters that should force the LBE to flow with velocities of 1, 2 and 3 m/s in the corresponding areas, respectively. A scheme of the test section is depicted in Figure 3. The tube specimens are placed in the centre of the test section tube in such a way that one original and one coated specimen are always in each one of the three velocity areas. The geometrical sizes are not correct; the scheme is compressed in direction of the LBE flow.

Figure 3. Test section for exposure of tubes to LBE with different flow velocities



A numerical calculation with the program FLUIDYN – MP, vers.5.0.2 yields the speed of the liquid LBE which has to be assumed inside the test section. The result is presented in Figure 4. It can be seen that the desired flow velocities are close to the intended ones.

Figure 4. Flow speed profile in the test section for different flow velocities



The test section for pressurised tubes contains two specimens. One is connected to a gas pipe for introduction of the gas from an external reservoir with 15 MPa pressure. The other is without pressure for comparison. The tangential stress σ_t in a thin-walled pressurised tube is given by [8]:

$$\sigma_t = Pd/2\delta$$

where P is the internal pressure in MPa, d the tube internal diameter and δ the wall thickness of the tube, both in mm. The diameter of the tube specimen is measured at five equidistant places along the tube axis before assembling the test section to allow determination of the strain rate.

Examination of specimens

After completion of the tests the tube specimens were removed from the working sections. Traces of LBE left on the surface are washed off with oil at 180°C. The surface was brushed with a coarse calico drenched with ethyl alcohol. Cleaning of the surface allows to identify possible corrosion damage and to find areas of interest for metallographic studies.

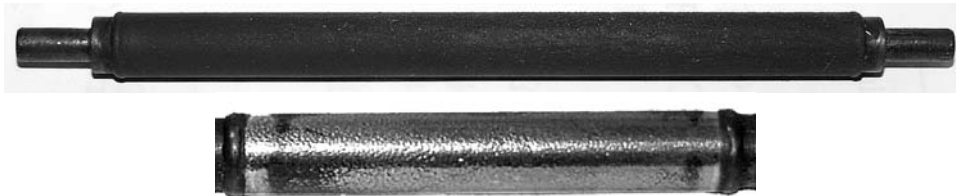
Discs were cut from the tubes at selected places that were ground and polished with a Struers Tegrapol 31. Light microscopy (LM) analyses were done by using the microscopes Leitz Aristomet and Olympus BX60H. Scanning electron microscopy (SEM) was conducted with the Leitz AMR1000 and Hitachi S800. The EDX analysis was performed with the Thomson WIN EDS that is attached to the Hitachi S800.

Results

Tests at different temperatures

After 2 000 h of exposure to flowing eutectic Pb-Bi melt (LBE) with 1.0-1.2 m/s at temperatures of 480 and 550°C, the tubes without surface modification exhibit an oxide scale of dark smooth appearance on the whole surface. The tube with surface modification by GESA shows a shiny metallic surface with only few dark places after exposure to 550°C and 600°C. The original and surface-coated tube specimens exposed at 550°C are shown in Figure 5.

Figure 5. Original (above) and surface coated (below) test tubes after 2 000 h exposure to LBE flowing with 1-1.2 m/s at 550°C



The metallographic analysis of the cross-sections of original specimen tubes after exposure to 480 and 550°C (see Figure 6) yields an oxide scale thickness of 18-25 and 25-45 μm , respectively. As expected, the oxide scale grows faster at the higher temperature. The upper magnetite scale and the spinel layer below can clearly be distinguished, as can the third zone in which oxygen penetrates into the bulk material by diffusion along the grain boundaries. The oxygen diffusion zone is very weak after exposure to 480°C but becomes prominent at higher temperatures. The figures are taken from the un-etched metallography to make the diffusion zone visible. The oxidation behaviour observed above is already well known from other experiments with ferritic steels in stagnant and flowing LBE [1-5].

A completely different appearance is offered in the cross-section in Figure 7 of the coated surface region after 2 000 h exposure to 600°C. Despite the higher temperature there is only a very thin oxide scale ($<1 \mu\text{m}$) on top of the surface. It is not visible from the metallography but can be recognised in the line scan below. It becomes clear from Figure 7 that the Al peak reaches its maximum about 0.5 μm before the Cr maximum. That means that the top oxide scale must consist mainly of alumina followed by a thin layer enriched in Cr. These layers protect the steel not only from LBE attack but also from oxygen diffusion into the coating and bulk material, although the temperature is higher than that in the original specimens which have thick oxide scales. The diffusion of Fe through the surface to form a magnetite layer on top is also prevented by the thin alumina scale.

Furthermore it becomes obvious from the line scan in Figure 7 that the depth of surface melting reaches down to about 30 μm represented by the range containing Al. Some small Cr peaks indicate the presence of precipitations enriched in Cr. The Al enrichment at the boundary between the melting zone and the steel bulk is also remarkable.

Figure 6. LM's of cross-sections of T91 steel specimens after 2 000 h exposure to LBE with 480°C (above) and 550°C (below), respectively

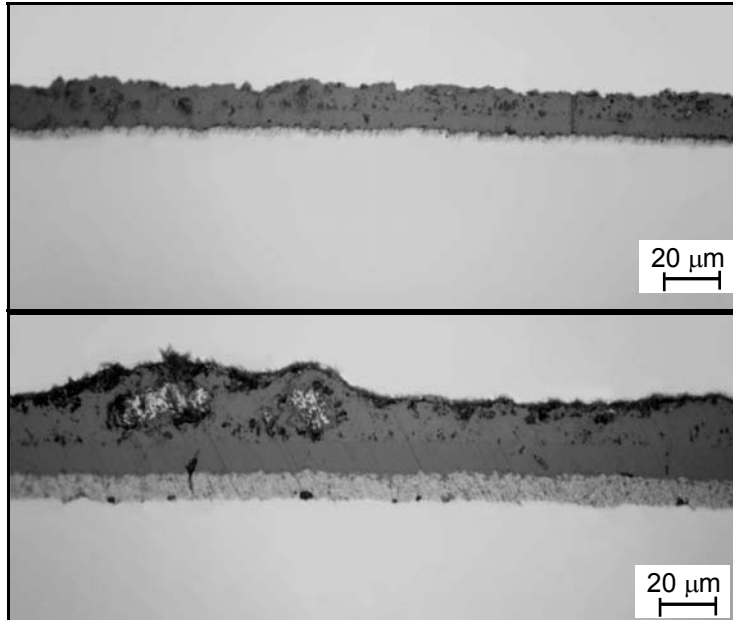
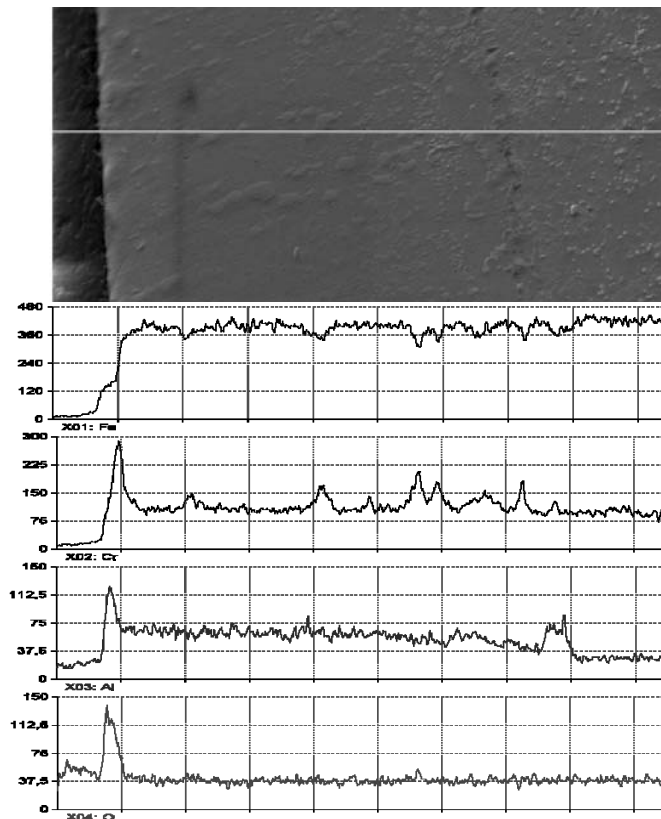


Figure 7. SEM of the cross-section of the coated T91 tube specimen after 2 000 h exposure to LBE at 600°C. Below is the EDX line scan through the surface region.



The extension of the region of GESA surface melting is also visible on the etched LM presented in Figure 8. It covers not only the coating but also some μm of the bulk material. This results in an improvement of the bonding between coating and bulk. The Al concentration in the melt region was analysed to be between 4-5 wt.%. The small zone of Al enrichment is visible on the border between melt zone and bulk material. On a few places of the surface there exists a multi-layer oxide scale like on original tube surface. Analysis of the Al concentration at these places yields less than 4 wt.%. This is obviously not sufficient for protective alumina scale formation.

Tests at different flow velocities

Original and coated tube specimens are exposed to LBE at different flow velocities of about 1, 2 and 3 m/s at 550°C for 2 000 h. The metallographic cross-sections of the original tube specimens are depicted in Figure 9. After all three flow velocities the specimens show a spinel and diffusion zone and only the 1 m/s specimen has a magnetite layer on top. On the 2 m/s specimen there are only some remains of the magnetite layer which is completely missing at the 3 m/s specimens that have a shiny spinel surface. This is probably due to erosion by the LBE stream at the high flow velocities. In any case there is still a stable protective oxide scale on top which consists of a dense spinel layer. The pictures of the cross-sections are taken from un-etched metallography to depict the oxygen diffusion zones that have about the same extension at all flow velocities.

The coated tube specimens show, once again, a different behaviour (Figure 10). After exposure for 2 000 h at 550°C to LBE with the three different flow velocities all specimens respond in the same way by formation of a thin oxide scale that consists mainly of alumina like that shown in the EDX line scan in Figure 6. The etched structure nicely depicts the extension of the surface zone re-melted by GESA which includes the FeCrAlY coating. The alumina oxide scale is too small to be visible on the metallographic pictures. There is only one small spot on top of the 3 m/s specimen which shows a visible oxide formation. It may be a place at which the Al concentration is below 4 wt.%.

Tests with pressurised tubes

The influence of an internal pressure of 15 MPa on the formation of the oxide scale at 550°C can be seen from Figure 11 by comparison of the cross-section through the wall of the tube without (left) and the one with pressure (right). The tube with pressure is protected as well as the tube without pressure, however, it has a thicker oxide scale. Since the oxygen diffusion zone is the same in both cases it can be assumed that the diffusion barrier for oxygen, the spinel layer, has the same effect in both cases. Indeed it is mainly the magnetite layer that is responsible for the difference in thickness, which does not influence oxygen diffusion into the bulk. The measurements of diameters before and after the exposure yield a strain of 0.7% after 2 000 h of exposure.

Discussion of results

Since oxide scales serve as a good protection against the attack by liquid LBE, coatings like those used for protection of turbine blades [9] appear to be a suitable choice. Therefore, a FeCrAlY coating is being chosen for protection of the high-temperature structures. It has an average thickness of 30 μm and is re-melted by the pulsed large area electron beam of GESA [10] to obtain a dense coating layer and to improve the bonding between the coating and the bulk material.

Figure 8. LM of the etched cross-section of the coated T91 tube specimen after 2 000 h exposure to LBE at 600°C

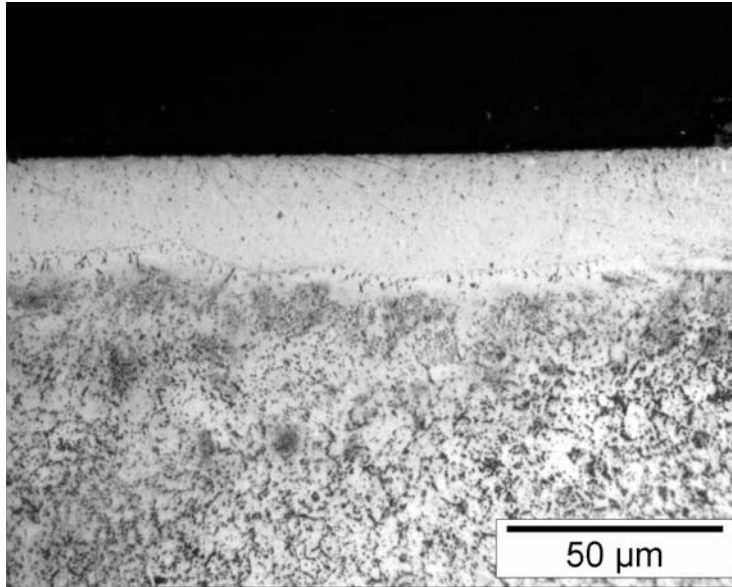


Figure 9. SEMs of the T91 steel tube specimens exposed 2 000 h at 550°C to LBE with a flow velocity of 1 (above), 2 (middle) and 3 m/s (below)

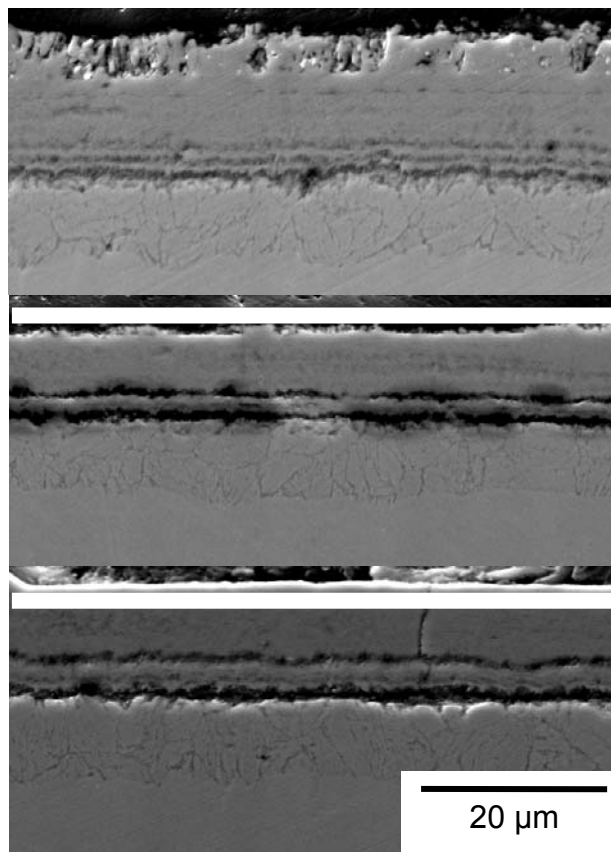


Figure 10. LMs of the coated T91 steel tube specimens exposed 2 000 h at 550°C to LBE with a flow velocity of 1 (above), 2 (middle) and 3 m/s (below)

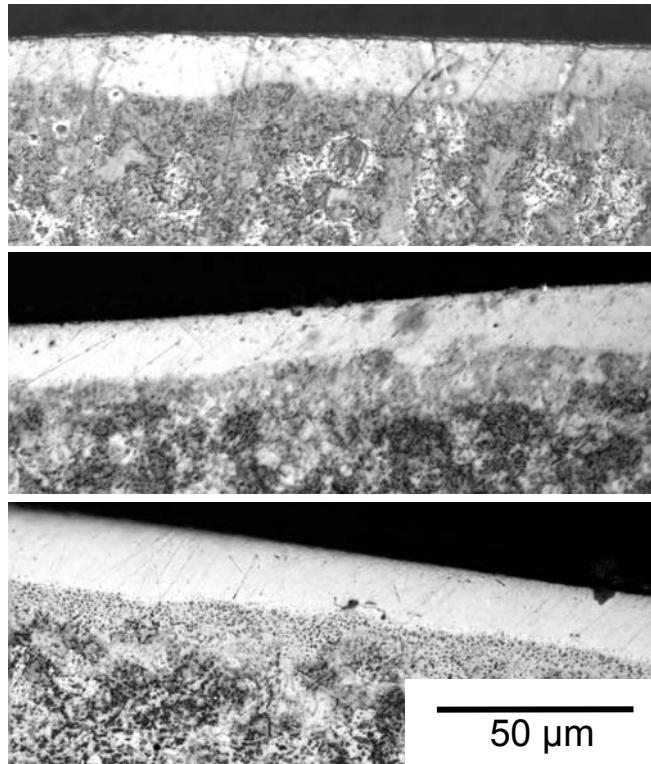
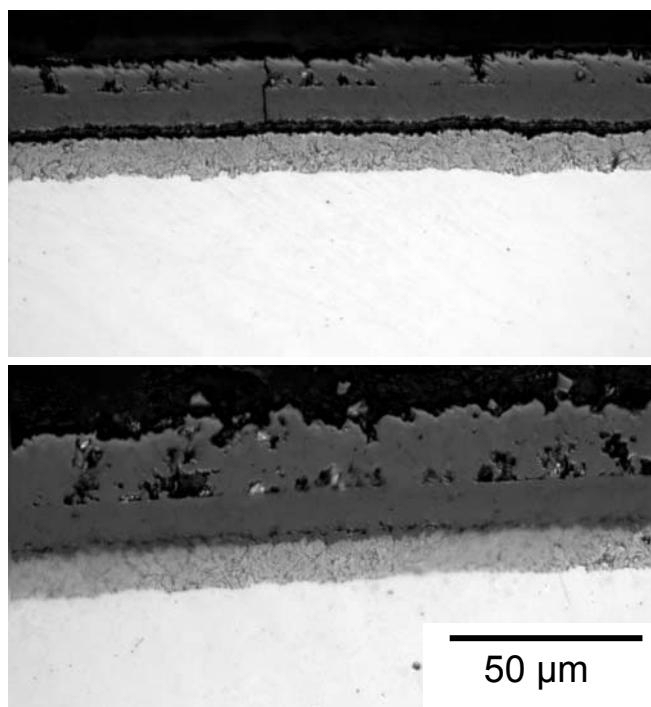


Figure 11. LMs of cross-section through the wall of a T91 steel tube without (left) and with (right) internal pressure of 150 bar after 2 000 h exposure to 550°C in LBE with flow velocity of 1 m/s



The beam energy of GESA is adjusted in a way to melt the entire coating together with a few μm thin region of the bulk to create a perfect intermixing at the boundary. This results in a new surface area of the cladding with an Al content between 4-5 wt.% that will be sufficiently high to grow thin stable oxide scales. This concept is proven for T91 steel tubes examined with the experiments described here. No negative response of such a modified coating on the mechanical properties and the stability under irradiation has been observed up to now [11].

The difference between the original and FeCrAlY coated tube specimens is the very thin alumina scale on top of the FeCrAlY surface which is stable also at higher temperatures like 600°C and has a much better thermal conductivity than the thick oxide layers that develop on original T91 surfaces. The thickness of oxide layers on original steel grows with temperature and is no effective barrier for oxygen diffusion into the bulk and for Fe diffusion through the surface that leads to a formation of magnetite on top of the surface. There are, however some places on the FeCrAlY coated tube specimen where oxide scales also grow like on the original material. They are caused by failures in the LPPS process which lead there to Al concentrations below 4 wt.%.

The tests at three different flow velocities of liquid LBE show clearly that at high flow velocities (>2 m/s) the Fe that diffuses through the spinel surface and gets oxidised is washed off by the passing liquid. Therefore, the tube specimen of the 3 m/s test develops no magnetite scale on the surface and has a shiny smooth appearance. Some small remains are observed on the surface of the 2 m/s specimen while the magnetite on the 1 m/s specimen has a magnetite layer of a thickness that is normally observed on ferritic steels under equivalent conditions [12]. The FeCrAlY coated tubes that were restructured by GESA pulses show no influence of the flow speed. All specimens have the same undisturbed, thin, protective alumina surface scale.

Pressure inside the tube specimens that expose the tubes to mechanical stress causes some creep in the tube wall which reaches a strain of 0.7%. But this is not the only effect. The strain obviously also increases Fe diffusion, leading to an enhanced growth of the magnetite layer which will not occur with the coated specimens that have no magnetite layer. This is another advantage of the coating applied.

The magnetite layers are in any case not desired. They tend to spall off, decrease the heat conductivity and have no influence on the prevention of liquid LBE attack.

Conclusions

Unprotected T91 steel in the as received condition is not suitable for the use with liquid LBE at temperatures above 500°C because it develops thick oxide scales including magnetite and spinel with low thermal conductivity. The magnetite tends to spall off.

Surface coating with FeCrAlY after homogenisation by melting with the GESA pulse avoids this disadvantage, as the coating develops a thin protecting alumina scale with good thermal conductivity.

The coating process needs some improvement to avoid coating regions which have aluminium concentrations below 4 wt.%. Measures are use of finer powder particles and cleaner preparation procedures and coating atmospheres.

There is an upper limit of LBE flow velocity of 2 m/s, above which no magnetite scale appears because it gets instantly removed.

Internal tube pressures of 15 MPa and the induced stresses increase the Fe diffusion and lead to enhanced magnetite scale growth.

Acknowledgements

The authors would like to thank the EC for funding the work presented in this paper under the EUROTRANS Project, No. FI6W-CT-2004-516520.

REFERENCES

- [1] Soler, L., F.J. Martin, F. Hernandez, D. Gomez-Briceno, *J. Nucl. Mat.*, 335, 174-179 (2004).
- [2] Müller, G., A. Heinzl, J. Konys, G. Schumacher, A. Weisenburger, F. Zimmermann, V. Engelko, A. Rusanov, V. Markov, *J. Nucl. Mat.*, 335, 163-168 (2004).
- [3] Fazio, C., G. Benamti, C. Martini, G. Palombarini, *J. Nucl. Mat.*, 296, 243-248 (2001).
- [4] Müller, G., G. Schumacher, F. Zimmermann, *J. Nucl. Mater.*, 278, 85 (2000).
- [5] Müller, G., A. Heinzl, J. Konys, G. Schumacher, A. Weisenburger, F. Zimmermann, V. Engelko, A. Rusanov, V. Markov, *J. Nucl. Mater.*, 301, 40 (2002).
- [6] Engelko, V., B. Yatsenk, G. Mueller, H. Bluhm, *Vacuum*, 62, 211-216 (2001).
- [7] Glasbrenner, H., J. Konys, G. Mueller, A. Rusanov, *J. Nucl. Mat.*, 296, 237-242 (2001).
- [8] Festigkeitslehre C40, Taschenbuch für den Maschinenbau / Dubbel. Hrsg. von W. Beitz K. – H. Küttner. – 17., neu-bearb. Aufl. – Berlin; Heidelberg; New York; London; Paris; Tokyo; Barcelona: Springer (1990).
- [9] Rickerby, D.D., A. Matthews, “Advanced Surface Coatings: Handbook of Surface Engineering”, London, Blackie & Son Ltd. (1991).
- [10] Weisenburger, A., G. Müller, A. Heinzl, V. Engelko, A. Rusanov, “Corrosion of Modified FeCrAlY Coated Cladding Tubes in Liquid PbBi”, *Proceedings of Eurocorr 2005*, Lisbon, Portugal, 4-8 September 2005.
- [11] Weisenburger, A., A. Heinzl, C. Fazio, G. Müller, V.G. Markow, A.D. Kastanov, “Low Cycle Fatigue Tests of Surface Modified T91 Steel in 10⁻⁶wt.% Oxygen Containing Pb45Bi55 at 550°C”, submitted to *J. Nucl. Mat.* (also, *Proceedings of IWSMT 8*, Taos, NM, USA, 16-20 October 2006).
- [12] Barbier, F., G. Benamti, C. Fazio, A. Rusanov, *J. Nucl. Mat.*, 295, 149-156 (2001).

SESSION IV

Fusion, High-power Accelerator Targets and Other Fission Reactor Systems

Chairs: L. Heikinheimo, D. Gómez Brinceño

ASSESSING SCC AND IASCC OF AUSTENITIC ALLOYS FOR APPLICATION TO THE SCWR CONCEPT

S. Teyseyre, G.S. Was
University of Michigan, USA

Abstract

From the standpoint of environmental degradation of material, the selection of alloys for use as structural material in a supercritical water-cooled reactor (SCWR) must include assessment of the corrosion and stress corrosion cracking susceptibility of the alloys in supercritical water. Moreover, as experience in current reactors showed that irradiation-assisted stress corrosion cracking (IASCC) is a major concern, a comprehensive study must include the assessment of the effect of irradiation on SCC in supercritical water. Therefore, such selection faces multiple obstacles. The first is the lack of data on the corrosion and SCC susceptibility of the candidate alloys in this environment. There is a need to produce basic data using complementary experimental techniques. The second is the difficulty to obtain material irradiated in conditions relevant for SCWR. Availability of such material is needed to determine the influence of irradiation and its influence on SCC. Techniques such as proton irradiation are appealing surrogates for neutron irradiation in assessing its effect of stress corrosion cracking initiation, and can be used for screening of various material and environmental conditions. However, neutron irradiation is required to confirm the role of in-core irradiation on crack growth and in performing final verification of the effect of alternative irradiation on candidate alloys. Another obstacle would be the lack of facilities for testing materials in the unirradiated and irradiated state in supercritical water.

The University of Michigan has developed a comprehensive programme to assess the stress corrosion cracking susceptibility of austenitic alloys in supercritical water in unirradiated, proton-irradiated and neutron-irradiated state. The cracking susceptibility of unirradiated alloys has been evaluated by a set of constant extension rate tensile, CERT, experiments and by determination of the crack propagation rate by DCPD technique under constant K loading in pure de-aerated supercritical water at temperatures ranging from 400-600°C. The effect of irradiation on alloy microstructure and on stress corrosion cracking were evaluated after proton irradiation. In addition, the construction of a new laboratory allowed the evaluation of the cracking susceptibility of neutron-irradiated JPCA alloy in 400°C and 500°C supercritical water. Results indicate that stainless steel 316L and nickel-based alloy 690 were susceptible to cracking at all temperatures and that the crack propagation rate under constant K loading mode decreased with increasing temperature. Results also showed that irradiation greatly increased the cracking susceptibility of the alloys and that the extent of the increase depends upon the alloy considered. Finally, the neutron-irradiated JPCA alloy showed severe susceptibility to IASCC.

Introduction

The supercritical water-cooled reactor (SCWR) is one of the Generation IV nuclear reactor concepts. In this design, the core coolant temperature is expected to be between 280 and 620°C at a pressure of 25 MPa and the structural materials should experience neutron damage levels of 15 dpa for the thermal reactor design and 100 dpa for the fast reactor design. While no experience exists with supercritical water nuclear reactors there is a significant operating history with supercritical fossil plants [1], therefore a significant industry experience with supercritical water in power generation. However, a nuclear reactor core is significantly different from a fossil-fired boiler. A fossil-fired boiler consists of a large number of fire tubes that circulate water on the inside. These tubes have relatively thick walls, approximately 6-12 mm in thickness and can easily withstand the formation of hundreds of micrometer thick oxide films. However, the core of an SCWR will be more complex with some 145 assemblies among which fuel rods, control rods and water rods. The wall thickness for the fuel rod cladding in the reference SCWR design is 0.63 mm and the wall thickness for the water rods is 0.40 mm. Therefore an oxidation rate acceptable in the fossil plant industry will be unacceptable for these components. This fact advocates for a modification in the choice of alloy. One consequence could be that stress corrosion cracking, not known as a problem for fossil fuel SCW plant, could be an issue in SCWR. In addition, irradiation will affect the microstructure of the structural materials and may influence their stress corrosion cracking resistance. Irradiation-assisted stress corrosion cracking (IASCC) is known to be a problem in light water reactors of all types and cover many austenitic and nickel-based alloys [2,3]. To date, little data exist on SCC and IASCC susceptibility of candidate alloys in a supercritical environment relevant for SCWR [4,5]. The SCC susceptibility of unirradiated alloys is commonly assessed with constant extension rate tensile (CERT) test, which is seen as a quick, easy technique relevant to determine crack initiation. However, the nature of a power plant requires knowledge of a crack propagation rate and crack growth rate (CGR) experiments should also probably be conducted even at the early stages of this project. To assess the effect of irradiation, techniques such as proton irradiation are appealing surrogates for neutron irradiation in assessing its effect of stress corrosion cracking initiation, and can be used for screening of various material and environmental conditions. However, neutron-irradiation is required to confirm the role of in-core irradiation on crack growth and in performing final verification of the effect of alternative irradiation on candidate alloys. Considering those facts, the University of Michigan developed a comprehensive programme to assess the stress corrosion cracking susceptibility of austenitic alloys in supercritical water in unirradiated, proton-irradiated and neutron-irradiated state.

University of Michigan programme

The University of Michigan developed a programme to assess the stress corrosion cracking susceptibility of unirradiated, proton-irradiated and neutron-irradiated austenitic alloys in supercritical water. This programme includes the development of testing capabilities to perform CERT and CGR experiments in supercritical water, the capability to test neutron-irradiated samples and the acquisition of alloys irradiated in conditions relevant for the SCWR. It was primarily focused on the cracking susceptibility of austenitic alloys in pure (conductivity < 0.1 $\mu\text{S}/\text{cm}$) de-aerated ($\text{DO} < 10$ ppb) supercritical water.

The stress corrosion cracking susceptibility of unirradiated alloys were investigated using stainless steels 304 (UNS S30400), 316L (UNS S31603) and nickel-based alloy 625 (UNS N06625) and 690 (UNS N06690) in solution annealed condition by constant extension rate tests in de-aerated pure supercritical water in the temperature range from 400°C to 550°C at a strain rate of $3 \times 10^{-7} \text{s}^{-1}$. The cracking was evaluated after rupture of the specimens from the gage surfaces in terms of crack density, average crack length and crack length per unit area, from the fracture surface and from the

cross-sectioned gage surface by measuring the maximum crack depth. In addition, the crack propagation rate of a 21% cold work 316L was determined using direct current potential drop (DCPD) technique under constant K loading mode in the subcritical regime from 288°C to 360°C and in the supercritical regime up to 500°C.

Proton irradiation was used in this programme to determine the effect of irradiation on the cracking behaviour of solution annealed alloys 316L and 690 in 400°C and 500°C de-aerated SCW. The alloys were irradiated in the Michigan Ion Beam Laboratory at the University of Michigan. Experimental doses and dose rates were calculated using SRIM03. As recommended in ASTM E521-89 [6], a displacement energy of 40 eV was used for all dose calculations. Sample temperature during irradiation was maintained at $400 \pm 10^\circ\text{C}$ and $500 \pm 10^\circ\text{C}$. Irradiations were performed using 3 MeV up to 7 dpa with a dose rate of approximately 1×10^{-5} dpa/s for displacement energy of 40 eV. The result is a relatively uniform damage rate through the first 35 μm of the total proton penetration depth of $\sim 40 \mu\text{m}$. Additional details on the techniques of the proton irradiations can be found in Ref. [7]. The irradiation was performed on tensile samples and on TEM bars. The irradiated TEM bars were used to measure irradiation hardening and to make TEM discs from which the irradiated microstructure (size and density of voids and loops, radiation induced segregation) were analysed. The cracking susceptibility of the irradiated tensile specimens was evaluated by CERT experiments in pure, de-aerated supercritical water at the irradiation temperature of the sample (either 400°C or 500°C). The samples fracture surface, gage surfaces and cross-sectioned gages were observed to determine the amount of cracking.

To assess the stress corrosion cracking susceptibility of neutron irradiated alloys, the University of Michigan undertook to develop the capability to conduct stress corrosion cracking experiments on neutron-irradiated materials. The Irradiated Material Testing Laboratory (IMTL) was designed to provide CERT and CGR capabilities of neutron-irradiated specimens in supercritical water, and for specimen analysis by Scanning Electron Microscopy (SEM). The facility was designed to minimise the occupation time of the hot cell by making both the load frame and the SEM column mobile. Hot cell #1 in Phoenix Memorial Laboratory (PML) is adjacent to the Irradiated Material Testing Laboratory (IMTL) and is used for specimen loading into the autoclave, autoclave closure and pressure testing in preparation for the experiment, and application of shielding. The autoclave is then rolled into IMTL, a 1 000 square foot laboratory located next to the hot cell, where the CERT or CGR experiment is conducted in supercritical water. Once the experiment is completed, the autoclave is rolled back in the hot cell for specimen unloading. Then, the SEM is installed in the hot cell for post-test analysis of fracture and gage sections. The material tested was a Japanese Prime Candidate Alloy (JPCA) that was irradiated in the Fast Flux Testing Facility (FFTF) for the US-Japan MOTA fusion programme. The material was irradiated in both solution annealed and cold work condition in the temperature range or 390°C to 520°C and to doses from 26.9 dpa to 43.9 dpa. The cracking susceptibility of those samples was determined in pure supercritical water and in neutral environment (argon at 400°C). The fracture surface and gage surfaces of each alloy were observed in SEM.

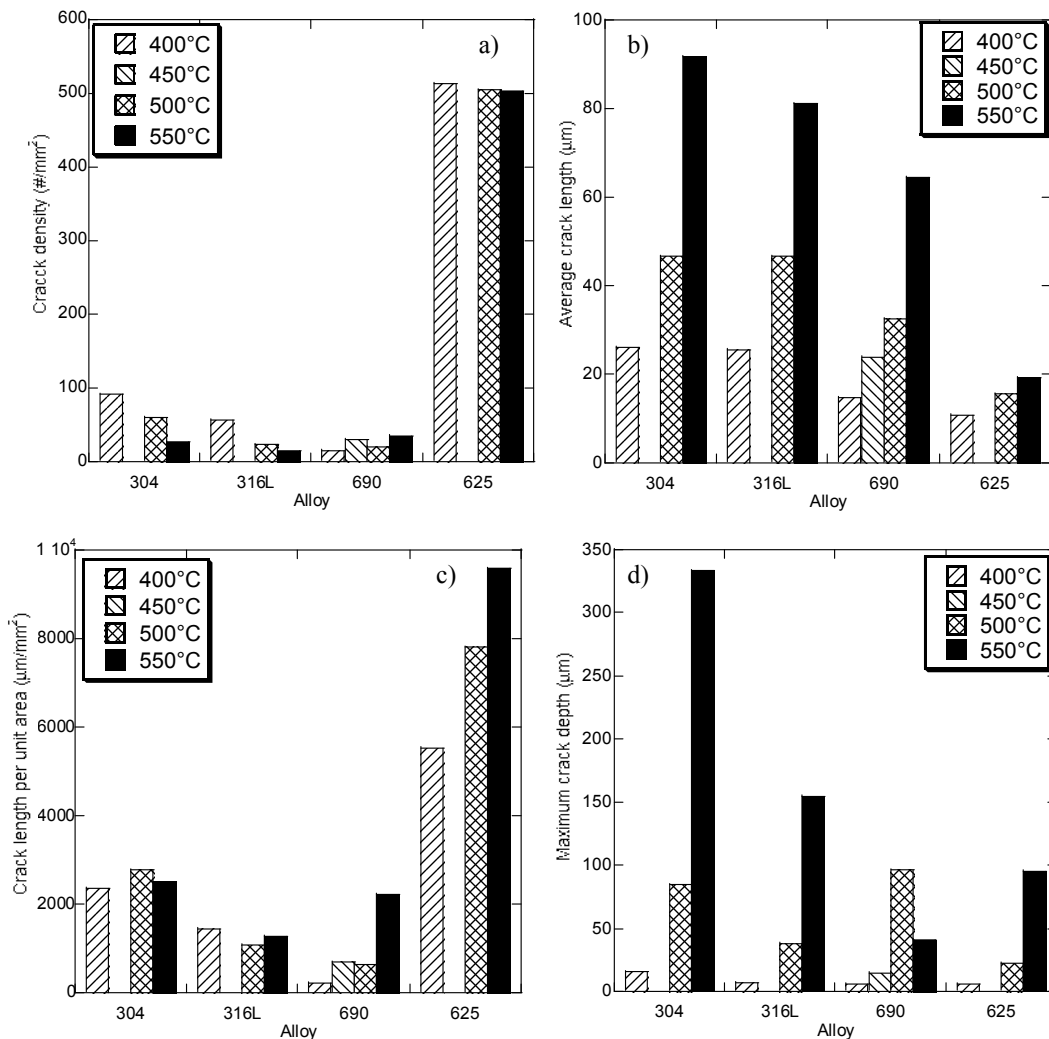
Results

Cracking susceptibility of unirradiated austenitic alloys in supercritical water

CERT experiments showed that both austenitic stainless steel alloys (304 and 316L) and the nickel-based alloys 625 and 690 undergo stress corrosion cracking in de-aerated SCW between temperatures of 400°C and 550°C. The study also showed that the fracture surface was not a good measure of cracking as results showed that extensive IG cracking occurred in multiple locations in the gage section, but very little was observable on the fracture surfaces. As such, a better measure of

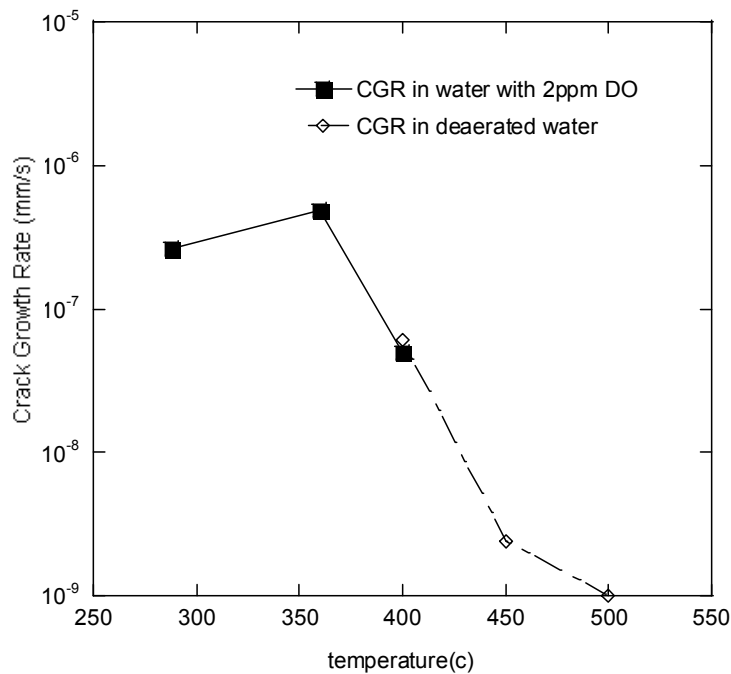
cracking is obtained through analysis of the gage section and the cross-section of the tensile bars. Cracking severity, as measured by the crack length per unit area (crack density \times crack length on the gage surface) incorporates both the density and length of the cracks. Overall, 304 and alloy 625 display the greatest degree of susceptibility as determined by the crack length per unit area [Figure 1(c)]. Observation of the gage surfaces showed that the average crack length and the maximum crack depth measured of the cross-sectioned sample [Figure 1(b,d)] increase with temperature while the crack density decreases. The crack growth rate determined using the maximum crack depth, is very temperature dependent. It results in activation energies between 84 and 105 kJ/mol [5]. Three distinct modes of cracking are observed, one that results in transgranular cracks perpendicular to the stress axis and appear to occur by a cyclic process consisting of cracking of the oxide followed by oxidation of the fresh metal, similar to the tarnish rupture mechanism. A second mode is a variation of TG cracking in which the crack morphology consists of finger-like projections closely grouped together and propagation occurs by the tarnish rupture mechanism. The last mode of cracking is characterised by intergranular cracking in which the crack path results in a characteristic jagged path along the grain. This mode led to the deepest cracks.

Figure 1. Crack density (a), average crack length (b), crack length per unit area (c), and maximum crack depth (d), obtained after straining in 400°C, 450°C, 500°C and 550°C SCW at $3 \times 10^{-7} \text{ s}^{-1}$ (blank indicates no data)



The propagation rate of a crack propagating in cold worked 316L under constant K loading mode ($K = 27.45 \text{ MPa } \sqrt{\text{m}}$) was measured in the subcritical regime from 288-360°C and in the supercritical regime up to 500°C. In the subcritical regime, an increase in temperature resulted in an increase in the crack growth rate by a factor of about 2 from $2.6 \times 10^{-7} \text{ mm s}^{-1}$ at 288°C to $6.3 \times 10^{-7} \text{ mm s}^{-1}$ at 360°C. The CGR increase is consistent with an activation energy for crack growth of 26 kJ/mol, which is within the range of experimentally determined values for stainless steels in water from 25-288°C [8,9]. Shifting from the subcritical to the supercritical condition caused a significant drop of the crack growth rate. The crack growth rate was further suppressed by temperature increases from 400-450°C and then to 500°C in supercritical water, in contrast to the increase in CGR between 288-360°C. The fracture surface showed that the crack propagated intergranularly. The crack propagation rates measured are presented Figure 2.

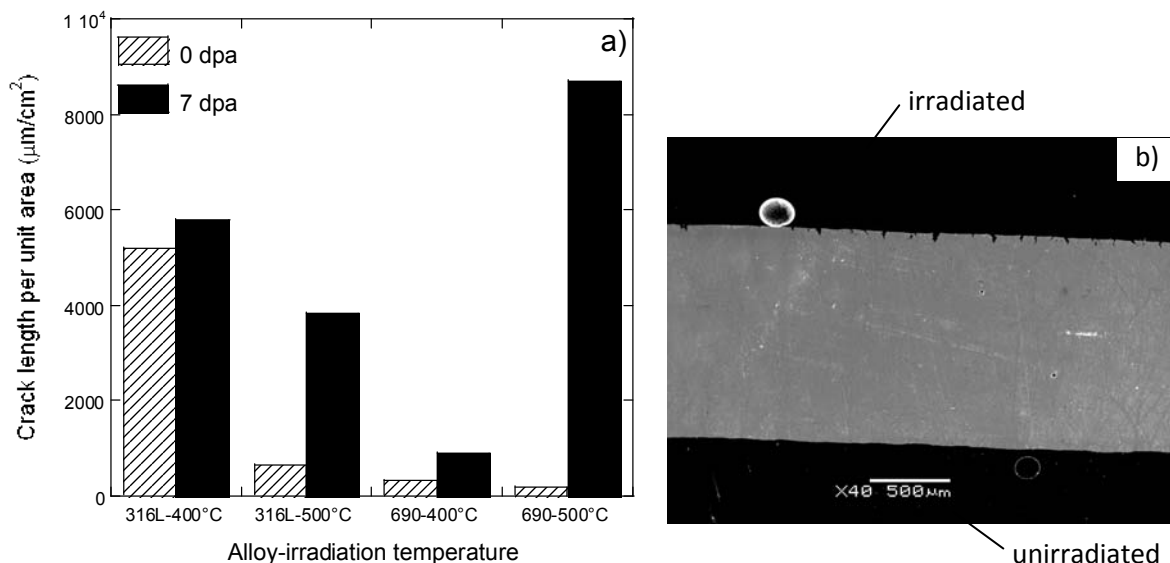
Figure 2. Crack propagation rate measured under constant K loading mode vs. temperature across the subcritical-supercritical line for a 0.5T CT specimen of 21% cold worked unsensitised type 316L stainless steel in pure water



Cracking susceptibility of proton-irradiated alloys

The microstructure analysis of the proton-irradiated samples indicates that irradiation results in grain boundary Cr and Fe depletion and Ni enrichment and that the extent of segregation increases with dose. The irradiated microstructure is dominated by small (7 nm) faulted Frank loops at 400°C and larger Frank loops (25 nm) and voids at 500°C. Irradiation hardening reached 237 kg/mm² for alloy 316L and 203 kg/mm² for 690 at 400°C and 126 kg/mm²s for 316L and 101 kg/mm² for 690 at 500°C. It is greater on 316L vs. alloy 690 at both temperatures and, as expected, irradiation hardening is less at 500°C than at 400°C. For all samples, the irradiated gage section of the samples exhibited more cracking than the unirradiated side. The measure of the extent of cracking for all samples tested is the crack length per unit area shown in Figure 3(a). At 400°C, the cracking susceptibility of 316L irradiated to 7 dpa is 1.11 times higher than that of an unirradiated sample. The susceptibility increase

Figure 3. Influence of irradiation on the cracking susceptibility of alloy 316L and 690 in 400°C and 500°C SCW 9a0 and cross-section of alloy 690, irradiated to 7 at 500°C, after completion of CERT test in 500°C SCW showing the unirradiated and irradiated sides of the sample



for alloy 690 at 400°C is 2.79. At 500°C, the increase of cracking with irradiation is much greater. Irradiated alloy 316L had a crack length per unit area 6 times than on its unirradiated side. This difference was even higher for 690 as a 7 dpa irradiation increased the amount of cracking by a factor of 48. As illustrated on Figure 3(b) with the post CERT test cross-section of alloy 690, irradiated to 7 dpa at 500°C, irradiation increased the crack penetration depth. At both 400°C and 500°C, the maximum crack depth increased with irradiation for both alloys. At 400°C, the fractional increase in crack depth due to irradiation was greater for the alloy 690 and at 500°C, the fractional increase in crack depth was greater for 316L [4].

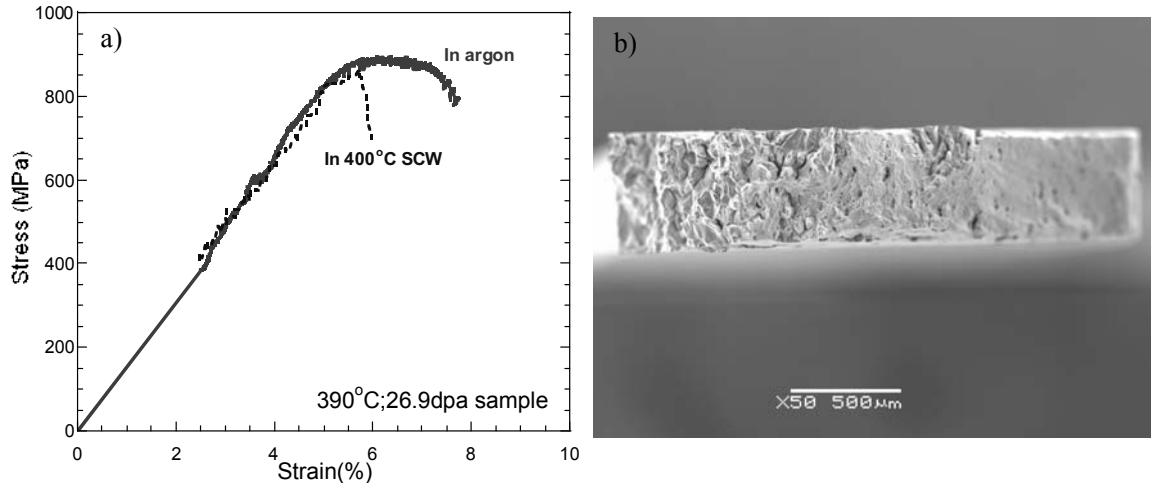
Cracking susceptibility of neutron irradiated samples

In 400°C argon, the neutron-irradiated samples exhibited a low engineering plastic deformation after rupture (3%), but no IG cracking on the fracture surface and about 40% of reduction of area. In supercritical water, all samples showed susceptibility to cracking. Some samples failed in the pinhole area with a fracture surface 100% intergranular. For the samples that failed in the gage section, a reduction of strain to failure was observed [Figure 4(a)], with samples failing before reaching the YS, presence of intergranular cracking on the fracture surface with up to 45% of the fracture surface intergranular [Figure 4(b)] and a decrease of reduction of area.

Discussion

One important result of the CERT experiments performed on unirradiated samples is that fracture surfaces are not good measures of IG cracking. Results showed that extensive IG cracking occurred in multiple locations in the gage section, but very little was observable on the fracture surfaces. It has been shown in many studies that ductile alloys that fail by IG fracture in service (e.g. alloy 600 in primary water), often exhibit only small amounts of IG cracking in constant extension rate tests [10]. Because CERT tests are typically conducted at relatively high strain rates compared to crack growth rates, the plastic strain tends to “outrun” the IG cracks that have initiated, resulting in a largely ductile

Figure 4. Stress-strain behaviour in 400°C argon and SCW, of JPCA irradiated at 390°C to 26.9, and fracture surface of the sample strained in SCW



fracture mode. For example, in these experiments, a rough measure of the crack growth rate can be obtained by dividing the maximum crack depth by the time of the test. For alloy 304, which exhibits the deepest IG cracks, this value falls between 1.0×10^{-8} mm/s (400°C) and 3.2×10^{-7} mm/s (550°C). So even the fastest crack growth rate is still an order of magnitude below the extension rate ($\sim 7 \times 10^{-6}$ mm/s) imposed by the test. It results in very shallow cracks and the statistical probability for the fracture surface to capture the extent of IG cracking is poor. Therefore, an observation of the gage surface and the cross-section of the gage surface are recommended to determine if the alloy is susceptible to cracking.

The CERT experiments on unirradiated samples showed an increase of cracking susceptibility with temperature. The results indicate that the maximum crack depth increases with temperature, suggesting that the crack propagation rate increases with temperature. Such an analysis would be consistent with the observation of a decrease of crack density and increase of the crack length per unit area measured. However, it is different from the CGR results that indicate a decrease of crack propagation rate with temperature. This observation likely results from the difference of loading mode and is related to the increase in corrosion rate [11]. In a CGR test with constant K loading, at high temperature, the oxidation rate is so high that oxide growth on the crack walls will approach that at the crack tip, blunting crack growth. The higher strain rates of a CERT test prevent blunting by causing film rupture. If the crack is blunted by rapid oxide growth at high temperature, then crack growth is reduced, but if the oxide is continually ruptured due to a comparatively high strain rate, then the effect of temperature is to increase the degree of cracking [12].

The results obtained with irradiated samples (proton and neutron) showed that IASCC would be a problem for the SCWR. The study with proton-irradiated samples showed that irradiation significantly enhances cracking susceptibility. It also suggests that IASCC studies should be done concurrently with SCC studies on unirradiated alloys. Alloy 690, which would be considered more resistant than 316L to SCC in unirradiated condition appeared to be less resistant after irradiation. The microstructure analysis also showed that neither RIS nor hardening can satisfactorily account for the changes in SCC susceptibility with irradiation temperature. The influence of irradiated microstructure on SCC susceptibility should be further studied in order to understand such results. The neutron-irradiated samples exhibited significant cracking in SCW at 400°C, supporting the results obtained with proton-irradiated samples. Unfortunately, there is no baseline for the unirradiated behaviour of JPCA

alloys in SCW. It would be of interest to use the same set of heats, irradiate them with protons and neutrons at the same temperature in order to compare the irradiated microstructure and the resulting cracking susceptibility. Once this is done for a limited set of heats, it will allow the use of proton irradiation to investigate other heats and various mitigation techniques, either related to water chemistry or to some alloy microstructure modifications, for a reduced cost and time before conducting the necessary, critical, experiments on neutron-irradiated samples. Another reason for the need for neutron irradiation of selected heats lies in the CGR results obtained with unirradiated 316L. Those results showed that the results obtained with CERT tests could not be trivially translated into crack propagation rate under constant K loading, which is the standard for the nuclear industry. There is no reason to believe that such observation would not apply on irradiated materials. Nevertheless, the set of JPCA samples tested is used to gain a better understanding of the material parameters (hardening, irradiation temperature, irradiation dose) influencing IASCC in SCW and how the water chemistry (water density, hydrogen content) would affect cracking.

Conclusion

To assess the SCC and IASCC susceptibility of the alloys for the SCRW concept, the University of Michigan developed the experimental capabilities to perform stress corrosion cracking experiments with unirradiated, proton-irradiated and neutron-irradiated samples in supercritical water. The CERT and CGR experiments performed with austenitic alloys showed that:

- Unirradiated stainless steel 304, 316L and nickel-based alloys 690 and 625 are susceptible to SCC in SCW in the temperature range of 400 to 550°C.
- CERT experiments showed an increase in cracking susceptibility with temperature whereas under constant K loading, the crack propagation rate decreases at higher temperatures.
- Irradiation by protons significantly enhanced the cracking susceptibility of alloys 316L and 690 in SCW and neither RIS nor hardening appear to be the main controlling factor.
- Neutron-irradiated JPCA is susceptible to IASCC in 400°C de-aerated supercritical water.

The present study suggests that:

- The measure of cracking after CERT experiments must incorporate analysis of the gage section and cross-sectioned gage section, as the observation of the fracture surface alone is insufficient to assess cracking susceptibility.
- CGR should be assessed independent of CERT result, as crack growth and crack initiation do not necessarily parallel each other for each alloy.
- IASCC experiments should be conducted in parallel with SCC studies on unirradiated samples, as the enhanced cracking susceptibility with irradiation is alloy-dependent.
- Proton irradiation is an appealing surrogate for neutron irradiation. However, neutron irradiation of the candidate alloys is required not only to benchmark the data obtained with proton irradiation, but also to characterise crack growth via crack growth rate measurements.

Acknowledgements

This research was supported by DOE subcontract 00038523 and A827761.

REFERENCES

- [1] Viswanathan, R., R. Purgert, U. Rao, “Materials for Ultra-supercritical Coal-fired Power Plant Boilers”, in Challenges for High Temperature Alloys for Aerospace, Land-based Gas Turbines, Power & Transportation Symposium, Session 2, High Temperature Alloys in Power Generation, *ASM Materials Solutions Conference*, Columbus, OH, 18-21 October 2004.
- [2] Was, G.S., P.L. Andresen, “Irradiation Assisted Corrosion and Stress Corrosion Cracking”, Chapter in *ASM Handbook*, Volume 13, Corrosion, American Society for Metals, in progress.
- [3] Was, G.S., P.L. Andresen, “Irradiation Assisted SCC in Austenitic Alloys”, *JOM*, 44 No. 4, 8-13 (1992).
- [4] Was, G.S., S. Teysseyre, “Challenges and Recent Progress in Corrosion and Stress Corrosion Cracking of Alloys for Supercritical Water Reactor Core Components”, *Proc. 12th Int. Conf. Environmental Degradation of Materials in Nuclear Power Systems – Water Reactors*, TMS, Warrendale, PA (2005), p. 1343.
- [5] Teysseyre, S., G.S. Was, “Stress Corrosion Cracking of Austenitic Alloys in Supercritical Water”, *Corrosion*, No. 12, Vol. 62, 1100-1116 (2006).
- [6] “Standard Practice for Neutron Radiation Damage Simulation by Charged-particle Irradiation,” ASTM Designation E 521-89, *Annual Book of ASTM Standards*, Vol. 12.02, p. D-9, American Society for Testing and Materials, Philadelphia, PA (1989).
- [7] Damcott, D.L., J.M. Cookson, R.D. Carter, Jr., J.R. Martin, M. Atzmon, G.S. Was, *Radiation Effects and Defects in Solids*, 118, 383-392 (1991).
- [8] Andresen, P.L., “Effects of Temperature on Crack Growth Rate in Sensitized Type 304 Stainless Steel and Alloy 600”, *Corrosion*, 49, p. 714 (1993).
- [9] Haruna, T., S. Zhang, T. Shibata, “Analysis of Initiation and Propagation of Stress Corrosion Cracks in Sensitized Type 304 Stainless Steel in High-temperature Water”, *Corrosion*, 60, p. 1104 (2004).
- [10] Begley, J.A., *Strain-rate Damage Model for Alloy 600 in Primary Water*, Electric Power Research Institute, Report no. NP-7008s, Palo Alto (1990).
- [11] Was, G.S., S. Teysseyre, Z. Jiao, “Corrosion of Austenitic Alloys in Supercritical Water”, *Corrosion*, No. 11, Vol. 62, 989-1005 (2006).
- [12] Peng, Q.J., S. Teysseyre, P.L. Andresen, G.S. Was, “Stress Corrosion Crack Growth in 316 Stainless Steel in Supercritical Water”, *Corrosion*, submitted (2006).

OXIDATION AND STRESS CORROSION CRACKING OF STAINLESS STEELS IN SCWRs

Dolores Gómez Briceño, Lucas Castro, Fernando Blázquez

Centro de Investigaciones Energéticas, Medioambientales y Tecnológicas (CIEMAT), Spain

Abstract

SCWRs are high-temperature, high-pressure, water-cooled reactors that operate above the thermodynamic critical point of water (374°C, 22.1 MPa). The SCWR offers many advantages compared to state-of-the-art LWRs including the use of a single phase coolant with high enthalpy, the elimination of components such as steam generators and steam separators and dryers, a low coolant mass inventory resulting in smaller components, and a much higher efficiency (~44% vs. 33% in current LWRs). In these systems high pressure (25 MPa) coolant enters the vessel at 280°C which is heated to about 500°C and delivered to a power conversion cycle.

Supercritical water (SCW) exhibits properties significantly different from those of liquid water below the critical point. Supercritical water acting essentially as a non-polar dense gas with solvation properties approaching those of a low-polarity organic. In this conditions, can dissolve gases like oxygen to complete miscibility. Depending upon what species are present and how much oxygen is present in the solution can becomes a very aggressive oxidising environment.

Most of the data on corrosion in supercritical water are from fossil plant or oxidation waste disposal systems. However there is very limited data on corrosion in low conductivity de-aerated SCW and less on stress corrosion cracking behaviour under operating conditions foreseen for SCWR.

Candidate materials for structural components are materials for high temperatures and include ferritic-martensitic alloys; oxide dispersion strengthened (ODS) ferritic/martensitic steels and strengthened steels by precipitation and for lower temperatures the austenitic stainless steels, such as 304 and 316, used in the LWR. Low swelling austenitic steels are also of high interest for areas with high dpa and high temperature.

A review of the available information on corrosion and stress corrosion behaviour of different types of stainless steels in supercritical water at high temperatures is presented in this paper. The experimental programme to be performed in our lab for the study of these topics is discussed.

Introduction

The supercritical water reactor (SCWR) design concept is one of six chosen for further development based on the criteria of economics, safety and sustainability by the Generation-IV International Forum and is one of two selected for primary research focus in the US. Advantages of SCWRs are their high thermal efficiency (45% vs. 33% for current LWR) and their more simple design. Several components such as the pressuriser, steam generators, steam separators and dryers are not needed, since the coolant remains single-phase throughout the system. SCWR construction will use experience from supercritical fossil-fired boilers and LWR.

The reference SCWR design for the US programme is a direct cycle system operating at 25 MPa with core inlet and outlet temperatures of 280 and 500°C, respectively. The coolant density came from about 760 kg/m³ at the core inlet to about 90 kg/m³ at the core outlet. All the reactor pressure vessel internals components will be designed for periodic replacement so that high fluences (20 dpa) will not need to be considered [1].

The European project HPLWR (high-performance light water reactor) has common objective with the SCWR of Generation IV. One of the work packages is devoted to materials and chemistry. For the definition of the scope of this work package the candidate materials identified in the Phase 1 of this project have been taken into account. The aim of Phase 2 regarding materials is the selection of tested materials and data for fuel rod cladding, core and RPV materials and specifications for the water chemistry. The following key areas have been identified: oxidation, corrosion and stress corrosion cracking; radiolysis and water chemistry; strength, embrittlement and creep resistance; and dimensional and microstructural stability [2].

In connection to materials, a major issue in a SCWR is the specification of the water chemistry to control the impurities in the required level. In the reactor core a transition from the subcritical to supercritical conditions occurs with the consequent diminution of the impurities solubility and the risk of precipitate formation. Radiolysis in supercritical core is being studied in different programme [3] and the first results are now available [4,5].

Materials to be into consideration for cladding and internals components included: ferritic/martensitic steels containing 9-12 wt.%Cr that has been selected as candidate materials for fuel cladding due to their combination of elevated temperature strength, irradiation swelling resistance and expected resistance to IASCC [6]; austenitic alloys such as 304 and 316 used as internal components in LWR with a good oxidation resistance but susceptible to IGSCC and IASCC in high-temperature water, moderate strength through the 400-500°C range and swelling at temperatures between 400-600°C, and nickel-based alloys for areas with low dpa. Oxide dispersion strengthened (ODS) steel are being considered as alternative material for areas in which a higher oxidation resistance and high-temperature properties will be needed.

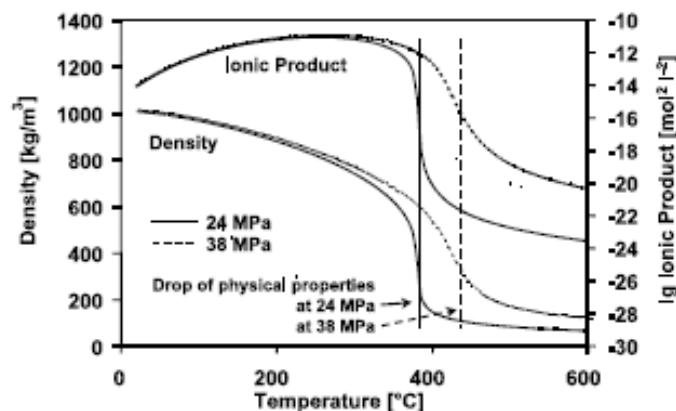
Candidate materials need to have adequate oxidation and SCC behaviour when exposed to supercritical water at temperatures up to 600°C. There is some information about these issues from materials used in supercritical fossil plants and from the supercritical water oxidation (SCWO) processes. However, available results are not directly applicable to the conditions foreseen for SCWR.

This paper tries to review the available information on oxidation and stress corrosion cracking of stainless steels: ferritic-martensitic, austenitic and ODS in supercritical water in order to identify the open points for future investigations. In addition to this, the experimental programme to be performed in our laboratory is presented.

Characteristic of supercritical water

Properties of water change with temperature and pressure for conditions above the critical point, 374°C, 22.1 MPa. Supercritical water (SCW) has both liquid-like and gas-like properties: density between states, high diffusivity and good heat transports. Supercritical water actuates as a non-polar dense gas, and has a complete solvency for most gases. The ionisation constant reduces from 10^{-14} at room temperature to 10^{-23} at 500°C, hydrogen bonding is greatly reduced or non-existent depending on the pressure and the dielectric constant is reduced by more than an order of magnitude. These changes mean that ionic solubility, pH and corrosion potential will be different at the core inlet compared to the outlet. To understand corrosion potential in the core of a SCWR would be needed to know the consequences of radiolysis on water decomposition, to identify the different radicals and species and to identify their contribution to corrosion potential. The variation of density and ionic product for temperature up to 600°C is presented in Figure 1 [7].

Figure 1. Physical properties of supercritical water at different pressures [7]



Oxidation in supercritical water

One of the first requirements for materials selection in the SCW environment is oxidation resistance. To minimise the impurities in the primary loop and the associated problems of activation transport, materials to be used in SCWR need to have a high corrosion resistance. The oxidation rate has to be lower than the acceptable for materials in supercritical fossil plants. In these plants, oxide films of several hundreds of micrometer thickness in tubes with wall thickness around 10 mm are assumed. However this situation is not acceptable for materials in SCWR.

Ferritic-martensitic steels (F-M steels)

Different types of 9%Cr and 12%Cr steels, more advanced alloys such as HCM12A (P112) and NF616 (T92), designed to improve high-temperature resistance creep up to 620°C, have been tested in supercritical water in an extended range of temperatures. HCM12A is an improved HT9 (12%Cr) by substituting more of the Mo by W and addition of Cu. The alloy NF616 (P92) is an advanced 9%Cr, developed by substituting part of the Mo in P91 with W [8].

9%Cr F-M steels have been tested by Yi [9] in water at 370°C and in SCW at 500°C, with an oxygen level below 10 ppb. In these experiments, a much thicker oxide layer was formed on sample tested under supercritical conditions. An oxide formed by two layers was observed on this sample. The

outer layer is formed by magnetite and the inner layer is composed by magnetite and FeCr_2O_4 . An internally oxidised region was detected beneath the inner layer in sample tested at 500°C . The surface oxide on the specimen tested in water at 370°C was also composed by two layers: an outer layer containing only iron and an inner layer containing iron and chromium. The corrosion rates of these samples were evaluated in terms of the weight gain. At 370°C the weight of all the samples decreases even though a surface oxide was observed on the sample. In supercritical conditions the weight of the samples increased. Process involving ions dominate the corrosion processes in aqueous solution. In the phase gas, the oxide growth is governed by the outward transport of the metals ions from the underlying metal substrate and the inward transport of oxygen. The diffusion rates of anions and cations in the oxide are the rate determining steps. From the analysis of the characteristic of the oxide layers, the authors suggest that the ionic dissolution was negligible on T91 in the supercritical conditions and that the corrosion behaviour of T91 in de-aerated SCW at 500°C would be similar to that in the gaseous environment rather than that in a liquid condition.

Hwang [10] studied the oxidation of three heats of 9%Cr steels, two of T91 and one of T92, and one heat 12%Cr (T122) in SCW with less than 10 ppb of dissolved oxygen, at temperatures from 370 to 600°C . At 370°C , materials showed weight loss. An evident effect of the temperature was observed, in particular from 500 to 600°C . The influence of the chromium contents on the oxidation rate seems to be not relevant for temperatures up to 500°C . At this temperature, corrosion rate of all alloys is $\sim 12 \text{ mg/dm}^2\text{day}$. However, at 600°C , corrosion rate of T91 and T122 is $\sim 40 \text{ mg/dm}^2\text{day}$ whereas T92 is $\sim 50 \text{ mg/dm}^2\text{day}$.

F82H (7.72%Cr) oxidation experiments in SCW with 200 ppb of dissolved oxygen, at temperatures from 280 to 650°C and 23.5 MPa were performed by Hirose [11]. A clear influence of the temperature was observed. For exposures time of 1 000 hours weight gain was five times higher at 550°C than at 470°C . The estimated oxidation rate at 550°C is 0.04 mm/year.

Oxidation of P91 (9%Cr) and pure Fe, Cr and Ni were determined by Betova [12] in deoxygenated ultra supercritical water at 500, 600 and 700°C and a pressure $>25 \text{ MPa}$, for a period of 100 hours. The thickness of the oxide layer was the lowest for Cr and the highest for Fe. For pure Ni, almost no increase of oxide thickness on temperature was found. The estimated apparent activation energies are 110 kJ/mol for the oxide on Fe and Cr and 77 kJ/mol for P91. A double layer structure of the oxide formed on P91 was observed. Oxide layers on the specimens tested at 600°C showed a high porosity. The inner layer is enrichment in Cr and Ni and the outer layer is formed almost exclusively by iron and oxygen. The enrichment of chromium of the internal oxide layer on P91 seems to be independent on temperature, being close to a factor 2. Nickel is enriched both the inner layer and the inner layer/interface, which reflects both its lower oxidation and transport through the inner layer. Mn is rather strongly enriched in the outlet layer of the oxide at all three temperatures.

P92 (9%Cr) and HCM 12 (11.9%Cr) were tested by Bojinov [13] in SCW at 650°C and pressure of 30 MPa, with an 1 ppm of oxygen, up to 900 hours. Both materials show a similar kinetic but the weight gain is higher in the P92 than in the HCM 12. A double oxide layer was observed on both materials. The porous, columnar type outer layer is formed by a hematite type oxide, whereas the denser inner layer contained iron-chromium spinel oxide with a clear enrichment of W and Mo and a detectable enrichment of Si. An enrichment of Ni exists at the alloy/film interface.

Jang [14] tested T91 and T92 in SCW with around 8 ppm of oxygen at temperatures from 350 and 627°C up to 500 hours. After 500 hours the oxidation rate at 627°C is 10 times higher than the one at 500°C ($\cong 5 \text{ mg/dm}^2\text{day}$), whereas differences among heats are not significant. Corrosion rates measured in sub critical water at 350°C and in supercritical water at 400°C are similar ($\cong 2.5 \text{ mg/dm}^2\text{day}$).

The same heats of T91 (8.4%Cr), HT9 (11.6%Cr) and HCM 12 (10.5%Cr) have been tested in SCW at 500°C at Wisconsin University [15-17] and at 400 and 500°C at Michigan University [18]. Oxygen contents were 25 wppb and 2 wppm in [15-17] and 10 ppb and 100 and 300 ppb in [18]. The alloy NF 616 (9%Cr) was also tested at Wisconsin University [19]. The comparison of the main results from these two programmes was presented by Allen [20]. Weight gain is very dependent on temperature. The oxide gain at 500°C is 4-5 times greater than at 400°C. The effect of the oxygen content from less than 10 ppb to 2 000 ppb is small, but the weight gain at 2 000 ppb is clearly the highest. For 25 ppb of oxygen, weight gain scales with bulk Cr content, but in a slight way. For Cr content from 8.5 and 11.5%, the weight gain goes from 1.7 to 1.4 mg/cm², for an exposure time of 333 hours. A heat of 9Cr ODS tested in the same condition shows a weight gain of 1.2 mg/cm². T91 and HCM12A [20] showed a double oxide layer: magnetite in the outer layer and iron-chromium spinel in the inner layer. The Mo content in the inner layer, closer to the bulk metal value, is higher than in the outer layer. The situation is similar for Cu and W in HCM12A. In this alloy there is a transition zone below the inner oxide layer, characterised by porosity or cracks running almost normal to the surface, and associated to an oxidation internal process.

Oxide dispersion strengthened steels (ODS)

The corrosion properties of ODS steels in de-aerated SCW at 510°C and 25MPa up to 600 hours was studied by Cho [21]. Materials tested were 9%Cr and 12%Cr ODS with different levels of yttrium and aluminium. ODS steels showed a similar oxidation rate that the ferritic-martensitic steels. No significant beneficial effects of yttrium (0.24-0.44 wt.%) were observed. Cr contents higher than 13% and Al concentration higher than 4.5 wt.% were effective in suppressing the corrosion in the tested conditions. New data for exposure time up to 2 400 hours has been reported by the same authors [22]. The materials tested were developed to investigate the influence of chromium (14%-22%). The obtained results point out that the ODS steels with 14%Cr showed higher resistance to corrosion than 316L and that ODS steels corrosion resistance increase with Cr content. Estimated corrosion rate for ODS steels are around 0.35 and 0.15 g/dm²day.

A 9Cr ODS ferritic steel was tested in SCW at 500°C and 25 MPa with 25 ppb of oxygen dissolved for 1 026 hours by Chen [23]. For comparison a heat of the F-M steel NF616 was included in the same experiment. The overall weight gain for the ODS steel was lower than for the NF616 steel. However, the ODS steel showed a more porous oxide structure. The oxidised thickness on 9Cr ODS consists of three layers: an outer formed by magnetite, an inner formed by (Fe,Cr)₃O₄ and an innermost internal oxidation zone, not detected in the NF616. This layer is associated with its finer grain size. Yttrium and chromium rich oxide ribbons were detected at the steel grain boundaries in the internal oxidation layer.

Austenitic stainless steels

Austenitic stainless steels, 304 and 316, are used for core internal components in light water reactor. There is a large database on their behaviour in high-temperature water in BWR and PWR conditions that could be used as reference. However, it is needed to have into account the differences between the corrosion/oxidation in subcritical and SCW.

Was [24] studied the oxidation behaviour of 304L and 316L in SCW at temperatures from 400 to 550°C with <10 ppb of dissolved oxygen. The 304L was tested in as received condition (grain size 40 µm) and the 316L after a heat treatment to remove carbide precipitation (grain size 44 µm). Weight gain increase accelerates with increasing temperatures for both alloys. At 550°C, gain weight of

4.8 and 6.2 mg/dm²day was measured for 304L and 316L, respectively. At 500°C the values obtained were 0.67 and 1.59 mg/dm²day. In both alloys, the oxide layer consists in a double layer: an outer layer of magnetite and an inner layer Cr-rich. Apparent activation energy of 210 and 214 kJ/mol for a temperature range from 400 to 500°C was calculated for 304L and 316L, respectively.

Betova [12] studied the oxidation behaviour of 316L in deoxygenated SCW at temperatures of 500, 600 and 700°C. The increase of weight gain seems to increase more significantly between 500 and 600 than between 600 and 700°C. The morphology of the oxide layer obtained at 500°C is similar to the observed on this material at subcritical temperatures. At 600°C, a double oxide layer was observed with a high porosity. Thickness of the oxide layer is smaller than the observed on P91 tested in the same experiments, with similar porosity.

Kaneda [25] reported oxidation rate of 304, 316L, and 310S, tested in supercritical water at 290, 380 and 550°C with 8 ppm of dissolved oxygen for 500 hours. At 290 and 380°C, weight loss is similar for the three materials. At 550°C, 304 had the largest weight loss, 12.5 mg/dm²day, and 310S the smallest, 2.4 mg/dm²day.

Allen [26] reported some oxidation data on an experimental low swelling austenitic alloy, named D9 (13.7%Cr, 15.8%Ni) and alloy 800. Tests were performed at 500°C and 25 MPa with 25 ppb of dissolved oxygen for exposures times up to 1 026 hours. A weight gain of 0.75 mg/dm²day for D9 was calculated. A dual oxide layer was observed, formed by magnetite and hematite. Si is present in the outer oxide layer. A Ni-rich layer remains on the metal side of the metal-oxide interface, formed by the Cr diffusion into the oxide from the metal. The alloy 800H showed a weight gain less than 0.48 mg/dm²day and presented a tendency to spall higher than D9. To improve the oxide scale adherence, alloy 800 H samples were thermo-mechanically processed to reduce the fraction of high-energy grain boundaries [27]. In this condition, the weight gain showed less fluctuation but higher values than for the annealed samples, according to the authors.

The austenitic alloys TP347H (Nb stabilised) and Sanicro 28 (26.7%Cr, 30.6%Ni) were tested by Bojinov [13] in SCW with 1 ppm of oxygen, at 650°C and 30 MPa up to 900 hours. The weight gain for the alloy TP347H was 4.8 mg/dm²day, whereas for Sanicro was almost negligible. Nodules like oxide formation was visible on TP 347H for short but after 900 hours a continue oxide layer was detected, formed by a double layer. On Sanicro, a very thin oxide layer rich in chromium was observed.

Stress corrosion cracking and corrosion fatigue

The SCC susceptibility of the F-M steel, T91, HT9 and HCM12A, were studied by Ampornrat [18]. CERT experiments were performed in SCW at 400°C with less of 10 ppb of dissolved oxygen and at 500°C with less than 10 ppb, 100 ppb and 300 ppb of dissolved oxygen. Strain rate used in all the tests was $3 \times 10^{-7} \text{ s}^{-1}$. In all the environments yield strength and maximum stress or HT-9 is highest, followed by HCMA 12A and T91. Samples tested at 500°C have lower strength, higher total elongation and lower uniform elongation than these tested a 400°C. Ductile fracture was observed in all the conditions. However, the gage surface of HT-9 revealed cracks that appeared to be intergranular. The density and depth of cracks increased with temperature and dissolved oxygen. Nevertheless, the greatest crack depth was 28 µm, which is about half the grain size. In oxidation experiments performed in the same conditions, HT9 showed the highest weight gain, followed by T91 and HCM12A.

Austenitic alloys 304L and 316L, were tested in SCW with less than 10 ppb of dissolved oxygen at temperatures from 400 to 550°C [1]. Strain rate used in the tests was $3 \times 10^{-7} \text{ s}^{-1}$. Fracture surfaces

were ductile at all the temperature for both alloys, except for 304L tested at 550°C in which a mixed fracture morphology, intergranular and ductile was observed. However, the gage surfaces exhibited a significant amount of cracking at all temperatures. The crack density is higher at the lower temperatures, but the cracks are longer. For evaluation of the SCC susceptibility, the authors used the crack length per unit area, which is the product of the crack length and crack density. This parameter increases with the temperature.

SSRT of sensitised 304 and 316L in supercritical water with 8 ppm of oxygen at temperatures from 290 to 550°C and 25 MPa were performed by Tsuchiya [28]. Strain rate used in the tests was $4 \times 10^{-7} \text{ s}^{-1}$. For sensitised 304, the fracture mode was totally intergranular at 290°C and transgranular and ductile at 550°C. Small cracks were observed at temperatures higher than 450°C. Cracks were also detected inside the specimen tested at 550°C. For 316L, fracture was ductile at all the temperatures. At 550°C, small cracks were observed on the side surface and inside the specimen. Stress-strain curves point out that maximum stress of sensitised 304 increased with increasing temperature until 400°C according to the decrease of IGSCC ratio. At temperatures higher than 400°C, maximum stress decreased with the temperature due to the decrease of mechanical strength. For 316L, stress-strain curves were obtained only at 290 and 550°C. The maximum stress was higher at 290°C since IGSCC did not occur at any temperatures. The cracks number per one square millimetre on side surface of sensitised 304 and 316L increased with increasing temperatures, for higher temperatures than pseudo critical point. Cracks observed inside the specimens at 550°C suggested a mechanical cause.

No data have been found on the SCC susceptibility of ODS steels in SCW. Cho [29] published some results on two ODS steel heats (19Cr-ODS and 19Cr-4Al-ODS) tested in water at 288°C with 8 ppm of dissolved oxygen. Strain rate influence on the stress-strain curves was studied. Results point out that no significant differences exist in the stress-strain curves for strain rates from 10^{-4} to $3 \times 10^7 \text{ s}^{-1}$ for both materials. Both ODS steels have very low SCC susceptibility. The heat with 4.5 of aluminium showed higher ductility and lower ultimate tensile strength and yield strength. No indications of susceptibility to SCC.

Corrosion fatigue tests of T91 at 370 and 500°C were performed for 3 000 cycles at the loading frequency of 0.0042 Hz [9]. Fatigue crack growth rate are higher in water than in air. The authors concluded that the corrosion fatigue of T91 in the supercritical condition was increased by a fatigue-oxidation interaction.

Results analysis: key parameters

Oxidation behaviour in supercritical water is similar to the observed in steam or gas phase. Materials undergo a weight gain instead of a loss weight as observed in water corrosion processes. Oxidation rate is higher for F-M steels than for austenitic alloys, and the few available data showed than the weight gains for ODS steel are lower than for austenitic alloys. However, the influence of F-M steels chromium concentration seems to be not significant at least up to 500°C.

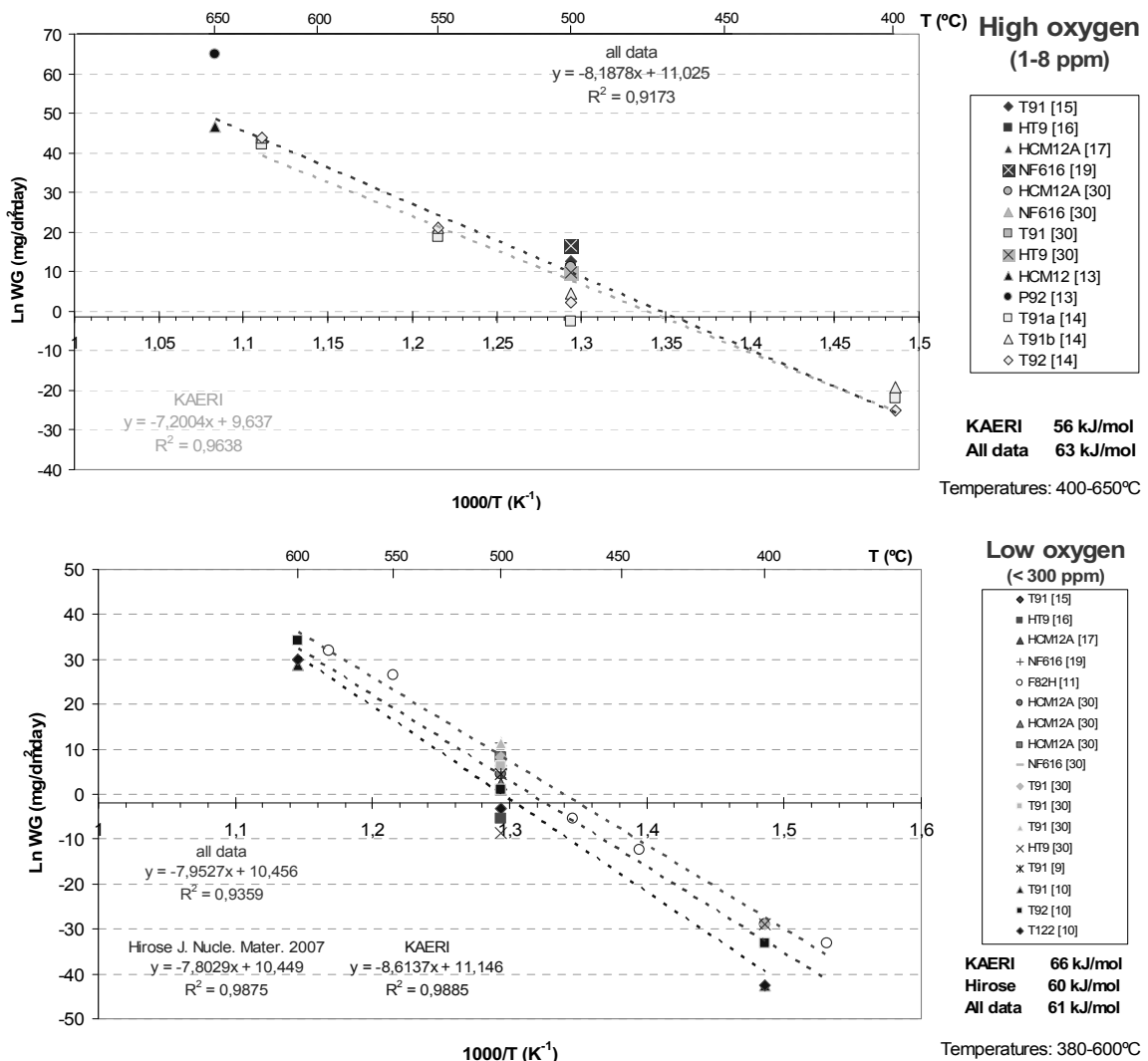
The experimental weight gain (ΔW) data can be fitted using the expression $\Delta W = k t^n$ where k is a constant, t is the exposure time, and n is the time exponent. Depend on time exponent the corrosion gain behaviour can be linear, parabolic, cubic, etc. Growth kinetics follow a parabolic law in the most of the cases [15-17].

An apparent activation energy of the oxidation process for F-M steel has been calculated for the weight gain data obtained in SCW with low oxygen dissolved (less than 10 ppb to 300 ppb) and with

high oxygen level (1 000 to 8 000 ppb). It is assumed that the influence of the F-M steels on the weight gain is not significant. Moreover, the weight gain data considered have been normalised to 100 hours, assuming that for short times its behaviour is linear. In case of parabolic behaviour the energy activation would be twice as much. Taking into account it in Figure 2, is showed average values are similar (63 and 61 kJ/mol has been obtained for high and low oxygen contents), in spite of the higher weight gain measured in high oxygen experiments. These values are similar to those calculated by Betova [12]. For austenitic alloys the activation energy calculated by Was [30] was of 210 and 214 kJ/mol for 304L and 316L respectively, assuming a parabolic growth law.

A minor SCC susceptibility has been detected in SCW conditions for F-M and austenitic steels, even with 8 ppm of dissolved oxygen. SCC susceptibility seems to disappear with the temperature. No data have been found for ODS steels.

Figure 2. Activation energy for oxide growth in F-M steels



Open points for future investigations and CIEMAT programme

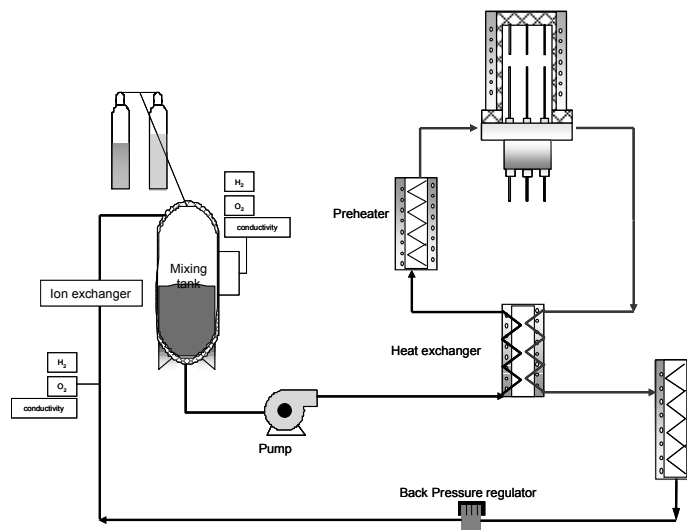
Oxidation rates for F-M and austenitic steels are now available but in most of the cases the exposure time is shorter than 1 000 hours. Oxide characterisation points out that porosity and spallation occur. Even if the oxidation rate of these alloys would be acceptable for materials to be used in SCWR, the evolution with time of the oxide layers stability is unknown. Longer oxidation tests are needed to establish the chemical-physical characteristics of oxide after long time in all the temperature range, but mainly at high temperature. In the case of ODS steels, the available data point out a high oxidation resistance. But oxidation rate data are very scarce and new data for different types of ODS, obtained after longer exposure times are needed.

In general, F-M and austenitic steels seem to be highly resistant to stress corrosion cracking under constant extension rate tests (CERT). However, the data are still scarce and new data are needed for sensitised and cold worked materials with high dissolved oxygen. No information has been found on the SCC behaviour of ODS steel. So, it is clear the necessity of SCC experiments to determine the susceptibility of ODS to this type of process in supercritical water. The influence of cyclic and constant load on the three types of materials should be studied.

Finally, all the experiments reported have been performed in "oxidant conditions". The influence of hydrogen dissolved in the coolant, as a possible remedy to mitigate radiolysis if needed, should be explored.

A new facility suitable to work under supercritical conditions is being built at CIEMAT, Figure 3. The supercritical loop is designed to work up to 600°C and 35 MPa. Four specimens can be tested simultaneously in the autoclave. CERT or constant load experiments are possible. Our experimental programme is focussed on the stress corrosion cracking of steels under different types of load, in a range of temperatures from subcritical to supercritical conditions in oxidised and reducing environments.

Figure 3. Schematic diagram of SCWR loop



REFERENCES

- [1] *Feasibility Study of Supercritical Light Water Cooled Reactors for Electric Power Production*, INEEL/EXT-04-02530, Final report.
- [2] Heikinheimo, L. *et al.*, “SCWR Materials and Coolant Interaction”, *EU-HPLWR – Materials Overview*, GEDEPEON, November 2006.
- [3] Katsumura, Y., *et al.*, “Research Program on Water Chemistry of Supercritical Pressure Water Under Radiation Fields”, *14th International Conf. on the Properties of Water and Steam*, Kyoto.
- [4] “Materials for Supercritical Water Systems. Programs in the United States”, *ICAP 2004*, Pittsburgh.
- [5] Sims, H.E., “Yield of Radiolysis Products from γ -irradiated Supercritical Water. A Re-analysis Data by W.G. Burns and W.R. Marsh”, *Radiation Physics and Chemistry*, 75, 1047-1050 (2006).
- [6] Totemeier, T.C., *et al.*, “Effect of Transient Thermal Cycles in a Supercritical Water-cooled Reactor on the Microstructure and Properties of Ferritic-martensitic Steels”, *Journal of Nuclear Materials*, 355, 103-113 (2006).
- [7] Krizer, P., “Corrosion in High-temperature and Supercritical Water and Aqueous Solutions: A Review”, *J. of Supercritical Fluids*, 29, 1-29 (2004).
- [8] Viswanathan, R., “Materials for Boilers in Ultra Supercritical Power Plants”, *2000 International Joint Power Generation Conference*, Miami, July 2000.
- [9] Yi, Y., *et al.*, “Corrosion and Corrosion Fatigue Behaviors of 9cr steel in Supercritical Water Conditions”, *Materials Science and Engineering*, A429, 161-168 (2006).
- [10] Hwang, S.S., *et al.*, “Corrosion Behavior of F/M Steels and High Ni Alloys in Supercritical Water”, *Global 2005*, Paper 043, Japan.
- [11] Hirose, T., *et al.*, “Corrosion and Stress Corrosion Cracking of Ferritic-martensitic Steel in Supercritical Pressurized Water”, to be published in *Journal of Nuclear Materials*.
- [12] Betova, I., *et al.*, “Composition, Structure, and Propertie of Corrosion Layers on Ferritic and Austenitic Steels in Ultrasupercritical Water”, *Journal of the Electrochemical Society*, 1153 (11), B464-B473 (2006).
- [13] Bojinov, M., *et al.*, “Characterization of Corrosion Film on Steels after Long-term Exposure to Simulated Supercritical Water Conditions”, *ICAPP’05*, paper 5349.
- [14] Jang, J., *et al.*, “Corrosion Behavior of 9CrF/M Steels in Supercritical Water”, *ICAPP’05*, paper 5136.

- [15] Chen, Y., *et al.*, “Corrosion Behavior of Ferritic-martensitic Steel T 91 in Supercritical Water”, *Corrosion Science*, 48, 2834-2854 (2006).
- [16] Ren, X., *et al.*, “Corrosion of Ferritic-martensitic Steel HT9 in Supercritical Water”, *Journal of Nuclear Materials*, 358, 227-234 (2006).
- [17] Tan, L., *et al.*, “Oxidation Behavior of Iron-based Alloy HCM12A Exposed in Supercritical Water”, *Corrosion Science*, 48, 3123-3138 (2006).
- [18] Ampornrat, P., *et al.*, “Corrosion and Stress Corrosion Cracking of Ferritic-martensitic Alloys in Supercritical Water”, *12th International Conference on Environmental Degradation of Materials in Nuclear Power System Water Reactors* (2005).
- [19] Chen, Y., *et al.*, “Corrosion Behavior of NF616 and D9 as Candidate Alloys for Supercritical Water Reactors”, *CORROSION 2005*, paper 5391.
- [20] Allen, T.R., *et al.*, “Corrosion of Ferritic-martensitic Alloys in Supercritical Water for GenIV Applications”, *GLOBAL 2005*, paper 419.
- [21] Cho, H.S., *et al.*, “Corrosion Properties of Oxide Dispersion Strengthened Steels in Supercritical Water Environment”, *Journal of Nuclear Materials*, 329-333, 387-391 (2004).
- [22] Cho, H.S., A. Kimura, “Corrosion Resistance of High Cr Oxide Dispersion Strengthened Ferritic Steel Exposed to Supercritical Water”, to be published in *Journal of Nuclear Materials*.
- [23] Chen, Y., *et al.*, “Microstructural Examination of Oxide Layers Formed on an Oxide Dispersion Strengthened Ferritic Steel Exposed to Supercritical Water”, *Journal of Nuclear Materials*, 359, 50-58 (2006).
- [24] Was, G.S., *et al.*, “Corrosion of Austenitic Alloys in Supercritical Water”, *CORROSION 2005*, paper 5397.
- [25] Kaneda, J., *et al.*, “Corrosion Film Properties of the Candidate Materials for the Fuel Cladding of the Supercritical Water Cooled Power Reactor”, *ICAPP’05*, paper 5594.
- [26] Allen, T.R., *et al.*, “Corrosion of Candidate Materials for Supercritical Water Cooled Reactors”, *12th International Conference on Environmental Degradation of Materials in Nuclear Power System Water Reactors* (2005).
- [27] Tan, L., *et al.*, “The Effect of Grain Boundary Engineering on the Oxidation Behavior of INCOLOY Alloy 800H in Supercritical Water”, *Journal of Nuclear Material*, 348, 263-271 (2006).
- [28] Tsuchiya, Y., *et al.*, “SCC Properties of Metals Under Supercritical Water Cooled Power Reactor Conditions”, *CORROSION 2004*, paper 4485.
- [29] Cho, H.S., *et al.*, “Evaluation of Susceptibility to Stress Corrosion Cracking of Oxide Dispersion Strengthening Steels in Hot Pressurized Water”, *ICAPP’05*, paper 5457.
- [30] Was, G.S., *et al.*, “Time, Temperature, and Dissolved Oxygen Dependence of Oxidation of Austenitic and Ferritic-martensitic Alloys in Supercritical Water”, *ICAPP’05*, paper 5690.

MICROSTRUCTURAL INFLUENCE ON THE CORROSION BEHAVIOUR OF STRUCTURAL MATERIALS FOR NUCLEAR POWER SYSTEMS

Lizhen Tan, Kumar Sridharan, Todd R. Allen
University of Wisconsin-Madison, USA

Abstract

INCOLOY alloy 800H is one of the candidate alloys for the Generation IV nuclear power systems. Grain boundary engineering (GBE) and shot-peening were employed to improve the material's corrosion resistance, specifically resistance to oxide exfoliation and minimising corrosion rate. The as-received, GBE-treated, and shot-peened samples were subjected to supercritical water (SCW) exposure tests to evaluate their corrosion behaviour. Scanning electron microscopy (SEM) incorporated with energy dispersive X-ray spectroscopy (EDS) and electron backscatter diffraction (EBSD), as well as optical microscopy and grazing-incidence X-ray diffraction were employed to analyse the microstructural evolution induced by GBE, shot-peening and SCW exposure tests. The GBE treatment greatly mitigated the oxide exfoliation that occurred on the as-received samples. The oxide exfoliation is attributed to the sharp strain change and the strong and anisotropic texture in the oxide scale on the as-received samples. The oxide scale formed on the shot-peened samples is thinner and more compact than that on the as-received samples, and is composed of a Cr-rich outer layer (FeCr_2O_4) and a highly Cr-enriched inner layer (Cr_2O_3). The shot-peening induced a nanocrystalline surface layer, which led to an enhanced Cr diffusivity, resulting in the Cr-rich oxide scale.

Introduction

A materials' resistance to corrosion is highly dependent upon the underlying microstructure. As part of an effort to develop materials for Generation IV nuclear power systems [1], the effect of grain boundary, grain size, strain and texture on corrosion behaviour in supercritical water (SCW) has been studied. SCW is a superfluid with temperature and pressure above the critical point of water at 374°C and 22.1 MPa. It has been used in modern power plants to improve thermal efficiency and reduce the release of deleterious gases such as carbon dioxide, nitrogen oxides and sulphur oxides. Due to the advantages, SCW has been selected as a candidate coolant for one of the Generation IV nuclear power systems [1].

As a fast diffusion path compared to bulk or lattice diffusion, grain boundaries play an important role in corrosion. The misorientation of grain boundaries can be described using the coincidence site lattice (CSL) model which introduced a parameter Σ to describe grain boundaries. The Σ is a value defined as the reciprocal density of coincident sites at grain boundaries. $\Sigma 1$ boundaries correspond to low-angle boundaries (LABs) with misorientation angle $<15^\circ$. Low- Σ CSL boundaries (CSLBs) with $3 \leq \Sigma \leq 29$ and random boundaries correspond to high-angle boundaries (HABs). The low- Σ CSLBs are considered to have special properties compared to random boundaries, such as low boundary energy, less susceptibility to impurity or solute segregation, smaller diffusivity, and greater resistance to grain boundary sliding and intergranular degradation. Among these low- Σ CSLBs, $\Sigma 3$ is a particularly important set of boundaries because they have very low energy and occur frequently via twinning in materials with low stacking fault energies. It has been found that intergranular oxidation takes place preferentially at random boundaries while low- Σ CSLBs, particularly $\Sigma 3$, $\Sigma 11$, $\Sigma 19$ and $\Sigma 27$ boundaries have excellent oxidation resistance [2]. Thus, materials with a high fraction of low- Σ CSLBs are expected to have superior corrosion resistance. With this as a motivation, grain boundary engineering (GBE) by means of thermomechanical processing was explored on INCOLOY alloy 800H to improve its corrosion resistance by tuning the grain boundary character distribution (GBCD) to obtain a high fraction of low- Σ CSLBs and disrupt the connectivity of random boundary network. Preliminary study indicates that the fraction of low- Σ CSLBs can be greatly enhanced with a greatly decreased fraction of random boundaries [3]. Supercritical water (SCW) exposure test results indicate that the oxide exfoliation of alloy 800H was greatly mitigated by the GBE treatment [4].

A second pathway for improving corrosion performance is grain refinement. Fine grained microstructure was reported to be preferable in case of steels with a high Cr content [5]. This is because the population of grain boundaries greatly increases with the decrease of grain size. As a result, a greater Cr enrichment in the inner oxide scale and subsequently a quicker formation of a protective layer of Cr-rich oxide can easily form due to enhanced Cr diffusion [6]. Shot-peening was employed for surface grain refinement, which is a cold-working process in which a metal part is bombarded by tiny balls of steel, cut-wire, glass or ceramic shot. It has been used in a wide variety of industries for decades. The effect of shot-peening on the corrosion behaviour of alloy 800H was studied by exposing the samples to SCW.

This paper presents the effect of GBE (grain boundary type) and shot-peening (grain size) on the corrosion behaviour of alloy 800H exposed to SCW. The effect of texture and strains formed in the oxide scale due to the SCW exposure on the oxidation behaviour of alloy 800H is also discussed.

Experiments

The material used in this study was commercial INCOLOY alloy 800H with a measured chemical composition listed in Table 1. The as-received alloy 800H was annealed at $\sim 177^\circ\text{C}$ for a time

Table 1. Chemical composition (wt.%) of INCOLOY alloy 800H

Alloy	Fe	Cr	Ni	Mn	Cu	Si	Ti	Al	C	P	S
800H	45.26	20.42	31.59	.76	.42	.13	.57	.50	.069	.014	.001

commensurate with section size followed by water quenching. Thermomechanical processing was performed on samples cut from the as-received alloy 800H by a low level of cold work followed by a high-temperature anneal and water quenching. Based on the previous experience [3], ~6% thickness reduction followed by annealing at 1 050°C for 90 minutes was employed for alloy 800H.

GBE-treated and shot-peened samples were subjected to SCW exposure tests. As-received samples were also tested at the same time for comparison. Rectangular samples (31.7 × 12.7 mm) with thickness of ~1 mm were cut from the as-received and the GBE-treated materials and polished down to 1 µm surface finish. A set of as-received samples with 1 µm surface finish was subjected to a shot-peening processing with stainless steel beads in a diameter of ~500 µm at ~0.28 MPa for 3 seconds. Thus, there are three types of samples in the as-received, GBE-treated and shot-peened conditions. Ultrasonic cleaning was performed on these samples prior to the SCW exposures. The SCW was maintained at 500 or 600°C and ~25 MPa with a test section inlet dissolved oxygen content of ~25 ppb and a flow rate of ~1 m/s.

A LEO 1530 field-emission scanning electron microscope (FESEM) was the major analytical tool employed in this study for microstructural characterisation. This FESEM is incorporated with energy dispersive X-ray spectroscopy (EDS) and electron backscatter diffraction (EBSD) capability. EBSD was employed for determining grain boundary misorientation using the TSL orientation imaging microscopy (OIM) system MSC2200. To obtain good quality EBSD data, the samples were metallographically polished with SiC abrasive paper down to 1 200 grit, followed by sequential polishing with 1 µm diamond paste, alpha alumina and colloidal silica solutions. The SEM was operated at 20 kV, and the automatic EBSD area scan was performed using a hexagonal grid with a variety of step sizes depending upon the microstructure of the examined materials.

In addition to the SEM/EDS/EBSD, other techniques such as optical microscopy for surface morphology and grazing-incidence X-ray diffraction (GIXRD) for surface layer grain size and strain analyses were employed in this study.

Results and discussions

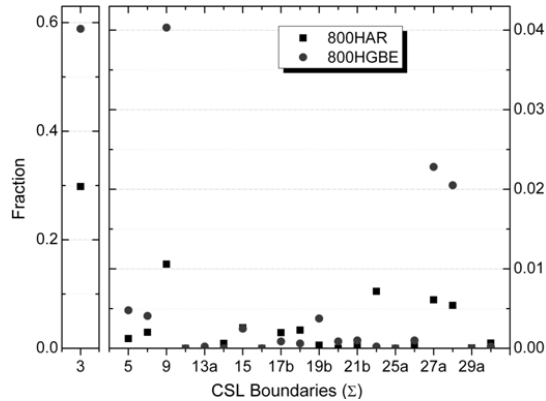
Grain boundary engineering (GBE)

The fraction of low- Σ CSLBs with Σ from 3 to 29 of the as-received and the GBE-treated samples is shown in Figure 1. The fraction of annealing twin boundaries $\Sigma 3$ and their twin variants $\Sigma 9$ and $\Sigma 27$ had been greatly increased by the GBE treatment. This phenomenon is consistent with the universal feature of grain boundary networks in face-centre-cubic (FCC) materials [7].

Thermal stability of the GBE-treated samples

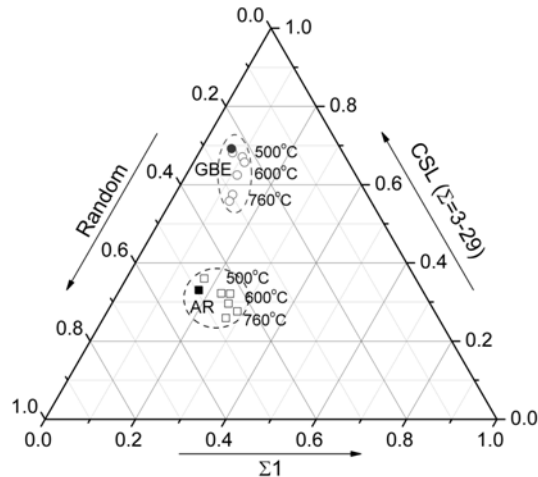
Since atomic migration is increased at elevated temperatures, GBE-promoted low- Σ CSLBs may become unstable and be transformed into random boundaries. Thus, it is necessary to evaluate the thermal stability of the GBE-optimised grain boundary character distribution (GBCD). The GBE-treated

Figure 1. The fraction of low- Σ CSLBs ($3 \leq \Sigma \leq 29$) of the as-received (AR) and the GBE-treated samples



samples were annealed at 500, 600, and 760°C for 4 and 6 weeks. As-received samples were also annealed at the same time as a reference. The GBCD of the as-received and the GBE-treated samples prior to and after the annealing is plotted in a triangle (an adapted ternary phase diagram) as shown in Figure 2 with the three axes denoting the fraction of the $\Sigma 1$, low- Σ CSL and random boundaries. The GBCD of the samples prior to the annealing indicates that the GBE treatment greatly increased the fraction of low- Σ CSLBs and decreased the fraction of random boundaries. The GBCD was slightly changed by the annealing for both of the as-received and the GBE-treated samples. The annealing at 760°C (~58% melting temperature of alloy 800H) did not significantly change the GBCD of the GBE-treated samples. Therefore, the GBE-treated samples are stable at their application temperatures up to 760°C. Although the test time was limited to 6 weeks, the degradation rate of the GBCD of the GBE-treated samples was slow.

Figure 2. Annealing effect on the GBCD ($\Sigma 1$, low- Σ CSL, and random boundaries) of the as-received (AR) and the GBE-treated samples annealed at 500, 600, and 760°C for 4 or 6 weeks

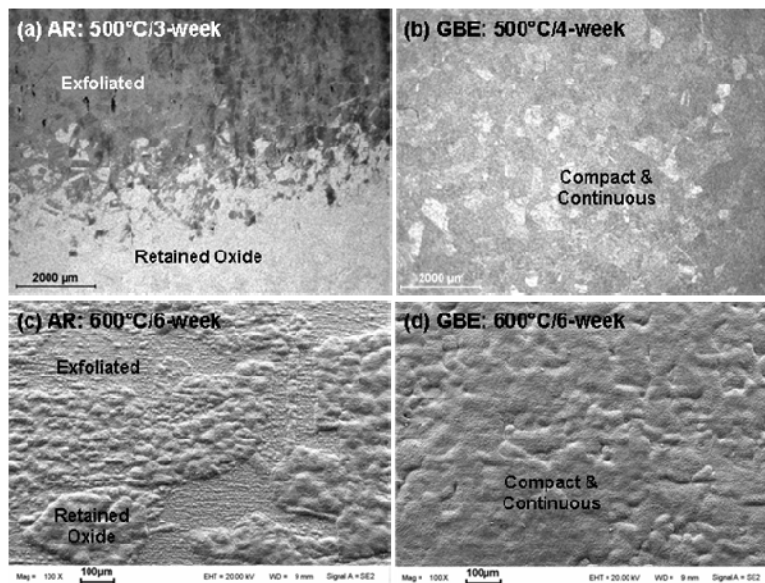


Supercritical water (SCW) exposure test

The as-received, GBE-treated and shot-peened samples were exposed to SCW to evaluate the GBE and shot-peening effects on the corrosion behaviour.

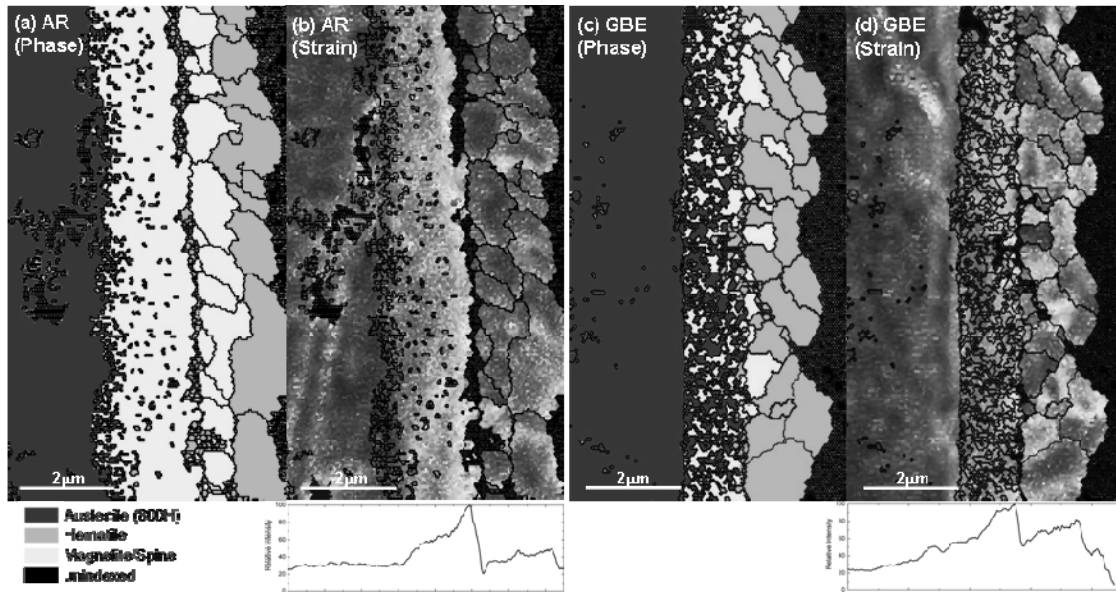
After the SCW exposure at 500 and 600°C for a variety of exposure times, surface morphology of the as-received and the GBE-treated samples was studied with optical microscopy and SEM, the results of which are shown in Figure 3. Extensive oxide exfoliation occurred on the as-received samples exposed to SCW at 500°C for three weeks [Figure 3(a)] and 600°C for six weeks [Figure 3(c)]. In contrast, the oxide scale is continuous and compact on the GBE-treated samples exposed to SCW at 500°C for four weeks [Figure 3(b)] and 600°C for six weeks [Figure 3(d)].

Figure 3. Surface morphology of the as-received (AR) and the GBE-treated samples exposed to SCW at 500°C for three or four weeks (a, b: optical images) and 600°C for six weeks (c, d: secondary electron images)



To analyse the reasons resulting in the distinct difference, cross-section samples were prepared for microstructural analysis by means of EBSD. Figure 4 shows the EBSD maps illustrating the distribution of phase and strain of the as-received and the GBE-treated samples exposed to SCW at 500°C for three weeks [Figures 4(a) and 4(b)] and four weeks [Figures 4(c) and 4(d)]. Austenitic phase (FCC structure), magnetite/spinel and hematite were identified by EBSD analysis as shown in Figure 4(a). Magnetite and spinel are not differentiable by EBSD due to their same crystal structure. But EDS analysis indicated that the inner layer is spinel and the outer layer is magnetite [8]. The strain distribution as shown in Figure 4(b) indicates that there is a strain accumulation close to the spinel-magnetite interface. Compared to the as-received sample, the spinel layer on the GBE-treated sample is mixed with FCC phase, and the outer layer has a lower fraction of magnetite and a higher fraction of hematite. The strain distribution as shown in Figure 4(d) is relatively uniform in the oxide scale on the GBE-treated sample compared to that on the as-received sample. By integrating the strain intensity along the direction parallel to the oxide surface, relative strain intensity as a function of the location across the oxide scale was obtained and is plotted below the Figure 4(b) and 4(d) for the as-received and the GBE-treated samples, respectively. The profiles indicate that there is a sharp strain change at the spinel-magnetite interface on the as-received sample compared to that on the GBE-treated sample. The sharp strain change contributed to the oxide exfoliation that occurred on the as-received samples.

Figure 4. EBSD maps of cross-section samples demonstrating the phase and strain distribution: (a, b) the as-received (AR) samples exposed to SCW at 500°C for three weeks and (c, d) the GBE-treated samples exposed to SCW at 500°C for four weeks

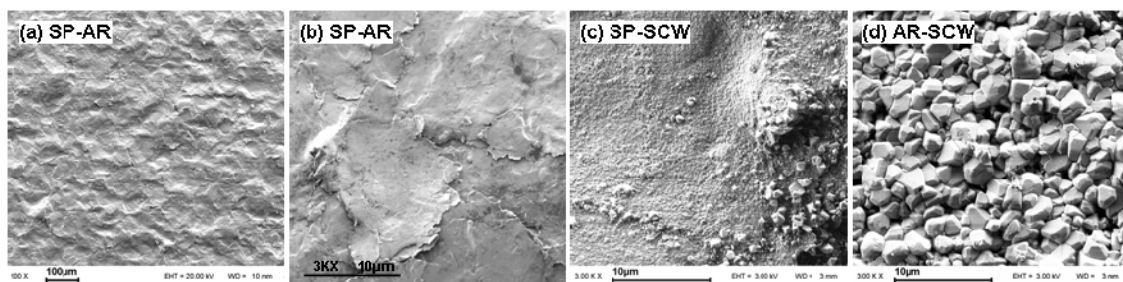


In addition to the sharp strain change, strong and anisotropic texture was observed in the oxide scale on the as-received sample [8]. In contrast, the texture in the oxide scale on the GBE-treated sample is weak and isotropic. The strong and anisotropic texture may promote the oxide exfoliation that occurred on the as-received samples due to the relationship among anisotropic texture, anisotropic grain boundary energy and growth stress [8].

Shot-peening effect on corrosion behaviour

The as-received and the shot-peened samples were subject to SCW exposure at 500°C for four weeks. The surface morphology of the as-shot-peened (SP-AR), the SCW-exposed shot-peened (SP-SCW), and the SCW-exposed as-received (AR-SCW) samples was analysed with SEM and is shown in Figure 5. The low-magnification secondary electron image (SEI) as shown in Figure 5(a) shows that the surface area was increased due to the dimples induced by the shot-peening. Overlapped dimples were often observed at high-magnification as shown in Figure 5(b). Compared to the SEI of the AR-SCW [Figure 5(d)], the SP-SCW [Figure 5(c)] is mainly covered by a compact oxide scale with a few dispersed oxide particles generally close to the edge of the overlapped dimples.

Figure 5. Surface morphology of the as-shot-peened (SP-AR) and the SCW-exposed (SP-SCW) samples



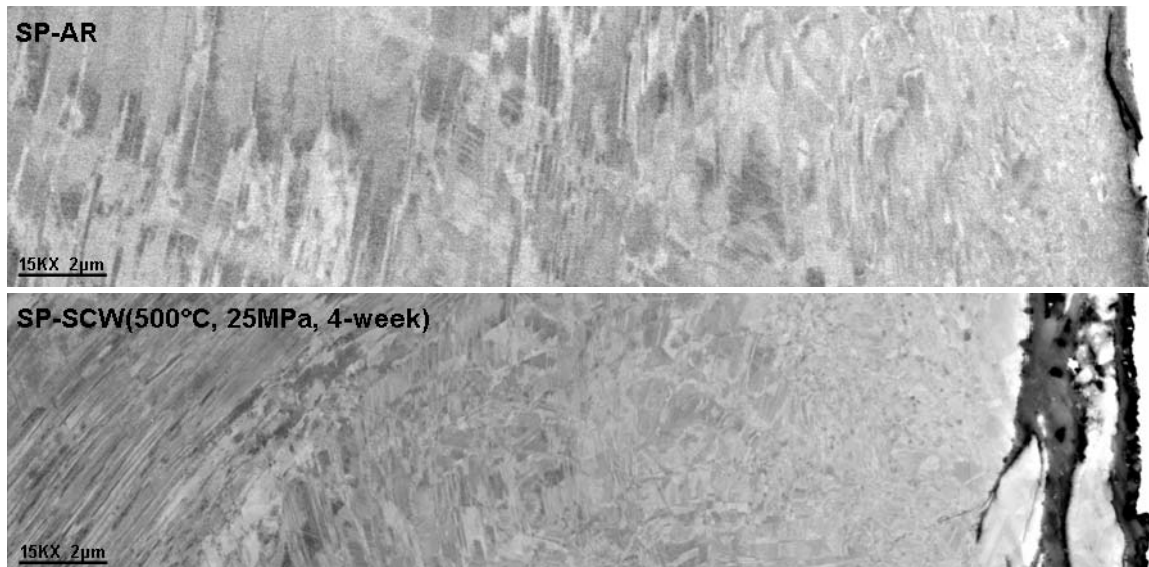
Grazing-incidence X-ray diffraction (GIXRD) with an incidence angle of 0.5° and conventional XRD (θ - 2θ) were performed on the as-received, SP-AR and SP-SCW samples. The effective analytical depth was calculated to be ~ 31 and $\sim 4\ 600$ nm for the GIXRD and the conventional XRD analyses, respectively. The shot-peening resulted in diffraction peak broadening. The effect of particle size and microstrain on the peak broadening was analysed by the Williamson-Hall method [9]. Integral breadth of the diffraction peaks was used for the calculation. The results, listed in Table 2, indicate that the shot-peening introduced a nanocrystalline surface with a thickness of a couple of microns. The grain size decreases but the strain increases when moving closer to the surface. The SCW exposure at 500°C resulted in some grain growth and strain alleviation.

Table 2. Average grain size and strain within the effective analytical depth of the as-shot-peened (SP-AR) and the SCW-exposed (SP-SCW) samples determined by grazing-incidence X-ray diffraction (GIXRD) and conventional XRD

XRD	Analysis depth (nm)	SP-AR		SP-SCW	
		Grain size (nm)	Strain (%)	Grain size (nm)	Strain (%)
GIXRD (0.5°)	~ 31	15	0.39	55	0.23
θ - 2θ	$\sim 4\ 600$	21	0.31	1 231	0.003

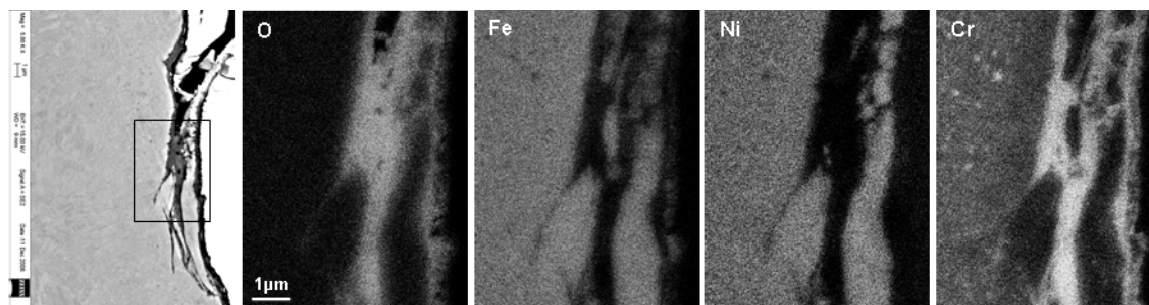
The cross-section SEIs of the SP-AR and the SP-SCW samples are shown in Figure 6. The effective depth of the shot-peening is more than $30\ \mu\text{m}$ from surface, and the thickness of the shot-peening resulted nanocrystalline surface is about $8\ \mu\text{m}$. Some cracks were observed close to the surface, which may correspond to the overlapped dimples as shown in Figure 5(b). The thickness of the oxide scale, resulting from the SCW exposure, on the shot-peened sample is $\sim 1\ \mu\text{m}$, which is much thinner than that on the as-received sample as shown in Figure 4 where the oxide thickness is roughly $4\ \mu\text{m}$. The cross-section SEI of the SP-SCW shown in Figure 6 was captured at the region close to a crack as shown in Figure 7, which indicates that oxidation occurred along the crack.

Figure 6. Cross-section SEIs of the SP-AR and SP-SCW samples



EDS elemental mapping of the oxide scale was performed at the region marked with a rectangle on the SEI of the SP-SCW sample as shown in Figure 7. The oxide scale is highly enriched with chromium. Associating the GIXRD results with the EDS maps, the oxide scale is determined to be composed of the outer thin layer (close to the oxide-SCW interface) of Cr-rich spinel, e.g. FeCr_2O_4 , and the inner layer of a highly Cr-enriched oxide, e.g. Cr_2O_3 . The formation of the Cr-rich oxides is attributed to the fine grain microstructure resulted from the shot-peening, which greatly increased the population of grain boundaries leading to an enhanced Cr diffusivity.

Figure 7. EDS maps of O, Fe, Ni, and Cr at the region marked with a rectangle in the secondary electron image



Conclusions

Grain boundary engineering (GBE) and shot-peening were employed on INCOLOY alloy 800H to improve its corrosion resistance. The as-received, GBE-treated and shot-peened samples were subject to supercritical water (SCW) exposure tests to evaluate the effect of GBE and shot-peening on the corrosion behaviour. The GBE treatment greatly mitigated the oxide exfoliation that occurred on the as-received samples. The sharp strain change and the strong and anisotropic texture in the oxide scale on the as-received samples resulted in the oxide exfoliation. The shot-peening processing produced a nanocrystalline surface layer with a thickness of $\sim 8 \mu\text{m}$. The effectively modified depth is over $30 \mu\text{m}$ deep. The oxide scale formed on the shot-peened samples is thinner and more compact than that on the as-received samples. The oxide scale is composed of a Cr-rich outer layer (FeCr_2O_4) and a highly Cr-enriched inner layer (Cr_2O_3), which was a result of the fine grain microstructure leading to an enhanced Cr diffusivity.

Acknowledgements

This work is supported by the DOE Generation IV initiative programme, NACE and the Office of Naval Research (ONR). The authors would like to thank Xiaowei Ren, Alan Kruienga and Yun Chen for their assistance in shot-peening and supercritical water exposure test.

REFERENCES

- [1] *A Technology Roadmap for Generation IV Nuclear Energy Systems*, US DOE Nuclear Energy Research Advisory Committee and the Generation IV International Forum, December 2002 (<http://gif.inel.gov/roadmap/>).
- [2] Yamaura, S., Y. Igarashi, S. Tsurekawa, T. Watanabe, “Grain Boundary Engineering for the Control of Oxidation Embrittlement”, *Properties of Complex Inorganic Solids 2, (Proceedings of the International Alloy Conference)*, A. Meike (Ed.), Davos, Switzerland, 8-13 August 1999, Kluwer Academic/Plenum Publishers, New York, NY, pp. 27-37 (2000).
- [3] Tan, L., T.R. Allen, “An Electron Backscattered Diffraction Study of Grain Boundary-engineered Incoloy Alloy 800H”, *Metall. Mater. Trans.*, A 36, 1921 (2005).
- [4] Tan, L., K. Sridharan, T.R. Allen, “The Effect of Grain Boundary Engineering on the Oxidation Behavior of Incoloy Alloy 800H in Supercritical Water”, *J. Nucl. Mater.* 348, 263 (2006).
- [5] Singh Raman, R.K., J.B. Gnanamoorthy, S.K. Roy, “Influence of Alloy Grain Size on the High Temperature Oxidation Behavior of Some Steels with Different Cr Contents”, *Trans. Indian Inst. Met.*, 45, 391-398 (1992).
- [6] Peng, X., J. Yan, Y. Zhou, F. Wang, “Effect of Grain Refinement on the Resistance of 304 Stainless Steel to Breakaway Oxidation in Wet Air”, *Acta Mater.*, 53, 5079-5088 (2005).
- [7] Schuh, C.A., M. Kumar, W.E. King, “Universal Features of Grain Boundary Networks in FCC Materials”, *J. Mater. Sci.*, 40, 847-852 (2005).
- [8] Tan, L., K. Sridharan, T.R. Allen, “The Effect of Grain Boundary Engineering on the Oxidation Behavior of Incoloy Alloy 800H in Supercritical Water”, *J. Nucl. Mater.*, 348, 263 (2006).
- [9] Williamson, G.K., W.H. Hall, “X-ray Line Broadening from Filed Aluminum and Tungsten”, *Acta Metal.*, 1, 22-31 (1953).

INFLUENCE OF STACKING FAULT ENERGY (SFE) ON THE DEFORMATION MODE OF STAINLESS STEELS

X. Li, W. Van Renterghem, A. Al Mazouzi

SCK•CEN, Reactor Materials Research Department, LHMA, Boeretang 200, B-2400 Mol, Belgium

Abstract

The sensibility to irradiation-assisted stress corrosion cracking (IASCC) of stainless steels in light water reactor (LWR) can be caused by the localisation of deformation that takes place in these materials. Dislocation channelling and twinning modes of deformation can induce localised plasticity leading to failure. Stacking fault energy (SFE) plays an important role in every process of plastic deformation behaviour, especially in twinning and dislocation channelling. In order to correlate localised deformation with stacking fault energy, this parameter has been experimentally determined by transmission electron microscope (TEM) using both dislocation node and multiple ribbons methods after compression in three different model alloys. Detailed deformation behaviour of three fabricated alloys with different stacking fault energy before and after tensile tests at temperatures from -150°C to 300°C, will be shown and discussed based on mechanical test and TEM observation.

Introduction

Irradiation-assisted stress corrosion cracking (IASCC) is a complex phenomenon, where irradiation modifies the response of a material to both mechanical loading and environmental interaction [1]. Current knowledge highlights radiation-induced segregation (RIS) [2] and radiation hardening [3] as the two main effects produced by neutron irradiation. The effect of radiation damage on hardening and plastic deformation of the material is considered as a dominating effect in IASCC in hydrogenated environment.

The stacking fault energy is forwarded as a key parameter of materials to affect the susceptibility to IASCC because it plays an important role in every process of plastic deformation behaviour and hardening [4]. SFE was linked to SCC resistance in stainless steels by Thompson and Bernstein, who found that increasing SFE correlates well with increasing reduction in area and decreasing SCC susceptibility [5]. Rhodes's and Thompson's [6], Schramm's and Reed's [7] plotted the IASCC susceptibility of several irradiated stainless steels as function of SFE showing that there is a good correlation between SFE and IASCC. But these correlations differ in the elements included in the alloys; they are also unable to account for several of the minor elements and therefore may deviate substantially from the true SFE, so it is necessary to determine the SFE accurately and build the correlation between SFE and IASCC. The effect of radiation hardening on IASCC can be simulated by mechanical deformation, although some differences exist in the types of defects produced by radiation and mechanical deformation. Since SFE influences the plastic flow behaviour of the material, the study of the impact of SFE variations on the deformation and SCC behaviour of irradiated and un-irradiated austenitic steels will contribute to the understanding of IASCC mechanism [8].

The aim of this work, as a task within the FP6-European Project PERFECT, is to investigate the influence of the SFE on IASCC susceptibility of stainless steels. In order to achieve this goal, three alloys were fabricated with different SFEs by controlling their chemical compositions. A systematic study is performed on these alloys to identify the correlation between the SFE, mechanical properties, microstructural defects and deformation behaviour before irradiation by using transmission electron microscope (TEM), tensile tests, scan electron microscope (SEM) and metallographical characterisation methods. Temperature has a strong effect on the SFE, which increases linearly with decreasing temperature by an amount of 0.08~0.11 mJ/m² per Kelvin [9]. To investigate this effect on mechanical properties and deformation mechanisms, the tensile tests have been done for three alloys in the temperature range from -150°C to 300°C. After tensile deformation, the strain mechanism was identified by microstructure analysis.

Experimental

Using high-purity starting elements, three alloys have been fabricated under highly controlled conditions. Then hot and cold rolled to reach the desired plate thickness and subsequently solution annealed to obtain a homogeneous microstructure. The resulted plates were analysed chemically and metallographically to check their homogeneity. The compositions are listed in Table 1.

Materials were characterised in the as-received state by optical microscopy and TEM. The specimens which were used for metallographic analysis, were mechanically polished and etched using nitric acid etching reagent for about 40-60 s at room temperature.

To determine the SFEs, the alloys were cold worked to ~3% to create partial dislocations and dislocation nodes, and then were annealed at 450°C for two hours to reduce the total amount of them. TEM specimens were prepared after compression test to 10%.

Standard tensile specimens [ASTM D638], round specimen with nominal gauge length of 12.4 mm, total length of 24.0 mm and diameter of 2.4 mm were used for the present experiments. Tensile tests were performed at a constant nominal strain rate of $3 \times 10^{-4} \text{ s}^{-1}$. The test temperature ranged from -150°C to 300°C , controlled by an automatically cooling/heating chamber system using electrical heating and nitrogen cooling. After tensile failure, the total elongation and reduction in area were measured optically. The load-displacement data were recorded, analysed and reported automatically.

After tensile tests, discs were cut from the deformed or fractured specimens along 45° with respect to the tensile axis and were polished to a thickness of about 0.1 mm or less. The thin discs were then thinned to perforation by a double jet electrochemical polisher. The deformation microstructures were observed by JEOL 3010 STEM operating at 300 kV.

Table 1. The name, composition and SFE of the selected alloy

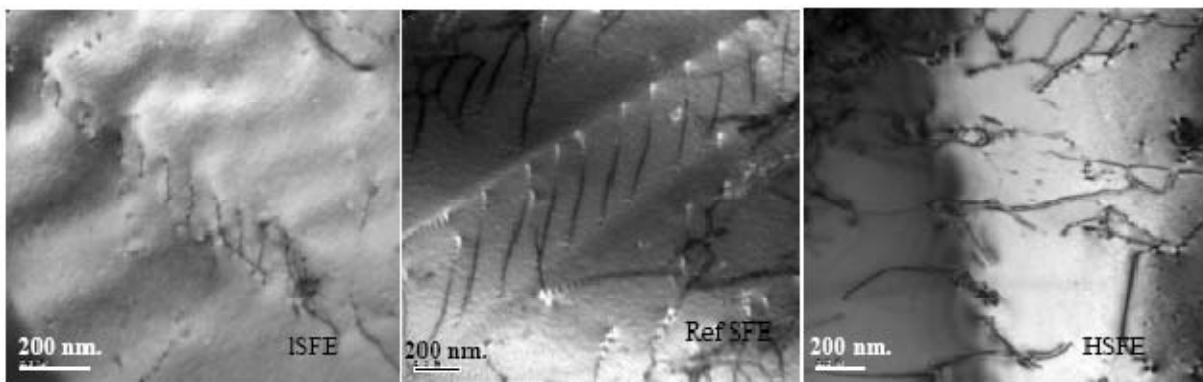
Alloy	C	N	Mn	Ni	Cr	Si	S	P
RefSFE	0.04	0.015	1.56	8.5	18.4	0.33	0.02	0.033
LSFE	0.01	0.08	1.56	8.5	18.4	1.0	0.02	0.033
HSFE	0.07	0.319	1.59	16.23	18.63	0.1	0.043	0.035

Results and discussion

Microstructure as the received state

The alloys in the as-received state were observed by TEM. In crystals with an fcc crystal structure, a $\{111\}$ type stacking fault is formed when a gliding dislocation $a/2\langle 110 \rangle$ dissociates into two partial dislocations $a/6\langle 112 \rangle$, separated by a stacking fault. This separation increases with decreasing SFE [11], which makes cross-slip difficult. Therefore, if the SFE is low, the gliding dislocations are confined to a thin slip band and show a banded, linear arrays dislocation microstructure. Cross-slip becomes easier for the high SFE alloys, where the mobile dislocations are tangled and arranged in cells, shown in Figure 1.

Figure 1. Microstructures of the three alloys in the as-received state



The SFE determination

Two methods, dislocation nodes (DN) and partial dislocations (PD) were applied to determine the SFEs of three alloys [10]. The PD method is the measurement of the separation of the partial dislocations when the equilibrium of the attractive and repulsive forces on the partial dislocation is established. The SFE γ can be determined by the equilibrium separation d of partial dislocations from the relation:

$$d = \frac{\mu b^2}{4\pi\gamma}$$

where μ is the shear modulus and b is the Burgers vector. An example is shown in Figure 2(a) for the LSFE alloy.

The ND method is the measurement of inner radius of the curvature when three sets of partial dislocations intersect and an equilibrium configuration of the node formed when the attractive and repulsive forces on each partial dislocation are equalled. The SFE γ can be determined by following equation:

$$\frac{\gamma\gamma}{\mu b_p^2} = 0.055 \left(\frac{2-v}{1-v} \right) - 0.06 \left(\frac{v}{(1-v)^2} \right) \cos 2\alpha + \left\{ 0.018 \left(\frac{2-v}{1-v} \right) + 0.036 \left(\frac{v}{1-v} \right) \cos 2\alpha \right\} \log_{10} \frac{R}{\varepsilon}$$

where ε is a cut-off parameter, related to the dislocation core radius, α is the angle between b_p and the line tangent to the partial dislocation at the centre of curvature, v is the Poisson ratio. An example is shown in Figure 2(b) for the Ref SFE alloy. The results were given in Table 2.

Figure 2. SFE determination by TEM

a) PD method to measure d , b) ND method to measure $2R$

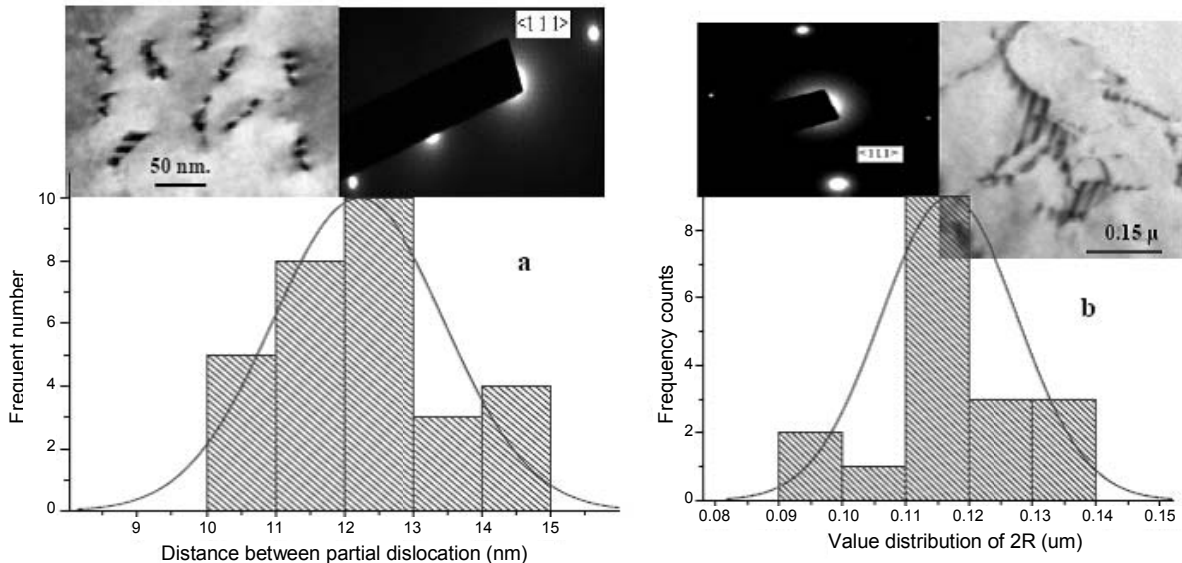


Table 2. The determined SFEs of the three model alloys

Alloy	LSFE	Ref SFE	HSFE
SFE (mJ/m ²)	11	31	46

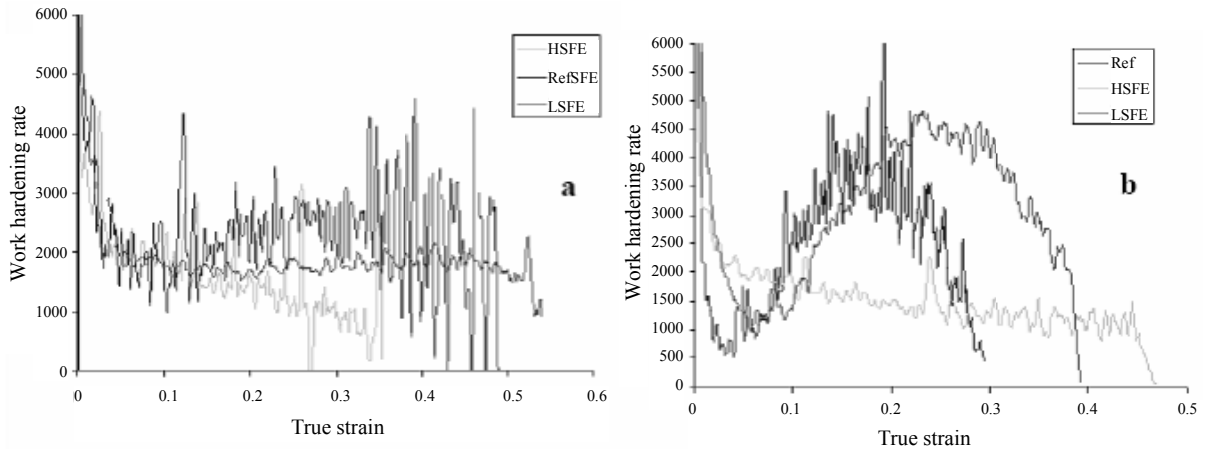
The engineering strain-stress curves of the three alloys show that for all three alloys the strength and ductility are strongly temperature dependent. To highlight this behaviour, the work hardening rate $\frac{d\sigma}{d\varepsilon}$ is plotted as function of the true strain $\varepsilon_{\text{true}}$ in Figure 3 at room temperature and -100°C.

Remarkable feature is change in curve shape with test temperature, which means the deformation mechanisms were changed with temperature. Below RT, LSFE and Ref SFE alloys show two-stage hardening behaviour, similar to other austenitic steels [11]. The HSFE alloy does not show this behaviour in the test temperature range considered.

Comparing the working hardening rates ($\frac{d\sigma}{d\varepsilon}$) vs. true strain curves of the three alloys at two selected temperatures, RT and -100°C, Figure 3 shows that at room temperature, the work hardening rates of all three alloys decrease monotonically with strain in the uniform deformation region, that is means in this temperature, the predominant deformation mechanism of both alloys does not change after plastic deformation with true strain. At -100°C, the work hardening rate curves of the LSFE and Ref SFE alloys display two-stage hardening behaviour, but the HSFE alloy does not, which means that at -100°C, the predominant deformation mechanisms of the LSFE alloy have changed, but of the HSFE alloy still has not.

Figure 3. Comparison of the work hardening rates of the three alloys

a) Room temperature, b) -100 °C



Deformation mechanisms

Significant variations in hardening behaviour must result from the deformation mechanism changes. TEM observation of tensile deformed alloys at each temperature gives a reasonable and logical explanation to the observed trends in mechanical behaviour.

At RT, the predominant deformation mechanisms of the LSFE and Ref SFE alloys are partial dislocations glide, trailing stacking faults. Some twinning is also observed. The HSFE alloy shows perfect dislocation glide (see Figure 5) and a cell structure is formed in this conditions, this is due to the narrow separation of dislocation into partials. For the LSFE and Ref SFE alloys, because twinning happens, twinning induced plasticity (TWIP) prevents necking to happen, which leads to a pronounced improvement of ductility and a little strength.

At -100°C , the strain-induced martensitic transformations happen in the lower SFE alloy. Twining, martensitic transformation are the predominant deformation mechanisms of LSFE and Ref SFE alloys, twinning is the main plasticity mechanism of HSFE alloy. If SFE increases linearly with the temperature decreases by an amount of $0.08\sim 0.11\text{ mJ/m}^2$ per Kelvin [9], the SFE of HSFE will decrease from 46 mJ/m^2 at RT to 38 mJ/m^2 at -50°C , so twinning is favoured at lower temperature. TEM observations of the low temperature deformation microstructure are shown in Figure 6. This result is similar to the mechanism observed in high strength austenitic FeMnCr steel [12]. For the LSFE and Ref alloys, from -150°C to -50°C , due to the strain-induced martensitic transformations. Work-hardening is strongly enhanced and ductility is reduced. In the HSFE alloy, twinning is the dominating strain mechanism. Twinning-induced plasticity (TWIP) leads to a pronounced improvement of ductility. In addition, a background of dense dislocations in Figure 6 suggests that the deformation starts with dislocation glide and then, twinning and martensitic transformation take over as stress rises due to strain hardening.

Figure 5. Deformation microstructures of the three alloys after deformation to 10% at RT, zone axis

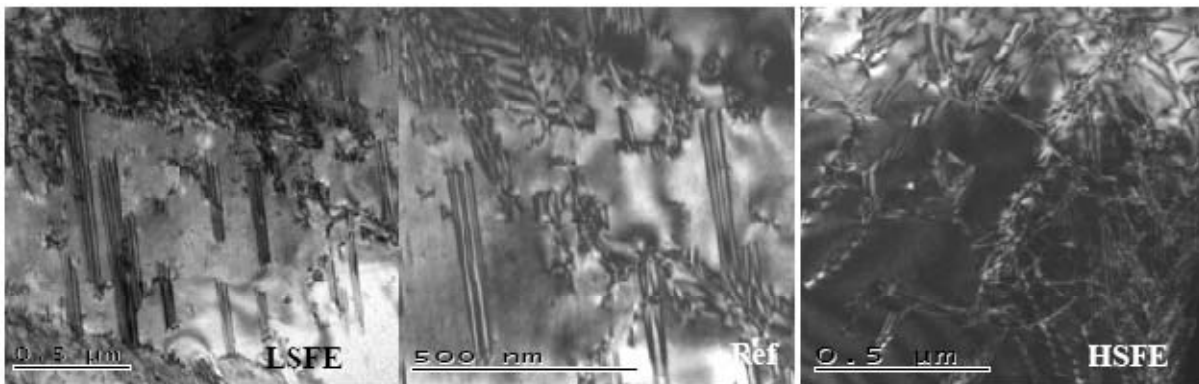


Figure 6. Deformation microstructures of the three alloys after deformation to 40% at -100°C , zone axis ([011])



Summary and conclusions

- 1) SFE and temperature strongly affect the deformation microstructure and mechanical properties of stainless steels. The LSFE alloy has a banded, linear array dislocation microstructure, while dislocations are tangled and arranged in cells of the HSFE alloy in the as received state.
- 2) At and above RT, all alloys strain hardening in a continuous way until fracture. At -50°C or below, however, transformation-induced two-stage hardening behaviour occurs in the LSFE and the Ref SFE alloys, while twinning is the predominant deformation mechanism of the HSFE alloy at low temperature.
- 3) From RT to -150°C, the plastic deformation mechanisms of the LSFE and the Ref SFE alloys are dislocation glide, stacking fault, twinning induced plasticity and martensite transformation induced plasticity, while the main deformation mechanisms of the HSFE are dislocation glide and twinning.

Acknowledgements

This work is partly supported by the FP6 European Project PERFECT with contract number F160-CT-2003-5088-40. The authors express special thanks to Drs. T. S. Byun, J. Bushy (ORNL) for their useful discussions and Sir L. Bracke (Ghent University, Belgium) for his help on TEM. The authors also would like to acknowledge the Reactor Materials Research Department of SCK•CEN, Belgium, microstructure analysis and mechanical test groups for their contribution.

REFERENCES

- [1] Kenik, E.A., R.H. Jones, G.E.C. Bell, IASCC, *J. Nucl. Mater.*, 212-215, 52-59 (1994).
- [2] Busby, J.T., G.S. Was, E.A. Kenik, *J. Nucl. Mater.*, in press.
- [3] Brummer, S.M., E.P. Simonen, P.M. Scott, P.L. Andresen, G.S. Was, J.L. Nelson, *J. Nucl. Mater.*, 274, 299 (1999).
- [4] Fukuya, K., S. Shima, A. Jacobs, G. Wozadlo, S. Suzuki, *6th Int. Conf. on Environ. Degrad. of Materials in NPS-Water Reactor*, TMS, 565 (1993).
- [5] Thompson, A.W., L.M. Bernstein, in *Advances in Corrosion Science and Technology*, Vol. 7, p. 53 (1980).
- [6] Rhodes, C.G., A.W. Thompson, *Met. Trans. A.*, 8A, 1901 (1977).
- [7] Schramm, R.E., R.P. Reed, *Met. Trans. A.*, 6A, 1345 (1975).

- [8] Was, G.S., "Recent Developments in Understanding IASCC", *11th Int. Conf. on Environ. Degrad. of Materials in NPS-Water Reactor*, TMS (2003).
- [9] Lantaniason, R.M., A.W. Ruff, *Metall. Trans.*, 2, 505 (1971).
- [10] Li, X., W. Van Renterghem, A. Al Mazouzi, *et al.*, *Stacking Fault Energy Determination – Theory and Procedure*, SCK•CEN R-4331, Feb. 2007.
- [11] Byun, T.S., N. Hashimoto, K. Farrell, *Acta. Mater.*, 52, 3889-3899 (2004).
- [12] Remmy, L., A. Pineau, *Mat. Sci. Eng.*, 28, 99 (1977).

EVOLUTION OF STRUCTURAL MATERIALS IN NUCLEAR REACTORS

Farhad Tavassoli

Commissariat à l'Énergie Atomique
CEA/Saclay, F-91191 Gif-sur-Yvette, Cedex France

Abstract

Structural materials used in conventional industry, their adoption and successive evolutions in the nuclear industry, from one generation of nuclear reactor to another, is presented. Specific examples for several steels are given, covering fabrication procedures, qualification methods, property databases and design allowable stresses, to show how the ever-increasing demands for better performance and reliability, in particular under neutron irradiation, have been met.

Particular attention is paid to the austenitic stainless steels types 304L, 316L, 316L(N), 316L(N)-IG, titanium stabilised grade 321, precipitation strengthened Alloy 800, conventional and low activation ferritic/martensitic steels and their ODS derivatives. For each material, evolution of the associated filler metal and welding techniques is also presented.

Introduction

The full family of structural materials is too large to be covered here. Even those used in the nuclear industry are numerous and diversified and can not be grouped in a single paper. This paper will focus on the steels used or envisaged for application in the structural components of pressurised water reactors (PWR), fast breeder reactors (FBR), International Thermonuclear Experimental Reactor (ITER), Fusion DEMONstration reactor (DEMO) and the forthcoming Gen IV fission reactors. Advanced structural materials developed for future fusion power reactors, such as Si_iC/SiC ceramic composites, vanadium alloys and tungsten alloys, are still at their very early stages of development and are not discussed here.

Austenitic stainless steels

Three steels are retained in this category: 304, 316 and 321.

Austenitic stainless steel type 304

This steel is the most familiar austenitic steel from the 300 series [1]. Its low carbon grade, 304L, has been used extensively in the internal structures of LWRs. It has also been used in the lower core structures of FBRs, and is retained for diverse parts of ITER components. In all these applications, the operating temperature is low: about 300°C in PWRs and ITER, and about 400°C in FBRs. In some out-of-core components, however, such as the sodium reservoir of Phénix, the service temperatures have been as high as 550°C.

The composition of 304L steel and its filler metal (308L) has remained relatively unchanged since the early days. Higher chromium content filler metal (type 309) is usually used in heterogeneous welds with low alloy steels for buttering, in order to avoid excessive dilution in chromium at the interface. Table 1 shows chemical compositions specified for 304L base metal and 308L filler metal in the French three-loop 900 MWe PWR [2].

Table 1. Chemical composition (wt.%) of type 304L steel and 308L filler metal used in the three-loop 900 MWe French PWR

	C	Mn	Si	S	P	Ni	Cr	Cu	Co	N	Ferrite (%)*
304L	≤0.040	≤2.0	≤1	≤0.03	≤0.04	9-10	19-20.0	≤1	≤0.11	≤0.08	
308L	≤0.030	≤2.5	≤1.0	≤0.030	≤0.030	9-12	18-20	–	≤0.20		5-15

* According to the De Long diagram.

The French 304L specification imposes an upper limit on the nitrogen content but not a minimum. Although, the actual analyses performed on several 304L heats used in Phénix and Superphénix give a nitrogen level close to the lower limit of the grade 304L(N), i.e. 0.06%.

For many years, the excellent ductility of austenitic stainless steels, in general, and 304 steel in particular (total elongation ≥40%), was considered more than adequate to be seriously affected by irradiation or thermal ageing. In fact, even today the design of these steels is based on the properties determined in the as-received conditions.

More recently, however, a greater attention has been paid to degradation of properties in service. Table 2 shows the operating conditions for the three-loop 900 MWe type reactors [2]. The calculated maximum fluence received by reactor internals are based on 32 effective full power years of operation at 2 785 MWt. The number of displacements per atom (dpa) is estimated using an average cross-section of 600 barns (for $E > 0.1$ MeV) for the baffle, which gives $1 \text{ dpa} = 6. \cdot 10^{-22} \times \text{fluence in n/cm}^2$ ($E > 0.1$ MeV). Under these conditions, significant reductions in toughness [3] and an increase in susceptibility to intergranular stress corrosion cracking [4] is expected.

Table 2. Maximum fluence on the internals of 900 MWe type French reactors

Structure	Materials		Temp. °C	Fluence			Dose (max.) dpa	Type of loading
	Type	State		Total	Fast	Fast		
			10^{21} n/cm^2	$E > 0.1 \text{ MeV}$	$E > 1 \text{ MeV}$			
Core barrel	AISI 304L	S.A.	286 ≈ 320	–	17	8	(10)*	Static
Core baffle	AISI 304L	S.A.	290 ≈ 370	≈ 296	137	60	82	Static
Formers	AISI 304L	S.A.	290 ≈ 370	–	80	35	(48)*	Static
Bolts	AISI 316	C.W.	300 ≈ 370	–	81	32	49	Static and cyclic

* Estimated with the mean cross-section of displacement of the baffle.

However, simple thermal ageing at 350°C has practically no effect, and only a small effect at 550°C, on the toughness of 304L steel [5]. Type 308L weld metal, in contrast, exhibits a greater sensitivity to thermal ageing due to its higher ferrite content. Examinations of 304L parts removed from the Phénix reactor have provided valuable information on the effects of long-term ageing under stress. These results show that degradation of properties after 20 years at 350°C is still limited, while at 550°C the changes are important but conform to initial predictions. The creep rupture tests performed on 304L parts aged in service show a reduction in life, confirming that part of the creep life has been spent in service [5].

Service failures observed, in the majority of cases, are due to bad manufacturing, under estimation of thermal fatigue or creep stresses, or faulted conditions.

Austenitic stainless steel type 316

The addition of molybdenum to the basic austenitic stainless steel composition not only improves the high-temperature properties,¹ but also increases resistance to corrosion and reduces the risk of segregation at the grain boundaries [6]. As a result, type 316L has been used in the primary circuit piping of PWRs and almost all major components of FBRs. Experience gained from its service in three generations of the French FBRs (Rapsodie, Phénix and Superphénix) has made this steel the *de facto* reference structural material for these reactors [7]. For the same reason, it has been selected for ITER vessel and in-vessel shielding components.²

¹ Thermal creep is ignored for 316 steel at below 475°C, as compared with 425°C for 304 steel.

² Cold worked grades of 316 steel have been used for bolting in PWRs.

Table 3 shows evolution of 316 steel compositions through successive generations of the French FBRs. The composition specified for ITER (316L(N)-IG) is based on the EFR specification for 316L(N), with added limitations on long-life radioactive elements [7].

Table 3. Evolution of type 316 SS from one generation to another of French FBRs. The steel is usually solution heat treated at 1 050-1 150°C for 30-60 minutes and quenched.

Element	ASTM 316L	316L Phénix	316L-CN	316L-SPH (SPX)	316L(N) (EFR)	316L(N)-IG (ITER)
C	0.03	0.030	0.045	0.030	0.030	0.03
Mn	2.0	1.40-2.0	2.00	1.6-2.0	1.60-2.00	1.60-2.00
Si	0.75	0.75	1.00	0.05	0.50	0.50
P	0.045	0.030	0.035	0.035	0.035	0.025
S	0.03	0.025	0.030	0.025	0.025	0.01
Cr	16.0-18.0	16.0-18.0	16.0-18.0	17.0-18.2	17.0-18.0	17.0-18.0
Ni	10.0-14.0	12.0-14.0	11.5-12.50	12.0-12.5	12.0-12.5	12.00-12.50
Mo	2.0-3.0	2.0-2.50	2.70	2.30-2.8	2.30-2.70	2.30-2.70
Cu		-	1.00		1.00	0.30
B		-	0.0020	-	0.0020	0.002 (0.001)**
Co			0.25		0.025	0.05
N	0.1		0.080	0.060-0.080	0.060-0.080	0.060-0.080
Nb+Ta+Ti					0.15*	0.15*

Note: ITER grade material is specified in five nuances (IG1-IG5). Unspecified element contents in all of them is considered “as low as possible” and not exceeding trace element levels.

* Ta <0.01% and Nb <0.1% for all nuances except IG2 and IG5 (low cobalt, niobium and boron).

** For materials that may require re-welding during service.

Much of the above achievements have become possible through improved steel-making practices. The steel used in the first generation of French FBRs was a low carbon grade, 316L. In order to improve its mechanical strength, in a subsequent nuance, the carbon content was slightly increased and nitrogen was added (316L-CN).³ This alloy had good mechanical resistance but not adequate resistance to grain boundary sensitisation. For Superphénix, a low carbon grade with a lower limit on nitrogen content (0.06 to 0.08%) was specified, 316L-SPH. Later, the overall composition was further narrowed to limit scatter in material properties, 316L(N) for EFR. Boron concentration was also restricted to less than 20 ppm, not only to avoid hot cracking during welding, but also to limit formation of helium from transmutation of ¹⁰B in irradiated materials [7].

Different filler metals are used for welding type 316 steel, the main ones used in France are: 316L for low temperature and 16-8-2 and 19-12-2 for high-temperature service [8]. The work on 19-12-2 has allowed definition of unique filler metal for welding in all positions, Table 4.

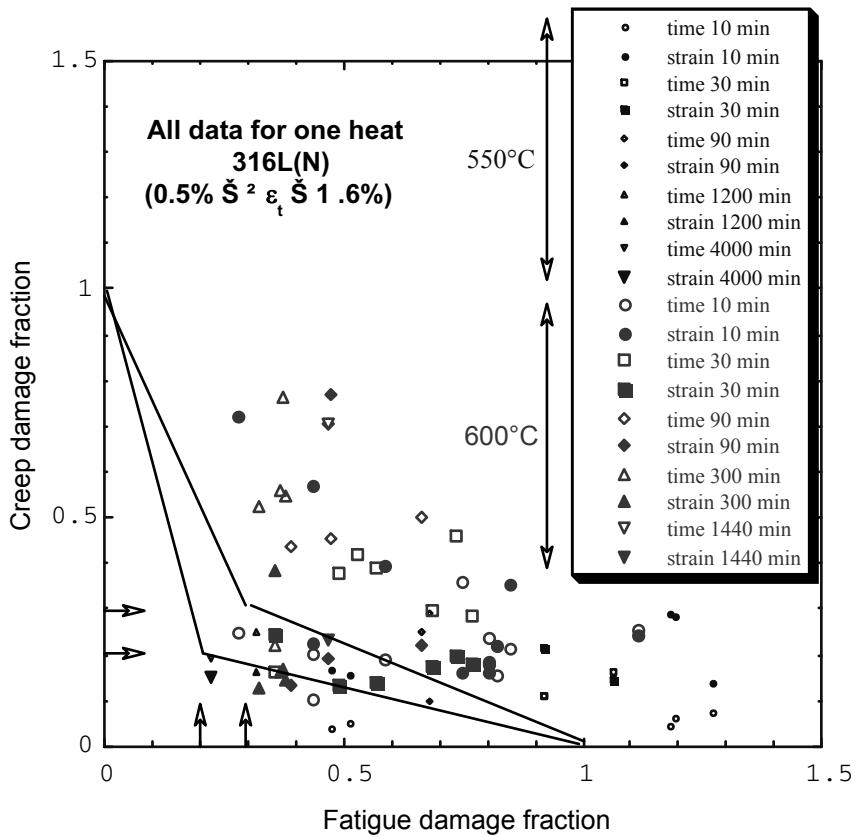
Throughout EFR development, international working groups were formed. Data from different laboratories were collected, sorted, harmonised, validated and put in common reference databases. From these reference databases, properties of 316L(N) products were re-evaluated and allowable stress values derived, see e.g. [9-14], and entered in the new editions of RCC-MR. Figure 1 shows an example of the results that contributed to redefinition of creep-fatigue damage diagram.

³ Nitrogen addition beyond 0.08% does not have a significant effect on strength and hence an upper limit of 0.08% was imposed.

Table 4. Evolution of 19-12-2 filler metal over the past 40 years

Element	Rapsodie (1967)		Phénix (1973)		Phénix (vertical welds)		Superphénix (1985)	
	Min.	Max.	Min.	Max.	Min.	Max.	Min.	Max.
C	0.50	0.065		0.040	0.045	0.055	0.045	0.055
Mn	1.2	1.50	1.2	2.0	1.0	1.5	1.2	1.8
Si	0.50	0.80	0.40	0.80	0.30	0.50	0.40	0.70
P				0.030	S+P	0.030		0.025
S				0.025	S+P	0.030		0.020
Cr	18.0	19.0	18.0	19.0	18.0	19.0	18.0	19.0
Ni	11.0	12.0	11.5	13.0	11.0	11.5	11.0	12.0
Mo	1.9	2.2	1.8	2.2	1.8	2.2	1.9	2.2
Nb+Ta+Ti								
Cu								
B								
Co								
d-ferrite %		5		5	5		3	7

Figure 1. Creep-fatigue damage evaluation for 316L(N) according to time and strain criteria. Notice that 0.3-0.3 rule does not cover all experimental results and 0.2-0.2 gives a better coverage.



With the selection of 316 steel for ITER, the R&D work took on new momentum and a wealth of new data were generated, see e.g. [15]. These gave rise to establishment of new Appendix A reports, new ITER Materials Properties Handbook property sheets and an advanced fusion Interim Structural Design Criteria (ISDC) that also included irradiation effects [16].

Currently work is concentrated on manufacturing of various components for ITER. Since the complexity of these components often require advanced manufacturing techniques, such as HIPing, diffusion bonding [17], further R&D work will be needed on materials subjected to additional heat treatments during such operations.

The service performance of components made from 316L(N) has been excellent. This grade has shown less susceptibility to delayed reheat cracking and to grain boundary sensitisation, and has retained better residual life than 304 steel. A surprising observation has been the good behaviour of 19-12-2 after 20 years of service in Phénix.

Austenitic stainless steel type 321

Titanium stabilised (321)⁴ and niobium stabilised (347) stainless steels have been used extensively in French, UK and German conventional power plants [18]. At the time when type 321 was selected for use in the first generation of French fast breeder reactors, the steel enjoyed the reputation of having excellent high-temperature creep resistance. Some researchers associated this to accidental pick-up of boron from furnace bricks used during its melting. Higher boron content grades thus enjoyed a good reputation. The problems mentioned above regarding welding have since put a limit on boron content.

These stabilised steels were later hit by another phenomenon known as “delayed reheat cracking”, see e.g. Figure 2. The crack starts at the root of the weld, which in general has a poor geometry, and propagates intergranularly at the interface between the heat affected zone (HAZ) and the weld metal. Cracking occurs in a delayed manner after several years of service at high temperature (in Phénix at 550°C). However, in a few cases cracking has been observed during stress-relieving treatment after few hours at very high temperature (750°C) [5].

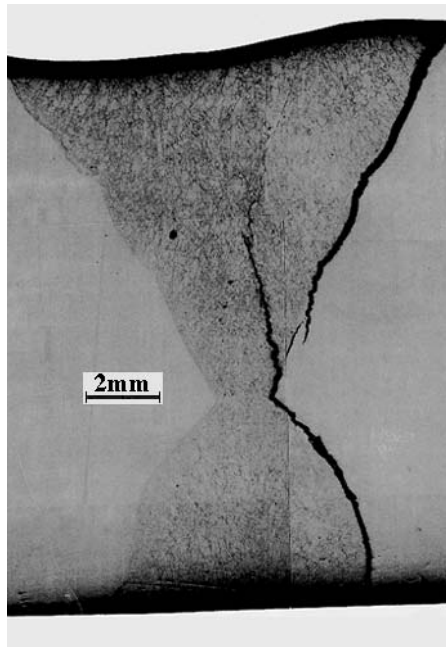
In general, the delayed reheat cracking occurs when a combination of conditions is met:

- The steel is stabilised with the addition of titanium or niobium.
- Significant local cold work is generated at the root of the weld and a bad weld geometry acts as stress raiser.
- Long-term exposure at high temperature ($\geq 550^\circ\text{C}$).

The present understanding is that during welding, carbides are dissolved in the HAZ with titanium or niobium atoms put back into solid solution. The local cold work after cooling creates a dense array of dislocations. During cooling and subsequent exposure to high temperatures, small titanium or niobium carbide precipitates are formed on these dislocations. The matrix thus becomes very hard and the relaxation of the residual stresses occurs through cracking at the grain boundaries.

⁴ Composition of the heat used in [18]: 0.050%C – 0.38%Si – 1.61%Mn – 11.30% Ni – 17.66% Cr – 0.008%S – 0.027%P – 0.27%Mo – 0.46%Ti – 0.0030%B – 0.16%Co.

Figure 2. Typical delayed reheat cracking observed in type 321 stainless steel



This kind of cracking has been observed many times in the secondary circuits of Phénix and PFR reactors. Although the titanium stabilised steel (321) appears to be less sensitive to such cracking than the niobium stabilised steel (347), it has been decided to discard both types of steels from use in subsequent generations of French FBRs. Note that such cracking has not been observed in unstabilised stainless steels such as 304 and 316 under similar service conditions.

Ferritic/martensitic steels

The iron-chromium phase diagram [19] has an austenitic phase loop⁵ at above about 850°C on the iron side, where steels with compositions up to 12% chromium can be heated and then quenched to obtain a martensitic structure. At above 13%Cr, the steel has a ferritic structure but is prone to sigma phase formation or alpha/alpha prime transformation at temperatures below about 820°C when chromium concentration is further increased. As a result, most of the ferritic/martensitic structural alloy development has centred around 9-12% chromium martensitic steels or 12-14% chromium ferritic steels.

Martensitic steels

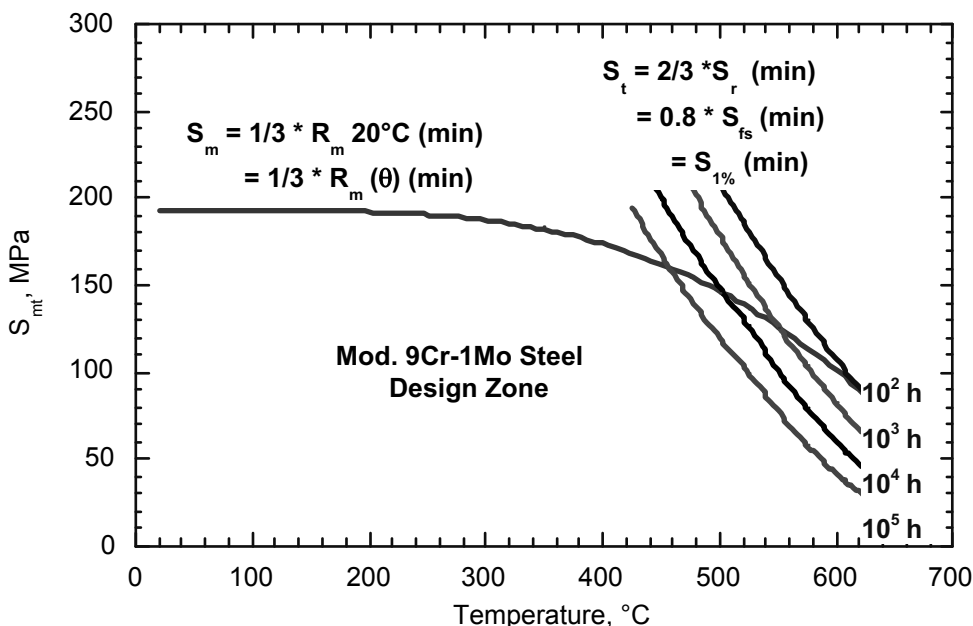
The basic 9Cr-1Mo steel (also known as EM10) was adopted in the late 1960s by the United Kingdom Nuclear Industry for use as steam generator tubing in both the advanced gas-cooled reactors and in the sodium-cooled Prototype Fast Reactor (PFR) at Dounreay. The first improvement of the basic steel occurred in the 1950s and led to 9%Cr2%MoNbV steel, commonly known as EM12 [20]. This steel, which possessed higher strength than the basic steel, was later adopted for superheater tubing in French fossil-fired power stations. However, the steel contains high amounts of delta ferrite, which together with the precipitation of laves phases during service at ~550°C caused it to become brittle and produce low ductility.

⁵ The position and extent of the austenite phase loop depend on the steel composition, particularly carbon content.

Grade 91 or Modified 9Cr1MoNbV steel is the third generation of the basic 9Cr1Mo ferritic steel [21]. Optimisation of its composition in the last two decades, in conjunction with its low thermal expansion, high thermal conductivity, *vis-à-vis* the austenitic stainless steels, has resulted in an attractive steel for elevated temperature operation in both the non-nuclear and nuclear power producing industries.

The Modified 9Cr-1Mo steel was selected for steam generator tubing of EFR and its properties updated for revision in RCC-MR, see e.g. Figure 3 and Ref. [22]. The work continues, however, on improvement of its filler metal, in particular for welding thick sections. Restrictions on certain elements, such as oxygen and phosphorous, has improved properties.

Figure 3. Determination of S_{mt} for Mod. 9Cr-1Mo steel



The industry has used a range of post weld heat treatments (650 to 800°C) for this group of steel. In some cases, a 20% drop in hardness after PWHT has been sufficient for a given service. However, in most cases a hardness level comparable to base metal has been sought. In the US, most of the development effort has been aimed toward achieving a room temperature Charpy-V notch energy of 68 Joules (8.5 daJ/cm²), in line with the non-mandatory Appendix G of Section III of the ASME Boiler and Pressure Vessel Code. In France, there is a restriction on the UTS (650 MPa) for components under pressure. Extensive work performed for EFR has shown that the above restriction is justified from the fracture toughness point of view in thick sections. To attain it, a PWHT at relatively high temperature (750-770°C) for long time is required.

In parallel with the EFR development, it was also clear to the fusion community that the austenitic stainless steel retained for ITER, will not satisfy the irradiation swelling resistance criterion for DEMO, where neutron doses higher than 70 dpa are expected. Experience from use of ferritic steels in FBR core subassemblies and in particular EM10 [23] had already shown superior resistance of these steels to swelling. As a result, ferritic/martensitic steels have also retained for DEMO.

Following extensive screening tests of various compositions (e.g. Manets 1 and 2 and Optifer in Germany), the composition of interest was finally narrowed to 9%Cr steels, but with high activation elements such as Mo and Nb replaced with their equivalent low activation elements (W and V, Ta).

Under the auspices of the IEA fusion materials implementing agreement, the first large industrial melts with 8%Cr-2%W were produced in Japan (F82H steel) and characterised by all international partners [24,25]. Later, EU fearing that 2%W could reduce the neutron sufficiency of the system, produced the Eurofer steel (9%Cr-1%W) and launched an intensive qualification programme [26-29]. The Eurofer steel is now practically ready for code qualification, though more work on its filler metal and joining techniques is needed. Since the initial qualification is for test blanket modules that will be tested in ITER, where maximum irradiation dose does not exceed 3 dpa and most of the joints have thin sections, it is believed that Eurofer steel will be fully qualified in time.

For the actual DEMO components, even the present 70 dpa irradiation experiments in fission reactors may not suffice. This is due to high He/dpa found in fusion reactors as compared with fission reactors. An Intense Fusion Materials Irradiation Facility (IFMIF) is proposed for testing fusion materials under conditions representative of a fusion reactor.

ODS ferritic/martensitic steels

Despite the improved performance of Mod 9Cr-1Mo steel, its strength sharply decreases at temperatures above 550°C. Fusion and fission researchers have been experimenting with different solutions to increase the strength of ferritic/martensitic steels. The preferred solution in both communities is oxide dispersion strengthening (ODS). Different volume fractions of Y₂O₃ oxide, with or without additions of other elements (e.g. Ti), have been tested.

The European fusion programme has produced several 50 kg heats of Eurofer ODS steels that show good high-temperature tensile and creep properties along with good ductility [30]. The second generation heats exhibit a DBTT below room temperature, but still remain sensitive to oxygen and carbon content, production method and heat treatments. More recently, a back-up route, with 12-14% chromium ferritic steels, has been added to the R&D programme. Already, the early results show that the 14% Cr has a DBTT above room temperature that can not be shifted to lower temperatures through heat treatments [31]. In contrast, the 12% Cr steel does respond to heat treatment.

The French Gen IV programme considers two ferritic steels, one with 13% and another with 18%Cr. Here, the intended application is mainly reactor core subassemblies, where swelling resistance to 200 dpa is targeted.

Much more work on ODS steels is still needed before they can be used in critical structural components, e.g. fusion welding is a major problem. Another factor that limits high-temperature application of ferritic/martensitic steels in fast flowing liquid metal is excessive corrosion and erosion of this steel. Development of a protective coating is of high priority for such applications.

Finally, a major concern in FBRs is sodium fire in case of a water leakage. In the austenitic stainless steel tubes such leaks occur through small cracks, often allowing their detection before serious consequences. It is feared that continuous erosion of the ferritic/martensitic steel tube wall may lead to the sudden appearance of a large hole and more serious Na/H₂O reaction.

Precipitation hardening stainless steels

The example chosen here is Alloy 800, which can also be placed in the austenitic stainless steel category. Other precipitation hardening grades are used for specific functions, i.e. grades A286 and 17-4PH are used for bolting due to their high yield strength. In such applications, small dimensional changes due to precipitation or irradiation creep can have significant effects on stress relaxation [32].

Alloy 800

Alloy 800 has been used in conventional power plants in standard (Alloy 800, Grade 1) and high-temperature (Alloy 800H or Grade II) grades. The latter is given an additional final heat treatment at a higher temperature (3 min. at 1 250°C) and has a larger grain size (ASTM GS No. 5). Both grades derive their extra resistance from precipitation of small spherical particles of Ni₃(Ti,Al), known as gamma prime, g' [33-35].

Grade 1 was selected for the steam generator tubing of Superphénix because of its superior ductility. It has also higher yield strength than the austenitic stainless steels (Rp min. at 20°C: 245 MPa for bars and 295 for tubes), as well as good resistance to stress corrosion cracking in pure water and chlorinated cooling media, and better behaviour in caustic solutions. Extensive R&D work has been performed for optimisation of its chemical composition (Table 5), which also covered variations in individual concentrations of Ti and Al and their ratio, before specifying a reference composition and heat treatment for Superphénix. Concurrently, microstructural examinations and mechanical tests were performed on each nuance, in relevant cooling media, with or without prior cold working. The work performed also included homogeneous and heterogeneous welds. All these contributed to code qualification of the specified grade for use in FBR, see e.g. Table 6.

Table 5. Chemical composition of Alloy 800 Grade 1 (grain size number between 6-10)

	C	S	P	Si	Mn	Ni	Cr	Ti	Al	Ti+Al	N	Cu	B	Co
Alloy 800	0.03 –	≤ 0.015	≤ 0.015	≤ 0.70	≤ 1.0	32.0 –	19.0 –	0.30 –	0.10 –	0.55 –	≤ 0.03	≤ 0.75	≤ 0.0015	≤ 0.25
Grade 1	0.06					35.0	23.0	0.50	0.25	0.75				

Table 6. Average stress rupture (MPa) of Alloy 800 Grade 1, as a function of Ti+Al (unaged)

T °C	Ti+Al%	10 ² h	10 ³ h	10 ⁴ h	10 ⁵ h	2. 10 ⁵ h
500	0.55	440	340	276	225	196
	0.63	–	360	295	–	–
525	0.55	395	290	240	170	148
	0.63	–	315	260	–	–
550	0.55	328	238	196	128	113
	0.63	330	270	230	146	127
	0.71	385	345	245	158	138
575	0.55	270	195	160	–	–
600	0.55	–	152	–	–	–

The final heat treatment applied to different products varied slightly. For a seamless tube of 25 mm external diameter and 2.6 mm thickness, it consisted of:

- an intermediate heat treatment between 970°C and 1 050°C;
- an import cold reduction (≥30%);
- a final heat treatment at 980°C ± 20°C in controlled atmosphere, followed by air cooling.

Conclusions

The overriding consideration in design and construction of nuclear power plants is safety. Materials that have performed well have been retained and improved from one generation of reactor to another and materials that have performed badly discarded.

For instance, austenitic stainless steels such as:

- types 304L and 316L(N) and ferritic/martensitic steels such as Modified 9Cr-1Mo steel;
- low activation grades such as F82H and Eurofer steels;

have performed well and continue to be widely used. Titanium and niobium stabilised stainless steel grades (321 and 347), in contrast, have performed poorly and have been discarded.

REFERENCES

- [1] Metals Handbook, Volume 3, Properties and Selection: Stainless Steels, Tool Materials and Special-Purpose Metals, 9th Edition, ASM (1980).
- [2] Tavassoli, A-A.F., P. Ould, E.A. Little, W. Dietz, *Evaluation of the Effect of Neutron Irradiation on Mechanical Properties of Internals of PWR*, CEC Study Contract Etnu-CT92-0056 (1992).
- [3] Tavassoli, A-A.F., “Effect of Neutron Irradiation on Mechanical Properties of Permanent Near Core Structures”, *Effect of Radiation on Materials: 14th Int. Symposium*, 27-29 June 1988, Andover, Mass., ASTM STP-1046 (Vol. 2), pp 684-699 (1990).
- [4] Andresen, P.L., *Irradiation Assisted Stress Corrosion Cracking. Stress Corrosion Cracking – Materials Performance and Evaluation*, ASM International (1992).
- [5] Petrequin, P., *Les matériaux pour applications à hautes températures*, Société Française de Métallurgie et Matériaux, Section Nord, Lille, 2 December (1999).
- [6] Escaravage, C., K. Williamson, E. Heesen, H. Breitling, D. Lehmann, A-A.F. Tavassoli, *Evaluation of Mo Containing Stainless Steel Weld Metal Stress Rupture Strength Factors for Use In Design*, CEC Study Contract RA01-0197-F, Novatome (1993).
- [7] *ITER Materials Properties Handbook*, Edition 2007.
- [8] Tavassoli, A-A.F., *Task Title: TW5-TVM-LIP: Rules for Design, Fabrication and Inspection: Sub-task: Modification of ITER Materials Documents, Assessment of Materials Data and Maintenance of a Database*, CEA-Euratom Annual Report (2005).

- [9] Forgeron, T., A-A.F. Tavassoli, J. Wareing, D. Lehmann, C. Escaravage, B. Breitling, C. Picker, *Effect of Thermal Ageing on Mechanical Properties of Type 316L(N) Base and Weld Metals*, CEC Study Contract CT-92-0211-F, CEA Report (1994).
- [10] Bergmann, H.J., A-A.F. Tavassoli, D. Lehmann, I. Curbuishley, *Comparison of Results From Interrupted and Uninterrupted Creep-Rupture Tests for 316L(N) Stainless Steel*, CEC Study Contract ETNU-CT92-0075-D, Siemens-KWU-NT-4/94/023 (1994).
- [11] Dietz, W., C. Picker, A-A.F. Tavassoli, “Structural Material Studies for the European Fast Reactor, Highlights and Progress”, *Structural Materials and Processes*, Vol. 6, No. 4 (1995).
- [12] Tavassoli, A-A.F., C. Picker, J. Wareing, “Data Collection on the Effects of Irradiation on the Mechanical Properties of Austenitic Stainless Steels and Weld Metals”, *Effects of Radiation on Materials, 17th International Symposium*, Sun Valley, ASTM STP 1271, D. Gelles, *et al.* (Eds.), ASTM, Philadelphia (1995).
- [13] Breitling, H., E. Stärk, V.B. Livesey, M. Mottot, A-A.F. Tavassoli, “Evaluation of Creep-fatigue Behaviour of Austenitic Stainless Steels”, *Structural Mechanics in Reactor Technology (SMIRT-12)*, BG12/2, Stuttgart, 15-20/08/93.
- [14] O’Donnell, I.J., H. Huthmann, A-A.F. Tavassoli, “The Fracture Toughness Behaviour of Austenitic Steels and Weld Metal Including the Effects of Thermal Ageing and Irradiation”, *Int. J. Pres. Ves. & Piping*, 65, 209-220 (1996).
- [15] Tavassoli, A-A.F., “Extending ITER Materials Design to Welded Joints”, *ICFRM-12*, ID No. 57140, Santa Barbara, Ca., USA, 4-9 December (2005).
- [16] ITER Interim Structural Design Criteria (ISDC), Revision 3.
- [17] Dänner, W., A. Cardella, L. Jones, P. Lorenzetto, D. Maisonnier, G. Malavasi, A. Peacock, E. Rodgers, A-A.F. Tavassoli, “Major Achievements of the European Shield Blanket R&D During the ITER EDA, and Their Relevance for Future Next Step Machines”, *ISFNT-5*, Rome (1999).
- [18] Tavassoli, A-A.F., J-N. Calvet, “Effet de la Variation de la Taille de Grain sur les Propriétés Mécaniques et Structurales de L’acier 18Cr-11Ni-Ti au Bore”, *Mem. Sci. Revue Métallurgie*, November 1979, 76, n°11, pp. 689-700.
- [19] Metals Handbook, Volume 8, Metallography, Structures and Phase Diagrams, 8th Edition, ASM (1973).
- [20] Caubo, M., J. Mathonet, “Properties and Industrial Applications of a Superheater Steel Containing 9%Cr 2%Mo V Nb”, *J. Review de Metallurgie*, Vol. 66, p. 345 (1969).
- [21] “Modified 9Cr-1Mo Steel – Technical Program and Data Package”, *ORNL Technology Transfer Meeting*, Knoxville, Tennessee, April (1982).
- [22] Tavassoli, A-A.F., “Assessment of Martensitic Steels for Advanced Fusion Reactors”, *Advanced Reactor Concepts, Structural Mechanics In Reactor Technology (SMIRT-13)*, Porte Alegre, 13-18 August (1995).

- [23] Séran, J-L., A. Alamo, A. Maillard, H. Tournon, P. Dubuisson, O. Rabouille, “Pre- and Post-irradiation Mechanical Properties of Ferritic-martensitic Steels for Fusion Applications: EM10 Base Metal and EM10/EM10 Welds”, *ICFRM-6*, Stressa, Italy, 27 September-1 October (1993).
- [24] Jitsukawa, S., M. Tamura, B. van der Schaaf, R.L. Klueh, A. Alamo, C. Petersen, M. Schirra, G.R. Odette, A-A.F. Tavassoli, K. Shiba, A. Kohyama, A. Kimura. “Development of an Extensive Database of Mechanical and Physical Properties for Reduced-activation Martensitic Steel”, *J. Nucl. Mat.*, 307-311, 179-186 (2002).
- [25] Tavassoli, A-A.F., J-W. Rensman, M. Schirra, K. Shiba, “Materials Design Data for Reduced Activation Martensitic Steel Type F82H”, *ISFNT-6*, San Diego, MS # 355, April (2002).
- [26] Möslang, A., E. Diegele, M. Klimianko, R. Lässer, R. Lindau, E. Lucon, E. Materna-Morris, C. Petersen, R. Pippan, J.W. Rensman, M. Rieth, B. van der Schaaf, H-C. Schneider, A-A.F. Tavassoli, “Towards Reduced Activation Structural Materials Data for Fusion DEMO Reactors”, *Nuclear Fusion* (2005).
- [27] Lucon, E., *RAFM Steels – Irradiation Performance*, EFDA Monitoring Meeting, TTMS-001, Garching, 7 January (2007).
- [28] van der Schaaf, B., A-A.F. Tavassoli, C. Fazio, E. Rigal, E. Diegele, R. Lindau, G. LeMarois, “The Development of Eurofer Reduced Activation Steel”, *Fusion Engineering and Design*, Vol. 69, Issues 1-4, September 2003, 197 (2003).
- [29] Tavassoli, A-A.F., *et al.*, “Materials Design Data for Reduced Activation Martensitic Steel Type Eurofer”, *ICFRM-11*, Kyoto, December (2003).
- [30] Lindau, R., A. Moeslang, M. Rieth, M. Klimiankou, E. Materna-Morris, A. Alamo, A-A.F. Tavassoli, *et al.*, “Present Development Status of Eurofer and ODS-Eurofer for Application in Blanket Concept”, *Fusion Engineering and Design*, Vol. 75-79, November 2005, pgs. 989-996, *Proceedings of the 23rd Symposium of Fusion Technology*.
- [31] EU Monitoring Meeting, Garching, Jan. 2007, EPFL results.
- [32] Barabash, V., *et al.*, *ICFRM-12*, Santa Barbara, CA, USA, 4-9 December (2005).
- [33] Tavassoli, A-A.F., G. Colombe, “Mechanical and Microstructural Properties of Alloy 800”, *Met. Trans. A.*, Vol. 9A, pp. 12031211, September (1978).
- [34] Tavassoli, A-A.F., Pozarnik, F., “Cinétique de la Précipitations de la Phase g' et son Influence sur la Limite d'Élasticité d'un Alliage Fe-Ni-Cr”, *J. Nuclear Materials*, 120, Nos. 2 & 3, pp. 293-303 (1984).
- [35] Tavassoli, A-A.F., “Metallurgical Instabilities and Creep Rupture Extrapolation, Alloy 800 (Fe-34 Ni-22 Cr-Ti, Al)”, *Proc. Int. Conf. on the Eng. Aspects of Creep*, University of Sheffield, Inst. of Mech. Eng., Vol. C 334/80, pp. 85-90, 15-19 September (1980).

SESSION V

Fundamental Research

Chairs: A. Al Mazouzi, S. Maloy

**QUALIFICATION OF STRUCTURAL MATERIALS FOR REACTOR SYSTEMS:
SYNERGIES IN MATERIALS FOR FUSION/FISSION
REACTORS AND ADVANCED FISSION REACTORS**

W. Dietz¹, B-C. Friedrich²

¹Consulting Metallurgist, ²AREVA NP, Germany

Abstract

In nuclear technology a lot of experience has been accumulated meanwhile from reactor programmes for ferritic alloys, austenitic steels and Ni-based alloys as main component materials during R&D, design, construction and operation. Generally materials are a key issue for a safe and reliable operation of NPPs. Many grades investigated are of interest for the design of GenIVs and fusion reactors.

Synergisms of materials, material technologies, mechanical data, corrosion and other topics for the qualification of materials for nuclear systems are generally discussed and information on a qualification procedure is compiled. Also some lessons learned from fabrication, test programmes or operation of NPPs are provided. A special problem is the fusion system because a final validation for alloy performance in the long term will need irradiation under realistic fusion condition anticipated in a high-energetic, fusion-specific intense neutron source such as (IFMIF), the International Fusion Materials Irradiation Facility.

Introduction

Advanced energy systems are under development to fulfil the needs for increasing energy demand world wide. Whereas non-nuclear power plants increase operation temperature and improve power-heat coupling systems the Gen IV reactor generation is an internationally defined programme to fulfil better public acceptance, environmental and economic requirements.

For Gen IV NPPs a revival of the fast breeder (FBR) and high temperature reactor (HTR) technology is considered after extensive programmes in the past. Less experience is available from the past for the other Gen IV reactor systems. Fusion reactors are the most complex system in nuclear technology and their viability has yet to be demonstrated with the ITER project, before a DEMONstration reactor (DEMO) can be constructed around 2030 or later.

In case of modifications for existing reactor designs, e.g. by changing the heat source, the transfer conditions of the coolant or the off-normal conditions, new design requirements have to be considered by mechanical and material engineers and also by the fabrication organisation of the designer or its subcontractor. Also new safety requirements such as considerations of earth quakes, plant crashes or special conditions of coolant chemistry may force activities for design verification through qualification testing of materials.

In the materials field design verification is mainly performed by qualification tests with specimens or, to some extent, also by prototypic components, e.g. simulating the creep-fatigue interaction of welded structures. During operation of the NPP specimens are tested in the frame of surveillance programmes.

Due to the time-consuming and costly process for the qualification and licensing of new materials with a final validation in reactor components, changes to new materials are rather scarce. Optimisation of code approved materials or their tailoring is mostly applied. In case of a new material a more extensive design verification is needed during the different phases of a project – a common case for all of the NPPs.

This paper recalls the relevant experience for the qualification of structural materials including near-core or core materials of fission reactors. The experiences are based on material's engineering activities in industry for reactor projects. A part was also material and design/component relevant R&D in co-operation with various research organisations [1,2].

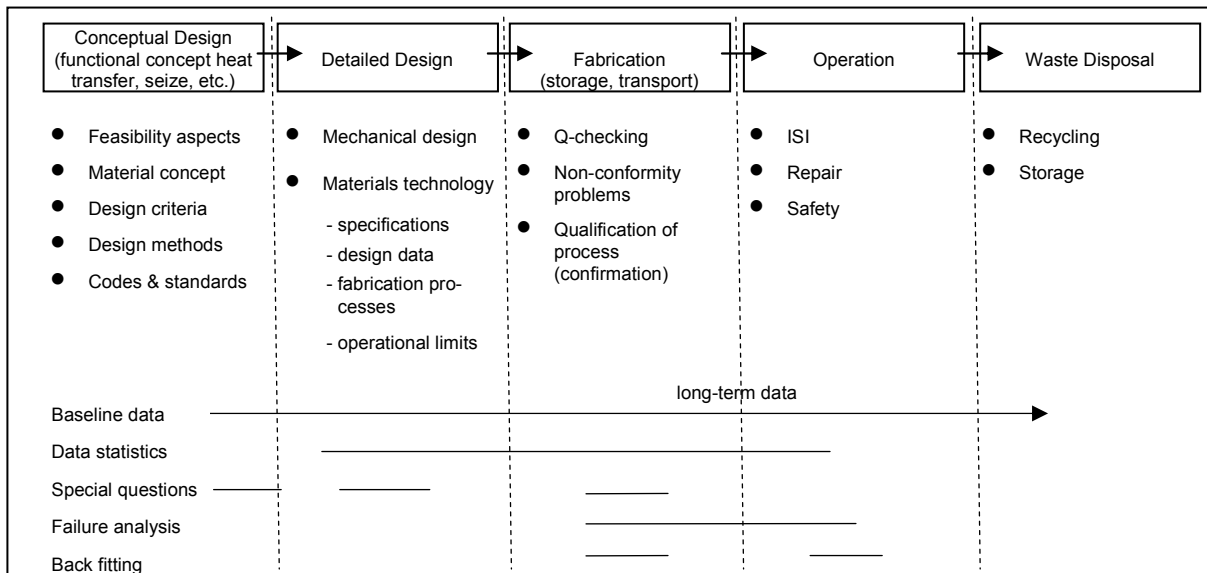
First, an example for a qualification scheme is provided, then the present materials used will be surveyed and the specific loading conditions for the different systems are considered. Finally, some examples are given for special events that could not easily have been foreseen in the basic qualification phases.

Scheme for the qualification of materials

The qualification of a material needs considerations of the different phases of a new project because the depth of investigations, data categories and their amount will be different. The principle scheme for the life cycle of a reactor is seen in Figure 1 with the different activities in project phases.

The principle selections of the materials occur in the Conceptual Design Phase, often already earlier in a phase for "project-definition" during R&D for a specific project line. Here the main features for materials technology are defined through the general boundary conditions for coolant, the heat source definitions, the safety approach, the core concept, etc.

Figure 1. Materials technology from conceptual design to waste disposal



The assessment for the qualification of materials may be defined by several steps as:

- Firstly, a *compilation of plant requirements* (e.g. temperature range, coolant specification, strength, loads, load cycles, ...). This will lead to the definition of the requested material properties in form of a “property and requirement specification”.
- Secondly, *available commercial materials* for similar applications in codes and standards will be considered which may have the capability to fulfil the requirements. A compilation of their base line properties is leading to a *reference material* and often to *alternative options*. An assessment about available data and knowledge compared with the requirements leads to the definition of additional investigations on an already available material grade. Various categories of materials data needed for a design have to be analysed. Examples are:
 - data for procurement specifications including non-destructive examinations (NDT) and relevant fabrication processes or for repair welding;
 - data for the mechanical design including safety and life assessments, corrosion or detailed design of specific areas such as acceptable flaw sizes for fatigue or creep crack growth...

Materials experts and designers have to analyse within a co-ordinated action whether available data: i) are sufficient for a design; ii) are insufficient; iii) are not at all sufficient (no data are available). Generally the amount of data for a reactor system with its different components and systems from the core to the outer auxiliary systems is numerous. Priorities for investigations have to be defined guided by the safety and reliability requirements for components. Alternative options for a component material should be dropped as soon as reasonable due to the costly investigations. The data needed are displayed in Table 1.

For many applications in a reactor system a number of materials exists in codes and standards with recommended data sets for pressure vessels (e.g. EN-, RCC-M/MR-, KTA-, ASME-standards,..). Most of the time, the specific data needed for the design of components in a radiation environment are missing. Often it is possible to adjust the specifications by modifications of the chemistry of the standard alloy taking into account an “environmental factor” for data [3]. From these experiences it is

Table 1. Aspects for materials selection in nuclear technology

<ul style="list-style-type: none"> • Thermophysical properties (stress factor) • Tensile strength • Creep strength • Toughness/DBTT • Ductility/uniform elong. • Fatigue resistance • Ductility irradiated 	<ul style="list-style-type: none"> • Swelling /irradiation creep • Resistance to crack propag. • Corrosion • Stress corrosion cracking • Reduced activation and radiological properties • Availability (qualified manufacturer) 	<ul style="list-style-type: none"> • Qualified fabrication routes • Weldability/joining • Dimensional stability of components fabricated • Non-destructive testing • Costs
---	---	---

strongly recommended to apply as far as possible such qualified materials from the past also for the future within new systems. A large amount of data was generated in the past within the FBR and HTR programmes, e.g. for austenitic materials such as Type 316 LN or Alloy 617. For the last one experimental data from the German HTR programme are in the *MAT-DB* data base of the JRC Petten, NL [4], however access to data needs agreements.

Changing to a new material it has to be considered that for qualification 10 years or even more have been needed from the first melt to the fabrication of reactor components. Success is not guaranteed in any case. A back-up solution often is needed! In case of the qualification of a new material (also if significant modifications of a standard alloy are needed) a principle scheme was used:

In a *first phase* the general alloy selection is made by “screening” of materials. For the principle alloy design different alloy options are considered using small R&D Heats (10-100 kg) for experiments. The result should be the draft of a specification with details of chemistry and heat treatment specifications and “preliminary design data”. The most crucial properties such as creep, aging and environment effects with a sufficient duration of the experiments have to be investigated. Also tests are done to simulate the microstructure of thick sections and check their properties.

In a *second phase* small industrial heats in the range of 1-10 tonnes are produced. The verification of properties defined in the draft specification is a main objective and also the generation of basic design data. In case that data are insufficient there is often a need to define “intermediate data sets” before “code data” with sufficient confidence can be provided. Important in this phase is the fabrication and joining work for the construction. Here, an interaction is needed between mechanical designers, the manufacturing engineer and the material’s engineer, all must be involved. Requirements must be identified for the joining processes, e.g. welding, brazing or bolting, and forming properties (elbow bending, etc.). For example, welding generates three “grades” of materials as base material, weld metal and the heat affected zone – each with specific properties in strength, ductility or corrosion which all have to fulfil the design requirements. Therefore, the properties of these features shall be included in any investigation programme from the beginning on.

These activities are started mainly in the phase of conceptual design (see Figure 1). Responsibilities for materials engineering in the phase of detailed design and construction generally are at industrial organisations which are later on responsible for the design, fabrication of a reactor and guarantee of operation.

In a *third phase* typical industrial heats in the range of 1-100 tonnes are produced depending on the design requirements for the semi-finished products.

In case of forgings or thick plates such as for LWR components the ingot size is more in the range of 50-100 tonnes. Mainly in this phase the design data base is finalised, failure criteria are defined, the sensitivity of NDT is checked or component tests are made in combination with the design methodology.

In case of long-term data often uncertainties exist for extrapolations e.g. due to the limited number of heats investigated. Then decisions about in-service inspections (ISI, see Figure 1) during plant operation or for surveillance tests have to be made.

Beside the data needed *for design*, metallurgists request additional generic information for the material – both for fabrication and design considerations. Examples are: i) effects of TMT and aging on properties; ii) interaction of mechanical properties and corrosion/stress corrosion; iii) dose-rate effects during irradiation; iv) microstructural evolution. These topics are issues of material conferences since a long time.

Some typical materials used in nuclear fission reactors of Gen I to Gen III and in the fusion programme are listed in Table 2. Most of these have been used also in modifications in conventional plants and they have been tailored following a fitness for purpose concept for reactors (e.g. the reduction of the Co content).

Table 2. Typical alloys used for fission reactor systems and in fusion programmes [5]

	Ferritic alloys*	Austenitic stainless steels	Ni alloys	Others
LWR	MnMoNi type	17Cr12NiMoN 18Cr10NiNb/Ti	Alloy 600 & 690 Alloy X 750	Zircaloy
FBR	2 1/4 Cr 1Mo 9-12Cr MoVNb	15Cr15NiMoTiB 17Cr12NiMo(N)	PE 16 Alloy 706/718	CrC
HTR	12 Cr 1MoVNb	20Cr32NiTi (Alloy 800)	Alloy 617 Hastelloy X	CrC, ZrO ₂
Fusion	9-12CrMoVNb 2 1/4Cr 2WV 7-10Cr WVTa	17Cr12NiMo(N)	Alloy 625	Cu-alloys ODS steels SiC/SiC

* Not included different types in the steam circuit.

Unique for conventional power plants and nuclear reactors is the use of ferritic-martensitic 9-12 Cr steels – tailored for fusion to low activation material – and from the austenitic steels e.g. 17Cr12NiMo(N), a type 316 LN. Assessments and detailed alloy selection for these types can rely on a broad data set in literature or in various codes including the ITER code. However, even if the same material is processed in the same way for components the application of property data from one system to another must be carefully checked due to different environments (temperature, coolant, stress corrosion, irradiation and cyclic operation). This is one of the aspects that synergies are rather scarce between the different systems. Differences in the nuclear systems will be highlighted in the following section.

Nuclear environment

One of the early observations made in the context of irradiation effects on a specific material grade was that the changes in the properties vary with the irradiation conditions as well as with the thermo-mechanical history of the material and its service loading. Embrittlement due to He production or dpa-level, void swelling, creep or structural instability may or may not occur, depending on the environment.

General operational conditions comparing the different reactor systems are summarised in Table 3. The data are more typical than exact and are linked to general designs. This is especially true for a DEMO FR. Especially the production of helium and hydrogen and the special neutron spectrum effects are part of discussions for materials performance, but this will not be considered in detail here.

Table 3. Operating and environmental condition of nuclear systems (general range) [5]

	LWR	FBR	HTR	Fusion systems
Coolant	Water	Sodium	Helium gas	Water; He (Pb-Li)
Coolant pressure (MPa)	15.8 (PWR)	1	4	Water: 15.5, He: 8
T range (°C)	270-325 (450)	360-650	400-950	150~600
Service life (years)	40-60	40-60	40-60	>30 2.5 (B)
Heat load (MW/M²)	4 (a)	8 (a)	n.a.	0,5
Number of cycles	100-1 000	1 000 (#)	1 000 (#)	> 10 000 ITER 1 000 DEMO (#)
Range of dpa (@)	5-50	1-200	1	50
He-appm/dpa (in Fe)	0.24 (b)	1	n.a.	10 (c)
H-appm/dpa (in Fe)	0.77 (b)	n.a.	n.a.	42 (c)

(a) Fuel pins (thin-walled); (b) HFR reactor; (c) DEMO; (B) Blanket modules
(#) Tentative figures; n.a.: not available; @: near core components/fuel elements

The mode of operation is another significant difference for the nuclear systems. It ranges from quasi-steady-state in the LWRs or FBRs to an extremely pulsed mode of operation in ITER. Pulsed operation in ITER will generate a high number of load cycles which will require a material highly resistant to fatigue damage under a low dpa dose level.

Environmental effects needed for design on fission reactor materials are determined by investigations on specimens after exposure in reactors or corrosion test loops. These experiences of material performance will provide valuable information on phenomena which need to be considered for material qualification for Gen IV reactors and ITER. However the base line properties for the design of a DEMO FR have to be provided by the International Fusion Materials Irradiation Facility (IFMIF). A direct extrapolation of irradiation performance to FRs is not possible due to the complex interaction of the neutron spectrum and temperature with the materials. Modelling may be a useful tool supporting the qualification of fusion materials.

Difference in the qualification process between reactor types

The qualification process of materials for different reactor types depend in detail upon: i) the component to be considered (thick or thin walled components, permanent structures, semi-permanent/removable structures or fuel elements); ii) the environmental conditions (corrosion, irradiation); iii) the mechanical loading and temperature conditions (time-dependent properties, creep range, low or high cycle fatigue, normal and transient loads or up-normal conditions,..); iv) needs and possibilities for in-service inspection, checking of crack growth,...; v) the risks of failures for mankind, investment and costs due to a shut down.

From these requirements materials and their semi-finished products are optimised for the specific application with specific properties. Thickness, heat treatment and joining effects need to be considered

in detail. Corrosion, irradiation and high temperature may raise specific questions on the effect of time and temperature. For example structural instability effects often need a rather long-term incubation period requiring adequate long periods for qualification tests.

Generally there is a broad range of parameters for material science and technology. To cover all effects will be extremely costly and time consuming. To do the right tests and optimise the test matrix within the frame of a project an interface between designers/manufacture and scientists is needed.

Due to the complex interrelations of environmental/loading conditions and material the transfer of know how from one reactor system to another is rather difficult. The general scheme for material qualification can be applied for all systems however the significance of properties is different for the various reactor systems. Each reactor system has specific material effects in the micro-structural scale. Properties to be considered are surveyed in the following table. The assessments in the table may be points of discussions depending in detail upon the materials/components considered.

Table 4. Properties and related effects

Effect on component → Material effect ↓ (Structure)	Design	Crack initiation	Change of dimensions	Wall thickness reduction	Wear	Handling (repair)	In-service inspection
Thermal ageing	□	■	*			(■*)	
Creep (thermal induced)	■*●	■*●	■*●				■*●
Fatigue (HCF, LCF, TMF)	□	□			□		□
Creep-fatigue (interaction)	■*●	■*●					■*●
Toughness/DBTT	□	□				□	□
High temperature embrittlement (He)	■*●	■*●					
Embrittlement at lower operation temperature	◆●					◆●	
Generation of voids (\leftarrow dpa/T)	■●		■●				■●
Creep (irradiation induced)	■●◆		■●◆				■●◆
Core reaction (atomic scale)/activation	□					□	□
Corrosion	□	□	□	□			□

□ General effect Predominantly: → ◆ LWR ■ Breeder * HTR ● Fusion reactor

Specialists can only become sensitive to experiences in special topics for the application of a material under other conditions. Also small deviations from experiences in a specific environment or temperature range compared to others can provide specific problems. Examples are the He plus impurities chemistry in a HTR, water chemistry in a LWR or sodium purity effects in FBRs – pointing out that corrosion is a system property. Therefore, carefully consideration of the interaction capability of all the relevant operation and environmental parameters are recommended.

Some specific problems observed during past qualification processes

In the following some observations from the qualification process of different reactor materials are compiled. Some events were observed in a late stage of the material qualification or even at operation – after a decade or more of the basic qualification tests. This needed special counteractive measures for the further steps in a project or for plant operation.

As a general rule the organisation of work and quality assurance (QA) is a very important item to be considered for all phases of a project (see Figure 1) including pre-normative R&D activities. Documentation of details in material processing and specimen fabrication is needed due to the long duration of irradiation experiments and creep tests (5-10 years). Scientists and technicians starting the programme often are not the same people for evaluation of the results.

As a consequence, the use of very well characterised material already with the first lots of processed materials with the beginning of the qualification process is stringent. Data from early screening tests often used for the generation of time dependent design data for which traceability is a key issue for the licensing of materials. It was observed that data from screening tests can determine e.g. the lower bounds of toughness for weld metal.

Problems occurred by the fact that a material or processes were qualified and later on the manufacturer stopped the production. Conclusion for the development is that generally more than one manufacturer should be available (knowledge redundancy) however cost aspects limit the qualification of more than one manufacturer often! This problem happened in past for the case of wear resistant coatings.

Some *specific observations* have been made in the reactor programmes which may be understood as “events of a general importance”.

In the *FBR programme*:

- Some *corrosion effects* have been underestimated. For the application of Type 304 the intergranular attack (IGA) was as a problem after fabrication of the reactor vessel [6]. Special programmes were initiated for the hydrogen-embrittlement – not expected for type 16Mo3 [7], also for problems of caustic corrosion after a sodium-water reaction or the ingress of water impurities in the system.
- Special *creep effects* have been observed: Reheat cracking appeared after more than 10 000 hrs operation for stabilised grades 18 8CrNi Ti (type 321) and 18 8CrNi Nb (type 347) for temperatures of 525-550°C [8]. It did not appear for stabilised grades of type 1613CrNiNb at about 600°C after 100 000 hrs. After more than 10 000 hrs a sudden drop/break in the creep properties of base metal of a ferritic-martensitic 11 Cr steels happens at 550-600°C [9]. These examples are of concern to the test methods applied and the reliability of extrapolations from short-term tests to the long term.
- There was a discussion about premature failures due to type IV cracking in the weak fine grained HAZ of weldments of 9-12 Cr steels for applications below 550°C. This effect is now also in discussion for the use of T91 and other 9-12 Cr steels in conventional plants for higher temperatures at 600°C or more [10].
- Problems occurred for the design of weldments since weldment creep properties showed low ductility data. This raised the needs for an extensive programme to demonstrate that standard design procedures for the elastic analysis can be applied.
- It is often not conservative to test at higher temperatures for extrapolation purpose due to a change of mechanisms. For type 304 hold time effect at 700°C were not conservative compared to 550°C data [11].
- For fuel assemblies, low ductility values for cladding in the range of 0.2% creep ductility and 0.5% plasticity needed inelastic design procedures with detailed knowledge for the creep

behaviour, data scattering and also assumptions for the loading conditions [12]. For the optimisation of austenitic steels as cladding material the incubation period for swelling was observed as a limitation of the material (small variations in chemistry such as Ti/C had significant effects and also process parameters). Due to these process effects on irradiation properties a special agreement was made with manufacturers for the long-term irradiation experiments of 5-10 years to assure later on a reproducibility of the fabrication of a tubing.

- For near core component materials the definition of radiation effects on design properties, e.g. fluence effect on number of cycle during fatigue, had to be handled through an environmental factor [3].

In the German *HTR* programme (in the 80s):

- A huge number of creep data was generated during the material qualification phase. For the data evaluation different methods were applied in order to generate the “minimum requirement values” as base for a creep code. Significant differences could be observed depending upon the data used for the analysis [13]. Recent assessments (e.g. ECCC) apply other data evaluation methods however international agreement is not present.
- Thermal aging induced the reduction of ductility (e.g. impact toughness and elongation at rupture) of some investigated materials after long-term exposure (e.g. 30 000 hrs and above). As a consequence discussions were raised for the application of impact data [14].

An example from *LWR* technology:

- A qualified material showed problems not anticipated in the phase of reactor operation. Intergranular stress corrosion effects were observed at Ti-stabilised materials of type 321 in boiling water reactors at temperatures above e.g. 200°C. Consequently the application of these steel grades were limited and further modifications of other grades were applied [15].

From the recent *fusion development programme*:

- The requirements for limitations of impurities in low activation 9 Cr steels are very strict and beyond the state of the art for raw materials and for the standard methods of chemical analysis (e.g. Nb in the ppm-range). Over a five-year period the quantities needed for the fusion programme are very small compared to productions in an industrial scale. The availability of interested manufacturer in Europe for a production therefore is very limited. The conclusion is that new materials or materials with strict requirements in advanced reactor technology can only be developed if there is synergy or interest also in the industry for other applications with a broader market. This may be true also for the development of dispersion strengthened alloys.

Summary and conclusions

Advanced energy systems are under development and operation loads and environments set challenges for the materials. In the past structural material were mainly selected from those materials that were experienced of other applications such as high temperature plants. Modifications of these materials were applied due to plant type specific requirements, e.g. a reduction of elements reducing activation or improvement of toughness. The development of really new material grades was rather scarce. The effect of irradiation on properties was taken into account mainly by reduction factors or by special material equations depending on the irradiation/stress conditions.

Due to large differences between the operation features of GenIV reactor types and fusion reactors the synergy on specific material properties is limited. Generally each reactor type has its specific “material effects”.

Due to the large efforts needed for the qualification and licensing of materials the use of materials from codes/standards with some tailoring is recommended for GenIV respectively fusion – in a similar manner, e.g. as in the past for HTR or FBR systems. In case of needs for new materials a close co-operation of scientists and designers is important because the test matrix especially for all the time and environmentally effected properties of base metal and joinings may enlarge too much for all material and design options. The development process for a new material starts at the manufacturing and examination of small ingots and includes detailed quality assurance of the material properties from the beginning on. All relevant processes needed for the manufacturing of large sized real plant components shall be included in the proceeding development process and also research on the joining techniques needed later on. Traceable and qualified material data being developed shall be stored in a data base accessible for all partners in a project and, the data evaluation procedure shall be internationally agreed in order to define minimum requirements for codes and standards needed to get licensing.

Experiences from the past showed that there were some events and material effects not anticipated in previous project phases. They needed counteractive measures – technically and by the project management in *ad hoc* programmes. Mostly engineering solutions were possible. They could be included in a “learner-curve” from today’s experience for new developments.

REFERENCES

- [1] Dietz, W., *Materials Science and Technology*, Vol. 10B, Nuclear Materials Part II, Chapter 8, VCH – Verlagsgesellschaft Weinheim (1994)
- [2] *Conference on Materials and Nuclear Power (EUROMAT'96)*, 21-23 October 1996, Bournemouth, United Kingdom, M. Erve, pp. 7-16, A. Seibold, *et al.*, pp. 149-156, W. Dietz, *et al.*, 243-256.
- [3] Dietz, W., H. Breitling, *IAEA-IWGR Specialist Meeting*, Gif-sur-Yvette, France, 1-3 December 1993.
- [4] Over, H.H., W. Dietz, these proceedings.
- [5] Dietz, W., K. Ehrlich, *Proceedings of the International Symposium on Advanced Energy Technology*, Sapporo, Japan, 2-4 February 1998.
- [6] Iversen, C., *Innovative Schweiß- und Lötverfahren*, DVS Verlag, pp. 187-196 (2002).
- [7] Stöhr, K.W., *et al.*, *Proc. Int. Conf. on the Interaction of Steels with Hydrogen in Petrol Industry Pressure Vessels Service*, M. Prager (Ed.), Material Property Council, New York (1990).
- [8] Picker, C., *Nucl. Energy*, 31, pp. 207-219 (1992).
- [9] Schirra, M., *et al.*, FZKA 5722, Forschungszentrum Karlsruhe, Okt. 1996J.A.
- [10] Francis, *et al.*, *Materials Science and Technology*, Vol. 22, No. 12, pp. 1387-1395 (2006).
- [11] Dietz, W., *Ibid* 1, p. 135.
- [12] Bergmann, H-J., *et al.*, FZKA 6864, Forschungszentrum Karlsruhe, Juni 2003.
- [13] Ennis, P., *Enlargement and Integration Workshop*, JRC Petten, 17-18 October 2005.
- [14] Nickel, H., *et al.*, *H. Engineering and Design*, 78, pp. 251-265 (1984).
- [15] Erve, M., *et al.*, *20 MPA-Seminar*, 6-7 October 1994.

UNDERSTANDING RADIATION DAMAGE IN FE-CR ALLOYS

Lorenzo Malerba, Abderrahim Al Mazouzi, Dmitry Terentyev, Milena Matijasevic
Nuclear Materials Science Institute, SCK•CEN, Boeretang 200, B-2400 Mol, Belgium

Abstract

We review the experimental evidence of the non-monotonic behaviour of Fe-Cr alloys versus Cr content, particularly under irradiation (ordering versus segregation tendencies, microstructure and phase evolution, ...), together with the theoretical efforts done at the electronic and atomic level to interpret them. We also present some of the experimental and modelling results on Fe-Cr produced at SCK•CEN in collaboration with other laboratories. In particular, we summarise how the use of *ab initio* calculations and interatomic potentials developed for this system allows model experiment results for the same system to be rationalised. Finally, we advance some opinions regarding some points that deserve further investigation in order to fully understand this important binary alloy, at the basis of the steels for current and future nuclear applications.

Introduction

High-Cr ferritic/martensitic steels are being considered as structural materials for a large number of future nuclear applications, from fusion to fission accelerator-driven systems and GenIV reactors. Independently of the specific reactor concept, a reliable guide for the assessment of the behaviour of these steels in operation is the quantitative understanding of the basic physical mechanisms acting from the atomic to the macroscopic level and determining the response of the material to the applied mechanical, thermal and environmental loads, under neutron irradiation. The build-up of this knowledge is beneficial for the safe operation and design of most future nuclear installations. For this reason in recent years significant effort has been put, particularly in Europe and in the USA, in the development of multi-scale models of the response to irradiation of FeCr alloys, the reference model system for high-Cr steels [1-21], and in the performance of model experiments aimed at providing physical insight, rather than parameters of design interest (see e.g. [22,23]). These models, benchmarked with reference model experiments, have the ambition of deducing the macroscopic response of the material to given conditions starting from a detailed knowledge of the fundamental interactions between atoms. It is a long-term approach that bears, however, the promise of being reliable, transferable and beyond empiricism.

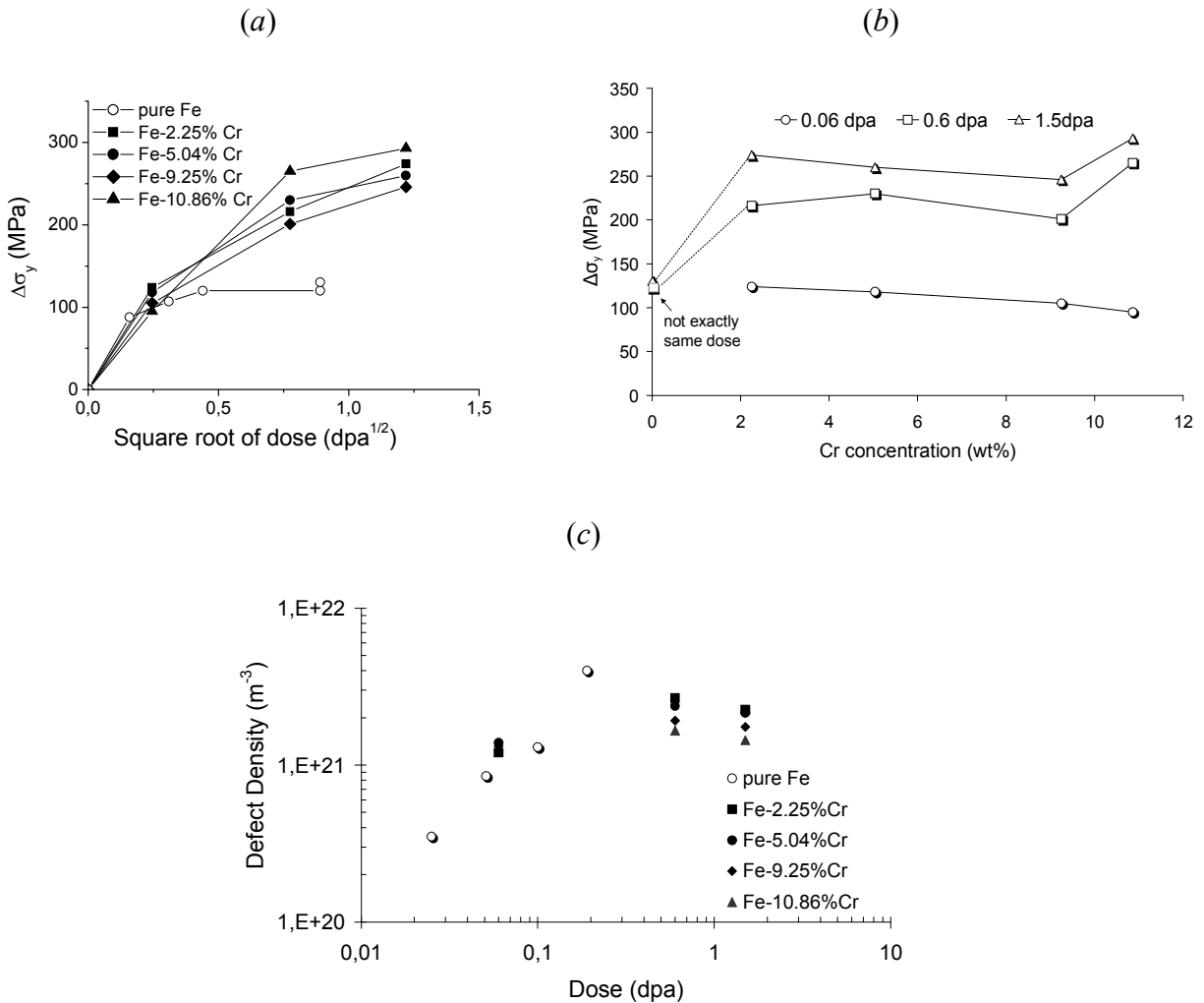
In this paper we give an overview of the current level of understanding of radiation damage in FeCr alloys, based on the results of this modelling and experimental effort. In particular, the change of sign of the mixing enthalpy with growing Cr content and the existence of a strong interaction between Cr atoms and self-interstitial atoms (SIA) is highlighted and used to provide a key for the interpretation of a number of experimental results. In turn, experimental results are used to provide a mechanistic framework to be used as a reference for further investigations, both theoretical and experimental, on this matter.

Experiments and *ab initio* calculations

Experiments clearly show that the addition of Cr to Fe influences significantly the response of the alloy to irradiation and this response is a non-monotonic function of the Cr content. The presence of even small percentages (0.1%) of Cr in ultra-pure Fe induces enhanced nucleation of small dislocation loops of interstitial nature in the early stages of neutron and electron irradiation, with a subsequently higher radiation-induced hardening [24,25]. Enhancement of loop density in electron-irradiated Fe10%Cr at 25°C, as compared to pure Fe, has been also reported [26]. More recently, Arakawa et al. studied the thermal stability of loops in ultra-pure Fe and Fe9%Cr, finding that in the latter loops are stable up to 820 K, while they disappear in the former at 620 K [27]. On the contrary, the formation of voids appears to be suppressed by the presence of Cr in Fe, as shown e.g. by Porollo *et al.* for alloys containing up to 18%Cr after neutron-irradiation up to about 5-7 dpa at 400°C [28,29]. Swelling is thus about one order of magnitude lower in FeCr than in Fe, at the same dose [28-32]: it decreases with the addition of small quantities of Cr, remains low for concentrations between 1 and 10% and then increases again for higher Cr contents. A remarkable effect of Cr concentration is also the reduction of the shift in the ductile-to-brittle transition temperature (ΔDBTT) in irradiated ferritic/martensitic steels. This shift was found to reach a minimum around 9%Cr [33,34], in a range of irradiation temperatures from 300 to 410°C and for doses from 7 to 36 dpa. Recent experiments on FeCr model alloys of concentration up to ~11%, neutron-irradiated at 300°C up to 1.5 dpa in the BR2 reactor, have also demonstrated that radiation-induced hardening ($\Delta\sigma_y$) is higher and saturates at higher dose, than in pure Fe, even though the density of visible defects remains essentially the same in both the pure element and the alloys [22,23]. Again, the dependence on Cr content is not regular: $\Delta\sigma_y$ is larger than in Fe already at low Cr concentration, remains almost independent of Cr content (or slightly decreases) up to ~9%, and then increases again above this critical concentration [22,23]. The

increase of radiation-induced hardening and embrittlement above 9%Cr is qualitatively understandable in terms of radiation-enhanced precipitation of the coherent, Cr-rich α' phase [35,36]. It is, however, not equally clear how to explain the radiation-hardening increase compared to pure Fe at equal concentration of visible defects and even less to understand the reason for the increase of the Δ DBTT caused by irradiation for Cr contents below 9%.

Figure 1. Hardening in irradiated FeCr model alloys vs. dose (a) and Cr concentration (b) (tests at 300°C). Dependence of visible defect density on dose for different Cr concentrations (c).



Even in the absence of irradiation, the FeCr system exhibits a number of peculiarities. Experimental measurement revealed the inversion of the sign of the short-range order (SRO) parameter from negative (at 5%Cr) to positive (at 15%Cr), the zero crossing occurring at about 8-10%Cr, both after thermal ageing and under irradiation [37-39]. This is equivalent to saying that, for example at $\sim 700^\circ\text{C}$, in Fe5%Cr solute atoms tend to be far apart from each other, eventually bringing long range order, in Fe15%Cr they tend to segregate (α' precipitation), and only Fe10%Cr corresponds to an ideal solid solution. An explanation for the origin of this phenomenon came recently from density functional theory (DFT) calculations, which showed that the mixing enthalpy of random or quasi-random FeCr solid solutions is negative below a critical concentration and becomes positive above it [1,12,13]. The analysis of the DFT results revealed that this effect is a consequence of the

magnetic properties of Fe and Cr [12]. Pure Fe is ferromagnetic in its ground state and pure Cr can be described as antiferromagnetic. Thus, if a single Cr atom is inserted in an Fe matrix its magnetic moment will be antiparallel to that of the surrounding Fe atoms. However, if a second Cr atoms is introduced nearby a situation of “magnetic frustration” is produced, because either Cr atom would like to have its magnetic moment antiparallel to both that of the surrounding Fe atoms and to that of the other Cr atom. Since this is impossible, when many Cr atoms are close to each other in Fe different magnetic configurations can result from the competition [12], but in practice the energetically most favourable situation is obtained when the Cr atoms are distributed sufficiently far from each other to avoid magnetic frustration (ordering). When, however, the concentration of Cr is high enough, Cr-Cr interactions cannot be avoided, leading to a positive formation enthalpy, i.e. to a tendency for Cr to form precipitates.

DFT calculations have been also performed to study in detail the interaction between Cr atoms and point-defects in Fe [17]. These studies show that, while the interaction energy between Cr atoms and vacancies in an Fe matrix is negligible (binding energy well below 0.1 eV), self-interstitials interact strongly with Cr atoms. In particular, not only is the mixed FeCr $\langle 110 \rangle$ dumbbell stable but also, and more importantly, both FeFe and FeCr dumbbells can be fairly strongly attracted or repelled by a Cr atom nearby the dumbbell [17]. Isochronal annealing resistivity recovery studies in dilute FeCr alloys showed that the mixed dumbbell is indeed stable and migrates with somewhat lower energy than in pure Fe [40,41]. Similar studies in concentrated FeCr alloys have been interpreted in terms of the existence of trapping configurations for the dumbbell, involving more than one Cr atom and capable of suppressing its migration [40,42]. It is of course rash to extrapolate results of DFT calculations in the presence of only one or two Cr atoms in an otherwise perfectly pure Fe matrix to explain trapping effects in concentrated alloys, but at least the qualitative consistency is worth mentioning.

Thus, the results of DFT calculations concerning single-defect/Cr interaction appear to be in agreement with experiments, for which they provide a key of interpretation. Another result of DFT, not directly comparable with any experimental measurement, but equally important, is that the interaction between a Cr atoms and a $\langle 111 \rangle$ crowdion is strongly attractive and also long-ranged [6,17]. The crowdion is not the ground state configuration for the single-interstitial in Fe and is unlikely to appear even at high temperature, thus in reality single crowdions will hardly ever interact with Cr atoms. Nonetheless this result suggests that the crowdion configuration is stabilised by the presence of high concentrations of Cr and this fact may have important consequences, not only on further lowering the migration energy of the single interstitial at high temperature, by making the crowdion configuration accessible [17], but also because crowdions are the building blocks for self-interstitial clusters of sufficiently large size and dislocation loops in Fe [43,44], so that a strong interaction between crowdions and Cr atoms is likely to translate into a strong effect of Cr atoms on the mobility of self-interstitial clusters and dislocation loops, as will be illustrated further on.

In summary, it is the interplay between the thermodynamic properties and the properties of point-defects and their clusters that determines the microstructure evolution and therefore the macroscopic response to irradiation of an alloy. In FeCr this interplay appears to be particularly involved. The development of quantitative models capable of allowing for these combined effects is highly challenging. One way to proceed is to produce empirical interatomic potentials capable of grasping at least the most important features of the system to be studied, as revealed by first principle calculations and experiments.

Interatomic potentials and their application

The first challenge for the development of an empirical interatomic potential for the FeCr system is the correct reproduction of the change of the sign of the mixing enthalpy, as this involves the introduction of an explicit or implicit dependence on concentration for the sign of the interactions. This task is out of the scope of the traditional embedded-atom method (EAM) [45] and calls for either modifications of this formalism or the development of a totally new formalism. The EAM formalism is based on the assumption that the total energy of the system is the sum of a pairwise interaction contribution and of an “embedding” energy contribution, which is a function of the local electron density. Two modifications of the EAM formalism have been hitherto proposed to fit a sign-changing mixing enthalpy, both focused on the proper fitting of the cross FeCr interaction only, and otherwise using for the pure elements already existing potentials.

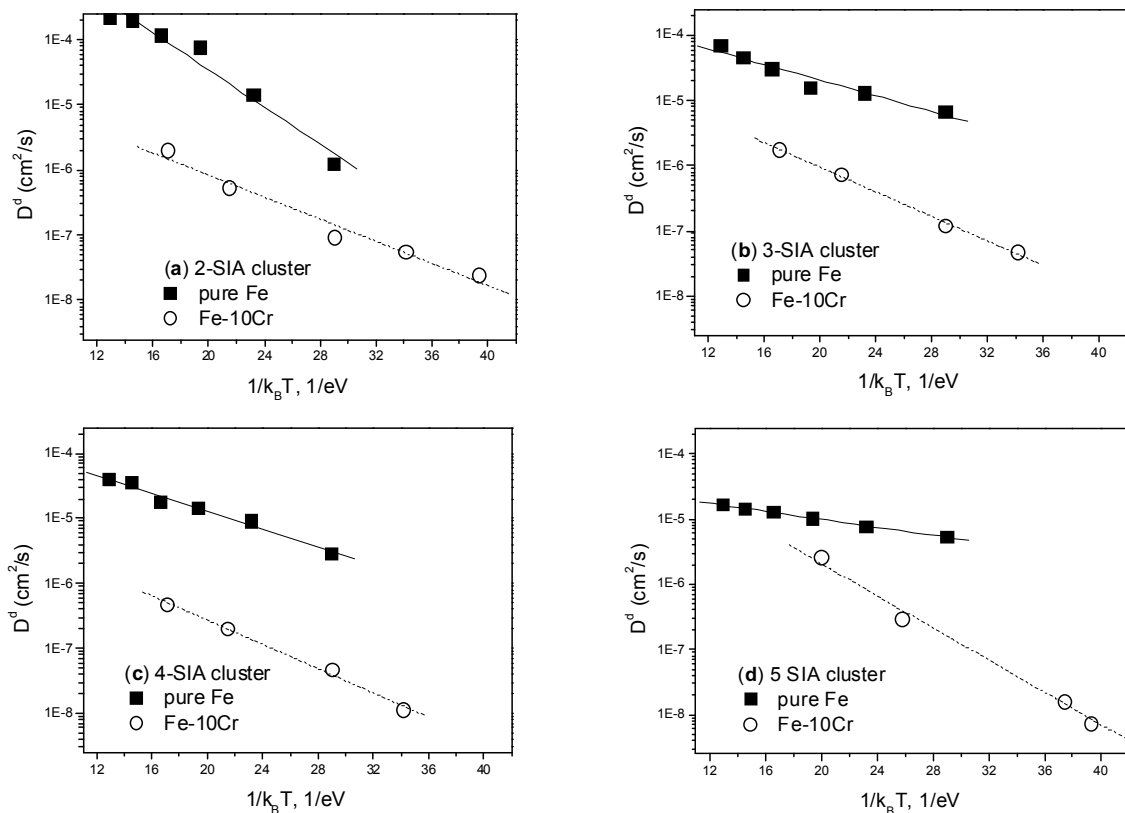
One modification [7], after renormalising the embedding function for the pure elements in such a way that its contribution to the mixing enthalpy becomes negligible, introduces an explicit dependence on concentration by multiplying the pair interaction term times a function $h(x)$, where x is the local concentration of one of the two species and is postulated to be given by the average at the two interacting atoms of the ratio between partial and total electronic densities [18]. The function $h(x)$ can be fitted to reproduce closely the given reference mixing enthalpy curve and enables in principle any shape of such curve to be reproduced. The only deviations will be the consequence of relaxation effects (largely negligible in FeCr, as the atom size misfit is negligible), of the small contribution from the embedding terms and of the accuracy whereby the local atomic concentration is correctly described by the electronic density ratio. This approach will be henceforth denoted as *concentration-dependence method* (CDM).

The other modification [8] introduces the dependence on concentration in an indirect way and follows a somehow opposite route, by working on the embedding part, rather than on the pairwise interaction. Namely, after drawing the attention on the fact that not only *d*-band electrons, but also *s*-band electrons participate in defining the energy of a transition metal alloy, Olsson, *et al.* introduce two separate embedding functions, one for each band, as well as correspondingly separate density functions. The concentration dependence is here contained in the *s*-band mixed electronic density (no *s*-band contribution is assumed in the case of the pure elements) and in practice the presence of the second embedding function provides sufficient degrees of freedom to fit closely any reference mixing enthalpy curve. This approach will be henceforth denoted, for obvious reasons, as *two-band method* (2BM) and we shall mainly focus here on results obtained with this one.

The mixing enthalpy curves at 0 K produced using both the CDM and the 2BM potentials fit closely the data-points obtained from DFT calculations performed as described in [13] in the low Cr concentration region. Even though magnetic effects are not explicitly accounted for in either empirical potential formalism, implicitly they are correctly reproduced, as the Cr-Cr pair repulsion, which is the main consequence of magnetic frustration, is qualitatively and also quantitatively captured by both CDM and 2BM potentials, when compared to DFT values from Refs. [12,13] (see e.g. Refs. [21,46]). It should however be noticed that, as discussed in another paper in these proceedings [47], the proper reproduction of the mixing enthalpy curve is not sufficient to guarantee that the thermodynamic properties of the alloy are correctly reproduced at all temperatures and concentration, so in what follows we shall not provide examples of applications of interatomic potentials for thermodynamic studies. Suffice it to say that, in the range of temperature and Cr concentration of technological interest, the 2BM potential has been shown to provide a reasonably correct prediction of the thermodynamic properties of FeCr to be safely used for other studies [8,16].

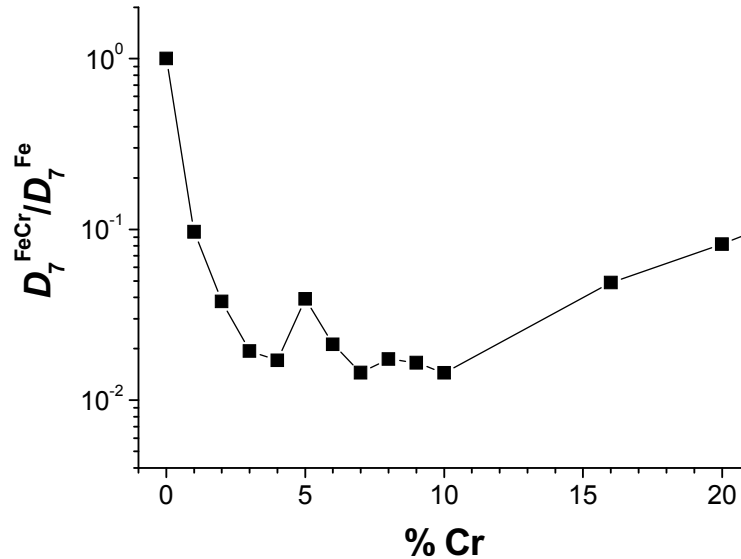
For example, in the fitting procedure for the 2BM potential care was taken to reproduce as correctly as possible also the interaction energies between self-interstitials and Cr atoms, as predicted by DFT calculations. In particular, the stability of the mixed dumbbell was fitted exactly [8] and this proved sufficient to allow the potential to reproduce satisfactorily the energy of a number of configurations involving Cr atoms and self-interstitials [19,46]. Among others, the potential succeeds in providing a satisfactory description of the Cr-crowdion interaction. Thus, the 2BM potential seems adequate to assess, at least qualitatively, the atomic-level consequences of the existence of a strong Cr/self-interstitial interaction and of the stability of the mixed dumbbell on the microstructure evolution under irradiation and for this reason has been extensively used to study the migration processes of self-interstitials and their clusters in FeCr alloys of different concentrations [6,10,48,49]. The diffusion coefficient of a number of small self-interstitial clusters in pure Fe and Fe-10%Cr is shown for example in Figure 2 in the Arrhenius representation, i.e. as a function of $1/k_B T$, k_B being Boltzmann's constant and T the absolute temperature. As can be seen, the diffusion coefficient is invariably orders of magnitude lower in FeCr than in Fe.

Figure 2. The MD calculated diffusion coefficient of small interstitial clusters in Fe and Fe-10%Cr



MD studies have also been performed in FeCr, using the 2BM potential, for the migration of larger self-interstitial clusters [6,10,19,48]. These are describable as collections of parallel $\langle 111 \rangle$ crowdions and diffuse mainly via one-dimensional glide along the direction of the crowdions [43,44]. In Figure 3 the results in the case of a 7-self-interstitial cluster at 640 K for different Cr concentrations in random alloys are summarised, by giving the ratio between the diffusion coefficient of the same cluster in FeCr and in Fe ($D_n^{\text{FeCr}}/D_n^{\text{Fe}}$, where n is the size of the cluster). These simulations are affected by the problem that, within the MD timeframe and space extension, the defect can only visit a limited amount of local atomic configurations, so the average provided by the simulation cannot be

Figure 3. The MD calculated diffusion coefficient ratio in Fe and FeCr vs. Cr content in the case of a 7 self-interstitial cluster at 640 K



quantitatively fully accurate (this problem also accounts for the rough profile obtained by showing all MD data points on the same graph in Figure 3). Nonetheless, qualitatively the result is relevant and clearly shows that, by adding Cr to Fe, the diffusivity of self-interstitial clusters may drop by about two orders of magnitude. This is of course the consequence of the already mentioned strong attractive interaction between Cr atoms and crowdions [17]. The resulting non-monotonic dependence has been rationalised within a formally simple model, which ascribes the drop in the diffusivity ratio to the time spent by the cluster in the different possible Cr configurations that trap it (assuming no influence on the migration mechanism and energy), see Refs. [6,10,11,48]. The delay in the migration will be maximum when each crowdion in the cluster, on average, interacts with one Cr atom only, a situation that will be reached at a critical Cr concentration that can be mathematically estimated [6,10]. Thus the diffusivity ratio will keep decreasing up to that critical concentration. Above it, the same crowdion will start to be “pulled” simultaneously by two Cr atoms, so the effective binding energy will decrease and, consequently, the diffusivity ratio will increase again. Figure 3 shows that the diffusivity ratio reaches a minimum around 10%Cr and then increases again, thereby reminding the swelling dependence on Cr content [28-32]. Indeed, the reduction of the self-interstitial cluster mobility with Cr content will enhance the probability of recombination with freely-migrating single vacancies. Consequently, the rate of formation of voids will decrease and this is equivalent to a reduction in swelling. The close resemblance between the dependence on Cr concentration of cluster mobility and experimentally measured swelling may thus not be accidental.

Microstructure evolution and mechanical property changes under irradiation

As shown, in FeCr the microstructure evolution under irradiation is the consequence of strongly coupled, concomitant phase changes and defect processes that inextricably influence each other. This is the case for all materials, but maybe in this system the problem appears particularly involved. Microstructure evolution models based on mean-field rate-theory approaches [49] or on the solution of the master equation using kinetic Monte Carlo methods (object KMC, see for example Ref. [50]) should therefore, in principle, contain a proper and coupled treatment of both phenomena. In dilute alloys, this is formally possible, up to a certain extent [50]. However, in the case of concentrated

alloys to our knowledge no self-consistent, fully developed methodology nowadays exists capable of treating both problems at the same time and effort is certainly needed in this direction. We can, however, use the inferences from *ab initio* and interatomic potential calculations reported above to qualitatively explain the microstructure evolution, and therefore the changes in mechanical properties, observed experimentally in irradiated FeCr alloys.

The fact that, as summarised in Figure 1, the visible microstructure cannot account, in FeCr, for the measured hardening, which is larger than in Fe at high enough dose (the density of visible defects, mainly dislocation loops, remains essentially constant, whereas the hardening increases with dose and has a non-monotonic dependence on Cr content) [22,23] can be explained by either supposing that a larger density of hardening, but invisible defects are accumulated in FeCr compared to Fe and/or that the visible defects have a different strength with respect to the motion of dislocations in FeCr than in Fe. The former effect can be qualitatively understood if, as suggested by our modelling results, small self-interstitial clusters diffuse more slowly in FeCr, as this situation will also slow down growth and enhance nucleation, thereby leading to the accumulation, with increasing dose, of a large number of small clusters that remain below the resolution of the electron microscope. The latter effect may, on the other hand, be related with a different proportion of $\langle 100 \rangle$ and $\frac{1}{2}\langle 111 \rangle$ dislocation loops depending on Cr concentration [51] and with the fact that $\frac{1}{2}\langle 111 \rangle$ dislocation loops are more effective barriers to dislocation slip than $\langle 100 \rangle$ loops [52]. MD studies to clarify these effects are ongoing. In addition, above $\sim 9\%$ Cr the formation of α' precipitates enhanced by irradiation is expected [35,36]. These precipitates, coherent with the matrix, are hardly visible for the electron microscope, unless they reach large enough sizes, but they are certainly expected to contribute to hardening. On the other hand, the above-mentioned tendency to order, that appears below $\sim 9\%$ Cr under irradiation [37-39], may also influence the mechanical response of the material. A simplified, mechanistic approach can be hence proposed, whereby the radiation-hardening, $\Delta\sigma_y$, in FeCr would be the result of the composition of different contributions:

$$\Delta\sigma_y(FeCr) = \Delta\sigma_y(Fe) + \Delta\sigma_y^{SRO} + \Delta\sigma_y^{invisible} + \Delta\sigma_y^{\langle 111 \rangle / \langle 100 \rangle}$$

Here, $\Delta\sigma_y(Fe)$ represents the hardening in pure Fe, which saturates at relatively low dose and remains, afterwards, essentially constant (Figure 1). The other three terms correspond to phenomena that only occur in the presence of Cr and at higher doses, namely: short-range order parameter changes ($\Delta\sigma_y^{SRO}$), allowing for either ordering or clustering (α'), depending on concentration; accumulation of invisible defects ($\Delta\sigma_y^{invisible}$), most likely small interstitial clusters; and, finally, effect of a different ratio of $\langle 100 \rangle$ -to- $\frac{1}{2}\langle 111 \rangle$ loops ($\Delta\sigma_y^{\langle 111 \rangle / \langle 100 \rangle}$), a term that could also include the effect of possible changes in the average size of the visible loops depending on Cr concentration, independently of the type. It is our belief that the accumulation of invisible defects provides the largest contribution to hardening, as compared to pure Fe, particularly at concentrations below 9%. The other two contributions “modulate” this hardening background. In particular, the zero SRO at 9% may be determining the presence of a local minimum of hardening at that concentration. Precise investigations are needed to confirm or reject these contentions and it is our opinion that this problem can be qualitatively addressed, with good probabilities of success, with the tools currently available, i.e. the existing interatomic potentials and, possibly, some support from DFT. Molecular dynamics simulations of dislocations mobility and their interaction with given microstructural features are indeed nowadays commonplace [53,54]. Simulations of this type with chosen microstructures are likely to provide at least a qualitative answer concerning hardening effects and their dependence on Cr concentration in the presence of defects.

Conclusions

Two main characteristics of the FeCr system, namely the change of sign of the mixing enthalpy from negative to positive in the low Cr concentration region, which is the cause, among other things, of a large solubility limit for Cr in Fe even at low temperature, and the existence of a strong interaction between self-interstitials and Cr atoms, which dramatically reduces the diffusivity of self-interstitial clusters in FeCr compared to Fe, seem to provide in many cases the key for the interpretation of the behaviour of these alloys under irradiation as observed experimentally. In spite of the difficulty of modelling in detail the response to irradiation of concentrated alloys, the integration of model experiments and computer modelling studies, even using already existing tools, is expected to enhance even further our understanding of radiation damage in FeCr alloys, certainly qualitatively and, hopefully, also with a certain degree of quantitative reliability.

Acknowledgements

This work was partially supported by the European Commission (EC) under the contract of Association between EURATOM and the Belgian State and carried out within the framework of the European Fusion Development Agreement (EFDA), task TTMS-007, as well as under contract no. FI6W-CT-2004-516520 (EUROTRANS/DEMETRA Integrated Project).

REFERENCES

- [1] Olsson, P., I.A. Abrikosov, L. Vitos, J. Wallenius, *J. Nucl. Mater.*, 321, 84 (2003).
- [2] Malerba, L., D.A. Terentyev, P. Olsson, R. Chakarova, J. Wallenius, *J. Nucl. Mater.*, 329-333, 1156 (2004).
- [3] Terentyev, D., L. Malerba, *J. Nucl. Mater.*, 329-333, 1161 (2004).
- [4] Wallenius, J., I.A. Abrikosov, R. Chakarova, C. Lagerstedt, L. Malerba, P. Olsson, V. Pontikis, N. Sandberg, D. Terentyev, *J. Nucl. Mater.*, 329-333, 1175 (2004).
- [5] Terentyev, D.A., L. Malerba, M. Hou, *Nucl. Instr. & Meth. in Phys. Res. B*, 228, 156 (2005).
- [6] Terentyev, D.A., L. Malerba, A.V. Barashev, *Phil. Mag. Lett.*, 85 (11), 587 (2005).
- [7] Caro, A., D.A. Crowson, M. Caro, *Phys. Rev. Lett.*, 95, 075702 (2005).
- [8] Olsson, P., J. Wallenius, C. Domain, K. Nordlund, L. Malerba, *Phys. Rev. B*, 72, 214119 (2005).
- [9] D.A. Terentyev, L. Malerba, R. Chakarova, K. Nordlund, P. Olsson, M. Rieth, J. Wallenius, *J. Nucl. Mater.*, 349, 119 (2006).

- [10] D.A. Terentyev, "Study of Radiation Effects in FeCr Alloys for Fusion Applications Using Computer Simulations", PhD dissertation, Free University of Brussels (2006), available on-line at: https://www.sckcen.be/sckcen_en/publications/theses/PhD_Terentyev_v3_06112006.pdf.
- [11] Terentyev, D.A., L. Malerba, SCK•CEN Scientific Report BLG-1026 (June 2006).
- [12] Klaver, T.P.C., R. Drautz, M.W. Finnis, *Phys. Rev. B*, 74, 094435 (2006).
- [13] Olsson, P., I.A. Abrikosov, J. Wallenius, *Phys. Rev. B*, 73, 104416 (2006).
- [14] Shim, J-H., H-J. Lee, B.D. Wirth, *J. Nucl. Mater.*, 351, 56 (2006).
- [15] Caro, A., M. Caro, E.M. Lopasso, D. Crowson, *Appl. Phys. Lett.*, 89, 121902 (2006).
- [16] Malerba, L., SCK•CEN External Report ER-16 (June 2006).
- [17] Olsson, P., C. Domain, J. Wallenius, *Phys. Rev. B*, 75, 014110 (2007).
- [18] Lavrentiev, M.Yu., R. Drautz, D. Nguyen-Mahn, T.P.C. Klaver, S.L. Dudarev, *Phys. Rev. B*, 75, 014208 (2007).
- [19] Terentyev, D.A., P. Olsson, L. Malerba, "Migration of Single Self-interstitials in Dilute and Concentrated FeCr Alloys: an Atomistic Study", submitted.
- [20] Wallenius, J., P. Olsson, L. Malerba, D. Terentyev, *Nucl. Instr. & Meth. in Phys. Res. B*, 255, 68 (2007).
- [21] Caro, A., M. Caro, T.P.C. Klaver, B. Sadigh, E.M. Lopasso, S.G. Srinivasan, *JOM*, 59 (4), p. 52 April 2007.
- [22] Matijasevic, M., A. Al Mazouzi, "Structural and Refractory Materials for Fusion and Fission Technologies", *MRS Proceedings*, Vol. 981E, 0981-JJ07-06 (2006).
- [23] Matijasevic, M., A. Almazouzi, "Effect of Cr on the Mechanical Properties of Fe-Cr Model Alloys", *J. Nucl. Mater.*, submitted.
- [24] Okada, A., N. Kawaguchi, M.L. Hamilton, K. Hamada, T. Yoshiie, I. Ishida, E. Hirota, *J. Nucl. Mater.*, 212-215, 382 (1994).
- [25] Okada, A., H. Maeda, K. Hamada, I. Ishida, *J. Nucl. Mater.*, 271&272, 133 (1999).
- [26] Yoshida, N., A. Yamaguchi, T. Muroga, Y. Miyamoto, K. Kitajima, *J. Nucl. Mater.*, 155-157, 1232 (1988).
- [27] Arakawa, K., M. Hatanaka, H. Mori, K. Ono, *J. Nucl. Mater.*, 329-333, 1194 (2004).
- [28] Garner, F.A., M.B. Toloczko, B.H. Sencer, *J. Nucl. Mater.*, 276, 123 (2000).
- [29] Porollo, S.I., A.M. Dvoriashin, A.N. Vorobyev, Yu.V. Konobeev, *J. Nucl. Mater.*, 256, 247 (1998).
- [30] Little, E.A., D.A. Stow, *J. Nucl. Mater.*, 87, 25 (1979).

- [31] Little, E.A., D.A. Stow, *J. Metal Sci.*, 14, 89 (1980).
- [32] Konobeev, Yu.V., A.M. Dvoriashin, S.I. Porollo, F.A. Garner, *J. Nucl. Mater.*, 355, 124 (2006).
- [33] Kayano, H., A. Kimura, M. Narui, Y. Sasaki, Y. Suzuki, S. Ohta, *J. Nucl. Mater.*, 155-157, 978 (1988).
- [34] Kohyama, A., A. Hishinuma, D.S. Gelles, R.L. Klueh, W. Dietz, K. Ehrlich, *J. Nucl. Mater.*, 233-237, 138 (1996).
- [35] Dubuisson, P., D. Gilbon, J.L. Séran, *J. Nucl. Mater.*, 205, 178 (1993).
- [36] Mathon, M.H., Y. de Carlan, G. Geoffroy, X. Averty, A. Alamo, C.H. de Novion, *J. Nucl. Mater.*, 312, 236 (2003).
- [37] Mirebeau, I., M. Hennion, G. Parette, *Phys. Rev. Lett.*, 53, 687 (1984).
- [38] Filippova, N.P., V.A. Shabashov, A.L. Nikolaev, *Phys. Met. & Metall.*, 90, 145 (2000).
- [39] Sagaradze, V.V., I.I. Kositsyna, V.L. Arbutov, V.A. Shabashov, Yu.I. Filippov, *Phys. Met. & Metall.*, 92, 89 (2001).
- [40] Maury, F., P. Lucasson, A. Lucasson, F. Faudot, J. Bigot, *J. Phys. F: Met. Phys.*, 17, 1143 (1987).
- [41] Abe, H., E. Kuramoto, *J. Nucl. Mater.*, 271 & 272, 209 (1999).
- [42] Nikolaev, A.L., *J. Phys.: Condens. Matter*, 11, 8633 (1999).
- [43] Terentyev, D.A., L. Malerba, M. Hou, *Phys. Rev. B*, 75, 104108 (2007).
- [44] Osetsky, Yu.N., D.J. Bacon, A. Serra, B.N. Singh, S.I. Golubov, *Phil. Mag.*, 83, 61 (2003).
- [45] Daw, M., M.I. Baskes, *Phys. Rev. B*, 29, 6443 (1984).
- [46] Malerba, L., A. Caro, J. Wallenius, "Multiscale Modelling of Radiation Damage and Phase Transformation: The Challenge of FeCr Alloys", *J. Nucl. Mater.*, submitted.
- [47] Bonny, G., R.C. Pasianot, P. Olsson, L. Malerba, "Interatomic Potentials Consistent with Thermodynamics", these proceedings.
- [48] Terentyev, D., L. Malerba, A.V. Barashev, "Modelling of the Diffusion of Self-interstitial Atom Clusters in FeCr Alloys", *Phil. Mag.*, submitted.
- [49] Golubov, S.I., B.N. Singh, H. Trinkaus, *Journ. Nucl. Mater.*, 276, 78 (2000).
- [50] Domain, C., C.S. Becquart, L. Malerba, *J. Nucl. Mater.*, 335, 121 (2004).
- [51] Gelles, D.S., *J. Nucl. Mater.*, 108 & 109, 515 (1982); *ibid.*, 225, 163-174 (1995).
- [52] Gelles, D.S., R. Schäublin, *Mater. Sci. & Eng. A*, 309-310, 82 (2001).
- [53] Bacon, D.J., Yu.N. Osetsky, *Mater. Sci. & Eng. A*, 400-401, 353 (2005).
- [54] Domain, C., G. Monnet, *Phys. Rev. Lett.*, 95, 215506 (2005).

A NEW COMPUTATIONAL METHOD FOR STUDIES OF 3-D DISLOCATION-PRECIPITATE INTERACTIONS IN REACTOR STEELS

Akiyuki Takahashi¹, Nasr M. Ghoniem²

¹Tokyo University of Science, Chiba, Japan

²University of California, Los Angeles, USA

Abstract

To enable computational design of advanced steels for reactor pressure vessels and core structural components, we present a new computational method for studies of the interaction between dislocations and precipitates. The method is based on three-dimensional parametric dislocation dynamics, Eshelby's inclusion and inhomogeneity solutions, and boundary and volume element numerical models. Results from this new method are successfully compared to recent molecular dynamics (MD) simulation results, and show good agreement with atomistic simulations. Then the method is first applied to the investigation of the critical shear stress (CSS) of precipitates sheared by successive dislocation cuttings. The simulations reveal that the CSS is reduced when dislocations cut precipitates, and that it can be as low as half the original value for a completely sheared precipitate. The influence of precipitate geometry and the ratio of precipitate-to-matrix elastic shear modulus on the CSS is presented, and the dependence of the interaction stress between dislocations and precipitates on their relative geometry is discussed. Finally an extension of the method to incorporate the dislocation core contribution to the CSS is highlighted.

Introduction

Alloy design requires optimisation of many, and often conflicting requirements, such as strength, ductility, corrosion resistance, etc. Precipitation strengthening is one of the most effective techniques to design advanced alloys with superior strength characteristics. The mechanism is based on blocking the motion of dislocations by second phase precipitates that are dispersed in the alloy's matrix, and thus results in significant improvements in the yield strength and hardness of the alloy. It is therefore essential that the interaction between dislocations and precipitates is accurately and efficiently modelled in order to explore the basic physics of these interactions and to enable rational alloy design.

When dislocations approach precipitates, they experience attraction/repulsion forces that can significantly retard their motion. Such forces result from a number of factors: (1) mismatch between the elastic properties of the matrix and precipitate; (2) coherency strains between the precipitate and matrix; (3) misfit dislocations at incoherent precipitate-matrix interfaces; (4) changes in the core structure of dislocations as they penetrate precipitates. In practice, however, not all these factors exist simultaneously, and one or several of them are utilised for strengthening. We will focus here on the influence of the first two factors on precipitation strengthening.

Several theoretical studies on precipitation strengthening have been based on statistical assumptions for precipitate distributions and shapes, and on simplified dislocation geometry [1-4]. During a dynamic interaction process, dislocations can have a complicated shape, and frequently change their shapes. Moreover, precipitates are not generally spherical. Recently, Van der Giessen and Needleman developed a computer simulation technique to simulate dislocation dynamics in a finite volume with boundary conditions based on a superposition principle [5]. The method is a hybrid of dislocation dynamics (DD) and finite element method (FEM). Shin, *et al.* applied the idea to the simulations of the interaction between a dislocation and impenetrable precipitate [6,7]. However, up till now, no method has been advanced for studies of the interaction between dislocations and penetrable precipitates in the most general sense.

The objective of this work is to develop a computational method for solving dislocation-precipitate interaction problems based on linear elasticity theory, which enables us to investigate the interaction between flexible dislocations and penetrable precipitates. Based on the superposition principle, the solution for the dislocation-precipitate interaction problem can be obtained as the sum of the solutions to two different problems: (1) a dislocation problem with image stresses from interfaces between precipitates and the matrix; (2) a precipitate problem with initial stresses, which result from the elastic constants mismatch between the precipitate and the matrix and the *eigen* strain in the precipitate. The dislocation problem is solved here by the parametric dislocation dynamics (PDD) method. For the precipitate problem with initial stresses, a boundary integral equation is formulated and solved by the boundary element method (BEM). The accuracy of the method is confirmed by comparing the numerical results to MD simulation results. Then, the method is applied to investigations of the critical shear stress (CSS) of precipitates. Finally, an extension of the method to incorporate the dislocation core effect is discussed.

Computational method

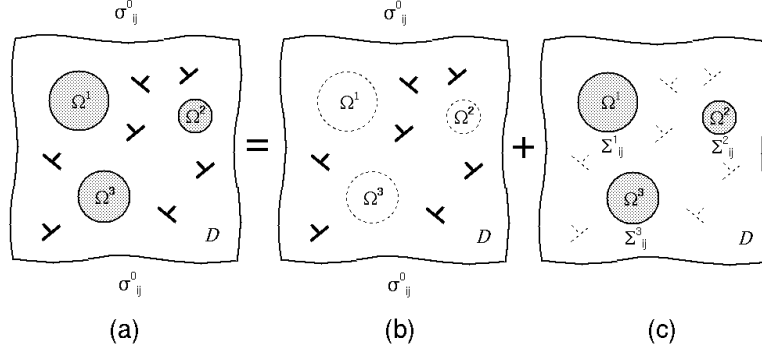
Let us consider N_p coherent precipitates with eigen strains ϵ_{ij}^m and elastic constants C_{ijkl} in an infinite body with elastic constants C_{ijkl} . The superscript m denotes the m^{th} precipitate. The infinite body D contains an arbitrary number of dislocations, and is subjected to an external stress σ_{ij}^0 at infinity. Following Mura [8], we describe the stress in $D-\Omega$ and Ω^m as:

$$\begin{aligned}\sigma_{ij}^0 + \sigma_{ij} &= C_{ijkl} (\varepsilon_{kl}^0 - \varepsilon_{kl}) & \text{in } D - \Omega \\ \sigma_{ij}^0 + \sigma_{ij} &= C_{ijkl}^m (\varepsilon_{kl}^{m,0} + \varepsilon_{kl}^m - \varepsilon_{kl}^m) & \text{in } \Omega^m\end{aligned}\quad (1)$$

where, $\varepsilon_{ij}^0 = C_{ijkl}^{-1} \sigma_{kl}^0$, $\varepsilon_{ij}^{m,0} = C_{ijkl}^{m,-1} \sigma_{kl}^0$, and ε_{ij} is the strain produced by dislocations and the external stress. The domain Ω contains the total volume of N_p precipitates.

Figure 1. Schematic for the dislocation-precipitate interaction problem with the superposition principle

(a) Original problem, (b) the dislocation problem with image stresses, and (c) the correction problem with initial stresses Σ_{ij}^m



As shown in Figure 1, using the superposition principle, the problem can be decomposed into two problems: (1) a dislocation problem in an infinite homogenous body; (2) a correction problem, which is an elastic problem of precipitates. At first, the stress in the original problem is described by a summation of the stress $\tilde{\sigma}_{ij}$ in the dislocation problem and the stress $\hat{\sigma}_{ij}$ in the correction problem. Then the stress $\tilde{\sigma}_{ij}$ in the dislocation problem is defined by:

$$\tilde{\sigma}_{ij}^0 = C_{ijkl} (\varepsilon_{kl}^0 + \tilde{\varepsilon}_{kl}) \quad \text{in } D \quad (2)$$

where, $\tilde{\varepsilon}_{ij}$ is the strain produced by dislocations in D . The stress $\hat{\sigma}_{ij}$ in the correction problem can then be defined by:

$$\begin{aligned}\hat{\sigma}_{ij} &= C_{ijkl} \hat{\varepsilon}_{kl} & \text{in } D - \Omega \\ \hat{\sigma}_{ij} &= C_{ijkl}^m \hat{\varepsilon}_{kl}^m - C_{ijkl}^m \varepsilon_{kl}^m + (C_{ijkl}^m - C_{ijkl}) (\varepsilon_{kl}^{m,0} + \tilde{\varepsilon}_{kl}) = C_{ijkl}^m \hat{\varepsilon}_{kl}^m + \Sigma_{ij}^m & \text{in } \Omega^m\end{aligned}\quad (3)$$

where $\Sigma_{ij}^m = -C_{ijkl}^m \varepsilon_{kl}^m + (C_{ijkl}^m - C_{ijkl}) (\varepsilon_{kl}^{m,0} + \tilde{\varepsilon}_{kl})$. From above equations, the correction solution can be considered as the solution to an inhomogeneity problem with an initial stress Σ_{ij}^m . In this work, the dislocation problem and the dynamics of dislocations are computed by the parametric dislocation dynamics (PDD) method [9]. The detail of the PDD method can be found in elsewhere [9,10]. Boundary integral equations for the infinite body and precipitates can be derived as:

$$\begin{aligned}c_{ij}(P) \hat{u}_j(P) &= \int_{\Gamma} (U_{ij}(P, Q) \hat{t}_j(Q) - T_{ij}(P, Q) \hat{u}_j(Q)) d\Gamma & \text{for } D - \Omega \\ c_{ij}(P) \hat{u}_j^m(P) &= \int_{\Gamma^m} (U_{ij}^m(P, Q) \hat{t}_j^m(Q) - T_{ij}^m(P, Q) \hat{u}_j^m(Q)) d\Gamma - \int_{\Omega^m} \Sigma_{jk}^m(q) U_{ij,k}^m(P, q) d\Omega & \text{for } \Omega^m\end{aligned}\quad (4)$$

where, c_{ij} is the shape factor, U_{ij} and T_{ij} are the kernel functions. u_j and t_j are respectively the displacements and tractions on the interface Γ between the infinite body and precipitates.

Assuming that the infinite body and precipitates are perfectly bonded, the displacements and the tractions on the interfaces must satisfy the continuity condition for displacements and the equilibrium condition for tractions. Using the conditions, we can solve Eq. (4) and compute the displacements and tractions on the interfaces. Once the displacements and tractions are obtained, the stress at any point can be easily computed by:

$$\hat{\sigma}_{ij}(p) = \int_{\Gamma} (D_{ijk}(p, Q)\hat{t}_k(Q) - S_{ijk}(p, Q)\hat{u}_k(Q))d\Gamma \quad (5)$$

It is worth noting that there is a singularity in the stress calculation by the boundary element method when the calculation point is close to the boundary. Also the stress of the dislocation involves a strong singularity within a range of the dislocation core. In this work, these singularities are simply removed by introducing a cut-off radius $2b$, which is typically used as a radius for the dislocation core. The stresses within the cut-off distance are kept to be a constant.

Comparison with molecular dynamics

One of the key phenomena that determine the degree of embrittlement of pressure vessel steels is the interaction between dislocations in an iron matrix with small copper precipitates in steels. Several MD simulations have been carried out to determine the atomistic origins of this interaction [11,12]. Kohler, *et al.* performed MD simulations of the interaction between an edge dislocation and a copper precipitate in iron, and determined the critical shear stress for the edge dislocation to break away from the interaction with the copper precipitate [12]. In this work, we compare the results of MD with those of the present method to examine the accuracy and consistency with the MD results. In the simulations, the size of the simulation volume is $19.7 \times 9.73 \times 19.7$ nm, and the x, y and z axes are along [111], [1 $\bar{1}$ 0] and [11 $\bar{2}$] directions, respectively. A spherical copper precipitate with a diameter d_{Cu} and an edge dislocation with [111] Burgers vector on (1 $\bar{1}$ 0) slip plane are placed in the volume. The centre of the copper precipitate is on the slip plane of the dislocation. Periodic boundary conditions are applied along [11 $\bar{2}$] direction, which implies that the edge dislocation is infinitely long, and that the precipitate is one of a periodic array in the [11 $\bar{2}$] direction. The CSS is evaluated by gradually increasing the external shear stress by 5 MPa each 1 000 time steps. Their calculated shear modulus for the iron matrix and copper precipitate are $\mu_1 = 69.76$ GPa and $\mu_2 = 21.842$ GPa, respectively. Although the experimental values of the shear moduli are higher, we used the same elastic constants of Kohler, *et al.* in the present simulations. This allows direct comparison between the elasticity results (present method) and the results of MD simulations, which are based on interatomic potentials. In order to examine the convergence of the accuracy of the present method, we used different boundary and volume element mesh densities resulting in successively higher resolution, while the length of each parametric segment is set to be 1 nm in all simulations. In this work, the density of the boundary element meshes is expressed with a parameter γ , which is the ratio of the average area for one boundary element and total area of the surface of the precipitate.

Figure 2 shows the dislocation configurations during the interaction with a 3 nm diameter copper precipitate. In the figure, the dislocation is first attracted by the copper precipitate. It then moves spontaneously to the middle of the copper precipitate to achieve equilibrium in the precipitate interior. A higher force is required to pull the dislocation out of the precipitate, and thus the precipitate temporarily pins the dislocation till a higher force is applied. Finally the dislocation cuts through the copper precipitate when the external shear stress is sufficiently increased resulting in a break-away condition.

Figure 2. Configurations of the edge dislocation interacting with the copper precipitate with $d_{Cu} = 3$ nm. (a) and (b) are the configurations during the process to reach an equilibrium configuration from the initial straight dislocation. (c) is the configuration of the most bent dislocation configuration due to interaction with the precipitate. (d) is after the interaction.

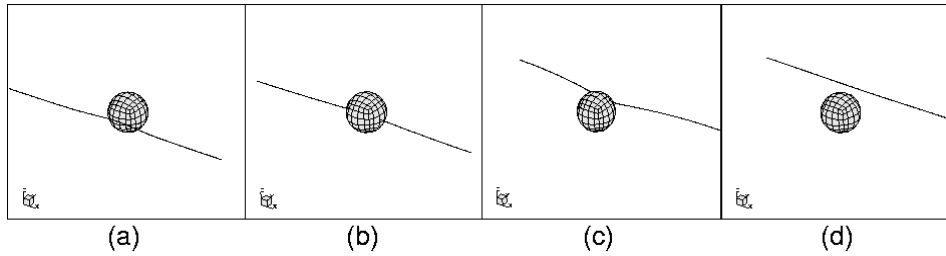
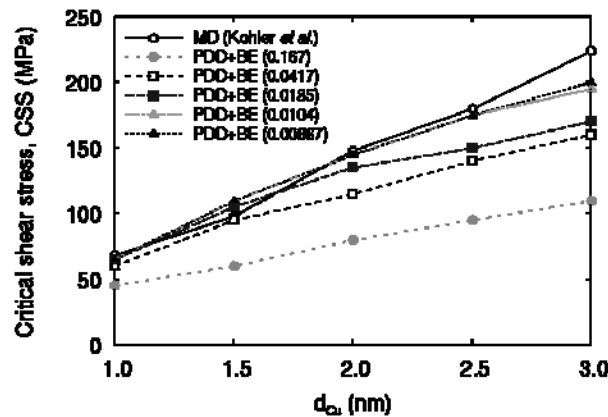


Figure 3 shows the dependence of the CSS on precipitate diameter, calculated by the present method and compared to the results of MD simulations. In the figure, the CSS calculated with a coarse mesh ($\gamma = 0.167$) displays a large deviation from MD simulation results. However, the CSS converges gradually to MD results as the mesh resolution is increased (smaller γ values). Note that the results for $\gamma = 0.0104$ and 0.00667 are almost the same indicating convergence, and that the results are in reasonable agreement with MD simulations.

Figure 3. Dependence of the critical shear stress (CSS) for an edge dislocation in Fe cutting through a copper precipitate on its diameter. Results of the calculations are compared to the MD computer simulations by Kohler, *et al.* The numbers in brackets are the γ values, indicative of the boundary element mesh resolution.



Applications

Dislocation interaction with sheared precipitates

When the shear modulus of precipitates is below the Orowan limit, they can be sheared by the passage of dislocations through them. Every time a dislocation shears, its resistance to dislocation motion is reduced. If the precipitate is sheared a number of times, and the overall resistance of the two sheared pieces becomes sufficiently low, many dislocations can slip through the sheared region in an avalanche fashion, and a zone of localised plastic deformation is formed in the matrix. This mechanism can result in plastic flow localisation and the formation of cleared dislocation channels in precipitation hardened materials. In this section, we evaluate the CSS of precipitates with a diameter of 2.5 nm and an

elastic shear modulus $\mu_p = 54.6$ GPa cut by dislocations in an Fe matrix. Every time the precipitate is completely sheared, the two halves are shifted relative to one another by the magnitude of Burgers vector and two new surfaces on the slip plane of the dislocation are formed. In the following series of simulations, we use a volume of $19.7 \times 9.73 \times 19.7$ nm, with the x, y and z axes along the $[111]$, $[1\bar{1}0]$ and $[11\bar{2}]$ directions, respectively. An edge dislocation with $[111]$ Burgers vector on the $(1\bar{1}0)$ slip plane that cuts through the middle of a spherical precipitate are placed in the simulation volume. Periodic boundary conditions are applied along the $[11\bar{2}]$ direction, which correspond to a periodic 1-D array of precipitates. The elastic constants of the iron matrix is taken as $\mu_m = 81.8$ GPa.

Figure 4 shows the dislocation configuration during the interaction with a 2.5 nm diameter precipitate that has been completely sheared by the passage of 10 previous dislocations. As the dislocation glides along the surfaces of the two precipitate halves, it is partially locked at the edges, thus forming bow-out pinned configurations. The dislocation bow-out is slightly exerted by the external shear stress and the pinning effect of the precipitate. Finally, the dislocation breaks away from the precipitate when the external shear stress is sufficiently increased. Figure 5 shows the calculated “relative” CSS of slipped precipitates as a function of the number of previous dislocation passages or “cutting” through the precipitate. Note that the CSS is normalised by $\tau_o = \mu_m b/L$, where L is the spacing between the precipitates. It is shown the CSS rapidly decreases each time the precipitate is cut by a dislocation. As the number of the dislocation cuttings is increased, the CSS decreases further, but gradually converges to a constant value. We also performed a simulation for the interaction between an

Figure 4. Configurations of the edge dislocation interacting with the slipped copper precipitate. The precipitate halves are displaced by $10b$. (a) and (b) are the configurations during the process of reaching equilibrium from the initial straight dislocation configuration. (c) is the most bent dislocation configuration by the precipitate. (d) is after the interaction.

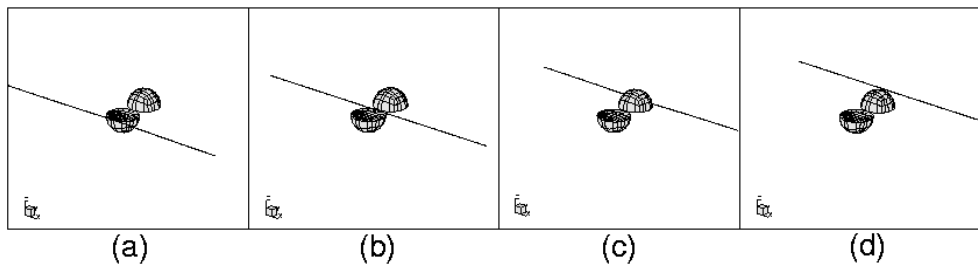
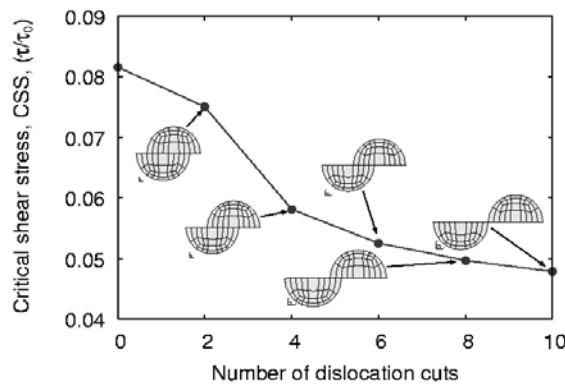


Figure 5. The dependence of the relative critical shear stresses of the slipped precipitates on the number of dislocation “cuttings”. The critical shear stress is normalised by $\tau_o = \mu_m b/L$.



edge dislocation and half of a precipitate, which corresponds to a precipitate slipped an infinite number of dislocation cuttings. The calculated relative CSS was found to be $0.0431\tau_0$, which is almost half of the CSS of the spherical precipitate. The simulations with the present method reveal that the resistance of precipitates to dislocation motion is rapidly weakened by previous dislocation cuttings, and may decrease to about half of the CSS of an uncut spherical precipitate.

Influence of precipitate geometric & elastic parameters on strength

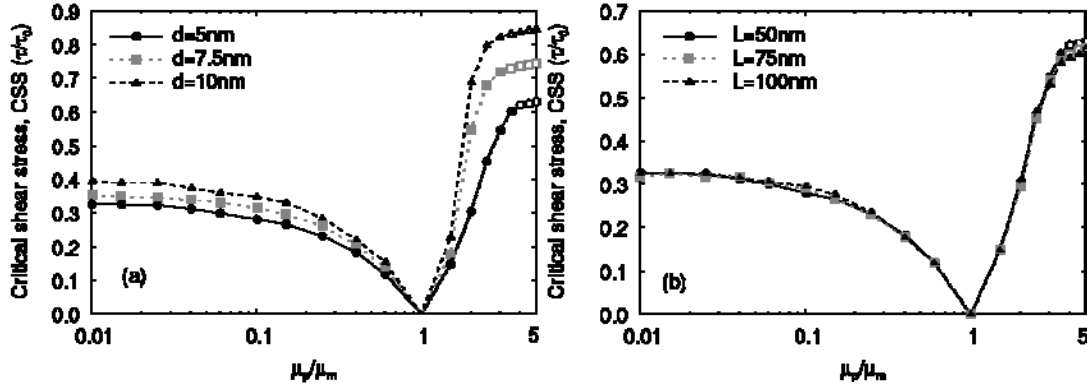
Precipitation strengthening is derived from a number of factors, such as precipitate geometry, spatial arrangement, and the relative magnitude of the elastic modulus compared to the host matrix. One of the important aspects here is the effect of the elastic modulus mismatch between the precipitate and the host matrix. If the shear modulus of the precipitate is smaller than that of the matrix, dislocations can easily cut through the precipitate. Even if the precipitate shear modulus is somewhat larger than that of the matrix, the dislocation can still cut through the precipitate and reconfigure to its original form before the interaction. However, precipitates with much larger elastic modulus compared to the matrix can present impenetrable obstacles to dislocation motion. In this case, dislocations must completely encircle the precipitate and leave a small loop surrounding the precipitate before they reconfigure and break-away from the precipitate. This interaction limit is known as the Orowan mechanism.

Utilising the present method, we investigate the influence of a number of important geometric and elastic parameters on the CSS, and hence on the strengthening effect of precipitates. These are: (1) the precipitate diameter; (2) the spacing between precipitates; (3) the ratio of the precipitate-to-matrix shear modulus. The simulation volume is $50 \times 50 \times 50$ nm, with the x, y and z axes taken along the $[111]$, $[1\bar{1}0]$ and $[11\bar{2}]$ directions, respectively. A spherical precipitate with a diameter of 5 nm is placed in the middle of the simulation volume. A straight edge dislocation with $[111]$ Burgers vector on the $(1\bar{1}0)$ slip plane is also introduced, and is initially placed 10 nm away from the precipitate. Periodic boundary conditions are applied along the $[11\bar{2}]$ direction to simulate the interaction of a one-dimensional precipitate array with the dislocation. The elastic shear modulus of the matrix material μ_m is taken as 81.8 GPa, and of the precipitate shear modulus, μ_p , is changed in the range from $0.01 \leq \mu_m/\mu_p \leq 5$ in order to investigate the effect of the elastic modulus mismatch between the precipitate and the matrix on the CSS.

To investigate the influence of the precipitate diameter and modulus on the strength, a set of simulations were performed for a range of precipitate-to-matrix shear modulus ratios, and for initial precipitate diameters of 5, 7.5, and 10 nm. The results of the simulations are shown in Figure 6(a), where the CSS is normalised by the reference shear stress $\tau_0 = \mu_m b/L$. It is shown that larger precipitates have a stronger strengthening effect, and that the CSS is dependent also on the relative elastic modulus mismatch. Softer precipitates ($\mu_p/\mu_m \leq 1$) still result in strengthening ($\tau/\tau_0 > 0$), and in the limit of very soft precipitates, the strengthening effect saturates to $\tau/\tau_0 \approx 0.3 - 0.4$. On the other hand, harder precipitates are still shearable up to μ_p/μ_m ratios on the order of 3-4, where the Orowan looping mechanism sets in, as shown in the figure with hollow symbols. It is also noted that the strength sensitivity to the μ_p/μ_m ratio in the Orowan regime is considerably smaller than in the shearable precipitate regime.

The transition from the shearable precipitate to the Orowan regime depends on the precipitate size, as shown in the figure. The self-force on the dislocation surrounding the precipitate mainly depends on the diameter of the precipitate, and is large when the diameter of the precipitate is small. For small precipitates, the dislocation prefers to cut through them as a result of the strong self-force on the dislocation. Therefore, the precipitate with a small diameter must have a large elastic shear modulus to stop the dislocation from cutting it, and hence the onset of the Orowan mechanism must take place at larger μ_p/μ_m values for a precipitate with a smaller diameter.

Figure 6. Dependence of the CSS on the precipitate-to-matrix shear modulus ratio. The effect of (a) the precipitate diameter and (b) the spacing between precipitates on the strength is shown, where the solid symbols are for dislocations cutting through precipitates while the hollow symbols are for dislocations looping around the precipitate by the Orowan mechanism.



Next, we investigate the effect of the inter-precipitate spacing on the strengthening effect by changing the length of the simulation volume in the $[11\bar{2}]$ direction to 50, 75, and 100 nm. The results of the simulations are shown in Figure 6(b), where the CSS is normalised by the reference shear stress with different values of L . It is clear from the figure that the normalised shear stress is insensitive to the inter-precipitate spacing over a wide range of μ_p/μ_m ratios. This is indicative of the direct inverse proportionality between the CSS and L , as predicted by the Orowan formula. Small deviations from the inverse proportionality can be seen for very large μ_p/μ_m ratios, indicating a slight dependence on the precipitate size as well.

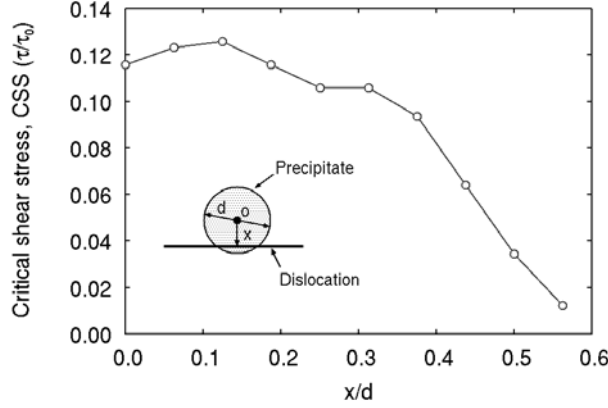
Influence of position of slip plane

In the previous sections, only the dislocation-precipitate interactions at the middle of the precipitate are simulated. However, in many cases, dislocations interact with precipitates not only at the middle of precipitates, and also at the different positions. The CSS of precipitates may be a function of the position of the interaction, and approach to zero when the distance between the precipitate and the dislocation becomes sufficiently large. To investigate the distribution of the CSS within the precipitates, we performed simulations of the dislocation-precipitate interaction at different positions of the precipitate using the present method. In the simulations, the simulation volume and the boundary conditions are the same as those used in the previous section. The elastic shear modulus of the precipitate is $\mu_p = 54.6$ GPa, and that of the matrix is $\mu_m = 81.8$ GPa. The diameter of the precipitate is $d = 5$ nm and the spacing between the precipitates is 50 nm. The position of the slip plane of the dislocation is changed in a range from 0 to $0.55d$ from the centre of the precipitate. Figure 7 shows the simulation results. As shown in the figure, the CSS is almost equal near the centre of the precipitate. However, the CSS sharply drops down to a small value, when the position goes from $0.3d$ to the interface between the precipitate and the matrix. When the position is $0.55d$, the CSS is almost 10% of that at the centre of the precipitate. The results tell us that the interaction force from the precipitate has a large dependence of the position of the interaction and works only in a very close range from the precipitate.

Dislocation core effects

The present method can accurately simulate the elastic interaction between dislocations and precipitates. However, a change in the dislocation core structure can also give a great contribution to the

Figure 7. Dependence of the CSS on the position of interaction with a dislocation. The CSS is normalised by a reference stress $\tau_o = \mu_m b/L$.



strengthening mechanism. Thus, modelling of the dislocation core effects on the dislocation-precipitate interaction is of another interest to find an effective way to achieve an requirement for the strength of alloys. An idea to incorporate the dislocation core effects into the simulations with the present method is to utilise the Pierels-Nabarro (PN) model [13]. The PN model gives an equation to give the distribution of the dislocation core displacement based on an elastic interaction between the dislocation core displacements u_c , and the lattice restoring stress p that is:

$$p = \alpha \int_{-\infty}^{\infty} \frac{1}{x' - x} \frac{du_c}{dx'} dx \quad (6)$$

where α is a constant, $\mu/\pi(1 - \nu)$ for edge dislocations and μ/π for screw dislocations. Generally, in the DD simulation, one dislocation is represented with one line with a perfect Burgers vector. In order to describe the distribution of the dislocation core displacement, one dislocation line is represented by N lines with b/N Burgers vector, where b is the magnitude of the perfect Burgers vector. The dislocation core displacement can be written as $u_c = b/2N$. Then Eq. (6) can be transformed into a discretised form as [14]:

$$p_i = \alpha \frac{b}{2N} \sum_{j \neq i}^N \frac{1}{x_i - x_j} \quad (7)$$

where, p_i is the lattice restoring stress on the i^{th} dislocation. The right hand side of Eq. (7) is the elastic interaction term, and can be naturally calculated by the DD method, because the DD method is essentially based on the elastic interaction between dislocations. Then the modification for the implementation of the discretised form of the PN model into the DD simulation is only to add the lattice restoring stress to the total stress. One of the ways to calculate the lattice restoring stress is:

$$p_i = -\nabla \gamma(u_i) \quad (8)$$

where, γ is the generalised stacking fault (GSF) energy, which can be obtained by the *ab initio* calculations [15]. Additional data for the hybrid PDD-BEM-PN simulation of the dislocation-precipitate interaction with the dislocation core effects is only the GSF energies for the matrix, precipitate, and near the interface between the precipitate and the matrix. Therefore, the hybrid PDD-BEM-PN method is very promising to model both the elastic interaction and dislocation core effect.

Conclusions

We successfully developed a new computational method for the dynamics of the most general dislocation-precipitate interaction in 3-D, which is based on a hybrid of the parametric dislocation dynamics (PDD) and the boundary element method (BEM). The method shows excellent agreement with MD simulation results. Then the method was applied to the investigation of the CSS of the sheared precipitate, and revealed that the resistance to dislocation motion is reduced by the successive passage of a dislocation, and it goes down and converges to the half of its original CSS when the two halves of the precipitate is displaced to a very long distance. The method was also applied to the investigation of the CSS with different precipitate-to-matrix elastic modulus. The simulation found out that the most critical range for the effect of this ratio is between 0.1 and 4, and that the Orowan looping regime occurs for the ratios above approximately 3-4. Moreover, the change in the interaction force within the precipitate is studied using the present method. The resistance force from the precipitate effectively works only in the range from $-0.3 d$ to $0.3 d$, and is sharply reduced to a very small value. The interaction range was very narrow from the interface of the precipitate. Finally, we presented an idea to incorporate the dislocation core contribution to the present method, which must be very promising to realise more realistic simulation of the dislocation-precipitate interactions.

Acknowledgements

Research for this project has been funded by the Department of Energy (DOE), Office of Nuclear Energy, under grant number DE-FC07-06ID14748 with UCLA.

REFERENCES

- [1] Friedel, J., *Dislocations*, Pergamon Press, Oxford (1964).
- [2] Nembach, E., *Phys. Stat. Sol. (a)*, 581, pp. 571-581 (1983).
- [3] Fleischer, R.L., *Acta Metall.*, 9, pp. 996-1000 (1961).
- [4] Fleischer, R.L., *Acta Metall.*, 11, pp. 203-209 (1963).
- [5] van der Giessen, E., A. Needleman, *Modelling Simul. Mater. Sci. Eng.*, 3, pp. 5499-5518 (1995).
- [6] Shin, C.S., M.C. Fivel, M. Verdier, K.H. Oh, *Philos. Mag.*, 83, pp. 3691-3704 (2003).
- [7] Shin, C.S., M. Fivel, W.W. Kim, *Modelling Simul. Mater. Sci. Eng.*, 13, pp. 1163-1173 (2005).
- [8] Mura, T., "Micromechanics of Defects in Solids", Martinus Nijhoff, Dordrecht (1982).
- [9] Ghoniem, N.M., S-H. Tong, L.Z. Sun, *Phys. Rev. B*, 61, pp. 913-927 (2000).

- [10] Ghoniem, N.M., L.Z. Sun, *Phys. Rev. B*, 60, pp. 128-140 (1999).
- [11] Osetsky, Y.N., D.J. Bacon, *Philos. Mag.*, 83, pp. 3623-3641 (2003).
- [12] Kohler, C., P. Kizler, S. Schmauder, *Modelling Simul. Mater. Sci. Eng.*, 13, pp. 35-45 (2005).
- [13] Nabarro, F.R.N., *Proc. Phys. Soc.*, 59, pp. 256-272 (1947).
- [14] Banejee, S., N.M. Ghoniem, N. Kioussis, *Proc. MMM-2*, pp. 23-25 (2004).
- [15] Lu, G., N. Kioussis, V.V. Bulatov, E. Kaxiras, *Phys. Rev. B*, 62, pp. 3099-3107 (2000).

ON THE THEORETICAL DEVELOPMENT OF NEW CREEP RESISTANT ALLOYS AND THEIR EMPIRICAL VALIDATION

D. Gaude-Fugarolas, N. Régent, Y. De Carlan

CEA Saclay

SRMA/LA2M Bât. 453

F-91191 Gif-sur-Yvette Cedex France

Abstract

In anticipation to the present revival of nuclear power, and to obtain more efficient, secure and environmentally-friendly power plants, new families of high temperature resistant, low activation materials are under development. This work presents an example of work performed at CEA during the development of novel ferrito-martensitic reduced activation alloys for Generation IV and Fusion applications.

In the past, the process of designing a new material was mostly heuristic, requiring repeated experimental trial and error, but nowadays, synergies between the accuracy of current scientific knowledge in thermodynamics and transformation kinetics and increased computer capacity enables us to design successful new alloys using minimal empirical feedback. This work presents this comprehensive and multi-model approach to alloy and microstructure design. The CALPHAD method, thermo-kinetic modelling of precipitation reactions and artificial neural network analysis are combined in the development of new alloys having their compositions and microstructures optimised for maximum creep resistance.

To complete this work, a selection of the alloys designed has been cast and the results obtained during alloy design and the modelling of various heat treatments have been verified. Optical and electronic microscopy have been used to characterise the microstructure. Uniaxial tensile tests have been used to measure the mechanical performance of the alloys presented at room, service and higher temperatures. The characterisation of the behaviour of the material in service conditions is underway with relaxation and creep tests.

Introduction

The development of new and improved alloys for critical applications had been hitherto (and in a great measure still is) a lengthy and expensive process, requiring multiple iterations of alloy design, casting and testing. However, the present level of scientific knowledge and the use of modern computational methods permit to ease and reduce this process substantially. One of the fields can benefit the most of the improved methods and the shorten development time is, undoubtedly, the power generation industry.

In order to satisfy more demanding efficiency requirements and to achieve better environmental and economic performance, modern power generation industry requires a continuous process of improvement. New materials able to outperform present ones in safety, mechanical properties and service temperature are a continuous need in this process. In order to achieve these goals better materials are needed, which enable to work under more demanding requirements of service temperature, life length, and creep resistance. In particular, in the case of nuclear power generation, critical components are required to withstand their service conditions for the complete operation life of the power plant, sometimes up to 50 or 60 years. In cases like that, it is also important to be able to predict accurately the evolution of the microstructure during and to the end of the service life of each component. Obviously, it is not practical to perform life tests of all possible conditions, and specially tests of the duration of the real working life of the component.

The work presented here exemplifies the use of various thermodynamic and statistic tools in the design of new creep resistant alloys for the nuclear industry, and the prediction of their microstructural evolution during service life. The design process is still iterative, each stage leading to a more refined definition of the final alloy. The difference with the traditional approach is that most of the work is performed theoretically or computationally, involving the production of only a few essential experimental casts to corroborate the suitability of the final composition and thermo-mechanical treatments required to obtain an optimal performance.

Design methodology

Summary of the method

The design method starts by a stage of exploration of the scientific literature and the industrial *expertise* in order to delimit the choices of composition and microstructure that will be analysed and optimised later on.

In order to narrow the range of composition and heat treatment for the alloy to obtain good creep resistance, an advanced statistical method has been used, an artificial neural network. By using this type of multi-dimensional non-linear regression method, it was possible to analyse a large quantity of data on creep resistance of many alloys and to obtain guidelines as to design an improved material.

After a narrow composition has been selected, CALPHAD-based thermodynamic models like ThermoCalc, MTDATA or MatCalc were used to ascertain whether a suitable microstructure could be obtained. Finally thermo-kinetic model like MatCalc, which is able to calculate the kinetics of multiple simultaneous precipitation reactions in multi-component alloys, was used to find the heat treatment necessary to obtain the optimal microstructure (i.e. the finest precipitate distribution).

Comprehensive validation of the alloys developed must follow the theoretical design, starting with the static mechanical properties at room temperature and high temperatures, and high temperature relaxation and creep tests.

Step 1: General composition and microstructure

To illustrate the potential of modern materials design methods, a new family of alloys for the nuclear power industry has been developed. Ferritic-martensitic steels are known to perform well as low-activation materials, due to their low swelling under radiation and long service life at high temperature and even moderate corrosion resistance, therefore they have the potential to become optimal candidates for various critical applications in the thermal and nuclear power generation and petrochemical industries [1-3]. A Fe8-12Cr ferritic-martensitic alloy has been selected as base material.

Some elements commonly used in the power generation industry and other high temperature applications like Mo, Ni, Nb, Si, Mn, Co and B need to be reduced or even excluded and are commonly substituted by W, V and Ta in alloys that need to work under radiation [1-3]. Thermodynamic software packages like MTDATA and Thermocalc were used to perform the necessary calculations on the thermodynamic stability of the phases of interest [3,4].

One effective method to enhance the creep resistance of an alloy is by producing a fine precipitate distribution that minimises the deformation mechanisms at service temperature. MX precipitates like TaC, VN are especially suitable for this task, due to their morphology, homogeneous distribution and their slow coarsening (especially in comparison with $M_{23}C_6$ -type carbides). Moreover, and VN precipitates are stable at higher temperatures than $M_{23}C_6$ precipitates, allowing an increase in the working temperature of the alloy. Nevertheless, an alloy with high nitrogen content could present some problems, including the formation of porosity during manufacturing [5].

A general range of possible compositions including the elements Fe, Cr, W, V, N, and C but with limited content of Ni, Si, Mn or B was therefore selected following the above criteria.

Step 2: Main target property: Creep resistance

The main mechanical property that had to be optimised was creep resistance. The physical phenomena governing creep behaviour of metals is extremely complex, but ultimately related to the composition, precise microstructure and service conditions of the alloy. Present physical models for creep phenomena are either simple empirical models or physical models of particular creep mechanisms very limited in application [2,6], and therefore, an advanced statistical method, an artificial neural network model has been used to narrow the range of compositions to be considered [5,7]. A Bayesian-based neural network has been used to perform non-linear regression analysis on a large database of creep data with multiple input parameters [8,9]. The database used includes information on over 2 000 data points of creep resistant alloys, each of them described in terms of composition, heat treatment and creep life, creep test temperature and creep fracture stress [7]. This model is publicly available at the Materials Algorithms Project web site [10]. With this tool the effect of variations in composition on the creep rupture strength after 100 000 hours was analysed and a well defined composition was defined that would potentially maximise creep resistance.

Figure 1 and Figure 2 show just two examples of the analysis performed using the neural network model to study the effect of small changes in composition, corresponding to the effect in the predicted rupture time of tungsten and nitrogen respectively [5,7]. The predictions for each set of conditions are plotted in solid lines and surrounded by dashed lines representing the *error bar* or confidence estimation of the prediction [8,9].

Figure 1. Creep rupture strength predicted using a neural network as a function of tungsten content

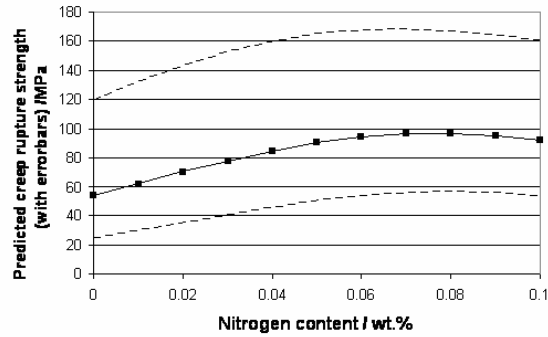
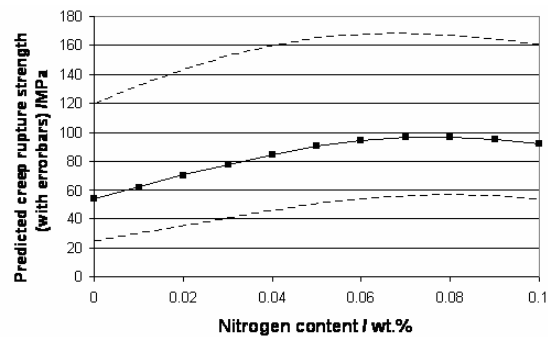


Figure 2. Creep rupture strength predicted using a neural network as a function of nitrogen content



From the neural network analysis [5,7] it was found that for some elements there was an optimal composition range (represented as a maximum in the predicted creep rupture strength at 10 000 hours), like is the case of tungsten around 2 wt.% (Figure 1).

Other elements, for instance carbon, which produces a strong solid strengthening effect, present a creep rupture strength that increases monotonically with the element content of the alloy. However, this type of trend needs to be taken cautiously, and it would be unwise to extrapolate too far. Using again the case of carbon, not all of it stays in solid solution but it tends to precipitate as $M_{23}C_6$. $M_{23}C_6$ precipitates have rapid coarsening kinetics and therefore produce little improvement in the mechanical properties, and on the other hand steal Cr from the matrix of the alloy, reducing its oxidation resistance.

In the case of nitrogen, the predictions of the neural network suggest that the optimal nitrogen content lies around 0.07 wt.%, as shown in Figure 2. This amount will need to be matched stoichiometrically with that of vanadium for instance, to form the reinforcing MX precipitates. Moreover, an excessive N content could lead to porosity in the cast [4,11].

Finally, the neural network analysis shows that the predicted creep rupture strength increases with boron content. It has been known that even small additions of boron have important influence on creep behaviour of Cr-steels [12,13]. Boron is an element that, on its natural form is deleterious in alloys exposed to radiation. However, if only small amounts are needed, isotope B^{11} could be used, which does not form helium under radiation like B^{10} , and still be able to benefit from the effect of boron [5].

As shown, it is possible to interrogate the neural network model to obtain a narrower definition of composition and heat treatments needed. To conclude, after examining the related literature and analysing the possible compositions with the help of advanced statistical methods, several alloy compositions optimised to maximise the creep rupture strength and presenting good oxidation properties were chosen. One of the proposed composition, referred to as *Alloy VY1* is approximately (all compositions are in wt.%) Fe 9.5Cr 0.14C 2.5W 0.35V with up to 0.07N relying mainly on the reinforcement by VN. Additionally, a second alloy composition with lower N and small (less than 0.1 wt.%) additions of B¹¹. The limit on nitrogen was found as a compromise between the reinforcing role of nitrogen by the formation of nitrides and by solid solution on one hand and on the other hand, the need to be able to keep all nitrogen in solution during manufacturing (i.e. to avoid the occurrence of porosity), as it will be described in a later section, and in the alloys including B, the avoidance of the formation of boron nitrides.

Step 3: Microstructure and heat treatments

Once the composition of the alloy has been selected, the heat treatment to obtain the desired microstructure need to be carefully designed. In order to obtain the fine precipitation of vanadium nitrides the alloy needs to be austenitised to dissolve completely all existing precipitates. Subsequent quench to transform the austenite matrix in martensite and a temper to release internal stresses and to precipitate MX and M₂₃C₆ and therefore to stabilise the microstructure will finish the treatment. Using a thermo-mechanical treatment would also be feasible, adding stages of hot rolling prior to annealing to increase the density of precipitate nucleation sites and hence, accelerate the precipitation reaction and reduce the average size of the precipitate distribution. The optimisation of the heat treatment parameters (temperature and duration of each stage of the heat treatment) is possible using a thermodynamics and precipitation kinetics package like MatCalc, using the database “TWS_Steel”, both developed at TU Graz [14-16].

A package like MatCalc, combines the equilibrium phase stability calculations with calculations on the kinetics of precipitation, (nucleation, growth and coalescence of precipitates), and the prediction of the size distribution obtained with each set of conditions [14-16].

Figure 3 shows the calculated phase stability diagram as a function of temperature for steel VY2. Using this diagram we can define the temperatures different stages of the heat treatment to obtain the optimal microstructure.

Using Figure 3 as a reference we can define the austenitisation temperature at 1 200°C, and then a subsequent quench in oil. Then two different heat treatments have been considered. The first one (*standard*) consists in a single over-ageing annealing at 720°C. The second one (*optimised*) consists in a double annealing treatment, at 600°C and 720°C for one hour each, to promote a finer distribution of reinforcing phases and to avoid excessive over-ageing of the microstructure.

Using a software package that includes at the same time thermodynamics and precipitation and coarsening kinetics simplifies considerably the selection the optimal heat treatment conditions to obtain the desired microstructure, precipitate distribution, avoiding incomplete precipitation reactions or excessive precipitate coarsening. This procedure has been used to determine the evolution of the precipitate distribution during the two heat treatments considered, as shown in Figure 4 and Figure 5.

Moreover, a similar calculation could be performed to study the evolution of the microstructure during service conditions, for instance to predict the degree of coarsening of the reinforcing phases during long thermal ageing.

Figure 3. Phase distribution as function of temperature for designed alloy. Diagram calculated using MatCalc.

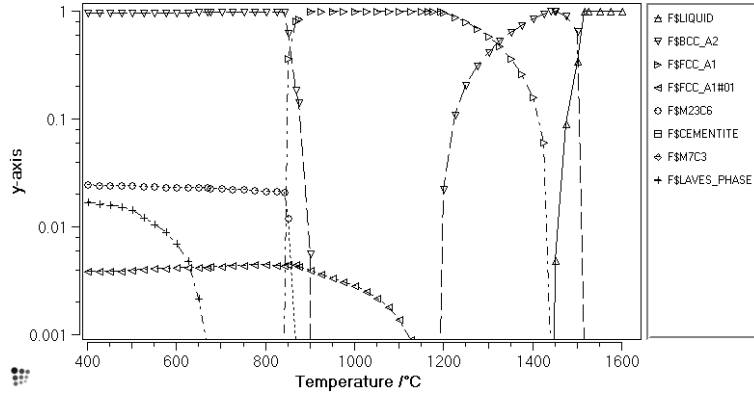


Figure 4. Simulation of the evolution of the average radius of MX and $M_{23}C_6$ precipitates on the designed alloy during the *standard* heat treatment)

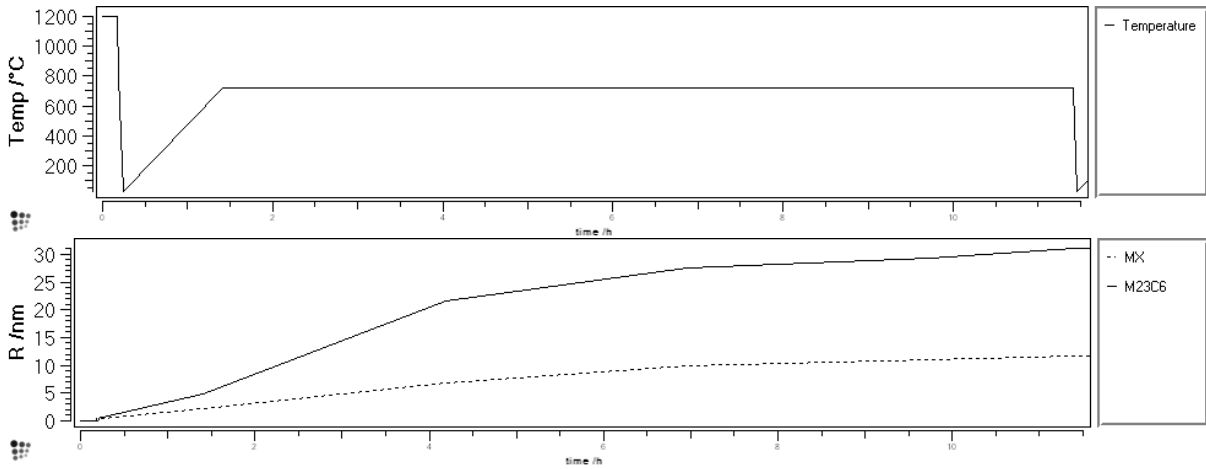
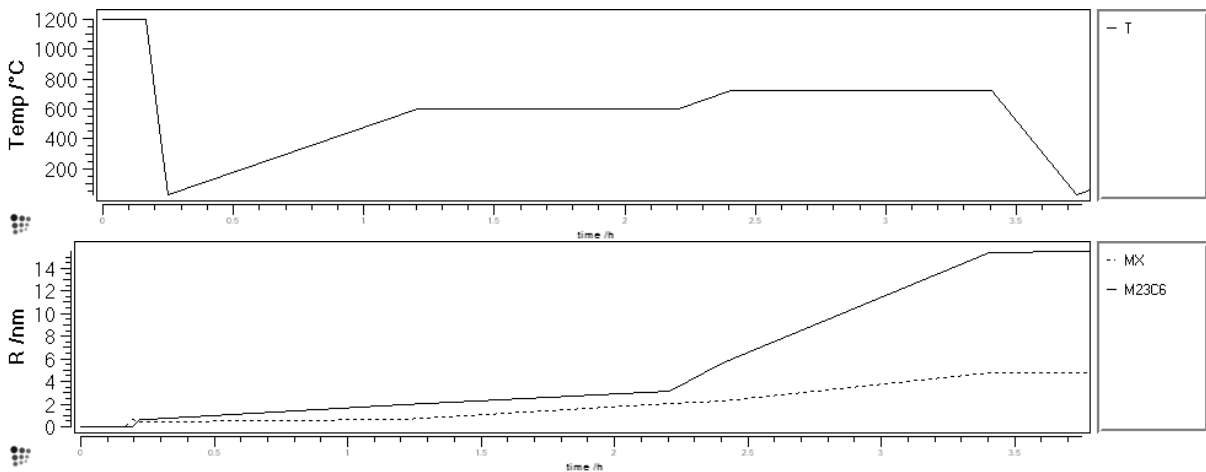


Figure 5. Simulation of the evolution of the average radius of MX and $M_{23}C_6$ precipitates on the designed alloy during the *optimised* heat treatment)



Experimental assessment

After the theoretical design of the alloy, a careful experimental assessment is necessary. The main points of the assessment are to make sure that the phase stability and kinetics calculations predict the correct phases in the real material, and that the microstructure obtained lead to the expected optimised mechanical behaviour.

Undesirable phase: Nitrogen gas

In this section, an example of an unexpected (and undesirable) phase found in some of the alloys designed is shown.

As the nitrogen content of the alloy is increased to produce a larger extent of precipitation of the reinforcing phase VN, there is an increased risk that the matrix of the alloy will not be able to keep in solution all the nitrogen and some will be released as gas, producing a degree of porosity. Several parameters influence the possibility of formation of porosity in high nitrogen content alloys, some thermodynamic, like the sequence of phases forming during solidification (as each phase presents a different nitrogen solubility curve) and others more of a technological character [5]. In order to avoid the risk of porosity the nitrogen content of the designed alloy has been kept at 0.04wt.% [5].

Mechanical properties

Tensile properties

A programme of tensile tests has been planned to characterise the tensile behaviour at room temperature and at high temperatures of the alloy under consideration. As high temperatures, two characteristic temperatures have been chosen, 650°C, which is the contemplated service temperature, and 820°C, indispensable to be able to predict the behaviour of the material in the event of *extraordinary* service conditions.

The tests have been performed on an INSTRON machine with a load capacity of 200 kN. The geometry of the specimens used is detailed below. The loading rate used in all cases was 0.84 mm/min. which is $= 4.7 \cdot 10^{-4} \text{ s}^{-1}$.

Figure 6 shows the comparison of the two different heat treatments considered with a PM2000 oxide dispersion strengthened (ODS) steel with different grain sizes (small grain $\sim 5 \mu\text{m}$, large grain $\sim 3 \text{ mm}$). This figure shows the substantial improvement in yield stress obtained at all temperatures by using an *optimised* heat treatment consistent in a double precipitation annealing instead of a single long over-ageing annealing. The yield strength obtained in both cases is of the same order of magnitude as that obtained in ODS steels, without the need of the complex manufacturing process needed for such type of materials.

Relaxation and creep properties

As a first approach to the long-term behaviour of the alloy under consideration, a relaxation test has been used to compare its behaviour with that of a T91 alloy (Fe-9Cr-1Mo-V-Nb). Although it is possible to extrapolate the results from a series of relaxation test to obtain the same type of information that would be obtained from full time creep tests [17], a programme of creep tests is under way. Figure 7 shows the comparison between the relaxation tests results for a T91 steel and VY2 alloy in the *standard* condition.

Figure 6. Comparison mechanical behaviour of alloy VY2 in two conditions with an ODS PM2000 alloy during uniaxial tensile tests between room temperature and 820°C

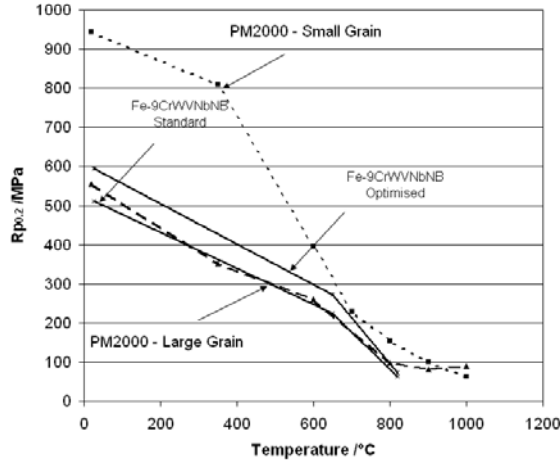
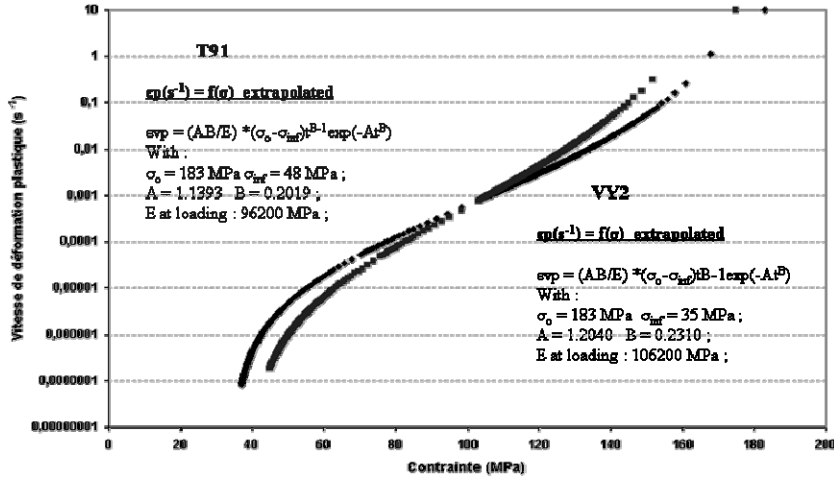


Figure 7. Comparison mechanical behaviour of alloy VY2 in the *standard* condition with T91 steel during stress relaxation test at 650°C



It is encouraging to see that the newly developed alloy, even in the *standard* condition behaves as well as a traditional alloy with good creep resistance. It is therefore expected that the creep tests on VY2 alloy in the *optimised* condition will present improved creep resistance (in the same way as it presents improved static mechanical properties), due to its optimised microstructure.

A comprehensive characterisation of high temperature creep behaviour of alloy VY2 in both conditions *standard* and *optimised* is at present under way in CEA Saclay.

Microstructure stability

The microstructure and carbide distribution in a commercial creep resistant, low activation alloy (F82H) has been simulated using a thermo-kinetic model package, MatCalc. The microstructure after long thermal ageing treatments (13 500 hours) at various temperatures, comparable to service conditions, have been considered. In all cases, the calculated carbide distributions describe with

remarkable accuracy experimental measurements (Figure 8), showing that it is possible to describe and predict accurately the evolution of the microstructure and carbide distribution even for long heat treatments, at temperatures comparable to service conditions found in power plant applications [18].

With this confidence, a similar calculation was performed for the designed alloy, obtaining that the $M_{23}C_6$ carbide distribution (Figure 9), has an average radius just under 100 nm after 10 000 hours.

Figure 8. Comparison of the predicted carbide distribution with experimental measurements in a F82H steel thermally aged at 550°C for 13 500 hours

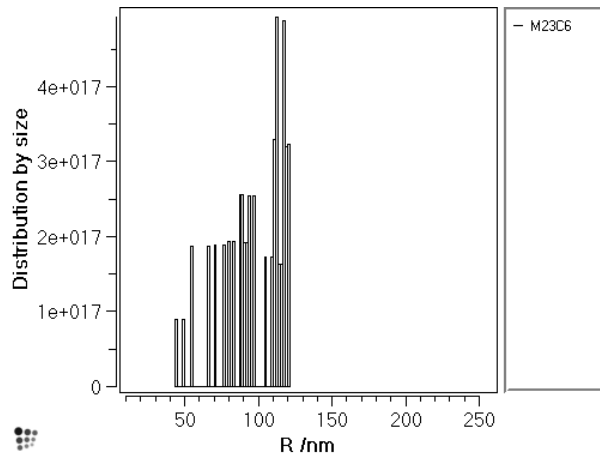
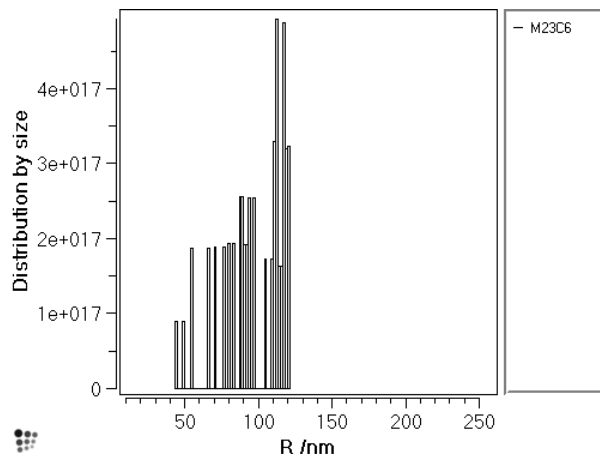


Figure 9. Predicted carbide distribution of VY2 steel thermally aged at 650±°C for 10 000 hours



Conclusions

The work presented here is a case study on how the present accuracy of thermodynamics and kinetics calculations allow for the design of new alloys responding to demanding solicitations and avoiding most of the experimental trial and error needed in the past. Software tools based on the CALPHAD method and various kinetics models are available that allow to predict not only the feasibility of some target microstructure but its evolution during various heat treatments.

The microstructural and mechanical characterisation of the alloy designed is presently under way, and preliminary results have been presented in this work.

Acknowledgements

The authors are grateful to V. Yardley, J-M. Lardon, J. Montagnon, A. Petit and F. Vivier for their collaboration in the development of this work and to H. K. D. H. Bhadeshia, E. Kozeschnik and J-C. Brachet for their invaluable advice on the use of the various methods employed in the present work and very fruitful discussions.

REFERENCES

- [1] Séran, J-L., J-C. Brachet, A. Alamo, “Ferritic-martensitic Steels for Fast Reactor Cores”, *Encyclopedia of Materials: Science and Technology*, Elsevier Science Ltd., pp. 2863-2866 (2001).
- [2] Bhadeshia, H.K.D.H., “Design of Heat Resistant Alloys for the Energy Industries”, *5th International Charles Parsons Turbine Conference*, pp. 3-39 (2000).
- [3] De Carlan, Y., M. Muruganath, T. Sourmail, H.K.D.H. Bhadeshia, “Design of New Fe-9CrWV Reduced-activation Martensitic Steels for Creep Properties at 650”, *Journal of Nuclear Materials*, 329-333:238-242 (2004).
- [4] Yardley, V.A., Y. De Carlan, *Progress in Fabrication of Experimental 9Cr Steel Compositions Optimised for Creep Resistance, Thermodynamic and Statistical Analysis and Proposed Solutions*, Technical report, CEA, France (2005).
- [5] Gaude-Fugarolas, D., V. Yardley, J-M. Lardon, J. Montagnon, Y. De Carlan, “Advanced Alloy Design Tools Applied to the Development of Vanadium Nitride Strengthened High-temperature Steels”, *Proc. 8th Liège Conference Materials for Advanced Power Engineering*, Liège, Belgium (2006).
- [6] Hertzberg, R.W., *Deformation and Fracture Mechanics of Engineering Materials*, John Wiley & Sons, Inc., New York (1996).
- [7] Cole, D., C. Martin-Moran, A.G. Sheard, H.K.D.H. Bhadeshia, D.J.C. MacKay, “Modelling Creep Rupture Strength of Ferritic Steel Welds”, *Science and Technology of Welding and Joining*, 5:81-89 (2000).
- [8] MacKay, D.J.C., “Bayesian Non-linear Modelling with Neural Networks”, *Mathematical Modelling of Weld Phenomena 3*, H. Cerjak (Ed.), pp. 359-389, The Institute of Materials, London (1997).
- [9] MacKay, D.J.C., “Probable Networks and Plausible Predictions – a Review of Practical Bayesian Methods for Supervised Neural Networks”, <http://wol.ra.phy.cam.ac.uk/mackay/>.

- [10] Materials Science and Metallurgy Department, University of Cambridge and National Physical Laboratory, *Materials Algorithms Project*, University of Cambridge, <http://www.msm.cam.ac.uk/map/mapmain.html>, 1995.
- [11] Yardley, V.A., Y. de Carlan, “Design Criteria for High-temperature Steels Strengthened with Vanadium Nitride”, *Journal of Phase Equilibria and Diffusion*, 27 (2006).
- [12] Kelly, T.F., D.J. Larson, M.K. Miller, J.E. Flinn, “Three-dimensional Atom Probe Investigation of Vanadium Nitride Precipitates and the Role of Oxygen and Boron in Rapidly Solidified 316 Stainless Steel”, *Materials Science and Engineering A*, A270:19-26 (1999).
- [13] Abe, F., T. Horiuchi, M. Taneike, K. Sawada, “Stabilisation of Martensitic Microstructure in Advanced 9Cr Steel During Creep at High Temperature”, *Materials Science and Engineering A*, A378:299-303 (2004).
- [14] Svoboda, J., F.D. Fischer, P. Fratzl, E. Kozeschnik, “Modelling of Kinetics in Multi-component Multi-phase Systems with Spherical Precipitates I: Theory”, *Materials Science and Engineering A*, A385:166-174 (2004).
- [15] Kozeschnik, E., J. Svoboda, P. Fratzl, F.D. Fischer, “Modelling of Kinetics in Multi-component Multi-phase Systems with Spherical Precipitates II: Numerical Solution and Application”, *Materials Science and Engineering A*, A385:157-165 (2004).
- [16] Kozeschnik, E., J. Svoboda, F.D. Fischer, “Modified Evolution Equations for the Precipitation Kinetics of Complex Phases in Multi-component Systems”, *Computer Coupling of Phase Diagrams and Thermochemistry*, 28:379-382 (2004).
- [17] Auzoux, Q., “Fissuration en Relaxation des Aciers Inoxydables Austénitiques – Influence de l'Écrouissage sur l'Endommagement Intergranulaire”, PhD thesis, École Nationale Supérieure des Mines de Paris (2004).
- [18] Gaude-Fugarolas, D., Y. De Carlan, “Modelling Precipitate Distribution on F82H and JLF-1 Reduced Activation Steels During Manufacturing and Service Conditions”, submitted to *Journal of Nuclear Materials* (2007).

MODELLING OF NUCLEAR-GRADE GRAPHITE USING X-RAY TOMOGRAPHY DATA

C. Berre, G. Hall, B.J. Marsden, S.L. Fok, T.J. Marrow, P.M. Mummery
The University of Manchester, Manchester, England, UK

Abstract

A number of designs for the next generation of nuclear fission reactors use graphite components as integral parts of the reactor core. It is known that nuclear-grade graphite will undergo significant dimensional and material property changes due to the fast neutron fluence at elevated temperature within the core. Ongoing studies at the University of Manchester have demonstrated the feasibility of predicting graphite bulk material property and dimensional changes employing microstructural information derived from a non-invasive measurement technique, X-ray micro-computed tomography. High-resolution three-dimensional images of nuclear-grade graphite were obtained from tomography, and transformed into finite element models. The relationship between the bulk properties and the microstructural changes with thermal oxidation has been investigated using a reproduction technique, with successful comparison of prediction and measurement. Also, the irradiation-induced behaviour of graphite has been simulated using a multi-scale finite element methodology. The results from both approaches are presented and discussed, as well as a proposed combination of both modelling approaches. It is suggested that such a methodology, when used with an economic materials testing programme, could help in the qualification and design of nuclear-grade graphites for the next generation of reactors.

Introduction

Graphite is widely used in the nuclear industry for its very good thermo-mechanical properties and its neutron moderation efficiency. In gas-cooled reactors, nuclear graphite is subjected to fast neutron irradiation, radiolytic oxidation as well as thermal oxidation at high temperatures. These extreme conditions of operation modify the microstructure and hence the mechanical behaviour of the material during its life time. A good understanding of the underlying mechanisms is required to predict the material behaviour changes in time. Predictions of the bulk thermo-mechanical property changes can be derived from the microstructure of the material using novel modelling methods. In this paper, the graphite grade used for study is Gilsocarbon, a semi-isotropic graphite composed of coke filler particles embedded in a coal-tar pitch matrix, and containing around 20% of porosity.

Using a reproductive approach [1], very accurate finite element meshes of the microstructure of graphite were obtained from X-ray tomography images of thermally oxidised Gilsocarbon. Finite element analysis allowed the micro-mechanical behaviour to be analysed in details and to calculate the bulk mechanical properties from a representative volume. Numerical results were compared to the existing database from the literature for an isotropic graphite grade. This study showed that bulk Young's modulus changes could be well predicted using a linear elasticity analysis.

A multi-scale modelling approach was adopted to simulate the neutron irradiation effect on the microstructure of the same isotropic graphite and to calculate the bulk mechanical property changes with increasing neutron dose. Considering the mechanical properties of a crystal and a polycrystalline model composed of randomly orientated and distributed crystals, the bulk Young's modulus changes were calculated for different temperatures of operation. Numerical predictions showed a good agreement with experimental data [2].

Numerical models

Reproduction method

X-ray tomography is a non-invasive imaging technique that allows the visualisation of the microstructure of a material in three dimensions. The specimen is scanned by an X-ray beam and the projected image is captured by a charge couple device camera (CCD). A series of radiographs are taken at different angles between 0° and 180° . A three-dimensional image is then reconstructed from the two-dimensional information using a back-filtered projection algorithm. Typical resolutions are in the order of the micrometer, depending on the size of the sample. Figure 1 shows a schematic representation of the tomography device.

X-ray tomography images are coded in 16 bits using a greyscale containing 65 536 grey levels. The greyscale depends on the material density, higher densities being represented by brighter voxels (three-dimensional elementary image). A set of semi-isotropic graphite samples was thermally oxidised in air. Specimens were originally cylindrical, with a diameter $D = 8$ mm and a length $L = 15$ mm. After oxidation at different levels, high-resolution three-dimensional images of the microstructure of the samples were obtained (Figure 2).

In Figure 2, the effects of oxidation is characterised by the enlargement of the pores within the binder phase and by the contrast difference between filler particles and binder matrix as a result of the preferential oxidation of the binder [3].

Figure 1. Schematic of the X-ray tomography device

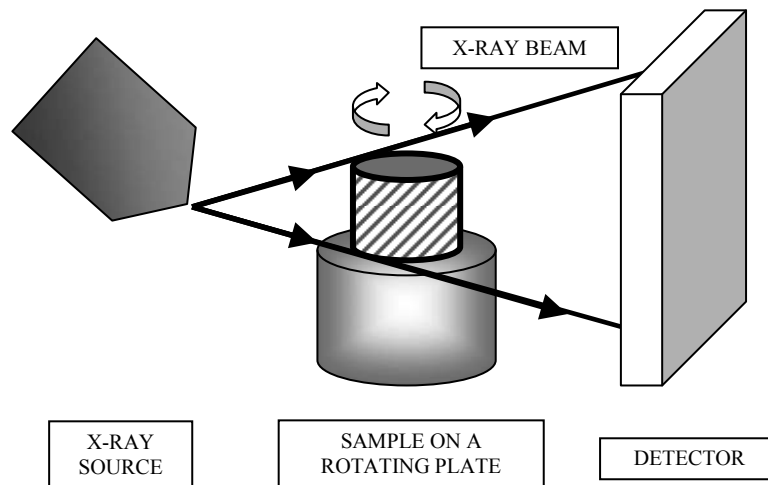
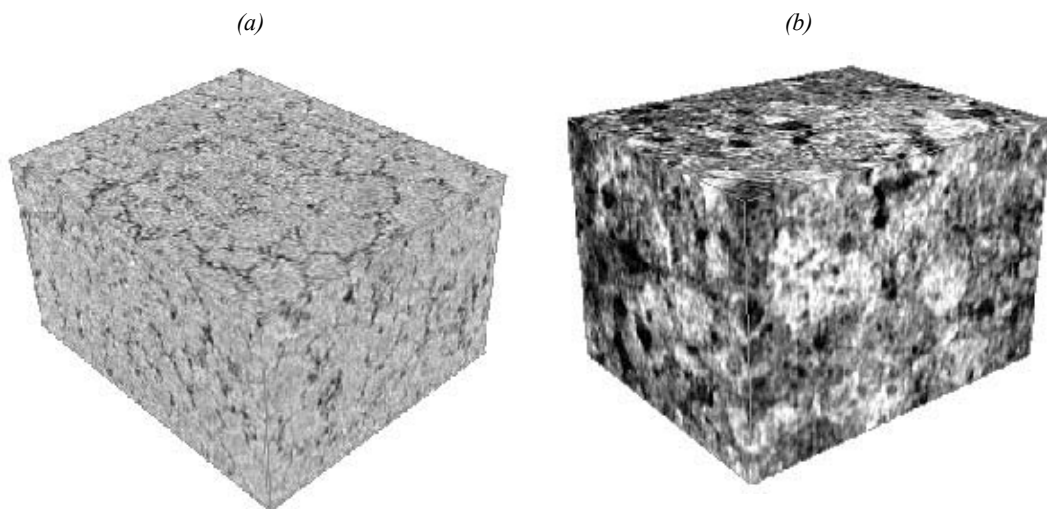


Figure 2. X-ray tomography images of (a) unoxidised and (b) oxidised graphite



Pore connectivity in the material can be seen after a segmentation process [4]. As a first assumption, the pore phase was separated from the solid material during this process. From knowledge of the crystallite density the pore volume fraction contained in the finite element meshes was set according to the specimen weight and volume measurements. The segmented images were then transformed into finite element meshes (Figure 3).

X-ray tomography images of each sample were transformed into finite element meshes using the commercial package Simpleware [4]. Generated meshes are very accurate since the pores are larger than the tomographic image resolution, i.e. $19\ \mu\text{m}$, is precisely rendered in the model. Finite element analysis was performed using ABAQUS [5]. The volume of each sub-model was limited to $V = (1\ \text{mm})^3$ due to the very large memory requirements ($\sim 4\ \text{GB}$ RAM): the finite element meshes contained around 125 000 mixed tetrahedral and hexahedral elements (ABAQUS C3D4/C3D10). Linear elastic analysis was conducted on each numerical model whilst subjected to uniaxial applied strain $\varepsilon = 0.01$. Tensile stresses and effects of the microstructure are shown in Figure 4.

Figure 3. (a) Three-dimensional mesh of the microstructure of an unoxidised graphite and (b) porosity network (2mm × 2mm × 2mm)

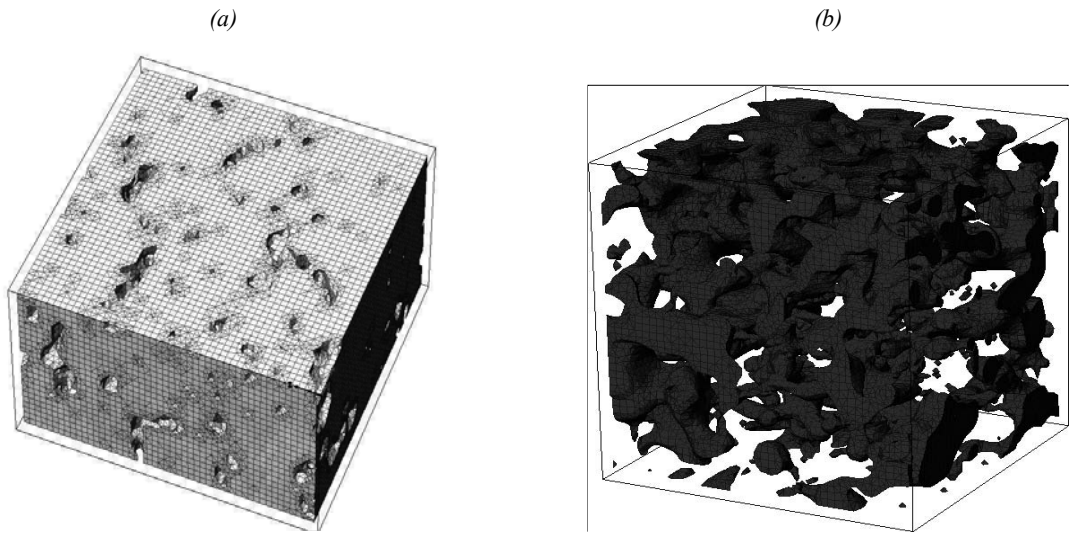


Figure 4. Tensile stresses in the direction 3 of a finite element model of unoxidised graphite

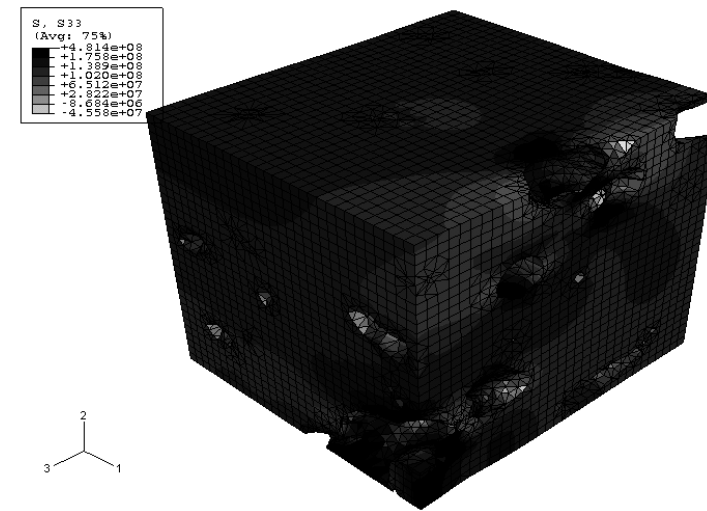
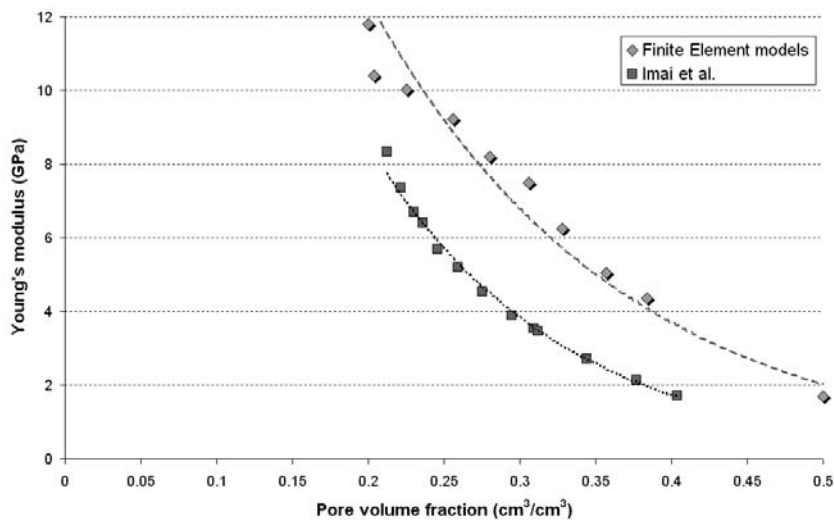


Figure 4 shows that high stress regions (dark areas) are located near the pores and near the edges of the model. The pores also shield the load path and cause stress concentrations. In each numerical model the bulk Young's modulus was calculated from the reaction force R_f at the fixed surface and its area S by:

$$E = \frac{R_f}{\epsilon S} \quad (1)$$

In an experimental investigation of quasi-isotropic-grade SM1-24, Imai, *et al.* [6] determined the Young's modulus changes with thermal oxidation. Using the reproduction approach, numerical Young's modulus of thermally oxidised Gilsocarbon were plotted against the pore volume fraction P and compared to Imai's results (Figure 5).

Figure 5. Bulk Young's modulus changes with increasing pore volume fractions and comparison with experimental data from the literature [6]

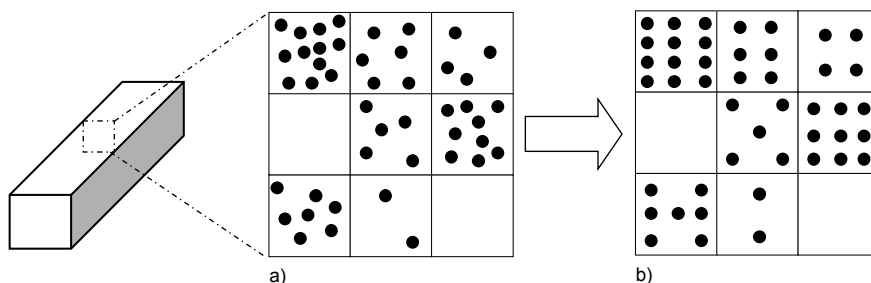


The density of SM1-24 graphite grade before oxidation is similar to the density of Gilsocarbon. However, SM1-24 has a lower initial Young's modulus (~8 GPa) than Gilsocarbon (~11 GPa). In Figure 5, considering the initial Young's modulus of Gilsocarbon and SM1-24 before oxidation, the trend of the changes with increasing pore volume fraction is similar in both experiments and numerical models. Hence, a good agreement between the numerical and experimental Young's modulus changes with increasing thermal oxidation was found [6]. Therefore, it can be concluded that the reproduction approach is a suitable numerical method to investigate and predict the elastic property changes with oxidation. This methodology can also be applied to other physical properties such as strength or thermal conductivity.

Multi-scale approach

The multi-scale or hierarchical approach has also been applied to modelling the bulk changes in nuclear-grade graphite. This technique approximates a heterogeneous material using a range of unit cells (Figure 6). The complexity of the actual material can be reduced by assuming uniformity at local levels through the use of different local cell models. The non-uniform global model can then be constructed from these local cell models. A disadvantage with this is that the creation and analysis of a range of local models can be time consuming.

Figure 6. Multi-scale approach: a) globally and locally non-uniform, b) globally non-uniform but locally uniform

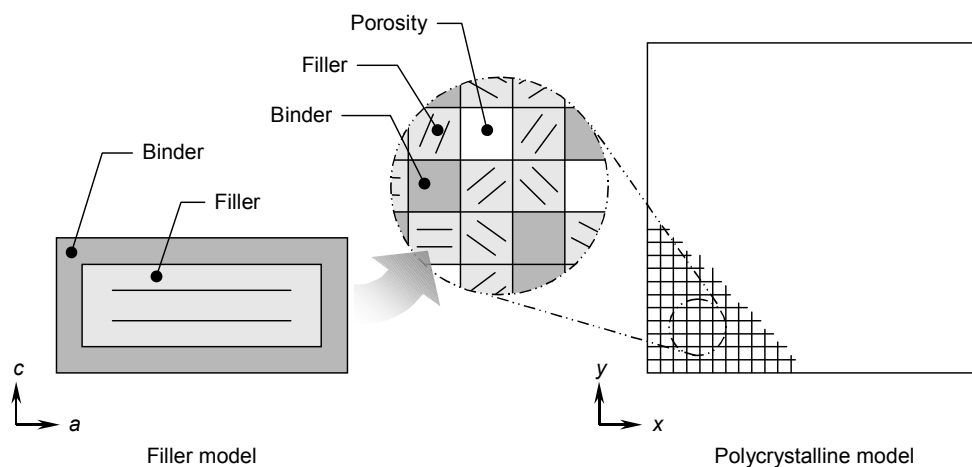


The underlying assumption for this modelling procedure was that the bulk or mesoscale changes in nuclear-grade graphite are dominated by the changes at the microscale. Thus, two-dimensional models of the microscale (an idealised coke or filler particle) and mesoscale (polycrystalline graphite) were created using the finite element method (Figure 7). The idealised filler particle model was based upon the work by Sutton and Howard [7] and White [8], and consisted of a region of well-crystallised graphite (filler) containing a lenticular crack that represented the microporosity found in graphite [7,8], referred to here as accommodation porosity. A layer of amorphous graphite (binder) surrounded the filler material and acted as an effective medium, providing a restraining effect to the filler. Numerous filler models with different dimensions, material ratios, and accommodation porosity percentages were created in order to provide a full range of behaviours.

The filler particle was assigned the irradiation-dependent dimensional and material properties of the closest representative material, highly-oriented pyrolytic graphite (HOPG) [9-13]. The binder, however, was assigned only the unirradiated properties of an isotropic graphite [14]. The analyses were conducted using a subroutine facility in the commercially available finite element package ABAQUS called a User Material (UMAT). This allows for the definition of a material's constitutive equations which, in the case of the filler material, were anisotropic, temperature and fast neutron irradiation-dependent relationships. The filler models were subjected to loading conditions (fast neutron irradiation and temperature) akin to those found in a thermal nuclear reactor and the apparent changes in properties obtained. These filler model behaviours were then applied in the mesoscale, polycrystalline modelling stage.

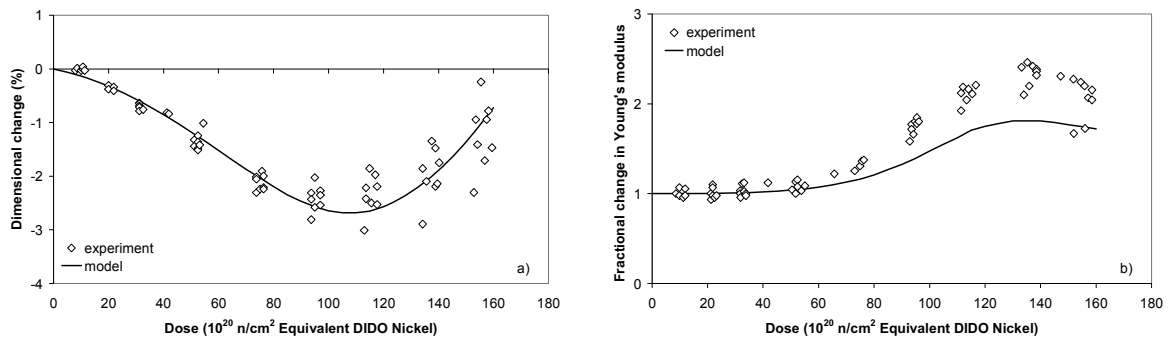
The polycrystalline model comprised of a square mesh where elements could be assigned filler model properties determined in the previous modelling stage, binder properties, or negligible properties in order to represent the larger scale porosity found in graphite (Figure 7). The allocation of the elements was made randomly throughout the polycrystalline model but the ratio of porosity, binder and filler was based upon manufacturing information [16]. In order to create an isotropic material, the filler elements were given an even orientation distribution. However, a range of filler model behaviours were assigned to the filler elements to account for an assumed distribution in accommodation porosity [7]. The polycrystalline model was loaded as per the filler model, and the apparent bulk dimensional and elastic modulus changes extracted.

Figure 7. Multi-scale finite element method model of nuclear-grade graphite



Comparison of the multi-scale modelling approach with experimental data [15] showed good agreement at lower temperatures (450-600°C), especially in the case of bulk dimensional changes (Figure 8). At higher temperatures (above 600°C), the approach was able to simulate the general trends of the dimensional and elastic modulus changes, but the magnitudes did not compare as well as those at lower temperatures. The main contributor to the differences at higher temperatures was assumed to be the scarcity of input HOPG data for the filler model at the higher temperatures. However, another factor may have been the oversimplification of the graphite structure in the multi-scale approach.

Figure 8. Comparison of experimental data and a multi-scale modelling approach for nuclear-grade graphite: a) dimensional changes at 450°C, b) fractional change in elastic modulus at 450°C



Combined reproduction and multi-scale approach

To address the oversimplification in the multi-scale approach, and due to the success of the reproduction method, it is proposed that a combined reproduction/multi-scale modelling technique would be more effective in the simulation of nuclear-grade graphite properties. The concept is to use high-resolution computed tomography images to create reproduction-type, finite element models of the graphite microstructure (Figure 9). These sub-models could then be restrained and loaded as in the multi-scale model discussed earlier. The apparent behaviour of these sub-models would then be implemented into a reproduction, finite element model of the bulk material, again created from tomographic images. Subjecting the bulk model to suitable loading conditions would then hopefully provide material property changes that are comparable to experimental data.

If the combined technique does prove to be successful, it may provide a means to quantify the oxidation and fast neutron irradiation-induced changes in a nuclear-grade graphite from non-invasive examination of unirradiated and unoxidised graphite. It is not proposed that this approach will remove completely the need to conduct irradiation and oxidation test programmes, but that it will provide a tool to identify candidate graphite grades for new reactor builds and aid in the development of new graphite grades.

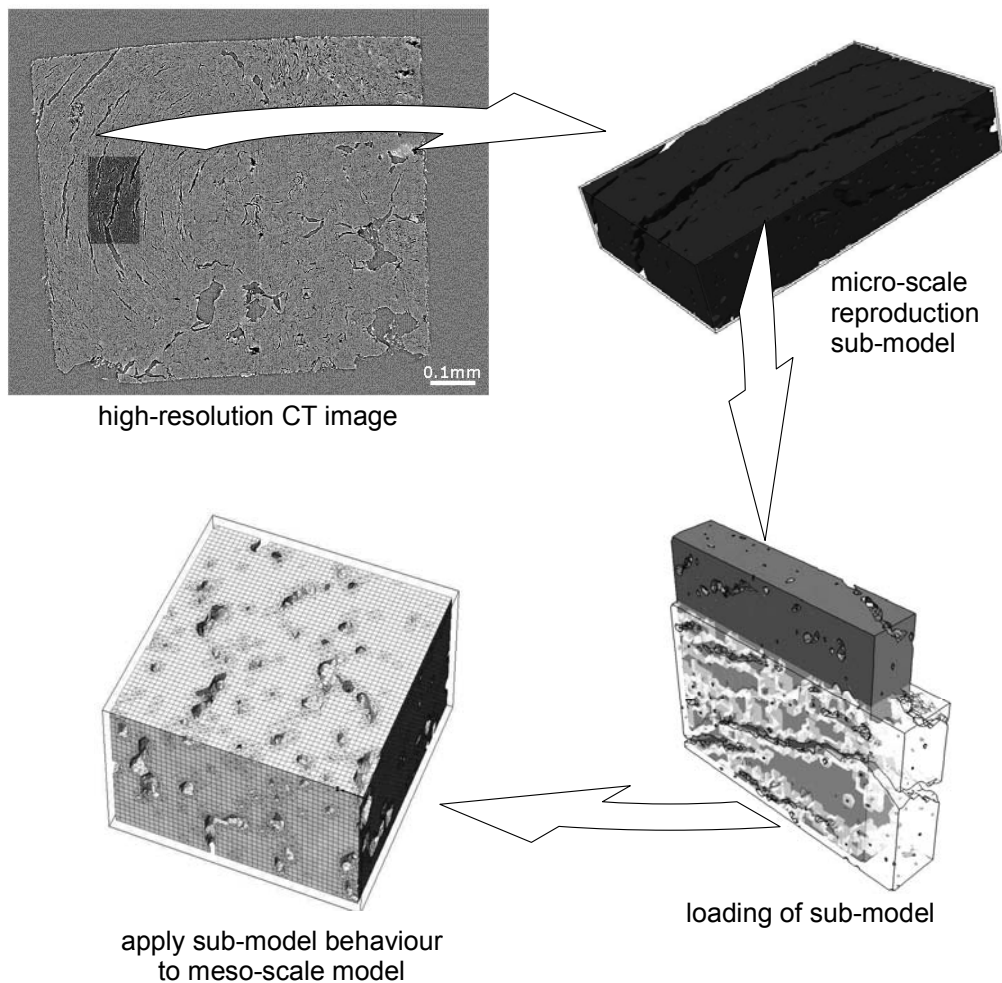
Conclusion

This work has demonstrated the possibility of using numerical models to predict the mechanical property changes of graphite when subjected to fast neutron irradiation or oxidation. Using a non-destructive reproductive approach, X-ray tomography images were used to generate detailed finite element meshes of the microstructure of thermally oxidised graphite. Subsequently the models were analysed using finite element analysis. Bulk mechanical property changes with increasing oxidation

were calculated for each sample. The predicted results showed good agreement when compared to experimental values. The effect of fast neutron irradiation on polycrystalline graphite has also been simulated using a multi-scale finite element approach. Predicted dimensional and Young's modulus changes were found to be in good agreement with experimental data, although there were slight discrepancies at high fast neutron doses. This work is now being applied to other thermal/mechanical properties, such as strength, coefficient of thermal expansion and thermal conductivity.

Both of these methodologies have been proved to be successful on an existing grade of graphite and can be combined to obtain an improved model. A better understanding of the underlying mechanisms between microstructural arrangement, stress flow and mechanical behaviour of nuclear graphite was also obtained. Similar studies can be conducted on newly developed materials to evaluate the mechanical behaviour and the mechanical property changes of such materials under irradiation.

Figure 9. Proposed reproduction/multi-scale modelling approach for nuclear-grade graphite



Acknowledgment

Dr. G. Neighbour, University of Hull, is gratefully acknowledged for providing the thermally oxidised graphite specimens.

REFERENCES

- [1] Berre, C., S.L. Fok, B.J. Marsden, L. Babout, A. Hodgkins, T.J. Marrow, P.M. Mummery, "Numerical Modelling of the Effects of Porosity Changes on the Mechanical Properties of Nuclear Graphite", *J. Nucl. Mat.*, 352, 1-5 (2006).
- [2] Hall, G., B.J. Marsden, S.L. Fok, "The Microstructural Modelling of Nuclear Grade Graphite", *Journ. Nucl. Mat.*, 353, 12-18 (2006).
- [3] Babout, L., P.M. Mummery, T.J. Marrow, A. Tzelepi, P.J. Withers, "The Effect of Thermal Oxidation on Polycrystalline Graphite Studied by X-ray Tomography", *Carbon*, 43, 765-774 (2005).
- [4] Simpleware Ltd., *ScanIP and ScanFE Manual Reference Guide Version 2.0* (2004).
Website: <http://www.simpleware.co.uk>
- [5] HKS, *ABAQUS/Standard User's Manual*, Version 6.6 (2006).
- [6] Imai, H., K. Fujii, T. Kurosawa, S. Nomura, "Changes in Young's Modulus and Electrical Conductivity of Nuclear Grade Graphites Oxidized with Air", *Journ. Nucl. Mat.*, 118, 294-302 (1983).
- [7] Sutton, A.L., V.C. Howard, "The Role of Porosity in the Accommodation of Thermal Expansion in Graphite", *Journ. Nucl. Mat.*, 7, 58-71 (1962).
- [8] White, E.S., "Some Factors Affecting the Anisotropy of Extruded Carbon", *Proc. 4th Carbon Conf.*, University of Buffalo, Buffalo, New York, 685-681 (1960).
- [9] Mrozowski, S., "Mechanical Strength, Thermal Expansion and Structure of Cokes and Carbons", *Proc. 1st and 2nd Conf. Carbon*, 31-45 (1956).
- [10] Brocklehurst, J.E., B.T. Kelly, "The Dimensional Changes of Highly-oriented Pyrolytic Graphite Irradiated with Fast Neutrons at 430°C and 600°C", *Carbon*, 31, 179-183 (1993).
- [11] Bokros, J.C., G.L. Guthrie, D.W. Stevens, "Irradiation-induced Dimensional Changes in Imperfect Graphite Crystals", *Carbon*, 9, 349-353 (1971).
- [12] Kelly, B.T., "The Basal Thermal Expansion of Graphite and a Relationship Between the Bond Bending Resistance and the In-plane Elastic Constants", *Carbon*, 13, 350 (1975).

- [13] Bailey, A.C., B. Yates, "Anisotropic Thermal Expansion of Pyrolytic Graphite at Low Temperatures", *Journ. App. Phys.*, 41, 5088-5091 (1970).
- [14] Blakslee, O.L., D.G. Proctor, E.J. Seldin, G.B. Spence, T. Weng, "Elastic Constants of Compression-annealed Pyrolytic Graphite", *Journ. App. Phys.*, 41, 3373-3382 (1970).
- [15] Brocklehurst, J.E., B.T. Kelly, "Analysis of the Dimensional Changes and Structural Changes in Polycrystalline Graphite Under Fast Neutron Irradiation", *Carbon*, 31, 155-178 (1993).
- [16] *Nuclear Graphite*, R.E. Nightingale (Ed.), Academic Press (1962).

**BASIC EXPERIMENTS FOR UNDERSTANDING
MICROSTRUCTURE EVOLUTION UNDER IRRADIATION:
TEM AND KMC CHARACTERISATION OF IRRADIATED PURE IRON**

**M. Hernández-Mayoral¹, M.J. Caturla²,
D. Gómez-Briceño¹, J.M. Perlado³, E. Martínez^{3,4}, J. Marian⁴**

¹CIEMAT, Madrid, Spain

²Dept. Física Aplicada, Universidad de Alicante, Spain

³Instituto de Fusión Nuclear, Universidad Politécnica de Madrid, Spain

⁴Lawrence Livermore National Laboratory, Livermore, CA

Abstract

We present a combined effort of experiments and simulations to understand damage evolution under irradiation in pure Fe. Basic experiments, under well known and controlled conditions, were performed in order to validate the models developed using a combination of *ab initio*, molecular dynamics and kinetic Monte Carlo methods. The experiments consisted of ion irradiation of ultra-high-pure iron at 300°C and analysis of the accumulated damage using transmission electron microscopy (TEM). The concentration of defects and average defect size was obtained for different doses, as well as defect types. Kinetic Monte Carlo calculations were performed to model the same experimental conditions. The model includes the migration of self-interstitials and vacancies using information from *ab initio* and molecular dynamics calculations, as well as the nucleation and growth of different clusters. It assumes that the formation of <100> loops occurs through the reaction of <111> loops. The results of the simulations are discussed in comparison to those obtained in the experiments.

Introduction

The experimental validation of simulation tools developed to reproduce the long term evolution of irradiation-induced hardening defects is required to ensure the reliability of the obtained final product. The experiments performed to do such experimental validation should fulfil some requirements that basically consist in performing the experiments under well known and controlled conditions. Also, they have to be simple enough to be reproduced by computational simulation. These kinds of experiments are being named “model oriented experiments”. The methodology of experimental validation presented here is being followed in several fields where the effect of irradiation on materials behaviour is an issue, as the development of new energy production systems. The general objective is to obtain reliable experimental data for the experimental validation of simulation tools.

As an example of the experimental validation methodology, a basic ion irradiation experiment carried out to investigate the irradiation response of ultra high pure iron is presented. The relevance of ion irradiation experiments stems in their allowance to perform systematic studies in relative short time and where above mentioned conditions of model oriented experiments are fulfilled. In parallel, this experiment is modelled using Kinetic Monte Carlo with input data from *ab initio* and molecular dynamics. The objective is double: to get the understanding of mechanisms that take place under irradiation and the experimental validation of computational simulation codes. The experimental characterisation technique used, and which results are presented here, has been transmission electron microscopy (TEM). These microstructural characterisation results are directly compared to results from KMC simulations. Possible mechanisms for loop formation and growth during irradiation of ultra-high-pure iron are discussed.

Experiments: irradiation and TEM measurements

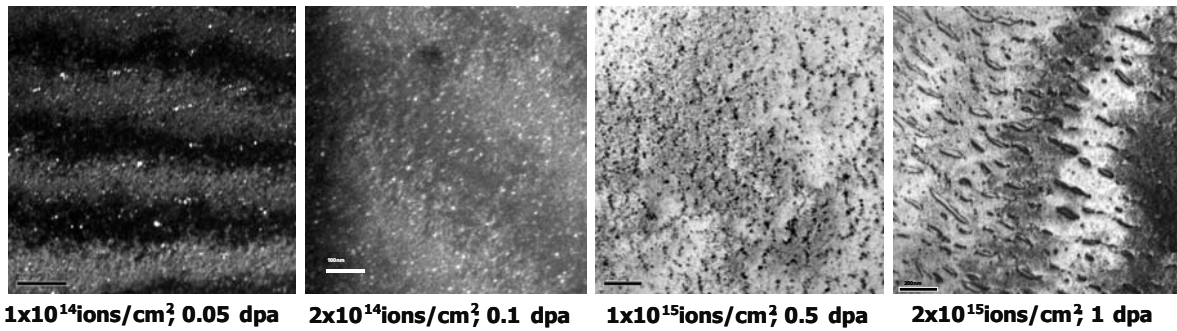
The material considered in this study has been ultra-high pure iron (UHP-Fe), provided by Prof. J. Le Coze, École des Mines de Saint-Étienne. About impurity content, it is worth to note that carbon content is less than 5 ppm, about 1 ppm, nitrogen, less than 5 ppm, about 1 ppm or less; and silicon content is less than 10 ppm, which is the detection limit of the analysis method.

The materials were irradiated in the form of thin foils suitable for TEM examination. They were irradiated at the IRMA implanter at CSNSM, Orsay, in collaboration with Drs. M.O. Ruault, O. Kaitasov and H. Bernas. TEM specimens were irradiated with 150 keV iron ions (Fe^{2+}), with an ion flux of 4×10^{11} ions/cm²s (2×10^{-4} dpa/s). In order to study ion dose effect, four groups of specimens were irradiated up to four different doses: 1×10^{14} ions/cm² (0.05 dpa), 2×10^{14} ions/cm² (0.1 dpa), 1×10^{15} ions/cm² (0.5 dpa), 2×10^{15} ions/cm² (1 dpa). The irradiation temperature was 300°C.

Microstructural characterisation of samples has been carried out in a transmission electron microscope JEOL, model JEM-2010 of 200 keV and LaB₆ filament, in CIEMAT. Thin foils for TEM analysis were prepared by jet polishing using an electrolyte of 5% perchloric acid in methanol at -60°C and 20 V, in a Metalthin machine.

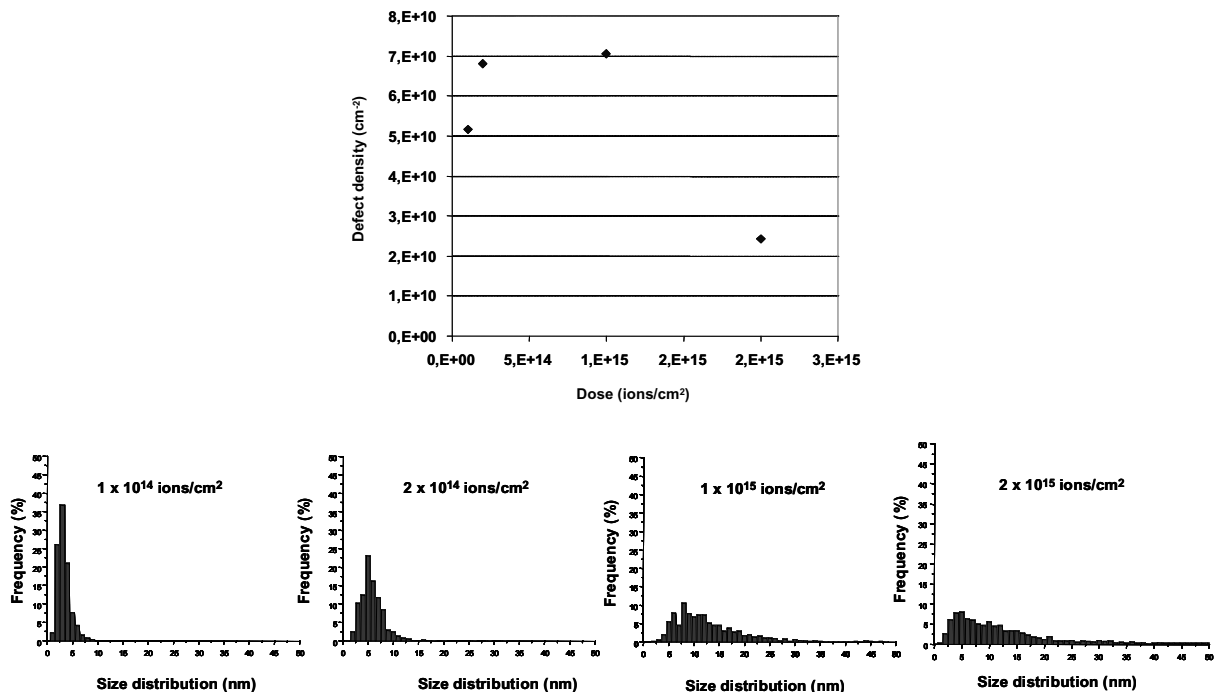
Figure 1 shows TEM images of the microstructure of UHP-Fe after ion irradiation up to 1×10^{14} ions/cm² (0.05 dpa), 2×10^{14} ions/cm² (0.1 dpa), 1×10^{15} ions/cm² (0.5 dpa) and 2×10^{15} ions/cm² (1 dpa).

Figure 1. TEM images at different doses for 150 keV Fe²⁺ irradiation in UHP-Fe



Irradiation with Fe²⁺ ions of 150 keV produced observable defects at all the irradiation doses studied, in particular at the lowest dose, 1×10^{14} ions/cm², (0.05 dpa), as shown in TEM images. Defects were distributed homogeneously in the matrix, though a tendency of defects to align along a particular crystallographic direction, forming rafts was observed in some cases. These defects are clusters of point defects created by irradiation and they have formed dislocation loops. At the highest dose, loops grow to a larger size interacting with each other and forming large dislocation loops and tangled dislocations. From these images quantitative information was obtained: areal defect density and defect size distribution as shown in Figure 2.

Figure 2. Experimental cluster size distribution for 150 keV Fe⁺ irradiation in UHP-Fe at different doses



Defect density increases rapidly at low doses and then, saturation seems to take place between 0.1-0.5 dpa. At high dose, 1 dpa, density decreases due to loop coarsening. Regarding size distribution, a comparison of the distributions for each dose level indicates that loop growth occurs with increasing dose. A population of defect cluster with size as low as TEM resolution limit, 1.5-2 nm, was observed

for all the doses and the maximum size increases as dose increases. These observations imply that new clusters of defects are being created as dose accumulates, and that, at the same time, growth of existing clusters takes place. Therefore, point defects created as irradiation proceeds have two destinations, the creation of new clusters and contribution to the growth of the existing ones.

Average size values correspond to those clusters that continuously grow more or less from the beginning. Mean size of the loop distributions increases with dose beyond a dose of 1 dpa where a bimodal size distribution is observed. At 1 dpa clusters start to overlap and this gives place to an apparent reduction in density when dose increases in the region of high dose.

Except at lower dose, the majority of dislocation loops were found to be $\frac{1}{2}\langle 1,1,1 \rangle$ type. A systematic study to investigate dose effect on evolution of Burgers vector is been undertaken. An effect of TEM sample thickness on Burgers vector type has been observed in these specimens irradiated with ions as thin foils. At thinner areas, Burgers vector with $b = \langle 100 \rangle$ type were observed, but at thicker areas $\frac{1}{2}\langle 1,1,1 \rangle$ were the type predominant.

Model: kinetic Monte Carlo calculations

The nucleation and growth of defects and clusters is followed using a kinetic Monte Carlo (kMC) model for the same conditions used in the experiments reported above. In order to do these calculations information about the migration energies of different types of defects, self-interstitials and vacancies, the binding of defects to clusters and the initial distribution of the damage produced by the irradiation must be known. Such information can be obtained from *ab initio* and molecular dynamics simulations. *Ab initio* calculations have shown that small clusters of both vacancies and self-interstitials in α -Fe are mobile [1]. This information was used to reproduce the resistivity curve measured experimentally in electron irradiation α -Fe using a kinetic Monte Carlo approach [1]. The same values of mobilities of vacancies and self-interstitials, as well as binding energies of defects included in Ref. [1] were used in this work.

However, the migration and growth of self-interstitial clusters in α -Fe poses still many questions. The behaviour of small self-interstitial clusters (up to size 5) is known from *ab initio* calculations [2]. These calculations show that up to size 4, the most stable self-interstitial clusters are of $\langle 110 \rangle$ type and should move with migration barriers similar to that of single self-interstitials, on the order of 0.3-0.4 eV. However, for self-interstitial clusters of size 5 the most stable configuration is that of a $\langle 111 \rangle$ type. These type of clusters have much lower migration barriers, on the order of 0.1 eV. Since it is not possible to perform *ab initio* calculations for systems sizes of several thousands of atoms only empirical potential calculations exist on the mobility of large $\langle 111 \rangle$ loops. These calculations point towards low migration barriers for these clusters for all sizes studied. This is, however, still a controversial issue. Since $\langle 111 \rangle$ loops are observed experimentally there must be a trapping mechanism for these clusters. Several approaches to include this trapping have been used in the literature. Hardouin-Duparc, *et al.* [3] have used a rate theory model where only single self-interstitial and single vacancies are mobile species and all clusters are immobile. With this model they were able to reproduce electron irradiation experiments. On the other hand Domain, *et al.* [4] have shown that in order to reproduce neutron irradiation experiments it is necessary to introduce the mobility of self-interstitial clusters and the presence of traps for these clusters. The nature of these traps is also still not clear. Some results seem to point to the interaction of loops with impurities, such as carbon. However, *ab initio* calculations [5] point towards a repulsive interaction between self-interstitials and carbon atoms. OKMC calculations including elastic interactions between mobile self-interstitials and spherical impurities also show an effective trapping for these defects [6].

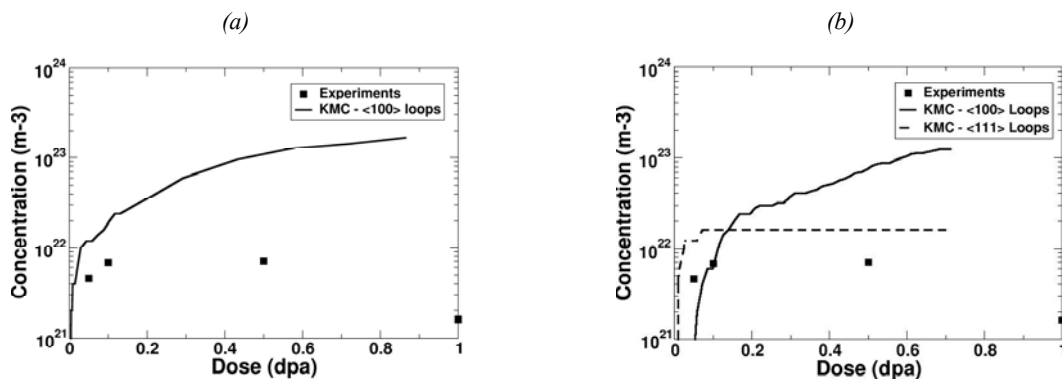
Experimental measurements, on the other hand, of irradiated α -Fe show the presence of two different types of loops, $\langle 111 \rangle$ and $\langle 100 \rangle$ loops [7]. The mechanism to form the later is also not yet fully understood. The formation of $\langle 100 \rangle$ loops through the reaction of $\langle 111 \rangle$ loops was first proposed by Masters in 1965 [8]. Molecular dynamics simulations [9] have shown that a reaction between $\langle 111 \rangle$ loops can result in the formation of a $\langle 100 \rangle$ junction, although the $\langle 100 \rangle$ loop was not observed in the time scale of the simulations. More recent molecular dynamics calculations have shown that in order to obtain $\langle 100 \rangle$ loops it is necessary to have an interaction between three $\langle 111 \rangle$ loops [10]. In our kinetic Monte Carlo model we have implemented a mechanism of formation of $\langle 100 \rangle$ loops by the reaction of two $\langle 111 \rangle$ loops.

Therefore, the model used in these calculations considers the following mechanisms for migration and growth of self-interstitial and vacancy clusters. Vacancies up to size 4 are mobile with values from *ab initio* calculations [1]. Self-interstitial clusters up to size 5 are considered to be of $\langle 110 \rangle$ type and therefore migrate using values obtained also by *ab initio* calculations, between 0.34 and 0.4 eV and their migration is in three-dimensions [2]. Those self-interstitial clusters of sizes larger than 5 are considered to be of $\langle 111 \rangle$ type with mobilities of approximately 0.1 eV and one-dimensional migration [2,11]. The formation of $\langle 100 \rangle$ loops can occur through the reaction of two $\langle 111 \rangle$ loops as long as both loops have at least 15 defects each and the sum of their burgers vector is such that a $\langle 100 \rangle$ loop can be formed. Moreover, we consider the possibility of having impurities in the sample, although the nature of these impurities is not yet know. As mentioned above, previous calculations [3,4] have shown that it is necessary to include some type of trapping of self-interstitial clusters in order to reproduce the experimental observations both in electron irradiation and in neutron irradiation. The trapping model included consists simply of trapping the mobile $\langle 111 \rangle$ loops when they are within the capture radius of one of the impurities. Simulations with and without impurities are presented below. The initial distribution of the damage produced by the irradiation and included in the model was obtained from molecular dynamics simulations from a data base of cascades by Roger Stoller [12]. Cascades were distributed according to TRIM calculations for a 150 keV Fe irradiation in Fe. Sample thickness was 50nm and surfaces are considered to be perfect sinks for defects.

Results: comparison between experiments and model

Figure 3 shows the concentration of loops as a function of dose as obtained from the kinetic Monte Carlo model (solid and dashed lines) compared to the experimental measurements (squares) for two different conditions.

Figure 3. Defect concentration as a function of dose. Comparison between experiments (dots) and simulations (solid line) for (a) no impurities included in the simulations (b) 0.2 apm traps for self-interstitial atoms

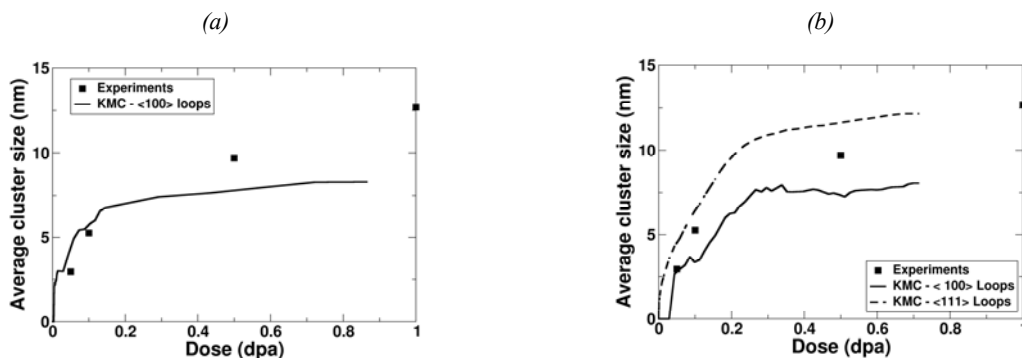


In Figure 3(a) no traps were included in the model while in Figure 3(b) a concentration of 0.2 appm traps was included. In order to compare the experimental measurements and the results of the calculations it is necessary to define the minimum size of clusters that are visible in the microscope. In this case we considered that only those clusters larger than 1 nm in radius are clearly observed under the TEM. Therefore, the simulation values are the total concentration of clusters larger than 1 nm in radius. Experimental values presented are the total concentration of clusters independently of the character of the loop, while for the case of simulations we present the concentration of $\langle 100 \rangle$ and $\langle 111 \rangle$ loops separately. In the case when no traps are included in the simulation, such as in Figure 3(a) the only types of loops in the simulations are $\langle 100 \rangle$ loops, since all $\langle 111 \rangle$ loops are mobile and quickly scape to the surfaces. Note that the simulations were performed in a sample 50 nm in thickness. On the other hand, when a small amount of traps are included in the simulation, 0.2 appm in this case, as shown in Figure 3(b) both $\langle 111 \rangle$ and $\langle 100 \rangle$ loops can be observed in the simulations, in better agreement with experimental measurements. At low doses most of the clusters are of $\langle 111 \rangle$. The total concentration of $\langle 111 \rangle$ loops saturates when all trapping sites are occupied by a $\langle 111 \rangle$ loop.

Comparing the total concentration of defects obtained experimentally and from the simulations we can observe that at low doses there is quite a good agreement between them. However, at higher doses simulations overestimates the total defect concentration. In particular, simulations do not reproduce the decrease in cluster concentration at the highest dose, 1 dpa, observed experimentally. This is due to the lack of coarsening between adjacent immobile clusters in the model. In general, it is important to point out that the comparison of total defect concentration between experiments and simulations is not unambiguous since assumptions must be made regarding the visible cluster size, as noted earlier. Moreover, there are also issues regarding the dependence with sample thickness.

More significant is probably the correlation between the average cluster sizes measured experimentally and those obtained from the simulations. Figure 4 presents also the comparison between experiments and simulations. Figure 4(a) shows the simulation results when no impurities are considered in the model while Figure 4(b) shows the results when 0.2 appm impurities are included. The agreement between the measured average cluster sizes and those predicted are quite remarkable. Only at the higher doses the average cluster size obtained by the simulations is underestimated, again possibly due to the lack of coarsening in the model.

Figure 4. Average cluster size as a function of dose. Comparison between experiments (dots) and simulations (solid line) for (a) no impurities included in the simulations (b) 0.2 appm traps for self-interstitial atoms



Conclusions

In summary we have presented results from experiments produced by irradiation of 150 keV Fe²⁺ on UHP-Fe at different doses. The damage produced has been characterised by TEM. These experiments show that the defect density increases rapidly at low doses, with saturation occurring at a dose between 0.1 and 0.5 dpa. At higher doses density decreases due to loop coarsening, with the creation of new clusters and loop growth. The character of the defects were analysed in detail. Large loops at thicker areas and doses higher than 0.5 dpa are identified as type $b = a/2\langle 111 \rangle$ interstitial dislocation loops, only a small fraction are $b = a\langle 001 \rangle$ type. At thinner areas they are mainly $b = \langle 100 \rangle$.

Parallel to the experimental measurements a kinetic model was developed with input parameters from *ab initio* and molecular dynamics simulations. The model assumes that $\langle 100 \rangle$ loops are formed by the reaction between two $\langle 111 \rangle$ loops. Using this model the total cluster concentration as a function of dose, as well as the average cluster size was compared with the experimental measurements. It is observed that for low doses both the defect concentration and average cluster size agree with the values measured experimentally, while there is a discrepancy at the highest doses due to the lack of coarsening in the current model. The model also shows that the observation of $\langle 111 \rangle$ loops, at least in thin films, is only possible in the presence of traps, since otherwise these loops migrate quickly to the surfaces. This is in agreement with the experimental observation that in thinner areas mostly $\langle 100 \rangle$ loops are observed. Although the mechanism of formation of $\langle 100 \rangle$ loops through reactions between $\langle 111 \rangle$ loops is not the only possible explanation for the experimental observation of these types of loops, these simulations show that this is indeed a possible one which provide reasonable quantitative agreement with experiments.

Acknowledgements

This work was supported by the European Commission in the framework of the Project PERFECT. Simulations were performed at the Matcon Cluster of the UA built and managed by GuiriSystems.

REFERENCES

- [1] Fu, C.C., J. Dalla Torre, F. Willaime, J-L. Bocquet, A. Barbu, *Nature Materials*, 4, 68(2005).
- [2] Willaime, F., *Nucl. Instrum. and Methods*, B 228, 92-99 (2005).
- [3] Hardouin Duparc, A., C. Moingeon, N. Smetniansky-de-Grande, A. Barbu, *J. of Nucl. Mater.*, 302, 143 (2002).
- [4] Domain, C., C.S. Becquart, L. Malerba, *J. of Nucl. Mater.*, 335, 121-145 (2004).
- [5] Domain, C., C.S. Becquart, *J. Foct, Phys. Rev.*, B 69, 144112 (2004).

- [6] Hudson, T.S., S.L. Dudarev, M.J. Caturla, A.P. Sutton, *Phil. Mag.*, 85, 661 (2005).
- [7] Ward, A.E., S.B. Fisher, *J. Nucl. Mater.*, 166, 227 (1989).
- [8] Masters, B.C., *Phil. Mag.*, 11, 881 (1965).
- [9] Marian, J., B.D. Wirth, J.M. Perlado, *Phys. Rev. Lett.*, 88, 255507(2002).
- [10] Terentyev, D., Ph.D Thesis (2006).
- [11] Soneda, N., T. Diaz de la Rubia, *Phil. Mag.*, A 81, 331 (2001).
- [12] Stoller, R.E., G.R. Odette, B.D. Wirth, *J. of Nucl. Mater.*, 251, 49(1997).

COMBINED TEM, PAS AND SANS INVESTIGATION OF NEUTRON-IRRADIATED PURE IRON

F. Bergner¹, A. Al Mazouzi², M. Hernandez-Mayoral³, A. Ulbricht¹

¹Forschungszentrum Dresden-Rossendorf, Germany

²SCK•CEN Mol, Belgium

³CIEMAT Madrid, Spain

Abstract

Fission spectrum neutron irradiation of pure Fe at irradiation temperatures of about 300°C gives rise to the formation of two populations of defects: planar dislocation loops and spherical vacancy-type clusters. Knowledge of the type and size distributions of these populations is important for the purpose of multi-scale modelling of the mechanical behaviour of Fe-based alloys. Among the experimental techniques with nanometer size resolution, transmission electron microscopy (TEM) and small-angle neutron scattering (SANS) allow to gain information on both nature and size distribution of particular types of defects. Furthermore, positron annihilation spectroscopy (PAS) is sensitive to sub-nanometer size open-volume defects. However, there is no single experimental technique capable of providing the full set of information required for calibration and validation of advanced models. Complementarity between the three techniques to identify and quantify the defects created by irradiation in pure Fe is emphasised in the paper. It is shown that while TEM allows direct size-resolved evidence of dislocation loops, PAS a qualitative appreciation of the existing sub-nanometer size vacancy-type clusters, SANS yields indirect size-resolved evidence of vacancy-type clusters, which form a sound basis for the quantification of the size distributions.

Introduction

Neutron irradiation of pure Fe under fission reactor conditions gives rise to the formation of two populations of defects on the nanometer size scale: planar dislocation loops and spherical vacancy-type clusters. Knowledge of the type and size distributions of these populations is important for the purpose of multi-scale modelling of the mechanical behaviour of Fe-based alloys. Among the experimental techniques with nanometer size resolution, transmission electron microscopy (TEM) and small-angle neutron scattering (SANS) allow to gain information on both nature and size distribution of particular types of defects. Furthermore, positron annihilation spectroscopy (PAS) is sensitive to sub-nanometer size open-volume defects. However, there is no single experimental technique capable of providing the full set of information required for calibration and validation of advanced models. Previous work on pure Fe including the application of TEM [1-3], PAS [2,4,5] and SAXS [6] was focused on the effect of neutron irradiation on defect evolution in Fe irradiated at lower temperatures or on the effect of solutes with results for pure Fe serving as reference condition [7]. There are few publications on pure Fe neutron-irradiated at about 300°C using individual techniques [8-11], while the application of the present combination of techniques (TEM, PAS and SANS) to the same lot of pure Fe neutron-irradiated at 300°C seems to be unique.

Results obtained using TEM, PAS and SANS for the same lot of pure Fe neutron-irradiated at 300°C are presented and confronted with one another. The paper will emphasise the complementarity between the three techniques to identify and quantify the defects created by irradiation in pure Fe. It will be shown that while TEM allows direct size-resolved evidence of dislocation loops, PAS a qualitative appreciation of the existing sub-nanometer size vacancy-type clusters, SANS yields indirect size-resolved evidence of vacancy-type clusters, which form a sound basis for the quantification of the size distributions.

Experiments

Materials and irradiation

Commercially pure Fe (<30 ppm C, average grain size 250 µm, dislocation density $7 \times 10^{13} \text{ m}^{-2}$) was neutron-irradiated in the Callisto rig (IPS2) in the Belgian reactor (BR2). An irradiation temperature of 300°C and a neutron fluence rate of about $9 \times 10^{13} \text{ n/cm}^2\text{s}$ ($E > 1 \text{ MeV}$) were maintained. The neutron fluence covered the range from $1.7 \times 10^{23} \text{ n/m}^2$ to $1.3 \times 10^{24} \text{ n/m}^2$ ($E > 1 \text{ MeV}$). This fluence range corresponds to the range of neutron damage dose from 0.026 to 0.19 displacements per atom (dpa).

Small-angle neutron scattering (SANS)

The SANS measurements were carried out at the SINQ facility of PSI [12] at a wavelength of 0.50 nm with a sample-detector distance of 2 m. The samples were placed in a saturation magnetic field. For the analysis including corrections related to both sample holder and detector, absolute calibration as well as separation of magnetic and nuclear contributions of SANS data, we refer to [13]. For a number of N homogeneous spherical scatterers of radius, R , in the probed volume, V_p , the coherent scattering cross-section can be expressed as:

$$\left(\frac{d\Sigma}{d\Omega} \right)_c(\vec{Q}) = \frac{N}{V_p} \Delta\eta^2 V^2(R) |F(\vec{Q}, R)|^2 \quad (1)$$

with the volume, V , of the sphere, the scattering vector, $\vec{Q} = (Q_x, Q_y, Q_z)$, and the form factor, F :

$$|F(\vec{Q}, R)|^2 = \frac{9(\sin QR - QR \cos QR)^2}{(QR)^6} \quad (2)$$

Magnetic and nuclear scattering are not distinguished in Eq. (1). The scattering contrast, $\Delta\eta$, is given by:

$$\Delta\eta_i^2 = \left[(n\bar{b}_i)_S - (n\bar{b}_i)_M \right]^2 \quad (3)$$

where $i = m$ for magnetic scattering and $i = n$ for nuclear scattering. Subscripts S and M refer to scatterer and matrix, respectively, and \bar{b}_m and \bar{b}_n denote the average scattering length for magnetic and nuclear scattering, respectively. In the case of non-magnetic scatterers ($\bar{b}_{m,S} = 0$) in pure Fe:

$$\Delta\eta_m^2 = (n_{Fe} b_{m,Fe})^2 \quad (4)$$

For dislocation loops [14] the above separation of terms is impractical and the cross-section is approximately expressed as:

$$\left(\frac{d\Sigma}{d\Omega} \right)_c(\vec{Q}) = \frac{N}{V_p} \Delta\eta^2 \frac{1-2\nu}{1-\nu} \cdot \frac{2\pi b R \sqrt{Q_x^2 + Q_y^2}}{Q^2} J_1 \left(R \sqrt{Q_x^2 + Q_y^2} \right) \quad (5)$$

where ν is Poisson ratio, b is Burgers vector of the dislocation loop of radius, R , and J_1 is the Bessel function.

The indirect transformation method [15] based on a description of the size distribution by a number of 40 cubic splines with nodes uniformly distributed in the radius range from 0 to 15 nm is applied to obtain, by means of a weighted least squares procedure, the size distribution of scatterers without assuming a certain type of distribution. The unirradiated control for pure Fe is subtracted after performing the transformation in the present case.

Transmission electron microscopy (TEM)

Microstructural characterisation of samples has been carried out in a transmission electron microscope JEOL, model JEM-2010 of 200 keV and LaB₆ filament, in CIEMAT. Samples were electropolished in a Metalthin machine with 5% perchloric acid in methanol at -60°C and 20 V.

TEM is particularly sensitive to image irradiation-induced dislocation loops. For the irradiation conditions investigated, the majority of the loops detected is characterised by a Burgers vector of <100>-type. The size distribution of dislocation loops was determined by means of direct counting taking into account both the size of the probed volume and the fact that some families of loops are invisible under the imaging conditions selected.

Positron annihilation spectroscopy (PAS)

The positron lifetime spectrometer (PLT) described in detail in [16] has been recently installed in the laboratory for high- and medium-level activity at SCK•CEN. The PLT set-up consists of a digital oscilloscope (LeCroy WaveRunner 6100A, 1GHz, 4-Channel, 5 GS/s, 4 Mpts), three movable scintillation detectors based on single crystal BaF₂ scintillators and Hamamatsu H3378-51 photomultipliers (PM) (optimal selected for transit time spread, typical 0.37 ns, HV = 3000 V). Time differences are measured between the arrivals of a 1 274 keV start gamma (birth of positron) from ²²Na and two positron-electron annihilation gammas (stop- γ -rays) of 511 keV.

The digitalisation of the PM signals in the oscilloscope allows a clear definition of the coincidence events and also a reduction of the background signals. The time resolution of 170 ps full-width at half-maximum (FWHM) is achieved for the positron lifetime measurements of radioactive specimens. The measurement of irradiated steels was possible thanks to the mobility of the detectors that allow the decrease of their dead time even in the presence of high activity sources. The obtained spectra were analysed using the LT code developed by “kansys” assuming two components contribution after the subtraction of the background and the positron source contribution.

Results

Measured total and separated nuclear coherent SANS cross-sections obtained for pure Fe exposed to a neutron dose of 0.19 dpa are presented in Figures 1 and 2, respectively. The total coherent SANS cross-section is compared with corresponding results for pure Fe exposed to a neutron dose of 0.038 dpa [17] in Figure 1. The differences in the scattering curves for the unirradiated reference conditions can be due to the degree of purity and grain size. However, the irradiation effects are observed to be similar in both cases: there is a pronounced irradiation-induced increase of the scattering cross-section at larger values of the scattering vector, $Q > 0.5 \text{ nm}^{-1}$, and a marginal increase for $Q < 0.5 \text{ nm}^{-1}$. In Figure 2 the scattering cross-section calculated for a measured distribution of dislocation loops is also included (see below).

Dislocation loops were observed by means of TEM. A typical TEM micrograph is shown in Figure 3 for pure Fe exposed to a neutron dose of 0.19 dpa. The size distributions of loops calculated by direct counting are displayed in Figure 4 for three different doses. Average loop diameter and total loop density are about 5 nm and $0.85 \times 10^{21} \text{ m}^{-3}$, 7 nm and $1.3 \times 10^{21} \text{ m}^{-3}$, and 10 nm and $4 \times 10^{21} \text{ m}^{-3}$ for 0.051 dpa, 0.1 dpa, and 0.19 dpa, respectively. We have found a monotonic growth of both number density and diameter with increasing dose.

Figure 1. Total coherent SANS cross-section for pure Fe exposed to doses of 0.19 dpa (full circles) and 0.038 dpa (full triangles [17]), unirradiated references marked as open symbols

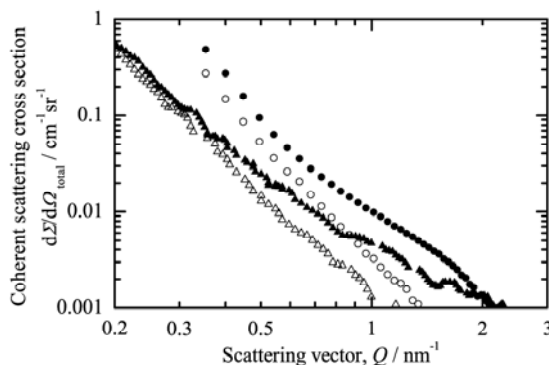


Figure 2. Coherent nuclear scattering cross-section obtained by SANS for pure Fe exposed to a dose of 0.19 dpa (full symbols), unirradiated control (open symbols) and calculated scattering cross-section due to loops (solid line)

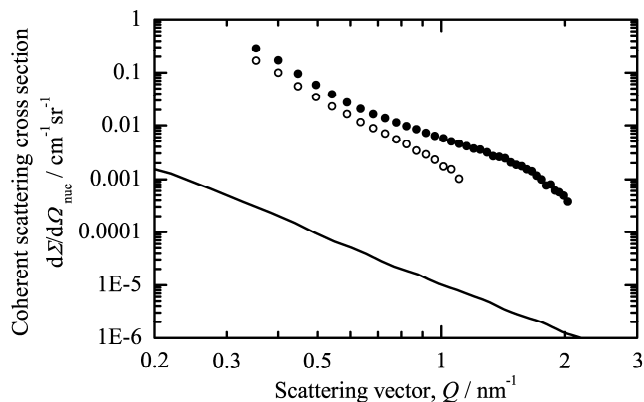


Figure 3. TEM micrograph showing irradiation-induced dislocation loops for pure Fe exposed to a neutron dose of 0.19 dpa

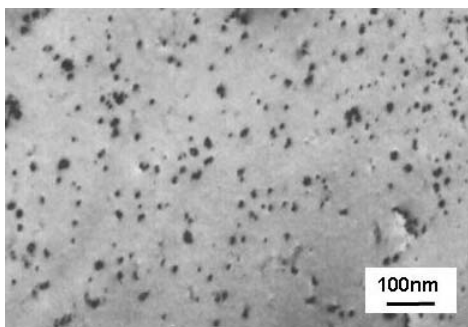
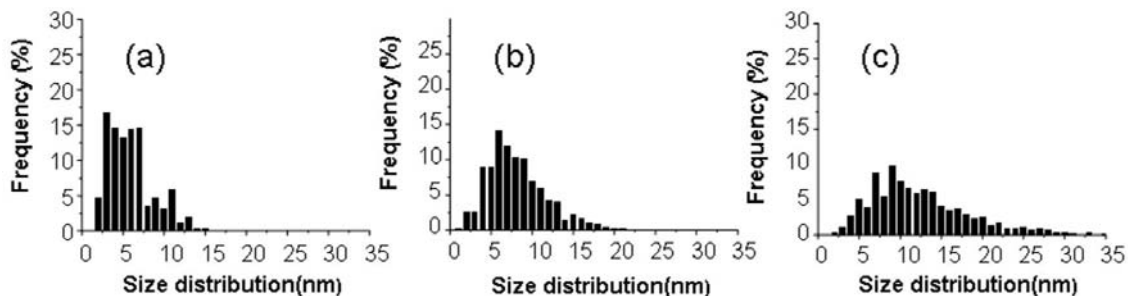
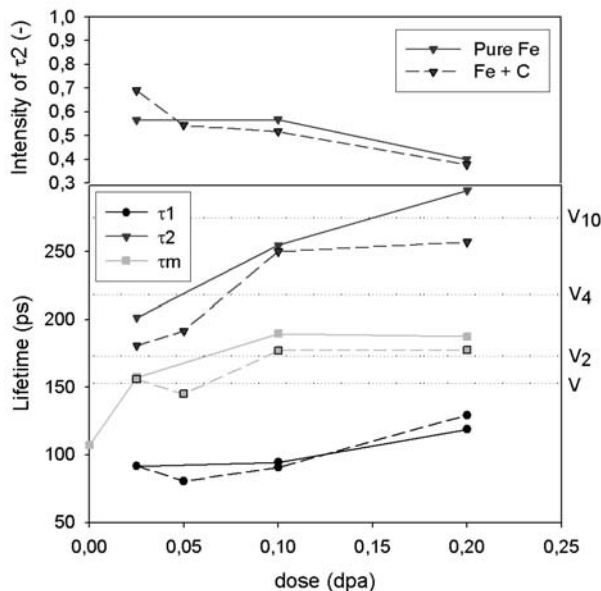


Figure 4. Size distribution of dislocation loops obtained by TEM for pure Fe exposed to neutron doses of 0.051 dpa (a), 0.1 dpa (b) and 0.19 dpa (c)



The positron lifetime results can say more about the size of the clusters, in particular about the amount of vacancies (at numbers less than about 100 [5]) inside the cluster. In computer simulations [18] specific lifetimes for clusters with one, two and more vacancies were found. Some of the results are shown in Figure 5 along with the measured lifetime evolution during irradiation for pure iron and Fe+C.

Figure 5. Positron lifetime of pure iron and Fe+C given as function of dose. The results are divided into two lifetime-components (τ_1 and τ_2), their average is given as well (τ_m).



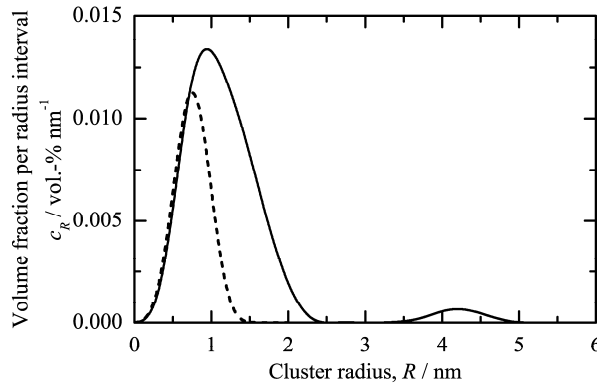
Discussion

The first question to be answered is whether or not there is an overlap of the features detected by means of TEM and SANS. In order to do this we have calculated the nuclear scattering cross-section caused by the distribution of dislocation loops observed for the 0.19 dpa irradiation. The calculated cross-section caused by loops are confronted in Figure 2 with the extra scattering obtained in the SANS experiment for the same irradiation condition. We have found that scattering caused by loops is orders of magnitude less than the observed extra scattering. Therefore, it can be concluded that the features detected by SANS belong to another population of defects, we assume spherical (as opposed to planar) vacancy-type defects.

If we further assume these defects to be pure vacancy clusters, size distribution can be calculated according to Eqs. (1) to (3) in absolute units. This size distribution is compared in Figure 6 with the size distribution obtained on the same assumptions for pure Fe exposed to a neutron dose of 0.038 dpa [17]. The second part of the question posed above is related to the possible contribution of the defect population detected by SANS to what is interpreted as loops in the TEM analysis. For the 0.038-dpa irradiation, the size distribution obtained from SANS essentially decays below the detection limit of TEM of about 1 nm in radius. For the 0.19-dpa irradiation, comparison of the corresponding size distributions in Figures 4(c) and 6 shows that there is only a marginal overlap of both defect populations with respect to size, if any. We conclude that the present analysis is not biased by overlap effects.

For pure iron, it is observed by means of PAS that the vacancy-clusters are growing to form nanovoids during irradiation. The clusters are growing due to a supply of new vacancies during the irradiation, but as the intensity slightly decreases, also some small clusters gather together. Even at high doses, the vacancy-type clusters are very small. The measured positron lifetimes indicate that vacancy-clusters containing some 10 vacancies are formed due to the irradiation up to a dose of 0.19 dpa. If a certain amount of carbon is added, the clusters will not grow that big. The carbon-atoms will be nucleation-sites for the vacancy-clusters, so some more clusters will appear.

Figure 6. Size distribution of irradiation-induced defect clusters calculated from SANS cross-sections on the assumption of spherical non-magnetic clusters for pure Fe exposed to 0.19 dpa (solid line – this work) and to 0.038 dpa (dashed line – [17])



The parameters characterising the defect population detected by SANS are summarised in Table 1. A pronounced increase of the total volume fraction of irradiation-induced clusters with dose is observed. This increase is caused by both cluster growth and increase of number density. The dependence of peak radius and number density on neutron dose for spherical clusters is weaker than for dislocation loops. There is a significant amount of clusters of sizes in excess of 1 nm radius, i.e. larger than expected from the PAS data. The detailed nature of the irradiation-induced defects detected by SANS is not clear. The *A*-ratio (defined as ratio of total and nuclear SANS cross-section) of 1.4 supports any type of self-defects in Fe, but cannot differentiate between pure spherical compact vacancy clusters and a sponge-like morphology containing vacancies or small vacancy clusters and Fe. A decision on the latter point should be possible on the basis of a detailed quantitative confrontation of SANS and PAS results. It is beyond the scope of this paper.

Table 1. Integral parameters characterising the defect populations detected by SANS

Dose (dpa)	Peak radius (nm)	<i>A</i> -ratio	Volume fraction (%)	Number density (m ⁻³)
0.19	0.95	1.4	0.014	4×10^{22}
0.038	0.78	1.4	0.006	3×10^{22}

Conclusions

It has been shown that while TEM allows direct size-resolved evidence of dislocation loops, PAS a qualitative appreciation of the existing sub-nanometer size vacancy-type clusters, SANS yields indirect size-resolved evidence of vacancy-type clusters, which form a sound basis for the quantification of the size distributions. We conclude that the size distributions of loops obtained by TEM and the size distribution of vacancy-type defects obtained by SANS are not biased by overlap effects. There seems to be a discrepancy between the sizes of vacancy-type clusters derived from SANS and PAS.

Acknowledgement

This work was supported by the European Commission in the framework of the Project PERFECT. The assistance of M. Große during the SANS experiment at PSI is gratefully acknowledged.

REFERENCES

- [1] Eyre, B.L., A.F. Bartlett, *Phil. Mag.*, 12, 261-272 (1965).
- [2] Eldrup, M., B.N. Singh, S.J. Zinkle, *et al.*, *J. Nucl. Mater.*, 307-311, 912-917 (2002).
- [3] Zinkle, S.J., B.N. Singh, *J. Nucl. Mater.*, 351, 269-284 (2006).
- [4] Hautojärvi, P., L. Pöllänen, A. Vehanen, J. Yli-Kaupilla, *J. Nucl. Mater.*, 114, 250-259 (1983).
- [5] Eldrup, M., B.N. Singh, *J. Nucl. Mater.*, 323, 346 (2003).
- [6] Franz, H., G. Wallner, J. Peisl, *Rad. Eff. Def. Solids*, 128, 189-204 (1994).
- [7] Nagai, Y., K. Takadate, Z. Tang, *et al.*, *Phys. Rev. B*, 67, 224202 (2003).
- [8] Horton, L.L., J. Bentley, K. Farrell, *J. Nucl. Mater.*, 108 & 109, 222-233 (1982).
- [9] Robertson, I.M., M.L. Jenkins, C.A. English, *J. Nucl. Mater.*, 108 & 109, 209-221 (1982).
- [10] Okada, A., T. Yasujima, T. Yoshiie, *et al.*, *J. Nucl. Mater.*, 179-181, 1083-1087 (1991).
- [11] Singh, B.N., A. Horsewell, P. Toft, *J. Nucl. Mater.*, 271-272, 97-101 (1999).
- [12] Kohlbrecher, J., W. Wagner, *J. Appl. Cryst.*, 33, 804-806 (2000).
- [13] Keiderling, U., *Appl. Phys. A*, 74 [Suppl.], S1455 (2002).
- [14] Seeger, A., M. Rühle, *Ann. Phys.*, 11, 216-229 (1963).
- [15] Glatter, O., *J. Appl. Cryst.*, 13, 7-11 (1980).
- [16] Jardin, M., M. Lambrecht, A. Rempel, *et al.*, *Nucl. Instr. and Methods in Phys. Res. A*, 568, 716-722 (2006).
- [17] Bergner, F., A. Ulbricht, M. Hernandez-Mayoral, P.K. Pranzas, *J. Nucl. Mater.*, submitted.
- [18] Kuriplach, J., O. Melikhova, C. Domain, *et al.*, *Appl. Surf. Sci.*, 252, 3303-3308 (2006).

SYNCHROTRON LIGHT TECHNIQUES FOR THE INVESTIGATION OF ADVANCED NUCLEAR REACTOR STRUCTURAL MATERIALS

M.A. Pouchon, A. Froideval, C. Degueldre, D. Gavillet, W. Hoffelner
Paul Scherrer Institute, CH-5232 Villigen PSI, Switzerland

Abstract

In the frame of the Generation IV initiative, different structural material candidates are investigated at the Paul Scherrer Institute. These are oxide dispersion strengthened (ODS) steels, intermetallic materials and ceramic composite materials. The response of the material to different potential loads (irradiation, temperature ...) is addressed in a multi-scale approach, both, modelling wise and also experimentally. The investigation of each scale delivers at least a qualitative understanding of possibly evolving damage in the material and also delivers a validation of the corresponding scale on the modelling side.

From the experimental side, the lower end of the scale, the atomistic and structural level, can be investigated by conventional techniques, as for example transmission electron microscopy (TEM) and X-ray diffraction (XRD). However, the use of synchrotron radiation techniques offers an ideal, complementary way to investigate the material structure and other properties. This paper presents applications in the field of the ODS research, where the structural behaviour of the nanoscopic dispersoids can selectively be investigated, although only being present with roughly 5 wt % in the matrix. A study showing the structural behaviour of these oxide particles as a function of irradiation illustrates the potential of the extended X-ray absorption fine structure (EXAFS) technique. Using X-ray magnetic circular dichroism (XMCD), which is a difference-signal of two X-ray absorption spectra recorded for positive and negative helicities of the beam, the magnetic structure and some magnetic parameters, can be resolved. An example shows, how this can be applied to understand (Fe,Cr) systems, which is the base alloy of the investigated ODS steel. The results deliver an important crosscheck for modelling.

Beside the presentation of these techniques, this paper shows how beamline techniques can serve nuclear research, with possibly activated materials. At the Paul Scherrer Institute, a sample holder for highly active materials has been developed, and has already served for EXAFS measurements at the Swiss Light Source (SLS). The set-up of this sample holder is briefly presented here.

Introduction

Generation IV Initiative/HT-Mat Group at PSI

The Generation IV International Forum (GIF) is an international R&D effort for future nuclear reactor designs [1]. For an increase in efficiency, many of these systems are foreseen to run at high temperatures. At the Paul Scherrer Institute in Switzerland, the High Temperature Materials (HT-Mat) Group mainly concentrates on the Very High Temperature Reactor (VHTR), a gas-cooled system, which is foreseen to achieve gas temperatures up to 1 000°C; not only significantly increasing efficiency with a gas turbine, but also having the possibility to use the system for direct heat applications (e.g. hydrogen production, using the sulphur-iodine cycle [2], or the high temperature electrolysis).

Addressing material issues

The very high temperatures in the reactor and economic aspects, which imply long component lifetimes, demand novel classes of materials. Long-term experience for such candidate materials under irradiation conditions is missing. In order to address the damage process, a multi-scale approach is chosen for the experimental work, and for modelling; for both methods the goal is to develop the understanding of the damage development, from point defects to component failure.

Materials of interest

Several materials are of interest to the VHTR community. Very attractive classes of candidates are Fe-Cr based alloys and especially some oxide dispersion strengthened (ODS) versions of them. The addition of oxide particles to a metal matrix provides pinning points for dislocations, thus enhancing the creep behaviour of the material. Ceramics, especially black ceramics, are another class of materials with very advantageous high temperature behaviour and good irradiation properties. Depending on the application, the disqualification due to the brittle behaviour of ceramics can be overcome by the use of composite materials. Finally intermetallics are under discussion, which show very good high temperature properties. This paper concentrates on the Fe-Cr system, and its creep resistant modification, the ODS steels.

Fe-Cr system

The Fe-Cr system is the base for many high performance steels. Table 1 gives an overview of such alloys, as a function of their Cr content, ranging from 1 up to 23 wt.%. In this list especially the 2¼Cr1Mo, 9-13 Cr(W), ODS steels (such as PM2000) and Alloy 800 H are of interest to the VHTR community. Among the numerous Fe-based binary alloy systems, Fe-Cr plays a particularly significant role. This stems from its interesting magnetic and crystallographic properties. Concerning the magnetic properties, it is especially interesting in the regime of Cr concentration between 0 and 20 wt.%; alloying of ferromagnetic Fe with anti-ferromagnetic Cr, leads to magnetic frustration [3,4]. This effect is important for atomistic modelling as molecular dynamics [5] and kinetic Monte Carlo [6], and is addressed by *ab initio* calculations. An experimental validation is important, being addressed by the PEEM/XMCD experiment described later (for a full description see [7]).

Table 1. Overview of some Fe-Cr alloys which are of technical interest. Some of them are of special interest for the VHTR community. The Cr content varies from 1 up to 23 wt.%.

Type of steel	Typical chromium content (wt.%)	Characteristics and typical applications
1CrMoNiV	1	Ferritic/bainitic steels for turbo-machinery and structural parts up to 450°C.
2¼Cr1Mo	2.25	Ferritic/bainitic vessel steels for temperatures up to 500°C. Candidate for reactor pressure vessel of VHTRs.
12 CrMoV	12	Martensitic steels for turbomachinery and corrosion resistant plants for temperatures up to 550°C.
9-13 Cr(W)	9-13	Newly development martensitic steels for steam turbines, fusion plants, and VHTR reactor pressure vessels for temperatures up to 600°C. Currently ODS version in development.
316	16-18	Austenitic creep resistant steel for temperatures up to 750°C.
PM2000	20	Ferritic, oxide dispersion strengthened steel for structural applications up to 1 050°C. The oxide dispersion particles act as obstacles for dislocations improving therefore the creep strength. Part of the NES HIG Temperature Materials project.
Alloy 800 H	19-23	Austenitic Fe-based superalloy for piping and structural parts up to 900°C. Candidate for VHTR piping applications.

ODS material

The idea of introducing fine obstacles, in order to impede the dislocation movements, is very old and commonly applied. Precipitation hardening is a widely used technique, where the formation of the precipitates is achieved by alloy design and special heat treatment techniques. Nickel-based superalloys, and many structural materials based on aluminium and titanium are based on this principle. The obstacles are metallic or intermetallic phases, which differ from the matrix. In the ODS materials, the dispersoids are oxides, and therefore of ceramic nature. Because of high hardness and good thermal properties, the behaviour of these classes of materials promised to be superior. For most of these materials the production is an expensive powder-metallurgical process. This includes high energy milling to achieve a solid solution which contains a uniform dispersion of the oxide. The powder is consolidated using hot isostatic pressing followed by a hot and cold rolling procedure. The process is finalised by a thermal treatment [8]. Attempts are underway to simplify the process into a dispersion injection technique, where the material can be cast [9].

Experimental and theoretical background

Beamline methods

General background of synchrotron-radiation

Synchrotron radiation has many advantages, which are often based on its tuneable energy, the very high flux, the possibility to focus and to use polarised photons. Some of these advantages and their application are shortly described here. With the very high flux, it is often possible to perform

in situ experiments, because good statistics can be generated in a short time. Combined with the possibility of short pulses, intense synchrotron beams can be used to characterise dynamic effects. As the beam can be focused, one can address very small regions, even being able to characterise microscopic parts within a matrix, or to perform a scan of a surface and map it with regards to different properties. Certain techniques, which rely on energy-specific properties of elements, as for example the absorption, offer the possibility to concentrate on one element, and therefore characterise its properties within a matrix. Because of the element specificity, one does not suffer background effects from the other elements (except if the absorptions are overlapping); EXAFS (see description below) is an important example. The possibility of polarised photons results in the ability to study the spin and orbital moments of electrons/atoms, and therefore to explore the magnetic properties of materials. This is applied in the XMCD/PEEM technique further described below.

EXAFS/XANES

Extended X-ray absorption fine structure (EXAFS) is an experimental method of determining the co-ordination environment of selected elements, by analysing oscillations in the absorption versus the photon energy of the incoming X-ray beam. This oscillation is caused by interferences between the outgoing photoelectron wave with the scattered components of this wave from the neighbouring atoms. The measured absorption spectrum is a superposition of two components. The first of these is the structureless background, which shows the typical edge at the absorption energy of the excited atom, and then steadily decreases with increasing photon energy. The second component is the oscillations due to the interferences. The EXAFS $\chi(k)$, with k being the photoelectron wave vector, is then the oscillation part normalised to the structureless spectrum, and therefore delivers the structure information. The typical energy range, being of interest for EXAFS is from shortly before up to 1 000 eV beyond the absorption edge. When concentration on the near edge range, from shortly before up to 5-150 eV beyond the absorption edge, one talks about the X-ray absorption near edge structure (XANES). This modification is advantageous if one is especially interested in the first neighbours of the absorbing atom, this can for example give useful information about the oxidation state.

EXAFS (as XANES also) is a highly sensitive and element specific technique. The element specificity is due to the specific absorption edge. Therefore EXAFS represents a very useful tool to determine the co-ordination environment of species, which occur in very low abundance or concentration in the sample, without suffering the disadvantage of having a dominant background.

XMCD

X-ray magnetic circular dichroism (XMCD) is a difference spectrum of two X-ray absorption spectra taken with oppositely circularly polarised photons (left and right). The absorption spectra are different if there is an imbalance between spin-up and spin-down 3-D electrons of the absorbing atom. Therefore the difference spectrum is sensitive to magnetic properties of the sample [10].

PEEM

Photoemission electron microscopy (PEEM) is a surface-imaging technique which is based on the secondary-electron intensity distribution as a function of the photon energy. The emitted electrons are detected with an electron microscope allowing a spatial distinction of different regions of the sample surface having different magnetisation. The technique was already developed in the early

1930s [11] but has reached special interest in connection with the XMCD technique; it allows magnetic regimes at the surface to be visualised [12]. The technique typically delivers information on the first 5 nm from the surface. Therefore, any potential surface modification, as for example an oxidation layer, strongly influences the result.

The multi-scale approach

Multi-scale modelling can be seen as a chain of methods, which operate on an increasing scale, where each section acts as a qualitative input for the next one: *ab initio* – molecular dynamics (atomistic modelling) – kinetic Monte Carlo (atomistic modelling) – dislocation dynamics (mesoscopic modelling) – finite element method (macroscopic modelling). This is an inherent multi-scale approach. Similarly, the testing of materials properties is performed on many different scales, mainly because miniaturised samples and/or testing of small regimes offer important cost and time effectiveness, but real components are macroscopic. Therefore the different dimensions must be bridged in a multi-scale approach. Another reason for applying experimental multi-scale methods is the validation of the corresponding modelling scale. Table 2 shows on the left side experimental methods, which address physical effects, represented in the middle column. Each of those physical effects is also addressed by a modelling method and scale. In the figure the range of modelling scales is presented from the *ab initio* up to the macroscopic modelling.

Table 2. Scheme which illustrates the relation between experimental and modelling

The middle column lists the different effects, which have been approached. The left column contains the different experimental methods being addressed (therefore incomplete with regards to what is possible), and the right column shows the correspondence in the modelling scale. The different shading in the matrix arrangement illustrates the applicability of the method or the modelling scale to the physical effect.

Experimental	Observed Effect	Modelling
EXAFS PEEM/XMCD ARD TEM Indenter/Punch-Test Creep/Tensile-Test AFM		Ab Initio Atomistic Modelling Mesoscopic Modelling Macroscopic Modelling
	Microstructure: Point Defects Crystal Structure Clusters Dislocation ↔ Cluster Dislocation ↔ Dislocation	
	Magnetism: Magnetic Microstructure Spin/Orbital Moments	
	Volume: Lattice Swelling Void Swelling	
	Mechanical Properties: Hardness Toughness Yield Point Creep	

For the investigation of the nano micro- and macro-structure, many different methods, ranging from optical to highly sophisticated synchrotron radiation methods, are deployed. These investigations deliver important inputs for modelling and for the understanding of results from mechanical testing. Together with miniaturised mechanical-testing devices, up to the large-scale testing, this all together represents a multi-scale – multi-method approach, for understanding mechanical behaviour under irradiation.

Experimental and results

Several experiments, applying the beamline techniques, have already been performed. This paper concentrates on a small selection of these, demonstrating the potential of synchrotron radiation based techniques. Two examples are presented, showing the EXAFS and the XMCD/PEEM techniques. Furthermore, special shielding is shown, which allows radioactive samples to be investigated with beamline techniques. This is an important issue, as some activated materials might best represent structural components after long term exposures.

EXAFS experiment and results

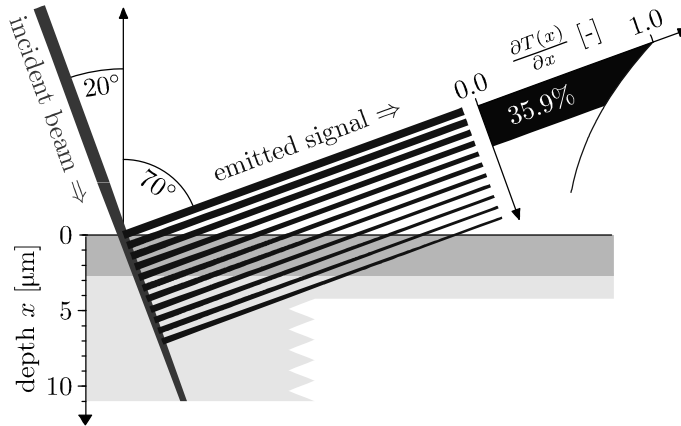
This experiment demonstrates the irradiation stability of yttria particles within an ODS steel. In order to detect radiation damage, which is potentially a major accumulation of point defects and clusters, an EXAFS study is performed. Table 2 shows that it is an appropriate method. This is especially true, because the investigated particles, are only present in a very low percentage in the matrix (0.5 wt.%), and the EXAFS technique allows the selective analysis by tuning to an elements absorption edge. From the modelling side, point defect creation is simulated by *ab initio* calculation.

The tested material is PM2000, a commercial product from Plansee [13]. It is composed of 73.5 wt.% Fe, 20 wt.% Cr, 5.5 wt.% Al, 0.5 wt.% Ti and 0.5 wt.% Y₂O₃, manufactured by mechanical alloying as described earlier and in [8]. The material has already been investigated with regards to some of its radiation properties [14-17]. Polished PM2000 samples are irradiated with a tandem accelerator (ETH, Zürich, Switzerland) implanting 1.5 MeV He ions up to a matrix damage of 1 dpa at ambient temperature and under an incident angle of 0-66° [14,15]. Figure 1(a) shows a sketch of the EXAFS probing the irradiated region (upper 2.7 µm), with a fraction of 36% of the total fluorescence signal. The EXAFS spectra are taken at ambient temperature at the Y edge (APS, Argonne National Laboratory, USA). In a later experiment, another set of samples are through irradiated using 0-24 MeV He ions from a cyclotron (FZJ, Jülich, Germany). The irradiation temperature here is at 570 K. The EXAFS spectra are taken at 50 K and the Y edge, using a cryostat (ESRF/France). Here the whole emitted signal derives from the irradiated region, as the samples are through irradiated.

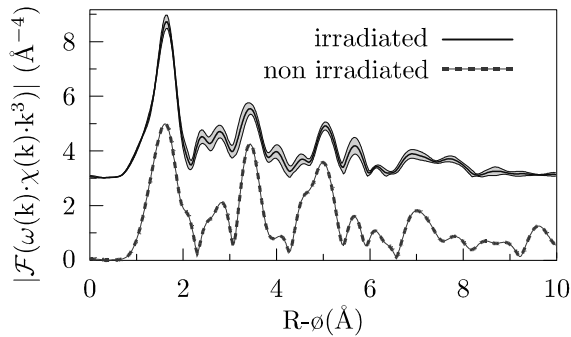
Figure 1(b) shows the Fourier transforms of the spectra taken from the surface irradiated sample, compared to a non irradiated sample. There is almost no difference visible. At ambient temperature and an irradiation damage of 1 displacement per atom, the structure of the dispersoids seems to remain unaffected [16]. On the other hand, the sample being irradiated at 570 K to 0.7 dpa, show a clear difference in its spectra [see 18]. Although the associated change in structure still has to be interpreted and understood, it appears that the first neighbours remain stable while second neighbours structure seems distorted. See also an earlier EXAFS study of PM2000 [19]. The observation of stable dispersoids is promising for the materials-performance under the given radiation conditions. On the other hand, the observed structural change must be further investigated, but could be an indication for a degradation of the dispersoids, with a potential loss of their materials enhancement (for this enhancement see for example [20]).

Figure 1. EXAFS samples irradiated at ambient temperature using a tandem accelerator (1.5 MeV, different angles) [14,15]

a) EXAFS set-up with incident and emitted signal, 36% of the signal derive from the irradiated region (here green, top 2.7 μm , 1 dpa) [16]



b) Fourier transforms of EXAFS spectra taken on irradiated (blue) and a non-irradiated (red) samples. No significant change in the structure of the yttria particles is detected [16].



PEEM/XMCD experiment and results

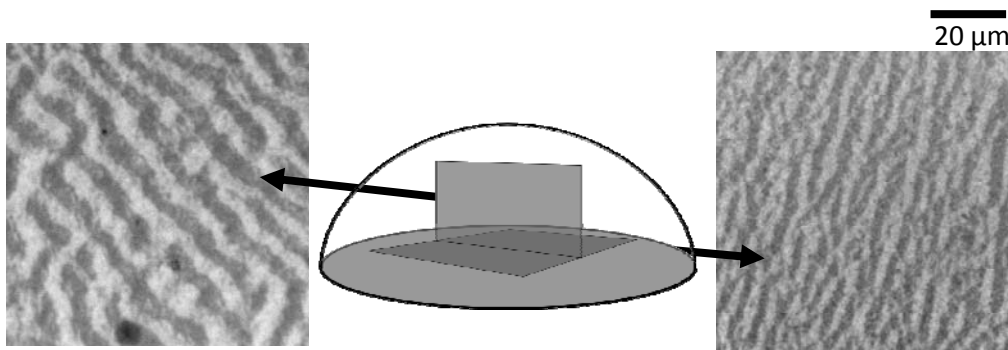
The Fe-Cr system is an important base for many alloys. Therefore a basic understanding of its behaviour is important. As already described earlier, its magnetic properties promise to be interesting. In Table 2 one can clearly identify, that the PEEM/XMCD technique is associated with the magnetic properties of materials, which from the modelling side is addressed by *ab initio* calculations. This kind of modelling is performed in the HTMat group [21], and the experiment described here is part of its validation [7].

An Fe-Cr sample with 5.8 wt.% Cr is prepared by the arc-melting technique in the appropriate stoichiometric proportions. The constituents are 99.995% pure Fe and 99.999% pure Cr. The melting was done under argon atmosphere, with previous vacuum pumping; repeating it several times to ensure compositional homogeneity. A thermal treatment of 1 h at 950°C followed this procedure and was finalised with an annealing step in the furnace at 790°C under vacuum. Different sections are extracted from the resulting button, as illustrated in Figure 2.

Figure 2. Magnetic domains on the surface of a Fe-6%Cr alloy. Two orientations are investigated, the transversal and the in-plane cutting planes.

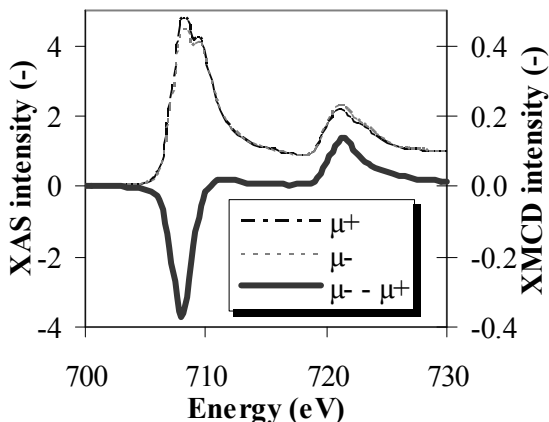
(a) In-plane surface [7]

(b) Transversal surface, see also [7,22]



The extracted sections are polished and magnetised up to their remanence state. Then they are investigated by means of PEEM using circularly polarised soft X-rays at the WERA beamline of the German ANKA synchrotron facility (Forschungszentrum Karlsruhe) [22,7]. Figure 2 presents magneto-optical images showing the magnetic surface microstructure of the Fe-Cr alloy containing 5.8 wt.% in Cr for the transversal and the in-plane cutting planes. The domain structure consists of a regular column pattern with domains magnetised parallel and antiparallel to the polarisation vector of the beam. Only domains with black and white contrast level coexist at the surface of the sample whatever the investigated plane (longitudinal or in-plane). This means that a rotation of the sample surface by 90° leads to two remanent magnetisation directions of the domains suggesting the formation of out-of-plane domains at the surface of the Fe-6%Cr sample. By taking the difference of images recorded at resonance with right and left-handed circularly polarised X-rays, the magnetic dichroism contrast is clearly visible (Figure 3). Quantitative evaluation of the iron spin and orbital magnetic moments and their ratio can be determined from the XAS and XMCD spectra extracted from the PEEM images [7]. This allows the validation of *ab initio* calculations, which on their hand support the potentials used in molecular dynamics. Therefore these results indirectly contribute to the modelling of radiation damage [23].

Figure 3. In plane Fe-6%Cr sample. Fe $L_{2,3}$ absorption edge spectra extracted from magnetic domains with opposite character ($\mu+$ and $\mu-$) and their difference corresponding to the XMCD signal



Special equipment for the use of beamlines in the nuclear field

For the analysis of radioactive specimens on the μ -XAS [24] beamline of the Swiss Light Source (SLS), a dedicated infrastructure including a specimen holder, a (XYZ) manipulator, local shielding and a complex detector holder structure has been designed and constructed [25]. The holder has been especially designed for safe containment of up to three specimens using Kapton foils as windows material for the X-ray beam. Procedures have been designed to realise a safe transfer of the radioactive specimens from the PSI hot laboratory into the hutch of the beam line and insure a contamination free analysis of the specimens. Local 8 cm shielding can be installed around the holder in order to shield the radiation field of the specimens and allow the investigation of relatively strongly radiating specimens. The Swiss regulatory authorities have licensed the infrastructure for analysis of β - γ emitting specimen with dose rate up to few mSv/h at 5 cm. For material containing α -emitters, the holder is licensed up to a total activity per specimen of 100 authorisation limit (LA) according to the Swiss regulation [26] (LA = Limite d'autorisation or in German „Bewilligungsgrenze“).

With this infrastructure, specimens can be investigated in both transmission and fluorescence modes with a micro-beam as small as 1 μm in diameter. Actually the specimens are positioned at a 45° angle with the horizontal incident beam as seen in Figure 4 and the detector is installed on top of the holder along the vertical axis for fluorescence measurement or beyond the holder for transmission measurement. In the future, different geometries with the detector in the horizontal plane will be available to reduce the elastic scattering and allow better measurement of dilute specimens. A container for liquid specimens is also in the licensing process.

Figure 4. Active specimen holder surrounded by shielding



Conclusions

This paper describes two beamline techniques, EXAFS and PEEM/XMCD, and describes their impact on a multi-scale understanding of advanced structural materials with the modelling and its validation. Two examples demonstrate the potential of these techniques. EXAFS is used for investigating the co-ordination environment of the absorbing atom. This technique should allow detecting a major creation of point defects, or a phase change. Because of the element specificity, this technique can also be used to investigate minor phases in a dominant matrix. XMCD in conjunction with PEEM can depict and analyse magnetic domains. This is important to understand the magnetic behaviour of materials, with its potential influence to other mechanisms. Finally a shielded XAS sample holder is presented. It is important for the future, having the option to investigate activated or contaminated materials. Especially when it comes to the investigation of radiation damage, neutron or high energy ion irradiated specimen are important.

Acknowledgements

The work was partially supported by the EU projects RAPHAEL and EXTREMAT. The authors would especially like to thank M. Nazmy from Alstom for providing the Fe-Cr samples.

REFERENCES

- [1] *The Generation IV International Forum*, OECD Nuclear Energy Agency, last retrieved 1 May 2007, <http://www.gen-4.org/>.
- [2] Dokiya, M., T. Kameyama, K. Fukuda, *Int. J. Hydrogen Energy*, 4 (4), 267-277 (1979).
- [3] Olsson, P., I.A. Abrikosov, J. Wallenius, *Phys. Rev. B*, 73, 1044161 (2006).
- [4] Klaver, T.P.C., R. Drautz, M.W. Finnis, *Phys. Rev. B*, 74, 0944351 (2006).
- [5] Samaras, M., P.M. Derlet, H. Van Swygenhoven, M. Victoria, W. Hoffelner, unpublished.
- [6] Lavrentiev, M.Y., R. Drautz, D. Nguyen-Manh, T.P.C. Klaver, S.L. Dudarev, *Phys. Rev. B*, 75, 0142081 (2007).
- [7] Froideval, A., R. Iglesias, M. Samaras, S. Schuppler, P. Nagel, D. Grolimund, M. Victoria, W. Hoffelner, accepted for publication in *Phys. Rev. Lett.*
- [8] Czyska-Filemonowicz, A., B. Dubiel, *Materials Processing Technology*, 63, 53-64 (1997).
- [9] Almazouzi, A., SCK•CEN, private communication
- [10] Wende, H., *Rep. Prog. Phys.*, 67, 2105-2181 (2004).
- [11] Brüche, E., *Z. Physik*, 86, 448-450 (1933).
- [12] Scholl, A., H. Ohldag, F. Nolting, S. Anders, J. Stöhr, "Magnetic Microscopy of Nanostructures, 2", *Study of Ferromagnet-antiferromagnet Interfaces Using X-Ray PEEM*, H. Hopster, H. Oepen (Eds.), Springer, 29-50 (2005).
- [13] *Dispersion-strengthened High-temperature Materials/Material Properties and Applications*, Prospectus from Plansee, 706 DE.04.03(1000)RWF (2003).
- [14] Pouchon, M.A., J. Chen, M. Döbeli, W. Hoffelner., *J. Nucl. Mater.*, 352 (1-3), 57-61 (2006).
- [15] Pouchon, M.A., M. Döbeli, R. Schelldorfer, J. Chen, W. Hoffelner, C. Degueldre, *Proceedings of 16th International Conference on Physics of Radiation Phenomena and Radiation Material Science*, Alushta, Crimea, 3-7 September 2004 (VANT, Voprosy Atomnoi Nauki i Techniki, ISSN 1562-6016), Vol. 3 (86), p. 122 (2005).

- [16] Pouchon, M.A., A.J. Kropf, A. Froideval, C. Degueldre, W. Hoffelner, *J. Nucl. Mater.* 362 (2-3), 253-258 (2007).
- [17] Chen, J., P. Jung, M.A. Pouchon, T. Rebac, W. Hoffelner, *J. Nucl. Mat.*, forthcoming (2007), doi:10.1016/j.jnucmat.2007.04.051.
- [18] Pouchon, M.A., J. Chen, C. Degueldre, A. Froideval, H. Emerich, W. Van Beek, *Mater. Sci. Forum*, 561-565, 1761-1764 (2007).
- [19] Degueldre, C., S. Conradson, W. Hoffelner, *Comput. Mater. Sci.*, 33, 3-12 (2005).
- [20] Bakó, B., D. Weygand, M. Samaras, J. Chen, M.A. Pouchon, P. Gumbsch, W. Hoffelner, *Philos. Mag.*, 87 [24], 3645-3656 (2007).
- [21] Iglesias, R., A. Froideval, M. Samaras, M. Victoria, W. Hoffelner, "Spin and Orbital Surface and Bulk Magnetism of Fe-Cr Alloys", talk presented at the 3rd *ChiralTEM Workshop*, Trieste, Italy, 31 May-1 June 2007.
- [22] Hoffelner, W., A. Froideval, M. Pouchon, J. Chen, M. Samaras, *Met. Mat. Trans. A*, forthcoming (2007).
- [23] Samaras, M., W. Hoffelner, M. Victoria, *J. Nucl. Mat.*, 371, 28-36 (2007).
- [24] "SLS Web Site – MicroXAS", last retrieved 1 May 2007 from the following URL: <http://sls.web.psi.ch/view.php/beamlines/mxas/index.html>.
- [25] Heimgarnter, P., R. Restani, D. Gavillet, "New Specimen Holder for XAS-analyses of Radioactive Specimens at the Swiss Light Source (SLS)", European Working Group, Hot Laboratories and Remote Handling, Plenary Meeting, Petten, the Netherlands, 23-25 May 2005.
- [26] Swiss Law – SR: 814.501 – Strahlenschutzverordnung vom 22, Juni 1994 (StSV), Anhang 3, last retrieved 1 May 2007 from: http://www.gesetze.ch/sr/814.501/814.501_041.htm.

FIRST-PRINCIPLES MODELLING OF ADVANCED NUCLEAR FUELS: PROBLEMS AND PROSPECTS

P. Van Uffelen¹, E. Kotomin^{1,2}, E. Heifets¹, D. Gryaznov^{1,2}

¹European Commission, Joint Research Centre, Institute for Transuranium Elements
D-76125 Karlsruhe, Germany

²Institute of Solid State Physics University of Latvia (ISSP LU)
8 Kengaraga str., LV-1063 Latvia

Abstract

In view of the progress achieved in the materials research community as well as with the advent of more extensive experimental data for nuclear fuels, first principles (or *ab initio*) calculations have been applied over the past few years to shed light on some fundamental issues of these materials. On 5-6 March 2007 a workshop was held at ITU, which aimed at bringing together both users and developers of *ab initio* computer codes involved in these calculations, in order to discuss the recent results along with the needs for detailed knowledge of actinides and f-elements. More precisely, the workshop aimed at exploring ways to acquire more and more accurate material properties relevant for fuel fabrication processes, hence contributing to the selection of advanced nuclear materials, as well as to improve our understanding of underlying basic mechanisms governing the fuel behaviour during its entire lifetime. The workshop participants evaluated how the results of first principles approach can be used in larger scale atomistic calculations, such as pair potential and force field calculations, or fuel performance codes that are being used by safety authorities. In addition to the outcome of the workshop, an overview of the multi-time-scale approach at ITU for nuclear fuels is presented in the second part of the paper, along with suggestions for further development like in cladding materials for example.

Multi-time-scale modelling at ITU

ITU has a long tradition of research and development activities devoted to the safe handling of radioactive materials, as reflected in the actions on nuclear fuel safety, partitioning and transmutation, as well as the characterisation of spent fuel. A common feature across these interlinked disciplines is the analysis of advanced materials for achieving a more sustainable nuclear fuel cycle, by either optimising the use of natural resources and/or improving the safety of the spent nuclear materials that will be stored for long periods of time. To this end, it is essential to shed light on the underlying basic mechanisms governing the behaviour of the materials under irradiation conditions, as well as during the long-term storage after irradiation. The detailed understanding of the atomic and electronic structures, the defect structures and mobilities under various conditions require a multi-time-scale modelling approach. Such an approach integrates various experimental and computational techniques, is hierarchical and based on passing information or parameters, starting from the electronic/atomic up to structural length and time scales [1].

At present ITU performs various stages of the multi-time-scale approach. On the theoretical side, the fuel rod behaviour over time scales from milliseconds to years is predicted phenomenologically by means of the TRANSURANUS code [2], while more detailed models for the behaviour of the fission gas atoms are also available for specific situations as illustrated in Until recently, most calculations for the radiation defects in nuclear fuels and fission gas diffusion were performed using the effective potentials and shell model (SM) [3-5] and focused mostly on UO_2 fuel. This technique permits to obtain the defect formation and migration energies, provided the interatomic potentials are properly fitted to the experimental or *ab initio* calculated basic properties of materials. In recent years, this approach demonstrated its great potential for UO_2 surface calculations [6] and for materials with partly covalent chemical bonding, like ABO_3 perovskites [7-8]. However, it is important to check SM-based calculations by *ab initio* modelling, in order to control whether the chemical bond covalency is properly taken into account via empirical parameters, and if there is not considerable charge redistribution at the saddle point of defect (Xe atom) migration hops. Recently, SM was also successfully applied to the modelling of Pu and U atom accommodation in $\text{A}_2\text{B}_2\text{O}_7$ pyrochlore compounds [9-10]. The MD simulations were performed so far only for preliminary understanding of basics of the radiation damage of simple ionic oxides, like MgO [11] and spinels [12], as well as for a first attempt to evaluate thermal properties of UO_2 and MOX [13-15].

Until recently, most calculations for the radiation defects in nuclear fuels and fission gas diffusion were performed using the effective potentials and shell model (SM) [3-5] and focused mostly on UO_2 fuel. This technique permits to obtain the defect formation and migration energies, provided the interatomic potentials are properly fitted to the experimental or *ab initio* calculated basic properties of materials. In recent years, this approach demonstrated its great potential for UO_2 surface calculations [6] and for materials with partly covalent chemical bonding, like ABO_3 perovskites [7-8]. However, it is important to check SM based calculations by *ab initio* modelling, in order to control whether the chemical bond covalency is properly taken into account via empirical parameters, and if there is not considerable charge redistribution at the saddle point of defect (Xe atom) migration hops. Recently, SM was also successfully applied to the modelling of Pu and U atom accommodation in $\text{A}_2\text{B}_2\text{O}_7$ pyrochlore compounds [9-10]. The MD simulations were performed so far only for preliminary understanding of basics of the radiation damage of simple ionic oxides, like MgO [11] and spinels [12], as well as for a first attempt to evaluate thermal properties of UO_2 and MOX [13-15].

The *ab initio* computational methods enable to obtain quantitative properties of specific materials like the lattice constants, the structural stability (cohesive energy), the elastic and bulk moduli, which permits in principle, to extract the interatomic potentials for the classical (SM and MD) modelling and

Figure 1. Schematic set of modelling tools envisaged by ITU and its partner institutes for multi-time-scale modelling of nuclear fuels

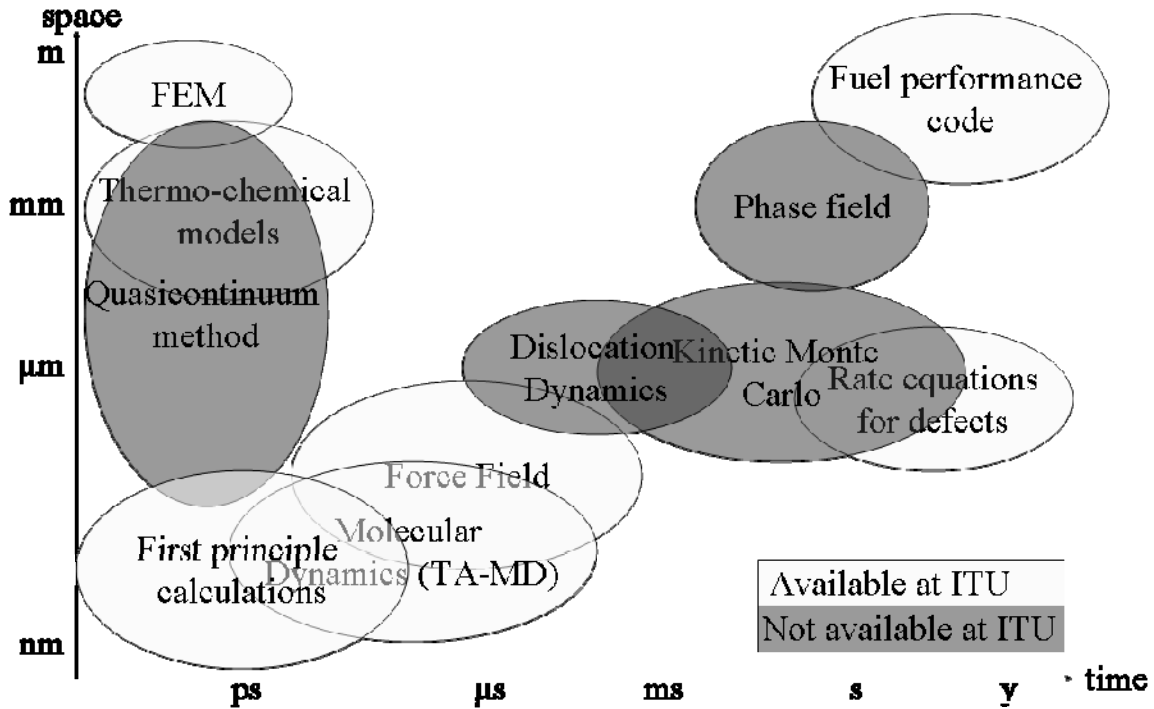
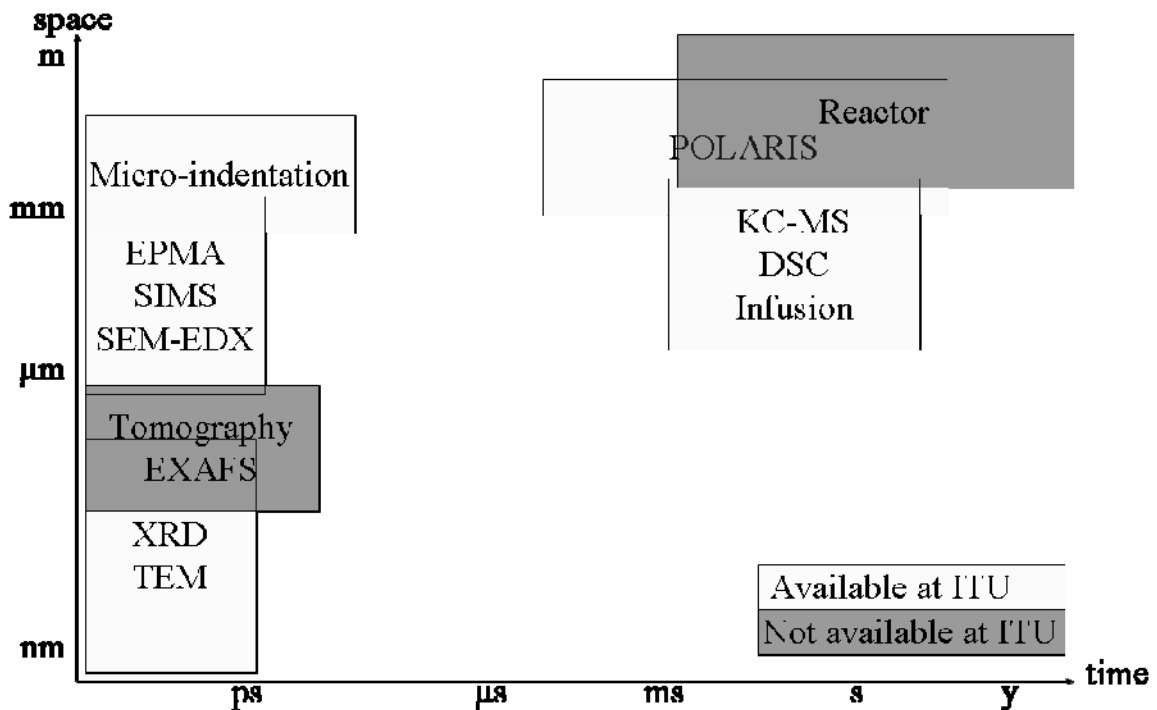


Figure 2. Schematic set of experimental tools envisaged by ITU and its partner institutes for multi-time-scale modelling of nuclear fuels



to adjust force field parameters. Simultaneously, such calculations give the electronic density distribution and energy bands of materials, including the defect energy levels within the bandgap of the pure material. *Ab initio* calculations of UO_2 and point defects therein were first based on LMTO Density Functional Theory (DFT) calculations [16] and further continued with plane-wave DFT calculations with pseudopotentials [17]. This approach was extended for the modelling of some fission products (Kr, I, Cs, Sr and He) [18] and comparison of LDA and GGA [19-20]. First-principle calculations for ThO_2 , SrThO_3 and SrZrO_3 have also been reported very recently [21].

Using nitrides as a fuel in a fast transmutation reactor offers potentially enhanced performance compared to conventional oxide fuels, due to higher thermal conductivity, good sodium compatibility, and in the case of fuel reprocessing, high solubility in nitric acid [22-23]. The first pilot calculations of basic defects in UN were performed only in 2007, essentially as a result of collaboration between ITU and Imperial College London [24].

Summary of the workshop on *ab initio* calculations

In view of the challenges brought about by the 5f electrons in actinide materials, the large amount of materials to be considered for the new generation of reactors, and because of the variety of calculations launched at various research centres worldwide, it was felt necessary to organise a workshop. One of the main advantages this workshop offered was the presence of both code developers and users. As a result, experience acquired in the first-principles calculations by means of plane-wave computer codes (VASP, CASTEP, ABINIT, WIEN-2k) and LCAO (GAUSSIAN-2003 and potentially CRYSTAL-2006) was discussed. It was clearly demonstrated that these codes, combined with large supercells and appropriate methods to account for the specific role of the 5f electrons, are able to reproduce basic properties of nuclear fuels (mostly, UO_2 , PuO_2 , and UN) and defects therein. These first encouraging results and experience will be applied in the near future to a wide range of materials (e.g. UC, (Zr,U)N and (U,Pu) O_2 solid solutions), with defects and impurities (He, Xe, Sr and fission products). As a result of the workshop, also several key problems were identified as follows.

Importance of electron correlations in actinides

Standard LDA and GGA calculations predict commonly used UO_2 fuel to be a metal, which is at odds with experimental observations indicating UO_2 to be a semiconductor. To resolve this disagreement, on-site electron correlations should be more correctly taken into account by means of DFT+U or hybrid functionals. Hybrid functionals are universal in nature, i.e. the same for any element in any compound; they reduce the calculation speed, but pose difficulties for the PW basis set since current implementations are only suitable in computations for insulators. Furthermore, hybrid functionals are in an implementation stage for PW codes (e.g. VASP [25]) and very time consuming. For localised basis sets with the f-elements they are currently only available in the Gaussian-2003 code. The DFT+U approach is fast and suitable in some variants of the PW computations (e.g. PAW implemented in VASP [26]) but it has not been used so far for local basis sets. It works successfully if the respective energy bands are empty or when electrons are well localised. Particularly, VASP has already been applied for calculating different properties of UO_2 [27]. However, the DFT+U approach faces problems for intermediate localisation of electrons (e.g. in nitrides). Another potential drawback of this approach is the non-transferability of the U parameter (it might differ for the cation in UN and UO_2), which would complicate the comparison of calculations for different materials.

Comparison of different pseudopotentials for actinides

Different types of Effective Core Pseudopotentials (ECP) are currently available in LCAO and PW calculations due to peculiarities of these two kinds of the basis sets: the PWs need much softer ECP in order to reduce the cut-off energy. In addition, there is a well developed set of standard ECPs for the LCAO calculations, unlike for the PW calculations where in many cases ECPs are generated ad hoc. This makes a comparison of results of the LCAO and PW calculations quite complicated. It is unclear whether LDA generated ECPs can be used in computations with GGA functionals, which is a possibility often used in PW codes. At the moment, it is strongly advisable for authors to explicitly mention the type of pseudopotentials and exchange-correlation functional they apply in the computations. It is well known that in lanthanides that the f-electrons practically do not participate in chemical bonding. The questions raised for actinides read “What is the role of semi-core electrons for heavy actinides like U?”, and “Could one include these electrons into the ECP or do we have to treat them in the same way as valence electrons (explicitly)?” It appears that a proper treatment of the degenerate states and magnetic properties of U compounds requires an explicit treatment of 5f electrons, which is not straightforward.

Inert gases

Inert gases such as Xe, Kr and He are produced in large amounts in nuclear fuels under operational and prolonged disposal conditions. The theoretical study of their behaviour is of great technological importance. However, the main problem of the DFT approach is the absence of the van der Waals interaction. An attempt to incorporate this interaction into DFT was performed by Prof. B.I. Lundqvist and co-workers at the Chalmers University of Technology [28]. However, the so-called van der Waals DFT is not yet implemented in the commonly used DFT codes and, consequently, was not applied to actinides.

During the workshop it was also underlined how various groups using the same code could come up with different values, for example for the He incorporation energy in UO_2 . In the present paper, we present an example of an *ab initio* calculation for He energetics in bulk UO_2 performed at ITU by means of the VASP code. It should be underlined that only the interstitial position for He in UO_2 was applied in view of recent experimental [29] and previous theoretical studies [30], indicating this to be the energetically most favourable site. Consequently, the incorporation energies were calculated for different supercells varying the number of atoms according to the definition proposed by Grimes and Catlow [31]. We took into account the experimental fact that UO_2 is an anti-ferromagnetic (AFM) insulator at low temperature [32] and compared the corresponding incorporation energies with those obtained for the non-magnetic case (indicated as NM in Table 1). For the same reason, we applied the appropriate Hamiltonian to account for the on-site correlation corrections (indicated as DFT+U in Table 1) in the form suggested by Dudarev which is available in VASP [33]. The latter is particularly important because it allows us to compare our non-magnetic incorporation energies with previous plane wave calculations [18,20] for the 24 atoms supercell. This supercell represents a $1 \times 2 \times 1$ extension of a crystallographic cubic fluorite unit cell of UO_2 . Also, the results are given for the crystallographic cubic unit cell (12 atoms) and 48 atoms supercell (a $2 \times 2 \times 2$ extension of tetragonal primitive unit cell). Please notice, all the supercells with He incorporated were fully relaxed. For the first time, we analysed how the incorporation energy depends on the concentration of He. It reduces from the value of 1.6 eV for the 12 atoms supercell to 0.7 eV for the 48 atoms supercell and AFM configuration, at least in the framework of the PW91 exchange correlation functional applied (Perdew and Wang, see [34]). When the same functional is applied for the non-magnetic UO_2 , the incorporation energy is higher, confirming the result of Crocombette [18] but contradicting with the results of Grimes [29] and Freyss [20]. In order to reproduce their result we needed to combine the PBE

Table 1. The incorporation energies of He in UO₂ (the interstitial site) expressed in eV. All the results for AFM phases were obtained applying the DFT+U approach in the VASP code. PS and LSD denote a pseudopotential and local spin density approximation, respectively. In the calculation the parameter U = 4.6 eV was from the previous experimental work [37]

PS	Functional	12 atoms		24 atoms		48 atoms	
		AFM	NM	AFM	AFM	AFM	AFM
PW91	PW91	1.6	1.3	0.8	0.7		
LSD	PBE	–	-0.1	-0.8	-6.2		

exchange correlation functional (Perdew, Bucke and Ernzerhof [35]) with the LDA pseudopotential. Such inconsistent combination can often be met in the literature, although it can hardly be considered a reasonable model. This clearly indicates room for clarification, benchmarking and improvement which will be addressed in a future paper [36].

Perspectives for nuclear fuel rod modelling

Nuclear fuel

In view of the importance of He in various nuclear materials, experimental collaborative projects (JP 05-04 and JRP01-35) such as “A separate effects study of the behaviour of helium in uranium dioxide” have been launched in the frame of the ACTINET network of excellence. As a complement to these studies that address, among other, the solubility and mobility of He in various nuclear matrices, a complementary theoretical project has recently been submitted to ACTINET. The primary aim of this project is to develop collaboration between the dispersed theoretical groups in Europe working on modelling of advanced nuclear fuels (extending the activities of the Theoretical User Laboratory for solid state/defects/surfaces) and associated experimental groups. This will focus their activities on key problems of long-term storage of nuclear fuels and will result in the development of a robust predictive capability that can be used to investigate the physics and chemistry of exotic Generation-IV fuels.

The precise aim of this project is to calculate properties of He in perfect and defective advanced and conventional nuclear fuels including UO₂, PuO₂, MOX, UC, PuC, UN, PuN, ZrN, and (U,Zr)N solid solution. Several first-principles computer codes (Wien-2k, VASP, CASTEP, ABINIT) for parallel large-scale atomic/electronic structure calculations of actinides will be used for a reliable prediction of equilibrium He atom positions, migration paths, aggregation as well as incorporation, solution and migration energies in single crystals and those containing different configurations of vacancies. To this end, the partners in this project plan to apply the above-mentioned four first-principles parallel computer codes – Wien-2k, VASP, CASTEP and ABINIT – for the large scale modelling of He behaviour in the nuclear fuels under consideration. This will not only allow us to predict their behaviour under normal and accident conditions, but more importantly to benchmark these codes and develop a method which most effectively and reliably predicts actinide properties. Specifically, we plan to:

1. Determine the reliability of these calculations (where some “hidden” parameters such as exchange-correlation (LDA, GGA or GGA(LDA)+U) functionals and different type pseudopotentials are involved). We will, initially, compare results for perfect UO₂ single crystals. These calculations will be directly compared to results obtained through the current experimental Actinet project on helium behaviour (very low dose helium diffusion, determination of the He location in the UO₂ lattice, and infusion/effusion tests).

2. Identify the equilibrium He trapping sites in perfect and point-defect containing oxides, nitrides and carbides.
3. Calculate the corresponding solution and incorporation energies.
4. Identify the mechanisms and associated migration energies for He, from which diffusion coefficients will be obtained and compared to data determined from Knudsen cell experiments being carried out at ITU.

In addition to the proposal for analysing the He properties in various nuclear fuels by means of *ab initio* codes, another collaborative project has been submitted for funding from the 7th EURATOM framework programme with a much wider scope. With the CEA as the co-ordinator, it brings together various European research groups and is called Science for Advanced Fuels and Irradiation Effects (SAFIRE) aiming at:

1. identifying and sharing the concept-dependent key criteria for fuel selection, translating them in terms of generic materials science issues;
2. undertaking basic research on fuel materials in a consistent multi-scale approach coupling experimental simulation and modelling;
3. undertaking a multi-scale modelling exercise for UO₂, encompassing techniques such as *ab initio* codes, molecular dynamics, kinetic Monte Carlo code, forced field codes, etc.;
4. preparing the transfer of basic knowledge to fuel designers and applied scientists.

In summary, SAFIRE intends to address thermodynamics (phase diagrams of U-Pu-O-C-N) systems, impact of minor actinides and fission products, fuel environment interaction; transport and microstructure evolution (experimental and modelling approach, effects on macroscopic properties); and the thermo-mechanical evolution.

Cladding

With respect to the metallic cladding based on zirconium, few atomic scale calculations have been found in the open literature, despite the large amount of research on reactor materials. Within the SIRENA project, which was funded by the 5th EURATOM Framework Project, both molecular dynamics (MD) [38-39] and kinetic Monte Carlo calculations [40] have been reported for zirconium. The MD computations were used to investigate primary damage created by displacement cascades in high-energy particle irradiation. Some general features about the primary defect creation in HCP α -Zr were obtained: the number of Frenkel pairs created in displacement cascades in α -Zr turned out to be insensitive to the temperature, both vacancy and self-interstitial atom (SIA) clusters were reported to be stable in α -Zr in the whole temperature range considered, and the SIAs showed a higher tendency to agglomerate in clusters than vacancies. Voskoboinikov, *et al.* [39] also identified three typical SIA categories and three typical vacancy categories. Based on the information from these MD calculations, Arevalo and co-workers [40] have analysed the influence of self-interstitial mobility on damage accumulation in zirconium (total defect concentration and size) under fission irradiation conditions by means of the kinetic Monte Carlo technique. At present the KMC technique is being extended to include other modes of diffusion along different directions.

The difficulties encountered for achieving a full multi-time-scale approach for cladding materials seem to be associated with the composition of the alloy as well as the texture of the technological material. Besides the zirconium, the fuel claddings adopted in LWRs may contain some Sn, Fe, Cr, Ni and Nb. Applying techniques such as DFT or molecular dynamics to such alloys is therefore still a remarkable challenge. Nevertheless, these techniques may prove helpful in addressing basic questions about:

1. the nature of diffusing hydrogen species and the diffusion mechanism in Zr/ZrO₂ under accidental conditions;
2. the energetics and mechanism of the interfacial oxidation reaction under accidental conditions;
3. the atomic-scale feature of the Zr-ZrO₂ interface resulting from these fundamental processes,

in a similar way as a combination of first-principles computations, atomistic modelling and selected experiments enabled to investigate oxygen transport through a multi-scale oxide on ultra-high temperature ceramic composites such as ZrB₂-SiC [41].

In addition to the composition, which affects the corrosion resistance for instance, the macroscopic behaviour of the cladding is strongly determined by the fabrication route. Indeed, the degree of cold work (area reduction) as well as the heat treatment (temperature level and hold-time) of the fabrication process affect the final anisotropy of the hexagonal closed packed α -phase ($T < 800^\circ\text{C}$) at room temperature and under normal operating conditions. More recent techniques and/or methods dealing with the material at larger scale such as the phase field modelling may prove helpful in simulating the fabrication process and the in-pile behaviour of the cladding alloys. They might, for example help understand why the onset temperature for the α - β crystallographic phase transition occurs in standard Zry4 and differs from that reported in Nb-containing zircaloy, or why the corrosion resistance of Zircaloy-4 in PWRs is improved when the size of second-phase particles is greater than about 100 nm, unlike for zircalloys in BWRs or the Nb-containing zircalloys in PWRs [42].

Acknowledgements

All participants of the workshop, and in particular detailed discussions with Prof. R.W. Grimes, Prof. R.A. Evarestov, Prof. D. Sedmidubsky, Dr. C. Valot and Dr. M. Freyss.

REFERENCES

- [1] Wirth, B.D., G.R. Odette, J. Marian, L. Ventelon, J.A. Young-Vandersall, L.A. Zepeda-Ruiz, *J Nucl. Mater.*, 329-333, 103 (2004).
- [2] Van Uffelen, P., C. Gyori, A. Schubert, J. Van de Laar, *J. Nucl. Mater.*, forthcoming (2007).
- [3] Catlow, C.R.A., *Proc. R. Soc. London*, A 353, 533 (1977).
- [4] Jackson, R.A., A.D. Murray, J.H. Harding, C.R.A. Catlow, *Phil. Mag.*, A 53, 27 (1986).
- [5] Nikoll, S., Hj. Matzke, C.R.A. Catlow, *J. Nucl. Mater.*, 226, 51 (1995).
- [6] Tan, A.H.H., M. Abramowski, R.W. Grimes, S. Owens, *Phys. Rev.*, B 72, 035457 (2005).
- [7] Kotomin, E., A. Popov, *NIM*, B 141, 1 (1998) (review article).
- [8] Heifets, E., E. Kotomin, J. Maier, *Surf. Sci.*, 462, 19 (2000).
- [9] Williford, R.E., W.J. Weber, *J. Nucl. Mater.*, 299, 140 (2001).
- [10] Cleave, A., R.W. Grimes, K.E. Sickafus, *Phil. Mag.*, 85 (9), 967 (2005).
- [11] Uberuga, B.P., R. Smith, A.R. Cleave, F. Montalenti, G. Henkelman, R.W. Grimes, A.F. Voter, K.E. Sickafus, *et al.*, *Phys. Rev. Lett.*, 92 (11), 115505 (2004).
- [12] Bacorisen, D., R. Smith, B.P. Uberuga, K.E. Sickafus, R.W. Grimes, *Phys. Rev.*, B, 74, 214105 (2006).
- [13] Sobolev, V., *J. Nucl. Mater.*, 344 (1-3), 198 (2005).
- [14] Kourosaki, K., K. Yamada, M. Uno, S. Yamanaka, K. Yamamoto, T. Namekawa, *J. Nucl. Mater.*, 294, 160 (2001).
- [15] Van Brutzel, L., M. Raviromanantsoa, D. Ghaleb, *J. Nucl. Mater.*, 354 (1-3), 28 (2006).
- [16] Petit, T., C. Lemaignan, F. Jollet, B. Bigot, A. Pasturel, *Phil Mag.*, B, 77 (3), 779 (1998).
- [17] Crocombette, J.P., F. Jollet, L.T. Nga, T. Petit, *Phys. Rev.*, B 64, 104107 (2001).
- [18] Crocombette, J.P., *J. Nucl. Mater.*, 305, 29 (2002).
- [19] Freyss, M., T. Petit, J-P. Crocombette, *J. Nucl. Mater.*, 347, 44 (2005).
- [20] Freyss, M., N. Vergnet, T. Petit, *J. Nucl. Mater.*, 352, 144 (2006).

- [21] Shein, I.R., K.I. Shein, A.L. Ivanovskii, *J. Nucl. Mater.*, 361, 69 (2007).
- [22] Matzke, H.J., *Science of Advanced LMFBR Fuels*, North Holland, Amsterdam (1986).
- [23] Thetford, R., M. Mignanelli, *J. Nucl. Mater.*, 320, 44 (2003).
- [24] Kotomin, E.A., R.W. Grimes, Y. Mastrikov, N.J. Ashley, *J. Phys: CM*, 19 (10), 106208 (2007).
- [25] Kresse, G., J. Furthmüller, *Comp. Mater. Sc.*, 6, 15 (1996).
- [26] Kresse, G., D. Joubert, *Phys. Rev.*, B, 59, 1758 (1999).
- [27] Geng, H.Y., Y. Chen, Y. Kaneta, M. Kinoshita, *Phys. Rev.*, B, 75, 054111 (2007).
- [28] Rydberg, H., B.I. Lundqvist, D.C. Langreth, M. Dion, *Phys. Rev. B*, 62, 6997 (2000).
- [29] Garrido, F., L. Nowicki, G. Sattonnay, T. Sauvage, L. Thome, *Nucl. Ins. Meth. Phys. Res.*, B, 219-220, 196 (2004).
- [30] Grimes, R.W., R.H. Miller, C.R.A. Catlow, *J. Nucl. Mater.*, 172, 123 (1990).
- [31] Grimes, R.W., C.R.A. Catlow, *Phil. Trans. R. Soc. Lond.*, A, 335, 609 (1991).
- [32] Cracknell, A.P., M.R. Daniell, *Proc. Phys. Soc.*, 92, 705 (1967).
- [33] Dudarev, S.L., G.A. Botton, S.Y. Savrasov, Z. Szotek, W.M. Temmerman, A.P. Sutton, *Phys. Stat. Sol.*, (a), 166, 429 (1998).
- [34] Perdew, J.P., Y. Wang, *Phys. Rev.*, B, 45, 13244 (1991).
- [35] Perdew, J.P., K. Burke, M. Ernzerhof, *Phys. Rev. Lett.*, 77, 3865 (1996).
- [36] Gryaznov, D., E. Kotomin, E. Heifets, P. Van Uffelen (in preparation).
- [37] Baer, Y., J. Shoenes, *Solid St. Comm.*, 33, 885 (1980).
- [38] Voskoboinikov, R.E., Y.N. Osetsky, D.J. Bacon, *NIM Phys. Res.*, B 242, 68 (2006).
- [39] Voskoboinikov, R.E., Y.N. Osetsky, D.J. Bacon, *NIM Phys. Res.*, B 242, 530 (2006).
- [40] Arevalo, C., M.J. Caturla, J.M. Perlado, *J. Nucl. Mater.*, 362, 293 (2007).
- [41] Bongiorno, A., C.J. Först, R.K. Kalia, J. Li, J. Marschall, A. Nakano, M.M. Opeka, I.G. Talmy, P. Vashishta, S. Yip, *MRS Bulletin*, 31, 410 (2006).
- [42] Yilmazbayhan, A., A. Motta, R. Comstock, G. Sabol, B. Lai, Z. Cai, *J. Nucl. Mater.*, 324, 6 (2004).

POSTER SESSIONS

HIGH TEMPERATURE CORROSION PROPERTIES OF ALLOY 230 IN THE ENVIRONMENT OF GAS-COOLED REACTORS

Céline Cabet, Fabien Rouillard, Brigitte Duprey
DEN/DANS/DPC/SCCME, CEA Saclay

Abstract

Despite high-level gas-tightness and purification, cooling helium of advanced gas-cooled reactors (GCR) is expected to be polluted by low level of impurities, i.e. traces of hydrogen, water vapour, methane, carbon monoxide. Structural metallic materials for pipes and heat exchangers must be resistant against corrosion at temperatures as high as 850-950°C in this unique atmosphere which has a low oxidising potential and a significant activity of carbon.

Experience from the former HTR shows that corrosion effects such as oxidation, carburisation or decarburisation may occur depending on temperature, gas chemistry and alloy nature. As in any other high temperature process, in GCR the corrosion resistance of chromium-rich alloys relies on the growth of a surface scale that can act as a barrier against corrosive or oxidising species. In any case, impure helium must thus stabilise surface chromia.

This paper focus on the high temperature behaviour of candidate alloy 230 in GCR service conditions.

In a first part, we have studied the environmental conditions that could promote oxidation of the alloy. The reactivity is investigated in the temperature range 800-1 000°C under various impure helium atmospheres. It was observed that chromia scale can form but above a critical temperature the surface oxide becomes instable due to interaction with carbon. This critical temperature depends on the helium composition.

In a second stage, alloy 230 has been exposed at 950°C to selected helium mixtures up to 1 000 hrs. Oxidation as well as carburisation modes were assessed. Observations of the corroded specimens indicate that oxidation induces growth of the surface scale whereas carburisation causes in-depth changes in the microstructure.

Introduction

Selection and qualification of structural materials for gas-cooled reactors (GCR) represent critical issues. In relation to the elevated helium temperatures (maximum 850-950°C), the thermal and gaseous environment in the primary circuit is highly demanding toward metallic materials in terms of structural stability, creep strength and chemical compatibility. Reference commercial alloys for such temperature ranges are for instance Inconel 617 and Hastelloy X/XR that are rich in chromium (22 wt.%) for the oxidation resistance and strengthened by addition of molybdenum (plus cobalt). Alloy 230, which also contains 22 wt.% chromium and 14 wt.% tungsten, could be an attractive alternative candidate. CEA, in close collaboration with Areva NP and EDF, has launched a R&D programme on high temperature metallic materials for the primary circuit and the intermediate heat exchanger (IHX). It mainly intends to compare the performances of Alloys 617 and 230 for GCR applications regarding aging, creep and corrosion properties. The programme achievements are globally presented in another contribution [1] and this paper's focus concerns the corrosion of Alloy 230 in impure helium.

It is expected that the GCR cooling gas is polluted by air ingresses during maintenance and refuelling or by out-gassing of adsorbed species out of insulation and graphite. These gasses can react with hot graphite. Impurity level is said to reach a steady state as a dynamic balance is set up between contamination rates, reactions of the pollutants with graphite or other hot materials, and purification efficiency [2]. Based on the analysis of the coolant in experimental GCRs, the composition may be estimated. Helium may contain H₂, CO, CO₂, CH₄ and N₂ ranging from few Pa to tens of Pa, while water vapour content may be a tenth of Pa or so [2-4]. Such a medium is reactive toward metallic materials at high temperature. Assuming that due to low contamination level, collision between gasses is very unlikely in GCR atmosphere, impurity/surface reactions can be regarded as independent [5]. Accordingly a set of possible reactions can be established at a metallic surface (Me), considering the formation of an oxide MeO_x and the transfer of dissolved carbon C_S:



The high temperature resistance of chromia former alloys relies upon the formation of a chromium-rich oxide scale that must be adherent, dense and slow-growing and so, protects the metallic surface against corrosive species. GCR atmosphere must thus definitely promote oxidation though Eq. (1) [and possibly (4)]. However besides reactions (1) to (4), a further specific process was evidenced in diluted atmospheres [5-7]. From the experimental standpoint, it is as if Eq. (4) with chromium and Cr₂O₃ reverses above a critical temperature T_A:



In destabilising the oxide scale, reaction (5) can expose chromia former alloys to an active corrosion mode.

We examine here the surface reactivity of Alloy 230 in impure helium at high temperature is examined here. In particular, the formation of a chromia scale and its stability versus reaction (5) is discussed. Eventually, the alloy corrosion behaviour in the oxidation mode and in conditions where reaction (5) occurs is characterised.

Experimental

Material

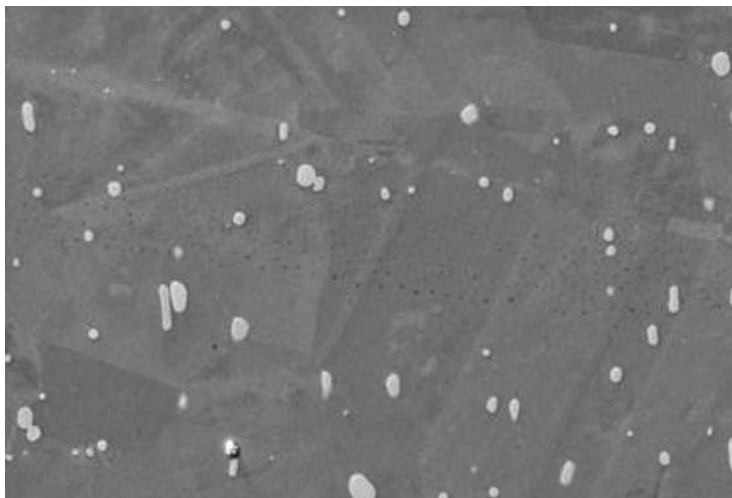
Table 1 reports the chemical composition of the tested Alloy 230 sheet which was manufactured by Haynes International in the mill-annealed condition (annealing at 1095°C and quench). Rectangular specimens were machined (thickness: about 2 mm, area: 6 cm²); they were ground to 1 200 grit (corrosion test) or to 2 400 grit and finished with 1 µm alumina powder (surface reactivity study), then ultrasonically cleaned in an acetone/ethanol mixture.

Figure 1 shows a SEM picture of the as-received alloy. Large tungsten carbides (about 5 µm) are present inside the grains. Other carbides much smaller were detected by TEM along grain boundaries [1].

Table 1. Alloy chemical composition (in wt.%)

	Ni	Cr	W	Co	Mo	Fe	Al	Mn	Ti	Si	C	B
Alloy 230	base	22.0	14.7	0.2	1.3	1.3	0.4	0.5	0.1	0.4	0.105	0.002

Figure 1. SEM image (BSE contrast) of the as-received Alloy 230



Test loop

Specimens were exposed to flowing impure helium at high temperature and at atmospheric pressure. Purposely added impurities are: H₂, CO and CH₄. Concentrations of impurities were analysed at the test section inlet and outlet by gas phase chromatography. In any case, oxygen, nitrogen and carbon dioxide partial pressures were below the chromatography detection limit (about 0.01 Pa). No water was directly introduced but the residual vapour partial pressure reaches 0.1 Pa or so; moisture is on-line monitored via a chilled mirror dew point hygrometer. Blank tests were carried out without specimen in order to check that the loop material and specimen holder do not significantly react with gaseous impurities, or influence the gas composition.

Experimental conditions for studies of the surface reactivity

Table 2 gives the impurity concentrations and water vapour content in test mixtures that are likely GCR atmosphere. ^1He to ^5He were used for this part. Two identical specimens were together exposed to a gas flow rate of about 0.7 ml/s per cm^2 of metallic surface. The experimental procedure, adapted from Ref. [6], consisted of a two-step thermal programme:

- *Step 1:* Oxidation step – heating to 900°C at 1°C/min and 25-hour plateau at 900°C under impure helium.
- *Step 2:* Study of the oxide stability – heating to 980°C at 0.5°C/min and 20-hour plateau at 980°C under impure helium.
- *Cooling:* Natural cooling under pure helium.

Table 2. Composition of the experimental impure helium mixtures and measured critical temperatures T_A – ^1He to ^5He relate to the study of the surface reactivity and ^6He to ^8He relate to the corrosion tests at 950°C

	H_2 (Pa)	H_2O (Pa)	CO (Pa)	CH_4 (Pa)	T_A (°C)
^1He	20.0±0.4	0.55±0.24	0.60±0.01	1.80±0.04	892±5
^2He	19.6±0.4	0.03±0.02	2.20±0.04	1.99±0.04	944±5
^3He	19.3±0.4	0.16±0.08	4.9±0.1	1.90±0.04	971±5
^4He	19.5±0.4	0.17±0.08	5.0±0.1	2.02±0.04	974±5
^5He	19.6±0.4	0.04±0.02	5.3±0.1	2.10±0.04	979±5
^6He	18.9±0.7	0.15±0.10	5.2±0.2	2.00±0.06	
^7He	20.0±0.6	0.07±0.05	0.5±0.06	2.10±0.05	
^8He	50.0±1.0	0.05±0.03	1.5±0.1	30.0±0.5	

Experimental conditions for corrosion tests

The corrosion tests were isothermal at 950°C for different times up to approximately 1 000 hrs; specimens were heated up and cooled down in pure helium at 1°C/min. Maximum six specimens, each one in a separate gas flow line, were together exposed in order to avoid downstream effect due to interferences between materials. The gas flow rate was about 0.15 ml/s per cm^2 of metallic surface. We validated that no significant depletion of impurities occurred throughout the test section. Considering the previous surface reactivity study, we designed test helium with the following characteristics at 950°C:

- ^6He should oxidise chromium into chromia.
- ^7He and ^8He should destabilise chromia; to test the effect of methane, ^7He and ^8He possess respectively a moderate (~2.1 Pa) and a high (~30 Pa) partial pressure of methane.

Specimen observations and analyses

After exposure, metallic specimens were weighed then sawed. Surface was directly characterised by X-ray diffraction (XRD with Cu-K α radiation). The global carbon content was analysed by LECO. For observations by scanning electron microscopy and analysis by energy-dispersive X-ray spectroscopy (EDS), coupons were prepared: they were sputtered with a gold film using cathodic evaporation and then coated by an electrolytic nickel deposit (both layers are visible on micrographs). Mounted coupons were eventually ground to 2 400 grit and finished with 1 μ m alumina powder.

Results and discussions on the surface reactivity at high temperature: chromia formation and stability in impure helium

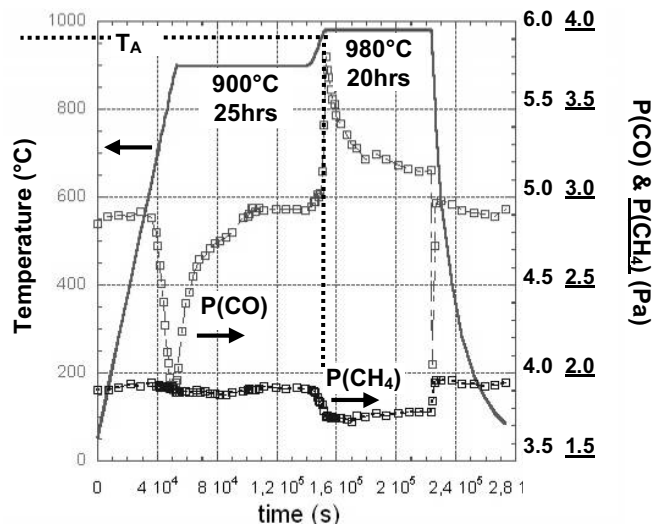
The following experiments aim at characterising the high temperature oxidation products of Alloy 230 in impure helium and at evidencing if this specific oxide scale may suffer from reduction according to reaction (5).

Gas phase analyses

Figure 2 presents the gas phase analysis by chromatography during testing in impure helium ^3He . In Step 1 (heating to 900°C and stay for 25 h) the P(CO) curve exhibits a negative CO peak.

During Step 2 (heating to 980°C and stay for 20 h) the carbon monoxide partial pressure increased; starting roughly at 970 \pm 5°C, the CO release reached 0.9 Pa. Afterward, the carbon monoxide production lowered and stabilised at about 0.3 Pa when the temperature is kept constant at 980°C. Furthermore, a decrease of about 0.15 Pa in the CH $_4$ level concurrently occurred. In agreement with Ref. [5] the critical temperature for the steep CO production was called T $_A$.

Figure 2. Temperature programme and changes in P(CO) and P(CH $_4$) during testing in ^3He as a function of time in seconds



Mass changes

Table 3 reports mass changes of Alloy 230 during testing in impure helium ^3He interrupted after Step 1 or completed up to Step 2. For both treatments, the mass increased but average mass gains after Step 2 appeared to be twice less than after Step 1. As spalling-off did not occur, the difference in the mean masses can definitely be related to a mass loss during Step 2.

Table 3. Mean mass changes and approximate surface scale thicknesses of Alloy 230 specimens after Step 1 and after Step 2 in ^3He

	Δm (mg/cm ²)	δ_{ox} (μm)
After Step 1	+0.11±0.01	~0.7
After Step 2	+0.05±0.01	~0.3

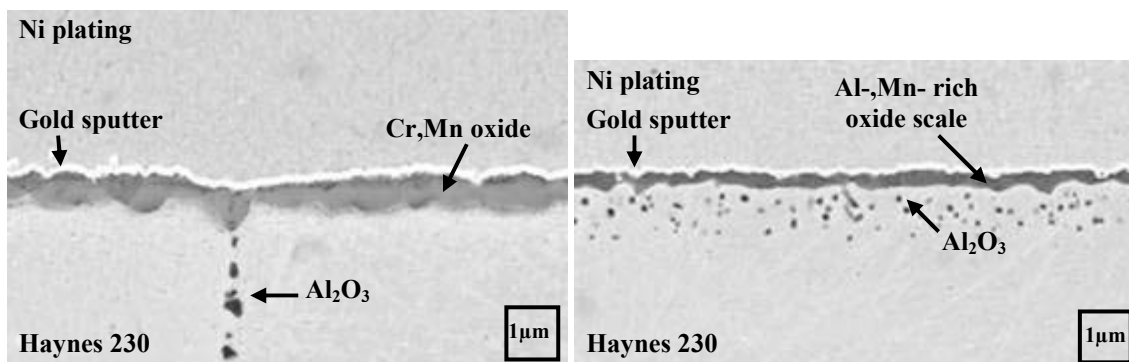
Observations and analyses of Alloy 230 surface corrosion products after Step 1

Figure 3, left-hand side, is a cross-section SEM image of the surface after Step 1 in ^3He . A continuous scale about 1 μm -thick has formed. Grazing XRD examinations at 1° identified Cr_2O_3 and a spinel phase of the type $\text{Mn}_{1.5}\text{Cr}_{1.5}\text{O}_4$. EDS analysis through the layer indicated that the Cr,Mn spinel was in the upper part whereas the inner part was mainly constituted by the chromium oxide. EDS also revealed that a discontinuous aluminium-rich oxide developed underneath the chromium-rich layer and that some aluminium oxidised along the grain boundaries up to 10 μm .

Observations and analyses of Alloy 230 surface corrosion products after Step 2

Figure 3, right-hand side, shows the cross-section of Alloy 230 after Step 2 in ^3He . A continuous surface oxide film can still be evidenced. However, this layer is significantly thinner than after Step 1 (Figure 3, left-hand side, and Table 3). When compared to the oxide developed after Step 1, EDS linescans through the scale suggested that the amount of chromium decreased relatively to manganese. The small nodules that are also detected in Figure 3 are alumina particles.

Figure 3. SEM images (BSE contrast) of specimens tested in ^3He after Step 1 (left-hand side) and after Step 2 (right-hand side)



Oxidation of Alloy 230 in impure helium: Step 1

Alloy 230 oxidised during Step 1 (up to 900°C) in ^3He . Two oxidising species are ready to react with the metallic surface: water vapour and carbon monoxide according to Eqs. (1) and (4). Oxidation by CO produced a negative peak in Figure 2. As the consumption eventually stopped (plateau in Figure 2), it is assumed that after some hours water vapour was the only impurity that took part to oxidation. It was elsewhere demonstrated [8] that the reactivity of the carbon monoxide depends on the water vapour content in helium: the higher the $P(\text{H}_2\text{O})$, the smaller the consumption of CO.

Oxidation resulted in the formation of a continuous surface scale. This oxide is rich in chromium and contains manganese. As already observed by Lupton [9], Mn is concentrated in the outer scale; it is partly incorporated in a spinel phase. Besides, aluminium exhibited a tendency to internal oxidation. It was proposed [10] that in the given conditions carbon monoxide may mainly react with minor elements Al, Si... following Eq. (4) whereas water vapour may largely oxidise chromium according to Eq. (1).

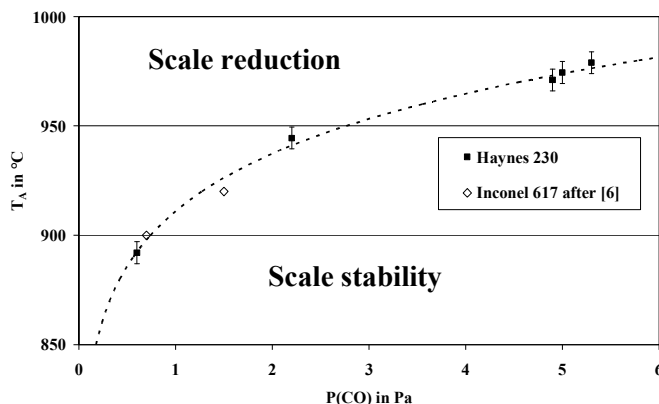
Oxide scale reduction: Step 2

Figure 2 shows an increase in the partial pressure of carbon monoxide during heating in Step 2. It started at about $970\pm 5^\circ\text{C}$ in ^3He . As was observed for other alloys [5-7,11], Eq. (5) is the only reaction that can produce such an important amount of CO. Eq. (2) coupled to Eq. (3) can also produce CO but the consumption of water vapour (maximum 0.16 ± 0.08 Pa) and of methane (about 0.15 Pa in Figure 2) was too low to account for the whole CO peak (up to about 0.9 Pa).

Moreover during Step 2, specimens lost mass and the surface scale became significantly thinner (Table 3). Scale analysis strongly suggests that chromium oxide is first reduced by carbon from the alloy following Eq. (5). Eventually manganese oxide reacts. After test in ^1He , the whole surface oxide (except alumina inclusions) has actually been removed. On the contrary, alumina cannot be reduced in such conditions.

According to Brenner's terminology [5], the critical temperature at the beginning of the steep peak in Figure 2 is called T_A . Determined by the test gas mixture, T_A changed from 892 to $974\pm 5^\circ\text{C}$ and the experimental values are given in Table 2 for ^1He to ^5He . Figure 4 plots the evolutions of T_A

Figure 4. Measured critical temperature T_A in $^\circ\text{C}$ for Haynes 230 in impure helium with different $P(\text{CO})$ in Pa (see Table 2: ^1He to ^5He); comparison to published data for Inconel 617 from Ref. [6] in helium containing 50 Pa H_2 , 2.2 Pa CH_4 and ~ 0.05 Pa H_2O



with respect to P(CO). It clearly appears that the higher the level of carbon monoxide in the gas phase, the higher the T_A value. Quadackers [6] studied Inconel 617 and his results are also reported in Figure 4. Both sets of data fall within the same scatter band. Furthermore, the author proposed that T_A is the equilibrium temperature of Eq. (5).

In summary Eq. (5) consumes chromium rich surface oxide plus carbon from the alloy and releases gaseous carbon monoxide; it likely produces chromium as well that should dissolve back in the metallic phase. As the surface scale is of prime importance for the protection against corrosion at high temperature, Eq. (5) puts a high risk on the material integrity. The critical temperature for the oxide reduction largely depends on the gas chemistry, firstly on P(CO), and Figure 4 helps in choosing the gas composition for longer corrosion tests.

Corrosion behaviour in impure helium: results and discussion

In the previous section, we evidenced two main reactivity modes for Haynes 230. Depending on the environment [temperature and P(CO)], a surface scale either develops or the surface oxide is irreversibly reduced by the carbon from the alloy. Brenner [5] and Quadackers [6] described that chromium-rich alloys actually demonstrate at least five reactivity types. In the following the medium term corrosion behaviour of Haynes 230 is studied in impure helium at 950°C. According to Figure 4, we have designed several test mixtures: ^6He promotes oxide scale formation; ^7He and ^8He destabilise the chromium oxide. In order to address the effect of methane, P(CH_4) is low in ^7He and high in ^8He .

Table 4 summarises the observations and analyses on the corroded specimens for the three gas compositions and various exposure times. Column 3 is the mass gain of oxygen by direct weighting. Column 4 gives the mean thickness of the surface scale as estimated by microscopy. Column 5 indicates the mass gain corresponding to the thickness in column 4. Column 6 gives the global carbon content from the LECO analysis and Column 7 shows the mass gain equivalent to the carbon uptake.

Table 4. Mass gain Δm , thickness of the surface scale δ_{ox} and global carbon content for specimens exposed for various times at 950°C in ^6He , ^7He and ^8He

	Time [h]	Measured Δm [mg.cm ⁻²]	Measured δ_{ox} [μm]	Calculated $\Delta m(\text{O})$ [mg.cm ⁻²]	Elemental C [wt.%]	Calculated $\Delta m(\text{C})$ [mg.cm ⁻²]
As-received					0.10	
^6He	25	0.11	0.7	0.1	No analysis	
	226	0.29	1.5	0.3	No analysis	
	239	0.38	2	0.4	0.11	
	498	0.46	2	0.4	No analysis	
	518	0.43	2	0.4	0.12	
	813	0.66	3	0.5	0.11	
	1 027	0.63	3	0.5	No analysis	
^7He	240	0.06			0.11	0.04
	500	0.44			0.17	0.60
^8He	240	7.64			1.29	7
	500	11.99			1.78	10
	1 000	15.65			2.49	14

Corrosion in “oxidising” ^6He

As shown in Table 4, all specimens gain mass in ^6He and the longer the test duration, the higher the mass gain. Figure 5 is a SEM picture of the surface of a specimen tested for 813 hours at 950°C in ^6He . As described in the previous part, Haynes 230 developed a surface oxide scale. It is rich in chromium and contains manganese. Table 4 shows that the scale was thicker for longer exposure times. Alumina is also observed at grain boundaries and the internal oxidation went deeper when the test time increased (up to approximately 20 μm after 1 013 hours).

Figure 5. SEM image (BSE contrast) of the specimen tested for 813 hours in test gas ^6He

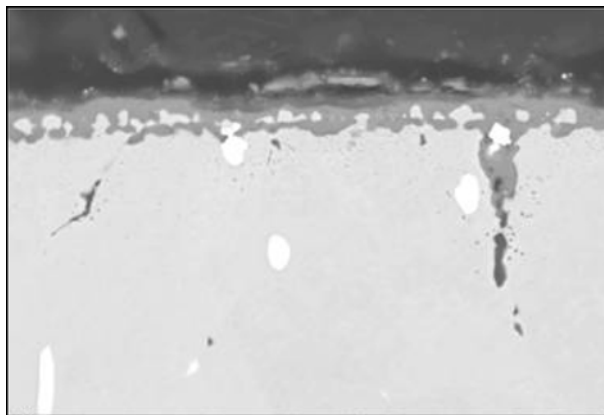
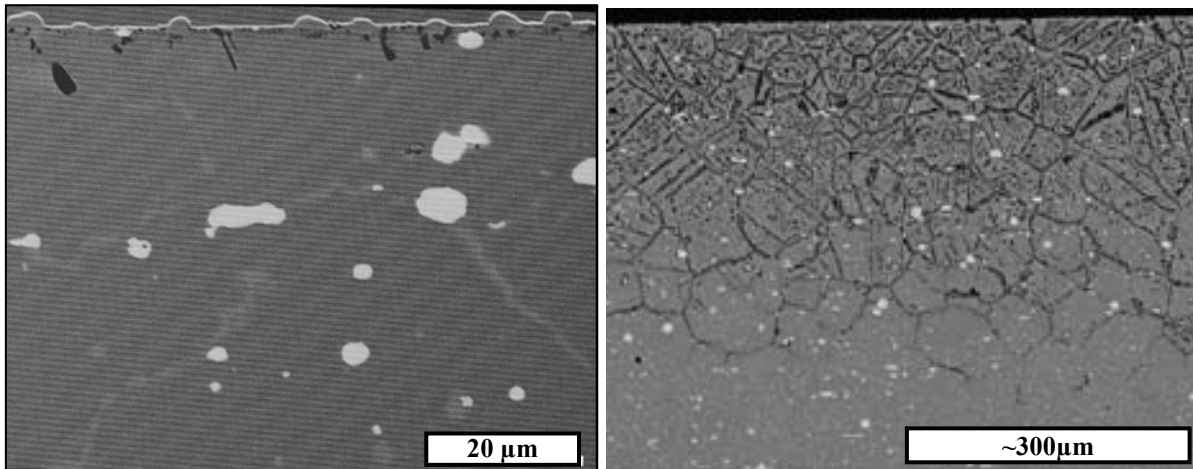


Table 4, last column, gives the total carbon content in specimens measured by the LECO analyser. There was a very small increase of the carbon weight percentage after treatment in ^6He . An increase in carbon corresponds to a deposition in the alloy by carbon-bearing gasses CO and/or CH_4 . In the case of ^6He , reactivity of carbon monoxide and methane following Eqs. (3) and (4) was thus very limited. This indicates that the oxide scale acts as an impervious barrier against gasses. If the mass gain corresponding to carbon deposition is neglected, the measured mass gains only correspond to oxygen deposition by Eq. (1). The thickness of the scale can therefore be estimated from the mass gain assuming the growth of dense chromia ($d = 5.2 \text{ mg/cm}^2$). The calculated values are in good agreement with the direct estimation by microscopy.

Corrosion in ^7He and ^8He (reduction of the oxide scale)

Specimens took weight after treatment in gas mixtures ^7He and ^8He . However, the mass gains were moderate in ^7He and very high in ^8He . Figure 6 reveals that there is no covering oxide scale. Instead, nodules are observed on the surface (see Figure 6, left-hand side). They are chromium-rich carbides. XRD analysis of the right-hand side specimen detected Cr_2C_3 and Cr_{23}C_6 (plus possibly Cr_7C_3). Some aluminium internally oxidised (dark phase). After 500 hours in ^7He , chromium-rich carbides also precipitated along grain boundaries up to about 150 μm deep (white precipitates in Figure 6, left-hand side). In ^8He , carburisation was massive on the surface, inside the grains and at joint boundaries. The front of coarse carbides went deeper when exposure time increased. After 240 hours, it reached approximately 500 μm and after 1 000 hours it crossed throughout the 2 mm-thick specimen that became brittle. Element analysis by LECO confirms that carbon was deposited in the specimens. Carbon uptake is very important for treatment in ^8He and accounted for the high mass gains as shown

Figure 6. SEM images (BSE contrast) of the specimens tested for 500 hours in test gas ^7He (left-hand side) and for 240 hours in test gas ^8He (right-hand side)



in the right column of Table 4. In conditions where surface oxide is reduced, it was observed that Inconel 617, another Cr-rich alloy, in fact suffered from carburisation in methane-rich helium and from decarburisation in helium with a low methane content and a relatively high water vapour partial pressure [5,6].

Conclusion

High temperature corrosion of Alloy 230 was investigated in impure helium representative of GCR atmospheres. In the given conditions, this material exhibits two main modes of surface reactivity: in balanced environments, it oxidises forming a scale while at the highest temperatures, the chromium rich oxide scale is reduced by carbon. It was evidenced that the critical temperature for the reactivity change essentially depends on the partial pressure of carbon monoxide in helium. It was therefore possible to design experimental gas mixtures with different natures for midterm corrosion tests at 950°C. The first (^6He) promotes oxidation. The two others (^7He and ^8He) cause reduction of chromia.

In weakly oxidising conditions, a sustainable Cr-rich oxide grows over at least 1 000 hours and the scale protects the metallic surface from exchanges with the gas phase. On the other hand if the scale is destabilised by reaction with carbon, the bare alloy interacts with impurities. In the given test gasses (which contain CH_4), carburisation rapidly proceeds. Its intensity is related to the partial pressure of methane. After 1 000 hours in atmosphere with 30 Pa CH_4 , coarse carbides precipitate throughout a 2 mm-thick specimen that becomes brittle.

It is thus obvious that, within the primary circuit, atmosphere must in any situation allow the development of a surface oxide scale. Excursion out of the stability conditions causes in-depth changes in the material microstructure that jeopardise the component lifetime. This puts a criteria on the partial pressure of CO in the reactor coolant. $P(\text{CO})$ has to be higher than a critical level that changes according to the temperature; the critical value, including necessary safety margins, can be estimated based on curves such as those presented in Figure 4.

Longer experiments are required to confirm the corrosion resistance of Alloy 230 in oxidising conditions where the behaviour depends on the properties of the slow growing surface scale.

Acknowledgements

The authors are thankful to the experts of Areva NP and EDF R&D, especially M. Blat, P. Combrade, G. Girardin, D. Kaczorowski and J. Chapovaloff, for the fruitful discussions within the framework of the joint research programme on high temperature metallic materials for the ANTARES project.

REFERENCES

- [1] Bulet, H., J-M. Gentzittel, C. Cabet, P. Lamagnère, M. Blat, D. Renaud, S. Dubiez-Le Goff, these proceedings.
- [2] Graham, L.W., M.R. Everett, D. Lupton, F. Ridealgh, D.W. Sturge, M. Wagner-Löffler, *Proc. of a Symposium on Gas-cooled Reactors with Emphasis on Advanced Systems*, Jülich, Germany, 13 October 1976, pp. 319-352.
- [3] Yao, M.S., R.P. Wang, Z.Y. Liu, X.D. He, J. Li, *Nuclear Engineering and Design*, 218, 163-167 (2002).
- [4] Sakaba, N., Y. Hirayama, *Proc. GLOBAL 2005*, Tsukuba, Japan, 9-13 October 2005, Paper no. 263.
- [5] Brenner, K.G.E., L.W. Graham, *Nuclear Technology*, 66, n°2, 404-414 (1984).
- [6] Quadackers, J.W., H. Schuster, *Nuclear Technology*, 66, n°2, 383-391 (1984).
- [7] Warren, M.R., *High Temperature Technology*, 4, n°3, 119-130 (1986).
- [8] Rouillard, F., C. Cabet, A. Terlain, K. Wolski, “Gas Cooled Reactors: Corrosion Behavior of a High Strength Nickel Base Alloy”, *Proc. Eurocorr 2005*, Lisbon, Portugal, 3-9 September 2005, Paper O-358-8.
- [9] Lupton, D.F., Report JÜL-1639, Kernforschungsanlage Jülich, Germany, January 1980.
- [10] Rouillard, F., C. Cabet, K. Wolski, M. Pijolat, *Oxidation of Metals*, accepted for publication.
- [11] Chapovaloff, J., D. Kaczorowski, K. Wolski, *Proceedings Matériaux 2006*, Dijon, France, 13-17 November 2006.

MATERIALS MODELLING – A POSSIBLE DESIGN TOOL FOR ADVANCED NUCLEAR APPLICATIONS

W. HOFFELNER, M. SAMARAS, B. BAKO, R. IGLESIAS
Paul Scherrer Institute
CH-5232 Villigen PSI

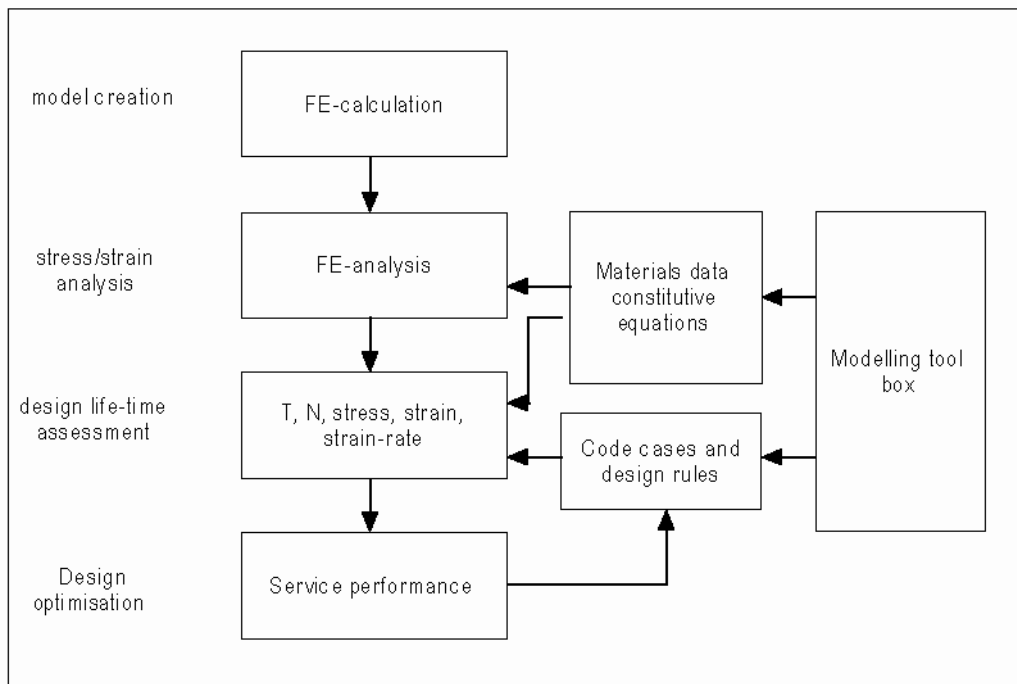
Abstract

The design of components for power plants is usually based on codes, standards and design rules or code cases. However, it is very difficult to get the necessary experimental data to prove these lifetime assessment procedures for long-term applications in environments where complex damage interactions (temperature, stress, environment, irradiation) can occur. The rules used are often very simple and do not have a basis which take physical damage into consideration. The linear life fraction rule for creep and fatigue interaction can be taken as a prominent example. Materials modelling based on a multi-scale approach in principle provides a tool to convert microstructural findings into mechanical response and therefore has the capability of providing a set of tools for the improvement of design life assessments. The strength of current multi-scale modelling efforts is the insight they offer as regards experimental phenomena. To obtain an understanding of these phenomena it is important to focus on issues which are important at the various time and length scales of the modelling code. In this presentation the multi-scale path will be demonstrated with a few recent examples which focus on VHTR applications.

Introduction

Components of plants and equipment operating under extreme conditions are usually subjected to a variety of exposures leading to damage and aging of the materials used. Safe operation of components requires methods which predict materials degradation as accurately as possible. In applications where the components are easily accessible and typical maintenance intervals are short (e.g. automotive applications) or where non-destructive evaluations are easily performed during service, investigation of components taken out of service prematurely help to improve the reliability of a certain design. This approach for design optimisation, however, fails for long-term applications (50 years and more) and for components which cannot be exchanged (e.g. reactor pressure vessel) and it is therefore necessary to implement improvements to schemes. The left-hand side of Figure 1 schematically illustrates the usual design procedure employed for long-term applications. Once the geometry of a component has been defined, the stresses and strains are determined by finite element (FE) calculations. These calculations are based on material properties (experimentally determined in the laboratory) and material laws (constitutive equations). Design rules and code cases are used to include complex loading situations and uncertainties. To obtain a more quantitative understanding, the inclusion of multi-scale modelling can provide physically based inputs into constitutive equations and finally can provide a very valuable input into design rules and code cases for damage interactions [1] and is thus included on the right-hand side of Figure 1. In this context, the term modelling does not refer to the well-established FE methodology used to date, but to calculations whose foundations rest upon quantum mechanical calculations at the microscale and move through the meso- and macroscales using the input of these quantitative smaller scaled calculations. To implement such a model successfully, scientists must understand and pinpoint the relevant issues and the related time and length scales on which the phenomenon in question occurs and subsequently implement the appropriate codes. For example, although failure of a component is usually considered as a macroscopic event, the main portion of damage during exposure time occurs on a microscopic and even nanoscopic level.

Figure 1. Schematic of the design process



Inclusion of data obtained using atomistic simulations of the various components which lead to failure, would greatly strengthen the quality of results obtained in design codes. Another example is the technically important prediction of phase diagrams using this multi-scale modelling approach. Results from quantum mechanical calculations which provide information of interatomic forces can be used in combination with thermodynamics-based programs, to obtain a good prediction of phases which can form with time. Thus the addition of this multi-scale modelling toolbox to the current design scheme is an attractive approach to increase the accuracy of life time assessments and consequently the safety of plants.

Modelling approach

The determination of the local mechanical properties from the microstructure is of utmost importance, indicating the necessity of approaching the issue using a multi-scale modelling scheme which encompasses broad time and length scales. This necessitates an approach that begins at the atomistic level using *ab initio*, molecular dynamics (MD) and kinetic Monte Carlo (kMC) techniques moves through the mesoscale using dislocation dynamics (DD) and ultimately ends at the larger spatial scales by employing FE methods and finally more general continuum models such as those used in current design schemes. As many of the related effects occur on a time scale which cannot be accomplished in the laboratory, modelling such phenomena is expected to enhance basic understanding and thereby improve the accuracy of design life assessments.

In this paper we address strength as the designer understands it and studies it – top-down – looking first at constitutive equations, then moving down a scale to the interaction of dislocations and their role in the mechanical behaviour of materials and then moving to smaller scales, often not visible by the experiments undertaken and overlooked by designers, but which indeed contain vital information which is important to include and which have been proven to be reputable methods to provide insight into materials' behaviour. This multi-scale procedure is highlighted top-down, with examples applicable to advanced VHTR reactor materials which are investigated within the international Generation IV initiative.

Discrete dislocation dynamics (DDD) taking ODS as an example

Increasing a material's strength in order to extend its lifetime is of great interest for many high temperature applications. Oxide dispersoids such as fine ceramic (yttria) particles dispersed in a matrix (e.g. ferritic) perform such a strengthening function by providing obstacles which hinder dislocation movement. This phenomenon and mechanisms therein can be understood and portrayed by modelling the dislocation-dispersoid interaction using the mesoscopic computational methodology known as discrete dislocation dynamics (DDD). From such calculations, the yield strength of materials and optimum particle size and distribution can be studied.

The DDD technique can also be used to analyse strength contributions from additional phases formed during long-term operation or from eventual helium bubbles formed as a result of irradiation. An extension of DDD simulations to high temperatures and to creep, necessary to understand materials degradation in high temperature reactors needs the quantitative inclusion of atomistic mechanisms for dislocation-obstacle interactions, dislocation-dislocation interactions and diffusion controlled dislocation movement. Such information requires data from atomistic scale modelling using MD and kMC simulations.

Atomistic simulations

Atomistic simulation methods such as MD and kMC can also be used to analyse point defect movement and other irradiation induced material damage which can become important during transient operations such as in the case of reactor start-up. The possible growth of creep induced grain boundary voids by point defects created during irradiation is another example of the application of MD/kMC [3].

Figure 2. Scheme of interaction between experiment and modelling (discrete dislocation dynamics, DDD) after [2]

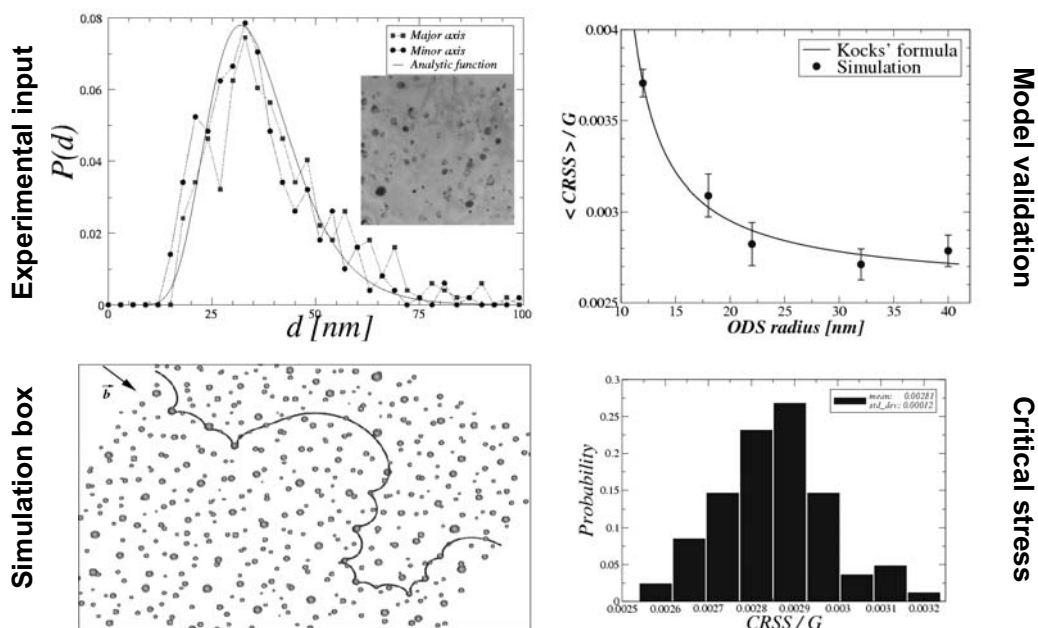
Upper left: Determination of size distribution of dispersoids with transmission electron microscope (TEM)

Lower left: DDD modelling of dislocation movement

Lower right: Determination of critical shear stress (CRSS) with model

Upper right: Comparison of experimentally determined CRSS with calculated value

Critical stress determination of PM2000 with Discrete Dislocation Dynamics

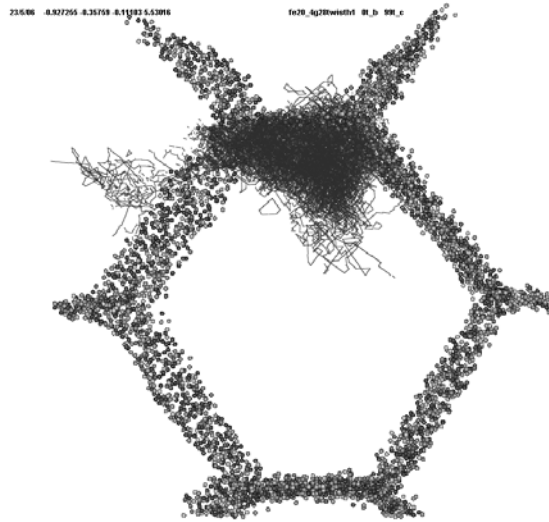


Accurate MD simulations need physically correct interatomic potentials. These potentials are fitted from a combination of quantum mechanical calculations and experimental results. Each element studied in an MD calculation needs to have the forces between the atoms of its own species and any other species in the simulation properly defined. This becomes a complex task when faced with the multitude of elements which make up the composition of today's highly developed steels. The main elements of many high temperature steels or alloys are iron, chromium and nickel which are all magnetic. Recently the role of magnetism, which hitherto has been a property ignored due to the increased difficulty to implement its inclusion, has been found to be of great importance in the case of iron, as it determines the most stable defect structures which indicates how deformations of the crystalline structure will form and move within the material and in the long term determines the material's lifetime. The importance of using a potential which includes magnetism is now illustrated in the following example of nanocrystalline bcc alpha-Fe. Initial comparisons of the displacement

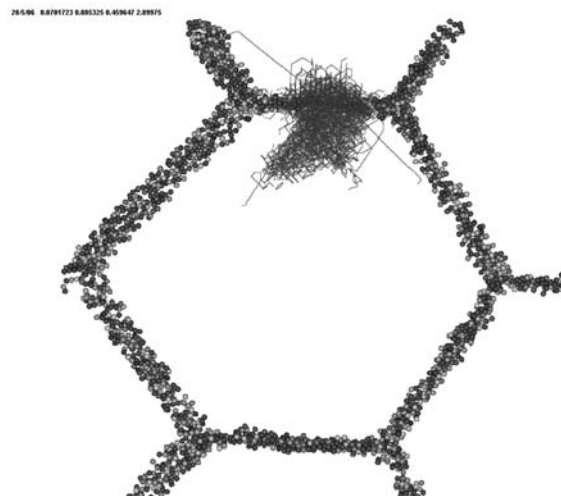
cascade of non-magnetic [4] with magnetic potentials [5] shown in Figure 3, reveal that the inclusion of magnetism produces cascades with different volumes and location within the structure. This result indicates that magnetism, which produces a dumbbell as the most stable interstitial rather than a crowdion [6], leads to an alternative movement of the interstitials within the sample and therefore affects the number of defects and the damage.

Figure 3

(a) Section of a grain in different orientations, showing the GB, with the movement of atoms during a displacement cascade with non-magnetic potential



(b) Section of a grain in different orientations, showing the GB, with the movement of atoms during a displacement cascade with magnetic potential



To properly include magnetism, it is therefore necessary to perform quantum mechanical investigations. Even using a top-down approach, as has been presented in this paper, brings forth the crucial role of performing quantum mechanical calculations to properly understand phenomena that may traditionally be thought of as purely macroscopic. From these considerations it becomes obvious that reliable lifetime models need to work within the whole range of dimensions (multi-scale approach).

Furthermore, to obtain robust, accurate models, it is important to validate them experimentally. Such experiments must first validate the calculations at the crux of the methodology – the quantum mechanical results. Testing of miniature samples and advanced analysis techniques like high resolution transmission microscope or beamline X-rays and neutrons are necessary for this purpose.

International collaborations

Modelling volumes are small and modelling times are short even when supercomputing facilities are used. Extension of the multi-scale approach to higher temperatures and longer times is a difficult challenge requiring international and interdisciplinary collaborations. With respect to the design of VHTRs, the following components and materials are of importance and the following work is envisaged within the VHTR GIF materials project; it is assumed that the reactor pressure vessel (RPV) will be made of an advanced martensitic 9% chromium steel (T91). As a result of temperature and eventually irradiation, microstructural changes and embrittlement can occur. To understand such materials it would be ideal to study Fe-Cr-C. Current modelling studies are performed on Fe-Cr.

Magnetism in this case is a very important factor that needs to be properly understood and implemented. Recently, studies on the complex inclusion of carbon in the Fe system have begun in a first step to study steel. It is also envisaged to use the Calphad approach with thermo-kinetic calculations, model the precipitation kinetic of secondary carbides in Fe-9Cr martensitic steels during the fabrication route and the dissolution/re-precipitation during the welding and the post-weld heat treatments.

New grades of materials (e.g. ODS) are considered as reactor internals, despite the well known austenitic steel 316. The ferritic Fe-Cr-C system (plus alloying elements) together with dispersoids, irradiation induced creep and thermal creep, creep-fatigue irradiation effects are the relevant processes to be studied. Multi-scale numerical simulation from the atomic scale is necessary to account for the mechanisms, and establish robust predictive models of the formation of atom nanoclusters in ODS steels as well as of their stability at high temperatures and under creep and irradiation conditions.

Piping and intermediate heat exchanger are outside the reactor and therefore irradiation effects do not need to be considered. *Ab initio* considerations have to be extended to FeNi (e.g. for 800 H) or NiCr (IN-617). Creep, fatigue and surface reactions are the life limiting factors in this case. ODS materials are also possible candidates for very advanced concepts. Mechanical performance, production and forming issues like optimisation of dispersoids or subgrain formation must be studied.

Atomistic modelling is equally important for non-metallic materials, too. As the basis of the multi-scale approach remains the same for metals and ceramics and as the scientific community working on metals and ceramics is basically identical it is advantageous to include the atomistic modelling requirements for ceramics here, too. A summary of the modelling work planned for the GIF VHTR materials project is shown in Table 1.

Conclusions

Modelling materials behaviour in principle has the capability of increasing the predictive aptitude of materials exposed to extreme conditions, thereby reducing the risk of premature failure of components and plants. A brief look at how creep and irradiation damage can be modelled in this multi-scale story, shows how component and materials design is being tackled by a new generation of scientists. This multi-scale scheme is far from complete and is at a far off stage from being directly incorporated into design rules. Time scales are very short, modelling temperatures are low, long-term effects and effects

of high temperatures are not yet developed. Model development can only become successful with experimental validation of the elementary structures modelled, indicating extra work for experimentalists as they need to go back and perform tests on non-industrial materials. For applications which need long-term predictions of damage under complex loading conditions, such as future nuclear fission plants, the current status of multi-scale modelling is still not mature for direct application to design procedures as it is still in development, however, even at this stage it is possible to obtain much insight into mechanisms that are present in the materials. Such a modelling scheme will benefit most by bringing together an international consortium of modellers, experimentalists and designers to work together in determining important phenomena and mechanisms, how to best tackle them with currently existing and/or new codes and methodologies, and to iteratively validate these models with experiments which are directly comparable in order to improve them. If a robust multi-scale modelling toolbox is constructed on a stable foundation, then a very interesting materials program will emerge in the future to predict the lifetimes of materials.

Table 1. Modelling collaborations planned within GIF VHTR materials project

Main topic	Subtask	Method
Microstructural stability of chromium steels and nickel-based alloys	FeCrC	<i>Ab initio</i> + Calphad
	NiCrC	Potentials
Damage assessment	Yield strength ODS	DD + inclusion of temperature
	Dislocation obstacle interactions	MD simulations
	Creep	Development of procedure
	Fatigue	DD (patterning)
	Irradiation/corrosion damage of bulk ceramics and ceramic compounds	MD, DD, kMC, FE
	Grain size effects	MD-irradiation
Constitutive equations	Life time assessment T91, IN-617	Norton-type, modified linear life fraction rule
	Dimensional link between constitutive equations and molecular modelling	Rate theory, constitutive-atomistic combinations
Experimental validation	Dislocation-dispersoid interactions	Tensile tests
	Magnetic properties	XMCD

REFERENCES

- [1] Samaras, M., W. Hoffelner, M. Victoria, “Modelling of Advanced Structural Materials for GEN IV Reactors”, *J. Nuclear Mat.* (2007), forthcoming.
- [2] Bako, B., D. Weygand, M. Samaras, J. Chen, M.A. Pouchon, P. Gumbsch, W. Hoffelner, “Discrete Dislocation Dynamics Simulations of Dislocation Interactions with Y_2O_3 Particles in PM2000 Single Crystals”, *Philosophical Magazine*, forthcoming (2007).
- [3] Samaras, M., W. Hoffelner, M. Victoria, *J. of Nucl. Mater.*, 352, 50 (2006).
- [4] Ackland, G.J., D.J. Bacon, A.F. Calder, *Philos. Mag. A*, 75, p. 713 (1997).
- [5] Dudarev, S.L., P.M. Derlet, *J. Phys. Condens. Matter*, 17, 7097 (2005).
- [6] Fu, C.C., F. Willaime, P. Ordejon, *Phys. Rev. Lett.*, 92, 175503 (2004).

CHARACTERISATION OF OXIDATION AND OXIDE LAYERS OF NICKEL-BASE SUPERALLOYS AT HIGH TEMPERATURE

Changheui Jang, Daejin Lee, Daejong Kim

Korea Advanced Institute of Science and Technology, Rep. of Korea

Abstract

Nickel-base superalloys are considered as materials for several key components in a very high temperature gas-cooled reactor. The high temperature properties of those alloys such as creep and creep-fatigue strongly depend on characteristics of surface oxide layer. Therefore, in the present study, the oxidation behaviours of several nickel-base superalloys such as Alloy 617, Haynes 214 and Haynes 230 were investigated at 900°C and 1100°C in air and helium environments. Also, to understand the surface oxidation process, oxide layers were analysed by XRD, XPS and EDX. The results showed that the oxidation behaviours were strongly depended on the stability of the surface oxides. In case of Alloy 617 and Haynes 230, Cr₂O₃ was dominantly formed on the surface, and the weight increased significantly due to oxidation at the initial stage, but followed by a decrease due to volatilisation of Cr₂O₃ layer, especially at 1100°C. Also, the partitioning of other minor alloying elements into the surface layer was observed but disappeared after long-term exposure. On the other hand, after forming transient phases like NiO and NiCr₂O₄, stable α -Al₂O₃ layer was dominantly formed later on the surface of Haynes 214, and the weight gain eventually reached to plateau. Based on the weight loss measurement and XRD analysis, the oxidation resistance of the alloys was discussed.

Introduction

The nickel-base superalloys are considered as main structural materials in a very high temperature gas-cooled reactor (VHTR). During the normal operation, the superalloys are subjected to very high temperature, 900°C and above. Also, they are exposed to the He gas containing reactive impurities, which lead to the degradation, in particular high temperature mechanical properties such as creep and creep-fatigue [1-3].

It has been known that nickel-base superalloys have considerably good oxidation and carburisation resistance, imparted by the Cr and Al. The stability of materials is high at the anticipated operating temperature because the external oxide prevents the direct interaction of metal with the contaminated He gas by small amount of gaseous impurities.

However, it still has many problems to adapt these alloys as structural materials for VHTR application. Superalloys as Ni-Cr-Al ternary alloys show huge different oxidation behaviours as a function of temperature and composition [4]. At the operation temperature above 1 000°C, its oxidation resistance dramatically decreases. The oxidation resistance is strongly related with the characteristics of the external oxide layer as a barrier against the potential damaging environment.

Therefore, in the present work, the oxidation behaviours of several nickel-base superalloys such as Alloy 617, Haynes 214 and Haynes 230 are investigated at 900°C and 1 100°C in air and high purity helium environments. The changes in composition and microstructural characteristics of the external oxide layer are analysed.

Experimental procedure

Commercial grade nickel-base superalloys such as Alloy 617, Haynes 230 and Haynes 214 were used in this study. Alloy 617 and Haynes 230 are candidate materials for VHTR, and Haynes 214, on the other hand, are used as a reference material to see the effect of high aluminium content. Chemical compositions of test materials are listed in Table 1.

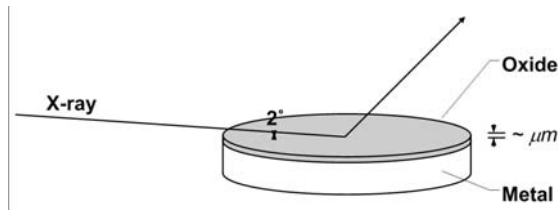
Table 1. Chemical compositions of nickel-base superalloys

	Cr	Al	C	Co	Fe	Mn	Mo	Ni	Si	Ti	W
Alloy 617	21.77	1.1	.08	12.0	1.2	.04	9.42	Bal.	.1	.38	–
Haynes 214	16.18	4.25	.05	.03	3.64	.188	.01	Bal.	.091	–	.001
Haynes 230	21.85	.38	.1	.19	1.48	.51	1.21	Bal.	.12	.01	14.0

The oxidation test was conducted using the tube furnace. Coupon specimens were oxidised in the high purity helium gas of 99.999%, containing small amount of impurities (1.8 ppm H₂O, 1.4 ppm O₂, 3.1 ppm N₂) and in atmosphere. The weight change caused by oxidation was measured using micro-balance.

The change in chemical composition and structure of oxides was analysed by X-ray photoelectric spectroscopy (XPS), energy dispersive X-ray (EDX) and X-ray diffraction (XRD). In particular, since the thickness of oxide layer is a few micrometers, we used the thin film XRD, considering the penetration depth of X-ray. The angle of the incident beam was fixed with 2° to reduce the penetration depth less than a few micrometers. Diffraction angle (2θ) was in the range of 20 to 80°. Tube current and voltage were 30 kV and 60 mA, respectively. The schematic diagram is illustrated in Figure 1.

Figure 1. Schematic diagram of thin film X-ray diffraction

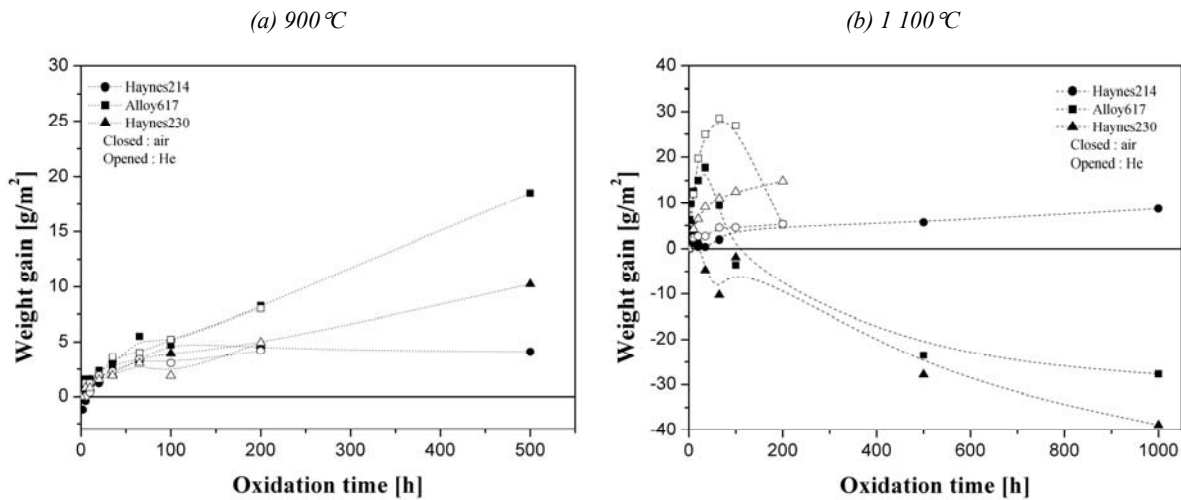


Results and discussion

Oxidation rates

Figure 2 shows the change in weight of Alloy 617, Haynes 214 and Haynes 230 during oxidation in air and helium at 900°C and 1 100°C. At 900°C, the weight increases as a function of oxidation time for three materials in both air and helium environments, because oxide layers are formed on the surface of the materials. In spite of a huge difference in oxygen contents between air (2×10^5 ppm O_2) and helium (1.4 ppm of O_2), the oxidation behaviours are similar in both environments. Therefore, amount of oxygen in He gas is considered high enough to oxidise superalloys. The rather continuous weight gain behaviour is observed for all three alloys tested at 900°C.

Figure 2. Weight changes of Haynes 214, Alloy 617 and Haynes 230 in He and air



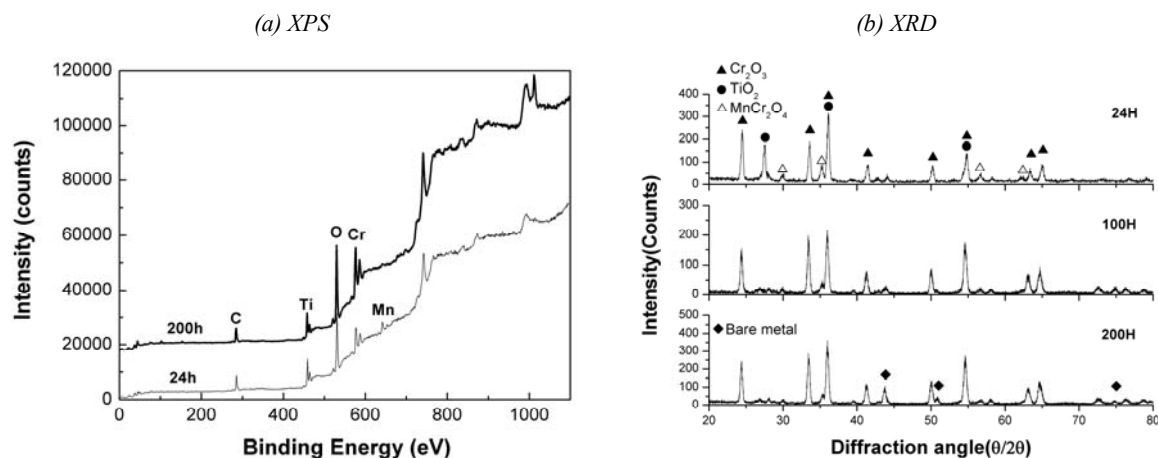
At 1 100°C, on the other hand, after an increase in weight at the initial stage, it decreases severely at for Haynes 230 and Alloy 617. The weight loss could be induced mainly by spallation and volatilisation of oxide layers on surface of specimens [5]. For example, the Cr_2O_3 layer becomes thermodynamically unstable and evaporated above 1 000°C [4]. Alloy 617 shows the delayed oxidation rate in high purity helium gas because of the limited oxygen contents. On the other hand, stable weight gain behaviour is observed for Haynes 214 at 900°C and 1 100°C in both environments. The weight gain reaches the plateau at approximately 100 hrs and very slow increase in weight is observed after that.

Characteristics of external oxides

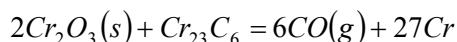
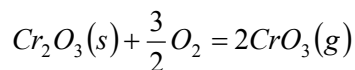
Oxidation of Alloy 617

Alloy 617 is a chromia-forming alloy, containing approximately 21.8 wt.% Cr. Cr_2O_3 forms mainly on the surface. Figure 3 shows the XPS and XRD analysis results of Alloy 617 oxidised at 1100°C. In Figure 3(a), C is a reference peak as a contaminated element. Main oxidation products are Cr_2O_3 (corundum), TiO_2 and MnCr_2O_4 , corresponding well to the result of XPS analysis. At the initial oxidation stage, Mn rapidly forms MnCr_2O_4 spinel because it has lower standard Gibbs free energy ($\Delta G \approx -830$ kJ/mol) than Cr_2O_3 ($\Delta G \approx -1160$ kJ/mol) at 1100°C [6]. Therefore, MnCr_2O_4 spinel develops preferentially on the surface at the beginning of oxidation. Local Mn depletion region is generated due to the limited Mn contents in Alloy 617 (0.04 wt.%). As oxidation progresses, MnCr_2O_4 is gradually covered by Cr_2O_3 layer, and eventually, peak of Mn is not detected in XPS result.

Figure 3. XPS and XRD analysis result of Alloy 617 oxidised in air at 1100°C



The peak intensity of Cr_2O_3 increases continuously with oxidation time. However, the peak intensity of metal substrate also increases with oxidation time suggesting that the external Cr_2O_3 layer get discontinuous and the matrix is exposed. Figure 4 shows evidence for the discontinuous development of external oxide layer. The decomposition of Cr_2O_3 layer by reaction with internal carbides, by the reaction shown below, also contributes to the continuous thinning of external Cr_2O_3 layer and the decrease in weight.



This phenomenon accelerates the diffusion of oxygen into metal matrix, which increases decarburisation as shown in Figure 5. The high temperature mechanical properties can be significantly degraded.

Figure 4. SEM micrograph of Alloy 617 oxidised in air at 1 100°C

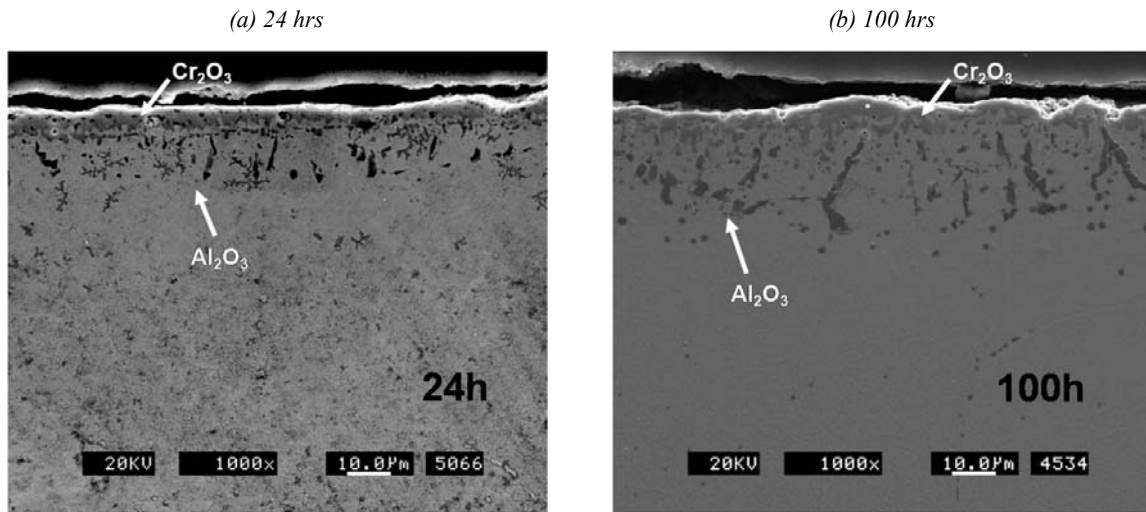
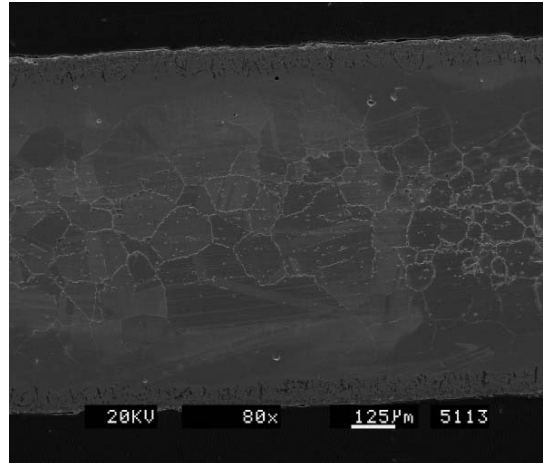


Figure 5. SEM micrograph of Alloy 617 oxidised at 1 100°C in air for 1 000 hrs



From the XRD results shown in Figure 3(b), TiO₂ peaks are almost disappeared after 100 hrs. However, Ti peak is still visible in the XPS analysis result. This discrepancy could be explained by the partitioning of Ti into the Cr₂O₃. At the early stage of oxidation, TiO₂ and Cr₂O₃ are formed separately. Then as the oxidation progresses, the formation of Cr₂O₃ becomes dominant, while TiO₂ is dissociated and partitioned into the Cr₂O₃. Therefore, Ti peak is observed from XPS, but TiO₂ peak is disappeared in XRD analysis.

Based on the XRD and XPS analysis, the oxidation behaviour for Alloy 617 is illustrated in Figure 7. After the formation of MnCr₂O₄, external Cr₂O₃ layer develops on the surface. While volatilisation of CrO₃ causes the thinning of protective layer, oxygen diffuses more rapidly into the matrix through thinned and discontinuous external Cr₂O₃ layer. The, Al₂O₃ nucleates on the grain boundary. Oxygen diffuses preferentially along the interface between internal Al₂O₃ islands and matrix because grain boundary is one of the most high diffusivity paths. It is called short circuit diffusion [8]. Therefore, extensive internal Al₂O₃ islands are formed in elongated shape. On the other hand, oxidation behaviour is a little different at 900°C. As shown in Figure 6(a), external oxide layer is more continuous, resulting in the shallow penetration depth of internal oxide.

Figure 6. EDX analysis result of Alloy 617 oxidised in air for 100 hrs exposure

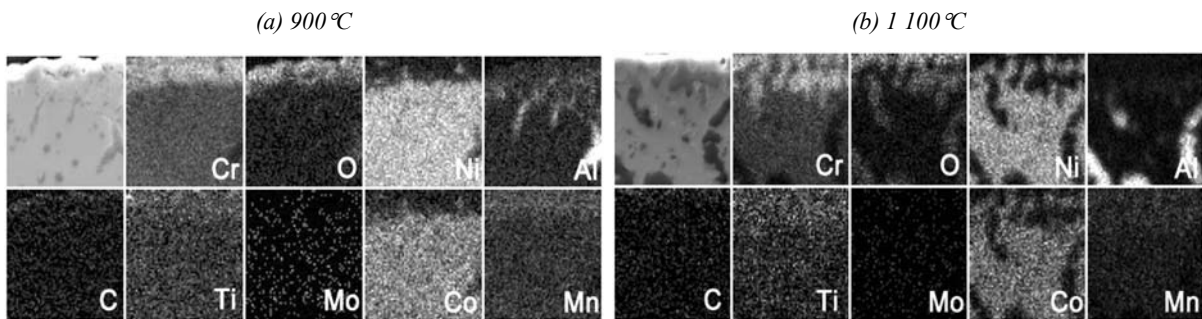


Figure 7. Schematic diagram of progress in oxidation for Alloy 617 at 1100°C

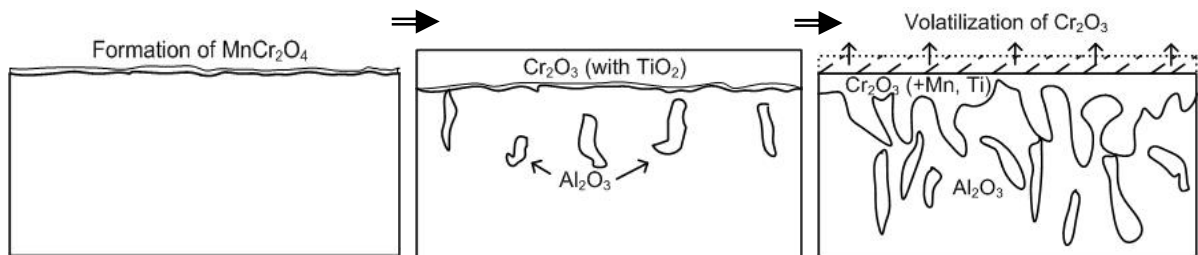


Figure 8 shows the XRD analysis results of external layer of Alloy 617 oxidised at 900°C. At the early stage, the external oxide, Cr_2O_3 and NiCr_2O_4 spinel are formed. Both Cr_2O_3 and NiCr_2O_4 spinel are slowly growing oxides at 900°C, which have low cation diffusion rate and, therefore, act as diffusion barriers for oxygen [4]. As results, the weight gain is rather slow as shown in Figure 2. Then as the oxidation progresses, the NiCr_2O_4 is completely dissolved. At the same time, surface Cr_2O_3 layer becomes discontinuous and irregular, resulting in the increase in the peak intensity of matrix.

Figure 8. XRD analysis results of Alloy 617 oxidised in air at 900°C

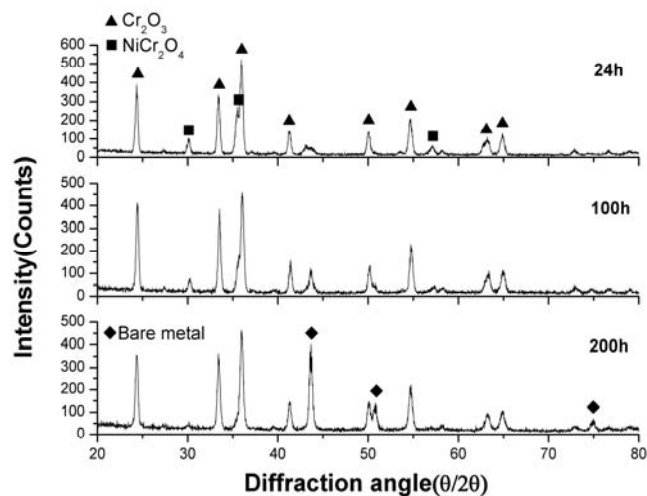


Figure 9 shows the XPS and XRD analysis results of Haynes 214 oxidised at 1 100°C in air. Peaks of Cr and Ni are detected after 24 hrs as shown in Figure 9(a). Cr and Ni form various oxides such as Cr_2O_3 , NiCr_2O_4 and NiO .

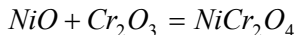
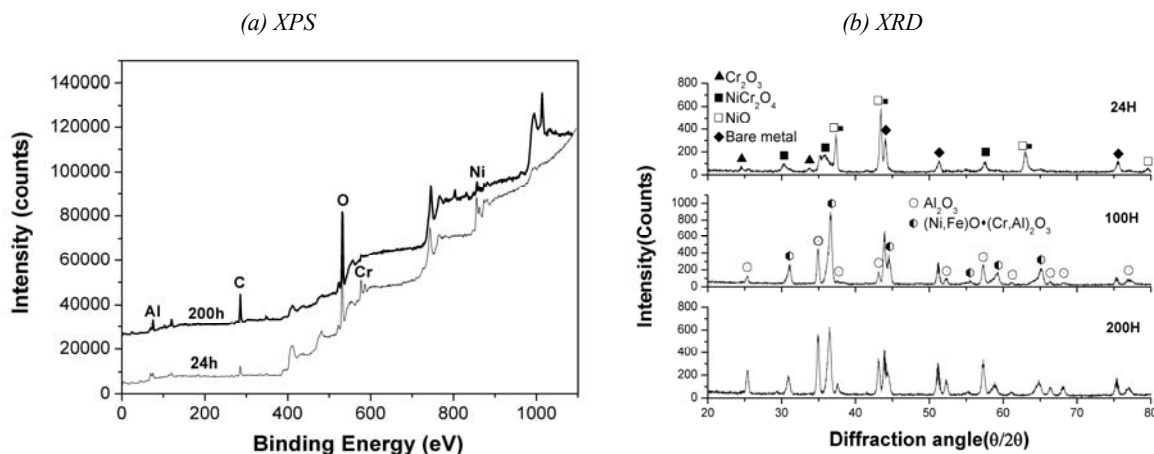


Figure 9. XPS and XRD analysis result of Haynes 214 oxidised in air at 1 100°C



However, these initial products are almost dissolved after 100 hrs in air. This phenomenon is known as transient oxidation and usually occurs in chromia-forming alloys [4]. Although Haynes 214 is an alumina-forming alloy, containing approximately 4.3 wt.% Al and 16.2 wt.% Cr, transient oxidation is observed in this study. As shown in Figure 9(b), peaks for Al_2O_3 and $(\text{Ni,Fe})\text{O}\cdot(\text{Cr,Al})_2\text{O}_3$ are observed from the XRD analysis. However, peaks of Fe and Cr are barely detected in XPS analysis, even at a very slow scanning rate. Therefore, it is thought that the oxide layer is a double layer consists of outer Al_2O_3 and inner $(\text{Ni,Fe})\text{O}\cdot(\text{Cr,Al})_2\text{O}_3$.

Among the oxides forming the double layer, the relative intensity of Al_2O_3 continuously increases with oxidation time. This could indicate that the inner $(\text{Ni,Fe})\text{O}\cdot(\text{Cr,Al})_2\text{O}_3$ is gradually transformed to Al_2O_3 as reported by Huang, *et al.* higher temperature [9]. But more analysis is needed to verify the transformation at current test condition. Peak intensity of metal substrate barely changes with oxidation time indicating that the thickness of oxide layer barely changes with time.

Figure 10 shows the Al 2p spectra of Haynes 214. The peak at the higher binding energy (BE) corresponds to Al 2p in metallic Al (72.9 eV). At the early stage of oxidation, Al 2p peak (71.6 eV) may be attributed to Al-rich oxides on the surface although aluminium oxide is not detected in XRD results as shown in Figure 9(b). This inconsistency needs further analysis. The existence of Al in oxide layer is confirmed by EDX analysis. After 200 hrs of exposure, the BE peak is at 73.9 eV, corresponding to Al^{3+} in $\alpha\text{-Al}_2\text{O}_3$ 2p. This result is consistent with the XRD result.

At 900°C, Haynes 214 forms completely different external oxides as shown in Figure 11. $\text{Ni}(\text{Cr,Al})_2\text{O}_4$ and NiO are detected instead of primary oxides such as Al_2O_3 and Cr_2O_3 . They are known as transient oxides at 1 000°C, but very stable at 900°C. Until 200 hrs, the peak intensity of matrix continuously decreases with oxidation time because external oxide layer grows slowly but steadily. Then, the weight gain eventually reaches to plateau as shown in Figure 2.

Figure 10. Al 2p spectra of Haynes 214 after oxidation in air at 1 100°C

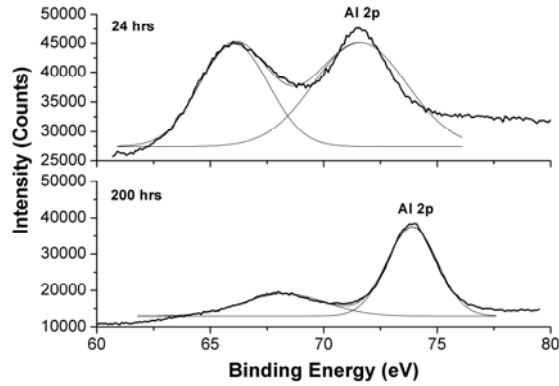
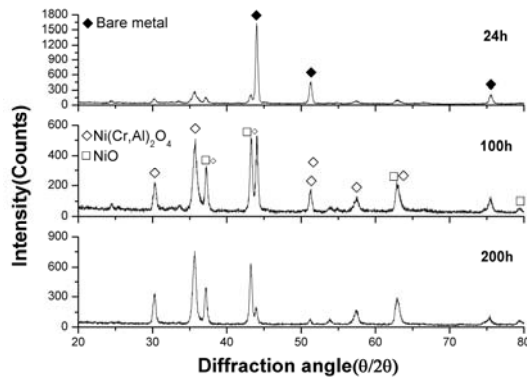


Figure 11. XRD analysis results of Haynes 214 oxidised in air at 900°C



Oxidation of Haynes 230

Haynes 230 is a chromia-forming alloy, containing approximately 21.9 wt.% Cr. Therefore, oxidation behaviour of Alloy 230 is similar to Alloy 617 as shown in Figure 12. The high Mn content leads to the intensive peaks of Mn and MnCr_2O_4 . Thick MnCr_2O_4 layer, which is earlier forming oxide than Cr_2O_3 , delays the weight loss at the initial stage of oxidation. With oxidation time, MnCr_2O_4 is dissociated and gradually replaced by Cr_2O_3 . As shown in Figure 12(a), Mn significantly disappears on the surface after 200 hrs because of the growth of Cr_2O_3 layer and duplex oxide layers. As the dissociation of MnCr_2O_4 increases, or Cr_2O_3 becomes dominant, substantial weight loss is observed. Moreover, relative peak intensity of matrix continuously increases by volatilisation of Cr_2O_3 .

Figure 13 shows that aluminium content is high in metal matrix just beneath the external oxide layer after 5 hrs at 1 100°C. But no Al-containing phase is formed yet. On the other hand, after 100 hrs at 1 100°C, Al oxides are clearly visible at grain boundary. The size of internal Al_2O_3 islands is relatively small compared to that in Alloy 617 due to lower Al and Ti contents in Haynes 230. The relatively continuous external oxide layer of Haynes 230 is also contributed to less internal oxidation. At 900°C, the same oxides form with at 1 100°C. The growth rate of oxide layer is much slow.

Figure 12. XPS and XRD analysis result of Alloy 230 oxidised in air at 1 100°C

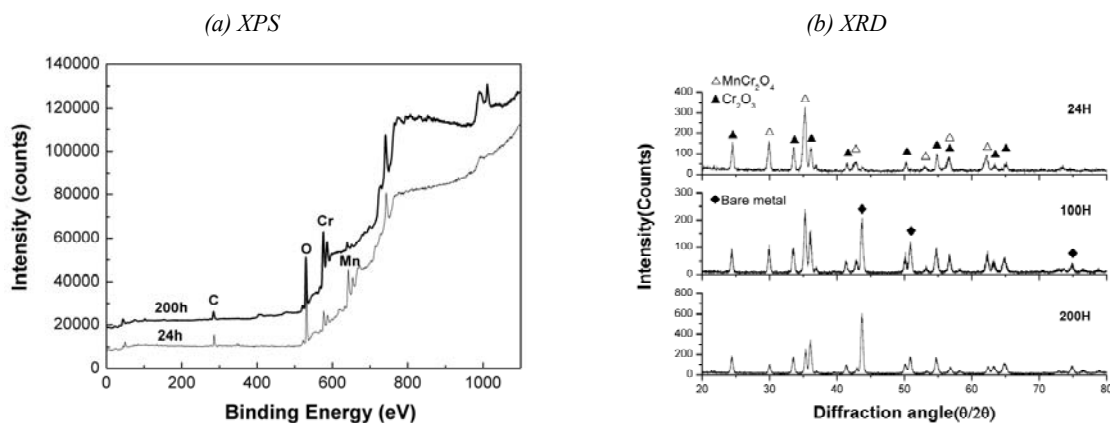
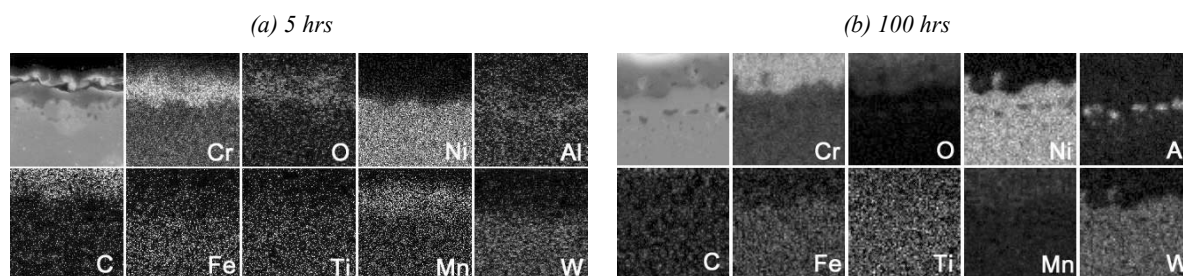


Figure 13. EDX analysis result of Haynes 230 oxidised in air at 1 100°C



Conclusions

The oxidation characteristics of nickel-base superalloys such as Alloy 617, Haynes 214 and Haynes 230 were investigated at 900°C and 1 100°C in high purity helium and air environments. The weight gain behaviours are measured and the surface oxides are analysed using XRD, XPS and EDX. Based on the analyses, the stability and the evolution of the oxides are investigated.

During the high temperature oxidation, several transient phases are formed on the surface and later disappeared. At 1 100°C, TiO_2 and MnCr_2O_4 are formed in Alloy 617, NiO , NiCr_2O_4 , Cr_2O_3 and $(\text{Ni,Fe})\text{O}(\text{Cr,Al})_2\text{O}_3$ in Haynes 214, MnCr_2O_4 in Haynes 230. And, at 900°C, NiCr_2O_4 is formed in Alloy 617, MnCr_2O_4 in Haynes 230. In case of low Al-containing alloys, the transient phases are gradually disappeared and replaced by the stable Cr_2O_3 as the oxidation time increases at both temperatures. On the other hand, high Al-containing Haynes 214 shows different stable phases depending on the temperature such that Al_2O_3 at 1 100°C but NiO and $\text{Ni}(\text{Cr,Al})_2\text{O}_4$ at 900°C.

The weight gain behaviours of the alloys are closely related to the stability of the surface oxide layers. When the surface oxide is Cr_2O_3 , as in Alloy 617 and Haynes 230, the oxide layers become discontinuous and lose the ability as a protective layer. On the other hand, Al_2O_3 and $\text{Ni}(\text{Cr,Al})_2\text{O}_4$ surface oxide layers formed in Haynes 214 are continuous and stable, thus provide good oxidation resistance at 900°C and 1 100°C.

Acknowledgements

This study was funded as the Basic Atomic Energy Research Institute (BAERI) programme of the Ministry of Science and Technology of Korea. Part of the funding was provided by the Second Phase BK21 programme of the Ministry of Education and Human Resource Development of Korea.

REFERENCES

- [1] Sankara Rao, K.B., “Creep-fatigue Interaction of Inconel 617 at 950°C in Simulated Nuclear Reactor Helium”, *Material Science and Engineering*, A104, 37-51 (1998).
- [2] *Review and Assessment of Codes and Procedures for HTGR Components*, NUREC/CR-6816 (2003).
- [3] Lu, Y., L. Chen, G. Wang, *et al.*, “Hold Time Effects on Low Cycle Fatigue Behavior of HAYNES 230 Superalloy at High Temperature”, *Material Science & Engineering*, A409, 282-291 (2005).
- [4] Birks, N., G.H. Meier, F.S. Pettit, “Oxidation of Alloys”, *Introduction to the High-temperature Oxidation of Metals*, Cambridge University Press, New York (2006).
- [5] Smialek, J., G. Meier, “High Temperature Oxidation”, *Superalloy II*, Wiley Interscience, New York (1987).
- [6] Jian, P., L. Jian, H. Bing, G. Xie, “Oxidation Kinetics and Phase Evolution of a Fe-16Cr Alloy in Simulated SOFC Cathode Atmosphere”, *Journal of Power Sources*, 158, 354-360 (2006).
- [7] Gleeson, B., M.A. Harper, “Effects of Minor Alloying Additions on the Oxidation Behaviour of Chromia-forming Alloys”, *Proceedings of EFC Workshop*, 34, 167-177 (2001).
- [8] Park, C.O., *et al.*, “High Diffusivity Path”, *Diffusion in Solids*, KAIST Press, Daejeon (2003).
- [9] Hwang, J., *et al.*, “High-temperature Oxidation Behavior and Mechanism of a New Type of Wrought Ni-Fe-Cr-Al Superalloy Up to 1 300°C”, *Oxidation of Metal*, 53, 273-287 (2000).

AN EXPERIMENTAL SURVEY ON MECHANICAL PROPERTY CHARACTERISATIONS OF ION-IRRADIATED SILICON CARBIDES

Weon-Ju Kim, Kyeong Hwan Park, Choong Hwan Jung, Ji Yeon Park
Nuclear Materials Technology Development Center
Korea Atomic Energy Research Institute
Republic of Korea

Abstract

SiC and SiC/SiC composites have a great potential for the structural material of advanced nuclear reactors. The irradiation behaviours of SiC are important and an ion irradiation is a useful tool to simulate the expected core conditions of fusion and GEN-IV nuclear reactors. Generally, however, the radiation-induced range by ion irradiation is limited to a few micrometers. Therefore, in the case of ion-irradiated SiC, a measurement of its mechanical properties is not straightforward and thus, advanced evaluation methods are continuously being requested to establish a data base for mechanical property changes of radiation-induced materials.

In this work, indentation tests are proposed for evaluating the mechanical properties of ion-irradiated SiCs. The low-temperature irradiation produced various defects in the SiC such as point defect clusters, dislocation loops and amorphous phases. These various irradiation defects were observed by TEM, which existed as a function of the penetrated ion depth. The amorphous phases and the other defects seem to provide contrary results for the hardness. The changes of the mechanical properties were exhibited with increasing indentation loads. The experimental evaluation by using the indentation techniques was discussed with relation between microstructures and the mechanical properties.

Introduction

Excellent high temperature mechanical properties, chemical stability and low radioactivity under neutron irradiation make silicon carbide (SiC) and SiC-based ceramic composites attractive materials for use in advanced nuclear energy systems. Monolithic SiC produced by a chemical vapour deposition (CVD) method has been considered as a containment material for fuel particles of high temperature gas-cooled reactor (HTGR) and a solid matrix material of fuel blocks for the gas fast reactor (GFR) [1,2]. SiC-based materials in a form of fibre-reinforced composites (SiC/SiC) have been considered as primary structural components in various gas-cooled and liquid metal-cooled blanket concepts of fusion reactors [3]. In addition, SiC/SiC composites are the advanced options for control rod components in very high temperature reactors (VHTR) [2,4] and also considered as a shield fuel pin in some GFR concepts [5].

These concepts of the structural design yield many material issues and the radiation effects of silicon carbide are recognised as one of important research subjects. All the applications mentioned above utilise near-stoichiometric SiC with a high crystallinity and purity due of its excellent irradiation tolerance [6,7]. SiC-based materials have been extensively studied to explore the irradiation-induced property changes such as mechanical properties [8], amorphisation [9], swelling [10], thermal conductivity [11] and microstructural evolution [12] although its irradiation effects are even less clear and not well understood. CVD-SiC under irradiation with a damage dose of 3 dpa could be divided by the three regimes with emphasis on an influence of the irradiation temperature [10]. The large swelling was occurred below the irradiation temperature of 200°C, which was caused by an irradiation-induced amorphisation. The diffused diffraction pattern at the damaged region was a clear evidence of the formation of an amorphous phase. In the irradiation temperature between 200° and 1 200°C, the point defects and clusters were mainly observed as a form of the black dots in TEM image and the swelling was decreased with increasing the irradiation temperature. The irradiation-induced cavities were exhibited above the irradiation temperature of 1 200°C. But the irradiation effects of CVD-SiC at high temperature have not still been clear yet.

In the present work, the grain size effects on the irradiation behaviours of SiC were investigated with four different types of SiC having various grain sizes. One of the convenient approaches for an analysis of the irradiation damage is to use an ion irradiation at low temperature. An ion irradiation has been used as an excellent tool for the simulation study of neutron irradiation because of its good advantages such as simplicity, economical efficiency, capability of high-fluence bombardment, high temperature irradiation, helium co-implantation and target versatility. Meanwhile, an irradiation at low temperature is often used for a preliminary study of radiation effects because of the preservation of irradiation-induced defects due to the low degree of the dynamic recovery. In this work, the Si ions with MeV acceleration energy were irradiated to various SiC materials at room temperature. Then the microstructure and mechanical property were investigated by TEM and nano-indentation, respectively.

Experimental procedure

Four different grades of SiC ceramics were used for the ion irradiation experiment and the characteristics of the materials used in this study are shown in Table 1. Commercial SiC materials labeled as SiC-01 and SiC-02 in Table 1 are the α phase single crystal SiC with 6H structure produced by CREE systems and the β phase polycrystalline SiC with 3C produced by Rohm and Haas Advanced Materials, respectively. The materials labelled as SiC-03 and SiC-04 are the lab-made β phase polycrystalline SiCs with 3-C structures, which were produced by chemical vapour deposition. The samples had different grain sizes with a decreasing order of SiC-01, SiC-02, SiC-03 and SiC-04.

Table 1. Characteristics of the SiC samples used in this study

Sample ID Explanation	SiC-01	SiC-02	SiC-03	SiC-04
Manufacturer	CREE, Inc.	Rohm and Haas, Co.	KAERI	KAERI
Structure	6H (hexagonal)	3C (cubic)	3C (cubic)	3C (cubic)
Fabrication temp.	Sublimation	~1 500°C	1 300°C	1 100°C
Grain size	Single crystal	Large ~30 µm	Medium 0.2-5 µm	Small 0.05-1 µm

The ion beam irradiation was conducted by a high voltage accelerator (a NEC model 5SDH-2, a tandem Van de Graaff) with the condition of 5.1 MeV Si²⁺ ions (1.7 MeV terminal voltage). The accurate temperature increase by the ion beam heating could not be measured. The irradiation temperature of the specimens was in the range of 100 to 200°C, which was estimated by the thermal couple attached on the edge of the specimen stage. The silicon ions were irradiated for the four types of materials simultaneously in order to evaluate the irradiation effects at the completely same conditions. The displacement damage rate was 2.24×10^{-3} dpa/s and the damage dose was 20 dpa at the depth of 1 400 nm along the normal to the entry face of the ion-irradiated specimens. The damage profile was calculated by a SRIM2003 code [13] assuming the average displacement threshold energy of 35 eV, a stoichiometric chemical composition and a mass density of 3.21 g/cm³.

Microstructures of ion-irradiated SiC were investigated by TEM. The Focused Ion Beam (FIB) milling system (Model NOVA200, FEI Co., Netherlands) was used for preparing the samples for the TEM observation. The evaluation of the mechanical property changes before and after ion irradiation was carried out using the nano-indentation tester (NanoTest, Micro Materials Ltd.) and a Berkovich diamond tip. To simulate the effects of a neutron irradiation, the correct evaluation of the hardness and the elastic modulus in ion-irradiated SiC is necessary and it is dependent on the relation between zone of the irradiation damage and the deformation induced by indentation. It has previously been discussed [14] that the cross-sectional TEM observation beneath the residual indentation impression has provided good information to determine the penetration depth of a diamond indenter tip for the effective evaluation of ion-irradiated SiC. In this work, the diamond tip penetrated into ion-irradiated SiC with the maximum depth of 100 nm, where the indenting depth was estimated with considering the factors such as the round shape of diamond tip, the pile-up/sink-in effects and the elastic recovery. The penetration of the diamond tip was likely to make a deformation zone with the depth of 1 000 nm, which was estimated from an empirical TEM observation.

Results

Displacement damage profile and depth distribution of implanted Si ions calculated by SRIM are shown in Figure 1. A peak damage region occurred at a depth of 2.0 µm from the irradiated surface.

Figure 2 shows TEM images of the single crystal SiC (SiC-01) and the small-grain polycrystalline SiC (SiC-04) after the ion irradiation. The diffused diffraction pattern with the diffused spots exhibited in the microstructure of the SiC-01 sample indicates that a large amount of amorphous phase was produced in single crystal SiC. Dislocation loops with less than 20 nm diameter are observed at the damage dose of more than 30 dpa. It is likely that the small clusters appearing as black dot defects develop into dislocation loops as the damage dose increases. On the other hand, the SiC-04 sample shows little difference between the damaged and undamaged regions. The almost same diffraction patterns with crystal spots indicate no amorphisation.

Figure 1. Displacement damage profile and depth distribution of Si ions

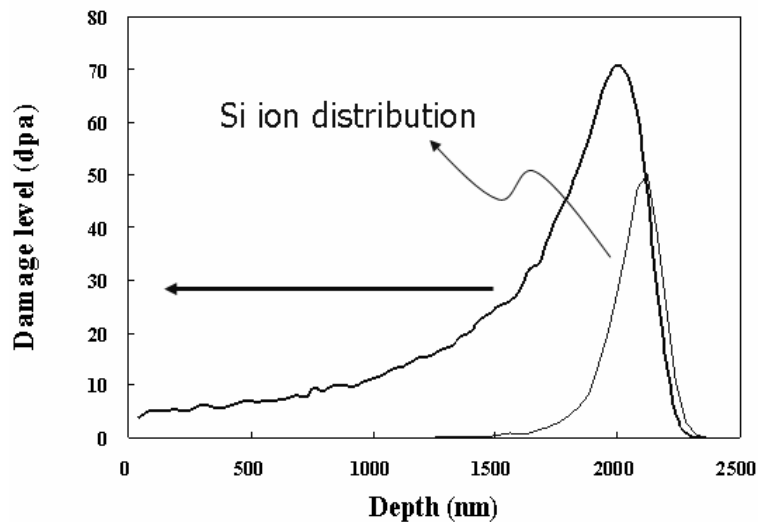


Figure 2. TEM images of the samples (a) SiC-01 and (b) SiC-04 after ion irradiation

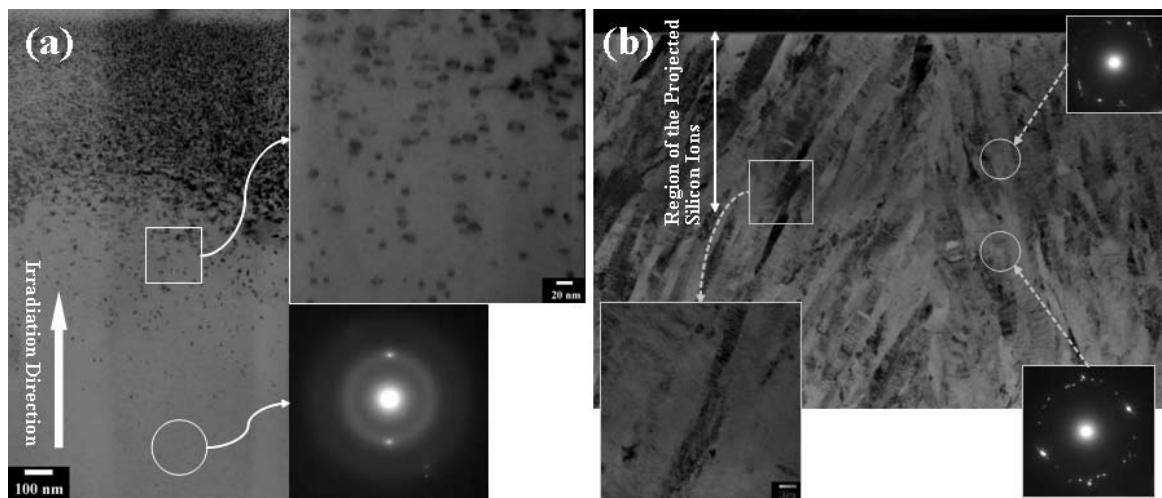


Table 2 summarises the hardness changes for the four types of SiC samples after ion irradiation. The single crystal SiC that was irradiated with 20 dpa experienced a $\sim 1.3\%$ reduction in hardness, whereas the irradiated sample exhibited the large difference resulted in a $\sim 27.3\%$ reduction in elastic modulus. For the SiC-02 sample, the increased hardness and elastic modulus were shown by the ion irradiation, where the averaged values were 30.8 GPa (un-irradiated) to 33.9 GPa (ion-irradiated) in hardness, and 436.2 GPa (un-irradiated) to 494.0 GPa (ion-irradiated) in elastic modulus, respectively. The medium- and small-grain samples made by KAERI exhibited the similar tendency of the mechanical property change before and after the ion irradiation. An increase of the hardness (5.5% increase in SiC-03, and 2.7% increase in SiC-04) and a reduction of the elastic modulus (2.6% reduction in SiC-03, and 1.1% reduction in SiC-04) were revealed after the ion irradiation.

Table 2. Summary of mechanical properties of SiC materials before and after ion irradiation

Properties Materials	Hardness				Elastic modulus			
	Virgin		Irradiated		Virgin		Irradiated	
	Mean	m	Mean	m	Mean	m	Mean	m
SiC-01 (CREE)	31.14	29.83	30.37	16.69	702.56	17.11	400.90	26.99
SiC-02 (R&H)	30.75	31.68	33.88	22.67	436.17	38.57	493.95	16.59
SiC-03 (KAERI)	27.49	16.67	30.68	18.29	378.76	26.99	359.86	24.26
SiC-04 (KAERI)	28.56	14.94	30.16	16.95	374.28	19.11	365.99	39.13

Discussion

The microstructure and the mechanical property were investigated in four types of SiC with different grain sizes to fundamentally understand the irradiation behaviours with emphasis on an effect of the grain size. It is well known that the irradiation temperature is the most important factor on SiC amorphisation. In the case of self-ion (Si) irradiation to SiC, the threshold temperature of amorphisation has been known about 150°C, which was dependent on the acceleration energy of bombarding ions [9]. In this work, the irradiation temperature was selected to be close to the amorphisation threshold temperature of SiC. Evolution of the irradiation-induced amorphous phase and the other defects was expected at this irradiation temperature.

The single crystal SiC showed a good agreement with the previous report on the amorphisation behaviour under the ion irradiation [9]. The hardening could occur by the production of the point defects and clusters, where the defects act as obstacles dislocation movement [6] because of its stress-free structure (SiC-01). On the other hand, the hardness reduction could occur due to the formation of the amorphous phase in SiC, where the amorphisation was observed by selected diffraction pattern [see Figure 2(a)]. It has been reported [15] that the irradiation-induced amorphisation in SiC contributed to the reduction of mechanical properties like hardness and elastic modulus. Two phenomena seemed to occur dynamically in the single crystal SiC under the present ion irradiation condition. Eventually, the hardness of the single crystal SiC exhibited a slight reduction, which seems to be largely affected by the amorphous phase. The elastic modulus was clearly reduced in the single crystal SiC, which is likely due to the amorphisation plus the effect of lattice expansion by the other irradiation-induced defects.

In the case of the SiC sample with coarse grains (SiC-02), increases of hardness and elastic modulus were exhibited after the ion irradiation. For the hardness increment, one of the possible mechanisms is the partial creation of the amorphous phase even though the TEM microstructures of the SiC-02 sample were not shown here. The sample consisted of a mixture of amorphous large grains and crystalline small grains after the ion irradiation. The minus effect for the hardness is expected by an irradiation-induced amorphisation. However, internal stresses between grains have to be considered. One of the possible explanations on the increment of hardness is the internal stress formation between fine and coarse grains by the partial amorphisation of large grains. It is noticeable that the amorphisation is accompanied with a large volumetric expansion [16] and thus the amorphisation of coarse grains may provide the compressive stress to the fine grains, which is contributed to the increase of the hardness as well as the elastic modulus.

Finally, in the case of medium- (SiC-03) and small-grain (SiC-04) SiC samples, the hardness slightly increased and the elastic modulus showed a marginal reduction. Little amorphous phase was observed in the TEM microstructures of these samples [Figure 2(b)]. The point defects and clusters were only observed as irradiation-induced defects. In this case, the hardening effect by point defects

and clusters and the reduction of elastic modulus by the lattice expansion seem to be considered as a mechanism. It has been reported [17,18] that the grain boundary acts as sinks for the radiation-induced point defects. Samaras, *et al.* [17] performed a molecular dynamic (MD) simulation on nano-crystalline Ni and stated that the radiation-induced point defects were removed by the surrounding regions of grain boundary and triple junction of grains at nanometer scale regime. Yoshiie and Kiritani [18] pointed out that the major annihilation sites for point defects are the opposite types of point defects and the permanent or fixed sinks like grain boundaries. They demonstrated that neutral permanent sinks act to change the destination of freely migrating point defects and compensate the unbalanced point defect reactions. The CVD-SiC used in the present study has almost no stress and defect free structure. Thus, the permanent sinks are mainly concern of the present case, where the permanent or fixed sinks include dislocations, stacking faults, grain boundaries and surfaces, etc. As can be seen in these results, the grain boundary and the grain size seem to influence on the defect production and accumulation which change the mechanical properties of SiC under the ion irradiation.

A defect production of SiC under the ion irradiation with MeV acceleration energy was strongly dependent on the grain boundary and grain size, where the fine-grained SiC showed superior irradiation stability than the coarse-grained SiC. However, the relation of irradiation-induced damages, dislocations, stacking faults and grain boundaries is still not clear and it has to be studied further. The irradiation behaviour in this work can give a good criterion for the fabrication of SiC-based materials for the advanced nuclear systems.

Conclusions

Effects of grain size on irradiation induced behaviours of microstructure and mechanical property have been discussed in SiC ceramics with different grain sizes. From the microstructure and mechanical property changes of SiC, it is suggested that the grain boundary and the finer grain size suppress a production of the amorphous phase in SiC. The hardness and the elastic modulus behaviours provided a good estimation on the relations between grain size and irradiation-induced defects. The polycrystalline SiC with fine grains revealed an irradiation stability of microstructure and an improved behaviour of the mechanical properties. To improve the understanding on the effect of grain size (grain boundary) for highly pure and near-stoichiometric SiC, further studies on low temperature irradiations in connection with the behaviours at high temperature irradiations are needed.

Acknowledgements

This work was financially supported by Ministry of Science and Technology (MOST) through the nuclear R&D programme.

REFERENCES

- [1] Nabielek, H., W. Kühnlein, W. Schenk, W. Heit, A. Christ, H. Ragoss, *Nucl. Eng. Des.*, 121, 199 (1990).
- [2] Katoh, Y., N. Hashimoto, S. Kondo, L.L. Snead, A. Kohyama, *J. Nucl. Mater.*, 351, 228 (2006).
- [3] Giancarli, L., H. Golfier, S. Nishio, R. Raffray, C. Wong, R. Yamada, *Fus. Eng. Des.*, 61-62, 307 (2002).
- [4] Windes, W.E., Y. Katoh, L. Snead, C. Henager, *Topical Meeting on Nuclear Fuels and Structural Materials for the Next Generation Nuclear Reactors*, Reno, Nevada, 4-8 June 2006.
- [5] Kohyama, A., T. Hinoki, T. Mizuno, J.S. Park, H. Kishimoto, *Proc. of the International Congress on Advances in Nuclear Power Plants*, p. 351, Reno, Nevada, 4-8 June 2006.
- [6] Osborne, M.C., J.C. Hay, L.L. Snead, D. Steiner, *J. Am. Ceram. Soc.*, 82, 2490 (1999).
- [7] Snead, L.L., Y. Katoh, A. Kohyama, J.L. Bailey, N.L. Vaughn, R.A. Rowden, *J. Nucl. Mater.*, 283-287, 551 (2000).
- [8] Park, K.H., Y. Katoh, H. Kishimoto, A. Kohyama, *J. Nucl. Mater.*, 307-311, 1187 (2002).
- [9] Snead, L.L., S.J. Zinkle, J.C. Hay, M.C. Osborne, *Nucl. Inst. Meth. Phys. Res.*, B 141, 123 (1998).
- [10] Katoh, Y., H. Kishimoto, A. Kohyama, *J. Nucl. Mater.*, 307-311, 1221 (2002).
- [11] Kowbel, W., C.A. Bruce, K.L. Tsou, K. Patel, J.C. Withers, G.E. Youngblood, *J. Nucl. Mater.*, 283-287, 570 (2000).
- [12] Kondo, S., K.H. Park, Y. Katoh, A. Kohyama, *Fus. Sci. Technol.*, 44, 181 (2003).
- [13] Jiegler, J.F., Chap. 7 in *The Stopping and Range of Ions in Solids*, Pergamon Press, New York (1985).
- [14] Park, K.H., S. Ikeda, T. Hinoki, A. Kohyama, *Proceedings of the International Congress on Advances in Nuclear Power Plants*, Paper# 5468, Seoul, Korea, 15-19 May 2005.
- [15] McHargue, C.J., J.M. Williams, *Nucl. Inst. and Meth. Phys. Res.*, B80/81, 889 (1993).
- [16] White, C.W., C.J. McHargue, P.S. Sklad, L.A. Boatner, G.C. Farlow, *Mater. Sci. Reports*, 4, 41 (1989).
- [17] Samaras, M., P.M. Derlet, H. Van Swygenhoven, M. Victoria, *Phys. Rev. Lett.*, 88, 1 (2002).
- [18] Yoshiie, T., M. Kiritani, *J. Nucl. Mater.*, 271-272, 296 (1999).

NEW ASPECTS OF OXYGEN CONTROL IN LBE SYSTEMS

H. Steiner, C. Schroer, Z. Voß, O. Wedemeyer, J. Konys

Forschungszentrum Karlsruhe

Institut für Materialforschung III, P.O. Box 3640, D-76021 Karlsruhe, Germany

Abstract

In recent years, liquid metal alloys have been examined in the light of various applications in technical systems the most famous example is the sodium-cooled fast breeder reactor. One major problem in non-isothermal heavy liquid metal systems lies in the corrosion of their structural components. The formation of oxide scales on the structural components is considered as a viable measure in limiting the dissolution rates in the hot parts in lead and lead-bismuth loops. Hence, one has to develop concepts of oxygen control enabling the formation of oxide scales on the structural components but preventing from the formation of oxides of the liquid metal alloy itself. The oxygen level in the liquid metal must be maintained actively at appropriate levels.

There are thermo-hydraulic limitations on oxygen supply from the liquid metal to the structural material, the oxygen mass transfer coefficient in the liquid metal being rate-determining. This explains, for example, why in the first stage of oxidation of stainless steels slowly growing, dense single layer Fe/Cr spinel scales are formed.

Introduction

Liquid metal alloys have various applications in technical systems the most famous example being the sodium-cooled fast breeder reactor. Recently, lead-bismuth eutectic (LBE) is foreseen as coolant and target for neutron generation in accelerator-driven nuclear systems (ADS) [1,2]. Also, Pb-17Li alloy is considered as a coolant and breeding medium in future fusion reactors [3,4]. The advantage of these liquid metal alloys lies in their high thermal conductivity and their relative safety in case of an accident. But a major problem in non-isothermal liquid metal systems lies in the corrosion of their structural components, consisting mainly of ferritic/martensitic and austenitic stainless steels, as the solubility of structural components in the liquid metal depends in general on the temperature. The formation of oxide scales on the structural components is considered as a viable means in limiting the dissolution rates in the hot parts of the system, as the solubility of the oxides is in general much smaller than that of the metal alloys [5,6].

Oxide scales might not be stable as for example in Pb-17Li alloy, but there may also be a problem in LBE loops at low oxygen concentrations. Hence, the prediction of the oxide scale evolution is of great importance. Also precipitation of oxides at cooler parts of the system can have consequences as there may be clogging and plugging of components having small cross-sections. This may also affect the maintenance and repair of the system as in an accelerator driven nuclear system and in a fusion reactor there will be activation of steel components and there will be transport and deposition of activated material.

Concepts of oxygen control in Pb and Pb-Bi loops had already been developed in Russia some years ago [7,8]. Oxygen control in the loop can only be of practical use if the oxygen solubility in the liquid metal is high enough for oxide scale formation on structural components as is the case for Pb and Pb-Bi alloys [9]. From Pb loops it is also known that there is a critical oxygen level below which no oxide scale is formed and dissolution attack of the metal alloy occurs [8]. In Pb-Li on the other hand oxygen solubility is very low. If a Pb-Li loop is operated with oxide scales on structural materials as protective layers, the uptake of oxygen by the liquid metal due to dissolution effects may eventually constitute a problem. In this paper we are mainly concerned with oxygen control in the CORRIDA loop with lead-bismuth eutectic (LBE) as the coolant material. An oxygen control system requires the continuous measurement of the oxygen activity in the liquid metal [10,11]. It must be assured that no oxides of the liquid metal itself are formed; otherwise the loop can be clogged.

The locations of dissolution and precipitation are mainly determined by the temperature dependence of the solubility of the oxides or of the metal alloys if no oxide scale is present. This means that we have dissolution in the hot parts of the system and precipitation in the cold parts, irrespective of the nature of the dissolution process, whether it is exothermic or endothermic. Depending on the local oxygen concentration at the surface of the structural component there can be duplex scale formation or formation of a single layer Fe/Cr spinel scale with the solubility depending on the nature of the oxide scale. Thus, it is indispensable to calculate the axial profiles of oxygen concentration in the bulk of the fluid and at the surface of the structural components. It is in general not sufficient to use only the value of oxygen activity level given by the oxygen control system.

In two previous papers [12,13] information on a recently developed computer code (MATLIM) for the calculation of iron mass transfer in a liquid metal loop was given. The code is meant to deal with multi-modular liquid metal loops as are the two loops operated at FZK, namely PICOLO and CORRIDA (see Ref. [14]). In this report focus is laid on the modelling aspects of oxygen behaviour and oxide scale formation and growth. We are going to discuss the implementation of the respective models in the recently developed computer code MATLIM in more detail.

Oxygen mass balance

We are not going to derive (exact) solutions for the oxygen concentration in the loop as has been tried in Ref. [15], but we will describe oxygen behaviour with the help of two characteristic values, namely c_o^b and c_o^w . The parameter c_o^b represents the mean value of the oxygen concentration over the cross-section of the coolant channel at an axial position x and the parameter c_o^w the oxygen concentration at the channel walls. Under turbulent flow conditions the oxygen distribution in the coolant channel is rather flat except in a very thin boundary layer of a few microns as the Schmidt-number is in the order of 10^3 . In this case the mean oxygen concentration is very near to the oxygen concentration in the bulk of the fluid. The two characteristic values of oxygen concentration in the liquid metal are linked by the oxygen mass transfer coefficient. This parameter can be calculated with the help of empirical correlations, depending on the oxygen diffusion coefficient and thermo-hydraulic parameters (see also Ref. [16]). In this way we have a sound experimental basis for our model.

Approximating the velocity profile in the cross-section of the coolant channel by the mean velocity of the fluid u_{fl} (the so-called flow velocity) one can derive simple differential equations for the mean values of the solute concentrations (see Refs. [12-14]). In the meantime we have also included in these differential equations the effect of (oxide) particles in the liquid metal. Thus, the mass balance for the oxygen in the bulk of the fluid c_o^b reads as follows:

$$\frac{\partial c_o^b(t, x)}{\partial t} + u_{fl} \cdot \frac{\partial c_o^b(t, x)}{\partial x} = \frac{U_{ch}}{A_{ch}} \cdot j_o^w(t, x) + n_p \cdot A_p \cdot j_o^p \quad (1)$$

where n_p is particle density, A_p is particle surface area, t is time, x is axial position, $j_o^{w,p}$ is oxygen mass flux to the wall and the particles, U_{ch} is circumference and A_{ch} is the cross-section of the flow channel

Except for a relatively short period after the start of the operation of the loop and for special circumstances like a very fast change of the oxygen activity given by the oxygen control system and may be oxide scale spalling, the partial time derivative of c_o^b can be neglected. In the following we will apply Eq. (1) only for quasi-stationary conditions, meaning under conditions slowly varying with time.

Particles in an oversaturated solution can only grow in a stable way by atomic or molecular deposition if the particle radius is above a certain critical limit. Particles below the critical radius are dissolved even in an oversaturated solution. But such particles could, of course, grow by coagulation.

We have not included in Eq. (1) a term for the time variation of the particle density n_p as we are for the time being not in a position to describe the relevant processes like spalling of oxide scales, coagulation and trapping of particles, etc. in a quantitative way. Thus, the iron mass equivalent contained in particles, their shape (spherical or cylindrical) and the particle radius must be specified by the user of the code. The oxygen mass flux to the channel walls j_o^w and to the particles in the fluid j_o^p are linked to the respective iron mass flux.

We have also assumed that the channel walls are oxidised. Therefore the mass flux due to oxidation itself j_{ox} appears in Eq. (4). If a parabolic law for oxide scale growth is given then we have:

$$j_{ox} = \frac{k_{ox.m.}(T)}{\delta_{ox}} \quad (2)$$

where $k_{ox.m.}(T)$ is the mass related oxidation rate constant, δ_{ox} the oxide scale thickness and T is temperature.

Oxygen content at the surface of structures

Knowing the oxygen content in the bulk of the fluid c_o^b , the oxygen content at the channel wall c_o^w can be calculated with the help of the following equation:

$$j_o^w = \bar{K}_o \cdot (c_o^w - c_o^b) \quad (3)$$

The mass transfer coefficient \bar{K}_o for oxygen can be calculated in the same way as that for iron (see Refs. [13,16], we have only to replace the iron diffusion coefficient in LBE by the respective diffusion coefficient for oxygen. For this we have taken the correlation for the oxygen diffusion coefficient in LBE given in Ref. [17]:

$$D_o^{LBE}(T) = 10^{-0.813-3612./T} \text{ in cm}^2/\text{s} \quad (4)$$

Evolution of oxide scale thickness

The change of the oxide scale thickness in a time increment Δt is given by:

$$\Delta \delta_{ox}(t) = \left(\frac{K(T, c_0)}{2 \cdot \delta_{ox}(t)} + b \right) \cdot \Delta t \quad (5)$$

where b is the dissolution/precipitation rate of the oxide in cm/s.

Consequences of thermo-hydraulic limitations on the oxygen supply to structural materials

The oxygen needed for the growth of the oxide scale is supplied by the liquid metal. The main parameter for this is the oxygen mass transfer coefficient. This mass transfer coefficient is determined by the thermo-hydraulic conditions in the loop. Besides, there may be contributions to the oxygen flux coming from dissolution or precipitation of oxide. Upon dissolution of oxide oxygen is released into the coolant channel and upon precipitation oxygen is consumed. Thus, the balance equation for oxygen mass flux needed for oxide scale growth is as follows:

$$\bar{K}_o \cdot (c_o^b - c_o^w) + j_o^{diss/precip} = j_{ox} \cdot f_{ox}^O \quad (6)$$

$$j_o^{diss} > 0 \quad j_o^{precip} < 0 \quad (7)$$

where $j_o^{diss/precip}$ is the oxygen mass flux due to dissolution/precipitation of iron oxides and f_{ox}^O is the mass ratio oxygen/oxide.

Eq. (6) can be considered under two point of views, namely one can ask what level of oxygen concentration in the bulk of the fluid one must have if one wants to adjust to a certain value of oxygen concentration at the surface of the structural material, or one can ask whether for a certain value of oxygen concentration in the bulk has a physical solution at all under the assumed mode of oxidation.

One must understand that the oxygen diffusion coefficient in liquid metals is about six orders of magnitude lower than in gas atmospheres. Also, one should note that it is a technical goal to operate LBE loops at rather low levels of oxygen concentrations (0.005-0.01 wppm). This has certain consequences for the oxide scales to form.

The oxygen mass transfer coefficient is especially low under laminar flow conditions and it might be of some interest to compare for this flow regime the situation in a gas atmosphere (steam + oxygen for example) to the situation in an LBE loop like CORRIDA. We have derived from the work of Fuller, *et al.* [18] the following correlation for the diffusion coefficient of oxygen in steam:

$$D_{H_2O,O_2}(T, p) = 1.251E - 5 \cdot \frac{T^{1.75}}{p} \quad (8)$$

where p is the total gas pressure in bar .

The oxygen diffusion coefficient in LBE can be calculated with the help of the respective correlation given in Ref. [17]. Under laminar flow conditions the Sherwood number in a fully circular cross-section is 3.66. Neglecting for this case dissolution and precipitation effects we have calculated the oxygen concentration difference in the coolant channel to supply the oxygen mass flux in case of an oxide scale on AISI316 of 1 μm thickness if the oxygen concentration at the surface is at 0.01 wppm. The relevant values are to be found in Table 1.

Table 1. Comparison of thermo-physical values relevant for oxidation of structural material

	Gas atmosphere H ₂ O+O ₂	LBE
Temperature (K)	823	823
Oxygen diff. coeff. (cm ² /s)	1.582	6.28 E-6
Ox. mass tr. coeff. (cm/s)	7.24	2.87 E-5
$c_o^b - c_o^{surf}$ (wppm)	1.6 E-6	0.42

In order to be definite we have used for the calculations an empirical correlation for the oxidation rate constant of AISI316, although it is doubtful, whether it can be applied for such thin oxide scales. Thus, the oxygen concentration difference is much higher in an LBE loop than under gas atmosphere. A value of 0.42 wppm can certainly not be neglected. For turbulent flow and a mass transfer coefficient of 0.0175 cm/s (a value typical for turbulent flow in the test section of CORRIDA) we obtain of course a much lower value for the oxygen difference, namely about $0.7 \cdot 10^{-3}$ wppm. The oxygen concentration difference depends mainly on the flow regime and on the oxide scale thickness and certainly on the structural features in the oxide scale (density, grain size, etc). In a situation with precipitation taking place the problem with the oxygen difference in the coolant channel would be even more acute, as precipitation consumes oxygen. Thus, except for rather high oxygen activities in LBE we think that one has in the low temperature part of the CORRIDA loop only precipitation of oxide on the channel walls and no additional proper oxidation of the structural material. This conclusion could probably be checked by respective examinations.

Results of calculations with the code MATLIM

The code MATLIM allows a 1-D simulation of multi-modular loops. The relevant differential equations are solved with the help of finite difference techniques by dividing each module into a certain number of axial meshes. In the actual version of the code a mesh length of 1 cm is used

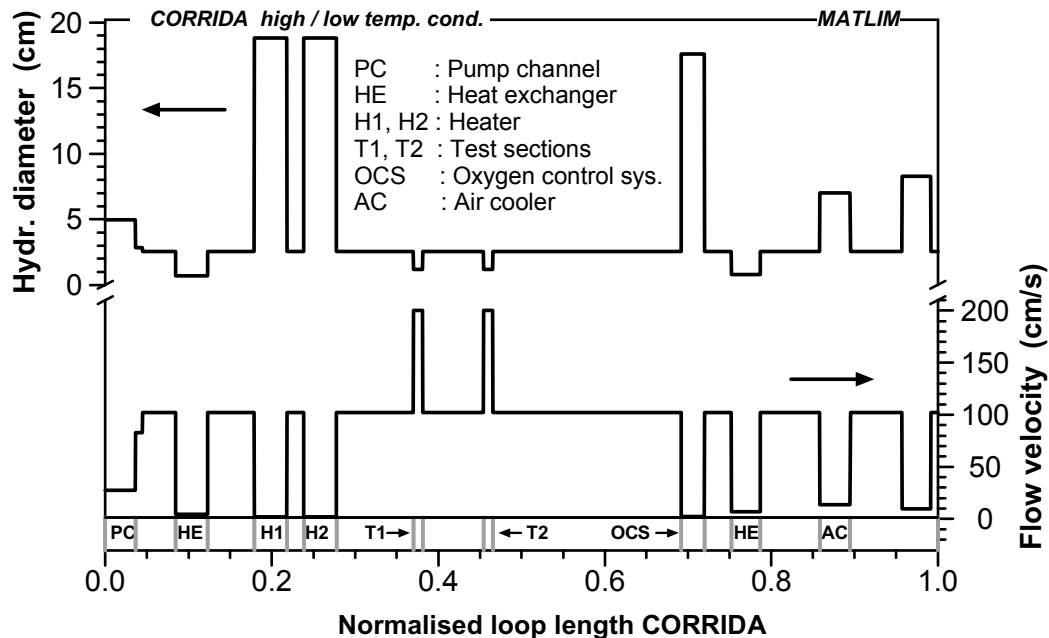
allowing integer mesh numbers for all modules of the loop. Specific values for the relevant parameters can be assigned for each axial mesh. Calculations were done for the CORRIDA loop, which is operated with LBE as a coolant [12-14,19]. The main characteristics of this loop are described in Ref. [19]. The loop contains among other modules two test-section and an oxygen control system. The oxygen control system consists of a tank, which is located downstream of the test-sections. The liquid metal flows through the tank together with an oxygen-containing gas stream.

There are mainly three different types of physical properties and parameters, which determine material behaviour in a liquid metal system. The first group concerns the thermo-hydraulic data of the system like the flow velocity and the hydraulic diameter but also the temperature distribution along the system. The second group concerns material data like viscosity of the liquid metal, diffusivity and solubility of the solutes. The third group encompasses properties of the structural material itself like oxidation rates.

For the calculations we have assumed that the structural material and the specimens in the test-sections consist of AISI316 and we have covered an operation period of 1 000 h. For the oxygen concentration supplied by the oxygen control system we have taken three different values, namely 0.05, 0.001 and 0.005 wpm in order to investigate the response of the loop as simulated by the MATLIM code. For all the calculations we have assumed duplex scale formation on the structural material. Thus, only magnetite will be dissolved and precipitated.

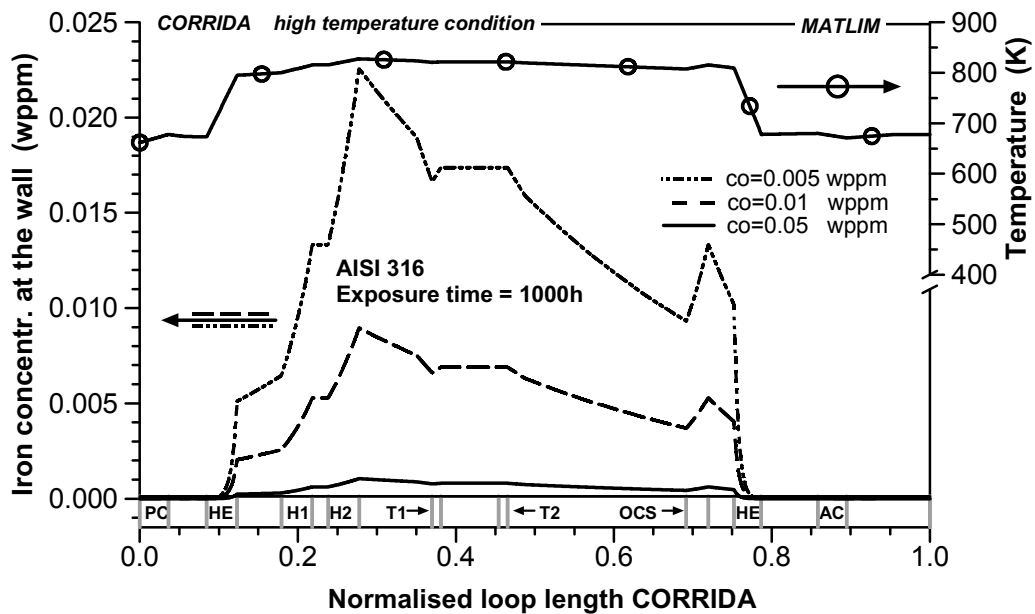
The single most important thermo-hydraulic parameter is the mass transfer coefficient for the solutes of interest. In our case it is that for oxygen. The mass transfer coefficient depends on the temperature and on hydraulic parameters like the flow velocity and the hydraulic diameter (see also Ref. [16]). Information on this can be found in Figure 1. This gives also some evidence about the simulation of the CORRIDA loop features with its different modules within the frame of the MATLIM code. The flow velocity in the test-sections, for example, comprises 2 m/s.

Figure 1. Axial profiles of the hydraulic diameter and of the flow velocity for the CORRIDA loop



Up to now the CORRIDA loop was operated in a low and in a high temperature mode with nominal values of 380 and 550°C in the test-sections respectively. In this report we are only concerned with the high temperature mode. The relevant temperature distribution is to be found in Figure 2. In this figure one can also find axial profiles for the iron concentration at the channel walls for the three values of oxygen concentration. As a consequence of the solubility product over magnetite we find that the lower the oxygen concentration the higher is the iron content dissolved in the liquid metal. For the calculation of the respective iron mass flux we have assumed an iron diffusion coefficient of $1 \cdot 10^{-6} \text{ cm}^2/\text{s}$ (see also Refs. [12-14]).

Figure 2. Axial profiles of temperature and iron concentration at the channel walls dissolved in the liquid metal for three values of the oxygen control system



Information on the oxygen concentration profiles along the loop (bulk and surface) as well as on dissolution/precipitation rates can be found in Figure 3 and on the oxide scale in Figure 4. For an input value for the oxygen level of 0.05 wppm the dissolution rates are rather low and can be neglected, but they increase with decreasing oxygen concentration. Dissolution/precipitation rates depend among others on the iron diffusion coefficient and on the solubility product over magnetite. For the time being we have no experimental data on dissolution rates of magnetite, only some hints from post test examinations that there might be an effect [19]. In case of single layer Fe/Cr scales the dissolution rates would be much lower than for magnetite decreasing with increasing Cr content. This is a consequence of the free enthalpy of formation of Fe/Cr spinels.

The mean oxygen concentration in the bulk of the liquid does not vary very much along the loop. For an input value of 0.05 wppm the variation is nearly imperceptible in the scale generated by the plot routine. It should be noted that the situation shown in Figures 3 and 4 is for time equal 1 000 h, where oxidation is no longer progressing very fast. For the two lower input values (0.01 and 0.005 wppm) the oxygen concentration at the surface is in the high temperature leg of the loop higher than that in the bulk of the liquid metal. This is due to oxygen release by dissolution of magnetite. The low values of oxygen concentration at the surface of the structures in the cold leg of the loop are a consequence of magnetite precipitation in this axial zone. The oxide scales in the cold leg of the loop are entirely due to precipitation. Thus, the lower the oxygen input value by the oxygen control system the higher is the mass transfer from the hot leg to the cold leg.

Figure 3. Axial distributions of dissolution/precipitation rates and oxygen concentration in the bulk of the fluid (c_o^b) and at the channel wall (c_o^w) (0.05 wppm for the oxygen control system)

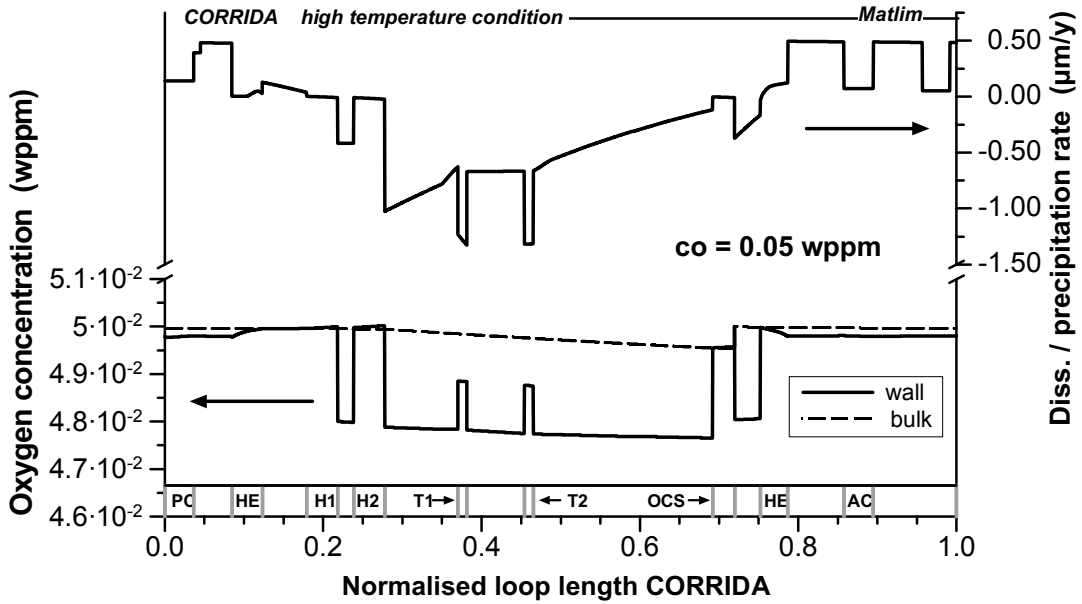
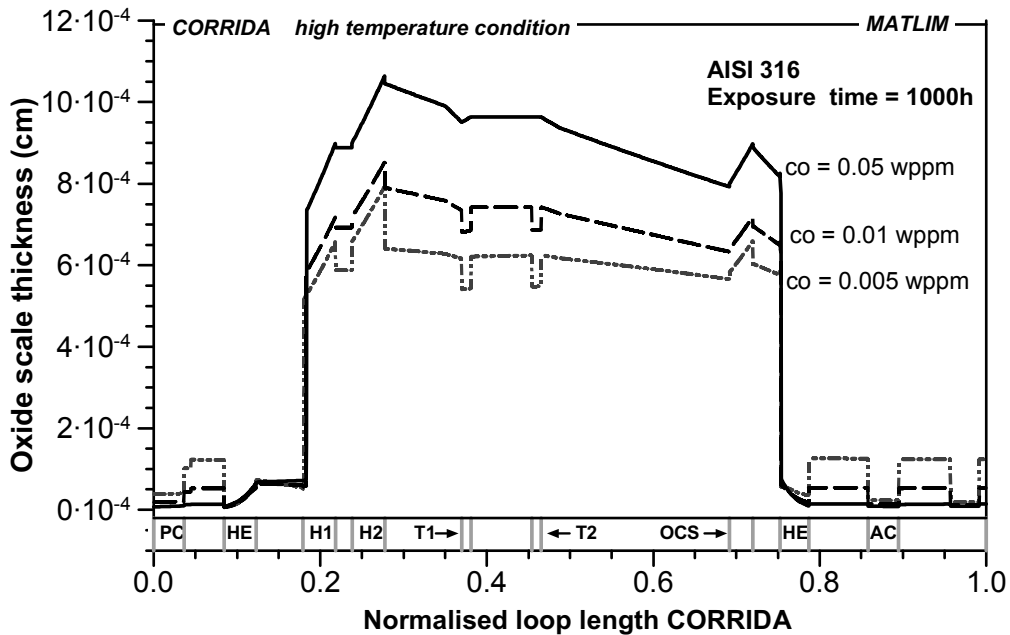


Figure 4. Axial distributions of the oxide scale thickness for AISI316 structural material after 1 000 h of operation in the CORRIDA loop for three input values of oxygen content



Conclusions

Oxygen control in liquid lead and lead-bismuth loops is of great importance as the formation of protective oxide scales must under all circumstances be assured. Otherwise, severe dissolution attack of structural components is to be expected. There are certain thermo-hydraulic limitations of oxygen supply towards the structural materials. This point has not been fully recognised in the past. The mode

of oxidation of stainless steels (single layer Fe/Cr spinel or duplex scales) does not only depend on the level of the oxygen supply system but may also be influenced by thermo-hydraulic parameters and also by the characteristics of the loop. Our analysis suggests that for moderately high values of oxygen concentration the first stage of oxidation is with slowly growing dense single layer scales. The length of this first stage should then depend on the level of oxygen content in the loop.

A main assumption of this work is that oxidation correlations gained from tests under gas atmosphere can also be used in liquid metals if they are in a suitable form with temperature and oxygen partial pressure as parameters. Oxide scale thickness in liquid metals under forced convection flow is then due to the combined effect of oxidation and of dissolution/precipitation mechanisms. Dissolution should increase with lower oxygen content in the liquid metal and it is presumably considerably higher for magnetite than for Fe/Cr spinel scales. Evolution of oxide scales can be calculated with the recently developed computer code MATLIM, which performs a 1-D simulation of heavy liquid metal loops like CORRIDA. From the oxidation rate constants of stainless steels one can deduce with the help of Wagner's theory empirical diffusion coefficients of iron and oxygen through the oxide scales.

REFERENCES

- [1] Carminati, F., R. Klapisch, J.P. Revol, Ch. Roche, J.A. Rubio, C. Rubbia, CERN/AT/93-47(ET) (1993).
- [2] Rubbia, C., J. Rubio, S. Buono, F. Carminati, N. Fietier, J. Galvez, C. Geles, Y. Kadi, R. Klapisch, P. Mandrillon, J.P. Revol, Ch. Roche, CERN/AT/95-44(ET) (1995).
- [3] Casini, G., J. Sannir, *Jour. Nucl. Mat.*, 179-181, 47-52 (1991).
- [4] Konys, J., W. Krauss, Z. Voss, O. Wedemeyer, *Journ. Nucl. Mat.*, 329-333, 1379-1383 (2004).
- [5] Asher, R.C., D. Davies, S.A. Beetham, *Corr. Science*, 17, 545-551 (1977).
- [6] Müller, G., FZKA report 6422 (2000).
- [7] Gromov, B.F., Yu.L. Orlov, P.N. Martynov, K.D. Ivanov, V.A. Gulevski, "Physical-chemical Principles of Lead-bismuth Coolant Technology", in *Liquid Metal Systems*, H.U. Borgstedt, G. Frees (Eds.), Plenum Press (1995), p. 339.
- [8] Markov, V., "Corrosion of Structural Materials in PbBi and Pb", *Seminar on the Concept of Lead-cooled Fast Reactor*, Cadarache (1997).
- [9] Müller, G., G. Schumacher, F. Zimmermann, *Journ. Nucl. Mat.*, 278, 85-95 (2000).
- [10] Konys, J., H. Muscher, Z. Voss, O. Wedemeyer, *Journ. Nucl. Mat.*, 296, 289-294 (2001).
- [11] Muscher, H., J. Konys, Z. Voss, O. Wedemeyer, FZKA report 6690 (2001).

- [12] Malkow, T., H. Steiner, H. Muscher, J. Konys, *Journ. Nucl. Mat.*, 335, 199 (2004).
- [13] Steiner, H., J. Konys, *Journ. Nucl. Mat.*, 338, 18-25 (2006).
- [14] Steiner, H., J. Konys, FZKA report 7212 (2006).
- [15] He, X., N. Li, M. Mineev, *J. Nucl. Mater.*, 297, 214-219 (2001).
- [16] Balbaud-Celerier, F., F. Barbier, *Journ. Nucl. Mat.*, 289, 227-242 (2001).
- [17] Ganesan, R., T. Gnanasekaran, Raman S. Srinivasa, *Journ. Nucl. Mat.*, 349, 133-149 (2005).
- [18] Fuller, E.N., P.D. Schettler, J.C. Giddings, *Ind. Eng. Chem.*, 58, 19 (1966).
- [19] Schroer, C., Z. Voß, O. Wedemeyer, J. Novotny, J. Konys, *Journ. Nucl. Mat.*, 356, 189-197 (2006).

CORROSION BEHAVIOUR OF STAINLESS STEELS IN LEAD-BISMUTH EUTECTIC AND LEAD EXISTING EXPERIENCE AND NEEDS

L. Soler Crespo, F.J. Martín Muñoz, D. Gómez Briceño

Centro de Investigaciones Energéticas, Medioambientales y Tecnológicas (CIEMAT), España

Abstract

Lead (Pb) or lead-bismuth eutectic (LBE) were proposed as coolant and/or spallation target for accelerator-driven systems (ADS). The understanding and mitigation of corrosion of structural material in LBE and Pb are essential issues for the demonstration of technical feasibility of ADS and, therefore, several EU projects have dedicated an important effort to study this subject. Within TECLA project (5FP) important knowledge was gained on the comprehension of basic corrosion phenomena and a first screening on several steels in LBE was carried out. The results obtained showed that for tests conducted both in stagnant and in flowing LBE/Pb, most stainless steels form oxides that are protective below 500-550°C, specially for an oxygen concentration above 10^{-6} wt.%, for short- to medium-term applications. Within the DEMETRA domain of the EUROTRANS project (6FP), the evolution of long term corrosion kinetics in flowing LBE/Pb for T91 and 316L steels, chosen as candidate structural materials for ADS, is being studied.

It is possible to transfer some aspect of this know-how to future Gen-IV lead-cooled fast reactor (LFR) system. However, LFR will operate, in its long-term option, at temperatures up to 800°C and will be refrigerated by pure lead and the use of new materials will be mandatory. Within VELLA projects (6FP), some preliminary tests are being carried out in Pb on new materials with a better high temperature resistance. However, several issues remain still open regarding materials performance at high temperatures in molten lead.

This paper will give an overview on the existing data on the corrosion behaviour of stainless steels in LBE/Pb and on the identification of the possible transfer of knowledge and of different research issues still needed to expand the database in Pb at high temperature.

Introduction

Lead (Pb) or lead-bismuth eutectic (LBE) have been proposed as coolant and/or spallation target for accelerator-driven systems (ADS) [1] and as coolant for lead-cooled fast reactor (LFR) system, one of the options considered within Generation IV initiative [2]. However, Pb and LBE show a high aggressiveness for conventional structural materials. The main constitutive elements of stainless steels (Ni, Cr, Fe) show a high solubility in the liquid metal that prevents their use as structural materials without any protection at high temperatures. With an adequate control of the oxygen concentration in the liquid metal, the formation of oxide films on the surface of the structural materials occurs, limiting further dissolution. For the optimum effectiveness, the oxygen concentration in the liquid metal has to be adequate to passivate the material but not sufficiently high to promote the precipitation of lead oxide. For Fe containing alloys, such as structural steels, the minimum oxygen concentration is defined by the magnetite (Fe_3O_4) decomposition potential, considering this oxide the less stable of the ones that can be formed on structural steels. The maximum value is fixed by the precipitation of lead oxide. After the formation of oxide films, the dissolution of the structural materials becomes negligible due to the low diffusion rate of the alloying elements of steels in the oxides [3].

The understanding and mitigation of corrosion of structural materials in LBE and Pb are, therefore essential issues for the demonstration of technical feasibility of ADS and LFR. In addition, the availability of technologies that allow for safe operation of lead alloy facilities is also essential. Several European projects have dedicated an important effort to study the compatibility of structural materials, mainly stainless steels, with lead-bismuth eutectic and lead, dealing with the corrosion mechanism and rate.

Background

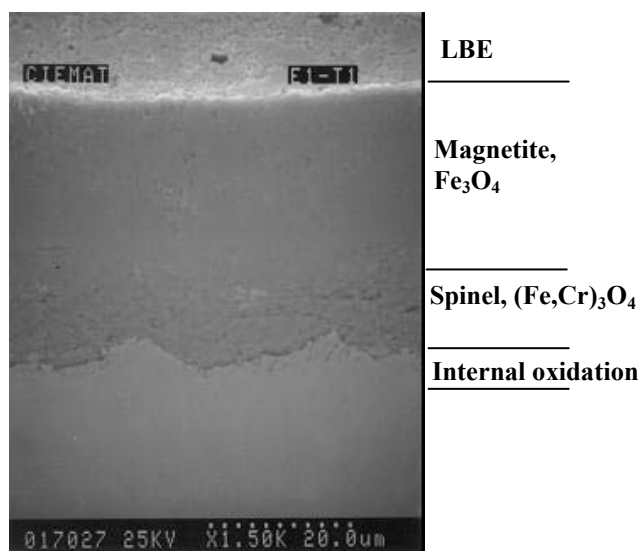
Within TECLA project (TEChnologies, materials and thermal-hydraulics for Lead Alloys, 5th Framework Programme of the EU) important knowledge was gained on the comprehension of basic corrosion phenomena and a first screening on several steels was achieved. Tests were conducted to evaluate the behaviour of several stainless steels in contact with LBE at high temperature in order to pre-select the most promising ones. The importance of several parameters involved in the corrosion process as materials composition, temperature, temperature gradient, time, oxygen activity, impurities, etc., was also evaluated. Besides, the viability of protection by means of the *in situ* formation of an oxide layer on the steel surfaces was studied using the control and measurement of the oxygen activity in the liquid metal, with special attention to the use of oxygen sensors.

The temperature range explored was between 450 and 600°C, with oxygen contents in the liquid metal from saturation to 10^{-8} wt.% and times from 100 to 3 000 hours on a wide variety of steels [4,5]. The main results point out that the protection method by the *in situ* oxide layer formation on the steel surface is feasible. However, there is a threshold temperature over which the steel protection is not perfectly effective [6]. This temperature depends on the oxygen concentration in the liquid metal, the material composition and time.

The influence of chromium content is evident both under oxidant and reductive environments. Under oxidant conditions, steels with lower chromium content showed thicker oxide layer [7]. The austenitic steels presented thinner and more adherent oxide layers. For oxygen concentrations lower than 10^{-6} wt.%, however, dissolution takes place in most of the steels, especially austenitic steels, due to the high solubility of nickel in LBE/Pb. For tests temperatures higher than 550°C, the formation and protectiveness of oxides is uncertain, and protection usually fails due to dissolution for long times.

Similar compositions of the oxide layers formed in LBE and Pb experiments have been described by several authors. In general, the steels show a double oxide layer formed by an outer layer with a composition comparable to that of magnetite and an inner layer where Cr content is higher than in the material bulk. The composition of this inner layer correspond to $\text{Fe}(\text{Fe}_{1-x}\text{Cr}_x)_2\text{O}_4$. Figure 1 shows the general morphology of an oxide scale formed on T91 steel tested in LBE at 600°C for 3 000 hours under oxidant conditions. The acceptable limit for oxide layer thickness would be around 20 μm .

Figure 1. General morphology of an oxide scale on T91 steel

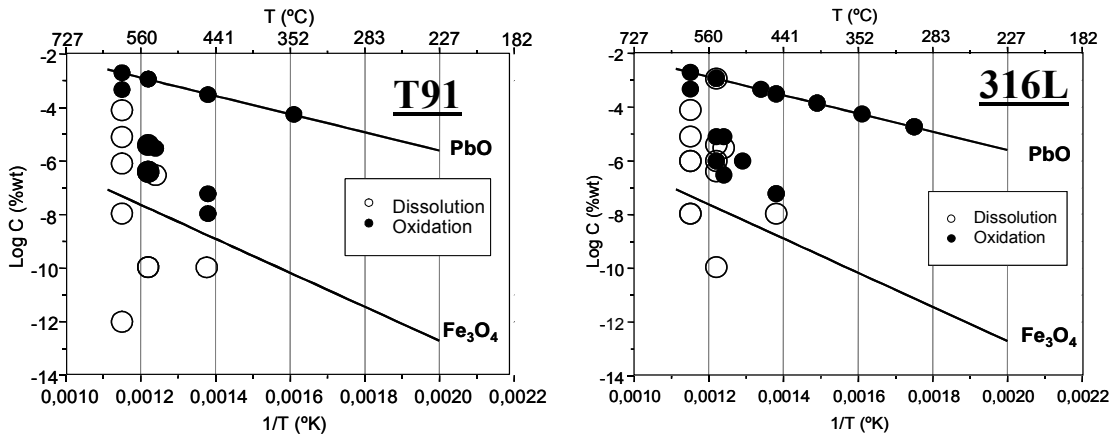


The OECD/NEA Working Group on LBE technologies in the frame of the Working Party of Fuel Cycle (WPFC) has elaborated a handbook entitled *Lead-bismuth eutectic*, in which Chapter 6, “Compatibility of structural materials with LBE and Pb: standardisation of data” includes the existing data on corrosion of steels in contact with LBE and Pb until the year 2005 [8]. Corrosion tests of a variety of materials under wide ranging conditions were carried out in both stagnant and flowing LBE/Pb. The steels tested include Fe-Cr steels, with chromium contents from 1.2 to 16.24 wt.% and austenitic steels. The test temperatures range from 300 to 650°C, times from 100 to 10 000 hours and oxygen concentration in LBE/Pb from 10^{-12} wt.% to saturation. For tests conducted both in stagnant and in dynamic (flowing) LBE/Pb within the oxygen control band, most Fe-Cr and Fe-Cr-Ni steels form oxides that are protective below temperatures in the range 500-550°C, specially for an oxygen concentration above 10^{-6} wt.% for short- to medium-term applications.

Figure 2 shows the graphics for the martensitic steel T91 and the austenitic steel AISI 316L tested in LBE in stagnant conditions. In these graphics, the line of formation of magnetite and the saturation line (PbO formation) are indicated. Even though these graphics are semi-quantitative, they are very useful to determine the temperature and oxygen concentration areas for which the protection by oxide layer formation is feasible. In all the cases, below the magnetite formation line dissolution takes place. There is also dissolution at 600°C and below 10^{-6} wt.% oxygen concentration.

Under flowing conditions, there were few data and the maximum temperature tested was 470°C, and it was not possible to get any conclusions. For steels tested in lead, there were spare data both under stagnant and flowing conditions. Thus, much more experiments in these conditions should be conducted in the future in order to assure an adequate system design.

Figure 2. Corrosion behaviour of T91 and 316L steels in LBE under oxygen control in stagnant conditions



Current activities

The activities carried out have improved the heavy liquid metal (HLM) scientific/technological knowledge and the main results obtained were a good approach to the study of the compatibility of structural materials with LBE/Pb. However, there are still some basic aspects that need to be covered to provide with a complete database for the design of a prototype. To this end, additional data is required in the following areas:

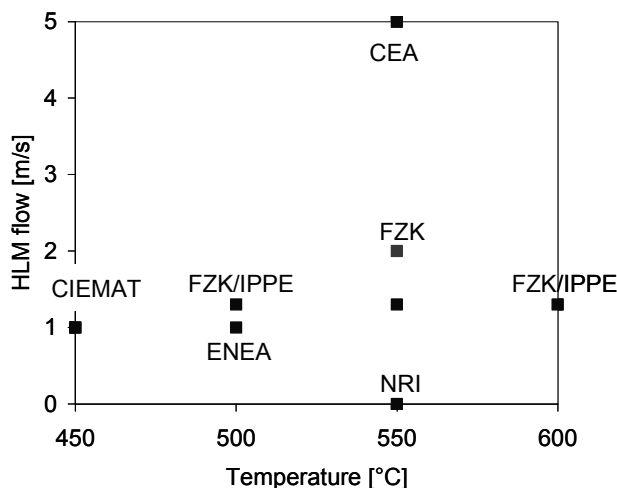
- Long-term tests (15 000 hours) in dynamic conditions to confirm the actual oxygen-temperature areas, especially for T91 and 316L steels to support the design of future systems in which these steels have been chosen as reference.
- Influence of several parameters (surface state of steels, stresses, welding, etc.) on the corrosion response of steels to improve the knowledge about the dissolution/oxidation process and to support models and mechanisms.
- Tests in stagnant and flowing lead to expand the database in Pb at high temperature
- For high temperature systems (above 550°C), development and testing of advanced materials will be also needed.

Within the EUROTRANS (EUROpean TRANsmutation) project, the DEMETRA domain (DEvelopment and assessment of structural materials and heavy liquid METal technology for TRANsmutation systems, 6th Framework Programme of the EU) is devoted to the development and evaluation of the necessary technology for the use of materials and HLM for transmutation systems. The selected reference structural materials are the 9Cr martensitic steel T91 for the components highly stressed (claddings, wrapper tubes, etc) and the austenitic steel AISI 316L for vessel and in-vessel component materials.

From the corrosion point of view, the main objective of the project is the assessment of the long-term behaviour of the reference steels in flowing liquid metal. Tests are being carried out in several forced convection loops of large dimensions cooled by LBE with an oxygen concentration of 10⁻⁶wt.%, which cover a wide range of temperatures: CORRIDA (FZK) loop will operate at 550°C, LINCE (CIEMAT) at 450°C and CU2 (IPPE/FZK) at 500, 550 and 600°C. LECOR (ENEA) loop will

operate at 450°C in LBE with an oxygen concentration of 10^{-10} - 10^{-8} wt.%. CHEOPE III (ENEA) loop will operate at 500°C in Pb with an oxygen concentration of 10^{-6} wt.%. Besides, some experiments are being conducted under not normal conditions, e.g. high flow rates in CICLAD loop (CEA) and fluctuations in oxygen content and temperature in COLONRI (NRI). Figure 3 shows the test matrix for the long-term assessment of the reference materials in HLM [9]. A detailed description of the experimental facilities is given in Chapter 12, “Existing HLM facilities for experimental applications”, of the *Lead-bismuth technology* handbook [10].

Figure 3. Test matrix for the long-term assessment of the reference materials in HLM



Besides, modelling activities are being carried out to predict the long-term behaviour of reference materials and to help to the definition of a corrosion kinetic model. The development and testing of high temperature surface barriers, as GESA method, for high heat loaded elements (e.g. fuel claddings) are also under investigation. In addition, the influence of some metallurgical parameters (surface finishing, welding, stresses) on corrosion/protection processes is also being studied.

Some results have been obtained in the forced convection loops after 2 000 hours of operation. T91 and 316L were tested in flowing LBE (2 m/s) in CORRIDA loop at 550°C and 10^{-6} wt.% oxygen content. An oxide layer was formed but no magnetite was detected. T91 cladding tubes were tested in CU2 loop at IPPE at 550°C, 10^{-6} wt.% oxygen content and different flow velocities from 1 to 3 m/s. For the lowest flow rate (1 m/s) the normal oxide scale, with magnetite at the outer side, is observed. However, the samples tested at 3 m/s do not show any magnetite. T91 and 316L steel samples were tested in LECOR loop at 450°C and 10^{-10} - 10^{-8} wt.% oxygen content. Both steels show liquid metal penetration, stronger for T91 steel. Some experiments have been also carried out in Pb. T91 and 316L steels were tested in CHEOPE III loop at 500°C and 10^{-6} wt.% oxygen content. Both steels show oxidation. Test on the influence of the surface finishing on the corrosion/protection process have finished, showing a no significant influence [11].

Integrated Infrastructure Initiative VELLA (Virtual European Lead Laboratory, 6th Framework Programme of the EU) has as main objective to homogenise the European research area in the field of lead technologies for nuclear applications in order to produce a common platform of work. It is articulated in Networking Activities (NA), Transnational Access Activities (TA) and Joint Research Activities (JRA). Within JRA, some tests are being performed in stagnant lead on materials with a better high temperature resistance. Within NA, the development of guidelines for relevant issues for future HLM systems (e.g. materials corrosion tests) is being conducted.

Another current European Project related with lead technology is ELSY (European Lead-cooled System), which aims to demonstrate that it is possible to design a competitive and safe fast power reactor using simple technical engineered features. The general objective of the ELSY project is to design an innovative lead-cooled fast reactor complemented by an analytical effort to assess the existing knowledge base in the field of lead-alloy coolants (i.e. lead-bismuth eutectic (LBE) and also lead/lithium) in order to extrapolate this knowledge base to pure lead. This analysis effort will be complemented with some limited R&D activities to acquire missing or confirmatory information about fundamental topics for ELSY.

Future needs

Generation IV Initiative aims to develop and demonstrate advanced nuclear energy systems that meet future needs for safe, sustainable, environmentally responsible, economical, proliferation-resistant and physically secure energy. Six nuclear systems were selected, being one of them lead-cooled fast reactor (LFR) system. The LFR features a fast-neutron-spectrum Pb or LBE liquid-metal-cooled reactor with a closed fuel cycle. The LFR is cooled by natural convection with a reactor outlet coolant temperature of 550°C, possibly ranging to 800°C with advanced materials. The higher temperature enables the production of hydrogen by thermochemical processes.

The assessment of the effect that high temperature and interactions with molten HLM have on the properties of potential materials for LFR has been initiated in several FP6 projects. As mentioned above, EUROTRANS-DEMETERA domain focuses on compatibility of T91 and 316L steels, candidate materials for ADS, with LBE. And VELLA and ELSY projects are dedicating an important effort to lead technologies. It is possible to transfer some aspect of this know-how to future Gen-IV lead-cooled fast reactor (LFR) system. However, several issues remain still open regarding materials performance at high temperatures in molten lead.

LFR will operate, in its long term option, at temperatures up to 800°C and will be refrigerated by pure lead. These high temperatures require the use of new materials with a better high-temperature resistance. Oxide Dispersion Strengthened (ODS) steels are well known to have good corrosion resistance at high temperature oxidant media due to their ability to develop adherent compact oxide scales at their surface. However, it is necessary to gain experience on the use of ODS steels in lead at high temperature. In VELLA project, some preliminary tests are being carried out commercial ODS steels in lead at temperatures up to 700°C. But, it is necessary to complete the database in terms of materials, covering a wide range of ODS, and conditions.

REFERENCES

- [1] Rubbia, C., J.A. Rubio, S. Buono, F. Carminati, *Conceptual Design of a Fast Neutron Operated High Power Energy Amplifier*, CERN/AT/95-44 (ET), 29 September 1995.
- [2] *Gen IV Technology Roadmap*, GIF-002-00, December 2002.
- [3] Gromov, B.F., *et al.*, *Nucl. Eng. Design*, 173, p. 207 (1997).

- [4] Benamati, G., C. Fazio, H. Piankova, A. Rusanov, “Temperature Effect on the Corrosion Mechanism of Austenitic and Martensitic Steels in Lead-bismuth”, *Journal of Nuclear Materials*, 301, p. 23 (2002).
- [5] Müller, G., A. Heinzl, J. Konys, G. Schumacher, A. Weisenburger, F. Zimmermann, V. Engelko, A. Rusanov, V. Markov, “Behavior of Steels in Flowing Liquid PbBi Eutectic Alloy at 420-600°C After 4000-7200 h”, *Journal of Nuclear Materials*, 335, p. 163 (2004).
- [6] Gómez-Briceño, D., L. Soler, F.J. Martín Muñoz, F. Hernández, “Influence of Temperature in the Oxidation-corrosion of F82Hmod. Martensitic Steel in Lead-bismuth”, *Journal of Nuclear Materials*, 303, 137-146 (2002).
- [7] Soler, L., F.J. Martín, F. Hernández, D. Gómez-Briceño, “Corrosion of Stainless Steels in Lead-bismuth Eutectic Up to 600°C”, *Journal of Nuclear Materials*, 335, pp. 174-179 (2004).
- [8] Soler, L., F.J. Martín Muñoz, D. Gómez-Briceño, “Compatibility of Structural Materials with LBE and Pb: Standardization of Data, Corrosion Mechanism and Rate”, Chapter 6 of the Handbook *Lead-bismuth eutectic*, of the OECD/NEA Working Group on LBE Technologies, WPFC, forthcoming.
- [9] Fazio, C., A. Al Mazouzi, F. Groeschel, J. Henry, F. Roelofs, L. Soler, P. Turrone, “Development and Assessment of Structural Materials and Heavy Liquid Metal Technology for Transmutation Systems (DEMETRA) Within EUROTRANS”, *Actinide and Fission Product Partitioning & Transmutation*, 9th Information Exchange Meeting, Nîmes, France, Sept. 2006.
- [10] Fazio, C. “Existing HLM Facilities for Experimental Applications”, Chapter 12 of the Handbook *Lead-bismuth eutectic*, of the OECD/NEA Working Group on LBE Technologies, WPFC, forthcoming.
- [11] Second year DEMETRA technical review meeting, FZK, Karlsruhe, Germany, March 2007.

THE LEAD AND LBE CORROSION RESEARCH AT KAERI

Tae Yung Song, Chung Ho Cho, Choon Ho Cho and Eung Ho Kim
Korea Atomic Energy Research Institute, Korea

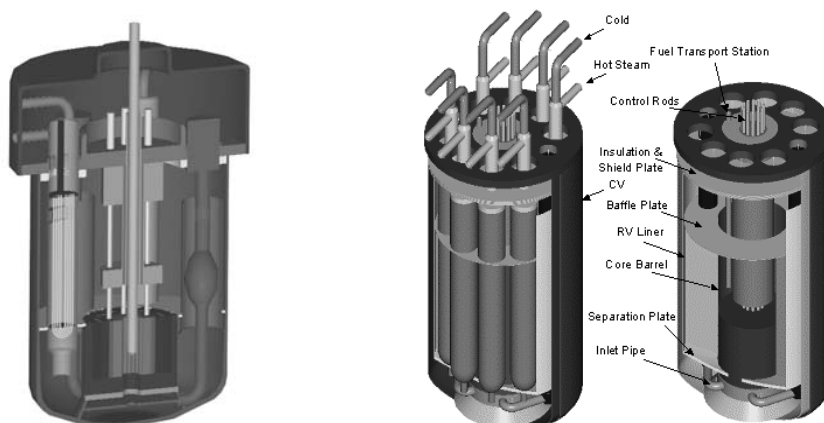
Abstract

KAERI has been developing the facilities needed to study the corrosion of lead-alloy. KAERI fabricated a static corrosion test facility in 2003. The static corrosion tests of HT-9, 316L and T91 have been performed at 600°C and 650°C since 2003. KAERI completed the construction of Pb-Bi corrosion test loop, KPAL-I (KAERI Pb-Alloy Loop I) and the first stage of Pb corrosion test loop, KPAL-II (KAERI Pb-Alloy Loop II) in 2006. The Pb-Bi loop is an isothermal loop. Although the Pb loop is designed to be operated with $\Delta T = 150^\circ\text{C}$ ($T_{\min} = 450^\circ\text{C}$ and $T_{\max} = 600^\circ\text{C}$), it is operated as an isothermal loop since only the first stage of the loop construction was completed in 2006. We will complete the second stage of the Pb loop construction in the near future. The corrosion tests were performed using KPAL-I and KPAL-II. The tested samples were 316L, T91 and HT-9 which are candidate materials for the reactor structure, a beam window of an ADS and the fuel cladding respectively. The tests were performed at temperature of 570°C. The flow velocities were measured by electromagnetic flow meter (EMF). The samples were tested up to the maximum of 450 hrs and analysed by using SEM.

Introduction

Korea Atomic Energy Research Institute (KAERI) has been developing an accelerator-driven system (ADS) and a lead-cooled fast reactor (LFR). Pb-Bi and Pb are adopted as the coolant/target and coolant materials for the ADS and LFR respectively. Most serious problem in using lead-alloy is a corrosion of the steel structure materials in contact with the high temperature lead-alloy. Therefore, we should establish the methods of preventing a corrosion. If we cannot establish an appropriate method to prevent a corrosion, the design parameters of the reactor systems should be modified so that the maximum temperature decreases. The accelerator-driven transmutation system developed by KAERI is called HYbrid Power Extraction Reactor (HYPER) [1]. HYPER can reduce plutonium, minor actinides and environmentally hazardous fission products from the nuclear waste coming from a conventional nuclear power plant. In addition, it can be used to produce electricity. HYPER is designed to transmute TRU and fission products such as ^{99}Tc and ^{129}I . Figure 1 shows the outline of HYPER.

Figure 1. The outline of HYPER (left) and the LFR (right) developed by KAERI



HYPER uses Pb-Bi as the coolant and target material which is not separated. The inlet temperature of Pb-Bi is designed to be 340°C for HYPER. The average outlet temperature is 490°C . The maximum temperature exists at the cladding surface, which is about 570°C . The candidate cladding materials are 12Cr steels such as HT-9. We considered 9Cr steels such as T91 as the candidate beam window materials. The maximum temperature of the beam window in contact with Pb-Bi is designed not to exceed 500°C . In the case of the beam window, the Pb-Bi corrosion effect can be combined with the radiation damage to produce more severe damage.

Pb is adopted as the coolant in the case of the LFR developed by KAERI [2]. The inlet and average outlet temperature of the liquid Pb coolant are 420°C and 540°C respectively. The maximum temperature exists at the cladding surface, which is about 620°C . The candidate cladding material is HT-9. We set the maximum temperature of the LFR higher than that of HYPER since Pb-Bi is more corrosive than Pb. The general structure material can be 316L for both the HYPER and LFR system.

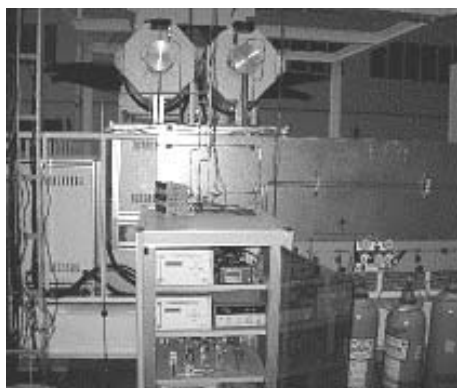
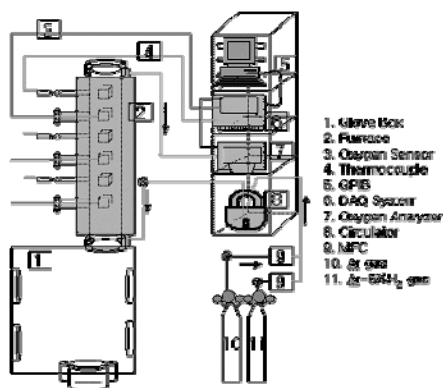
We need to investigate the corrosion behaviour of the structure materials such as HT-9, T91 and 316L at a high temperature. We also need to find methods to prevent a corrosion if it is too severe. One method is to form a stable oxide layer on the material through an oxygen control in lead-alloy [3]. Another one is to modify the material compositions or the surface of the material. KAERI constructed three corrosion test facilities for the corrosion study. They are a static test facility, a Pb-Bi loop and a Pb loop. The lead-alloy loop is named KAERI Pb-Alloy Loop (KPAL). The Pb-Bi and Pb loops are named KPAL-I and KPAL-II respectively.

Corrosion test facilities

Static corrosion test facility

Figure 2 shows the static corrosion facility installed at KAERI. It is mainly composed of tube furnaces, a gas system and a glove box. The furnace is a three-zone type. There are two furnaces which are connected to the glove box. The rail and tray inside the quartz tube make it possible to control the movement. Six Al_2O_3 crucibles are located inside the tube. Each crucible was designed to hold a maximum of four samples. To improve the reliability of the accurate data, three sensors to measure the oxygen concentration and three thermocouples are implemented. The oxygen control system is installed to investigate the effect of the oxide layer on a corrosion resistance. Oxygen control is performed by flowing Ar/H_2 gas mixed with H_2O vapour. When a reduced atmosphere is needed, $\text{Ar}5\%\text{H}_2$ gas is forced to flow. When a certain oxygen content is required, the pressure ratio between H_2O and H_2 is controlled. The gas concentration of the furnace is monitored at the inlet and outlet. The static corrosion test facility can also be used as a facility to calibrate the YSZ oxygen sensor which is used to measure the oxygen content inside lead-alloy.

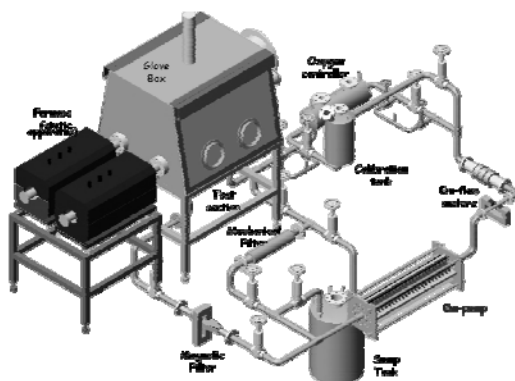
Figure 2. The static corrosion facility of KAERI



Pb-Bi corrosion loop (KPAL-I)

Figure 3 shows the Pb-Bi corrosion loop which was installed at KAERI. The LBE loop is an isothermal loop. The flow velocity in the test section was designed to be around 2m/s and the charging volume of the LBE is around 0.03 m^3 in the circulation loop. The temperature can be up to 600°C .

Figure 3. The Pb-Bi loop KPAL-I



The LBE loop is mainly composed of a main test loop, bypass loop for filtering LBE and a mixture-gas supplying system. The liquid metal in the main test loop circulates in the following order: electromagnetic pump (EMP) – EM flow meter – oxygen controller – test section – magnetic filter – EM pump. Major specifications of the KAERI's loop are summarised in Table 1.

Table 1. Major specification of LBE corrosion loop

Temperature	Max. 600°C
Pb-Bi volume	0.08 m ³
Test-section	3/4 inch SUS 316, $V_{\text{mean}} = 2 \text{ m/s}$ (at 45 lpm)
Piping system	1.5 inch-Schedule 40, SUS316 pipe
Flow measurement	EM flow meters
Pumping	EM-pump (60 lpm – 4 bar – 40 kVA)
Oxygen control	H ₂ /H ₂ O
Purification	Magnetic filter, mechanical filter

The LBE is circulated with an electromagnetic pump (60 lpm – 4 bar – 40 kVA), which is a kind of annular linear induction pump and it was designed by an equivalent electric-circuit method. By considering the uncertainty, the pump head was conservatively determined as 4bar under a maximum flow rate to overcome the pressure loss of the LBE flow.

The flow rate is measured with electromagnetic flow meters based on Faraday's induction law. Several types of electromagnetic flow meters will be serially installed to investigate the effects such as a contact impedance due to a wall oxidation and others. The performance of every EM flow meter can be calibrated with a calibration tank in the loop.

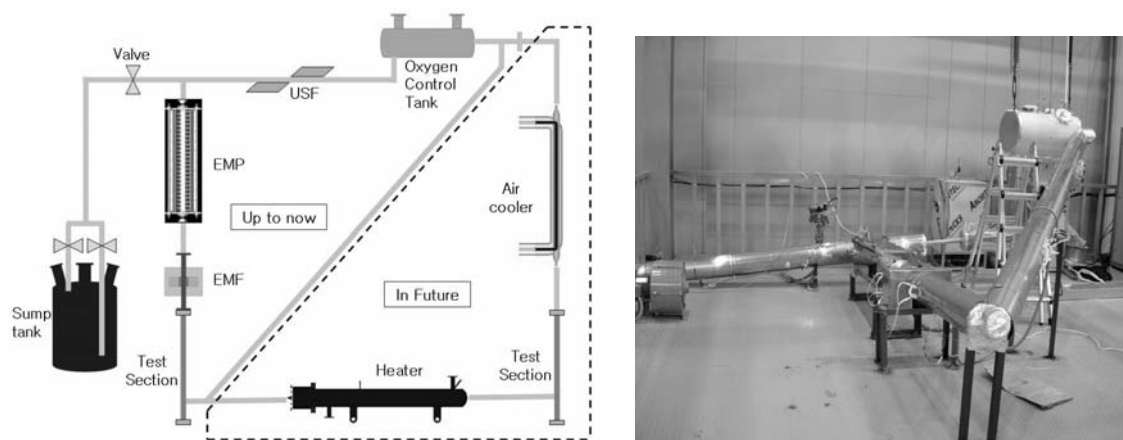
A total of 0.08 m³ of LBE is stored in the sump tank before charging it into the test loop. Most parts of the piping system are made of stainless steel pipe with 1.5 inch in inner diameter (SUS316, 1.5-inch schedule 40) and they are connected by a welding for the prevention of a leakage of the LBE. The oxygen concentration is controlled by the chemical equilibrium between the mixture gas of hydrogen-argon and the water vapour. The oxygen concentration in the LBE and mixture gas is measured with an oxygen sensor made of a yttria-stabilised zirconia.

Test samples are installed in the test-section with an annular cross-section. In order to treat the test samples in a regulated oxygen environment, the upper part of the test-section is installed inside the glove box. The test-section is made of a seamless pipe (SUS316, 3/4 inch schedule 40). Most LBE flows in the test-section have to be turbulent due to a high density. Test samples are mounted from a distance of 15~20 D_h (hydraulic diameter of test section). In fact, the distance of the entrance zone is longer than this distance. However, we determined the distance to be as small as possible by considering the pressure drop, the static head and the height of set-up space.

Pb corrosion loop (KPAL-II)

KAERI's Pb-Bi loop is an isothermal loop, but the Pb loop is designed to have ΔT . It is designed to be operated with a flexible ΔT , ΔT_{hot} and ΔT_{cold} . Figure 4 is the Pb corrosion test loop. The Pb loop consists of an EMP, flow meter, heater, cooler and an oxygen control system. EMP and EM flow meter will have the same configuration as the ones used for the Pb-Bi loop. A calibration tank and dedicated bypass were installed for the EM flow meter of the Pb-Bi loop, but an ultrasonic flow meter will be used for the calibration of the EM flow meter of the Pb loop. The ultrasonic flow meter will be located in the cold part of the loop since the flow meter can be operated under a limited temperature. EMP is also installed at the cold part of the loop to reduce the heat load.

Figure 4. The Pb corrosion test loop KPAL-II



Oxygen control system is also the same as that of the Pb-Bi loop and the static test facility, where H_2 and H_2O vapour are used for a control of the oxygen concentration. There are two test sections, one in the cold part and the other in the hot part. The lowest temperature of the cold part is $450^\circ C$ and the highest temperature of the hot part is $600^\circ C$. ΔT can be 50, 100 and $150^\circ C$. Thus, many combinations of the cold-hot temperatures are possible such as $450-500^\circ C$, $450-550^\circ C$, $450-600^\circ C$, $500-550^\circ C$, $500-600^\circ C$ and $550-600^\circ C$.

It is hard to form hot parts when the temperature of the hot part is $600^\circ C$. The loop will be operated under an oxygen control so that the materials used for the loop can also be protected by an oxide layer. It is known that the oxide layer can be formed and protect materials somewhat successfully up to a temperature of about $550^\circ C$, but oxygen control alone may not be good enough for a protection above $550^\circ C$. In that case, we need to choose hot part material which shows a better corrosion resistance to Pb without an oxide layer and replace the material periodically. KAERI is surveying such materials. Table 2 shows the main loop parameters such as the pressure drop, velocity, flow rate, etc., in the case that the hot and cold part temperatures are 550 and $450^\circ C$ respectively.

Table 2. Major specification of Pb corrosion test loop

Temperature of hot part	550°C
ΔT (hot – cold)	100°C
System pressure	0.4 MPa
Maximum flow rate	20 litre/min
Maximum velocity at test section	3.4 m/s
Heater and cooler power	45 KW
Number of test sections	2 ea
Volume of Pb in the corrosion loop	55 litre
Total pressure drop (normal operation)	0.2 MPa
Flow rate (normal operation)	12 litre/min
Velocity at the test section	2.03 m/s

Although the Pb loop is designed to be operated with ΔT , it is operated as an isothermal loop since only the first stage of the loop construction was completed in 2006. We will complete the second stage of the Pb loop construction in the near future.

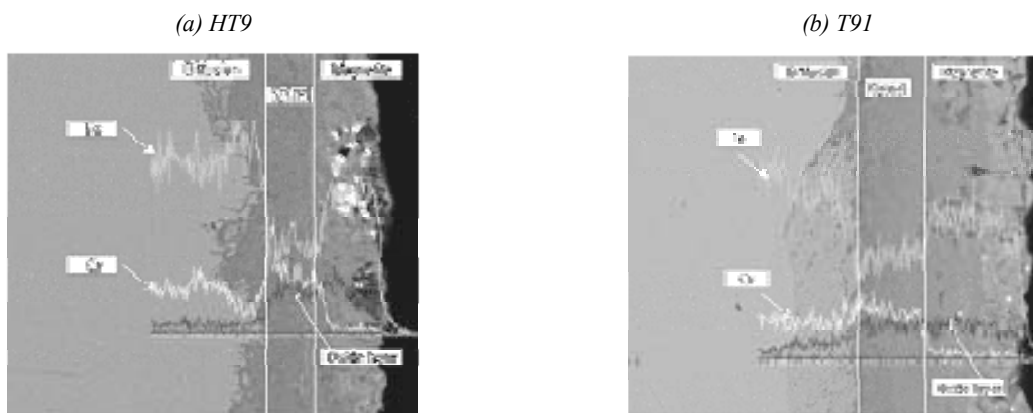
Operation of test facilities

Corrosion test using static test facility

The static test facility has been operated since 2003. It was used to study the corrosion behaviour of steel structure materials. The corrosion tests were performed at 600°C and 650°C. The test materials were 316L and some ferrite/martensitic steels such as HT9, T91. The dimensions of the samples were 10 mm × 18 mm × 2 mm. The samples were annealed at 1 050°C for 1 hour and a heat treatment was implemented at 750°C for 2 hours except for 316L. The tests were performed under both reduced and oxygen-controlled atmospheres. The oxygen concentration was controlled by adjusting the H₂ and H₂O vapour ratio. The oxygen concentration of the oxygen controlled cases were about 10⁻⁶ wt%. The H₂O pressure was set to be 15.94 mbr. Ar gas was forced to flow with the rate of 100 ml/min and the corresponding rate of the Ar-5%H₂ gas was also forced to flow. The exposure time was 200-1 500 hrs. We also tested the corrosion resistance of the surface-treated samples. Al coating and N ion implantation were adopted for the surface treatment. Nitrogen ion implantation was considered to improve the chemical and mechanical property of a material surface. Nitrogen ion implantation was performed by using the 100 keV ion beam accelerator. The acceleration voltage of 75 keV and beam current of 0.8 mA were employed for the investigation. The specimens were implanted at a dose of 1 × 10¹⁷ ions/cm².

The results show that the oxygen control method does not work well at 650°C since the oxide layer was not formed successfully. In the case of the 600°C tests, the oxide layer was formed well when the lead-alloy was Pb. Al coating and N ion implantation turned out to be effective for preventing a corrosion for both Pb and Pb-Bi at 600°C.

Figure 5. Samples exposed to Pb under oxygen content of 10⁻⁶ wt% at 600°C for 500 hours



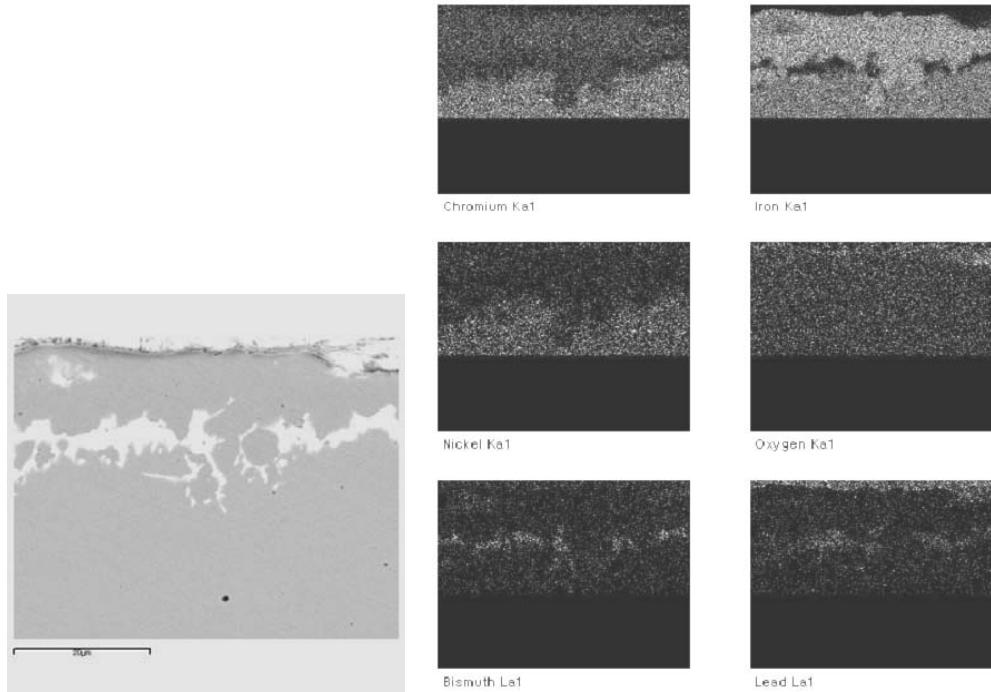
Corrosion test using Pb-Bi loop (KPAL-I)

A corrosion test was performed by using KAERI's Pb-Bi loop KPAL-I. The test temperature and time were 570°C and 300 hours respectively. The test samples were 316L, T91 and HT-9. Oxygen was controlled by mixing Ar, Ar5%H₂ and H₂O vapour.

A YSZ oxygen sensor was not used for this test. Therefore, the oxygen content in Pb-Bi was just estimated based on the flow rates of Ar, Ar5%H₂ and H₂O vapour. The estimated oxygen content was 10⁻⁶ wt%. The velocity of Pb-Bi flow was measured by electromagnetic flow meter (EMF). Since the calibration of EMF showed some uncertainty, the flow velocity was measured to be in the range of 1.1-1.8 m/s.

SEM/EDX analysis was performed after the test was finished. The results show that oxide layer was formed on the small part of the T91 and HT-9 surface. The oxide layer was not formed in case of 316L. Therefore, a corrosion attack happened in 316L. Figure 6 shows the results of 316L. As shown in Figure 6, Cr and Ni were depleted and Fe was partially depleted. Pb and Bi penetrated into region where Fe, Cr and Ni were depleted.

Figure 6. The 570°C Pb-Bi test result of 316L



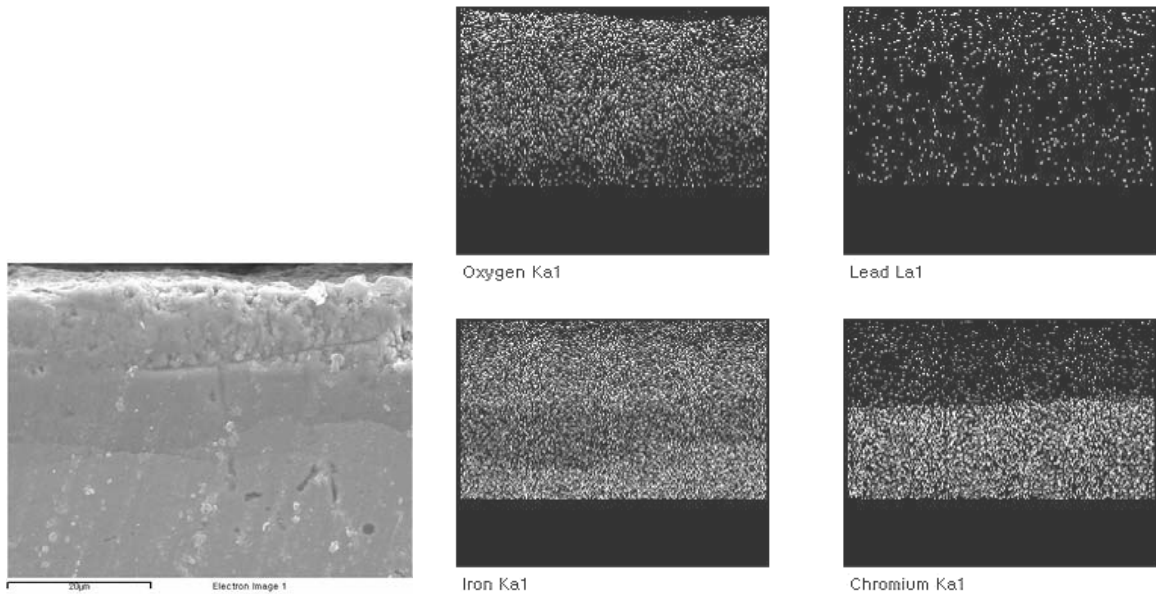
Corrosion test using Pb loop (KPAL-II)

The Pb corrosion test was also performed by using KPAL-II. The test temperature was the same as the Pb-Bi test, which is 570°C. But the test period was 450 hours which was longer than the Pb-Bi test. The test samples were 316L, T91 and HT-9. Oxygen was controlled by mixing Ar, Ar5%H₂ and H₂O vapour. The oxygen content was also estimated based on the flow rates of Ar, Ar5%H₂ and H₂O vapour. The estimated oxygen content was 10⁻⁶ wt%. The flow velocity was measured to be in the range of 0.8-4.8 m/s.

The corrosion test loop was heated up to 450°C inside sump tank. The liquid lead was filled into the loop from the sump tank by pressurising the argon cover gas in the sump tank. The pressure of the sump tank was 3.3 bar. Then Pb was heated to 570°C.

SEM/EDX results show that firm oxide layers were formed on the surface of T91 and HT-9. Figure 7 is the result of HT-9. The oxide layer of HT-9 consists of two different layers. The upper layer is Fe₃O₄ layer and the lower one is Cr spinel layer. In case of 316L, no oxide layer was observed by SEM analysis, but no corrosion attack was observed unlike Pb-Bi test.

Figure 7. The 570°C Pb test result of HT-9



Summary

KAERI has been developing an accelerator-driven system (ADS) and a lead-cooled fast reactor (LFR). Pb-Bi and Pb are adopted as the coolant/target and coolant materials for the ADS and LFR. The most serious problem in using lead-alloy is a corrosion of the steel structure materials in contact with a high temperature lead-alloy. KAERI has been developing three facilities needed to study the corrosion of lead-alloy. KAERI fabricated a static corrosion test facility in 2003. The static corrosion tests of HT-9, 316L and T91 have been performed at 600°C and 650°C since 2003. The static test facility can also be used for calibrating YSZ oxygen sensors. The construction of Pb-Bi loop (KPAL-I) and the first phase of Pb loop (KPAL-II) were finished in 2006. The rest of the KPAL-II will be constructed in the near future. KPAL-I and KPAL-II were operated for the corrosion tests of steel structure materials.

Acknowledgement

The authors gratefully acknowledge the financial support of The Korean Ministry of Science and Technology.

REFERENCES

- [1] Park, W.S., *et al.*, *Development of Nuclear Transmutation Technology*, KAERI Report KAERI/RR-1702/96 (1996).
- [2] Kim, Y., *et al.*, “A Proliferation Resistant Lead Cooled Reactor for Transmutation of TRU and FP”, *Proceedings of Korean Nuclear Society Conference*, Kyung-Ju, Korea, May 2004.
- [3] Orlov, Y.I., *et al.*, “The Problems of Technology of the Heavy Liquid Metal Coolants (Lead-bismuth, Lead),” *Proc. of the Heavy Liquid Metal Coolants in Nuclear Technology*, Obninsk (1998).

PERFORMANCE OF OXYGEN SENSOR AND CORROSION OF SURFACE-COATED STEELS, CERAMICS AND REFRACTORY METALS IN HIGH TEMPERATURE LBE

Minoru Takahashi¹, Abu Rivai Khalid², Tomoki Kumagai²

¹Research Laboratory for Nuclear Reactors, Tokyo Institute of Technology, Japan

²Department of Nuclear Engineering, Tokyo Institute of Technology, Japan

Abstract

Characteristics of zirconia solid electrolyte oxygen sensor with a reference electrode of oxygen saturated bismuth were investigated for measuring oxygen concentration in molten lead and lead-bismuth eutectic (LBE, 45%Pb-55%Bi). An alumina test pot was used for the test to avoid the effect of metallic impurities on the performance. Lead and LBE temperature ranged in 350-700°C. Oxygen potential in the melt was controlled in the range of 1×10^{-5} - 5×10^{-9} wt.%. The measured electromotive forces (EMF) in lead and LBE agreed well with theoretical ones above certain temperatures. Under the active control of oxygen concentration, Al-Fe-coated steel, refractory metals and silicon carbide were immersed in LBE at 700°C in the alumina test pot for 1 000 hours. After the immersion, a thin and stable protection layer of aluminium oxide was formed on the Al-Fe-alloy-coated steels and the coated surface layer still remained on the base specimen without penetration of LBE into matrix of specimen. No penetration of LBE into the refractory metals of W and Mo was observed with no appreciable weight changes after the immersion, although the penetration of LBE into Nb was observed. No penetration of LBE into silicon carbide (SiC) and titanium silicon carbide (Ti₃SiC₂) was observed with no appreciable weight changes.

Introduction

Lead and lead-bismuth eutectic (44.5%Pb-55.5%Bi, LBE) have been one of the candidates of coolants of the fast reactors and the spallation target of the accelerator driven system (ADS) [1-3]. Key issues for the utilisation of the lead alloys in the nuclear systems are the developments of oxygen control technique in the lead alloys, and the compatibility of cladding, structural and window materials with the lead alloys. For the monitoring of the oxygen concentration in the oxygen control, it is necessary to develop oxygen sensors.

Solid electrolyte sensors are made of magnesia-stabilised zirconia and yttria-stabilised zirconia. If steel is employed for test vessel and gas injection nozzle, hydrogen and impurities of iron oxide [4,5] are formed in the melts because of chemical reaction between steel and oxygen. Crespo, *et al.* [6] performed short-term static corrosion tests in LBE in porcelain crucible with gas injection using an austenitic steel tube and ceramic tube. Colominas, *et al.* [7] investigated the performance of oxygen sensors with In/In₂O₃ reference electrode in stagnant LBE using ceramic crucible with cover gas of N₂+5%H₂ and air at 300-500°C. More oxygen sensor tests in lead and LBE may be necessary using inert device such as ceramic crucible and tube.

Corrosion behaviour of the high chromium steels in flowing LBE at 550°C was reported [8,9]. A stable spinel layer of chromium oxide was formed on the high chromium steels. Thin and compact oxide layer could protect the steel from corrosion. There have been reported corrosion characteristics for surface-treated steels, refractory metals and ceramics. Aluminium alloying into the surface by surface melting with pulsed electron beam improved corrosion resistance in a stagnant lead at 550°C [10] and a flowing LBE at 550°C [11]. Refractory metals exhibited two orders of magnitude higher corrosion resistance than steels in a flowing LBE at 400°C [12]. In a stirred pool of LBE at 450°C, refractory metal of Mo exhibited more corrosion resistance than 12Cr steel [13]. SiC and Si₃N₄, showed good corrosion resistance in the liquid LBE flow with negligibly small weight loss, but showed cracked surfaces in flowing LBE at 550°C [14]. SiC and Si₃N₄ exhibited superior corrosion resistance with weight loss about 2-order less than those of 12% Cr steels, e.g. HCM12A, in the stirred pool of LBE at 450°C [13]. Investigations on corrosion behaviour of the materials in lead alloy at temperature above 650°C have been few.

In the present study, oxygen sensor test was carried out in lead and LBE using inert device under control of oxygen concentration via changing $P_{\text{H}_2}/P_{\text{H}_2\text{O}}$ ratio in gas at various temperatures. Corrosion behaviour was investigated for Al-Fe surface-coated steel, refractory metals, and silicon carbides types of ceramics materials in the molten LBE at temperature of 700°C.

Test apparatuses, test procedures and materials

Oxygen sensor test

Principle of oxygen control and measurement method

The oxygen control method using hydrogen and steam mixture gas have been employed for liquid lead alloy systems. Oxygen potential in the mixture gas depends on the ratio of hydrogen partial pressure to steam partial pressure ($P_{\text{H}_2}/P_{\text{H}_2\text{O}}$). As the zirconia solid electrolyte sensor exhibit oxygen ionic conductivity at high temperature, concentration cell are structured between lead alloy-side and internal reference-side by applying oxygen saturated bismuth for inside the electrolyte cell. Oxygen potentials in lead alloys can be calculated by applying measured EMF to the Nernst equation:

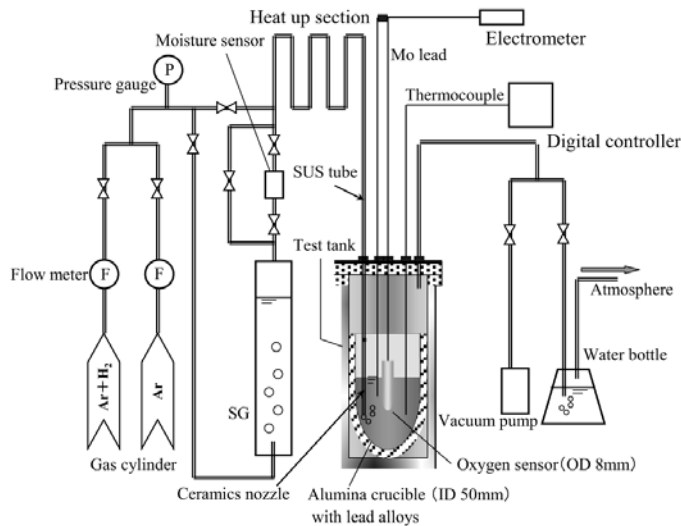
$$E = \frac{1}{2F} \left[\frac{\Delta G^{\circ}_{Bi_2O_3}}{3} - \Delta G^{\circ}_{H_2O} + RT \ln \left(\frac{P_{H_2}}{P_{H_2O}} \right) \right] \quad (1)$$

where E is the measured EMF of sensor, F is the Faraday constant, R is the gas constant, $\Delta G^{\circ}_{Bi_2O_3}$ is the Gibbs free energy of oxide formation of Bi_2O_3 , $\Delta G^{\circ}_{H_2O}$ is the Gibbs free energy of oxide formation of H_2O , and P_{H_2} and P_{H_2O} are hydrogen and steam partial pressure in injection gas.

Experimental apparatus

Figure 1 shows the schematic of stagnant liquid metal test apparatus. This apparatus mainly consist of a steam generator, a dew-point meter (moisture sensor), a heat up section of injection gas, a test section, and a gas exhaust system. In the test section, lead alloys are contained in the alumina crucible (120 mm in height and 50 mm in inner diameter). Oxygen sensor, molybdenum lead wire, ceramics nozzle and thermocouple (SUS316) were installed in the crucible. The gas injection tube was a ceramics tube in the crucible. Almost all parts that contacted with lead alloys were made of ceramics materials to prevent the formation of ferric oxide impurities and deposit on the electrolyte surface that affected the EMF.

Figure 1. Schematic of oxygen sensor test apparatus



Solid electrolyte oxygen sensor

The sensor cell was made of a yttria-stabilised zirconia ($Y_2O_3-ZrO_2$) 70 mm in height, 8 mm in outer diameter and 5 mm in inner diameter, with a reference electrode of oxygen-saturated bismuth ($Bi:Bi_2O_3 = 95:5$ wt.%). A molybdenum wire inserted into the reference electrode was used for EMF measurement with an electrometer with high impedance.

Oxygen sensor test procedure

The EMF signals of the oxygen sensor were measured by bubbling the gas through the melt. The injection gas mixture was controlled to have desired P_{H_2}/P_{H_2O} ratio by controlling Ar and Ar+3% H_2 gas flow rates and steam generator temperature, heated up, and then injected into the melt. The test conditions are summarised in Table 1. LBE and lead were beforehand reduced by injection of Ar+3% H_2 gas alone.

Table 1. Test conditions for oxygen sensor

Parameters	Conditions
System pressure	0.1 MPa
Ar and Ar+3%H ₂ mixture gas flow rate	40 mL/min
Ar and Ar+3%H ₂ mixture gas flow velocity	5.3 cm/s
Temperature of injection gas mixtures	200-500°C
Amount of lead or LBE in test section	1 150 g
Lead or LBE temperatures	350-700°C
Oxygen concentration in lead or LBE	1×10^{-5} to 5×10^{-9} wt.%

Corrosion test*Corrosion test apparatus*

The corrosion test was conducted in the same test apparatus as that for the oxygen sensor test. The parameters of test apparatus and test conditions are shown in Table 2. Oxygen concentration was controlled in the same way as the oxygen sensor test.

Corrosion test materials

Corrosion test materials chosen for the present test were surface-coated steels, refractory metals and ceramics. The surface-coated steel was Al-Fe-coated STBA26 which coated by physical vapour deposition (PVD) using Unbalanced Magnetron Sputtering (UBMS) method. The thickness of Al-steel-sputtering film was 21 μ m. are corrosion resistant in lead alloy at temperature up to 550°C according to previous publications. High chromium steels containing silicon and aluminium is more promising steels than the others. In this study a high-chromium steel Recloy10 was tested. Recloy10 contains 17.7%Cr, 1%Si and 0.9%Al. Refractory metals tested were tungsten (W), molybdenum (Mo) and niobium (Nb). Ceramics tested were SiC and Ti₃SiC₂ (3-ONE-2 LLC Company). SiC tested has composition of 98SiC-0.2SiO₂-0.1Si-1.2C. The density of the SiC is 3.1 g/cc.

Table 2. Test conditions and apparatus for corrosion test

Case/parameter	I	II
Injection gas	Ar	Ar+H ₂ (3%) and Ar
Type of sensor	Y ₂ O ₃ -ZrO ₂	Y ₂ O ₃ -ZrO ₂
Temperature of LBE	700°C	700°C
Oxygen concentration (wt.%)	$\sim 6.8 \times 10^{-7}$	$\sim 5 \times 10^{-6}$
Immersion time (hours)	1 000	1 000
Tested materials	Al-Fe-coated STBA26	Tungsten (W), molybdenum (Mo), niobium (Nb), SiC and Ti ₃ SiC ₂

Corrosion test procedure

Oxygen concentration which has main environmental factor on the corrosion process was controlled at 6.8×10^{-7} wt.% for the Al-Fe-coated STBA26 and at 5×10^{-6} wt.% for the high chromium steel, the refractory metals and the ceramics. The value of 6.8×10^{-7} wt.% was nearly the same of iron formation potential and that of 5×10^{-6} wt.% higher than the iron formation potential.

Each material has two specimens, i.e. one was for weight loss data and another for Scanning Electron Microscope (SEM) analysis/Energy Dispersive X-ray Microanalysis (EDX). For the measurement of weight change, all the specimens were immersed in a hot sodium pool at 260-280°C, and then washed with ethanol. Measurement of weight change was carried out by an electronic reading balance with the accuracy of 0.1 mg.

From Gromov's Fe, Cr and Ni solubility equations¹, it could be estimate that saturated level of Fe, Cr and Ni at 700°C were 4×10^{-3} wt.%, 4.3×10^{-3} wt.% and 4.6 wt.%, respectively. Metal concentrations in the molten LBE after 1 000 hours were estimated by specimen's weight changes. The concentrations of all metals were $< 2 \times 10^{-6}$ wt.% after immersed in molten LBE at 700°C for 1 000 h. It means that metal concentrations during experiment were much lower than saturations levels.

Corrosion characteristics were also investigated by SEM-EDX analysis. After immersed in molten LBE at 700°C, the specimens were washed in hot glycerin at 160-180°C to remove the residual LBE. Then, the glycerine was removed using water at 70°C-80°C. The specimen surfaces were coated by gold to protect oxide layers on the specimens. Afterwards, the specimens were cut in the middle, solidified by resin and polished with a mechanical grinder using polycrystalline diamond grains. The polycrystalline diamond grains used in this polishing treatment were 9 μm , 6 μm , 3 μm and 1 μm .

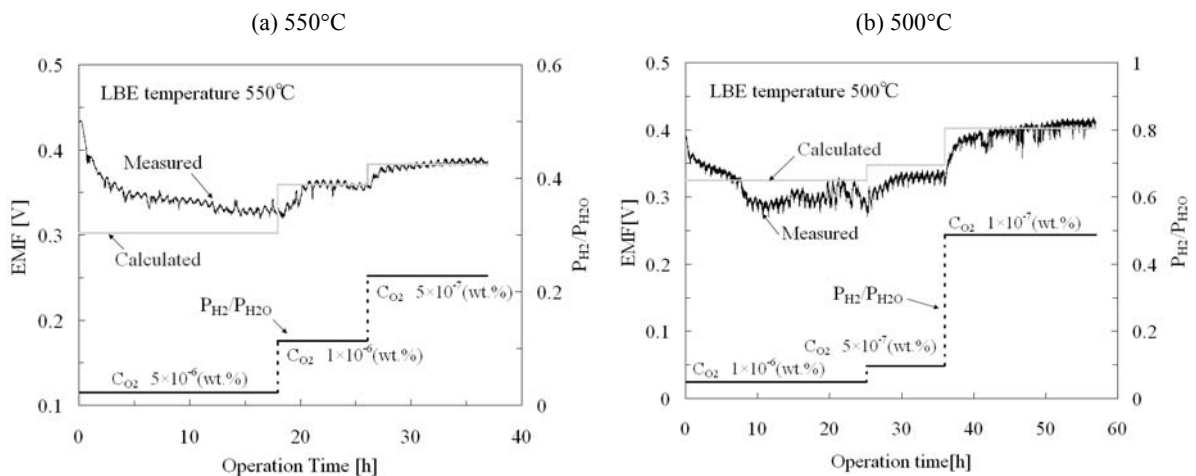
Results and discussion

Oxygen sensor test results

Characteristics of EMF of sensor in LBE

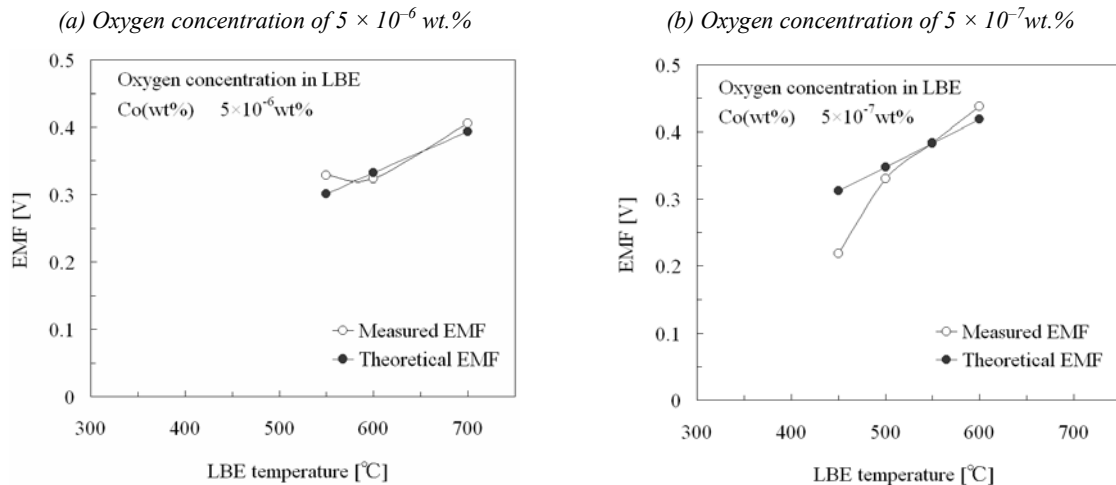
Figures 2(a) and 2(b) show the measured EMF of steam and hydrogen gas injection tests at LBE temperatures of 550°C and 500°C. $P_{\text{H}_2}/P_{\text{H}_2\text{O}}$ ratios were changed stepwise three times for each LBE temperatures so that LBE were reduced in three oxygen content levels. These measured EMF were compared with calculated EMF derived from Nernst equation. It is found that oxygen control in the melt was achieved properly, and the measured EMF agreed with calculated EMF in each $P_{\text{H}_2}/P_{\text{H}_2\text{O}}$ ratios.

Figure 2. Comparison of measured and calculated EMF under control of $P_{\text{H}_2}/P_{\text{H}_2\text{O}}$ ratio in three steps (injection gas 350°C)



Measured signals and theoretical EMF in oxygen concentrations of 5×10^{-6} wt.% and 5×10^{-7} wt.% in LBE are shown in Figures 3(a) and 3(b), respectively. The measured EMF were in good agreement with theoretical EMF over 500°C . In low temperature range, measured EMF deviated from theoretical EMF with decreasing the LBE temperatures and measured EMF were maintained low level voltages during operation at $350\text{--}400^\circ\text{C}$. That is, the solid electrolyte oxygen sensor had worked well at high temperatures ranged $500\text{--}700^\circ\text{C}$, while it had not worked accurately below 450°C .

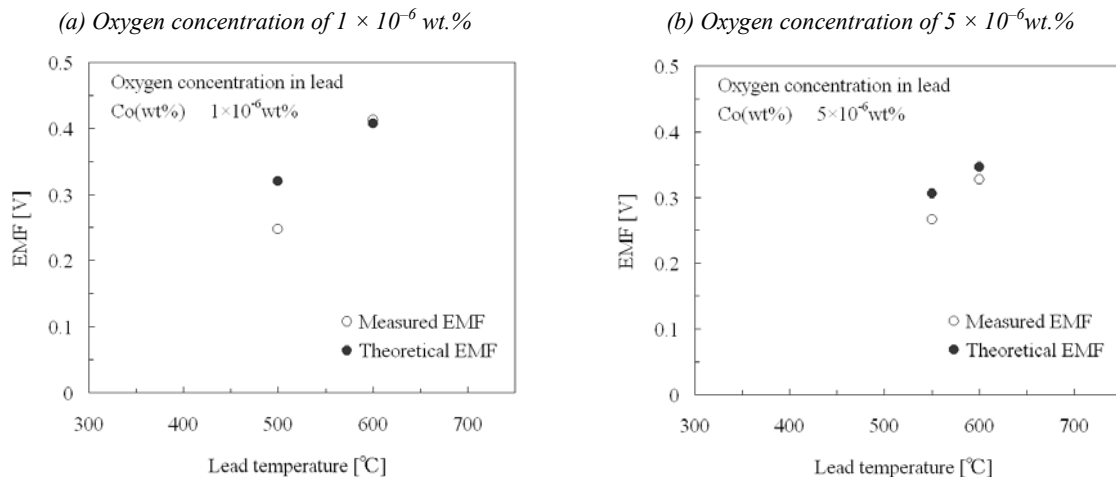
Figure 3. Comparison of measured and theoretical EMF



Characteristics of EMF of sensor in lead

Experiments were also carried out in molten lead in the oxygen concentration range of 1×10^{-5} to 5×10^{-6} wt.% at temperature range $500\text{--}600^\circ\text{C}$. Figures 4(a) and 4(b) show the comparison of measured and theoretical EMF at oxygen concentration of 1×10^{-6} wt.% and 5×10^{-6} wt.% at injection gas temperature of 500°C . It is found that measured EMF agree well with theoretical EMF at 600°C , while measured EMF deviate from theoretical EMF with decreasing the lead temperatures. The lowest limit of operating temperature in lead is 100°C higher than that in LBE (500°C).

Figure 4. Comparison of measured and theoretical EMF



Corrosion test results

Al-Fe-coated STBA26

SEM analysis of cross-section of Al-Fe-coated STBA26 is shown in Figure 5. It is found that the whole of sputtering-coated surface layer still remained on the base surface of STBA26. Al-Fe-coated layer was $\sim 21 \mu\text{m}$ in thickness which is as same as that before immersion in LBE. No penetration of LBE into this layer was observed after the immersion. This means that even Al-Fe-coated layer was not thick but could withstand from LBE at 700°C for 1 000 hours.

Figure 5. SEM micrograph cross-section of Al-Fe-coated STBA26 after immersed in LBE at 700°C with oxygen concentration of 6.8×10^{-7} wt.% for 1 000 hours

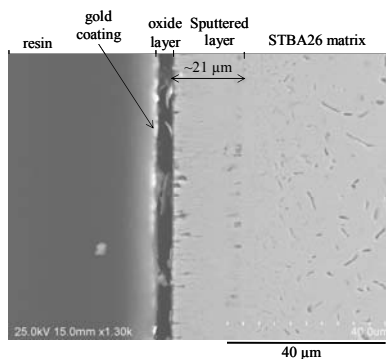
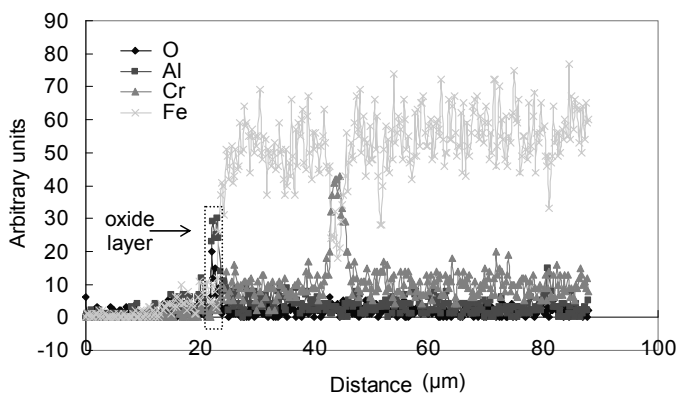


Figure 6 shows the atomic analysis of aluminium, iron, chromium and oxygen by using EDX analysis. The aluminium oxide layer was formed on the Al-Fe-coated surface layer, since aluminium spectrum had high peak in this oxide layer. Iron and chromium spectrum had no significant peak in this oxide layer. SUS304 which was used as a target in this UBMS technique mainly contains iron and 18-20% chromium. The oxygen concentration of 6.8×10^{-7} wt.% was much higher than the formation potentials of aluminium oxide and chromium oxide and was nearly the same of the formation potential of iron oxide. The SEM-EDX analysis showed that the aluminium oxide layer was thin and could well protect the surface from LBE at 700°C . There was no penetration of LBE into this layer after 1 000 hour immersion.

Figure 6. Atomic analysis of cross-section of Al-Fe-coated STBA26 after immersed in LBE at 700°C with oxygen concentration of 6.8×10^{-7} wt.% for 1 000 hours



The SEM micrographs of the cross-sections of tungsten, molybdenum, and niobium are shown in Figure 7. No penetration of LBE into tungsten and molybdenum matrices and no former traces of corrosion process were observed. The surfaces were smooth without any damage or cracks. It can be seen that no oxide layer was observed. There were no penetration of LBE into base metal and no dissolution of tungsten element into LBE. However, penetration of LBE into matrix of niobium was observed. This penetration of LBE was not only deep but also prevailed on all part of surface area.

Figure 7. SEM micrograph cross-section of tungsten after immersed in LBE at 700°C with oxygen concentration of 5×10^{-6} wt.% for 1 000 hours

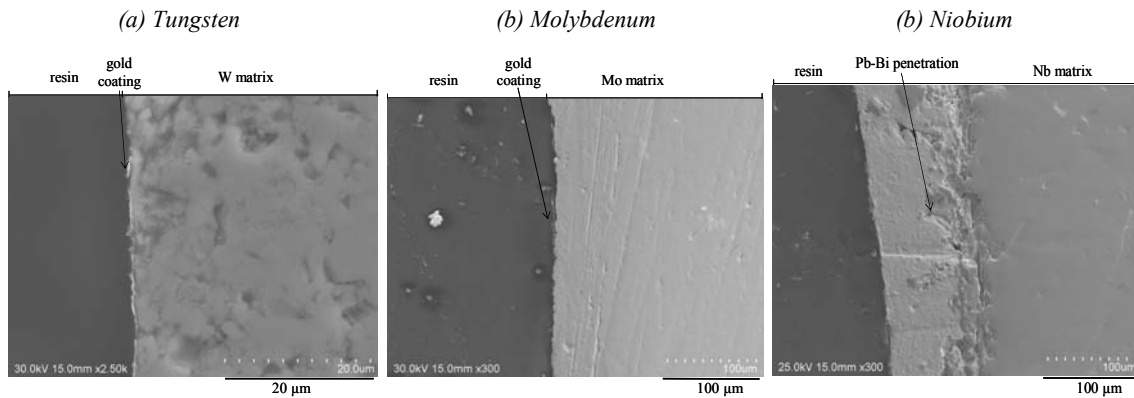
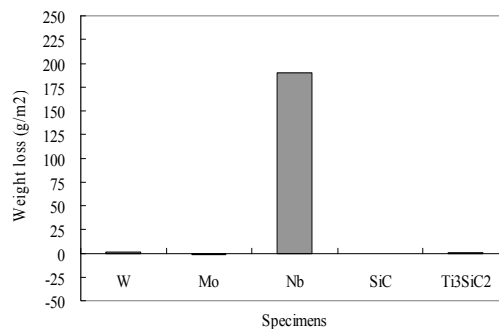


Figure 8 shows no significant weight changes of tungsten and molybdenum specimens after immersed in high temperature LBE up to 1 000 hours, although that weight loss of niobium was 190 g/m^2 . These results show that tungsten and molybdenum are compatible with LBE at 700°C, although niobium is not.

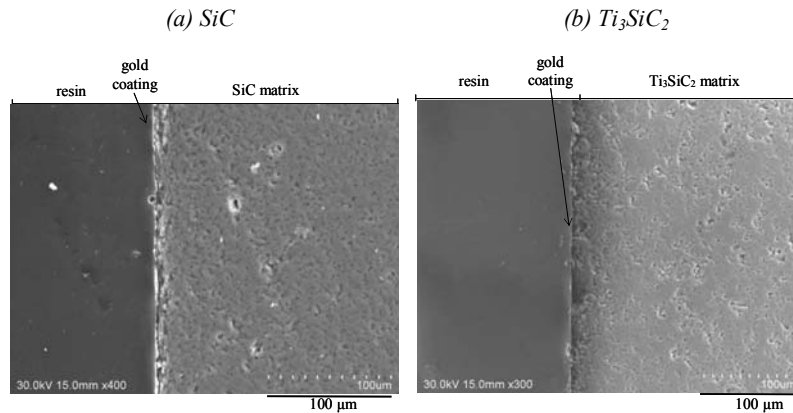
Figure 8. Weight loss of refractory metals and silicon carbide after immersed in LBE at 700°C for 1 000 hours



Ceramics

Figure 9 shows no penetration of LBE into SiC and Ti₃SiC₂ matrices and no former traces of corrosion process were observed. Figure 8 shows no significant weight changes of SiC and Ti₃SiC₂ specimens after immersed in high temperature LBE up to 1 000 hours. SiC and Ti₃SiC₂ have high performance of corrosion resistance in LBE at 700°C.

Figure 9. SEM micrograph cross-sections of ceramics after immersed in LBE at 700°C with oxygen concentration of 5×10^{-6} wt.% for 1 000 hours



Conclusions

The conclusions of the tests and analyses are as follows:

Oxygen sensor test

- (1) In the case of oxygen control in LBE, measured EMF were in good agreement with the theoretical EMF derived from Nernst equation at 500-700°C. Consequently, it is recommended that this sensor should be employed as oxygen sensor in high temperature region (higher than 500°C) for experimental loops.
- (2) In the case of oxygen control in lead, measured EMF agreed well with the theoretical EMF at 600°C. Therefore, it can be predicted that this sensor will be feasible for oxygen measurement in lead over 600°C.

Corrosion test

- (1) Sputtering technique could form good protection layer on the surface of steels. Aluminium oxide layer formed on the surface sputtering-coated layer was stable and effective for no penetration of LBE at 700°C.
- (2) Tungsten and molybdenum were high corrosion resistant in LBE at 700°C but niobium was not. SiC and Ti₃SiC₂ were high corrosion resistant in high temperature LBE at 700°C.

Acknowledgements

The authors would like to greatly thank to Mr. S. Yoshida, Mr. K. Hata, Mr. K. Hara, Dr. M. Kondo, Mr. T. Akashi of Tokyo Institute of Technology for their assistance in design, construction and operation of the experimental apparatus and for their instructions over the whole of these activities. The authors would like to express their gratitude to Dr. T. El-Raghy of 3-ONE-2 LLC Company for his supply of Ti₃SiC₂ and its information.

REFERENCES

- [1] Gohar, Y., *J. Nucl. Mater.*, Vol. 318, 185 (2003).
- [2] Sasa, T., *Progress in Nuclear Energy*, Vol. 47, 314 (2005).
- [3] Vantuyle, G.J., D.R. Bennett, J.W. Herczeg, E.D. Arthur, D.J. Hill, P.J. Finck, *Prog. in Nucl Energy*, Vol. 40, 357 (2002).
- [4] Courouau, J-L., P. Trabuc, G. Laplanche, Ph. Deloffre, P. Taraud, M. Ollivier, R. Adriano, S. Trambaud, *J. Nucl. Mater.*, Vol. 301, 53 (2002).
- [5] Courouau, J-L., *J. Nucl. Mater.*, Vol. 335, 254 (2004).
- [6] Crespo, L.S., F.J.M. Munoz, Gomez Briceno, *J. Nucl. Mater.*, Vol. 296, 273 (2001).
- [7] Colominas, S., J. Abella, L. Victori, *J. Nucl. Mater.*, Vol. 335, 260 (2004).
- [8] Kondo, M., M. Takahashi, *J. of Nucl. Mater.*, Vol. 356, 203 (2006).
- [9] Kond, M., M. Takahashi, N. Sawada, K. Hata, *J. of Nucl. Sci. and Tech.*, Vol. 43, No. 2, pp. 107 (2006).
- [10] Muller, G., G. Schumacher, F. Zimmermann, *J. of Nucl. Mater.*, Vol. 278, 85 (2000).
- [11] Heinzl, A., M. Kondo, M. Takahashi, *J. of Nucl. Mater.*, 350, 264-270 (2006).
- [12] Fazio, C., I. Ricapito, G. Scaddozo, G. Benamati, *J. of Nucl. Mater.*, Vol. 318, 325 (2005).
- [13] Hata, K., M. Takahashi, *Proc. of GLOBAL*, Tsukuba, Japan, 9-13 October 2005, Paper No. 446 (2005).
- [14] Takahashi, M., M. Kondo, *Proc. of GLOBAL*, Tsukuba, Japan, 9-13 October 2005, Paper No. 425 (2005).

LIQUID METAL-ASSISTED FRACTURE OF THE T91 MARTENSITIC STEEL

**J-B. Vogt¹, A. Verleene¹, I. Serre¹
F. Balbaud-Célérier², L. Martinelli², A. Terlain²**

¹Laboratoire de Métallurgie Physique et Génie des Matériaux ENSCL/USTL CNRS
Université des Sciences et Technologies de Lille, France

²CEA Saclay, Service de la Corrosion et du Comportement des Matériaux dans leur Environnement,
F-91191 Gif-sur-Yvette Cedex, France

Abstract

Use of liquid lead-bismuth eutectic (LBE) as spallation target or as cooling fluid in accelerated-driven systems rises the question of the reliability of structural materials in terms of liquid metal embrittlement, corrosion and corrosion-fatigue.

The paper analyses the risks of corrosion damage and of accelerated fatigue damage by liquid lead-bismuth eutectic (LBE) of the T91 steel and consists of three parts. Firstly, the corrosion of the T91 in LBE is studied at CEA paying attention on the oxygen concentration. This results in dissolution process when the oxygen concentration is low while a protective oxide film forms under high oxygen concentration. The second part is devoted to the experiments carried out at Lille University on the low cycle fatigue behaviour of the T91 steel. It is shown that the stress response to strain cycling is not influenced by LBE. However, the fatigue resistance is reduced by a factor at least of 2 when cycling at 300°C in LBE instead of air. Finally, the third part takes into account at once the effects of corrosion damage and the effects of fatigue damage. A pre-immersion of T91 fatigue specimens in a LBE bath is carried out at CEA. The immersion temperature was 600°C for about 600 h and the dissolved oxygen concentration less than 10⁻¹⁰ wt.%. The average relative loss of mass estimated from reference plates was less than 0.3% as a result of dissolution process. The specimens are then fatigued at Lille University in the as-received conditions (no modification of the specimen surface before fatigue testing). Fatigue tests are carried out with the same experimental procedure in LBE at 300°C. The results obtained on the pre-corroded specimens show that the fatigue life is reduced by a factor of about 10. The role of LBE is then discussed on the bases of SEM metallographic observations. LBE appears to be not only a source of microcracks in T91 when dissolution process occurs but promotes as well the growth of short cracks nucleated by cyclic plasticity or of the sharp defects induced by corrosion. Finally, an oxide layer formed in oxygen saturated LBE behaves like a protective coating against fatigue damage in LBE.

The present methodology and the obtained results are therefore of interest for innovative nuclear systems, such as Generation IV reactors, critical and subcritical transmutation systems and fusion devices.

Introduction

When materials are employed in presence of liquid metals, the main source of possible damages that are generally alarmed are corrosion and liquid metal embrittlement.

Liquid metal embrittlement is a particular feature of the environment-assisted fractures, which in contrast to pure corrosion damage, involves mechanical loading in addition to the environment. In a previous study [5], it has been shown that under monotonic loading, LBE can lead to a ductile → brittle transition with occurrence of cleavage in LBE instead of dimples in air. High yield stress as well as stress triaxiality promotes the effect even if LME has been observed on smooth disk using the small punch test [13].

Fatigue of materials is also important to take into account since it represents about 70 to 80% of the failure causes of components in service. The effect of liquid metal on fatigue behaviour is very few documented while it can accelerate the fatigue damage.

The present communication is an overview of the results obtained in the frame of the European research programme – Megapie-test – as well as in the frame of the French research network GEDEPEON. It will be focused on the reliability of structural materials in terms of possible detrimental interactions between environment and plasticity. Tests, results and their interpretation are carried out on a modified 9Cr1Mo steel deformed in the liquid lead-bismuth eutectic (LBE).

In this paper, it is proposed, to comment on two different sources of damage that can be promoted by liquid metal. The first one is related with LBE corrosion damage without any mechanical effect but with long time exposure. The second one is devoted to the mechanical behaviour of the T91 steel in the presence of LBE for rather short time exposure. Finally, a synergetic effect between corrosion damage and fatigue damage will be presented.

All these results are obtained from experiments carried out without irradiation and have been obtained jointly by the French Atomic Energy Commission (CEA) and by Lille University for their expertise in these areas.

Material

The chemical composition of the T91 steel which was supplied by Ascométal is given in Table 1.

Table 1. Chemical composition of the T91 steel (wt.%)

Cr	Mo	V	Mn	Si	Ni	C	Nb	Fe
8.50	0.95	0.21	0.47	0.22	0.12	0.10	0.06	Bal

The recommended heat treatment for the T91 steel consists of an austenisation at 1 050°C and air quenching followed by a tempering at 750°C for 1 hour. This results in a fully martensitic microstructure with an average grain size of 20 µm and a macro hardness of 220 HV.

Experimental procedure

Fatigue specimens

The fatigue specimens were smooth and cylindrical with a gauge length of 13 mm and a gauge diameter of 10 mm. For the study of the LCF behaviour without effect of pre-immersion, their surface was carefully electro polished before cycling. In the case of a pre-immersion in LBE, the surface was electro polished before introduction in the LBE loop but no further preparation of the surface was carried out before cycling

Pre-immersion conditions in LBE loop

Two batches of coupons ($10 \times 15 \times 2$ mm and $22 \times 25 \times 9$ mm) and fatigue specimens were pre-exposed in stagnant LBE vessel at CEA Saclay taking into account the control of oxygen concentration. A first batch of specimens was introduced in the LBE loop for 613 h at 600°C using a reducing atmosphere in order to reach an oxygen concentration less than 10^{-10} wt.%. The second batch was exposed in saturated oxygen (air over pressure of 200 mbar) LBE at 470°C for 502 h.

After immersion in LBE, the residual LBE adherent to the coupon surface was removed. The coupons were then weighed and compared to those before immersion in LBE, in addition with optical, SEM and EDX analysis.

Fatigue testing

All the fatigue tests were performed at 300°C in air and in the liquid LBE alloy using a servo-hydraulic MTS machine with a load capacity of 100 kN. No particular care was taken to control or measure oxygen activity.

The fatigue tests were carried out in a fully push pull mode ($R_\epsilon = -1$) at different imposed total strain amplitudes ranging from $\Delta\epsilon_t = 0.4\%$ to 2.5% . Some tests were done using a trapezoidal waveform (tension holding of 600 s). A strain gauge extensometer for the strain control, a triangular wave and a constant strain rate of 4.10^{-3} s^{-1} were used. During cycling, hysteresis loops were periodically recorded allowing the measurement of the stress variation $\Delta\sigma$ for each cycle. The fatigue life is defined as the number of cycles from which a 25% drop in the quasi stabilised tensile stress occurs.

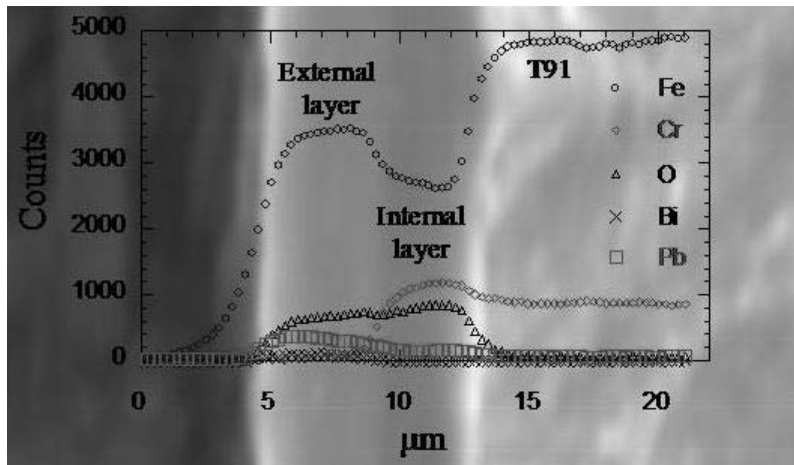
Results and discussion

Corrosion resistance in (free stress) LBE

A pre-immersion of the T91 steel in a LBE bath at 470°C for 502 h with an air over pressure of 200 mbar led to the formation of an oxide film $5 \mu\text{m}$ in thickness. The morphology was similar to that reported by [7,8] for T91 exposed in LBE in this range of temperatures, that is a double layer (Figure 1).

The EDX analysis were in agreement with the literature, and indicated magnetite for the external layer is and a $(\text{Fe,Cr})_3\text{O}_4$ spinel for the internal one.

Figure 1. SEM micrograph of the oxide film and EDX repartition of Fe, Cr O, Pb and Bi



In the low oxygen concentration LBE, corrosion proceeded by dissolution involving an intergranular attack of the surface [Figure 7(a)]. The average loss of mass estimated from reference coupons were in the range 1.5 to 5.6 mg/cm².

Effect of LBE on fatigue behaviour (continuous cycling on as-received specimens)

The evolution of the stress amplitude $\Delta\sigma/2$ as well as the stress amplitude values versus the number of cycles N does not vary from tests conducted at 300°C in air to tests conducted at 300°C in LBE.

The T91 exhibited a cyclic softening period, very pronounced at the beginning of the test and then more moderate. This is a typical response to strain cycling of the microstructure evolution of high density dislocation containing materials such as martensitic steels or cold worked materials [9].

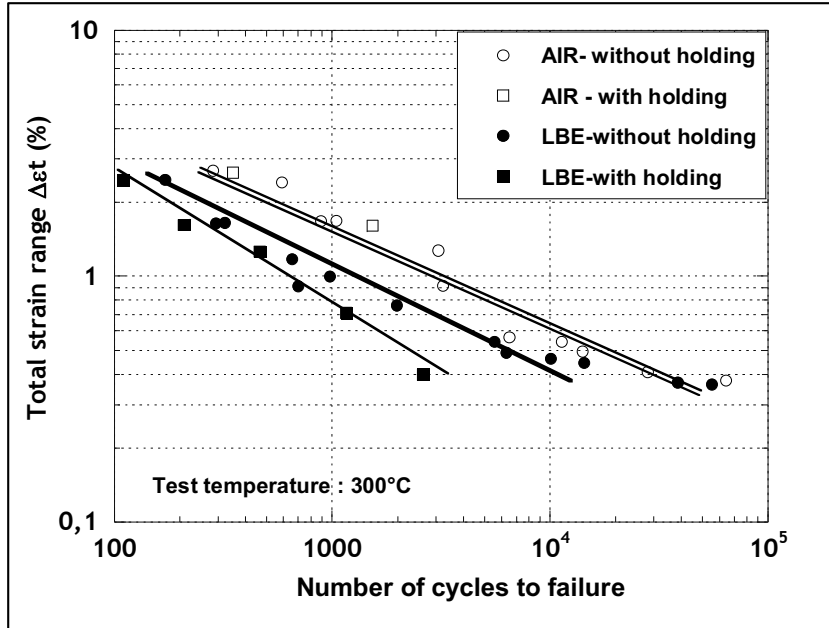
As occurs for corrosion-fatigue tests in aqueous solution, the LBE environment did not affect bulk properties as depicted by the macroscopic stress but can modify the surface properties. This effectively appears on the fatigue resistance which is at least twice lower in LBE than in air for a same strain amplitude (compare ○ and ● in Figure 2). Such detrimental effect of LBE on fatigue resistance has been also reported for a 10.5Cr steel Manet-II at 260°C [10]. This suggests a role of LBE on crack initiation and propagation.

Effect of testing conditions on fatigue behaviour (as-received specimens)

The introduction of a hold time did not modify the stress response to strain cycling as well for tests in air as in LBE as compared with continuous cycling. Especially, no stress relaxation was recorded. However, the effect of the cycling waveform appeared to act on the fatigue resistance according to the environment.

In air, the two tests performed with the hold time had the same fatigue resistance as the tests conducted under continuous cycling (compare ○ and □ in Figure 2). However, in LBE, a reduction in fatigue resistance was observed with the introduction of a hold time (compare ● and ■ in Figure 2).

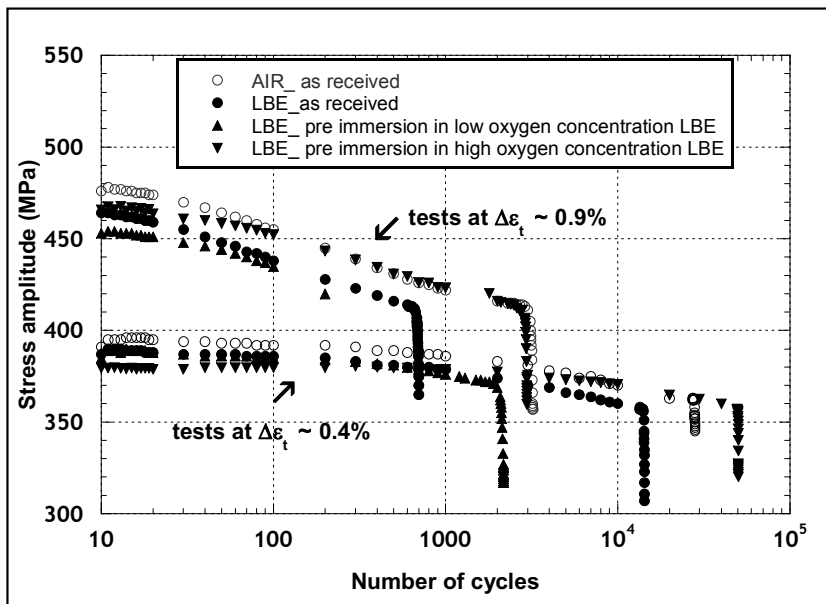
Figure 2. Fatigue resistance of the T91 steel according to the environment and the mechanical loading conditions



Effect of pre-immersion in LBE on fatigue behaviour

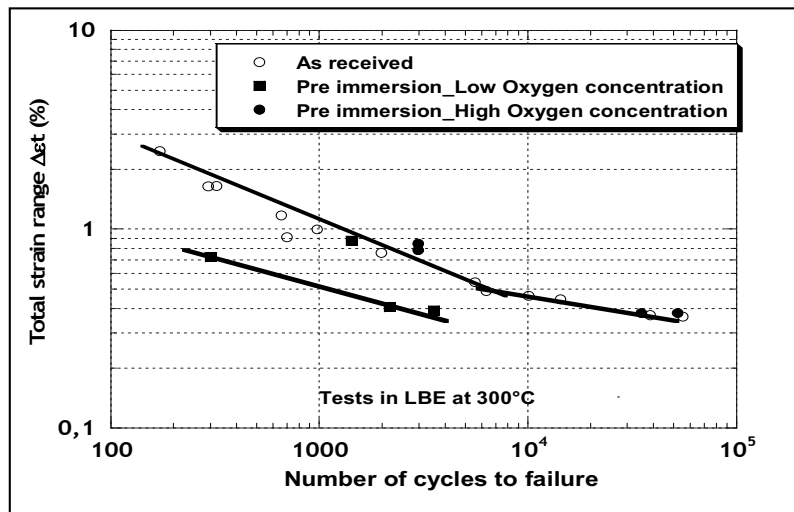
The stress response to strain cycling in LBE at 300°C of the T91 steel after a pre-immersion in LBE is reported Figure 3. For both conditions of pre-immersion in LBE, the response was similar to that of an as-received specimen in terms of cyclic accommodation.

Figure 3. Cyclic accommodation at 300°C in air and in LBE of the T91 steel in the as-received condition and after a pre-immersion in LBE according to the oxygen concentration



However, the fatigue resistance was considerably dependant on the pre-exposition condition (Figure 4). A pre-exposition in low oxygen concentration LBE bath followed by further cyclic deformation in LBE at 300°C resulted in shorter fatigue lives as compared with as-received specimens (except for one test). This contrasts with specimens pre-exposed in oxygen saturated bath which exhibited the same fatigue resistance as for received specimens after fatigue at 300°C in LBE. To our knowledge, no literature on fatigue properties after exposure in HLM is available. The only investigation on this topic concerns monotonic tensile properties [11] where a decrease in ductility was observed in the T91 after exposure at 400°C in LBE (low oxygen content) for 4 500 h.

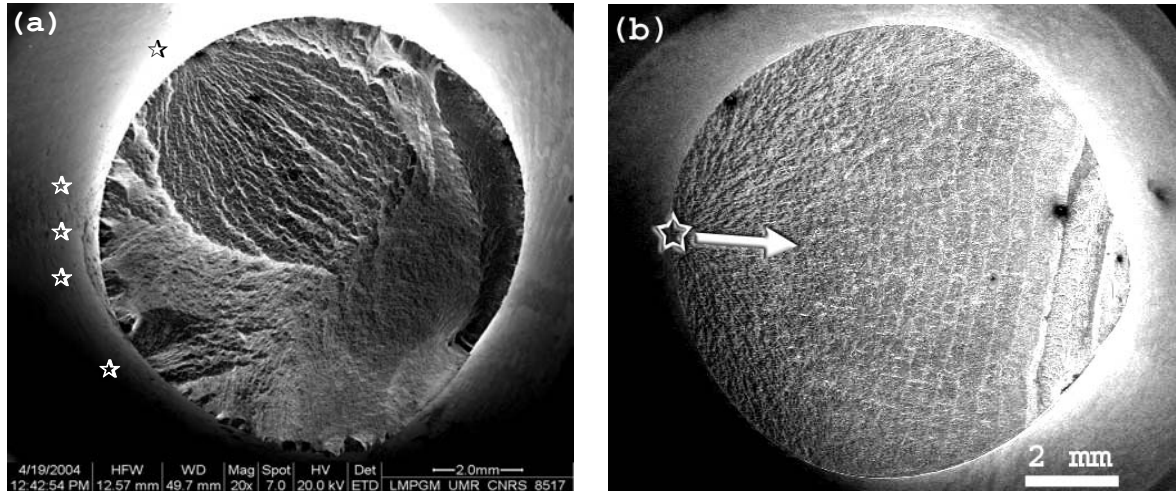
Figure 4. Effect of pre-immersion in LBE according to the oxygen concentration on the fatigue resistance in LBE at 300°C of the T91 steel



Role of LBE on fracture mode

At a macroscopic scale, the fractured LCF specimens can be classified into two groups according to whether crack initiation was single or multiple. The first one concerns the tests in LBE of as-received specimens. The second one is related with tests of as-received specimens fatigued in air and with tests in LBE of the specimens pre-exposed in LBE. The fracture surfaces of the as-received specimens fatigued in LBE were flat and perpendicular to the loading axis whatever the strain range [Figure 5(b)]. They only contained a single crack initiation site. Crack started from this unique initiation site and propagated along a plane perpendicular to the loading axis (arrows indicates the fatigue crack direction). For the specimens pre-exposed in LBE and then fatigue fractured in air or in LBE, the failure surfaces were rather tortuous with an inclined surface fracture with the loading axis in the centre of specimen. Multiple initiation sites were observed from which some cracks have propagated perpendicularly to the loading axis. Joining those propagation areas, the fracture surface appeared inclined to the loading axis [Figure 5(a)]. This is interpreted as a transition region, covering only few cycles. The classification into two groups of fractographies therefore suggests that the mechanisms of fatigue damage are different between the different conditions. At a microscopic scale, two modifications in the fractographic features have been observed. First, striations which are commonly observed on fatigue fracture surfaces of ductile materials, are indeed found after tests in air. They were also visible after LCF in LBE but the striation spacing was much higher in LBE (up to 100 μm) than in air (up a few μm). All these SEM observations are in agreement with an accelerated fatigue crack growth rate by LBE.

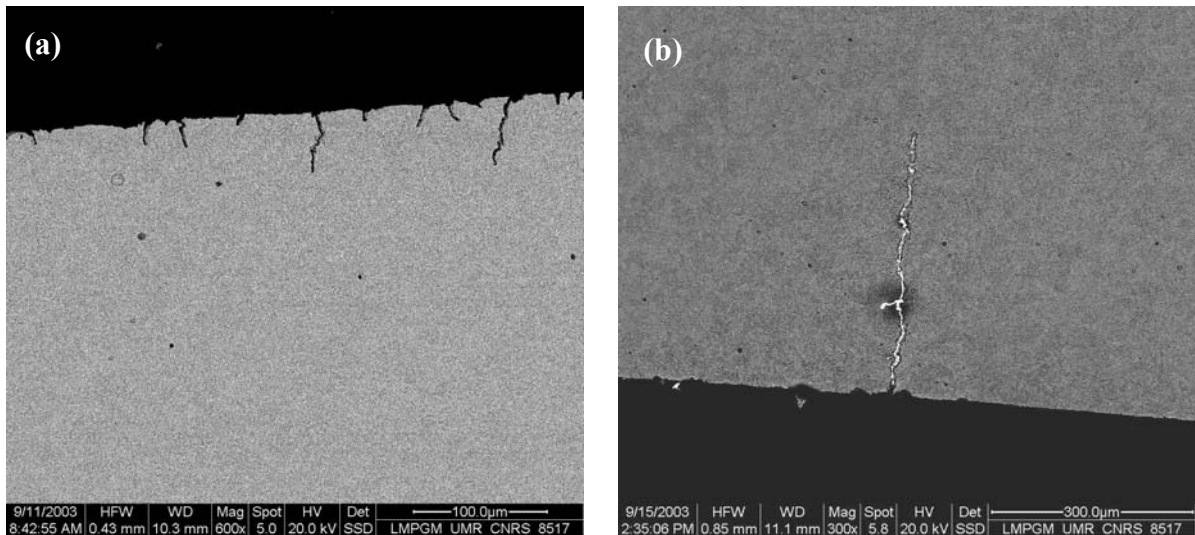
Figure 5. Macro views of typical fatigue fracture surfaces of the T91 after LCF tests in air (a) or in LBE (b) – the star indicates crack initiation site



Role of LBE on fatigue crack initiation

For both environments, cracks initiation was essentially transgranular. They also were growing through the grain, and occasionally at grain boundaries for the samples tested in LBE. The samples tested in air [Figure 6(a)] exhibited a high density of short cracks at the surface from extrusions/intrusions. In contrast, the specimens tested in LBE contained only the major crack propagated through the bulk and few secondary short cracks [Figure 6(b)].

Figure 6. Transversal cut of the T91 specimen after fatigue failure at 300°C and $\Delta\epsilon_t = 2.2\%$ in air (a) and in LBE (b)



A deep quantitative analysis of the distribution of the number of volumic cracks for different strain ranges according to the crack length in air (a) and LBE (c) is given elsewhere [12]. The growth of grain-sized cracks is limited by the grain boundaries which can be overcome after a given number of cycles. Crack extension therefore has occurred by crystallographic growth which again is limited by

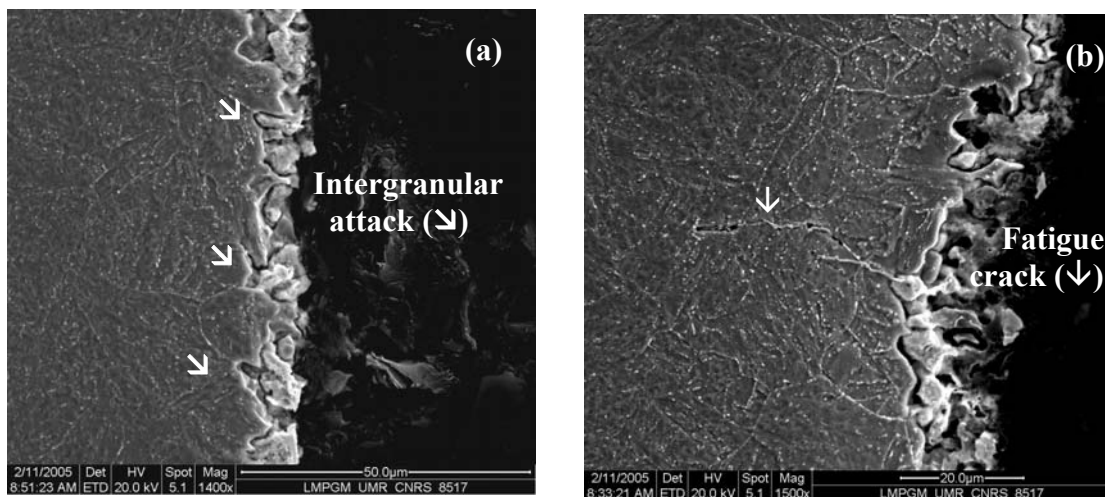
other grain boundaries but the length has reached now three or four grain sizes. Longer microcracks (up to ten grain sizes) can form by coalescence of the previous ones. Finally, only a very few of them have propagated in a plane perpendicular to the stress axis into the bulk. However, these different steps in the damage mechanism did not reflect the behaviour in LBE. LBE assists the propagation of the first short cracks so that it prevents nucleation and propagation of other cracks. The grain boundary resistance to crystallographic growth vanishes when LBE is in contact and allows easy extension of the crack into the bulk. To obtain such effects requires wetting of lips and tips of the cracks by LBE which was the case for most all the tests.

Role of pre-immersion in LBE on fatigue crack initiation

The two different surface evolutions resulting from the low and high oxygen concentrations in the LBE led to two different fatigue crack initiation modes.

The intergranular attack [Figure 7(a)] that occurred from dissolution process in the low oxygen concentration LBE behaved as defects similar to fatigue microcracks ready to propagate into the bulk with LBE under cyclic loading [Figure 7(b)]. In this case, a pre-immersion in LBE played a similar role as a cumulative cyclic solicitation in terms of short crack initiation, even if the mechanisms are totally different.

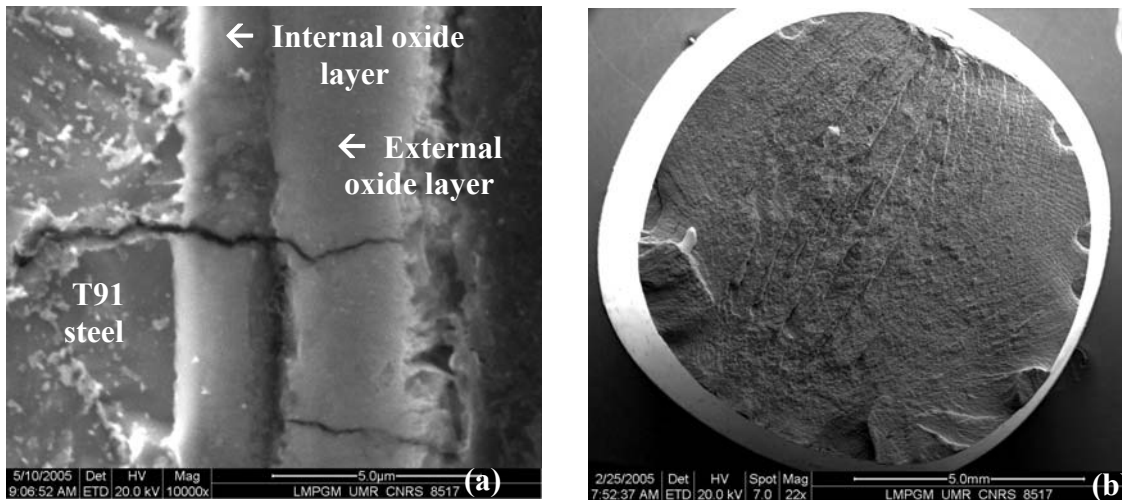
Figure 7. Transversal cut of the T91 specimen after pre-immersion for 613 h at 600°C in LBE with low oxygen concentration (a) before fatigue testing, (b) after fatigue failure in LBE at 300°C $\Delta\epsilon_t = 2.2\%$



The oxide film formed after a pre-immersion of the T91 steel in a LBE bath at 470°C for 502 h avoided the contact between LBE and T91 steel with further cyclic. Observation of the transversal cut of pre-oxidised specimens fatigued in LBE would tend to suggest that the oxide layer had good mechanical resistance in this range of solicitation. No obvious delamination or excessive cracking were observed. As can be seen in Figure 8(a), cracks can initiate in the external sublayer, stop at the interface between the two sublayers or cross the internal sublayer, and then propagate into the T91 steel.

On the fracture surface [Figure 8(b)], it is possible to observe fatigue crack propagation zones corresponding to multiple crack initiation sites. On the fracture surface of the major crack, widely spaced striations are visible which expresses a high rate of crack growth.

Figure 8. T91 specimen after pre-immersion in LBE with high oxygen concentration for 502 h at 470°C and then subjected to fatigue in LBE at 300°C $\Delta\epsilon_t = 0.4\%$ transversal cut (a) and fracture surface (b)



Conclusion

The present study which aimed at an evaluation of the interaction of LBE with the low cycle fatigue behaviour at 300°C of the T91 steel has first evaluated the corrosion resistance in LBE and then described the cyclic plasticity of the alloy.

Depending on the oxygen concentration in stagnant and free stress LBE, two different mechanisms of corrosion occurred at the T91 surface: dissolution with attack intergranular at low oxygen concentration and oxidisation at high oxygen concentration.

The stress response to strain cycling of the T91 martensitic steel at 300°C is a cyclic softening, similar in air and LBE. In air at 300°C, the fatigue damage proceeds by the classical steps: an evolution at the specimen surface consisting of a transgranular initiation at extrusion intrusion, a growth by crystallographic extension, a coalescence of short cracks to form a long crack and then propagation of the long crack into the bulk. The transfer from one step to another one is achieved with a cumulative plasticity. The marked variations in fatigue resistance according to the different situations studied involving the LBE indicates that the micro mechanisms in the fatigue damage are affected by LBE. LBE can act on each step of the fatigue damage and substitutes for a cyclic plasticity accumulation.

The first effect of LBE is to suppress the initial step of very short microcracks formation by cyclic plasticity. This requires a dissolution process, i.e. low oxygen content but not necessarily in the whole LBE bath but at least locally. It is interesting to note that a transgranular or intergranular initiation has no effect for the further evolution of the following steps. The second effect of LBE is to skip the growth by crystallographic extension and coalescence of short cracks at the steel surface. The third effect is to accelerate the growth of long crack in the bulk of the steel. For these two last effects, dissolution process is an unlikely cause because tests are carried out in saturated oxygen LBE and because the test duration is very short. On the other hand, oxidisation of the crack tip is possible. However, this requires time so that other kind of “reaction” such as adsorption of LBE on fresh steel effect must be taken into account. This suggests that LBE strongly affects plasticity dynamics at crack tip but additional work is still necessary to understand this point.

The effects produced by LBE occurred so locally that the reliability of a component should be greater by avoiding the use of a low oxygen LBE except if a protective coating is foreseen. To some extent, high oxygen LBE should limit the LBE fatigue damage due to the formation of the oxide film that avoids a contact between LBE and steel.

The present methodology and the obtained results are therefore of interest for innovative nuclear systems, such as Generation IV reactors, critical and subcritical transmutation systems and fusion devices.

Acknowledgements

This work has been supported by the French CNRS GdR GEDEON and GEDEPEON as well as by the European project MEGAPIE-Test part of the 5th FP EURATOM programme. Ascométal Dunkerque is acknowledged for providing the material.

REFERENCES

- [1] Fazio, C., R. Stieklitz, J.U. Knebel, F. Groeschel, W. Wagner, A. Strinning, H. Heyk, Y. Dai, B. Smith, W. Leung, G. Laffont, Th. Kirchner, A. Guertin, P. Agostini, D. Gorse, T. Auger, J-B. Vogt, A. Al Mazouzi, “The Megapie –Test Project”, *Proc. Int. Workshop on P&T and ADS Development 2003*, W. Haeck, G. Van den Eynde, Th. Aoust, H. Ait Abderrahim, P. D’hondt (Eds.), SCK•CEN, Mol (B), ESC-CEN BLG-959, ISBN 907 6971072.
- [2] Soler, L., F.J. Martin, F. Hernandez, D. Gomez-Briceno, *J. Nuclear Materials*, 335, 174 (2004).
- [3] Balbaud-Célérier, F., A. Terlain, *J. Nuclear Materials*, 335, 204 (2004).
- [4] Fernandes, P.J.L., D.R.H. Jones, *Engng. Failure Analysis*, 299 (1996).
- [5] Vogt, J-B., G. Nicaise, A. Legris, J. Foct, *J. Phys. IV*, Pr8.217 (2002).
- [6] Auger, T., G. Lorang, *Scripta Mater*, 52, 1323 (2005).
- [7] Aiello, A., M. Azzati, G. Benamati, A. Gessi, B. Long, G. Scaddozzo, *J. Nuclear Materials*, 335, 169 (2004).
- [8] Barbier, F., A. Rusanov, *J. Nuclear Materials*, 296, 213 (2001).
- [9] Nagesha, A., M. Valsan, R. Kannan, K. Bhanu Sankara Rao, S.L. Mannan, *Int. J. Fatigue*, 24, 1285 (2002).
- [10] Kalkhof, D., M. Grosse, *J. Nuclear Materials*, 318, 143 (2003).
- [11] Aiello, A., M. Agostini, G. Benamati, B. Long, G. Scaddozzo, *J. Nuclear Materials*, 335, 217 (2004).
- [12] Verleene, A., J-B. Vogt, I. Serre, A. Legris, *Int. J. Fatigue*, 28, 843 (2006).
- [13] Serre, I., J-B. Vogt, *Nuclear Engineering and Design*, 237, 677 (2007).

CONCEPTION OF OPERATION OF *IN SITU* OXIDE COATINGS CONCERNING LIQUID METAL COOLING SYSTEMS

O. Yeliseyeva¹, V. Tsisar¹, Ya. Matychak¹, V. Fedirko¹, T. Muroga², Z. Yao³

¹Physico-mechanical Institute of National Academy of Sciences of Ukraine, Ukraine

²Fusion Engineering Research Center, National Institute for Fusion Science, Toki, Japan

³Nuclear Engineering Research Laboratory, School of Engineering, University of Tokyo, Japan

Abstract

The corrosion aggressiveness of liquid metals with regard to the structural materials and protective coatings is one of the main issues of up-to-date reactor materials science. In this paper the interaction of components in the Fe[Cr]/Pb[O] and V[O]/Li[Er] systems was considered and the kinetic models of formation and growth of the oxide layers on the surface of structural materials during the contact with liquid metals were proposed.

The interaction of V-alloy with oxygen and liquid lithium is considered from the viewpoint of the coating operation at the interface. The *in situ* oxide coating, in turn, is considered as a synergetic object, which evolves (nucleates, grows, becomes stabilise and degrades). The charging procedure of V-4Ti-4Cr alloy by oxygen was considered using the concepts of theory of the low-temperature inner oxidation. The model of formation of the inner oxidation zone was proposed. The deoxidation of V-alloy during the contact with Li[Er] was considered as a surface reaction of oxygen with erbium and as a diffusion process accompanied by the structure-phase transformation in the bulk of solid metal.

The corrosion behaviour of Fe-based alloys in the Pb/Pb-Bi melts as a function of temperature; oxygen concentration in liquid metal, material composition and exposure time was investigated. The main existed experimental data concerning passivation of steels in heavy metal melts were described and generalised. The features of double oxide layer evolution depending on the various experimental conditions were revealed and discussed. Based on the experimental results and thorough analysis of the existed data the phenomenological model of growth of the duplex scale on the surface of steels contacting with heavy metal melts containing oxygen was proposed. The model demonstrates the main stages of origin, growth and degradation of double oxide layer in the liquid metal environment. The numerical simulation of the oxidation kinetics of a model material Armco-Fe in Pb melt saturated by oxygen (10^{-3} wt.%O) at 550°C was carried out.

Introduction

The corrosion aggressiveness of liquid metals (Pb, Pb-Bi, Li, Pb-Li etc.) with regard to the structural materials and protective coatings is one of the main issues of up-to-date reactor materials science [1,2]. An experimental activity aimed at the *in situ* developing of oxide coatings is still in progress. However, the basic understanding of the *in situ* oxide layer formation and operation on the surface of structural materials in liquid metal environment is still incomplete: the oxidation laws and regularities of interaction have not been determined yet. These gaps hamper the development of the satisfactory models for reliable prediction of the long-term viability of the *in situ* oxide layers and structural materials in the liquid metal coolants. In this paper, therefore, the existed experimental data concerning interaction of components in the V[O]/Li[Er] and Fe[Cr]/Pb[O] systems are generalised to develop the models of evolution of the oxide layers on the surface of structural materials during the contact with liquid metal coolants.

Physical and chemical interaction of oxygen-containing V-4Ti-4Cr alloy with liquid lithium doped by erbium

Development of effective and reliable insulating coating is a key to the viability of V/Li blanket concept. In order to mitigate the MHD pressure drop the continuous production of *in situ* insulator oxide layer at the interface “solid metal/liquid metal” should be sustained owing to diffusion inflows of oxygen from the vanadium alloy and active metal (Er) from the liquid lithium. Using the experimental results obtained at NIFS (Japan) [3-6], the conceptual model of interaction of V-4Ti-4Cr with dry oxygen and deoxidation of alloy under the contact with the liquid lithium doped by erbium is presented below.

The main tenet of kinetic model

The interaction of V-alloy with both gas and liquid metal medium is considered from the viewpoint of operation of Er_2O_3 coating at the interface during the contact of alloy with the melt. Thereupon the *in situ* oxide coating should be considered as a synergetic object, which evolves: originates, grows and becomes stabiliser and finally degrades, as illustrated on the scheme (Figure 1).

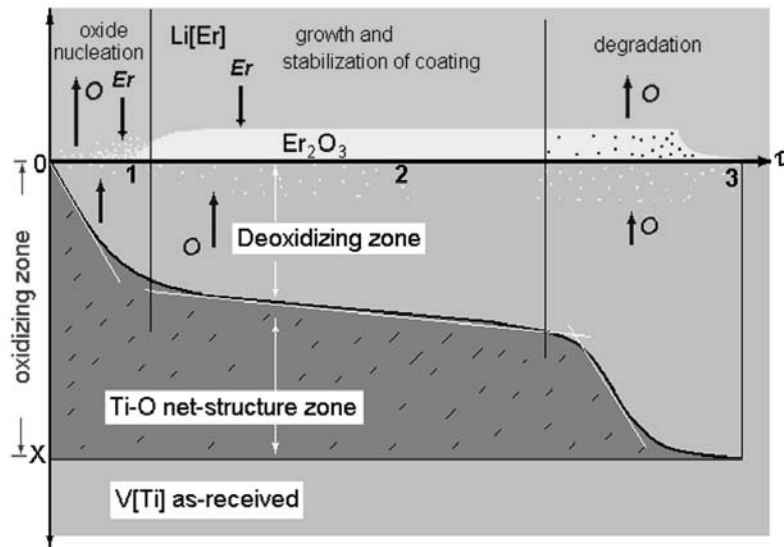
Synergetic status of a coating is based on the formulated hypotheses, which were confirmed experimentally:

- The coating behaviour on the interface $X = 0$ is controlled by the kinetics of physical-chemical processes in the solid metal, which obey the reactionary diffusion laws.
- The kinetics, in turn, is determined by the phase composition and structure of V-alloy specified at the previous charging procedure of alloy by oxygen.
- The process of reaction diffusion (at oxidising and deoxidising) are interconnected with the accumulation and relaxation of structural defects in the V-alloy.

The charging procedure of V-4Ti-4Cr by oxygen

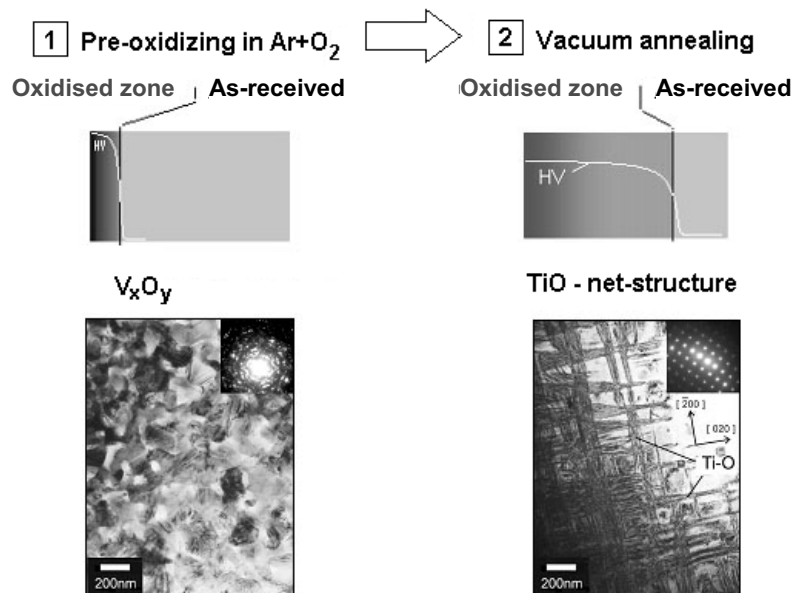
According to the hypotheses mentioned above the special attention should be focused on the charging procedure of V-4Ti-4Cr alloy by oxygen. The two-stage charging procedure was described previously [3,4]. After pre-oxidising in $\text{Ar} + \text{O}_2$ the thin film of vanadium oxides was formed on the

Figure 1. Kinetic model of interaction of oxygen-containing V-4Ti-4Cr alloy with Li[Er]



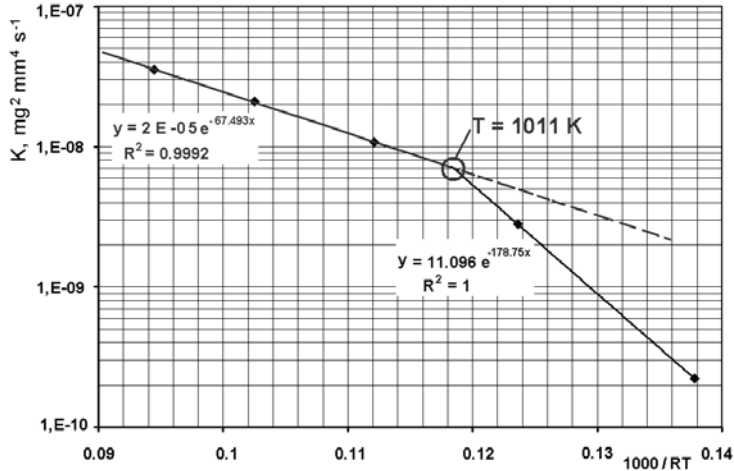
surface of alloy (Figure 2, stage 1). Then the samples were annealed in vacuum at 973 K for 16 h. After annealing the V-alloy contained a high density of $\langle 200 \rangle$ oriented TiO precipitates, so called net structure with the high Vickers hardness (~ 800) was formed in the oxidation zone (Figure 2, stage2).

Figure 2. Charging procedure of V-4Ti-4Cr by oxygen at 700°C and TEM structure after pre-oxidation and vacuum annealing [3,4]



Oxidation of V-4Cr-4Ti in the Ar + O₂ flow in the range 973-1 273 K testified that the mechanism of interaction between V-alloy and gaseous medium alters at around 1 011 K (Figure 3). At $T \leq 1\ 011$ K the oxygen diffusion is accompanied by the fine TiO precipitation limiting the deeper oxygen penetration into the alloy. An activation energy of this process is high $Q = 178.75$ kJ/mol. At $T > 1\ 011$ the interaction process is limited by oxygen absorption in the vanadium matrix as judged from the activation energy $Q = 64.493$ kJ/mol [7].

Figure 3. Parabolic rate constant K as a function of the reciprocal temperature for V-4Ti-4Cr oxidation in Ar-O₂, 1 h

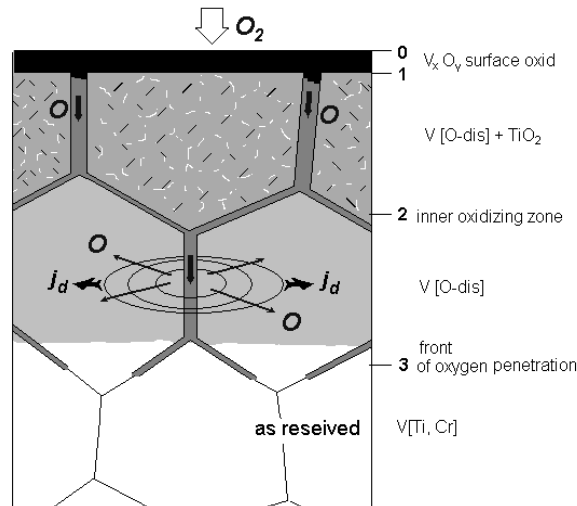


Thermodynamic estimation, TEM and XPS results, high hardness, and a parabolic dependence of oxidation on time indicated that in the low-temperature interval (873-1 011 K) the O diffusion into alloy is accompanied by TiO precipitation with high density [3,4,7].

But, these findings were in a conflict with the kinetic consideration. Specifically, at the temperature $T < 0.6 T_{\text{melt}}$ the absolute inequality $D_{\text{Ti}}C_{\text{Ti}} \ll D_{\text{O}}C_{\text{O}}$ is satisfied (here: D and C are diffusivity and concentration of Ti and O) [8]. It means that the growth of IOZ should be controlled by the titanium diffusion. Inasmuch as Ti atoms are almost immovable at this temperature, the nature of mass transfer of components and mechanism of TiO precipitation in the inner oxidation zone (IOZ) should be clarified. It is known that at $T = (0.5-0.6)T_{\text{melt}}$ the diffusion of interstitial impurities occurs predominately along the boundaries [9]. Because of the oxygen diffusion along the boundaries, the grains are subjected to a specific osmotic pressure. Even at relatively low content of impurities (0.1-1.0%), this pressure is assessed to be tens or hundreds atmosphere [9]. It is sufficient to generate the mobile dislocations (flow j_d), which transfer the oxygen atoms (flow j_o) into the grain (Figure 4). When oxygen attains its limit, the vanadium lattice becomes ordered ($\alpha \rightarrow \alpha'$). Ti-atoms are shifted no more than an interatomic distance. The ordered position of Ti and O atoms initiates the coherent Ti-O oxides ($\alpha' \rightarrow \text{TiO}_2$). The coherent precipitates add the inner stresses in the lattice and trigger an autocatalytic process of precipitation: fresh dislocations produced new oxides, etc. As a result, a net structure with very high precipitate density is formed in the IOZ.

According to the proposed model (Figure 4), the non-equilibrium defects play an important role in the creation of IOZ. They promote the penetration oxygen into the grain, contribute to the $\alpha \rightarrow \alpha' \rightarrow \text{TiO}$ transformation and keep oxygen in solid solution, perhaps as Ti-defect-O complexes. That is why the samples maintain a high level of hardness and abrupt gradient on the HV profiles after prolonged vacuum annealing (see Figure 1, stage 2). Different structural investigations (XRD, TEM, internal friction, measuring of diffusion parameters) of internally oxidised refractory metals showed that the saturated solid solution transforms to an ordered structure involving a complex of atom of alloying metal (Ti, Zr, Hf), non-metallic impurity (O, N, C) and structure defects (dislocations and vacancies) as well. Such non-equilibrium structure is stable at $T \leq 0.5-0.6 T_{\text{melt}}$ [8]. The following tests in Li(Er) showed that only TiO net-structure ensures the formation of Er₂O₃-layer on the surface of the charged V alloy [5,6].

Figure 4. Mechanism of the inner oxidising zone formation in V-4Ti-4Cr at 973 K



According to the proposed model (Figure 4), the non-equilibrium defects play an important role in the creation of IOZ. They promote the penetration oxygen into the grain, contribute to the $\alpha \rightarrow \alpha' \rightarrow TiO$ transformation and keep oxygen in solid solution, perhaps as Ti-defect-O complexes. That is why the samples maintain a high level of hardness and abrupt gradient on the HV profiles after prolonged vacuum annealing (see Figure 1, stage 2). Different structural investigations (XRD, TEM, internal friction, measuring of diffusion parameters) of internally oxidised refractory metals showed that the saturated solid solution transforms to an ordered structure involving a complex of atom of alloying metal (Ti, Zr, Hf), non-metallic impurity (O, N, C) and structure defects (dislocations and vacancies) as well. Such non-equilibrium structure is stable at $T \leq 0.5-0.6 T_{melt}$ [8]. The following tests in Li(Er) showed that only TiO net-structure ensures the formation of Er_2O_3 -layer on the surface of the charged V-alloy [5,6].

Deoxidation of V alloy at contact to Li[Er]

Figure 5 shows the Vickers hardness (HV) profiles of V alloy after exposure to Li[Er] at different temperatures. It can be seen, the configuration of HV profiles changes with time in a complicated manner. These changes are associated with the oxygen redistribution and phase transformation in the solid metal under exposure to lithium. In order to evaluate the kinetics of deoxidation the next points (values) were determined on the HV profiles (Figure 6).

The determined values (HV_{10} , S , L_{500}) versus time are presented on the Figure 7. Kinetics of coating growth is also given on these diagrams [3-6]. In general, the coating behaviour at the interface correlates with the changes in the bulk of solid metal represented by HV_{10} , S and L_{500} values. The next significant features of temperature influence should be underlined.

After exposures at 600°C, only a limited amount of oxygen was used to form the thin ($\sim 0.1 \mu m$) coating. The noticeable decreasing of H_{10} and S values and respective increasing of L_{500} zone of oxygen testify that the most part of a stored oxygen was consumed for the first 300 h. Then the rate of oxygen loss decreases. Even after exposure for 750 h the oxygen storage remained similar to exposure for 300 h [Figures 5(a) and 7(a)]. After contact at 650°C for 300 h the oxide coating get thicker ($0.5 \mu m$) at the nearly same characteristic H_{10} , S and L_{500} [Figure 5(b), 7(b)]. That means more effective oxygen

Figure 5. Vickers Hardness (HV) depth profiles in V4Cr4Ti[O] alloy after contact to Li[Er] for 0, 20, 100, 300 and 750 h at 600, 650 and 700°C [5,6]

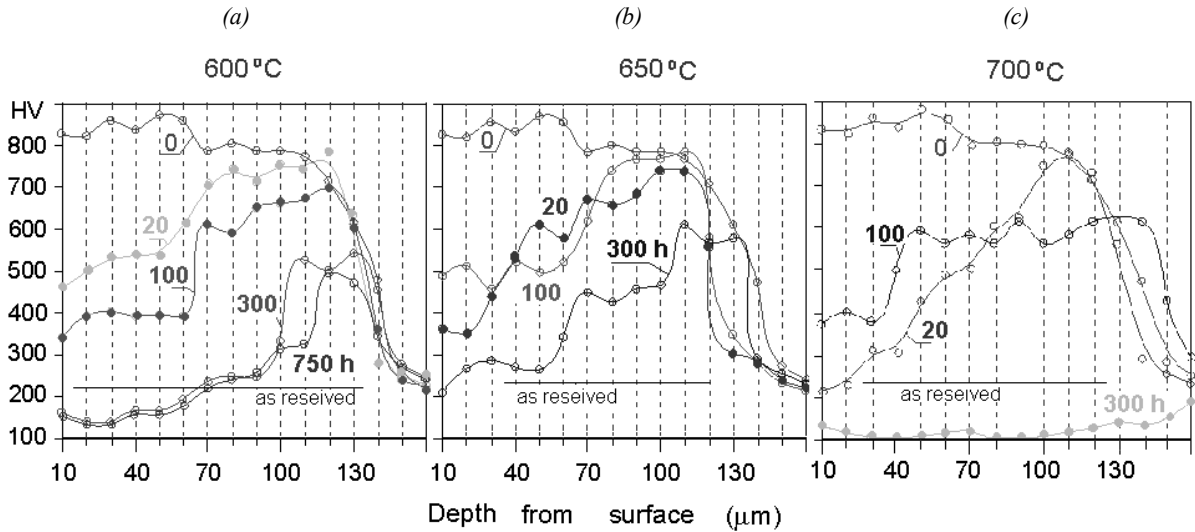


Figure 6. Evaluation of characteristics reflected the state of V alloy after contact with Li[Er]

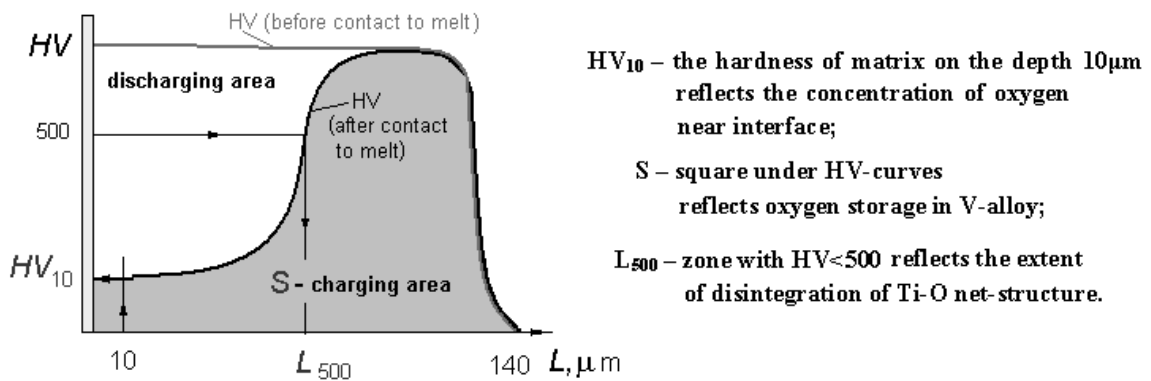
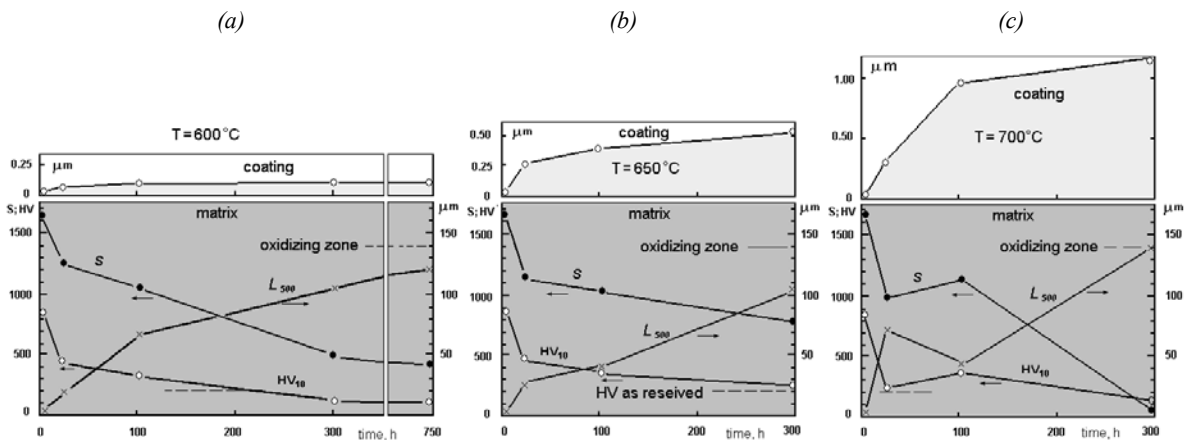


Figure 7. Kinetics of Er₂O₃ growth and deoxidation of V-Cr-Ti-O during the contact with Li[Er]



consumption at 650°C in comparison with 600°C. At last, the temperature 700°C provided the most intensive growth of Er_2O_3 at the interface accompanied by fast depletion of alloy by oxygen. Moreover, a little oxygen diffused deeper into matrix after 100 h exposure [Figure 5(c)]. After 300 h the H_{10} curve reflected surface oxygen concentration dropped to the initial level (before charging procedure) or even lower [Figure 5(c) and 7(c)]. Moreover, judging from L_{500} raise the TiO net structure, which was created previously at charging procedure, vanished after 300 h exposure [Figure 7(c)]. TEM investigation of the under surface region of alloy confirmed that after exposure in $\text{Li}[\text{Er}]$ melt initial TiO net structure dissipated completely [6].

Naturally, the rate of coating formation depends on both O and Er diffusion towards interface. It is known that solubility of Er in Li is very low (nearly 0.15 wt.% at 600°C). Therefore, it is reasonably to suppose that the formation and growth of Er_2O_3 layer at 600°C is controlled by the erbium delivering from the liquid lithium largely than by oxygen diffusion in the solid metal. Very likely, that oxygen redistribution started during the melt heating before the oxide coating could be formed.

Figure 8 illustrates SEM image of cross-section of oxygen-containing V-4Ti-4Cr with Er_2O_3 layer after exposure to $\text{Li}[\text{Er}]$ melt at 700°C for 100 h [4,6]. Figure 1.9 illustrates the mechanism of columnar structure formation in the deoxidising zone during contact V alloy with $\text{Li}[\text{Er}]$. During contact with $\text{Li}[\text{Er}]$ an oxygen atoms dissolves in lithium [Figure 9(a)]. The oxygen-free phase (V-Ti) originates near the initial interface $X = 0$, where the oxygen concentration reduces very quickly. New grain grows in opposite direction (v) where oxygen outflow causes dissipation of TiO net structure. In fact, it is reverse phase transformation relatively to that at charging procedure described above. Therefore, the non-equilibrium defects (dislocations, vacancies, etc.) accumulated in the oxidised zone at charging procedure release and rearrange creating the new grain boundaries [Figure 9(b)]. Since the lattice diffusion of oxygen is hindered at 600-700°C the new diffusion paths are primary importance in delivering of oxygen from the bulk to the interface to keep the integrity of Er_2O_3 coating.

Thus, due to high density of TiO (as the sources of oxygen) and structure defects (as the paths for oxygen diffusion) the oxygen concentration required for Er_2O_3 coating can be provided at the interface.

Consequently, as applied to *in situ* oxide coatings the essence of the V-4Ti-4Cr treatment by oxygen is to form the non-equilibrium structure contained both oxygen and defects.

Therefore, the charging procedure of alloy should be implemented in the restricted temperature interval around 1 011 K (923-1 023 K). On the one hand, the lower temperature ($T < 923$ K) is unacceptable because of hampering of diffusion processes. This temperature should be sufficient for

Figure 8. SEM image of cross-section of V-4Ti-Cr alloy with Er_2O_3 coating (a) and underlying deoxidation zone (b) [4,6]

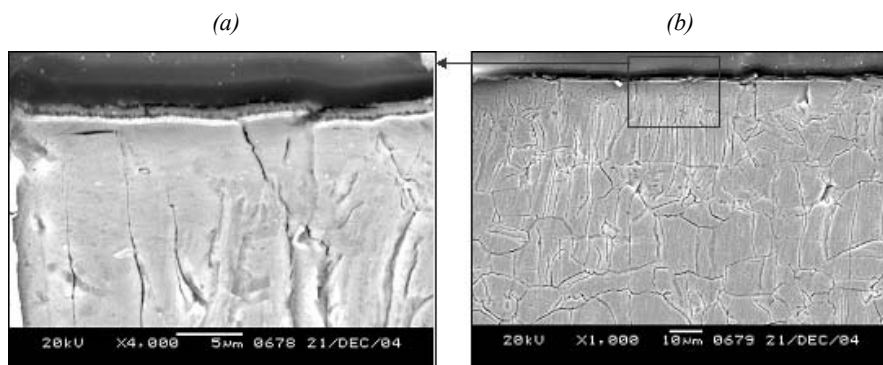
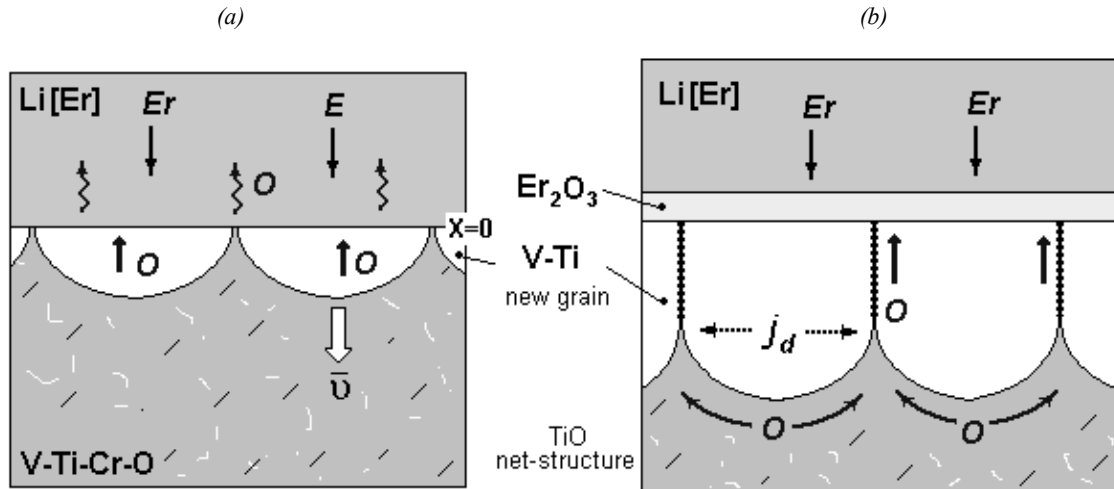


Figure 9. Formation of oxide coating and deoxidation zone in the oxygen containing V-4Ti-4Cr alloy under the contact with Li[Er] melt



oxygen diffusion along grain boundaries, producing mobile dislocations and thereby TiO precipitation in the grains. On the other hand, such kind of structure cannot be formed at the higher temperature (1 173, 1 273 K), where the bulk diffusion is more active, osmotic pressure decreases and the recovery process does not allow accumulate the defects in the oxidation zone.

Conclusions

Oxidising of V-4Cr-4Ti in the Ar+O₂ flow at 973-1 273 K was investigated. Mechanism of interaction between V alloy and gaseous medium alters at around 1 011 K. At $T \leq 1\,011$ K oxygen diffusion is accompanied with fine TiO precipitation limiting the deeper oxygen penetration into alloy. The growing of oxidised zone and content of oxygen in the alloy obeys parabolic law. At $T > 1\,011$ K the interaction process is limited by oxygen absorption in the vanadium matrix.

The charging procedure of V-4Ti-4Cr by oxygen should be implemented in the restricted temperature interval (923-1 023 K), where the diffusion of oxygen along the grain boundaries occurs producing mobile dislocations and TiO precipitation in the bulk of grains.

Severe restriction of temperature interval and oxygen partial pressure at pre-oxidising stage necessitates the following vacuum annealing at 973 K to reduce the surface oxygen concentration and extend the inner oxidation zone.

The deoxidation of charged V alloy at contact to Li[Er] is considered as a diffusion process accompanied by both surface reaction and phase-structural transformation in the bulk of alloy. Upon contact to the melt the oxygen dissolves in lithium reacting with erbium $Er_{(Li)} + O_{(V)} = Er_2O_3$. The lack of oxygen in solid solution provokes the Ti-O oxides dissociation and unblocking of non-equilibrium defects (dislocations, vacancies and other). Owing to the high density of TiO precipitation (as oxygen sources) and released structure defects (as paths for short oxygen diffusion) the Er₂O₃ coating can be formed on the V alloy.

Interaction of Fe-based alloys with Pb/Pb-Bi[O] melts

Generalisation of experimental results

The analysis of experimental results [10-38] indicate that regardless of the oxidising medium (Pb or Pb-Bi) and composition of steels the interaction, in general, is accompanied by the formation of the duplex scale composed of magnetite, providing that the oxidation potential of a liquid metal corresponds to the region between a thermodynamic stability of PbO and Fe₃O₄ oxides ($\sim 10^{-3} \dots 10^{-7}$ wt.% O). It was noticed that the complex oxide grows symmetrically with regard to the initial “solid metal/liquid metal” interface ($X = 0$) towards the melt and the base material simultaneously (Figure 10). The symmetry of growth is typical for the duplex scale, even if it is discontinuous (Figure 11). The outer columnar layer consists of magnetite (Fe₃O₄), while the inner oxide layer is composed of Cr-rich spinel Fe_{1+x}Cr_{2-x}O₄ (+ Ni for the austenitic steels). The inner oxidation zone (IOZ) demarcates usually the spinel and matrix and represents a vanguard of a propagation of an inner oxidation front into the bulk of steels. It is believed that the selective oxidation of elements (Cr, Si, Ti, etc.) with high affinity to oxygen than Fe occurs in the IOZ. With increasing temperature, concentration of oxygen in the liquid metal and exposure time the morphology, phase and elemental composition of the duplex scale change and get complicated: it becomes porous and permeable for liquid metal. For example (Figure 12), the thin ($\sim 3 \mu\text{m}$) Cr(Si)-rich oxide film was formed on the surface of EP823 steel under “low” oxygen concentration (10^{-5} wt.% O, 1 000 h) in the liquid Pb, while the thick ($\sim 300 \mu\text{m}$) magnetite scale totally penetrated by Pb was formed under “high” oxygen content (10^{-3} wt.% O, 50 h) [25,38]. It should be underlined that the penetration of the melt components (Pb and Bi) into the scale has a selective manner (Figure 13) [35,36]. The separation of eutectic components during scale growth occurs probably by the reaction-diffusion mechanism between clusters [Pb-O] existing in the melt and Fe-O oxides resulting in the formation of complex oxides (plumboferrites), especially under the high oxygen activity ($a_{\text{O}} \rightarrow 1$) in the melt [38]. Bismuth has less affinity to oxygen than Pb and therefore it accumulates in the pores of the scale [36]. The following rise in the defectiveness of the duplex scale leads to the penetration of liquid metal to the “scale/matrix” interface. As a result the exfoliation of scale often happens and the double oxide layer starts to form over again at the best [Figure 14(a)]. At worst, the melt, probably free of oxygen, reaches the steel surface and causes the dissolution of steel components accompanied by the penetration of the liquid metal into the steel core [Figures 14(b),14(c)].

Thus, the aforementioned data indicate that the nature of double oxide layer formation is complex and includes many stages. In spite of variety of existed data obtained under different experimental conditions it is worthwhile to connect the determined facts in order to elucidate the evolution of the double oxide layer at the different stages of interaction. However, there are some controversial points, which should be discussed additionally.

Figure 10. Morphology of scales formed on the surface of Fe-based materials during the contact with Pb melt (10^{-3} wt.% O) at 550°C

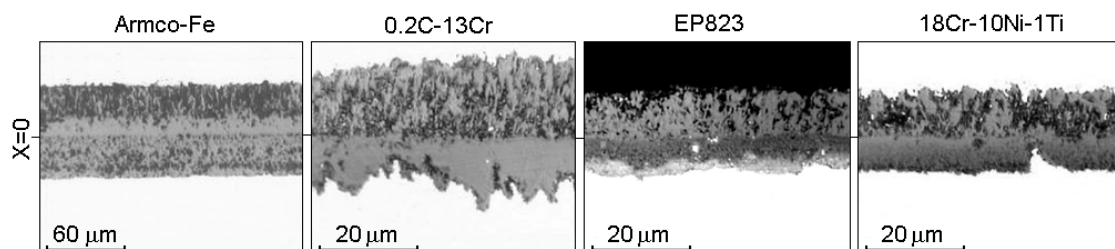


Figure 11. Lateral growth of duplex scale

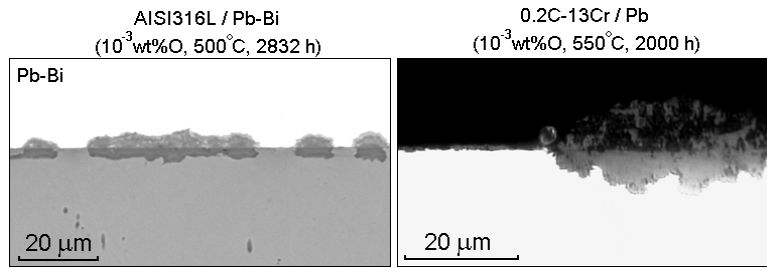


Figure 12. Influence of oxygen concentration on the intensity of oxidation of EP823 in Pb at 650°C

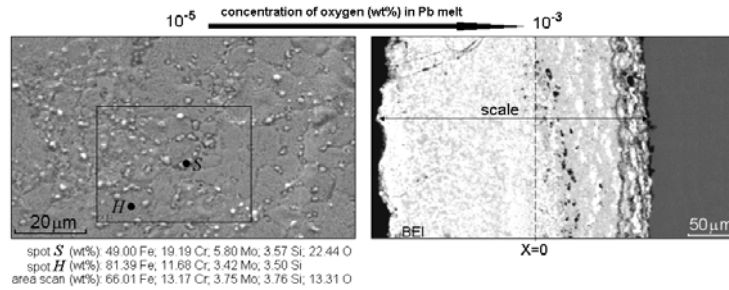


Figure 13. Selective penetration of liquid metal components (Pb and Bi) into the duplex scale

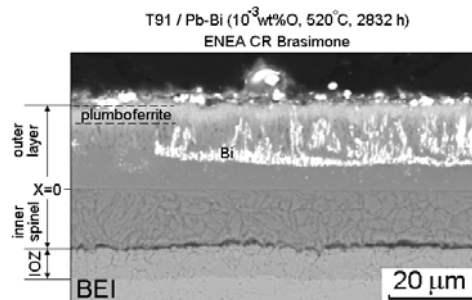
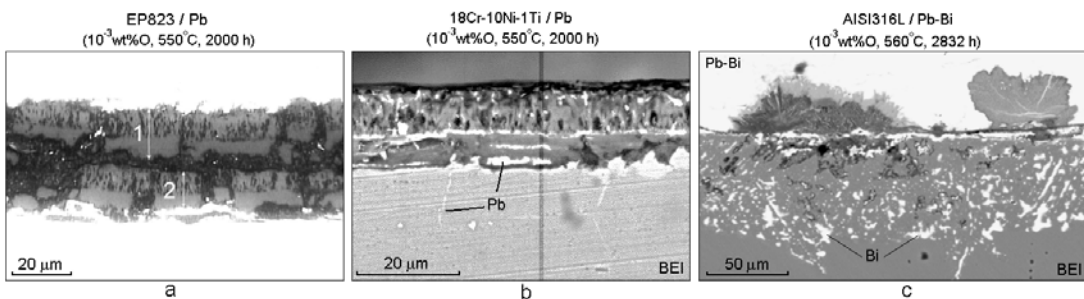


Figure 14. Degradation of duplex scale



First of all, the determined experimental fact, that the scale grows at the both the “scale/melt” and the “scale/matrix” interfaces, assumes the diffusion of oxygen into the iron matrix. However, the mechanism of oxygen diffusion into steel is questionable, since the oxygen diffusivity and solubility in the iron is too low (0.0006 mass.% at 700-850°C). Moreover, the magnetite spinel is a *p*-type oxide, which permits the diffusion of cations only [39]. Therefore, it is believed, the diffusion paths (grain boundaries and sub-boundaries, voids, pores, etc.) promote the fast oxygen delivery towards the

“scale/matrix” interface and intensify the growth of the inner spinel [39]. However, according to the performed evaluations [31], the diffusion of oxygen along the diffusion paths is also slow to provide the intensive inner oxide layer growth in the oxygen-containing liquid metals. Martinelly, *et al.* [35] performed the numerical calculation and proposed that the fast growth of the scale can be simulated by oxygen diffusion along the channels filled by Pb-Bi. In this case the oxygen diffusivity in liquid metal can be used ($D_{O[Pb]} \sim 10^{-6} \text{ cm}^2/\text{s}$). However the question arises why the diffusion of iron in Pb-Bi channels is ignored and only the bulk diffusion of iron cations through the magnetite was taken into account as a limiting factor. It is known [11], that the iron diffusivity in liquid metals ($D_{Fe[Pb]} \sim 10^{-6} \text{ cm}^2/\text{s}$, $D_{Fe[Bi]} \sim 10^{-8} \text{ cm}^2/\text{s}$) is well above than those corresponding to magnetite ($D_{Fe[Fe_3O_4]} \sim 10^{-12} \dots 10^{-20} \text{ cm}^2/\text{s}$). On our opinion, this approach is suitable for long-term exposure, when the liquid metal damages the duplex scale. However, experimental results indicate that the growth rate of the duplex scale is very high even if scale is free from the liquid metal (e.g. at the initial stages of interaction and/or under oxygen-controlled conditions). Zhang and Li [31] also exclude the fast growth of the spinel due to the oxygen diffusion along the porous channels filled in liquid metal.

Kinetic model of double oxide layer growth

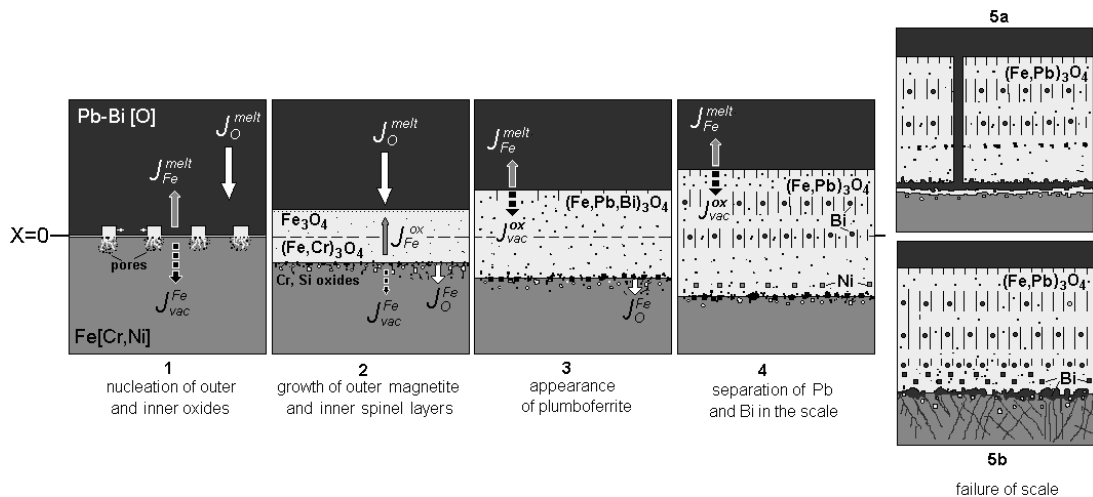
Using the obtained results and literature data [10-38] the oxidation process of steel in the lead melts doped by oxygen can be represented as the following main stages (Figure 15). At the first stage of interaction (Figure 15, stage 1) the iron atoms transfer through the initial interface ($X = 0$) into the melt (flow J_{Fe}^{melt}) and the magnetite islands arise due to the surface reaction among the iron and both [O] and [Pb-O] quasi-oxides dissolved in the melt by the following reactions: $3Fe(s) + 4[O] (\text{melt}) = Fe_3O_4 (s)$; $3Fe(s) + 4[PbO] = Fe_3O_4 (s) + 4Pb$.

The J_{Fe}^{melt} flow towards the melt causes the counter-flow of cation vacancies (J_{vac}^{Fe}). A condensation of vacancies at the defects (grain boundaries, twins, etc.) causes the formation of porous zone in the matrix beneath the interface $X = 0$. The oxygen penetrates into the formed pores (flow J_O^{Fe}), reacts with metal ($Me = Fe, Cr$) resulting in the formation of Cr-oxides and then spinel beneath the magnetite: $[O] + Me = MeO$; $3MeO + [O] = Me_3O_4$.

The islands of the outer magnetite and the inner spinel grow laterally along the $X = 0$ up to the formation of a continuous double oxide layer. During the lateral growth the main reacting components (Fe and O) diffuse easily enough along the outer “oxide/melt” and inner “oxide/matrix” phase boundaries. At this stage the oxidation obeys probably the linear or even quadratic law that is typical for the lateral growth of new surface phases [39].

At the *second stage* the formation of scale occurs at both “scale/melt” and “scale/matrix” interfaces (Figure 15, stage 2). The pores formed at the “spinel/matrix” interface hamper the motion of cations towards the melt. As a result, the magnetite becomes non-stoichiometric: the relative content of oxygen dominates in it. Both the growing porosity and the excess of oxygen promote the dissociation of oxide and the infill of the pores with oxygen (flow J_O^{Fe}). Now the spinel can grow due to the oxidation reaction occurring inside the pores. In this way the self-healing of pores takes place. As an effect, the integrity of the inner part of scale is restored and the diffusion of iron cations towards the melt renews. This leads to the appearance of new pores at the inner “scale/matrix” interface, their self-healing, etc. Thus, at this stage the defectless duplex scale grows owing to diffusion of cations towards the outer interface. The pores appear and self-heal permanently at the inner interface. The pores are closed and separated from the Pb-Bi melt and therefore the liquid metal does not penetrate into the pores. The growth of all scale is controlled by the transversal diffusion of iron cations and obeys the parabolic law.

Figure 15. Evolution of duplex scale on the steel during the contact with Pb-Bi [O] melt



Third stage. As the scale becomes thicker, the time of delivering of iron cations towards the outer interface increases (Figure 15, stage 3). Thus, the activity of iron at outer interface decreases gradually. Therefore the solid-phase reaction between magnetite and oxides of liquid metal (Pb) becomes possible. As a result the plumboferrites can form at the outer interface [11,18,36]. The general formula of plumboferrite can be represented as $m(\text{Fe}_{1-x}\text{Pb}_x)\text{O}\cdot n(\text{Fe}_{2-y}\text{Bi}_y)_2\text{O}_3$. In this compound the places of vacancies in the sublattice of wustite are occupied by the bivalent lead while trivalent bismuth associates with the sublattice of hematite. The main peculiarity of this stage lies in the variability of iron concentration at the interface(s). Therefore, the parabolic law assuming the constancy of concentrations at the interface(s) is being violated.

At the *fourth stage* the simultaneous growth of magnetite and plumboferrite take place (Figure 15, stage 4). As the growth of plumboferrite is accompanied by the diffusion of iron cations (Fe^{+2} , Fe^{+3}) through the scale, the substitution reaction can occur: the iron atoms replace the liquid metal atoms. The bismuth, as a more passive element, is forced out in the first place, while lead remains in the oxide composition. The possibility of realisation of such mechanism is confirmed by the distribution of lead and bismuth through the outer oxide layer: the concentration of iron decreases gradually while the concentration of lead increases towards the melt; bismuth is generally observed at the local spots [36]. Thus, during this stage the pure bismuth accumulates in the pores of scale by means of the aforesaid mechanism. As the scale grows, the oxygen activity decreases at the inner interface. As a result, the pressure in the pores becomes insufficient for oxidation of iron and a fortiori of nickel. Therefore, the non-oxidised islands of metal and the non-healed pores remain in the inner spinel layer, while the oxygen diffusion zone (ODZ) extends into the matrix.

At the *fifth stage* the unhealed porosity and accumulation of bismuth (lead) in the scale result in the violation of mass exchange and cause the failure of scale (Figure 15, stage 5). The rapid growth of pores results in the appearance of channels filled with liquid metal and scale exfoliation (Figure 15, stage 5a). When the pure bismuth accumulates in the scale the selective dissolution of non-oxidised areas, accompanied by penetration of Bi into the matrix, occurs (Figure 15, stage 5b).

During the growth of duplex scale all stages of interaction will occur. The duration of each stage depends on temperature and oxygen concentration in the liquid metal. The main task is to extend the stage corresponding to the protective operation of oxide layer (Figure 15, stage 2), short the kinetic dangerous stage 1 and exclude stages 3-5. This can be achieved by the co-ordinated influence on the liquid and solid metals.

Numerical calculations

The time dependence of the iron diffusivity in a magnetite must be taken into account in order to simulate analytically the interaction in Fe/Pb[O] system. This is caused by a gradual accumulation of the various defects in the scale. The growth of scale is defined by the total flow (j_{Fe}) of bivalent and trivalent iron cations. With time, the defects filled in liquid metal are accumulated in the magnetite scale. In this case the diffusion occurs by means of two ways: by slow bulk diffusion with diffusivity D_1 and by fast diffusion along the paths containing liquid-metal with diffusivity D_2 . Therefore, the diffusion of iron can be described by the following differential equations system:

$$\begin{aligned} D_1 \Delta C_1 &= \partial C_1 / \partial \tau + k_1 C_1 - k_2 C_2 \\ D_2 \Delta C_2 &= \partial C_2 / \partial \tau - k_1 C_1 + k_2 C_2 \end{aligned} \quad (1)$$

here C_1 and C_2 are concentrations of iron in the bulk of magnetite and in the fast diffusion paths respectively; k_1 and k_2 are coefficients, which characterise the oxide formation and dissociation. Assuming that $C = C_1 + C_2$ is the total concentration of cations, it is obtained that the equations of system (1) get similar to the Fick's equation. Here, the effective diffusivity of cations (D_{eff}) depends on both the time (τ) and the spatial value (x) in the scale. Assuming that the local chemical equilibrium between bivalent and trivalent iron cations exists, it is obtained that:

$$D_{eff} \Delta C = \partial C / \partial \tau, \text{ here: } D_{eff} = (D_1 k_2 + D_2 k_1) / (k_1 + k_2) \quad (2)$$

Under the non-stationary conditions of mass exchange at the phase boundaries the thickness of scale $Y(\tau)$ can be determined according to the following equation [40]:

$$(Y(\tau))^2 / (2D_{eff}) + Y(\tau) / H = F(\tau) \quad (3)$$

here:

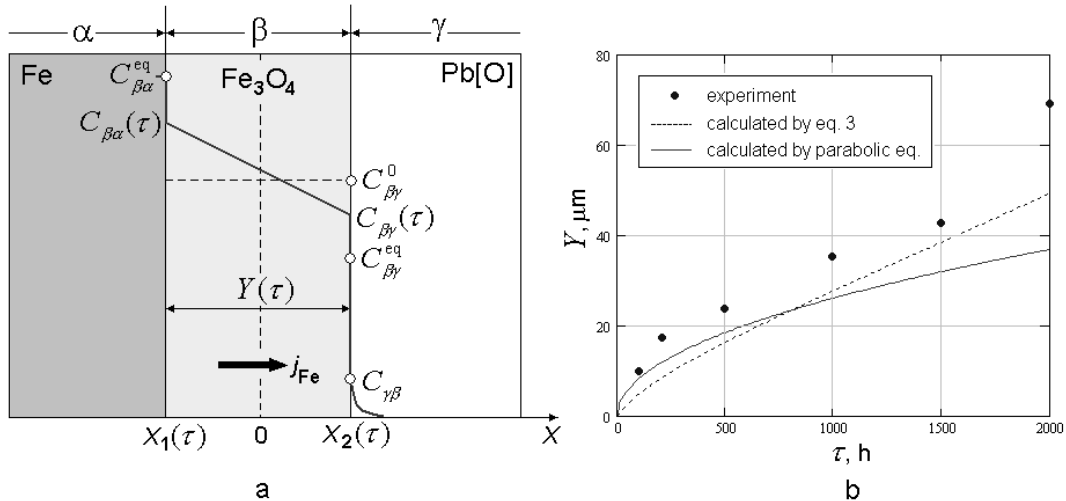
$$F(\tau) = \int_{\tau_0}^{\tau} \frac{C_{\beta\alpha}^{eq} - C_{\beta\gamma}(\tau)}{C_{\beta\gamma}(\tau) - C_{\gamma\beta}} d\tau, \quad C_{\beta\gamma}(\tau) = C_{\beta\gamma}^{eq} - (C_{\beta\gamma}^{eq} - C_{\beta\gamma}^0) \exp(-k_\gamma(\tau - \tau_0))$$

Figure 16(a) shows schematically the concerned system ($\alpha - Fe$; $\beta - Fe_3O_4$; $\gamma - Pb[O]$) and the iron distribution in the magnetite. The coefficient of mass transfer H in Eq. (3) allows to take into account the kinetic barrier (the accumulated pores) for mass exchange at the $x = X_1$ interface. The parameter k_γ characterises the time dependence of iron concentration at the outer $x = X_2$ interface. This dependence is caused by the generation of non-equilibrium cation vacancies and accumulation of the liquid metal components near $x = X_2$.

Figure 16(b) shows the kinetics of growth of the oxide layer (Fe_3O_4). The dotted line was plotted according to the proposed Eq. (3). Solid line represents the parabolic law of scale growth according to the Wagner's model, which postulates the constancy of iron concentrations at the phase boundaries. The curves are plotted using following parameters:

$$\begin{aligned} D_{eff} &\approx 10^{-12} \text{ cm}^2/\text{s}; D_{eff}/H = 0.5 \text{ cm}; k_\gamma = 2 \cdot 10^{-4} \text{ s}^{-1}; \\ C_{\beta\gamma}^0 / C_{\beta\alpha}^{eq} &= 0.5; C_{\beta\gamma}^{eq} / C_{\beta\alpha}^{eq} = 0.5; C_{\gamma\beta} / C_{\beta\alpha}^{eq} = 0.1; k_\gamma = 0.0002 \text{ s}^{-1} \end{aligned}$$

Figure 16. Scheme of kinetic processes in Fe/Pb[O] system (a) and the scale thickness (Y) versus time (τ) (b) formed on the surface of Fe after exposure to Pb (10^{-3} wt.% O) at 550°C



It is evident from the Figure 16(b) that the curve, calculated by Eq. (3), reflects qualitatively the experimental data obtained after exposure of Armco-Fe to Pb melt (10^{-3} wt.% O, 550°C , 2 000 h), but the scale grows faster. It is reasonable to suppose that the magnetite formed in the Pb melt differs essentially from that growing in the gaseous environments by the higher content of non-equilibrium cation vacancies, which ensure the faster diffusion of iron cations.

Conclusions

Based on the generalised experimental results the model demonstrating the main stages of the duplex scale evolution is proposed. The numerical simulation of oxidation of Fe in the Pb melt containing oxygen is carried out. The model takes into account the changing of iron diffusivity in the magnetite because of increasing defectiveness of scale with time. The numerical calculations, in the framework of the proposed model, reflect adequately the oxidation kinetics of Armco-Fe in Pb melt saturated by oxygen at 550°C .

REFERENCES

- [1] *Power Reactors and Sub-critical Blanket Systems with Lead and Lead-bismuth as Coolant and/or Target Material*, IAEA-TECDOC-1348, 1-223 (2003).
- [2] Pint, B.A., *et al.*, *J. Nucl. Mat.*, 329-333, 119-124 (2004).
- [3] Yao, Z., A. Suzuki, T. Nagasaka, T. Muroga, *Mater. Sci. Forum*, 475-479, 1445-1448 (2005).

- [4] Yao, Z., A. Suzuki, T. Muroga, K. Katahira, *J. Nucl. Mater.*, 329-333, 1414-1418 (2004).
- [5] Yao, Z., A. Suzuki, T. Muroga, O. Yeliseyeva, T. Nagasaka, *Fusion Eng. Des.*, 81, 951-956 (2006).
- [6] Yao, Z., A. Suzuki, T. Muroga, T. Nagasaka, *Fusion Eng. Des.*, 81, 2887-2892 (2006).
- [7] Yeliseyeva, O., T. Muroga, A. Suzuki, Z. Yao, A. Lukyanenko, *J. Nucl. Mat.*, forthcoming.
- [8] Korotayev, A., A. Tyumentsev, V. Sukhovarov, "Dispersion Hardening of Refractory Metals, Nauka", *Novosibirsk*, 211 p. (1989) (in Russian).
- [9] Bokstain, B., S. Bokstain, A. Zhukhovitskiy, "Thermodynamic and Kinetic of Diffusion in Solid Bodies", *Metallurgy*, Moscow, 280 p. (1974) (in Russian).
- [10] Eliseeva, O.I., *et al.*, *Materials Science*, 36, 5, 714-722 (2000).
- [11] Blohin, V.A., *et al.*, *Structure, Atomic Dynamics, Thermodynamics and Impurity State of Melts of Lead and Bismuth*, Review IPPE-0290, p. 76 (2000) (in Russian).
- [12] Barbier, F., *et al.*, *J. Nucl. Mat.*, 295, 2-3, 149-156 (2001).
- [13] Soler Crespo, L., *et al.*, 296, 273-281 (2001).
- [14] Barbier, F., A. Rusanov, *J. Nucl. Mater.*, 296, 231-236 (2001).
- [15] Glasbrenner, H., *et al.*, *J. Nucl. Mater.*, 296, 237-242 (2001).
- [16] Fazio, C., *et al.*, *J. Nucl. Mater.*, 296, 243-248 (2001).
- [17] Benamati, G., *et al.*, *J. Nucl. Mater.*, 301, 23-27 (2002).
- [18] Carbuicchio, M., *et al.*, *Hyperfine Interactions*, 141-142 (1-4), 403-408 (2002).
- [19] Kurata, Y., *et al.*, *J. Nucl. Mater.*, 301, 28-34 (2002).
- [20] Muller, G., *et al.*, *J. Nucl. Mater.*, 301, 40-46 (2002).
- [21] Briceño, D.G., *et al.*, *J. Nucl. Mat.*, 303, 2-3, 137-146 (2002).
- [22] Tsisar, V.P., *et al.*, *Materials Science*, Vol. 39, No. 4, 539-544 (2003).
- [23] Abramov, V.Ya., *et al.*, *Report on the ICON-11*, Tokyo, Japan (2003).
- [24] Matychak, Ya., *et al.*, *Defect and Diffusion Forum*, 237-240, 733-738 (2004).
- [25] Eliseeva, O.I., *et al.*, *Materials Science*, Vol. 40, No. 2, pp. 260-269 (2004).
- [26] Johnson, Allen J., *et al.*, *J. Nucl. Mat.*, 328, 2-3, 88-96 (2004).
- [27] Furukawa, T., *et al.*, *J. of Nucl. Sci. and Techn.*, 41, 3, 265-270 (2004).

- [28] Müller, G., *et al.*, *J. Nucl. Mat.*, 335, 2, 163-168 (2004).
- [29] Soler, L., *et al.*, *J. Nucl. Mat.*, 335, 2, 174-179 (2004).
- [30] Martín-Muñoz, F.J., *et al.*, *J. Nucl. Mat.*, 335, 2, 194-198 (2004).
- [31] Zhang, J., *et al.*, *J. Nucl. Mat.*, 336, 1, 1-10 (2005).
- [32] Kurata, Y., *et al.*, *J. Nucl. Mat.*, 343, 1-3, 333-340 (2005).
- [33] Martín-Muñoz, F.J., *et al.*, CD-R of EUROCORR-2005.
- [34] Soler, L., *et al.*, CD-R of EUROCORR-2005.
- [35] Martinelli, L., *et al.*, CD-R of EUROCORR-2005.
- [36] Yeliseyeva, O., *et al.*, CD-R of EUROCORR-2005.
- [37] Kondo, M., *et al.*, *J. Nucl. Sci. and Tech.*, Vol. 43, No. 2, 107-116 (2006).
- [38] Yeliseyeva, O., V. Tsisar, *The Journal of Cor. Sci. and Eng.*, 7, Paper 37 (2006).
- [39] Kofstad, P., *High Temperature Corrosion*, Elsevier, p. 206 (1988).
- [40] Matychak, Ya.S., *et al.*, *Metallofiz. Noveishie Tekhnol.* 21, 2, 78-83 (1999).

MODELLING OF PELLETT CLADDING INTERACTION DURING POWER RAMPS IN PWR RODS BY MEANS OF TRANSURANUS FUEL ROD ANALYSIS CODE

Valentino Di Marcello, Lelio Luzzi

Department of Nuclear Engineering, Politecnico di Milano, Italy

Abstract

Pellet-cladding interaction (PCI) in PWR type rods subjected to power ramps was analysed by means of TRANSURANUS (TU) fuel rod performance code. PCI phenomena depend on the fuel power history – i.e. by several irradiation and thermal induced phenomena occurring in the fuel rod and mutually interacting during its life in reactor – and may become critical for cladding integrity under accidental conditions. Ten test fuel rods, whose power histories and post irradiation experiment (PIE) data were available from the OECD/NEA-IAEA International Fuel Performance Experiment (IFPE) database through the Studsvik SUPER-RAMP Project, were simulated by TRANSURANUS. During a power ramp pellet gaseous swelling can be inhibited by cladding pressure and can be over-predicted by a normal operation swelling model. This phenomenon was simulated by a new formulation of a fuel swelling model already available in the code, in order to consider hot pressing of inter-granular fuel porosity due to the high hydrostatic stress resulting from PCI: it was found that TRANSURANUS, as a result of the proposed swelling formulation as well as of the accurate modelling of the other phenomena occurring during irradiation, gives correct predictions on PCI induced fuel rod failures. In addition, PCI failure threshold identified by TRANSURANUS was compared with the technological limits known in literature: the possibility of relaxing these limits for low burn-up values and the preponderance of the European fuel rod design in front of PCI emerged from TU analyses. Finally, a good agreement was found between TU evaluations and PIE data, with regard to fission gas release, fuel grain growth, and creep, corrosion and elongation of the cladding.

Introduction

Pellet-cladding interaction (PCI) [1] became a plant operation issue early in the nuclear fuel history [2,3]: it was one of the main failure mechanisms of fuel rods, which prevalently occurred in water cooled reactors during the 1960s and 70s. In the last decades PCI failures occurrence was strongly mitigated, owing to technological improvements on fuel rods (design remedies) as well as to definite power manoeuvrings (operating constraints) [4]: actually, in boiling water reactors (BWR) normal operation transients can bring about situations, in which PCI becomes dangerous, while in pressurised water reactors (PWR) it is critical only during accidental conditions [5]. In this paper the attention will be focused only on PWR type fuel rods. In the last years R&D programmes aimed at extending the discharged burn-up and the residence time of fuel rods in reactor [6], in order to reduce the total mass of spent PWR fuels and the fuel cycle costs. In these conditions PCI is still a fuel reliability concern and could become again a failure mechanism: therefore, it is necessary to guarantee adequate safety margins and to develop the so-called PCI-resistant fuel designs. In this context there are many incentives to progress on PCI modelling [4] and to adopt fuel performance codes [7] in order to understand better the involved phenomena, to rank their relative importance, to justify evolutions of the fuel rod design, and to allow reliable PCI predictions, which will contribute to the reduction and/or suppression of operating constraints, following the progressive introduction of PCI remedy fuel in commercial PWRs.

This paper is aimed at the further verification of the TRANSURANUS fuel performance code [8] as a suitable prediction tool on the behaviour and the PCI failures of PWR fuel rods subjected to very complete irradiation histories, which also contain fast power transients: in the present work validation and refinement of TRANSURANUS have been performed on the basis of post irradiation experiment (PIE) data available from the OECD/NEA-IAEA International Fuel Performance Experiment (IFPE) [9].

Preliminaries

Experimental database

Experimental data were taken from the Studsvik SUPER-RAMP Project [10], which investigated the PCI performance and failure propensity of typical LWR fuel in the form of test rods, when subjected to power ramps, after base irradiation to moderate burn-up. The Project power-ramped 28 individual PWR rods and 16 BWR rods. In this work reference is made to the PWR Subprogram, which consisted of 6 groups of rods with variations in design, material parameters and operative conditions: 19 rods (PK), manufactured by Kraftwerk Union AG/Combustion Engineering (KWU/CE), were base-irradiated in the power reactor KWO at Obrigheim (Germany), while 9 rods (PW) supplied by Westinghouse (W) were base-irradiated in the reactor BR-3 at Mol (Belgium). All rods were subsequently ramp tested in the research reactor R2 at Studsvik (Sweden). The main features of each group are summarised in Table 1.

Through non-destructive examination prior to ramping, measurements during ramping, and non-destructive and selected destructive examinations following the ramping, a wide experimental database is available [10], together with detailed records of fuel rods power histories [11,12].

TRANSURANUS code

Many different codes are available to model the fuel rod behaviour under reactor operation and PCI during power ramps [13-17]. In the present work TRANSURANUS code has been used: it is a

Table 1. Main features of base-irradiated rods in the PWR Subprogram (PK4 group is not used in this work); burn-up and linear heat rating refer to average values [10]

Group	Type	Burn-up [GWd/tU]	Linear heat rating [kW/m]
PK1	Standard	33-36	19-26
PK2	Standard	41-45	17-25
PK4	Standard plus Gd ₂ O ₃	33-34	18-25
PK6	Remedy: large grain	34-37	20-27
PW3	Standard	28-31	12-19
PW5	Remedy: annular pellets	32-33	9-21

well known computer program [18] developed at the Institute for Transuranium Elements (Karlsruhe, Germany) and employed by different licensing authorities as well as by different research and private industry groups. During its development [19,20] great effort was spent on obtaining an extremely reliable and efficient tool, which is easy to handle, exhibits very fast and stable solutions and can be employed for analysing the performance of the fuel rods found in the majority of nuclear reactors, in a wide range of different situations, as given in experiments, under normal, off-normal and accident conditions.

TRANSURANUS (in the following simply called TU) is a quasi two-dimensional code that exploits the superposition of a one-dimensional radial and axial description for the fuel rod thermal and mechanical analysis: it can process several components of strain (elastic, plastic, creep and thermal strains, as well as strains due to cladding growth and to fuel cracking, relocation, densification and swelling) and can be employed, both for steady state and transient analyses, in two different ways: as a deterministic and as a statistical code. TU is a well-structured computer program that consists of a clearly defined mathematical framework, into which are included the materials properties and the detailed models for the description of the intricate and mutually interacting phenomena occurring in the fuel rod during its life in reactor, whilst new data and models can easily be incorporated. The complete set of models and options available in the code is described in the TU Handbook [8]; in the present work deterministic analyses have been performed by means of v1m1j06 version of the code.

Input power histories

TU code calculations were performed coherently along with the power history and coolant conditions from beginning of life to the end of ramp test, using the manufacturing specifications and pre-irradiation characterisation data of the rods [11,12]. An example of base irradiation and power ramp is shown in Figure 1.

PK rods geometry is a short segment of about 390 mm, while PW rods are about 1 135 mm long. In the calculation each geometry is sub-divided into axial slices (three for PK group and six for PW group), on which the linear heat rate and the coolant temperature are given; only for PK rods, the three axial slices are subjected to the same linear power during base irradiation. Ten rods with their relative power histories were chosen from the whole SUPER-RAMP database: two rods for each group, with exception of the PK4 one. This choice is based on maximum severity in terms of conditions during the ramps (Table 2).

Figure 1. Input linear heat rate history during base-irradiation and power ramp for PK1-1 rod

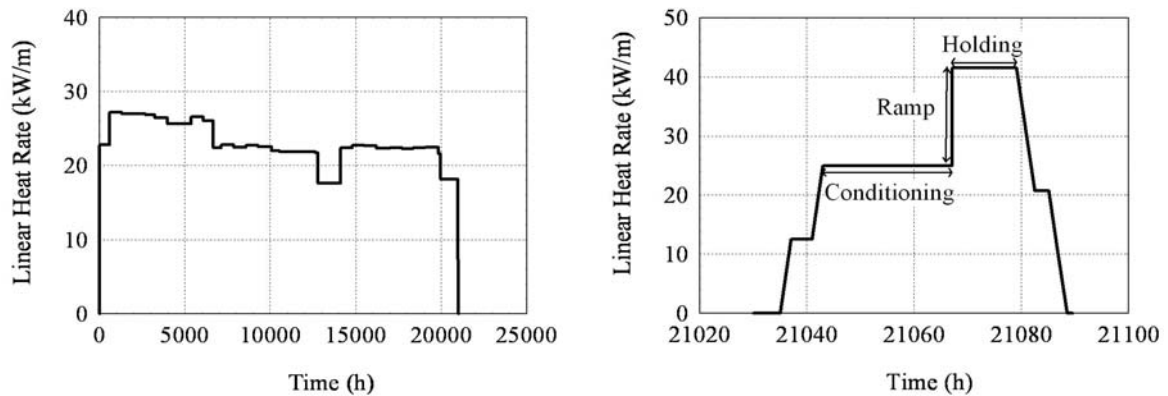


Table 2. Power ramping features in axial peak position of the analysed ten rods: the conditioning power level is the same (25 kW/m), except for PK6-4 rod (25.5 kW/m)

Rod no.	Burn-up [GWd/(tU)]	Power ramp rate [kW/(m·min)]	Ramp terminal level [kW/m]	Holding time [minutes]
PK1-1	35.4	9.0	41.5	720
PK1-4	33.1	9.5	47.5	720
PK2-2	45.1	9.5	46.0	720
PK2-3	44.6	8.5	49.0	720
PK6-3	36.5	9.0	43.0	720
PK6-4	33.6	10	44.0	60
PW3-4	38.6	9.5	37.7	12
PW3-S	35.1	10	40.5	17
PW5-3	41.4	9.0	38.2	38
PW5-4	39.2	8.5	38.0	72

Modelling

TRANSURANUS owns different optional models to describe the phenomena affecting the PWR fuel rod performance and the materials behaviour, i.e. two fission gas release algorithms; six relocation models, five swelling models, three densification models, and six conductivity correlations, for UO₂ fuel; as concerns the cladding in Zircaloy-4 (Zy-4), two correlations are available for creep, five for growth, and three for outer corrosion. On the basis of the SUPER-RAMP PIE database, a systematic sensitivity study was performed [21], so that it was possible to select the best combination of the available TU models and correlations; moreover, a new formulation for the fuel swelling was developed in order to consider hot pressing of inter-granular fuel porosity due to the high hydrostatic stress resulting from PCI.

Materials properties and phenomena models

The materials correlations and the phenomena models not reported here are the TU standard ones for PWR fuel rods, while the best combination found for the others is listed below (for all the details, see the TU Handbook and the reported references).

- Fuel thermal conductivity: Harding and Martin correlation for UO₂ [22], extended to include the effect of burn-up and the gadolinium dependence [8].
- Pellets relocation: modified KWU-LWR model, according to ITU calibration (1999) [8]; it calculates an equivalent deformation, which increases the fuel radius, being TU a non-3-D code.
- Fission gas release (FGR): URGAS algorithm [23], with thermal diffusion coefficient of Matzke [24] and athermal diffusion coefficient according to White [25].
- Gap conductance: URGAP model [26], second revised version by Lassmann (1994) [8], with thermal conductivity of the gas mixture according to Lindsay and Bromley [27].
- Fuel and cladding creep: Lassmann and Moreno correlations [28].
- Cladding growth: Knaab and von Jan correlation for Zy-4 [29]; it gives only the axial strain (the radial and hoop components are set to zero), and depends on the average burn-up in a section.
- Cladding outer corrosion: EPRI/CE/KWU waterside corrosion model [30,31] for PWR conditions; it takes into account several parameters as temperature, time, neutron flux and reaction activation energy.
- Axial PCMI model: no slip condition is assumed for axial pellet-cladding mechanical interaction (PCMI) [32]. This describes a situation characterised by anchorage between pellet and cladding: a static friction exists between them, hence their axial strain is the same when they are in contact.

The models adopted for the fuel swelling and densification as well as for the cladding stress corrosion cracking (SCC) are briefly presented below.

New formulation of a TU fuel swelling model

It is well known the contribution of solid fission products (FP) to the fuel pellet volume variation and its dependence on burn-up, while the gaseous FP swelling is still an open issue [4]: in operative conditions the gaseous contribute is less important [33], while in case of a power transient it becomes preponderant [17] and produces an increase of FGR [34,35]. On the other side, the stress field in the fuel pellet plays a significant role in the fission gas behaviour: the high hydrostatic stress resulting from PCI inhibits gaseous swelling by hot pressing of the inter-granular porosity, and therefore also limits FGR [4]. In this work a further modification of the MATPRO model [36] available in TU for the fuel swelling is proposed. The new formulation is based on the following assumptions: the gaseous contribution to the pellet strain (ε_i) is not considered when pellet and cladding are in contact, whereas the gaseous FP part contributes in increasing fuel porosity (P_{fuel}), even if gap is closed. For every time step (Δt), it means that:

$$\text{if } p_{contact} > 0.1 \text{ MPa} \Rightarrow \Delta V_{Gas} = 0$$

$$\Delta V = \Delta V_{Solid} + \Delta V_{Gas} + \Delta V_{HBS} \Rightarrow \varepsilon_i(t + \Delta t) = \varepsilon_i(t) + \Delta V / 3$$

$$P_{fuel}(t + \Delta t) = P_{fuel}(t) + \Delta V_{Gas}^*$$

where $p_{contact}$ is the contact pressure between fuel and cladding, and ΔV is the total pellet volume change due to solid FP (ΔV_{Solid}), to gaseous FP (ΔV_{Gas}) and to high burn-up structure (ΔV_{HBS}) formation; on the other hand, ΔV_{Gas}^* is the gaseous FP contribution calculated as if the gap had been open. This formulation gives the net result of increasing fuel conductivity degradation, fuel temperature and FGR.

Fuel densification model

The MATPRO fuel densification model [36], available in TU and adopted in this work, takes into account both thermal and irradiation induced densification. It needs as input parameters the initial and minimal porosity, the density, the plutonium concentration and the burn-up of fuel pellet; as regards the thermal contribution, the pellet density change due to the densification test and the sinterisation temperature are requested. Thanks to this model it was possible to describe the different densification behaviour exhibited by the analysed rods, due to their different pellet density increase at thermal densification test [10], and confirmed by their different fuel grain size [37]. Among the input parameters, the critical one (being experimentally not available [10] and playing a significant role in fuel densification behaviour) is the pellet minimal porosity, i.e. its porosity at the end of densification process: in order to establish it, a parametric study [21] on two different rods (PK1-1 and PW5-3) was performed by means of TU code, and the value that appears to describe the two different pellets behaviours resulted equal to 0.04.

Cladding Stress Corrosion Cracking (SCC) model

The TU SCC model [38] assumes that inter-granular phase is due to the chemical environment and depends on the mechanical stress state, while trans-granular phase is described by means of Linear Elastic Fracture Mechanics. The initial propagation of the crack starts only if critical conditions on local burn-up, cladding temperature, strain rate and hoop stress are satisfied; in order to establish the threshold stress intensity factor, K_{ISCC} , this TU model adopts a simple correlation depending on cladding yield strength [8].

Results and discussion

PCI failure predictions

TRANSURANUS code analyses were performed with both the new formulation (TU_mod version) and the MATPRO model available in TU (TU_orig version) for fuel swelling. Thanks to the above presented best selection of models, TU_mod predicts in a correct way the failure behaviour of 8/10 rods, whereas the right predictions with TU_orig are 7/10 (Table 3); in any case the code remains conservative, predicting the failure for those rods, which experimentally resulted not failed [10].

It is worth noting that the PK2 rods, whose failure is erroneously predicted by TU, differ from the others as to the cladding hydrides orientation [10]: in fact, the fraction of hydrides along the radial direction, measured on the inner radius of PK2 claddings, is quite an half in comparison with PK1 and PK4 rods. Many studies [39-41] have demonstrated that the majority of SCC cracks is situated where Zy-4 texture is prevalently circumferential, i.e. where the hydrides are along the cladding radial direction: thus the PK2 claddings have a greater SCC resistance, but TU does not take into account this local effect.

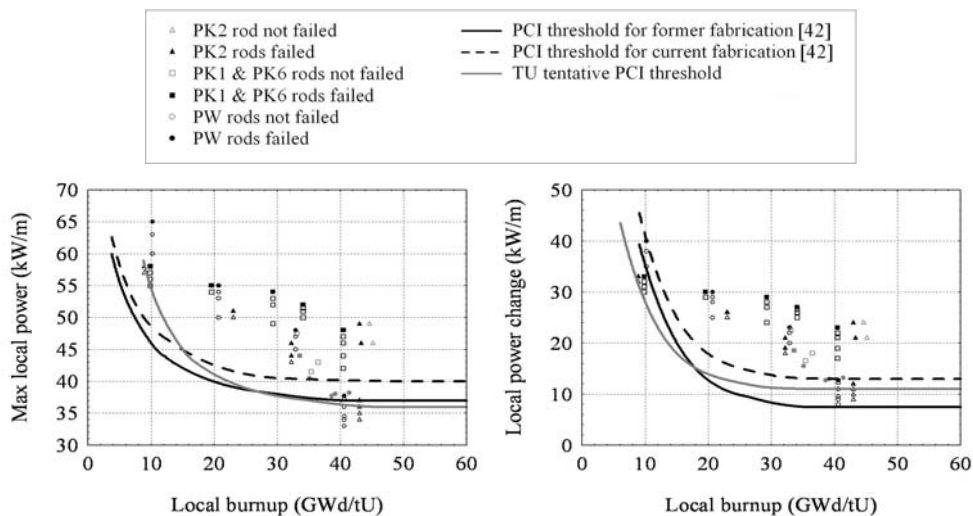
Table 3. Comparison between experimental and TU results: Failed (F) and Not Failed (NF) rods

Rod no.	Experimental (F/NF)	TU mod (F/NF)	TU orig (F/NF)
PK1-1	NF	NF	NF
PK1-4	NF	NF	NF
PK2-2	NF	F	F
PK2-3	NF	F	F
PK6-3	NF	NF	F
PK6-4	F	F	F
PW3-4	F	F	F
PW3-S	F	F	F
PW5-3	F	F	F
PW5-4	F	F	F

Technological limits

Technological limits of PCI are established by power ramp tests and represent the conditions under which rod failure does not occur. These limits can be expressed as the trend of the maximum power or the maximum power change with respect to burn-up [5]. The PCI failure threshold curves as function of burn-up according to Ref. [42] are shown in Figure 2 (the difference of the former and current fabrication stays in the Kearns’ factor of cladding material), together with the tentative PCI threshold achieved comparing TU_mod simulations with experimental data available from the SUPER-RAMP Project. As a result, in terms of maximum local power, TU suggests the possibility of relaxing the technological limits in the lower burn-up region, while it is a little bit more conservative in the higher burn-up zone. This does not happen in terms of local power change: TU threshold remains between the former and current fabrication technological limits in the higher burn-up region, while it is lower up to 17 GWd/tU. TU_mod threshold lower boundary is set by PK2 rods, which should rather obey to the current fabrication limit having a favourable hydrides orientation, as mentioned above; anyway, TU remains conservative, being not able to take into account this effect, which is therefore confirmed only experimentally.

Figure 2. Maximum power and power change during the ramps for experimental data (grey markers) and TU_mod calculations (black markers) compared with the PWR technological limits [42]



Looking at the experimental data in Figure 2, the PW test rods are located under the PK rods and failed during power ramps, though they were subjected to lower power ramp terminal levels in comparison with the PK ones. Moreover, the PCI threshold for current fabrication is not valid for PW rods, unlike the PK ones; this is also confirmed by TU_mod predictions, which suggest that PK1 and PK6 rods can reach higher linear power values in comparison with the PW rods.

The above comparison reveals a better PCI behaviour of the European rods (PK group). In order to explain this difference, the main design and material properties were compared (Table 4). Westinghouse rods (PW) are featured by a design, which brings to a certain worsening of pellet cladding interaction during the irradiation: actually, the higher pellet length and fuel grain size and the lower helium filling pressure and fuel densification likely contributed to their failure; moreover, for the PW5 rod group, the fuel pellet annular form did not compensate the mentioned disadvantages.

Table 4. Main design differences between the representative rods of each group

Design parameters	PK1-1	PK2-3	PK6-4	PW3-4	PW5-3
Rod type	Standard	Standard	Large grain	Standard	Annular
Pellet length [mm]	11.35	11.34	11.1	13.36	13.56
Average fuel grain size [μm]	6	5.5	22	10.5	16.9
Density increase at thermal densification test [g/cm^3]	0.04/2.2 h	0.07/2.2 h	0	0.03/10 h	0.03/10 h
He filling pressure [MPa]	2.25	2.25	2.25	1.38	1.38

Comparison with PIE data

PIE data, available from the Studsvik Report [10], were compared with TU results (Table 5). As far as FGR is concerned, both TU versions give good estimations, allowing to seize its behaviour during power ramps: the values predicted by TU_orig are lower than those achievable by TU_mod, which gives more accurate estimations for 3/5 rods in comparison with PIE data. It is worth noting that FGR is under-estimated for PK2 rods, which reached both higher burn-up and linear heat rate values during the ramp. Experimental values of cladding creep down are under-predicted by the code, but these values were achieved by means of non-accurate measurement – as affirmed in the Studsvik Report [10]. Reasonable predictions of the fuel grain growth were found: the TU_orig version is a little bit more accurate, because the new formulation of fuel swelling tends to enhance the fuel temperatures and its restructuring. As concerns the cladding, TU remains always conservative about the axial elongation, whereas it supplies under-predictions of the outer corrosion in all analysed cases. As final remark, it must be mentioned that a good agreement was found [21] between TU evaluations and literature data with regard to the SCC crack growth and to the value of K_{ISCC} .

Conclusions

The irradiation histories of different PWR fuel rod types, supplied by Westinghouse and KWU/CE, were modelled and analysed by means of the TRANSURANUS code (TU) on the basis of the SUPER-RAMP Project experimental database. TU was refined elaborating a new formulation of an existing model for the fuel swelling; thanks to this correlation and to a systematic study of the different models available in the code for all the other phenomena, it was possible to find the best combination of TU models that gives correct predictions on PCI induced fuel rod failures. Analysing the PCI failure threshold found with TU, it emerged that less restrictive limits may be defined in the

lower burn-up region. In the light of comparison between TU calculations, experimental data and current PCI technological limits, the preponderance of European (KWU/CE) fuel rod design was established: actually, the Westinghouse rods are featured by a design that brings to a certain worsening of pellet cladding interaction during irradiation, such effect being not compensated by the choice of annular pellets. Finally, a good agreement of TU evaluations with PIE data was found in regard to FGR, fuel grain growth, creep down, elongation and corrosion of the cladding.

Table 5. Comparison between the SUPER-RAMP experimental data and the TU results

Rod no.	FGR [%]			Max. cladding creep down [μm]			Grain size [μm]		
	Exp.	TU_mod	TU_orig	Exp.	TU_mod	TU_orig	Exp.	TU_mod	TU_orig
PK1-1	8.5	10.9	8.4	85	45	45	n.a.	–	–
PK1-4	13.0	21.9	17.5	n.a.	–	–	n.a.	–	–
PK2-2	32.1	27.4	23.8	n.a.	–	–	4.4 (P) 42*	5.5 68	5.5 39
PK2-3	44.9	32.6	29.2	75	39	39	n.a.	–	–
PK6-3	6.7	6.5	3.1	n.a.	–	–	23 (P) 25 (C)	22 46	22 26
PW3-4	n.a.	–	–	70	34	34	13 (P) 13 (C)	10.5 10.5	10.5 10.5
PW5-3	n.a.	–	–	50	33	33	17 (P) 21 (C)	16.9 17.2	16.9 17.0
PW5-4	n.a.	–	–	50	32	32	n.a.	–	–
Rod no.	Cladding elongation [mm]			Cladding corrosion layer [μm]			<ul style="list-style-type: none"> – n.a. means “not available” from the Experimental database (Exp.) [10]. – (P) and (C) indicate grain size measurement performed at periphery and centre of fuel pellet. – Cladding elongation measurements are given both before (b.r.) and after (a.r.) power ramp. * PK2-2 grain size comparison was made using measurement performed in the dishing region, where the maximum grain size (to be compared with the TU value) was reached. 		
Exp.	TU_mod	TU_orig	Exp.	TU_mod	TU_orig				
PK2-2	n.a.	–	–	19-38	14.2	14.2			
PK6-3	n.a.	–	–	26-36	9.2	9.2			
PW3-4	4.06 (b.r.) 4.21 (a.r.)	4.77 5.02	4.77 5.02	2-3	1.6	1.6			
PW5-3	3.46 (b.r.) 3.69 (a.r.)	5.17 5.45	5.17 5.45	3.8	1.5	1.5			
PW5-4	3.60 (b.r.) 4.34 (a.r.)	4.88 5.14	4.88 5.14	n.a.	–	–			

Acknowledgements

This work has been performed in the framework of a co-operation between ITU (Institute for Transuranium Elements, Karlsruhe, Germany), ENEA (Italian Agency for new Technologies, Energy and Environment, Bologna, Italy) and Politecnico di Milano. ITU is gratefully acknowledged for the support; special thanks are due to Prof. Klaus Lassmann, Dr. Paul Van Uffelen, Dr. Arndt Schubert and Dr. Jacques van de Laar.

REFERENCES

- [1] Cox, B., “Pellet-clad Interaction (PCI) Failures of Zirconium Alloy Fuel Cladding – A Review”, *Journal of Nuclear Materials*, 172, 249-292 (1990).
- [2] Roberts, J.T.A., *Structural Materials in Nuclear Power Systems*, Plenum Press, New York (1981).
- [3] “Nuclear Materials”, *Materials Science and Technology – A Comprehensive Treatment*, B.R.T. Frost (Ed.), Vol. 10A, Par. 3.6.6, and Vol. 10B, Par. 7.3.3, VCH, Weinheim (1994).
- [4] *Proceedings of the Workshop on Pellet-clad Interaction in Water Reactor Fuels*, OECD/NEA, Aix-en-Provence, France, 9-11 March (2004).
- [5] Bailly, H., D. Ménessier, C. Prunier, *The Nuclear Fuel of Pressurised Water Reactors and Fast Neutron Reactors – Design and Behaviour*, Commissariat à l'Énergie Atomique, Lavoisier Publishing (1999).
- [6] “Nuclear Fuel: Addressing the Future”, *Transactions of Int. Meeting on LWR Fuel Performance (Top Fuel 2006)*, European Nuclear Society, Salamanca, Spain, 22-26 October (2006).
- [7] Aybar, H.S., P. Ortego, “A Review of Nuclear Fuel Performance Codes”, *Progress in Nuclear Energy*, Vol. 46, No. 2, 127-141 (2005).
- [8] Lassmann, K., A. Schubert, P. Van Uffelen, Cs. Györi, J. van de Laar, *TRANSURANUS Handbook*, Copyright ©1975-2006, ITU (Institute for Transuranium Elements), Karlsruhe, Germany (2006).
- [9] Menut, P., E. Sartori, J.A. Turnbull, “The Public Domain Database on Nuclear Performance Experiments (IFPE) for the Purpose of Code Development and Validation”, *Proceedings of International Topical Meeting on LWR Fuel Performance*, American Nuclear Society, Park City, Utah, US, 10-13 April (2000).
- [10] Djurle, S., *The SUPER-RAMP Project. Final Report STUDSVIK-STSR-32*, Studsvik Energiteknik AB, Nyköping, Sweden (1984).
- [11] Turnbull, J.A., *QA Report for Studsvik SUPER-RAMP PWR Subprogramme Database Files* (1997).
- [12] Luzzi, L., *Validation of TRANSURANUS Code on the Basis of the Studsvik Super-Ramp PWR Database Files*, Technical Report JRC-ITU-TN-2002/08, Institute for Transuranium Elements, Karlsruhe, Germany (2002).

- [13] Massih, A.R., T. Rajala, L.O. Jernkvist, “Analysis of Pellet-cladding Mechanical Interaction Behaviour of Different ABB Atom Fuel Rod Designs”, *Transactions of 12th International Conference on Structural Mechanics in Reactor Technology (SMiRT-12)*, Vol. C, pp. 57-68, Elsevier, Amsterdam (1993).
- [14] Berna, G.A., C.E. Beyer, K.L. Davis, D.D. Lanning, *FRAPCON-3: A Computer Code for the Calculation of Steady-state, Thermal-mechanical Behaviour of Oxide Fuel Rods for High Burn-up*, NUREG/CR-6534, Vol. 2, PNNL-11513 (1997).
- [15] Cunningham, M.E., C.E. Beyer, P.G. Medvedev, G.A. Berna, *FRAPTRAN: A Computer Code for the Transient Analysis of Oxide Fuel Rods*, NUREG/CR-6739, Vol. 1, PNNL-13576.
- [16] Brochard, J., *et al.*, “Modelling of Pellet Cladding Interaction in PWR Fuel”, *Transactions of 16th International Conference on Structural Mechanics in Reactor Technology (SMiRT-16)*, Paper no. 1314, Washington, DC, US, August (2001).
- [17] Suzuki, M., H. Uetsuka, H. Saitou, “Analysis of Mechanical Load on Cladding Induced by Fuel Swelling During Power Ramp in High Burn-up Rod by Fuel Performance Code FEMAXI-6”, *Nuclear Engineering and Design*, 229, 1-14 (2004).
- [18] Lassmann, K., “TRANSURANUS – A Fuel Rod Analysis Code Ready for Use”, *Journal of Nuclear Materials*, 188, 295-302 (1992).
- [19] Lassmann, K., H. Blank, “Modelling of Fuel Rod Behaviour and Recent Advances of the TRANSURANUS Code”, *Nuclear Engineering and Design*, 106, 291-313 (1988).
- [20] Lassmann, K., *The TRANSURANUS Code – Past, Present and Future (Review Article)* Annual Report EUR 20252, Institute for Transuranium Elements, Karlsruhe, Germany (2001).
- [21] Di Marcello, V., “Verification and Refinement of the Transurans Code for PCI analyses in PWR Fuel Rods”, Nuclear Engineering Master Thesis (in Italian), Politecnico di Milano (2006).
- [22] Harding, J.H., D.G. Martin, “A Recommendation for the Thermal Conductivity of UO₂”, *Journal of Nuclear Materials*, 166, 223-226 (1989).
- [23] Lassmann, K., H. Benk, “Numerical Algorithms for Intragranular Fission Gas Release”, *Journal of Nuclear Materials*, 280, 127-135 (2000).
- [24] Matzke, H.J., “Gas Release Mechanisms in UO₂ – A Critical Overview”, *Radiation Effects*, 53, 219-242 (1980).
- [25] White, R.J., “A New Mechanistic Model for the Calculation of Fission Gas Release”, *Proceedings of International Topical Meeting on LWR Fuel Performance*, pp. 196-202, American Nuclear Society, West Palm Beach, Florida, US (1994).
- [26] Lassmann, K., F. Hohlefeld, “The Revised URGAP Model to Describe the Gap Conductance Between Fuel and Cladding”, *Nuclear Engineering and Design*, 103, 215-221 (1987).
- [27] Lindsay, A.L., L.A. Bromley, “Thermal Conductivity of Gas Mixtures”, *Industrial and Engineering Chemistry*, 42, 1508-1511 (1950).
- [28] Lassmann, K., A. Moreno, “The Light-water-reactor Version of the URANUS Integral Fuel-rod Code”, *Atomkernenergie (ATKE)*, Bd. 30, Lfg. 3, pp. 207-215 (1977).

- [29] Knaab, H., R. von Jan, “Fuel Performance Evaluation and Improved Fuel Utilization by Pool-side Fuel Services”, *Proceedings of International Topical Meeting on LWR Fuel Performance*, pp. 1-48, American Nuclear Society, Orlando, Florida, US (1985).
- [30] Garzolli, F., *et al.*, *Waterside Corrosion of Zircaloy Fuel Rods*, EPRI-NP-2789 (1982).
- [31] Pyecha, T.D., *et al.*, “Waterside Corrosion of PWR Fuel Rods through Burn-ups of 50 000 MWd/mtU”, *Proceedings of International Topical Meeting on LWR Fuel Performance*, American Nuclear Society, Orlando, Florida, US (1985).
- [32] Lassmann, K., *Treatment of Axial Friction Forces in the TRANSURANUS Code* Report EUR 13660 EN, pp. 185-202, Institute for Transuranium Elements, Karlsruhe, Germany (1991).
- [33] Lanning, D.D., C.E. Beyer, C.L. Painter, *FRAPCON-3: Modifications to Fuel Rod Material Properties and Performance Models for High Burn-up Application*, NUREG/CR-6534, Vol. 1, PNNL-11513 (1997).
- [34] Kogai, T., “Modelling of Fission Gas Release and Gaseous Swelling of Light Water Reactor Fuels”, *Journal of Nuclear Materials*, 244, 131-140 (1997).
- [35] Koo, Y.H., B.H. Lee, D.S. Sohn, “Analysis of Fission Gas Release and Gaseous Swelling in UO₂ Fuel under the Effect of External Restraint”, *Journal of Nuclear Materials*, 280, 86-98 (2000).
- [36] *MATPRO-Version 11, A Handbook of Material Properties for Use in the Analysis of Light Water Reactor Fuel Rod Behaviour*, NUREG/CR-0497 TREE-1280 (1979).
- [37] Une, K., M. Hirai, K. Nogita, T. Hosokawa, Y. Suzawa, S. Shimizu, Y. Etoh, “Rim Structure Formation and High Burn-up Fuel Behaviour of Large-grained UO₂ Fuels”, *Journal of Nuclear Materials*, 278, 54-63 (2000).
- [38] Mattas, R.F., F.L. Yaggee, L.A. Neimark, “Iodine Stress-corrosion Cracking in Irradiated Zircaloy Cladding”, *Proceedings of International Topical Meeting on Light Water Reactor Fuel*, CONF-790441-7, American Nuclear Society, Portland, Oregon, US (1979).
- [39] Sidky, P.S., “Iodine Stress Corrosion Cracking of Zircaloy Reactor Cladding: Iodine Chemistry (A Review)”, *Journal of Nuclear Materials*, 256, 1-17 (1998).
- [40] Nikulin, S.A., A.B. Rozhnov, “Corrosion Cracking of Zirconium Cladding Tubes (A Review) – I. Methods of Study and Mechanisms of Fracture”, *Metal Science and Heat Treatment*, 47, 71-79 (2005).
- [41] Murty, K.L., I. Charit, “Texture Development and Anisotropic Deformation of Zircaloys (Review)”, *Progress in Nuclear Energy*, 48, 325-359 (2006).
- [42] Kosaka, Y., N. Fukuda, T. Sendo, “Investigation of the High Burn-up Rim Structure in the PWR Fuel Pellet”, *Transactions of International Meeting on LWR Fuel Performance (Top Fuel 2006)*, pp. 163-172, Salamanca, Spain, 22-26 October (2006).

**MATERIALS DEMAND FOR FUSION POWER PLANTS:
IAEA PROJECTS, INITIATIVES AND DATABASES**

**R.E.H. Clark, G. Mank, N. Dytlewski, D. Humbert,
A. Malaquias, A. Mengoni, F. Mulhauser, A.L. Nichols, A. Stanculescu**
International Atomic Energy Agency, Vienna, Austria

Abstract

Use is made of a broad range of structural materials within nuclear power plants, accelerator-driven systems (ADS), spallation sources and fusion devices. Therefore, the International Atomic Energy Agency (IAEA) includes many of the most important aspects of materials research in atomic and nuclear programmes designed to assist member states in their related studies of such systems. These specific activities in nuclear fusion research and applications are described in this paper, while IAEA activities related to advanced materials development and fuel performance analysis in fission are covered in a separate paper.

Introduction

The primary goal of the International Atomic Energy Agency (IAEA) is to promote peaceful uses of nuclear energy. Many specific programmes included in this wide-ranging objective require materials properties data, and the IAEA co-ordinates research in such areas to fulfil this important need. Three main programmes of this type are discussed below: Databases for Materials Research, Materials Research for Fusion, and Materials Research for Accelerator-driven Systems (ADS).

Databases for materials research

The Atomic and Molecular (A+M) Data Unit of the Nuclear Data Section has the goal to establish databases for atomic, molecular and plasma-material interaction data in support of fusion energy research. With the ITER agreement in place (International Thermonuclear Experimental Reactor), materials properties have become issues of significant importance for fusion energy studies. Therefore, the A+M Unit sponsors and undertakes projects designed to generate information on a number of issues related to plasma-facing materials most likely to be used in ITER and other fusion devices.

A+M activities are reviewed and new projects suggested by the Subcommittee on Atomic Physics of the International Fusion Research Council (IFRC), which meets every two years to make recommendations for the following two-year budget cycle of the IAEA. The A+M Unit also supports a Data Centre Network (DCN), consisting of 11 data centres with strong links to fusion research that meet every two years to discuss their own work priorities.

The main method adopted to address atomic and nuclear data needs is through IAEA Co-ordinated Research Projects (CRPs). A CRP is a limited-term project focused on a specific issue (for 3 to 5 years). The A+M Unit operates three or four CRPs simultaneously, as recommended by the IFRC Subcommittee. Ten to fifteen researchers will participate in a typical CRP, and there will be two or three Research Co-ordination Meetings (RCM) during the course of such a project. Participants will summarise the current state of knowledge on the topic of the CRP during the first RCM, and a work plan for the next one- or two-year period will be formulated. Normally there will be co-ordination between theory and experiment as well as prioritisation of tasks. Over the course of the next one or two years, participants carry out their parts of the work plan and maintain contact through telephone, e-mail and informal meetings at conferences. Progress will be reported at the second RCM and, if appropriate, adjustments will be made to the work plan. If the CRP operates for over three years, a final RCM will be held in the last year at which the overall work plan will be reviewed, and the results obtained throughout the duration of the CRP will be summarised. Final results from the CRP will be published in an issue of the IAEA journal *Atomic and Plasma-material Interaction Data for Fusion* (APID). Participants are also encouraged to publish their results in external journals during the course of the CRP. Data from the CRP are also collected and reviewed, and may be added to the A+M electronic database available through the Unit home page (www-amdis.iaea.org).

The Unit has recently completed a CRP on “Tritium Inventory in Fusion Reactors” that brought together the work of eleven participants from seven member states. The CRP considered mechanisms by which tritium can be taken up by wall materials and subsequently be detected, as well as methods for releasing the trapped tritium. Participants reached the following specific conclusions:

- Increase of stored energy and pulse duration in ITER coupled with lack of experience in contemporary tokamaks with the plasma-facing materials proposed for this device make the choice of these materials arguably the highest risk factor for the plant.
- The tritium inventory is a major source term in accident scenarios.

- Erosion and tritium retention properties are decisive factors in the selection of plasma-facing materials. Tungsten demonstrates the lowest tritium-inventory risk when considering all of the proposed wall materials, while carbon presents the greatest risk in terms of the tritium inventory. Tritium removal techniques will have to be applied if carbon is used in the facility. Beryllium represents a major retention risk through co-deposition in the presence of oxygen-tritium removal techniques also need to be developed and applied for Be. Furthermore, our limited understanding of possible mixed-material effects increases tritium-inventory risks.

CRP participants made the following recommendations:

1. Focus more R&D on the effectiveness of tritium removal techniques from Be and BeO co-deposits with carbon and tungsten impurities.
2. Need capability in the plant design to change the materials in the first wall, arising from concern with respect to generating unacceptably high tritium inventories with current PFC materials.
3. ITER should explore the possibility of using high temperatures (400°C or more) to remove and reduce the tritium inventory.
4. Design a cooled co-deposit collector in the divertor that operates at room temperature and can be heated to >700°C for subsequent hydrogen release and removal.

The CRP participants are in the process of writing a summary article that describes the major results of the project for publication in the *Nuclear Fusion* journal. Furthermore, all participants will contribute relevant technical chapters to the next issue of *APID*.

Due to the importance of erosion issues in plasma-facing materials for fusion devices, the Subcommittee of the IFRC has recommended that the A+M Unit initiate a new CRP on the topic of “Data for Surface Composition Dynamics Relevant to Erosion Processes”. This first RCM will be held in October 2007, and the CRP will have an anticipated lifetime of five years focused on ITER-relevant materials. Experimentalists and theoreticians will apply techniques such as molecular dynamics simulations in which theory can be compared to precise, well-defined experiments. There are several large computational facilities working on numerical simulations with a need to interact closely with experimentalists. One hopes that this CRP will make achieve this particular objective.

The Nuclear Data Section maintains an extensive number of electronic databases for IAEA member states, and the resulting data files from CRPs are primary products for this service. Material-relevant A+M data are mainly concerned with particle-surface interactions – data for a number of processes are included, many with both energy and angular dependence. The A+M bibliographic database is collated from contributions from DCN members, and is updated as additional information is submitted; a yearly hardcopy publication is produced and distributed yearly (*International Bulletin on Atomic and Molecular Data for Fusion*). Both the numerical and bibliographic A+M databases can be accessed freely through the home page of the A+M Unit.

Materials research for fusion

The main driver for materials research within fusion is the demand for plasma facing components and blankets for ITER in which the average neutron flux will be greater than 0.5 MW/m² and the average neutron fluence will be higher than 0.3 MWa/m² [1]. The treatment systems for radioactive

wastes generated by ITER and future fusion power plants will be designed to minimise the dispersion of radioactive materials. Various aspects of a future fusion power plant have been presented at a recent Technical Meeting on “First Generation of Fusion Power Plants: Design and Technology” [2].

A major series of experiments on materials research for fusion components will be carried out on the International Fusion Materials Irradiation Facility (IFMIF). This materials test facility is based on the need for an intense neutron flux with an energy spectrum similar to the fusion neutron spectra. A 40-MeV proton beam impinging on a liquid lithium target could fulfil this requirement, and the resulting neutron flux will be of the order of 10^{17} n/(100 cm²s) if two beams hit the target simultaneously [3]. The neutron flux in the test area will provide a damage production of about 50 dpa/year in 0.1 L or about 20 dpa/year in 0.5 L (equivalent to 2 MW/m²). IFMIF presents some significant materials challenges with respect to power and flux.

Further to the needs of the magnetic fusion experiments, there are similar needs for inertial fusion experiments using lasers or particle beams to drive the fusion process. One realisation towards an inertial fusion power plant is FIREX in Japan (Fast Ignition Realisation EXperiment” – a very high temperature experiment driven by lasers.

DEMO is the proposed power-generating fusion reactor to follow, with flux and power more than ten times that of ITER. There is an essential role for research reactors in support of the next generation of fission and fusion reactors; if member states identify a common research theme, there are strong possibilities for IAEA programmes that will have a broad impact on the industry. The injected power is a maximum of ~10 MW for long pulse discharges, resulting in a total confined energy of about 1 GJ. ITER will operate at several tens of MW injected power, resulting in several tens of GJ. The situation for DEMO will be even more demanding, and these issues of operation and high heat fluxes on plasma facing components have been discussed at Technical Meetings on Steady State Operation [4].

The IAEA has finalised a CRP on Dense Magnetised Plasmas (DMP) in which several devices were built with the purpose of performing fundamental tests on candidate materials for application in fusion devices (April 2007). These devices are equipped with many sophisticated means of diagnosing and characterising the impinging flux and radiation into the specimen. Application of DMPs in support of fusion research started during the course of this CRP in which intense streams of plasma and fast ions generated in Plasma Accelerators (PA) and Dense Plasma Focus (DPF) were applied to the testing of materials intended for use as first wall and/or divertor elements in existing and future fusion devices. Such tests are being carried out in the Russian Federation (DPF, PA), Poland (DPF) and Ukraine (PA). For example, preliminary comparative round-robin tests of low-activating steels of various types (tungsten, carbon composites, and other ceramic and optical materials) have been performed with the financial support of the IAEA (TC project POL/013). The interaction of deuterium ions and dense plasma beams with ferritic steels and tungsten have also shown that damages of the surface layer of ferritic steels (10Cr9WV and Eurofer-97 types) were remarkably low compared with that of austenitic steels. Phase compositions of ferritic steels remained steady under the pulsed action of high power density beams (up to 10^{10} W/cm²) and at pulse durations up to 1 μs. However, the surface layer of tungsten after a 10-fold action of pulsed irradiation under harsh conditions ($q \sim 10^{10}$ W/cm², $t \sim 1$ μs) suffered significant damaged. Elongated surface cracks and extensive erosion of the material were observed, and the mean thickness of the evaporated layer per single pulse was 2 μm. Dense Plasma Focus (DPF) are a particular case of DMP devices that can generate neutron fluxes of $\sim 10^{11}$ n/s (DD), hard and soft X-rays (10^9 W/cm²/shot), electron and ion beams and plasma streams with heat fluxes up to 10^{10} W/cm² in a pulsed event lasting several nanoseconds.

The large potential of the Dense Magnetised Plasma devices results from their ability to recreate to some extent the harsh environment expected in future magnetic and inertial fusion confinement

devices. DMPs can be used to test the concepts, technologies and materials of some of the present and near-future fusion research topics, while larger testing facilities are being designed (such as IFMIF). The IAEA expects to support in the near future a CRP to utilise the DMP devices for research activities on the topics listed in Table 1, in which round-robin materials testing experiments will integrate all types of induced damage (neutron, heat flux, etc.) and provide basic physics understanding on the processes involved from the macroscopic down to the atomic level.

Table 1. Areas that DMPs are expected to contribute to our knowledge with respect to fusion materials research and technology

Magnetic confinement	Inertial confinement
<ul style="list-style-type: none"> ➤ Nanosecond time resolved testing and calibration of D-D and D-T neutron diagnostics ➤ Testing bench for charged fusion products diagnostics ➤ Compact neutron sources for use in characterisation of neutron fields and cross-calibration of MCNP codes ➤ Tests of fusion candidate materials under transient heat loads ➤ Tests of plasma-facing and construction materials under plasma and fusion products fluxes ➤ Fuelling systems ➤ Development of plasma sources for fusion applications 	<ul style="list-style-type: none"> ➤ Nanosecond time-resolved testing and calibration of D-D and D-T neutron diagnostics ➤ Testing bench for charged fusion products diagnostics ➤ Compact neutron sources for use in characterisation of neutron fields and cross-calibration of MCNP codes ➤ Investigate the possibility of developing PF technology to perform experiments for lithium blanket concepts under representative pulsed neutron fluxes. ➤ Test of plasma-facing and construction materials under plasma and fusion products fluxes ➤ Applications of DMP as intense x-ray sources (backlighting, pellet ignition, etc.) ➤ DMP as source for proton radiography in hohlraum characterisation

Accelerator-driven systems (ADS)

Challenges faced by long-term, sustainable utilisation of nuclear energy have led to increased R&D efforts to develop a technology aimed at reducing the amount of long-lived radioactive waste through transmutation in fission reactors or accelerator driven hybrids. At an international level, an increasing number of studies have been carried out on advanced and innovative waste management strategies [i.e. actinide separation and elimination, commonly called “partitioning and transmutation” (P&T)].

P&T is being revisited in several IAEA member states with the goal of reassessing the merits and investigating new approaches that could be followed by implementing this innovative fuel cycle and waste management option. Such a complex technology implies the availability of advanced reprocessing plants, facilities for fuel fabrication of transuranics, and irradiation facilities beyond existing nuclear reactors. Partitioning consists in extending the current reprocessing techniques beyond uranium, plutonium and ^{129}I to the extraction of the minor actinides (neptunium, americium and curium) and long-lived fission products ^{99}Tc , ^{93}Zr , ^{135}Cs , ^{107}Pd , and ^{79}Se from the high-level liquid waste. On the other hand, transmutation requires completely new fuel fabrication plants and irradiation technologies, and their implementation on an industrial scale. The use of existing nuclear reactors as transmutation devices results in modest incineration and transmutation yields, and is limited by safety and operational considerations. Therefore, new concepts (dedicated fast reactors) and subcritical systems (ADS and even fusion/fission hybrids) have been proposed as incineration and transmutation devices.

ADS rely on the availability of a hard neutron source produced from the spallation process induced by means of a high-energy proton beam impinging on a heavy nuclide target. While in theory the spallation neutron source can also be used to irradiate isotopes directly for transmutation purposes, utilisation as a supplementary external neutron source in a hybrid subcritical system such as the ADS is the only current application of interest. Although ADS possesses some attractive potential, various economic and technological issues remain to be solved (e.g. capital costs, additional energy consumption, accelerator reliability, specific physics and materials science issues linked to nuclear data, fuel performance, thermal-hydraulics, etc).

Any assessment of the potential of ADS technology must consider the fact that spallation neutrons are much less effective than those of fission, as can be seen from the following basic physics considerations: delivering 200-MeV energy obtained from one fission to the spallation target yields $200 \text{ MeV} \times \eta_{\text{th}} \times \eta_e \times \varepsilon = 200 \times 0.4 \times 0.5 \times 0.5 = 20 \text{ MeV}$ [typical figures were taken for η_{th} (efficiency of thermal to electrical energy transformation), η_e (efficiency of electric energy to proton current transformation in the accelerator), and ε (fraction of incident protons having kinetic energy \geq spallation nucleus dissociation energy, $\varepsilon \sim 0.5$ for the lead target)]¹. Along with 20-MeV energy, a spallation target yields 200-MeV $\eta_{\text{th}} \times \eta_e \times Z/E_p$ hard neutrons, where Z is the number of neutrons produced by each proton of energy E_p . Staying with the example of lead as the target material, Z is ~ 25 for 1-GeV protons, and hence the spallation process would yield 1 hard neutron. Studies have shown that the ADS design could be optimised (mainly with regard to the position of the spallation source) to enhance the spallation neutron importance ϕ^* and the number of spallation neutrons by a factor of up to 1.5. These basic considerations lead to the conclusion that transforming one fission (which yields roughly 200 MeV of energy and 3 hard neutrons) into spallation results in approximately 20 MeV of energy and 1.5 hard neutrons. Thus, in comparison with fission, the spallation source requires 180-MeV energy to produce half the number of neutrons. Clearly, the introduction of ADS with such an expensive neutron source can only be justified if there are conspicuous advantages in other areas. Such advantages are claimed in two areas: (a) improvement of the dynamics behaviour (and hence safety characteristics), and (b) enhanced flexibility linked to an improved neutron balance gained from the availability of an external neutron source. Both of these advantages have motivated R&D efforts aimed at substantiating the potential of ADS and studying their role in innovative reactor and fuel cycle strategies that include systems for large-scale utilisation and transmutation of actinides and long-lived fission products.

The IAEA has established the wide-ranging project “Technology Advances in Fast Reactors and Accelerator-driven Systems” that embraces a number of activities (both information exchange and co-ordinated research projects) on the utilisation of plutonium and transmutation of long-lived radioactive waste, accelerator-driven systems, thorium fuel options, innovative nuclear reactors and fuel cycles, non-conventional nuclear energy systems, and fusion/fission hybrids. As in all the other fields of advanced nuclear power technology development, the IAEA relies in the P&T area on the broad in-depth experience and perspectives of their staff. The framework for all IAEA activities in P&T is the Technical Working Group on Fast Reactors (TWG-FR), which acts as a catalyst for international information exchange and collaborative R&D.

As far as information exchange is concerned, the IAEA has prepared a Technical Report on heavy liquid metals (HLM) thermal-hydraulics [5]. A detailed knowledge of basic thermal-hydraulic

¹ Energy release by the spallation target in an ADS is amplified by the subcritical core, and the overall energy balance is positive – this means that more energy is produced by the ADS than is needed to feed the accelerator. The amplification factor can be expressed as $f = \left[\nu \left(\frac{1}{k_{\text{eff}}} - 1 \right) \right] / Z \times \phi^*$, where ν is the average number of prompt neutrons, and Z and ϕ^* are defined in the text.

phenomena is a necessary step for the development of the numerical codes to be used in R&D, as well as in the engineering design of HLM components. This need is particularly true in the case of high-power particle beam targets and the cooling of accelerator driven subcritical cores where the use of Computational Fluid Dynamic (CFD) design codes is mandatory. An assessment of the shortcomings of the present CFD codes used for HLM simulation has been carried out, and suggests future research activities in both the numerical and experimental areas [5]. State-of-the-art assessments of present CFD codes have been made by: (i) reviewing their degree of precision and accuracy, (ii) identifying open issues in current turbulence models, free surface phenomena, as well as in two-phase flows, (iii) addressing development requirements for adequate physical models in HLM flows, and (iv) defining code validation issues. Moreover, a review of the current and planned experimental HLM programmes has been carried out (definition of capabilities of existing and planned HLM facilities and work programmes, instrumentation and measurement techniques, description of existing and planned benchmark experiments and databases, thermal-hydraulic applications within ongoing projects on spallation targets and ADS, and prospects for international collaboration and co-ordination of the experimental activities), along with quantification of the needs in future activities [5] (definition of numerical and experimental benchmarks, including required databases and international collaboration, for example networking and co-ordination among institutions involved in HLM thermal-hydraulics). The key issues of CFD code characterisation (i.e. modelling, materials properties data, numerical problems and code performance), as well as code usability were addressed. Turbulence phenomena, two-phase and free-surface flows phenomena, as well as experiments and measurement techniques, were addressed.

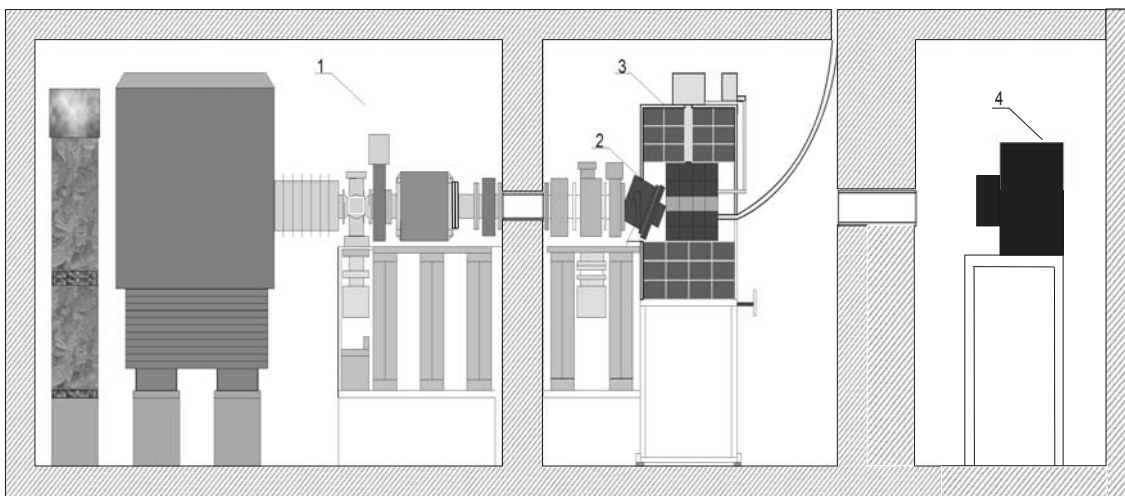
Training needs were considered in some detail, following on from various comments by member states. The IAEA has organised a Workshop on Technology and Applications of Accelerator-driven Systems, in collaboration with the International Centre for Theoretical Physics (ICTP), Trieste, Italy, from 17 to 28 October 2005. This workshop familiarised students with the status of the R&D activities in ADS for energy production and transmutation by means of a comprehensive review of the ADS designs currently under consideration. Thirty-four students from 19 countries studied the theoretical foundation of all ADS designs (i.e. high-power accelerator, spallation target and subcritical blanket), identified problematic areas, and considered the limitations of the simulation methods used. Modern theoretical models were used to predict nuclear reaction cross-sections. Evaluation methodologies, existing data libraries, data processing and transport calculations were studied. Based on discussions of the impact of the present uncertainties on the performance of ADS, the needs for data and methods development and validation work were identified. Students also studied various aspects of the fuel cycle, particularly the impact of transmutation on the repository. The workshop consisted of lectures, computer demonstrations and “hands-on” exercises, and participants were also invited to make short presentations of their own research and/or topics of interest that emerged during the workshop. The next IAEA/ICTP joint Workshop on *Physics, Technology and Applications of Accelerator-driven Systems (ADS)* will be held in Trieste from 19 to 30 November 2007.

With regard to collaborative R&D, the IAEA has two ongoing CRPs on *Studies of Advanced Reactor Technology Options for Effective Incineration of Radioactive Waste*, and *Analytical and Experimental Benchmark Analyses of Accelerator-driven Systems (ADS)*. The first CRP is attended by participants from 17 institutions in 13 member states and the EC (JRC). A major objective has been the production of a comparative assessment of the transient behaviour of advanced critical and subcritical transmutation systems. Benchmarks were performed on critical liquid-metal and gas-cooled fast reactors, heavy liquid-metal, and gas-cooled ADS, critical and subcritical molten salt concepts, and fusion-fission hybrid subcritical systems. The objective of the latter CRP is to improve the understanding of the physics of the coupling of external neutron sources with subcritical cores. A major thrust of this CRP has been the experimental backing of analytical benchmarks, and the participants are applying integrated calculation schemes to perform computational and experimental benchmark

analyses. While the main emphasis of the work has been directed towards ADS, transmutation concepts based on subcritical cores driven by non-spallation neutron sources have also been considered – particularly with respect to experimental benchmarking activities, since there are experimental demonstration projects using non-spallation targets [e.g. (D,D) or (D,T) neutron sources, and photon-neutron sources based on electron accelerators]. The CRP addresses all major physics phenomena of the spallation source for ADS, along with coupling to the subcritical core. Analyses for the detailed ADS calculations extend from the simulation of the high-energy proton beam down to thermal neutron energies in the subcritical core. At present, 27 institutions in 18 member states and two international organisations are actively involved in this CRP. Participants agreed to analyse the following benchmark problems: (i) YALINA-Booster (set-up of the YALINA facility assembled at the Joint Institute for Power and Nuclear Research Sosny JIPNR of the National Academy of Sciences of Belarus is shown in Figure 1); (ii) spallation target parametric studies with experimental validation; (iii) spallation source efficiency and energy dependence; (iv) analytical and numerical benchmarking of methods and codes for ADS kinetics; (v) ADS concepts; (vi) subcritical experiments; (vii) photonuclear based transmutation benchmarks; (viii) ADS performance [6].

Figure 1. Set-up of the subcritical facility YALINA

(1) *d*-accelerator; (2) neutron producing Ti-t (or Ti-d) target; (3) subcritical assembly; (4) gamma-ray spectrometer



Finally, the IAEA has implemented the “ADS Research and Development Database”, which provides information about ADS-related R&D programmes, existing and planned experimental facilities, as well as programmes, methods and data development efforts, design studies, and other materials. While operational on the WWW and open to all users (<http://www-adsdb.iaea.org/index.cfm>), this database relies on content contributed by interested communities. Data and information can be provided on-line, and contributions are solicited (upon request, the author will gladly provide access privileges as editor to anyone wishing to provide contributions).

Conclusions

The IAEA supports research on material properties for a variety of applications, and a number of CRPs are actively generating new data for applications. Technical meetings are held regularly on specific applications. Data are collected and disseminated in print and electronic form and are freely available to all member states.

REFERENCES

- [1] IAEA, ITER EDA Documentation Series No. 24 (2002).
- [2] *First Generation of Fusion Power Plants: Design and Technology*, IAEA, Proceedings Series, ISBN 92-0-106306-7 (2006).
- [3] *IFMIF Comprehensive Design Report*, IFMIF International Team, IEA (2005).
- [4] *Special Issue on Steady State Operation*, 4th IAEA Technical Meeting, Ahmedabad, India, 1-5 February 2005, *Nucl. Fusion*, Vol. 46, No. 3 (2006).
- [5] *Theoretical and Experimental Studies of Heavy Liquid Metal Thermal Hydraulics*, IAEA-TECDOC-1520, IAEA, Vienna, Austria.
- [6] Aït-Abderrahim, H., A. Stanculescu, "IAEA Co-ordinated Research Project on 'Analytical and Experimental Benchmark Analyses of Accelerator Driven Systems'", *Proc. PHYSOR 2006*.

EFFECT OF NEPTUNIUM IONS ON CORROSION OF ULTRA LOW CARBON TYPE 304 STAINLESS STEEL IN NITRIC ACID SOLUTION

Chiaki Kato, Takafumi Motooka, Masami Numata, Shinya Endo, Masahiro Yamamoto
Japan Atomic Energy Agency, Japan

Abstract

Major topics of materials in innovative nuclear systems, such as Generation IV reactors, are degradation or corrosion of metallic components. Corrosion of a nuclear fuel reprocessing plant is also important problem in not only the current but also an advanced nuclear fuel reprocessing system. The PUREX process is well known in the current system, and probably it will be used for the advanced system. In the process, nitric acid solution is used for dissolving spent nuclear fuels and solvent extraction method is used to separate U and Pu. Nitric acid is a known highly corrosive solution itself and the solution included oxidising agent, such as Pu, Np in transuranium elements (TRU) and Ru in fission products (FP) becomes more corrosive. In an advanced nuclear fuel cycle system, much higher TRU and FP should be treated for reprocessing spent nuclear fuels. It would be a much more severely corrosive environment. In this paper, an effect of Np addition to nitric acid solution on corrosion of ultra low carbon Type 304 stainless steel (SUS304ULC) was investigated. Two types of specimens were used. One is heat-transfer condition specimen, which is the heated condition with boiling. The other is immersed condition, which is non-heated condition with boiling. SUS304ULC sheets were used for corrosion tests. The corrosion tests were conducted in 9 kmol/m³ nitric acid solution adding Np. Also, a corrosion test with gamma-ray irradiation by ⁶⁰Co sources was investigated. The results showed that Np addition accelerated intergranular corrosion of SUS304ULC and the corrosion rate in the heat-transfer condition was larger than that in the immersed condition. It was found that Np(VI) ions elevated corrosion potential to noble direction. It was also found that the ratio of Np(VI+V)/Np (IV) ions increased after corrosion test. Furthermore, gamma-ray irradiation decreased corrosion rates. The reason for acceleration of corrosion rate by Np addition was estimated the cycle between the re-oxidising process of Np in the solution and reducing at the metal surface. Heat-transfer condition accelerated this Redox cycle, and gamma-ray irradiation decreased the cycle.

Introduction

Major topics of materials in innovative nuclear systems, such as Generation IV reactors, are degradation or corrosion of metallic components. Corrosion of a nuclear reprocessing plant is also an important problem in not only the current but also an advanced nuclear fuel reprocessing system. The PUREX process is well known in the current system, and probably it may be used for the advanced system. In this process, nitric acid solution is used to dissolve spent nuclear fuels and solvent extraction method is used to separate U and Pu. A stainless steel is one of important metallic materials used in a reprocessing plant. Nitric acid is a known highly corrosive solution itself and the solution with highly oxidising ions, such as Pu, Np in transuranium (TRU) and Ru in fission products (FP), becomes more corrosive [1-3]. Pu is the most abundant element and Np is second one in spent nuclear fuels except U from results calculated by ORIGEN2. Therefore, it is important to investigate the corrosion behaviours of stainless steel in nitric acid solution with Pu or Np.

The corrosion behaviours of stainless steel in nitric acid solution with Pu were reported [2]. However, the corrosion behaviours in nitric acid solution with Np are not well known. In this paper, an effect of Np ions on corrosion of ultra low carbon Type 304 stainless steel (SUS304ULC) was investigated by weight loss and polarisation measurements and spectrometry. We have also attempted to establish corrosion mechanism in nitric acid solution with Np.

Experimental procedures

Material and solutions

The chemical composition of SUS304ULC stainless steel used is shown in Table 1. Specimens for corrosion tests were cut and finely polished. Several test solutions were used for corrosion tests. The chemical concentration of test solutions is shown in Table 2. Solution A is pure 9 mol/dm³ HNO₃. Solution B is 9 mol/dm³ HNO₃ with 3.8 mmol/dm³ ²³⁷Np. Solution C is Solution B with Ru from fission products (FP). Purity and concentration of ²³⁷Np used in this study was checked by γ -ray spectrometry. The valence states of Np were Np(IV), Np(V) and Np(VI). Their ratios were not quantitatively analysed.

Corrosion tests

Two types of specimens were used. One is a heat-transfer specimen, which is the heated condition with boiling. The other is an immersed specimen, which is non-heated condition with boiling. It is known that heat-transfer condition accelerates corrosion [4,5]. The specimens were immersed for a total of 930 hours in those solutions. The solutions were newly changed every 310 hours in immersed and heat transfer corrosion tests. The ratio of solution volume to surface area of specimen was about 18 cm³/cm². The corrosion tests were examined under a boiling condition at 341 K in reduced pressure of 160 hPa in order to simulate vacuum evaporator for nitric acid recovery. The heat-flux was calculated by temperature difference between the thermocouples set at different positions from surface. The heat flux in the heat-transfer specimen was maintained at 60 kW/m² during the test. The appearance and schematic view in both specimens of apparatus used in this study are shown in Figure 1. Test specimen shapes for immersed condition and heat-transfer condition are shown in Figure 2. The condition of corrosion tests is summarised in Table 2.

From the weight loss measurement of specimens by use of an electric balance and the quantitative analysis of metallic ions (Fe, Cr and Ni) dissolved in test solutions by inductively coupled plasma arc

emission spectrometry (ICP-AES). The error in the weight measurements is under 0.1 mg. But, there is uneven in weight loss with 10% error even if it is the same condition and the error in corrosion rate would be about 10%. Surface morphology of specimens was observed by scanning electron microscopy (SEM).

Gamma-ray irradiation

The effect of gamma-ray irradiation on corrosion was examined by using ^{60}Co isotopes (300 GBq). The radiation dose was controlled 10 Gy/h in the centre of the heat-transfer specimen and ^{60}Co isotopes were layout around a test cell.

Photospectrometry

A Hitachi U-3400 photospectrometer with a spectral range from 190 to 2 600 nm was used to estimate the oxidation states of Np ion. It is reported that Np(V) has an absorption peak at 700 and 800 nm [7]. The solution in reference for compartment was pure 9 mol/dm³ HNO₃.

Results

Corrosion rates and SEM observation

Figure 3 shows the calculated corrosion rate of SUS304ULC in nitric acid with and without Np ions under immersed and heat-transfer conditions. Under immersed condition, corrosion rate of SUS304ULC in 9 mol/dm³ HNO₃ without Np ions (Solution A) was 0.0008 g/m²h and that in nitric acid with Np ions (Solution B) was 0.0162g/m²h. The corrosion rate in nitric acid with Np was about twenty times higher than that without Np. Under heat-transfer condition, corrosion rate in nitric acid without Np ions was 0.0093 g/m²h and that with Np was 0.0452g/m²h. The corrosion rate in nitric acid with Np was about five times higher than that without Np. Furthermore, the corrosion rate under heat-transfer condition was clearly higher than under immersed condition in both solutions.

Figure 4 shows periodic change of weight loss calculated by metallic ions dissolved. The corrosion rate increased with increasing time and the corrosion rate became constant value after 600 hours under the heat-transfer condition. The increased corrosion rate observed under the heat transfer condition would be caused by higher temperature (357 vs. 343 K) and increasing oxidation potential of nitric acid. It is reported that oxidation potential of nitric acid rises under the boiling heat transfer condition [5]

Figure 5 shows the surface SEM photographs of tested specimens under immersed and heat-transfer condition in both solution. SUS304ULC exhibited intergranular corrosion under heat-transfer condition in both solution and under immersed condition in nitric acid with Np ions. The groove of intergranular corrosion under heat-transfer condition was wider than under immersed condition. In addition, grains fell from the surface in the most corrosive condition, nitric acid with Np ions under heat-transfer condition.

The effect of γ -ray irradiation

Figure 6 shows the calculated corrosion rate of SUS304ULC in nitric acid with Np ions under γ -ray irradiation. In immersed condition, corrosion rate under non-irradiation was 0.0147 g/m²h and that under γ -ray irradiation was 0.0121 g/m²h. Under heat-transfer condition, corrosion rate under non-irradiation was 0.0147 g/m²h and that under γ -ray irradiation was 0.0121 g/m²h. It was found that the corrosion of stainless steel was decreased by γ -ray irradiation.

Figure 7 shows periodic change of weight loss calculated by metallic ions dissolved under γ -ray irradiation. The corrosion rate is clearly decreased under γ -ray irradiation in both conditions. The corrosion rate increased with increasing time. It seemed that the corrosion rate became constant value after 400 hours under γ -ray irradiation.

Absorption spectrum of Np(IV), (V) and (VI)

Figure 8 shows the absorption spectra of Np ions in the primary nitric acid solution and in solution after testing. Np(V) shows an absorption peak at 1 100 nm, Np(VI) at 1 225 nm, Np(IV) at 800 nm. It was found that Np ions had various states. In comparison with Np ions states after testing, Np(IV) was decreased and Np(V,VI) was increased. It shows that Np(IV) in nitric acid was oxidised to Np(V) or Np(VI) during corrosion tests.

Polarisation curves of SUS304ULC

Figure 9 shows the polarisation curves of SUS304ULC stainless steel in nitric acid without Np ions (Solution A) and in nitric acid with Np ions (Solution B) at room temperature. Ag/AgCl reference was used. The corrosion potential in pure 9 mol/dm³ HNO₃, E_a, is 0.723 V. The corrosion potential in solution with Np ions, E_b, is 0.750 V. The corrosion potential of SUS304ULC with Np ions became nobler than without Np ions. The only cathodic polarisation curve was shifted to noble potential by Np ions. On the other hand, anodic polarisation curves were similar in both solutions. It was found that the cathodic reaction was activated by Np ions.

Discussion

Corrosion acceleration by Np ion

Nitric acid is well known to be a highly corrosive solution itself, because of having noble Redox potential. The Redox potential of nitric acid is given as follows:



$$E = E_0 + (RT/2F)\ln(a_{\text{H}^+}^3 \cdot a_{\text{NO}_3^-} / a_{\text{HNO}_2}) \quad (2)$$

where E₀ = 0.934 V (vs. NHE). This noble Redox potential yields high oxidation power and highly corrosive in nitric acid solution.

It is reported that the Redox potential of Np(VI)/Np(V) equilibrium in acid solution is E₀ = 1.149 V (as NpO₂²⁺/NpO₂⁺ equilibrium) and the Redox potential of Np(VI)/Np(IV) equilibrium in acid solution is E₀ = 0.95 V (as NpO₂²⁺/Np⁴⁺ equilibrium) [6]. Those Redox potentials of Np ions are similar to that of nitric acid. Therefore, Np is easily oxidised to Np(V) or Np(VI) in nitric acid as shown in Figure 8. The activated cathodic reaction as shown in Figure 9 suggests that Np(VI) is reduced to Np(V) or Np(IV) on stainless steel. The reduced Np ion is re-oxidised promptly to Np(VI) in nitric acid and consequently electrons are continuously consumed on the stainless steel to lead to the acceleration of corrosion. Figure 10 shows the model for the corrosion.

Corrosion inhibition by γ -ray irradiation

It was found that the corrosion of stainless steel was decreased by γ -ray irradiation. The corrosion inhibition by γ -ray irradiation is probably caused by reduced species such as HNO_2 . It is reported that HNO_3 is decomposed into HNO_2 by γ -ray irradiation [8]. Those decomposed species reduce oxidants such as Np(VI) and consequently lead corrosion inhibition by γ -ray irradiation.

Conclusions

Corrosion tests of Type304ULC in boiling nitric acid with Np ions were examined under immersed and heat-transfer condition. The γ -ray irradiation test was also conducted. The following results were obtained:

- Np addition caused intergranular corrosion of SUS304ULC remarkably.
- Corrosion rate in heat-transfer condition was larger than that in immersed condition. It was obtained that Np(VI) ions rose corrosion potential to noble direction and the ratio of $\text{Np(V+VI)}/\text{Np(IV)}$ increased after corrosion test.
- γ -ray irradiation decreased corrosion rates.

Table 1. Chemical composition of tested SUS304ULC stainless steel and specification of SUS304ULC

	C	Si	Mn	P	S	Ni	Cr	Fe
SUS304ULC	0.011	0.34	1.71	0.013	0.001	10.8	19.0	Bal.
Specification SUS304ULC	<0.030	<1.00	<2.00	<0.045	<0.030	9.0~13.0	18.0~20.0	Bal.

Table 2. The condition of corrosion tests

Test solutions <i>Solution (a) [without Np]</i> <i>Solution (b) [with Np]</i> <i>Solution (c) [under irradiation only]</i>	9 mol/dm ³ HNO_3 9 mol/dm ³ HNO_3 + 3.8×10^{-3} mol/dm ³ Np 9 mol/dm ³ HNO_3 + 3.8×10^{-3} mol/dm ³ Np + 5×10^{-5} mol/dm ³ Ru
Test pressure	16 kPa (reduced pressure)
Solution state	Boiling
Solution temperature	343 K
Heat transfer condition <i>Surface temperature</i> <i>Heat flux</i>	357 K (estimated) 60 kW/m ²
Solution volume	300 mL
Renewal of test solution	Every 310 h

Figure 1. Testing apparatus for corrosion test

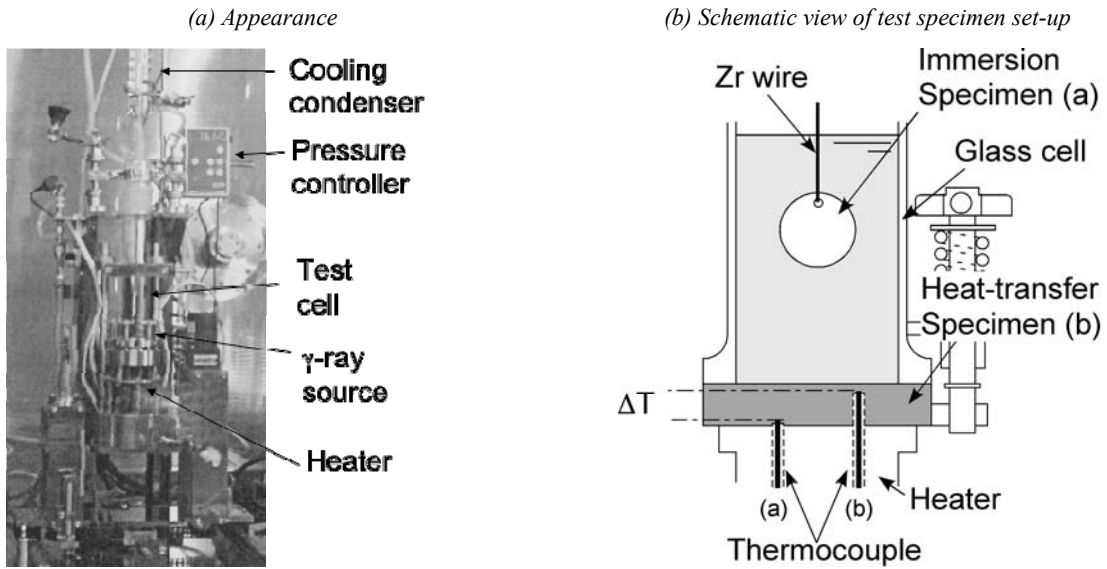


Figure 2. Test specimen shapes for immersion and heat-transfer conditions

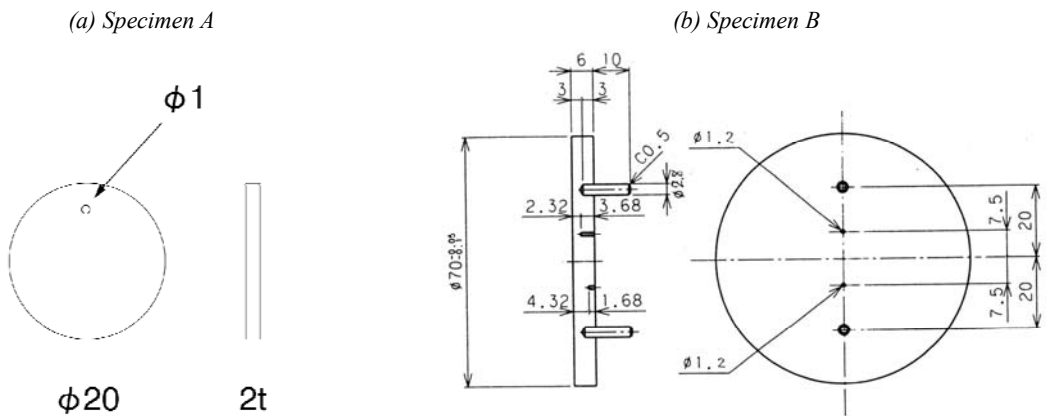


Figure 3. Calculated corrosion rate of SUS304ULC in nitric acid with and without Np ions on immersed and heat-transfer conditions

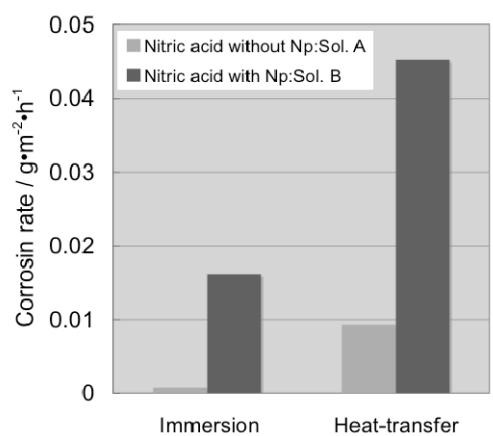


Figure 4. Periodic change of weight loss calculated by the concentration of dissolved ions in nitric acid with and without Np ions

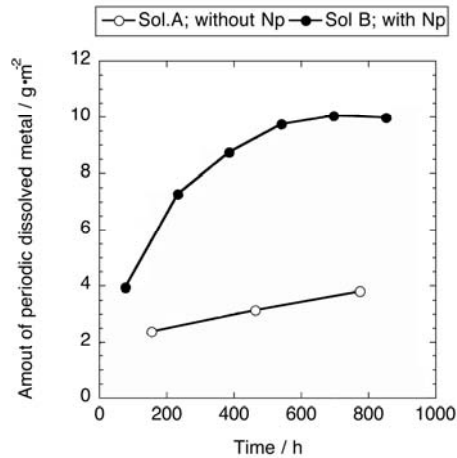


Figure 5. SEM photographs of SUS304ULC test specimens under immersed and heat-transfer conditions

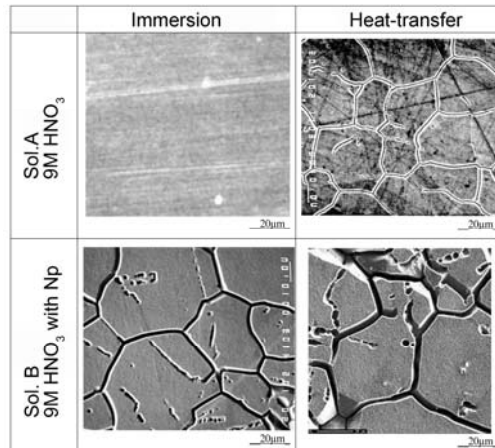


Figure 6. Calculated corrosion rate of SUS304ULC under no irradiation and γ -ray irradiation condition in nitric acid with Np ions

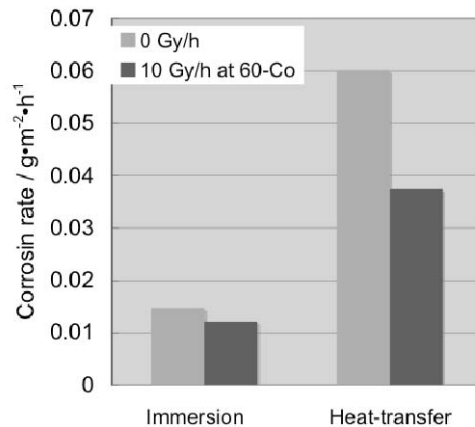


Figure 7. Periodic change of weight loss calculated by the concentration of dissolved ions under no-irradiation and γ -ray irradiation condition in nitric acid with Np ions

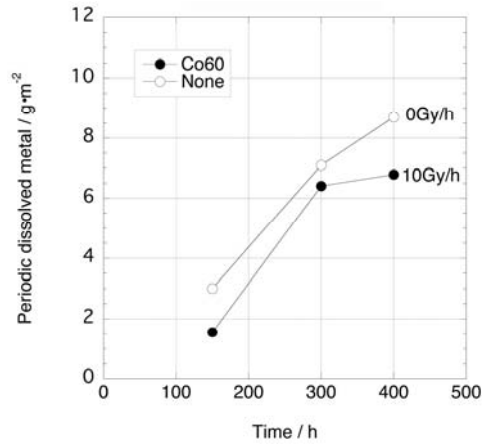


Figure 8. Absorption spectrum of 3.8mmol/dm³ Np in 9 mol/dm³ HNO₃ before and after corrosion tests

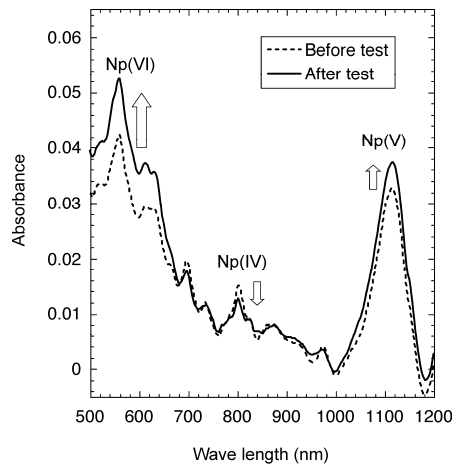


Figure 9. Polarisation curves of SUS304ULC stainless steel at room temperature

E_a and E_b are corrosion potential of SUS304ULC stainless steel

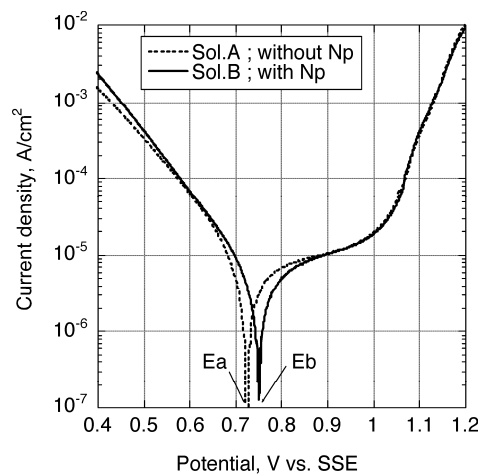
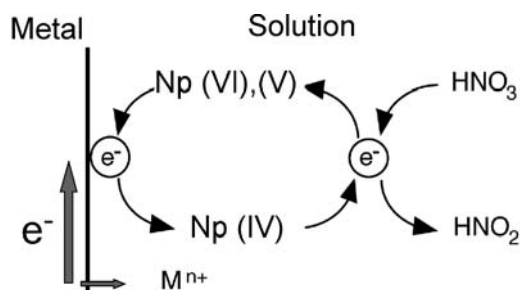


Figure 10. Schematic model of corrosion mechanism in nitric acid with Np ions



REFERENCES

- [1] Okubo, M., M. Shintani, H. Ishimaru, *et al.*, RECOD86, p. 1181 (1994).
- [2] Takeda, S., *et al.*, *Zairyou-to-Kankyou*, 45, 662 (1996).
- [3] Takeuchi, M., *et al.*, *Transactions of the Atomic Energy Society of Japan*, 4, 32 (2005).
- [4] Kato, C., *et al.*, *Corrosion Engineering*, 52, 53 (2003).
- [5] Kato, C., *et al.*, *Corrosion Engineering*, 52, 69 (2003).
- [6] Friedman, H.A., L.M. Toth, *J. Inorg. Nucl. Chem.*, 42, 1347 (1980).
- [7] Martinot, L., *et al.*, "Standard Potentials in Aqueous Solution", Allen J. Bard (Ed.), p. 651, Maecel Dekker Inc. (1998).
- [8] Katsumura, Y., "N-centered Radicals", Z.B. Alfassi (Ed.), p. 393, John Wiley & Sons Ltd. (1998).

NON-DESTRUCTIVE TECHNIQUES STUDY OF THE Fe-Cr BASED ALLOYS

Vladimir Kršjak, Marek Mikloš

Department of Nuclear Physics, Faculty of Electrical Engineering and Information Technology, STU
Ilkovičova 3, 812 19, Bratislava, Slovak Republic

Abstract

Non-destructive method, positron annihilation lifetime spectroscopy (PALS) was applied as an evaluation tool for microstructure study of the four different Fe-Cr alloys. This paper describes ion implantation technique as a tool for creating microstructure defect in structural materials, similar to radiation damage in nuclear facilities. In present state of the research non implanted specimens were measured using PALS, TEM and XRD. The results show the dependency of positron lifetime in defects on the Cr content. These results are necessary in further PALS spectra analysis of the implanted specimens.

Introduction

Reactor pressure vessel (RPV) is limiting factor of the nuclear power plant (NPP) operating lifetime. Lifetime extension of operating NPPs is the essential trend in the modern stage of nuclear power development and most efficient area for investments to maintain the existing generating capacities. This supports the ambition of research of the new structural materials for the non-replaceable parts of the primary circuit. The other important reason for do this large materials research is development of the fusion reactor and absolutely new requirements of the materials.

One of the important alloying elements with significant effect on the radiation embrittlement and swelling is chromium. There were several research made with regard to effect of Cr on the defect creation and stability [1,2], but this problematic is still not fully understood. This work will also attend on this research using the ion implantation as a material degradation tool and the positron annihilation lifetime spectroscopy (PALS) as an evaluation tool. This will enable to create material damage similar to the radiation damage, without problem with induced activity of the specimens. Moreover the PALS is perfect technique for measuring changes in the vacancy type defect density. Materials for specimens are four Fe-Cr alloys with different Cr concentration (2.5, 5, 9 and 11).

Materials specification

For study of Cr role in ferritic/martensitic steels were chosen four binary alloys with different chromium content. Fabrication process and cutting schemes are in details described in [3]. Chemical composition of the specimens is listed in Table 1.

**Table 1. Chemical composition the materials [wt.%]
(unlisted elements are below the 0.001 wt.%)**

For requirement of various non-destructive testing methods were the specimens prepared in dimensions of 10 × 10 × 0.5 mm, one side mirror-like polished

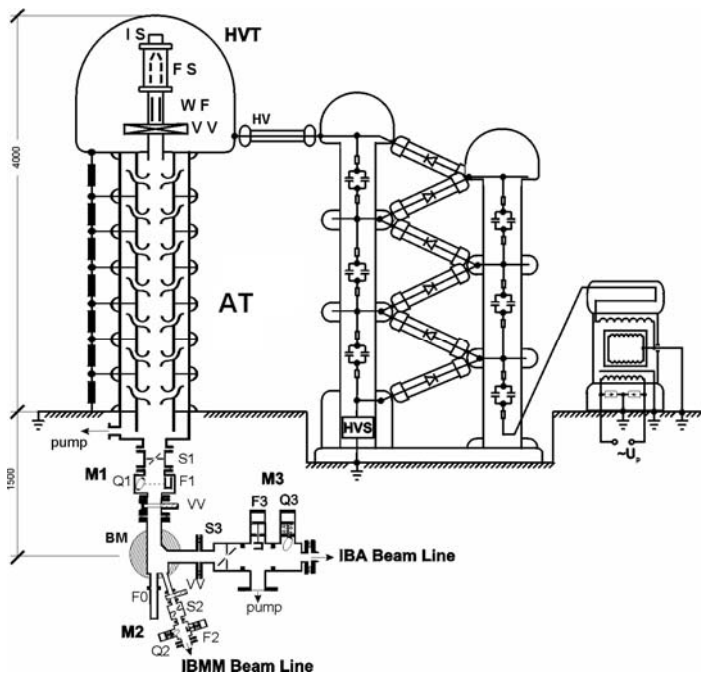
Material	Mn	P	Cr	Ni	C	N
L251	0.009	0.013	2.36	0.044	0.008	0.017
L259	0.02	0.011	4.62	0.06	0.02	0.034
L252	0.03	0.012	8.39	0.07	0.02	0.035
L253	0.03	0.05	11.62	0.09	0.03	0.039

Ion implantation and PALS method description

Ion implantation

Ion implantation of H and He was projected as material degradation tool for creation of vacancy type defects. Based on the previous results [4,5], was for this purpose used linear accelerator in Slovak university of technology in Bratislava. Its basic scheme and the main technical specification are shown on Figure 1. For implantation a different ions can be produced with the aid of four different ion sources: a universal Penning Ion Gauge (PIG) for H implantation, a He-dedicated PIG, a duoplasmatron and a radio frequency (RF) ion source. The accelerator has a possibility to accelerate ions in a wide energy range from 10 keV to 900 keV (single-charged). To keep beam focusing through all voltage range, the number of powered (“active”) accelerating gaps can also be controlled by short-cutting electrodes at the end of the accelerating tube [6].

Figure 1. Scheme of linear accelerator in STU Bratislava and technical specification (photo of accelerator hall – centre)



Abbreviations

- AT– Accelerating tube
- BM – Bending magnet
- pump – vacuum pump
- HVT– High voltage terminal
- HV – High voltage
- HVS – High voltage stabilisation
- IS – Ion source
- WF – Wien filter
- VV – Vacuum valve
- M – Monitoring chamber
- F – Faraday cup
- S – Slits
- Q – Quartz
- IBA – Ion beam analysis
- IBMM – Ion beam modification of materials

Technical specification

Total accelerating voltage: 0-1 MV
 Ripple factor: < 1%
 Energy range for singly charged particles: 5 keV to 1 MeV
 Energy spread: 70 keV-1 MeV: \approx 2 keV,
 < 70 keV: < 0.1%

Positron annihilation lifetime spectroscopy (PALS)

Positron annihilation lifetime spectroscopy (PALS) uses facts, that electron–positron annihilation is time-depending on the electron density in matter and therefore its defects density. The basic principle is shown on Figure 2. Positrons created by β^+ decay (^{22}Na) have continuous spectra with maximum energy of 540 keV. After short time thermalisation (~ 3 ps) to energy of surrounding lattice, positron diffuses in matter while annihilation occurs. The presence of any microstructure defects with local decreasing of electron density cause increasing of so called positron mean lifetime (MLT).

According the “trapping model”, positron annihilation lifetime spectroscopy is using time dependency of the e^+ lifetime on the amount and type of the microstructure defects. Typical measuring equipment contains two detectors (scintillator + photomultiplier), two energy analysers (SCA), time to amplitude converter (TAC) and a multi-channel analyser (MCA) for recording of particular events. Detailed description and specification of PALS equipment in laboratory of Slovak Technical University is shown on Figure 3.

Figure 2. Positron annihilation lifetime spectroscopy principle

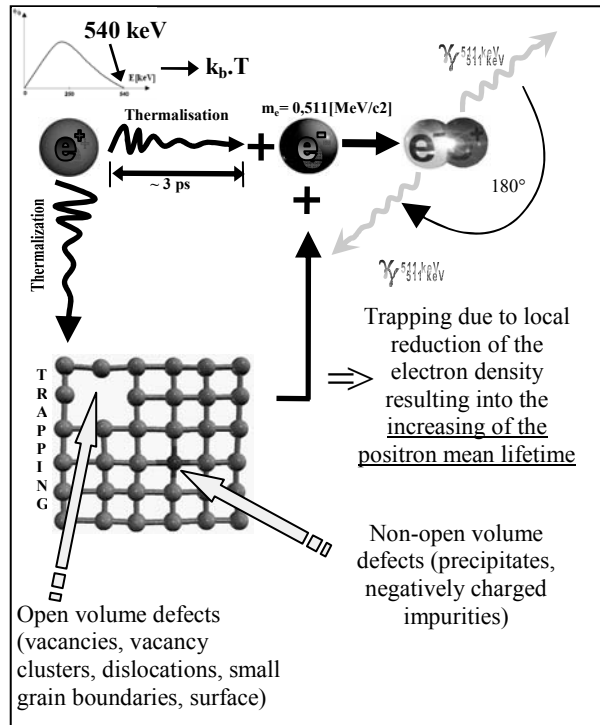
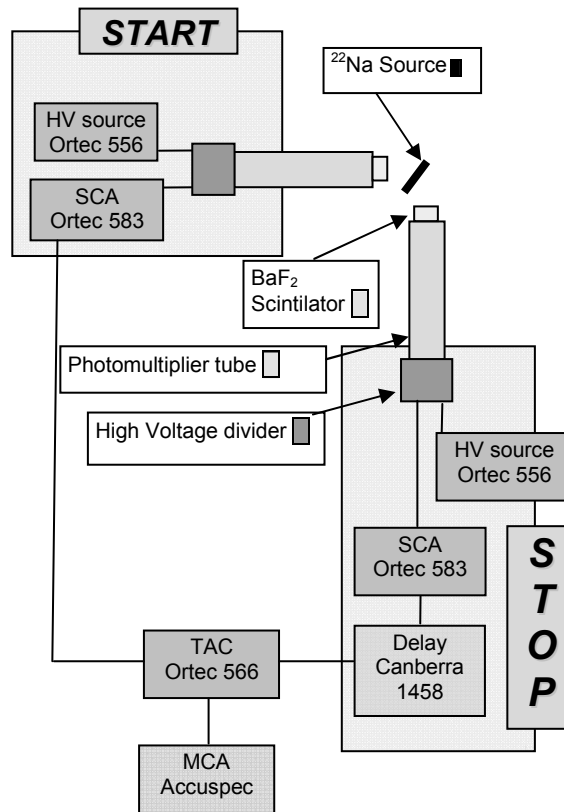


Figure 3. Scheme of “Fast-Fast” set-up of PALS equipment



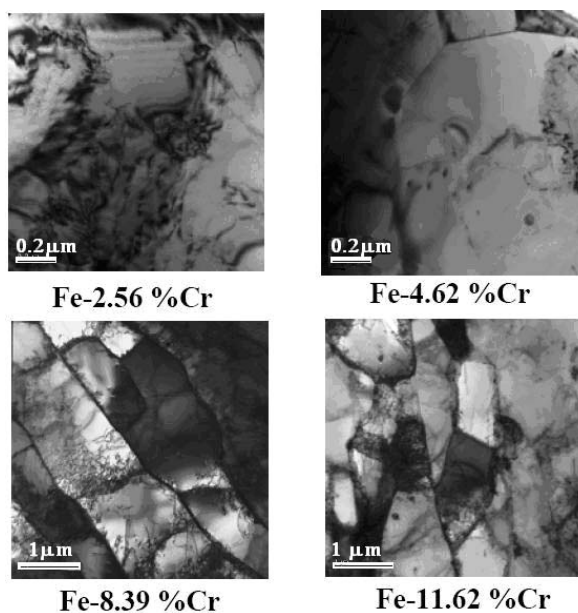
Present results

For evaluation of the PALS results is appropriate to make a comparison with some other techniques available to detect changes in microstructure. Very suitable is transmission electron microscopy. That, as well as metallographic examination was performed at Department of Metallurgy of Ghent University, Belgium [3].

TEM and XRD results

The metallography showed that in Fe-Cr binary alloys, the microstructure depends on Cr content (measured at OCAS, Belgium) [3]. The transmission electron micrographs on Figure 4 show this microstructure.

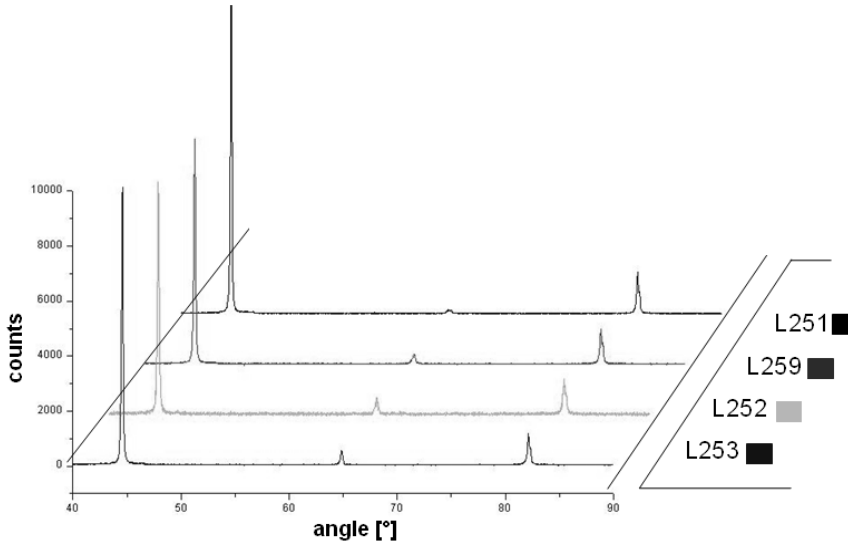
Figure 4. TEM micrographs (bright field) of Fe-Cr alloys [3]



Measured alloys can be classified in two groups. The two alloys with 2.56% and 4.62% Cr show similar microstructure and the 8.39% and 11.62% have also similar microstructure, but quite different from the other two with lower content of Cr. For Fe-2.56% and Fe-4.62% Cr micrographs have massive ferrite and they are showing irregular grain boundaries that are the signature of a fast cooling that prevent the formation of equiaxed ferrite. In Fe-8.39%Cr and Fe-11.62%Cr, the dominant microstructure consist of very small grains of the order of 1 micron and of bainitic ferrite due to rapid cooling after tempering. As for steels, the microstructure is typical of tempered F/M steels with high dislocation density sub-boundaries in the matrix and carbides ($M_{23}C_6$) on both the grain and sub-grain boundaries. The size of carbides varied from about 0.14-0.6 μm. The sub-boundaries are stabilised by the precipitation of carbides on them. Carbides also precipitate at the prior austenite grain boundaries [3].

X-ray diffraction analysis was performed at Slovak Academy of Sciences, Institute of Electrical Engineering. Measurements confirmed fact that all specimens are from the crystal lattice point of view in BCC phase without any indication of FCC. Figure 5 show all spectra compared with reference FCC iron spectrum. These measurements allow us to expecting, that any differences in PALS results of non-irradiated Fe-Cr alloys are caused mostly due to granularity of the materials and/or small amount of carbides, but not due to phase changes.

Figure 5. XRD measurements results of the binary alloys



PALS measurement results

PALS spectra fitted and analysed according “trapping model”, are listed in Table 2. Tau 1 corresponds to material bulk (BCC iron, decreased due to trapping model). Its intensity decreases with higher Cr content. Tau 2 and intensity I_2 describes qualitative and quantitative the microstructural defects. Component Tau 3 is not mentioned, because of its very small contribution ($I_3 \sim 1\text{-}2\%$). This component correspondent to in-flight or surface annihilation.

Table 2. PALS spectra fitting results

Spec.	% of Cr	Tau1 [ps]	I_1	Tau2 [ps]	I_2	Fit's variance	FWHM	MLT
L251	2.36	100	65%	185	33%	1.1	199	145
L259	4.62	88	45%	163	54%	1.14	196	142
L252	8.39	74	31%	158	68%	1.08	199	142
L253	11.62	76	33%	165	66%	1.02	201	155

In case of Fe-Cr specimens, there are several possible positron traps, which can be considered and attributed to Tau 2 component. The main contributions are dislocations, typical for tempered F/M steels. However the precipitates and vacancy type defects along the grain boundaries can more or less contribute to this component as well. Nevertheless, positrons may be trapped by grain boundary only when mean linear dimension of grains do not exceed a few μm . It means that grain size is comparable to (or smaller than) the positron diffusion length L_+ and some fraction of positrons have a chance to reach grain boundary by diffusion motion [7]. Because of typical distances achievable for the thermalised positrons are hundreds of nm, grain boundary trapping plays significant role in the 8.39Cr and 11.62Cr alloys, because their grains size are of the order of 1 micron. Therefore, the I_2 component increasing with the decreasing grain size (Figure 7). Initial higher value of the Tau 2 component should be assign to irregular grain boundaries and possible presence of point defects with higher lifetime.

The decreasing Tau 1 lifetime (Figure 7) can be explained through the standard trapping model as referred to in Ref. [8] according to Eqs. (1) and (2):

$$\lambda_1 = \lambda_{bulk} + (\lambda_{bulk} - \lambda_{def}) \cdot \frac{I_2}{I_1} \quad (1)$$

$$\tau_1 = \frac{1}{\lambda_{bulk}} \quad (2)$$

where λ_{bulk} is annihilation rate in bulk (αFe), λ_{def} is annihilation rate in defects (component 2), I_1 (I_2) is intensity of component 1 (2).

Figure 6. Intensities of Tau 1 and Tau 2 as a function of Cr content (contribution to the MLT)

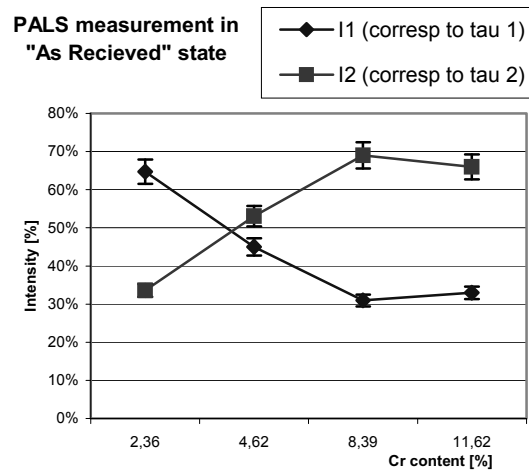
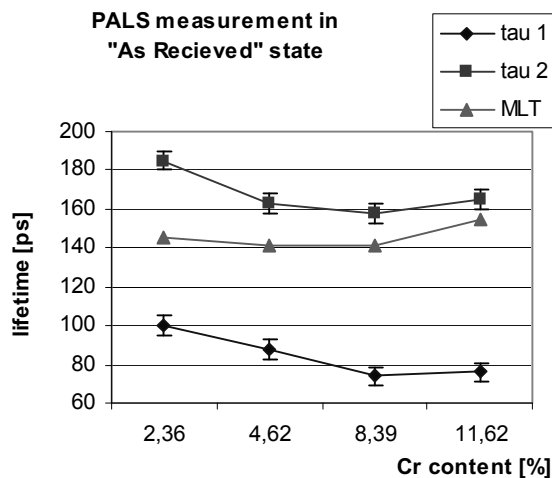


Figure 7. Tau 1, Tau 2 and mean lifetime as a function of the Cr content



Conclusions

PALS measurements complemented with TEM results show a strong dependency of positron lifetime on the material microstructure. In case of these binary alloys, in contrast with other crystal lattice materials, the granularity of the specimen plays an important role in positron lifetime values. If the grain boundaries are small enough to be achieved by positrons in diffusion process, they affect the annihilation and impact on the Tau 2 component. This can be seen on Figures 6 and 7, where

intensity I_2 of component assigned to annihilation at grain boundaries (characterised by lifetime τ_2) is increasing along decrease of the grain size. Higher than approximately 9% of Cr content does not cause significant granularity decrease, which is here close to dimensions of PALS maximum sensitivity. Decreasing of grain size also means decreasing of ferritic structures with regular BCC lattice, which cause the lower intensity (I_1) of bulk annihilation.

Effect of vacancy type defect mobility in different Fe-Cr structures will be observed using proton implantation in further experiments. Nowadays is running the implantation of the specimens on the level 0.1-0.5C using H and He ions with the energy based on the SRIM (The Stopping and Range of Ions in Matter, available on <http://www.srim.org/>) simulations.

Acknowledgements

This project was supported by FP6 of European Commission Fu-Ct-2005-00136: Microstructural Characterisation of Fe-Cr Alloys: Simulations, Positron Annihilation and Mössbauer Spectroscopy.

REFERENCES

- [1] Gelles, D.S., *J. Nucl. Mater.*, 329-333, 304-308 (2004).
- [2] Arakawa, K., M. Hatanaka, H. Mori, J.K.. Ono, *Nucl. Mater.*, 329-333, 1232-1236 (1988).
- [3] Matijasevic, M., A. Al Mazouzi, *Modelisation of Irradiation Effects: Modelling Oriented Experiments on Pure Fe-Cr-C*, Restricted contract report, SCK•CEN-R-4196, July 2005, RMO SCK•CEN, Boeretang 200, B-2400, Mol, Belgium.
- [4] Slugeň, V., J. Kuriplach, P. Ballo, P. Domonkoš, G. Kögel, P. Sperr, W. Egger, W. Triftshäuser, M. Domanková, P. Kováč, I. Vávra, S. Stanček, M. Petriska, A. Zeman, “Positron Annihilation Investigations of Defects in Copper Alloys Selected for Nuclear Fusion Technology”, *Fusion Engineering and Design*, 70/2, pp. 141-153 (2004).
- [5] Slugeň, V., G. Kögel, J. Kuriplach, P. Ballo, P. Sperr, W. Egger, W. Triftshäuser, P. Domonkoš, M. Petriska, A. Zeman, “Investigation of Defects in Copper Alloys Selected for Nuclear Fusion Technology”, *Material Science Forum*, Vols. 445-446, pp. 183-185 (2004).
- [6] Kováč, P., M. Pavlovič, J. Dobrovodský, “A 0.9 MV Accelerator for Materials Research at the STU Bratislava”, *Nucl. Instr. and Meth.*, B 85, 749-751 (1994).
- [7] Čížek J., “Investigation of Crystal Lattice Defects in Deformation and Irradiation Damaged Solids by Means of Positron Annihilation”, Doctoral thesis, Prague (2001).
- [8] Dupasquier, A., “Positron Trapping at Grain Boundaries”, *Physical Review*, Vol. 48, No. 13, October 1993.

THE INFLUENCE OF DIFFERENT CHEMICAL ELEMENTS IN THE HARDENING/EMBRITTELEMENT OF RPV STEELS

Marlies Lambrecht, Abderrahim Al Mazouzi
SCK•CEN, Department of Structural Materials, LHMA
Boeretang 200, B-2400 Mol, Belgium

Abstract

The hardening and embrittlement of reactor pressure vessel (RPV) steels is of great concern in the actual nuclear power plant life assessment. This embrittlement is caused by irradiation-induced damage, like vacancies, interstitials, solutes and their clusters. The current procedure to estimate material properties for the irradiated pressure vessels is based on Charpy-V tests of identical material located at the inner shell of the reactor. But the reason for the embrittlement of the materials is not yet totally known. The real nature of the irradiation damage should thus be examined as well as its evolution in time.

Fe-Cu binary alloys are often used to mimic the behaviour of such steels. Their study allows identifying some of the defects responsible of the hardening, especially when compared to pure iron or C-micro-alloyed iron. More recently the influence of manganese and nickel in low-Cu RPV steels has become a significant topic. Thus in contrast with the existing models in the literature, where it is predicted that the hardening saturates after a certain dose, alloys containing nickel and manganese irradiated at SCK•CEN up to doses of $1.3 \cdot 10^{20} \text{ n/cm}^2$ showed a continuing increase of the hardening. Positron Annihilation Spectroscopy analyses show that the main objects causing hardening are most probably interstitial clusters decorated with manganese in the Cu-free alloy. While in the RPV steel and Fe-CuMnNi alloy, the main effect is still due to Cu-rich precipitates at low dose, but the role of manganese becomes predominant at high dose.

Introduction

For the safeguarding of the nuclear power plants (NPPs), already a lot of investigations have been performed. In all these investigations it has been observed that the materials used for the reactor vessels [reactor pressure vessel (RPV) steels] are prompt to embrittlement due to the irradiation. The current procedure to estimate material properties for the irradiated pressure vessels is based on Charpy-V tests. Some capsules are installed at the inner shell of the reactor to perform these tests. But currently these capsules are used up. To extend the lifetime of the NPPS, there is an urgent need for predictive models based simultaneously on experiments and computer simulation. The study of defect formation under neutron irradiation and their thermal stability is of paramount importance for the understanding of radiation damage of structural materials.

The irradiation-induced embrittlement can be summarised by three main causes [1], precipitation, matrix damage and grain boundary segregation. The nature of these effects has to be known for the better understanding of the interplay of hardening and embrittlement. However and up to now, it is still uncertain to assess the main mechanism that gives rise to the matrix damage. Among others, L. Malerba [2] has shown that directly in the cascades some candidate cluster-solute complexes inducing small vacancy and interstitial clusters are produced. These defects aggregate to larger defects such as nanovoids and interstitial loops. At the same time, various solutes may diffuse to these clusters giving rise to complex defect-solute configurations.

Nowadays the progress achieved in advanced experimental techniques such as e.g. Transmission Electron Microscopy (TEM), Positron Annihilation Spectroscopy (PAS), Internal Friction (IF), Tomographic Atom Probe (TAP) and Small Angle Neutron Scattering (SANS) enables a detailed investigation of the nano-features induced by irradiation in RPV steels to be performed [3]. In this paper the experiments have been performed by PAS, which provides valuable information on this topic [4-7]. In PAS the positron is applied as probe. As anti-particle of the electron the positron will be trapped by defects with higher electron density like vacancies, vacancy clusters, interfaces, second phase particles, dislocations, etc. [8]. The annihilation characteristics are different in the neighbourhood of defects as for defect-free materials. Moreover, due to the difference in positron affinity of the different atoms, positrons will annihilate with another probability in the precipitates as in the bulk material. The power of PAS is its possibility to find very small defects (> 0.1 nm) with very low concentrations (> 1 ppm), its “self-seeking” nature and its non-destructive realisation. It is used in many different fields of material science, for instance in building materials (e.g. cement [9], polymers [10,11]), semiconductor-based systems for the information technology [12], as well as for the characterisation of nuclear materials ([4-6]).

Significant insight concerning potential vacancy clusters has been made by PAS during the past decades [13-16]. Focus is now being put on the nature of the clusters that are sensitive to positrons as well as to matrix damage. Positrons are also sensitive to precipitate-matrix interfaces. Therefore a substantial effort is being redeployed to use this technique to enquire the ultimate understanding of the hardening and embrittlement of RPV steels. Within this paper, the results obtained from the PAS investigations of different neutron-irradiated Fe and Fe-Cu alloys as well as a Fe-MnNi and a Fe-CuMnNi alloy are described and discussed. This is done in relation with the irradiation induced hardening data obtained from the same samples [17].

Materials and irradiation conditions

Starting from electrolytic iron, seven different materials were made, covering different model alloys in growing chemical complexity between the two extremes, pure iron and a real RPV steel.

These alloys are listed in Table 1. They were prepared using argon-arc melting and zone refinement methods. The resulting ingots were cold worked after austenisation tempering. A final heat treatment at 1 075 K is performed to release the stresses and to get well recrystallised materials. This was followed by water quenching.

Table 1. The chemical composition of the seven different alloys

Material	Nominal composition (wt.%)
Pure Fe	< 30 ppm C
Fe-C	> 30 ppm C
Fe-0.1%Cu	0.1 Cu (< 30 ppm C)
Fe-0.3%Cu	0.3 Cu (< 30 ppm C)
Fe-Mn-Ni	1.2 Mn, 0.7 Ni (< 30 ppm C)
Fe-Cu-Mn-Ni	0.1 Cu, 1.2 Mn, 0.7 Ni (< 30 ppm C)
French RPV steel	0.135 C, 0.009 S, 0.013 P, 0.04 Si, 0.37 Mn, 0.69 Ni, 0.13 Cr, 0.52 Mo, 0.065 Cu

The material has been irradiated in the test reactor BR2 at SCK•CEN. During irradiation with a flux of $9.54 \cdot 10^{13} \text{ n/cm}^2\text{s}^{-1}$ the temperature and the pressure were maintained constant at respectively 300°C and 150 bar.

This report will deal on the theoretical end of life of the NPPS, i.e. 40 years. As 0.1 dpa (or $7 \cdot 10^{19} \text{ n/cm}^2$) corresponds with about 40 years of irradiation, only the specimens with these irradiation conditions will be treated in this work.

Measurement and analysis

At SCK•CEN, both Positron Lifetime (PLT) and Coincidence Doppler Broadening (CDB) spectroscopy are used in complementary way. Thus, PLT measurements give information of the electronic structure of the material on the place of the annihilation, while CDB spectroscopy is used to measure the positron affinity of the atoms in the neighbourhood of the annihilation. Mechanical properties are also performed.

Hardening measurements

In addition to PAS, the mechanical properties of the samples have been determined. The tensile specimens used for these measurements have a gauge length of 15 mm with a diameter of 3 mm. The heads of the specimens have a diameter of 8 mm and the total length of the specimens is 26 mm. All measurements have been performed at room temperature.

Positron lifetime measurements

Irradiated specimens of $10 \times 10 \times 1 \text{ mm}^3$, have been firstly surface polished to mirror like, then chemically etched using a (HF + H₂O₂ + H₂O)-solution to remove the deformed surface layer. The two specimens are then mounted in the positron specimen holder under biologically shielded environment. The sandwich was then automatically loaded in the measurement cell between three BaF₂ detectors working on anti-coincidence mode. Depending on the radioactivity of the samples, the distance separating the detectors have been adjusted to minimise the background. Care was taken to separate correctly the γ -peaks coming from the specimens and those related to the positrons by following the

procedure described by M. Jardin, *et al.* in [18]. Due to their activity, the acquisition of statistically relevant number of counts, namely at least one million, has required more than one week for high dose irradiated samples. The analysis of the obtained spectra has been performed using the LT software by J. Kansy [19]. The resolution of the set-up was constantly checked to be about 175 ps, while the source contribution was set to 15% with a single lifetime of 393 ps. More detailed information about the experimental set-up is given by M. Jardin, *et al.* in [18] and [20]. All measurements were performed at room temperature using a ^{22}Na positron source of 2 MBq strength, wrapped in Kapton foils.

The lifetime spectrum $N(t)$ in time t obtained during the measurements is given by the equation below of the intensities I_i and the lifetimes τ_i . In this equation, there are k different kinds of defects assumed.

$$N(t) = \sum_{i=1}^{k+1} \frac{I_i}{\tau_i} \exp\left(-\frac{t}{\tau_i}\right)$$

The positron lifetime τ is a value which carries on information about the electron density at the annihilation site. Because the annihilation rate λ , the reciprocal of the lifetime, is given by the overlap of the positron density $n_+(\mathbf{r})$ and the electron density $n_-(\mathbf{r})$. This is given by following equation [21]:

$$\lambda = \frac{1}{\tau} = \pi r_0^2 c \int n_-(\mathbf{r}) \gamma(n_-(\mathbf{r})) n_+(\mathbf{r}) d\mathbf{r}$$

Here r_0 is the electron radius, c is the speed of light and $\gamma(n_-(\mathbf{r}))$ is the enhancement factor. More investigation on these values has been done by J. Kuriplach [22] and others. The electron density is related to amongst other things the amount of vacancies near the annihilation site.

To correlate the lifetime and the intensity parameters with the real properties of the defects, we need to solve the following set of differential equations:

$$\begin{cases} \frac{dn_B}{dt} = -\left(\lambda_B + \sum_{i=1}^k \kappa_i\right) n_B + \sum_{i=1}^k \delta_i n_{D_i} \\ \frac{dn_{D_i}}{dt} = \kappa_i n_B - (\lambda_{D_i} + \delta_i) n_{D_i} \end{cases}$$

In these equations B and D_i are the indicating the free and the trapped state, while λ is the annihilation rate, κ is the trapping rate and δ is the detrapping rate. When these equations are solved, with the knowledge of all parameters, it is possible to determine the number of each time of defects, using the intensities I_i . More detailed information can be found in [23].

Coincidence Doppler broadening measurements

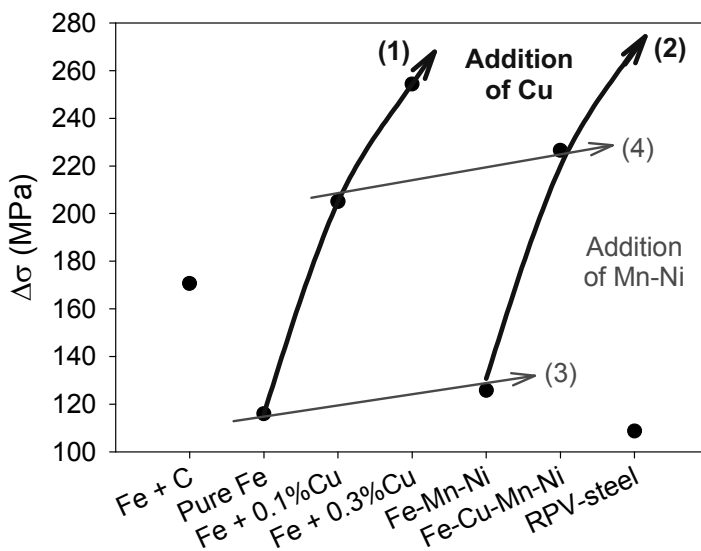
The CDB measurements have been performed as described by K. Verheyen, *et al.* in [17]. The analysis of the results was made using CDB ratio curves, obtained by normalising the momentum distribution to the one of unirradiated defect-free pure Fe. The S and W parameters are extracted from each spectrum. They are defined respectively as the ratio of low-momentum ($|cp_L| < 2.5 \cdot 10^{-3} mc$) and high-momentum ($15 \cdot 10^{-3} mc < |cp_L| < 25 \cdot 10^{-3} mc$) regions in the CDB spectrum to the total region (c is the speed of light and p_L is the longitudinal component of the positron-electron momentum along the direction of the γ -ray emission).

Results and discussions

Hardening measurements

Figure 1 shows that the irradiation-induced hardening depends strongly on the material composition. The hardening of pure iron is quite low. The addition of some carbon gives an increase of the hardening of about 50 MPa. The self-interstitials, trapped at the carbon atoms will thus block the dislocation movement. The trend due to copper-addition is indicated by Track 1 in Figure 1. Track 3 gives the tendency of the hardening due to an addition of manganese and nickel. Track 1 is very steep, thus copper leads to an enormous increase of hardness, while the hardening of manganese and nickel is much less pronounced. When 0.1% of copper is added to the Fe-MnNi alloy, the hardness follows the same trend as Track 1, i.e. Track 2. And if manganese and nickel are added to the Fe-0.1%Cu alloy, the hardness is following Track 4, which is again parallel to Track 3. There can thus be concluded that the hardening of both mechanisms is independent of each other.

Figure 1. The hardening (change of yield strength of the 0.1 dpa measurement compared to the unirradiated measurement) for all materials is illustrated. The effect of an addition of copper is shown as well as the effect of an addition of manganese and nickel.



As the hardening of the copper-addition is larger, the effect of this element will be the predominant one in medium- and high-copper steels. The effect of copper has therefore been investigated for many years [24]. It is now known that already at the start of the irradiation some copper-rich precipitates are formed, which block the dislocation movement [25]. Once the precipitates are formed, the hardening will saturate [17]. A higher copper concentration in the alloy will lead to more precipitates, thus they will have a higher hardening component.

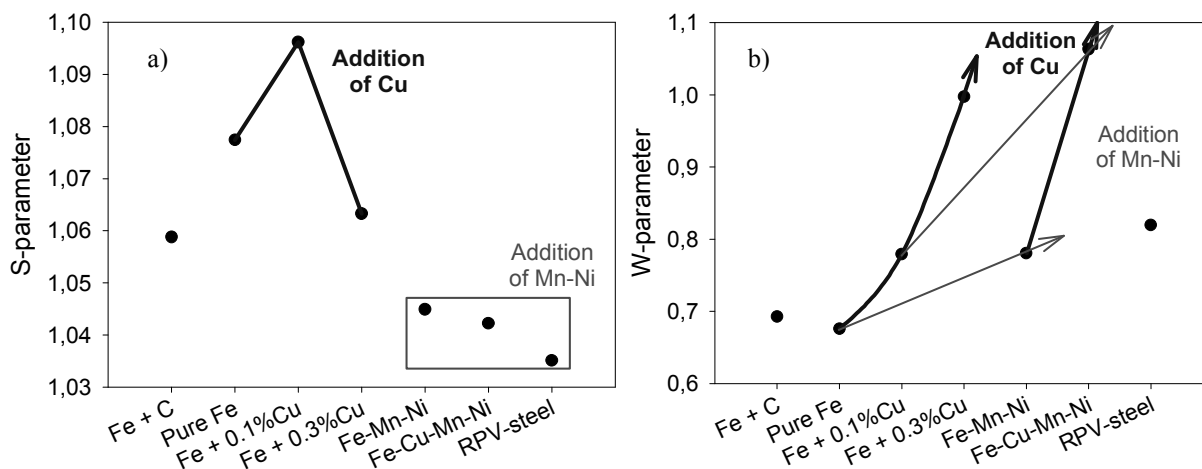
In contrary to higher-copper steels, the effect of manganese and nickel will not be negligible in low-copper steels. For that reason research should be focused on this hardening mechanism as well. There should already be mentioned, that these elements will not be located near the copper-rich precipitates, as their hardening is independent of the hardening due to copper.

The result for the low-copper RPV steel is very close to the alloy containing manganese and nickel and no copper. The small difference should be explained by a lower concentration of manganese and/or the initial microstructure. The model alloys are purely ferrite, while the steel is ferrite/bainite.

Coincidence Doppler broadening measurements

The low momentum part of the CDB results or the S parameter is especially due to electrons on the outer shell of an atom near the annihilation-site. Therefore this part of the curve will contain more information about the vacancy behaviour in the material. The high momentum part or the W parameter on the other hand deals with the inner shell electrons of the atom. This parameter is thus a fingerprint of the atoms near the annihilation sites. The values shown in Figure 2 are the ratio of the values obtained from the measurement of the investigated alloys to the one of non-irradiated pure iron. During irradiation, one expects that there will occur more vacancies, thus the S parameter [Figure 2(a)] will increase (higher than 1). At the same time fewer positrons will be able to annihilate with inner shell electrons, thus the W parameter [Figure 2(b)] will decrease (lower than 1). This is what happens for pure iron in Figure 2. If some carbon is added, a decrease of S is observed, while W is almost the same. The defects where the positrons annihilate will thus have the same chemical environment in both cases, but carbon seems to reduce the size of vacancy clusters observed.

Figure 2. The low [S parameter (a)] and high [W parameter (b)] momentum part of the CDB results is shown for all materials. The effect of a copper addition can be seen as well as the effect of an addition of manganese and nickel.



The binary iron-copper alloys show on the one side a continuous increase of W [Figure 2(b)]. On the other side S does behave differently [Figure 2(a)]. Puska, *et al.* [26] have shown that the positron affinity of the copper-precipitates is higher than the one of the iron-matrix. Therefore the W parameter will increase with the presence of precipitates, until it reaches the value of pure copper. The alloy with more copper contains more precipitates and will thus have a higher W value. For the medium-copper alloy an increase of the S value is observed. In [24] it has been illustrated that vacancies are located near the copper-rich precipitates and these will influence the behaviour of the S parameter. This value will be higher, due to the positron affinity of the copper in the vacancy-rich precipitates. When more copper is added, the S parameter decreases drastically. This behaviour should be explained by the fact that the created vacancies are forced towards more precipitates. In [24] it was also shown that in the alloy with 0.3% of copper some vacancy-free precipitates are formed, as a result of an augmenting amount of precipitates, while the amount of vacancies, created during irradiation is the same for the same irradiation conditions.

In contrary to the results of the yield strength increase, the effect of manganese and nickel during PAS measurements is not independent of the effect of copper. Nevertheless the theory of the two independent mechanisms is still assumed. When manganese and nickel are added to pure iron,

W [Figure 2(b)] increases, while S [Figure 2(a)] decreases drastically. As manganese has a lower positron affinity than the iron-matrix, while nickel has one compared to the one of copper [26], this can only be due to the influence of nickel. Manganese has no effect on PAS results. The drastic decrease of the S parameter illustrates that the nickel-rich regions do not contain many vacancies. The addition of copper to this alloy leads to an enormous increase of the W value. This means that most of the positrons will annihilate in the nickel-rich regions or in the copper precipitates. And almost no positrons will annihilate in the matrix. Nonetheless, it is not possible to distinguish between the annihilation in both regions. The enormous increase in W will induce a decrease of S, as a result of the equilibrium between the two parameters. In spite of this, the S value of the Fe-CuMnNi alloy is almost the same as the value for the Fe-MnNi alloy. This is caused by an increase of S, due to the vacancies located in the copper-rich precipitates.

The same explanation counts for the French RPV steel. This steel contains the same amount of nickel and a very low concentration of copper. Because of this the effect of nickel is more explicit.

Positron lifetime measurements

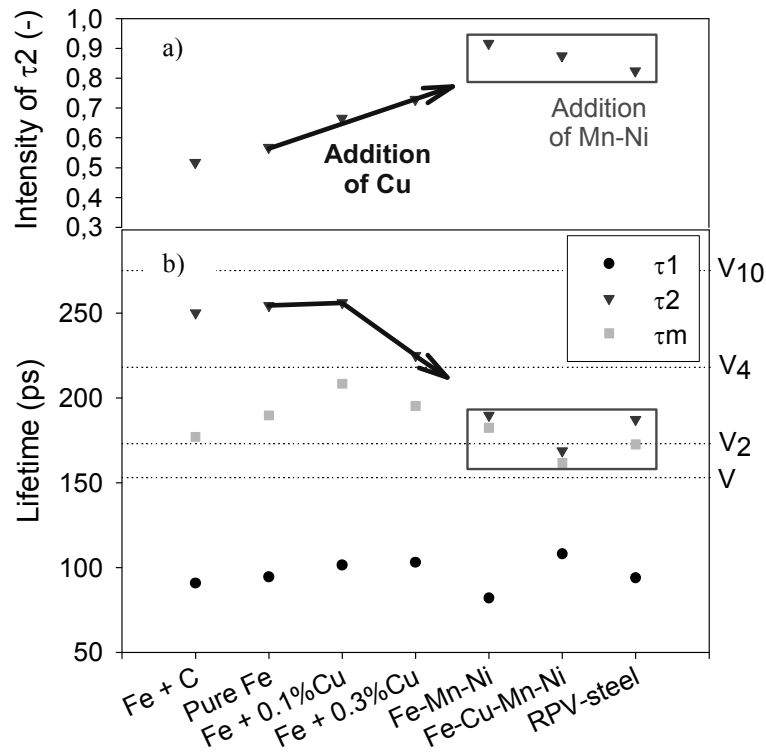
The lifetime results give more information about the amount of vacancy clusters (intensity) and the amount of vacancies in the clusters (lifetime). Pure defect-free iron has only one lifetime component, equal to 107 ps. When defects appear more components will occur. The first component relates to the iron-matrix and the second component is connected to the defects. The intensity of this second component is dependent of the amount of defects [23]. For the vacancy-type of defects, the second component increases with augmenting amount of vacancies in the defect. Figure 3 shows the PLT results for all the materials investigated. Here it is seen clearly that there are only few, but quite big vacancy clusters created in pure iron, during irradiation for 0.1 dpa. For the Fe-C alloy the same observations can be made. Nonetheless there are a little less clusters. This is also observed by the CDB results (Figure 2). While the interstitials are trapped by the carbon-atoms, the vacancies are thus having more chance to annihilate.

The copper will increase the intensity of the second component [Figure 3(a)]. As it is seen before, the copper-rich precipitate will be favourite annihilation-sites for the positrons. These precipitates will at the same time appear as nucleation-site for the vacancies. The vacancies created during irradiation will be divided between all precipitates. Therefore the amount of vacancies within one cluster will decrease with augmenting amount of precipitates. This difference is clearly seen between the alloy with 0.1% of copper and the alloy with 0.3% of copper [Figure 3(b)]. The same trend has already been observed with CDB (Figure 2).

On the part of the CDB results there has been concluded that almost all positrons annihilate near a defect in alloys containing manganese and nickel. This can also be observed within the PLT results. The intensity of the second component increases until more than 90% [Figure 3(a)]. The clusters observed are very small [Figure 3(b)]. This also was indicated by CDB. For the Fe-MnNi alloy the defects are divided between the nickel-rich regions and the vacancy clusters. In the Fe-CuMnNi alloy the vacancy clusters will be replaced by more Cu-rich precipitates, containing a smaller amount of vacancies. Thus the second component of the lifetime is even smaller than the alloy with no copper.

The result of the low-Cu steel resembles most the results of the Fe-MnNi alloy. The second component of the steel is almost the same as the one of the Fe-MnNi alloy, while its intensity is a little lower.

Figure 3. The positron lifetime results for all materials can be seen. The results are divided into two lifetime components (τ_1 and τ_2) and their average is given as well (τ_m). This is given in part (b) of the figure. I_2 (a) is the intensity of τ_2 ($I_1(\tau_1) + I_2(\tau_2) = 1$). In the figure, the theoretical values of positron lifetime in V clusters obtained by J. Kuriplach, *et al.* [27] are also reported. The effect of a copper and a manganese-nickel addition is visible.



There can thus be assumed that there are two main different mechanisms of irradiation-induced hardening in RPV steels. One is caused by the vacancy-rich copper precipitates, which have been proven by the PAS results. Secondly, *ab initio* calculations by E. Vincent, *et al.* [27] have illustrated that manganese is preferentially located in interstitial position. While its affinity to vacancies is found to be lower than the one of pure V clusters in iron [28]. Thus manganese will decorate the SIA loops, where no vacancies are available. This makes these defects invisible by PAS. They will nevertheless play an important role in the hardening mechanism of the material. More investigation has to be performed by other techniques, such as TAP to identify these manganese- and nickel-rich defects.

Conclusions

Most of the hardening is due to copper precipitation in RPV steels and their model alloys up to a dose of 0.1 dpa. Also matrix damage plays an important role. Positron Annihilation Spectroscopy, both Positron Lifetime and Coincidence Doppler Broadening are powerful techniques to analyse these Cu-rich precipitates and voids. The set-ups, available at SCK•CEN, are able to analyse active specimens with a high accuracy. PAS gives detailed information about the copper-vacancy complexes. The positron lifetime depends on the size and the volume fraction of vacancy clusters, so PLT extract information on the mean size. Due to the high affinity to copper of positrons, CDB gives information on the growth of the Cu precipitates.

The hardening in low-Cu steels is different from the one in high-Cu steels. PAS detects the Cu precipitates and voids as well as the Ni-rich regions. These regions are thus not located near the Cu precipitates. Mn is not visualised by the positron probe, while *ab initio* calculations have shown that the Mn is preferably located in interstitial positions. Therefore there can be assumed that the hardening in very low-Cu RPV steels is mainly induced by Mn decorated SIA loops.

Acknowledgements

This work is partly financed by the EU in the framework of PERFECT project.

REFERENCES

- [1] English, C.A., J.M. Hyde, Sr., *Proceedings of International Symposium on the Mechanisms of Materials Degradation and Non-destructive Evaluation in Light Water Reactors*, Osaka, Japan, 27-29 May 2002, p. 53; K. Fukuya, H. Nakata, K. Fujii, "Characterization of Radiation-induced Microstructural Changes in Reactor Vessel Steels".
- [2] Malerba, L., *J. Nucl. Mater.*, 351, 28 (2006).
- [3] *International School on Experimental Quantification of Irradiation Damage*, A. Al Mazouzi and L. Verdonck (Eds.), Rochehaut sur Semois, Belgium, 25-29 September 2006.
- [4] Nagai, Y., M. Hasegawa, Z. Tang, A. Hempel, K. Yubuta, T. Shimamura, Y. Kawazou, A. Kawai, T. Kano, *Phys. Rev. B*, 61, 6574 (2000).
- [5] Nagai, Y., Z. Tang, M. Hasegawa, T. Kanai, M. Saneyasu, *Phys. Rev. B*, 63, 134110 (2001).
- [6] Asoka-Kumar, P., B.D. Wirth, P.A. Sterne, *Philos. Mag. Lett.*, 82, 609 (2002).
- [7] Fujii, K., K. Fukuya, N. Nakata, K. Hono, Y. Nagai, M. Hasegawa, *J. Nucl. Mater.*, 340, 247 (2005).
- [8] Hessel Anderson, H., M. Eldrup, N. Hansen, D.J. Jensen, T. Leffers, O. Lillholt, B. Pedersen, B. Singh, *Proc. of the 5th Int. Riso Symposium of Metallurgy and Materials Science*, 133 (1984).
- [9] Salgueiro, W., A. Somoza, O. Cabrera, G. Consolati, *Cement Concrete Res.*, 34 (2004).
- [10] Jean, Y.C., *Microchem. J.*, 42 (1990); Y.C. Jean, *Mater. Sci. Forum*, 175-178, 59 (1995).
- [11] Jean, Y.C., P.E. Mallon, D.M. Schrader, *Principles and Applications of Positron and Positronium Chemistry*, World-Scientific, London (2003).
- [12] Krause-Rehberg, R., H.S. Leipner, *Positron Annihilation in Semi-conductors*, Springer, Berlin (1999).

- [13] Buswell, J.T., J.P. Highton, CEGB, *Berkeley Nuclear Laboratories*, TPRD/B/0787/R86 (1986).
- [14] Dai, G.H., P. Poser, J.C. Van Duysen, *ICPA-9*, Hungary (1991).
- [15] Carter, R.G., T. Onchi, N. Soneda, K. Dohi, J.M. Hyde, C.A. English, M.T. Hutchings, W. Server, J.F. Coste, J.C. Van Duysen, *Proceedings of the International Symposium on the Contribution of Materials Investigation to the Resolution of Problems Encountered in Pressurized Water Reactors*, Fontevraud IV (1998).
- [16] Valo, M., R. Krause, K. Saarinen, P. Hautojarvi, J.R. Hawthorne, *Effects of Radiation on Materials: 15th International Symposium*, R.E. Stoiler, A.S. Kumar, D.S. Gelles (Eds.), ASTM 1125, ASTM, Philadelphia, 172 (1992).
- [17] Verheyen, K., M. Jardin, A. Al Mazouzi, *J. Nucl. Mater.*, 351, 209 (2006).
- [18] Jardin, M., M. Lambrecht, A.A. Rempel, Y. Nagai, E. van Walle, A. Al mazouzi, *Nucl. Instr. and Meth. A*, 568, 716 (2006).
- [19] Kansy, J., *Nucl. Instr. and Meth. A*, 374, 235 (1996).
- [20] Jardin, M., A. Al Mazouzi, M. Lambrecht, A.A. Rempel, Y. Nagai, E. van Walle, *Proceedings of XIVth International Conference on Positron Annihilation*, Ontario, Canada, 23-28 July 2006.
- [21] Nieminen, R.M., M.J. Manninen, *Positrons in Solids*, P. Hautojärvi (Ed.), Springer-Verlag, Berlin, 145 (1979).
- [22] Kuriplach, J., O. Melikhova, C. Domain, C.S. Becquart, D. Kulikov, L. Malerba, M. Hou, A. Almazouzi, C.A. Duque, A.L. Morales, *Applied Surface Science*, 252, 3303 (2006).
- [23] Puska, M.J., R.M. Nieminen, *Rev. Mod. Phys.*, 66, 841 (1994).
- [24] Lambrecht, M., M. Jardin, A. Al Mazouzi, *Proceeding of the XIVth International Conference on Positron Annihilation*, Ontario, Canada, 23-28 July 2006.
- [25] Konstantinovic, M.J., A. Al Mazouzi, M. Scibetta, E. van Walle, *J. Nucl. Mater.*, 362, 283 (2007).
- [26] Puska, M.J., P. Lanki, R.M. Nieminen, *J. Phys. Condens. Matter.*, 1, 6081 (1989).
- [27] Vincent, E., C.S. Becquart, C. Domain, *J. Nucl. Mater.*, 359, 227 (2006).
- [28] Vincent, E., C.S. Becquart, C. Domain, *J. Nucl. Mater.*, 351, 88 (2006).

INTERATOMIC POTENTIALS CONSISTENT WITH THERMODYNAMICS

Giovanni Bonny¹, Roberto C. Pasianot², Pär Olsson³, Lorenzo Malerba¹

¹Nuclear Materials Science Institute, SCK•CEN, Boeretang 200, B-2400 Mol, Belgium

²Materials Dept., CAC-CNEA, Avda. Gral. Paz 1499, 1650 San Martín, Buenos Aires, Argentina

³EdF R&D, Dept. MMC, Les Renardières, F-77212 Moret-sur-Loing, France

Abstract

A most desirable property of interatomic potentials to be used in atomistic simulations of microstructure evolution of irradiated metallic alloys is consistency with the experimental phase diagram, the solid solubility and the phase stability in particular. A methodology to fit semi-empirical potentials with this goal in mind, recently developed by the authors, is here reviewed and critically discussed. The methodology is based on the seamless coupling of the Cluster Variation Method technique, a known sophisticated mean field theory for solid phase diagram computation, using the correlation function formalism to express energy and entropy, to other, more standard requirements, such as compliance with the energetics of some crystal structures, point defects, etc. The method has been successfully applied to the construction of an embedded-atom method (EAM) many-body potential for the FeCu system, a prototype alloy for the understanding of reactor pressure vessel steels embrittlement under irradiation. Coherence with *ab initio* computed formation energies of small point defect clusters, as well as vacancy migration energies in the vicinity of Cu atoms, has also been incorporated. The potential is shown to match very reasonably the Cu solubility in the Fe matrix vs. temperature, and also obtains enhanced point defect kinetics behaviour with respect to previous potentials. Efforts to apply a similar methodology to the more challenging FeCr and FeNi systems required the adoption, even within the same fitting formalism, of more flexible fitting techniques, which are here discussed, in the light of the uncertainties related with the construction of phase diagrams from the knowledge of atomic interactions, even when these are described with *ab initio* methods.

Introduction

Interatomic potentials are the core of atomistic computer simulations and determine the degree of reliability of the results obtained from these models. In the case of alloys, the microstructural evolution under irradiation is decided by the interplay between defect formation and migration, and thermodynamic driving forces. Thus it is very desirable that an interatomic potential reproduces as closely as possible the stability of the phases that can appear, so that compliance with the experimental phase diagram is implied.

Given a cohesive model, particularly an interatomic potential, there are accurate though expensive methods to compute its phase diagram [1]; inversion of those methods in order to derive the most consistent set of model parameters appears in general unfeasible. Therefore a practical procedure to build potential functions must include the thermodynamic information already at the fitting stage. Restricting ourselves to solid phases, a possible approach to this is the so called Cluster Variation Method (CVM) [2], that has been applied successfully for calculating the phase diagram of a wide variety of systems [3]. CVM is a mean-field theory that provides analytic expressions for the configurational entropy that transcend the regular solution model. On the other hand, the energy is generally handled via Ising-like spin Hamiltonians.

Here we review a methodology for building semi-empirical interatomic potentials that has recently been developed by the authors [4]. The method incorporates, among other more standard procedures, the CVM formalism, aiming at optimising the model parameters in order to obtain agreement with the experimental phase diagram. An interatomic potential based on the embedded-atom method (EAM) format, which possesses important improvements with respect to previous models, has already been constructed for the FeCu system. Presently however, the technique meets with difficulties when dealing with the FeNi and FeCr systems, so pointing to the need of further developments. The nature of those difficulties and possible ways of sorting them out are discussed.

Method

General framework

Thinking of a substitutional alloy as a lattice Ω whose sites can be occupied by either species A or B , on statistical mechanics grounds [5] free energies can be expressed as variational problems in this configuration space \mathbf{C}_Ω , namely, the probability distribution function $p(\sigma)$ must be optimal. In particular the Helmholtz free energy $F(T, V, c)$ is written as:

$$F = \min_{p \geq 0} \left\{ \sum_{\sigma} p(\sigma) [E(\sigma) + k_B T \ln p(\sigma)] \right\} \quad (1)$$

where σ stands for configuration, $p(\sigma)$ satisfies $\sum_{\sigma} p(\sigma) = 1$ and also must comply with the specified concentration c . The next important concept is that of correlation functions. Any function on \mathbf{C}_Ω admits the so called cluster expansion:

$$f(\sigma) = \sum_{\alpha \subseteq \Omega} f_{\alpha} \Pi_{\alpha}(\sigma) \quad (2)$$

where the Π_{α} 's constitute a complete and orthogonal set and are defined as products of spin-like functions:

$$\Pi_{\alpha} = \prod_{i \in \alpha} \hat{\sigma}_i, \text{ with } \hat{\sigma}_i(A) = +1 \text{ and } \hat{\sigma}_i(B) = -1 \quad (3)$$

The above expansion, when applied to $p(\sigma)$, allows the correlation functions ξ_{α} to be obtained, as:

$$p(\sigma) = \frac{1}{2^{|\Omega|}} \sum_{\alpha \subseteq \Omega} \xi_{\alpha} \Pi_{\alpha}(\sigma), \Rightarrow \xi_{\alpha} = \sum_{\sigma} p(\sigma) \Pi_{\alpha}(\sigma) \quad (4)$$

So, knowing the full set of ξ_{α} is equivalent to knowing $p(\sigma)$, wherefrom Eq. (1) can be translated into the language of the correlation functions, as well as all the conditions imposed on $p(\sigma)$; particularly, $p(\sigma) \geq 0$ defines a convex polyhedron in ξ_{α} space, which is the domain where the minimisation in Eq. (1) takes place.

For this approach to be effective, however, further assumptions are made. The clusters α that matter in the expansion are held to be relatively small and compact, so that no cluster beyond some largest (maximal) α_M needs to be considered. Summarising, the problem posed in Eq. (1) for an infinite crystal and on a *per-node* basis is rephrased as:

$$f = \min_{\xi} \left\{ \sum_{\alpha \subseteq \alpha_M} m_{\alpha} E_{\alpha} \xi_{\alpha} + k_B T \sum_{\alpha \subseteq \alpha_M} m_{\alpha} a_{\alpha} \sum_{\sigma} p_{\alpha}(\sigma) \ln p_{\alpha}(\sigma) \right\} \quad (5)$$

where $p_{\alpha}(\sigma)$ is the derived probability distribution for cluster α , expanded as in Eq. (4), and m_{α} stands for multiplicity (clusters/node). The first term on the right hand side is the energy contribution expressed as in Eq. (2); the second one represents the configurational entropy and is the specific ingredient coming from CVM, namely, a_{α} are constant coefficients depending only on lattice symmetry/topology.

Clearly, access to a thermodynamic potential grants access to all thermodynamic properties, particularly the phase diagram. Thus, one can use experimental data such as the two solute concentrations, c_1 and c_2 , that are in equilibrium on a phase boundary at temperature T , to force the common tangent equations derived from Eq. (5) to be compliant with this fact. A useful alternative approach is to consider Eq. (5) as a quick prototyping tool for obtaining the overall phase diagram appearance once the energy model is known, while using more sophisticated methods at later stages to perform the actual calculation. These equations are added to a larger set of more standard ones, such as compliance with alloy mixing enthalpies, formation energies of some defect structures (either from experiment or calculated by *ab initio* methods), etc. The enlarged set is proposed to be matched in a minimum square sense by optimisation on the potential parameters, eventually subject to extra constraints.

Some specifics

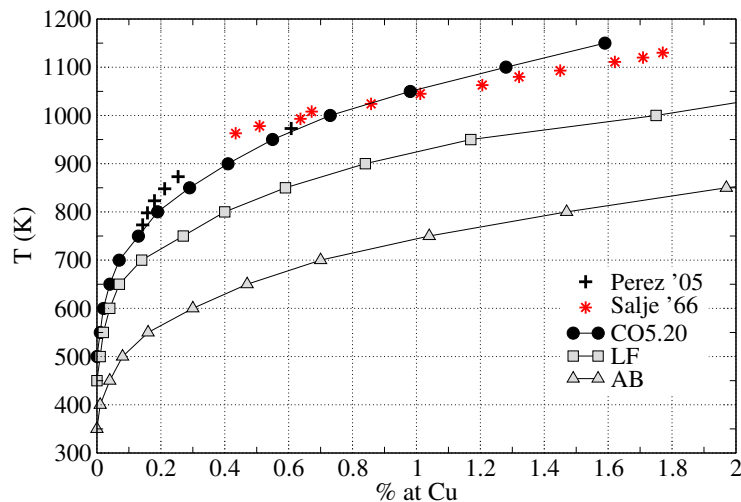
As anticipated, the energy model is taken from the EAM, which writes the energy per node e_i as:

$$\begin{aligned} e_i &= \frac{1}{2} \sum_{j \neq i} V(r_{ij}) + F(\rho_i) \\ \rho_i &= \sum_{j \neq i} \psi(r_{ij}) \end{aligned} \quad (6)$$

where V and ψ are pair-like functions and F is the so called embedding term; currently, the pure species potentials are chosen from the literature and the effort is concentrated on finding the most consistent mixed pair potential, $V_{AB}(r)$. An important issue here relates to the range of the interactions, because this determines the size, shape, and number of the clusters to be used in Eq. (5). The number increases very rapidly with size, so a compromise must be found with what is practically feasible. Thus, for the FeCu system discussed below, the energy was expanded up to triplets and the pair functions reached up to fifth nearest neighbours, leaving us with a total of 13/10 independent correlation functions for the bcc/fcc lattice. Finally, the configurational entropy was written in the so called tetrahedron approximation for the bcc lattice, and in the tetrahedron-octahedron approximation for the fcc one, both in a form suitable to the disordered lattice; the names refer to α_M in Eq. (5) (i.e. there are two of them for the fcc lattice).

The FeCu system

The outlined methodology was applied to fabricate a new FeCu potential meant to be used for the study of Cu precipitation in Fe under irradiation. Although there are in the literature a couple of many-body potentials for this system [6,7], neither of them appeared to be fully suitable for this kind of studies. For the pure species, two very refined potentials were selected from the literature [8,9]; the cross potential was fitted to 10 points of the mixing energy curve for the bcc phase, taken from Calphad-type calculations [10], and the maximum solubility of Cu and Fe at equilibrium in the coexisting bcc-fcc phases of the experimental diagram [11] (1.9 and 1.3 at.% respectively at $T \approx 1123$ K). The constraints included overall agreement with *ab initio* computed [12] binding energies for Cu-Cu at 1st, 2nd, and 3rd nearest neighbours, and Cu vacancy at 1st and 2nd ones. Also enforced was the overall agreement with the *ab initio* calculated barriers for the vacancy jumps nearest to a Cu atom, in order to reproduce the dragging of Cu atoms by vacancies, deduced on experimental grounds [13].



From the thermodynamic point of view, the most relevant result is presented in Figure 1, which shows the Cu solubility limit in the Fe matrix. The result for the current potential, CO5.20, is there compared to the ones of previous potentials, AB [6] and LF [7], and to experimental measurements [14,15]. Clearly, CO5.20 follows the experiment very reasonably, the other two potentials giving too high solubility.

The FeCr and FeNi systems

Some characteristics of the FeCu system, respected by the potentials chosen, did help the above sketched developments. Firstly, the two elements are almost insoluble into each other, meaning that no middle range concentrations needed to enter the picture, thus alleviating somewhat the stress on the CVM component. Secondly, the atomic sizes are rather well matched, so that essentially no local atomic relaxations were probed by the structures involved in the thermodynamics. Thirdly, some tests suggested that the vibrational contribution to the entropy could be neglected. Fourthly, the fitted mixing energy curve is a slightly skewed parabola, relatively easy to reproduce within a traditional EAM formalism.

For the FeCr and FeNi systems, on the other hand, the whole concentration range must be dealt with. FeCr shows a miscibility gap that closes at about 1100 K (neglecting a high temperature σ phase) while still in the solid phase. FeNi has a $L1_2$ ordered phase, Ni_3Fe , and there is also evidence that the $L1_0$ phase, $NiFe$, might be stable. In addition, at high temperature there is a region of complete solid solubility in the fcc structure. The potentials then must at least obtain the correct 0 K ground states and avoid possible unwanted ones; this may also require adoption of CVM entropy expressions tailored to ordered phases.

In the FeCr system, the mixing enthalpy of the random alloy predicted by *ab initio* calculations is slightly negative below ~8-10 at.% Cr [16] and becomes positive for the remaining concentrations. Such a shape cannot be handled within the EAM formalism, requiring the adoption of another energy model. We have selected the two-band model of [17], extended to work with two s embedding functions. The approach is able to fit quite nicely the mentioned mixing enthalpy, but if no care is taken the potential built in this way possesses some, apparently spurious and deep in energy, ordered ground states that completely dominate the predicted phase diagram, which turns out to be at variance with experiment. The situation in the literature is somewhat controversial. On the one hand, the *ab initio* cluster expansion of [18] suggests that some low energy structures dramatically impact on the phase diagram. On the other, the potential built in [19], where a new interaction model was developed, heuristically inspired on Calphad ideas, obtains about the same (random) mixing energy as in [18], but is free of those low energy states. Finally, the original two-bands potential advanced in [17] obtains an about symmetric mixing energy curve with a fairly lower maximum than the previous two, also possessing a low energy 50 at.% structure absent in those. Thus, it appears that the only way of improving the situation is to get rid of those deep ground states, while maintaining a reasonable fit to the mixing energy, using the methodology explained below. A last observation regarding this system refers to the relevance of the vibrational contributions; in spite of the small lattice parameter mismatch between Fe and Cr, on theoretical and experimental grounds [20] these contributions are deemed to be important. Rough estimates by the authors using the potential of [17] agree with this view; however the same estimates for the potential of [19] turned out to be negligible.

Regarding the FeNi system, some literature *ab initio* calculations suggest a small lattice mismatch [21]; this fact is however not correctly reflected by our currently selected pure element potentials, unfortunately. Consequently, rather large local atomic relaxations are expected [22], which need to be accounted for at the fitting stage. Initial tests at developing a potential confirmed these expectations. Within this scenario, also the vibrational contributions are expected to be of concern.

In order to cope with the mentioned difficulties, we are developing a technique that is able to address individual, small cell crystalline structures, built on the bcc and the fcc lattices. These structures can be subjected to quick static energy optimisations in order to feed the objective function or constraints of the overall optimisation cycle for the potential parameters. Specifically, we deal directly with the convex polyhedron in the correlation function space, mentioned in connection with

Eq. (1) above, described through its vertices (barycentric co-ordinates). The latter corresponds to known crystalline structures, all of them possible candidates to ground states. Currently, the polyhedron is built within the six-dimensional space spanned by the point and the first five pair correlation functions. For the bcc lattice we started with the 28 vertices polyhedron already advanced by Finel [23] and have augmented it to one of 99 vertices using the tools provided by the ATAT package [24]; for the fcc lattice the 87 structures of Kanamori and Kakehashi [25] analysis are currently used, aimed at representing the energy landscape of any pair interaction reaching up to the 4th neighbours. For both the fcc and bcc lattice, efforts to systematically augment the probability polyhedron are ongoing. The approach can also turn into a way of handling the vibrational entropy, due to the fact that not only an energy, but also a vibrational free energy, computed e.g. within a harmonic model, can be associated to each of those structures. The outcome of this work in progress will be reported in future publications.

Acknowledgements

The authors acknowledge support from the PERFECT integrated project and the Belgian Scientific Policy Office (BelsPO), under contract CO 90 03 31662.00 (TANGO Project). R.P. acknowledges support from ANPCyT and CONICET. Thanks also to Dr. A. Caro for providing a version of his FeCr potential, and Dr. M. Lavrentiev for details on his cluster expansion.

REFERENCES

- [1] Lopasso, E.M., M. Caro, A. Caro, P. Turchi, *Phys. Rev. B*, 68, 214205 (2003).
- [2] Kikuchi, L., *Phys. Rev. B*, 51, 988 (1951).
- [3] Inden, G., W. Pitsch, *Materials Science and Technology*, Vol. 5, J. Wiley & Sons, pp. 497-552 (1991).
- [4] Pasianot, R.C., L. Malerba, *J. Nucl. Mater.*, 360, 118 (2007).
- [5] Ducastelle, F., "Order and Phase Stability in Alloys", *Cohesion and Structure*, Vol. 3, North Holland (1991).
- [6] Ackland, G., D.J. Bacon, A.F. Calder, T. Harry, *Philos. Mag. A*, 75, 713 (1997).
- [7] Ludwig, M., D. Farkas, D. Pedraza, M. Schmauder, *Modelling Simul. Mater. Scie. Eng.*, 6, 19 (1998).
- [8] Mendeleev, M.I., A. Han, D.J. Srolovitz, G.J. Ackland, D.Y. Sun, M. Asta, *Philos. Mag. A*, 83, 3977 (2003).
- [9] Mishin, Y., M.J. Mehl, D.A. Papaconstantopoulos, A.F. Voter, J.D. Kress, *Phys. Rev. B*, 63, 224106 (2001).

- [10] Caro, A., P. Turchi, M. Caro, E.M. Lopasso, *J. Nucl. Mater.*, 336, 233 (2005).
- [11] *Binary Alloy Phase Diagrams*, T.B. Massalski (Ed.), 2nd Ed., ASM International, Metals Park, OH (1990).
- [12] Becquart, C., C. Domain, *Nucl. Instrum. and Meth. B*, 202, 44 (2003).
- [13] Nagai, Y., Z. Tang, M. Hassegawa, T. Kanai, M. Saneyasu, *Phys. Rev. B*, 63, 134110 (2001).
- [14] Salje, G., M. Feller-Kniepmeier, *J. Appl. Phys.*, 48, 1833 (1977).
- [15] Perez, M., F. Perrard, V. Massardier, X. Kebler, A. Deschamps, H. de Monestrol, P. Pareige, G. Covarel, *Philos. Mag.*, 85, 2197 (2005).
- [16] Olsson, P., I.A. Abrikosov, J. Wallenius, *Phys. Rev. B*, 73, 104416 (2006).
- [17] Olsson, P., J. Wallenius, C. Domain, K. Nordlund, L. Malerba, *Phys. Rev. B*, 72, 214119 (2005).
- [18] Lavrentiev, M.Y., R. Drautz, D. Nguyen-Manh, T.P. Klaver, S.L. Dudarev, *Phys. Rev. B*, 75, 14208 (2007).
- [19] Caro, A., D.A. Crowson, M. Caro, *Phys. Rev. Lett.*, 95, 75702 (2005).
- [20] Fultz, B., L. Anthony, J.L. Robertson, R.M. Niklow, S. Spooner, M. Mostoller, *Phys. Rev. B*, 52, 3280 (1995).
- [21] Mishin, Y., M.J. Mehl, D.A. Papaconstantopoulos, *Acta Mater.*, 53, 4029 (2005).
- [22] Ackland, G.J., V. Vitek, *Phys. Rev. B*, 41, 10324 (1990).
- [23] Finel, A., PhD. Thesis, Université Pierre et Marie Curie (1987).
- [24] van de Walle, A., M. Asta, G. Ceder, *CALPHAD*, 26, 539 (2002).
- [25] Kanamori, J., Y. Kakehashi, *J. de Physique C*, 7, 38, 274 (1977).

THE WEB-ENABLED DATABASE OF JRC-EC, A USEFUL TOOL FOR MANAGING EUROPEAN GEN IV MATERIALS DATA

H.H. Over

EC-Joint Research Centre, Institute for Energy, Netherlands

W. Dietz

Consulting Metallurgist/MECS, Germany

Abstract

Materials and document databases are important tools to conserve knowledge and experimental materials data of European R&D projects. A web-enabled application guarantees a fast access to these data. In combination with analysis tools the experimental data are used for e.g. mechanical design, construction and lifetime predictions of complex components. The effective and efficient handling of large amounts of generic and detailed materials data with regard to properties related to e.g. fabrication processes, joining techniques, irradiation or aging is one of the basic elements of data management within ongoing nuclear safety and design related European research projects and networks.

The paper describes the structure and functionality of Mat-DB and gives examples how these tools can be used for the management and evaluation of materials data for EURATOM FP7 Generation IV reactor types.

Introduction

Fast access and exchange of materials data between research, design and manufacturing teams working on different sites worldwide is a challenging issue to be addressed during the product cycle in materials engineering [1]. Another important issue is safeguarding high investments made into materials research, which means that experimental data must be properly conserved, easily located and quickly retrieved. Materials databases (MDBs) are powerful tools to address these problems. Various categories of MDBs exist for different requirements, for example containing standards data on metallic alloys [2,3] and plastics [4] or more complex database applications needed for the design analysis [5]. MDBs are also basic elements for establishing knowledge based and expert systems [6].

With the emergence of the Internet, the capability of MDBs has further increased. Web-enabled MDBs provide a more centralised management and conservation of the data. Finding and accessing the required data is much faster than to search for them in a traditional manner, e.g. from handbooks or EXCEL files. In particular the dissemination of public research results has improved significantly, as the data are accessible over the world-wide web. However, only few web-enabled materials applications exist at present on the market. Examples are the materials databases of National Institute for Materials Science (NIMS) in Japan [7], which offer a lot of data but their interface guidance is still very limited. Currently, acceptance and use of (web-enabled) MDBs is still hindered by the following problems:

1. Many organisations use proprietary MDBs, which are customised to their requirements and internal practices. The structures of the databases are not standardised and therefore interoperability and data exchange between different organisations is difficult.
2. Data entry and validation are necessary but time-consuming tasks in order to ensure high-quality data. Often, scientists do not invest the required time to store the data in MDBs, instead they keep them in simple EXCEL sheets or other customised formats.
3. Materials data from publicly funded R&D projects are not sufficiently made available in electronic format. Therefore immediate access to free, public data sets is limited.
4. Industrial companies often hesitate to make their experimental data freely available; publications often contain limited information (e.g. on material processing details) and experimental information on product specific features is difficult to retrieve.

It is the objective of the paper to describe in detail the present status of the JRC MDB and the aim to establish a materials database for EURATOM FP7 Generation IV reactor types.

Database description and structure

The JRC has been developing the material database Mat-DB for safeguarding and managing its experimental materials data resulting from in-house research some 20 years ago [8,9]: Mat-DB covers mechanical and thermo-physical properties data of engineering alloys at low, elevated and high temperatures for base materials and joints [10]. It includes irradiation materials testing in the field of fusion and fission, tests on thermal barrier coating for gas turbines and mechanical properties testing on a corroded specimen. Corrosion part refers to weight gain/loss data of high temperature exposed engineering alloys, ceramics and hot isostatic pressed powder materials and covers corrosion tests such as oxidation, sulfidation and nitridation. The extension to other types of corrosion is under consideration. The database structure has continuously grown and the application developed from the initial mainframe database without graphical user guidance, over stand-alone PC and client/server

applications to the new web-enabled application. All current applications use an identical database structure simplifying data exchange between the JRC and its external MDB partners. Mat-DB is being used as stand-alone PC or client/server application by a number of European industry and research organisations to manage their in-house experimental test results. Updates and further developments are presented and discussed during annual user meetings with these customers.

Mat-DB is designed for experimental data, which is delivered by the laboratories in defined formats and quality. The emphasis is on data from tests, which comply with existing or pre-normative standards. The data can be entered, stored and accessed with typical database routines and can be evaluated with integrated analysis tools.

In order to conserve as much information as possible, the database contains detailed meta-information and entry of many fields is mandatory to increase data quality (see Table 1). Thesauri are provided for many text and image fields facilitating and improving data entry and retrieval. All entities contain additional fields (customer internals), which can be used for company-specific purposes. In addition to the numerical and alphanumeric data, any type of binary files can be stored within the database, for example final reports of R&D activities, drawings or large amounts of raw data (unfiltered curve data, basic output of strain gauge measurements).

Table 1. Description of Mat-DB entities

Entity	Meta-information for e.g.
Data source	Organisation, laboratory, scientist, R&D project
Material	Material characterisation, chemical composition, heat treatment, process data, microstructure
Specimen	Sampling, orientation, geometry, coating layers
Test condition	Test environment, mechanical or thermal pre-exposure, irradiation
Joining	Process method, joining parameters, joining geometry, filler metal
Test result	See Table 2

In total, the database structure for base materials contains more than 130 tables and 1 850 fields, which are grouped into logical entities: *data source*, *material*, *specimen*, *test condition* and *test result* (see also Table 1). The entities are linked within a relation table. For tests on dissimilar joints, e.g. weldments a *joining* and also a second *material* entity are added. The entity '*test result*' is divided into different areas, which contain tables for storing test type specific mechanical (23) and thermo-physical (10) properties and corrosion data (see Table 2).

Web-enabled Mat-DB

Mat-DB of JRC Petten is deployed to the secure ODIN (On-line Data Information Network) Portal: (<https://odin.jrc.ec.europa.eu>). The ODIN portal provides access to various web-enabled database applications for engineering and nuclear safety. The applications share fast cabling, firewall, secure connection, redundancy to guarantee high availability, central data and user management, professional hard- and software infrastructure in order to facilitate maintenance and further development, e.g. ORACLE as a powerful RDBMS, and professional database servers with high-capacity raid arrays for the storage of data and documents. They are continuously maintained and updated.

Table 2. Mat-DB test result entity

Mechanical properties	Irradiation
Crack growth and fracture	Irradiation creep
Creep crack growth	Swelling
Cyclic creep crack growth	In-pile relaxation
Fatigue crack growth	Tensile
Fracture toughness	Compression
Impact	Multi-axial tensile
Creep	Uniaxial tensile
Cyclic creep	Small punch tensile
Multi-axial creep	Thermo-physical properties
Torsional creep	Density
Uniaxial creep	Electrical resistivity
Small punch creep	Emissivity
Relaxation	Linear thermal expansion
Multi-axial relaxation	Poisson's ratio
Uniaxial relaxation	Specific heat
Fatigue	Shear modulus
High-cycle fatigue	Thermal conductivity
Low-cycle fatigue (load control)	Thermal diffusivity
Low-cycle fatigue (strain control)	Young's modulus
Thermal fatigue	Corrosion
Thermo-mechanical fatigue	High-temperature corrosion

Final reports of R&D projects, drawings of any format and the whole project documentation including minutes of meetings can additionally be stored in a structured manner (e.g. public and confidential areas) in the related web-enabled documentation database DoMa and linked to project specific data sets.

One of the motivations for developing Mat-DB and DoMa was to provide fast access to public and confidential data sets together with other documentation on the Petten Server and help to conserve, manage and analyse data of European R&D consortia. Just by opening their browsers any authorised partner can immediately access and evaluate data sets entered and validated by other partners.

The final goal of JRC is to provide the full cycle of data entry, retrieval and analysis over the Internet. Furthermore it is planned to network with partners in order to increase both, the amount of available data and the tools for analysing the data.

The JAVA-programmed user interfaces and evaluation routines are further developed and improved. On-line help assists in using the applications. Manuals for describing the databases and the analysis tools including e.g. descriptions of image and text thesauri, curve file structures, definitions of the test types are available for Mat-DB users from the ODIN portal.

Data entry and exchange

The JRC aim is direct web-enabled data entry from the machine into Mat-DB for all European project and network partners by using XML (eXtensive Mark-up Language). XML is an established standard to exchange data over the Internet between organisations having dissimilar structured

databases or between machines and databases. Data are not only assigned by their values but also by their names and units. The nomenclature of the field names within Mat-DB is compatible with the standard MATML (www.matml.org), a library developed by the international materials society and maintained by NIST (US: National Institute of Standards and Technology).

Tools within the Mat-DB allow users to convert their data into XML providing they are available electronically in a database or a spreadsheet. Once correctly formatted in XML the upload into Mat-DB is fast and easy because the data are correctly identified and transferred to Mat-DB. The same is valid for post processing tools of the machines, which are extended to export into the defined XML format. Source, material, specimen, test condition and joining metadata can then manually be completed within separate steps. The metadata can be linked to uploaded tests results. The completed data sets can be checked, updated and validated before they are uploaded into the relational database part and released after validation for clients. The XML based data entry procedure [11] for base material is meanwhile pilot tested within the running European R&D project “TMF-Standard” [12]. The joining part will be implemented until end of 2007.

Figure 1 shows the “*Specimen geometry & production*” data entry screen. The yellow fields are mandatory. Alphanumeric expressions such as shown in the figure for the field ‘*Standard*’ are available from a thesaurus and can be selected from a text box. Unique specimen types can be selected from an image thesaurus. New expressions can be added to the thesauri. The data are automatically checked against constraints. Only after validation by the source responsible the data can be retrieved by other assigned users. Figure 2 shows the XML code for the entered expressions shown in Figure 1.

Figure 1. Mat-DB screenshot showing specimen details for data entry

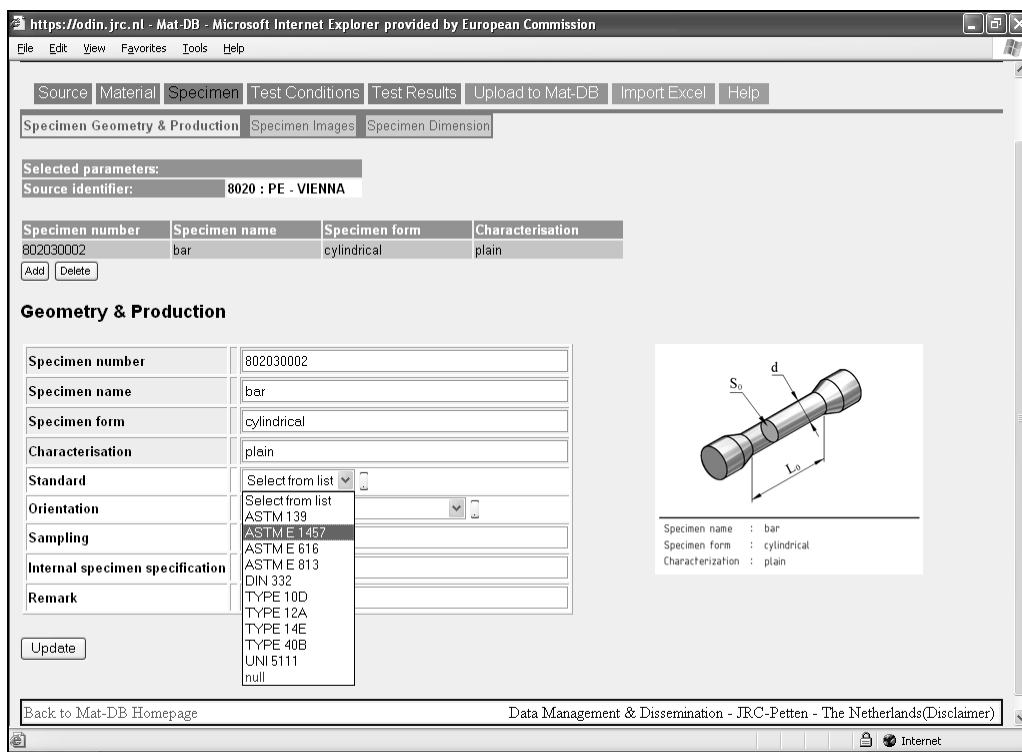
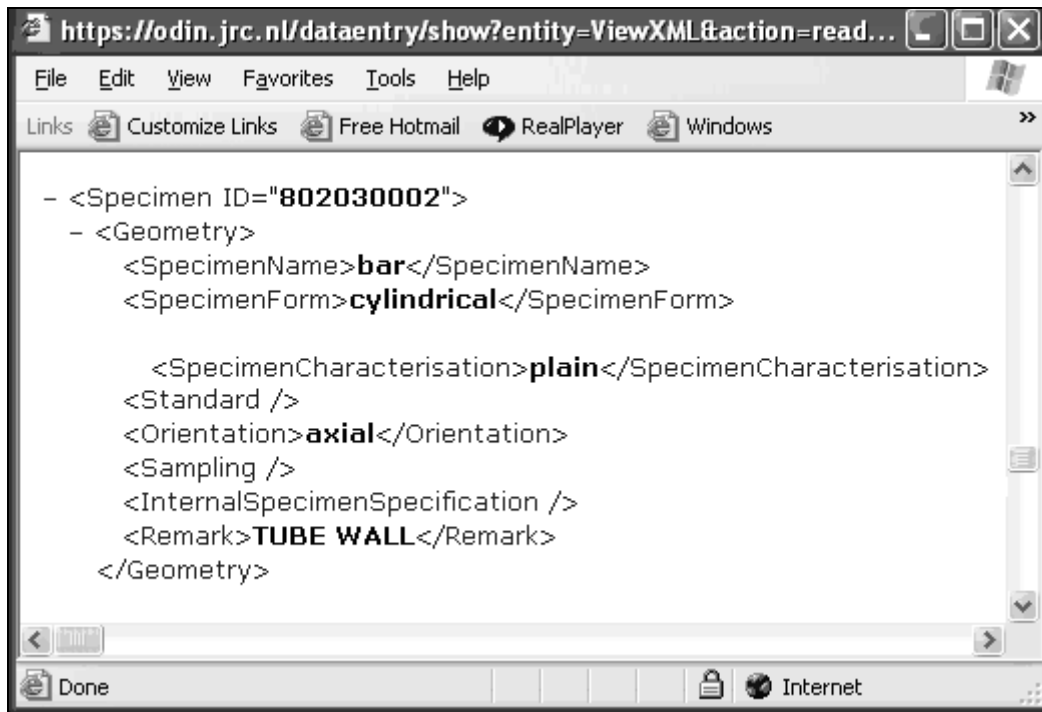


Figure 2. Mat-DB screenshot showing XML text for entered specimen details



Data retrieval and analysis

The web-enabled data retrieval user interface follows the principles of the well-established stand-alone PC and client/server applications, although it is slightly less sophisticated due to the limitations of the HTML protocol [13]. It allows constructing a query to retrieve the test results in three sequential levels. The first level starts with mandatory selections on *source*, *test type* and *material* following a hierarchical order. Data retrieval can then be continued with optional selections of a so-called *combined material*, which characterises special features of the material such as service exposed, irradiated, low carbon, etc., *batch identifier*, *specimen* (type) and (test) *environment*. Retrieval can be finished with optional selections on test type specific fields such as *time at rupture*, *test temperature*, *elongation* in the case of *uniaxial creep*.

After the mandatory fields have been specified the *Generate report* button is active allowing the user to create an overview report on the selected material tests. The report contains links to detailed information on e.g. source (including documentation), heat treatment, chemical composition, raw data sets or numerical and graphical curve information. Furthermore the report screen allows exporting the selected test data to pre-defined EXCEL charts or starting routines for analysing the test data.

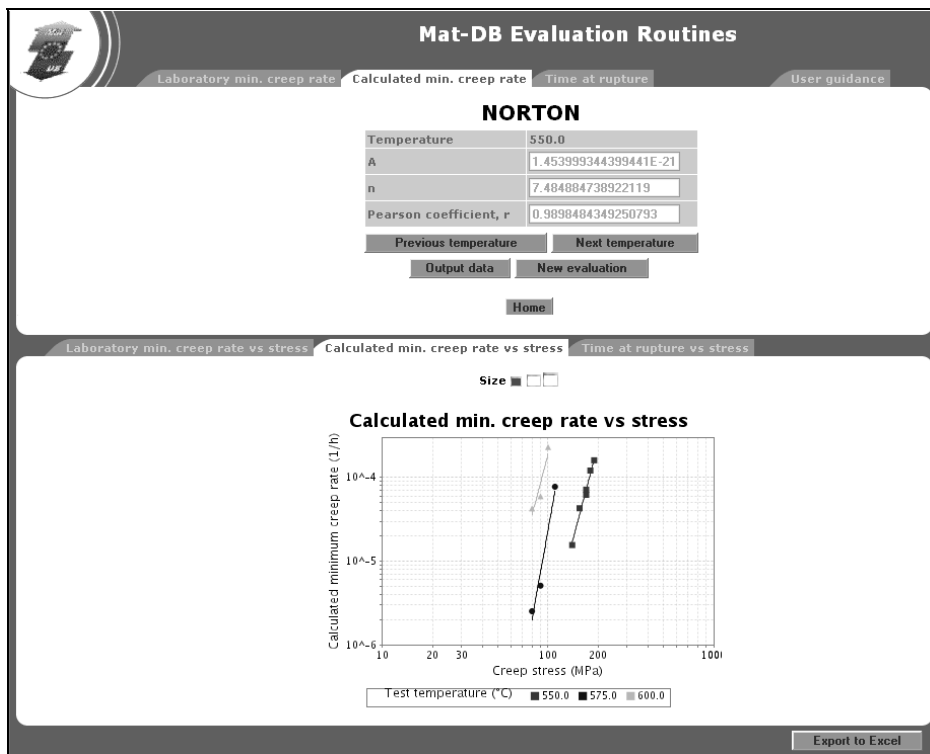
Mat-DB contains a number of test-type specific analysis routines, which allow a fast evaluation of the retrieved data. The evaluation program library (see Table 3) contains mathematical models, constitutive equations, parametric expressions and regression functions. The analysis routines allow a comparison of data sets against each other. Database customers often use the analysis results for their publications and reports [14]. The analysis routines are re-programmed with Java and implemented into the Mat-DB web-application, but they can also be used independently of Mat-DB. The data can be uploaded directly from the clients PC following a simple XML related transfer procedure.

Currently, most of the creep programs shown in Table 3 are implemented. The implementation of all other analysis routines should be finished by the end of 2007. The materials parameters calculated by the analysis routines are necessary for inelastic analysis calculations of high temperature exposed components. Figure 3 shows Norton creep law results for 10 CrMo 9 10. The program calculates numerically the temperature-dependent Norton parameters for the time at rupture and the laboratory as well as the calculated minimum creep rate. The laboratory minimum creep rate is the creep rate which has been entered by the data owner, the calculated minimum creep rate is automatically analysed by Mat-DB software by using a *seven point fitting method* as defined by ASTM E 647 while entering the creep curves. The evaluation program library is shown in Table 3.

Table 3. Mat-DB evaluation program library

Creep	Fatigue
<p><i>Creep relations:</i> Norton creep law, Prandtl creep law, Soderberg creep law, Monkman-Grant relation, Dobés-Milíčka relation</p> <p><i>Extrapolation methods:</i> Larson-Miller, Manson-Haferd, Manson-Brown, Orr-Sherby-Dorn, Spera, Minimum commitment method</p> <p><i>Constitutive creep equations:</i> Theta projection, McVetty equation, Kachanov equation</p> <p><i>Interpolation routines:</i> Polynomial creep curve fit, Polynomial stress dependence, Isochronous & isostrain determination</p>	<p>Ludvik law, Manson-Coffin relation, Basquin analysis, Frequency-modified Manson-Coffin relation</p>
	Crack growth
	<p>ASTM compliant creep crack growth analysis, Creep crack growth plot, Fatigue crack growth analysis</p>
	HT corrosion
	<p><i>Weight gain/loss analysis:</i> Power law, Power law-time, Parabolic Δm^2, Parabolic $t_{1/2}$, $K_p(t)$, Breakaway</p>

Figure 3. Screenshot of Norton creep law results for 10 CrMo 9 10



In addition to the existing database analysis routines, the JRC has integrated Fitit, – proprietary software of the Fraunhofer Institute in Germany designed for the calculation of complex material models. Fitit can be used for models defined as a set of differential equations and analytic functions, e.g. Chaboche and Kachanov. Data selected within the web-enabled Mat-DB can be sent to Fitit, which then fits the data to a selected model. Once the model parameters have been calculated, they are returned to Mat-DB and the user can apply them for Finite Element (FE) lifetime calculations of high temperature exposed components with commercial codes like ABAQUS or ANSYS, which improves safety and reliability and saves costs.

Generation IV data management

As documented before Mat-DB and DoMa are ideal applications for Generation IV data and document management and therefore part of the FP7 knowledge preservation strategy. Mat-DB provides access to public and confidential materials data. Confidential data sets are accessible by the related project participants only; they can be released into the public domain only after agreement by the data owners. The quality of validated data is the responsibility of the laboratory where they have been generated. JRC does not take any liability for the data.

Confidential Mat-DB data sets are for instance data of former German high temperature and fast breeder reactor programmes [15,16], which could be of interest for new reactor types as well as also the IAEA pressure vessel data. By managing these data pools Mat-DB has shown that it is a valuable platform with the right structure to handle nuclear related materials data which have to take into consideration irradiation and/or joining details. Taking that experience into consideration JRC as a supra-national institution is planning to create a Generation IV database for JRC owned experimental materials data and offer this data management to all European Generation IV R&D activities. The EURATOM FP7 Generation IV programme is related to the following six reactor types:

- sodium fast reactor;
- lead fast reactor;
- gas fast reactor;
- very high temperature reactor;
- supercritical water reactor;
- molten salt reactor.

Following a proposal of DG-RTD JRC will create separate entries to guarantee a straight user controlled access to these pools within Mat-DB. This procedure is similar to the IAEA policy. Nobody else but assigned IAEA members can see their data.

European FP7 R&D projects which refer to the six reactor types can use Mat-DB free of charge. By including JRC in their projects they have only to pay for the administrative Mat-DB work (user access control, creating individual data entry pools, data check, etc.) and for necessary project related updates and upgrades. They do not pay for server costs and maintenance. Additionally they can store all their documentation within DoMa. The access to data and documentation can directly be controlled and administrated by the project responsible via Internet for project members who have registered at ODIN.

Summary

The web-enabled Mat-DB is a state-of-the-art database for experimentally measured mechanical and thermo-physical properties and corrosion data of engineering alloys at low, elevated and high temperatures for base materials and joints. It is implemented within a powerful relational database management system and installed within a secure server portal which guarantees access control. Mat-DB offers the whole cycle from data entry via data retrieval to data evaluation. Additionally public and confidential project related data and documentation can be administrated in DoMa. Together Mat-DB and DoMa are ideal applications for Generation IV reactor materials data and document management and therefore part of the FP7 knowledge preservation strategy.

European FP7 R&D projects which refer to the Generation IV reactor types can use Mat-DB free of charge. By including JRC in their projects they have only to pay for the administrative Mat-DB work (user access control, creating individual data entry pools, data check, etc.) and for necessary project related updates and upgrades. They do not pay for server costs and maintenance. Additionally they can store all their documentation within DoMa. The access to data and documentation can directly be controlled and administrated by the project responsible via Internet for project members who have registered at ODIN.

REFERENCES

- [1] *Advanced Engineering Materials*, Vol. 4, No. 6, pp. 317-416 (2002). Special issue, "Materials and Process Selection".
- [2] Plantfacts Database of the German VDEh (Verein Deutscher Eisenhüttenleute – German Iron and Steel Institute): <http://www.vdeh.de/deutsch/arbeit/informat/plantfe.htm>.
- [3] WIAM[®]-METALLINFO database, IMA-Dresden: <http://www.ima-dresden.de/deutsch/startde.htm>
- [4] Materials Databases of MBase, Aachen, Germany: <http://www.m-base.de/main/en/index.html>.
- [5] MSC.Mvision Databanks, USA: <http://www.mssoftware.com>.
- [6] *Wirtschaftswoche*, No. 35 (2004).
- [7] Materials Databases of NIMS – National Institute for Materials Science, Japan: http://mits.nims.go.jp/db_top_eng.htm/
- [8] Hurst, R.C., H. Kröckel, H.H. Over, P. Vannson, "The Use of Models in Materials Databanks", *Materials 88 – Materials and Eng. Design*, The Institute of Metals, London (1988).
- [9] Kröckel, H., H.H. Over, "The Need for a European Approach to Materials Characterisation and Data Management", *International Symposium on Advanced Materials for Lightweight Structures*, March 1994.

- [10] Over, H.H., J.H. Rantala N. Taylor, W. Dietz, "A Materials Properties Database Approach to Cover Welded Joints", *2nd International Conference on Integrity of High Temperature Welds*, London, UK, 10-12 November 2003.
- [11] Nagy, M., H.H. Over, A. Smith, "XML Related Data Exchange from the Test Machine into the Web-enabled Alloys-DB", *19th International CODATA Conference, "The Information Society: New Horizons for Science"*, Berlin, Germany, 7-10 November 2004.
- [12] Thermo-mechanical Fatigue – the Route to Standardisation, CORDIS R&D Project No. GRD2-2000-30014.
- [13] Over, H.H., E. Wolfart, E. Veragten, "Data Retrieval and Evaluation within the Web-enabled Alloys-DB", *19th International CODATA Conference, "The Information Society: New Horizons for Science"*, Berlin, Germany, 7-10 November 2004.
- [14] Ennis, P.J., "Candidate Materials for a Modular High Temperature Reactor Power Plant in Engineering Issues in Turbine Machinery, Power Plant and Renewables", A. Strang, R.D. Conroy, W.M. Banks, M. Blackler, J. Leggett, G.M. McColvin, S. Simpson, M. Smith, F. Starr, R. Vanstone, Maney (Eds.), IOM3 Publications, Book Number B0800, ISBN 1-904350-20-8, pp. 1029-1037 (2003).
- [15] KFA Jülich, Endbericht zum Verbund-Forschungsvorhaben des BMFT, 'Auslegungskriterien für hochtemperaturbelastete metallische und keramische Komponenten sowie des Spannbeton-Reaktordruckbehälters zukünftiger HTR-Anlagen', Band IIB, 'Teil B: Metallische Komponenten', August 1988.
- [16] Bergmann, H-J., W. Dietz, K. Ehrlich, G. Mühling, M. Schirra, *Entwicklung des Werkstoffs X10CrNiMoTiB 15 15 als Strukturmaterial für Brennelemente*, FZKA 6864, Forschungszentrum Karlsruhe, Germany, June 2003.

Other contributions: Abstracts

The full texts of the presentations included in this section were unavailable at the time of printing.

ADVANCED MATERIALS DEVELOPMENT AND FUEL PERFORMANCE ANALYSIS FOR THE NUCLEAR ENERGY SECTOR*

V. Inozemtsev, C. Ganguly, G. Mank, N. Dytlewski, S. Paranjpe
International Atomic Energy Agency, Austria

Abstract

The paper presents an overview of programmes and projects of the International Atomic Energy Agency (IAEA) in the areas of advanced structural materials development and fuel performance analysis and illustrates how the IAEA project implementation tools work.

The IAEA activities related to R&D of fuels and core structural materials for fission reactors are mainly undertaken within the IAEA's major programme 1 (in the Department of Nuclear Energy and Department of Nuclear Sciences and Applications) based on the recommendations of the Technical Working Groups on Fuel Performance and Technology (TWGFPT) and on Nuclear Fuel Cycle Options (TWGFCO). The Agency's activities cover materials issues of both enhancing operational characteristics of existing nuclear reactors and developing advanced fuels and structural materials for innovative nuclear systems.

Since 2001 the Department of Nuclear Energy has been implementing a large interdisciplinary international project on innovative nuclear reactors and fuel cycles (INPRO). One of its present tasks is a study on fast reactor nuclear fuel cycle optimisation that includes the development of advanced and competitive fuel and cladding materials able to operate reliably up to very high level of radiation damage (150-200 dpa) and temperatures (>700°C) with tolerable changes of mechanical properties and dimensions. The requirements for materials in future fusion reactors as for the proposed prototype fusion reactor DEMO will be in the same or slightly higher range.

At present collaboration between the IAEA Departments of Nuclear Energy and Nuclear Science and Applications is being developed with an aim of facilitating the use of nuclear techniques including accelerators and research reactors for nuclear materials R&D for the benefit of the IAEA member states.

* *Overview*

SYNERGIES BETWEEN FUSION AND INNOVATIVE FISSION SYSTEMS FOR STRUCTURAL MATERIALS R&D*

Steven J. Zinkle

Oak Ridge National Laboratory
Oak Ridge, Tennessee, USA

Abstract

Durable, high-performance structural materials are the backbone for all innovative nuclear energy systems. In order to reduce the historical one- to two-decade development time for new structural materials, it is useful to share resources and information among innovative nuclear energy programmes. Many commonalities exist with regard to the materials research issues for innovative fusion and fission systems. In general, there is common interest in developing structural materials capable of prolonged operation at significantly higher temperatures compared to current commercial light water reactor systems (~290°C). The anticipated irradiation exposures in future fusion and innovative fission systems are also substantially higher than current fission reactors. Many of the structural material systems under consideration for future innovative nuclear systems are similar, including ferritic/martensitic steels, oxide dispersion strengthened ferritic steels, refractory alloys and ceramic composites (SiC/SiC and carbon/carbon). There are also many similarities in the chemical compatibility issues for proposed coolants, which include Pb-based alloys (Pb-Bi, Pb-Li), alkali metals (Li, Na), molten salts (LiF-BeF₂, etc.) and inert gas (He, He-Xe) systems. Recent research on the international fusion materials programme has demonstrated the value of using modelling and well-posed experimental validation experiments to investigate underlying fundamental physical phenomena responsible for controlling property degradation in irradiated structural materials. This has led in several cases to a transformational shortening of the development time for high-performance structural materials.

* *Session I*

AN INDUSTRIAL POINT OF VIEW ON R&D NEEDS FOR HTR MATERIALS AND COMPONENTS*

Dominique Hittner, Odile Gelineau, Eric Breuil
AREVA NP

Abstract

For industry, materials R&D needs are dependent on specific market prospects and on the possibility of going from laboratory results to industrial applications within a reasonable period of time.

HTR can be considered in some cases for electricity generation, but the main incentive for this type of system is its possible use for industrial process heat applications without CO₂ emission. It is also the main challenge for its development, as there is no experience at all of a direct coupling of a nuclear heat source with an industrial process without intermediate conversion into electricity.

The specifications of the system to be developed, in particular but not only the operating temperature, will depend of the precise characteristics of these applications. As far as the operating temperature is concerned, there are many industrial applications with high heat consumption at temperatures significantly below 800°C and also other applications which require much higher temperatures.

AREVA, together with its partners CEA and EdF, with the contribution of the European project RAPHAEL of the 6th Framework Programme and possibly in the future additional inputs from the VHTR materials project of the Generation IV International Forum, has undertaken a large R&D programme for assessing the potential of materials which can be available on an industrial basis for being used for critical HTR components, in particular the Intermediate Heat Exchanger (IHX), unavoidable for heat applications, the reactor vessel, the internals and the control rods.

From the results already obtained, it appears that the materials which could be available for an industrial development as soon as possible (next decade) have performance limits that would not authorise operating temperatures much above 800°C. In the longer term, if real market needs are identified, more advanced materials could be considered, but it is clear that they require a lot of R&D, not only to optimise them and assess their performance, but also to develop processes for forming and assembling them, which, very often do not exist at all for the time being.

Now the challenge is not only to develop and qualify high performance materials, but also to develop and manufacture high performance components made from these materials. Some of these components, in particular the IHX, are beyond the industrial state of the art, even if the aim is not to reach very high temperatures. Their development will require an extensive R&D and qualification programmes, which will necessitate large test facilities producing actual operating conditions (impure helium atmosphere, high temperature, transients).

Therefore the priorities of the development programme should be put in the right order: first of all, to make the demonstration of industrial feasibility of the coupling of a large scale reactor with an industrial process heat application at a reasonable temperature level, and therefore to develop and qualify the materials and components needed for the reactor and the coupling, then, in the longer term, to search for solutions for higher performances in terms of temperature, fuel burn-up, availability, lifetime, etc., if required by the market.

* *Session II*

COMPOSITES FOR NUCLEAR CORE APPLICATION AT TEMPERATURES ABOVE 800°C*

Lance L. Snead¹, Yutai Katoh¹, Steve Zinkle¹, Will Windes²
¹Oak Ridge National Laboratory
²Idaho National Laboratory

Abstract

Composite materials, specifically carbon fibre/carbon matrix (CFC), and silicon carbide fibre/silicon carbide matrix (SiC/SiC) have been considered for both fusion and fission core applications for over a decade. Both the potential benefits, such as their very high operating temperatures, and their drawbacks, such as the lack of understanding of how to design using these materials, are well known.

Less well known has been the performance under the extreme conditions of a reactor core, most importantly neutrons. For the past few decades the performance of both CFC's and SiC/SiC composites have been studied under low and intermediate temperature irradiation conditions and their properties are well understood. Moreover, a determined programme of materials development has produced materials which are fairly insensitive to irradiation. This paper will present a short review of the performance of the more irradiation-tolerant SiC/SiC and CFC materials at low and intermediate temperatures. Moreover it will present new information on the behaviour of these materials at temperatures greater than 900°C.

* *Session II*

BUCKLE, RUCK AND TUCK – THE RESPONSE OF GRAPHITE TO IRRADIATION*

Malcolm I. Heggie, C. Davidson, G. Haffenden, I. Suarez-Martinez, J.M. Campanera, G. Savini
Department of Chemistry, University of Sussex, Brighton, BN1 9QJ, UK

Abstract

The story behind radiation damage in graphite is framed in terms of interstitials and vacancies. First principles calculations all show that interstitials are immobile at low (e.g. liquid N₂) temperatures. We have performed the first serious and first principles calculations on dislocations in graphite and found some remarkable results, which give clear explanations for the dimensional change and creep in graphite under neutron irradiation.

Dimensional change can be substantial (sometimes exceeding 100%) and creep can be a linear (i.e. non-saturating) function of dose. We find that basal dislocations lie at the heart of nearly all these effects and not, as was originally thought, the Frenkel pairs formed from irradiation. The explanation lies in prismatic loops, screw dislocations and interactions with basal dislocations, so the structure and energetics of all of these will be discussed.

The physical effects they give are buckling and forming folds ruck and tuck defects. The findings are expected to be general to layered materials.

* *Session II*

GRAPHITES AND COMPOSITES IRRADIATIONS FOR GAS-COOLED REACTOR CORE STRUCTURES*

Jaap G. van der Laan¹, J.A. Vreeling¹, D.E. Buckthorpe², J. Reed³

¹Nuclear Research & Consultancy Group, Petten, The Netherlands

²AmecNNC, Knutsford, United Kingdom

³British Energy, Barnwood, United Kingdom

Abstract

Material investigations are undertaken as part of the European Commission 6th Framework Programme for helium-cooled fission reactors under development like HTR, VHTR, GCFR. The work comprises a range of activities, from (pre-)qualification to screening of newly designed materials. The High Flux Reactor at Petten is the main test bed for the irradiation test programmes of the HTRM/M1, RAPHAEL and ExtreMat Integrated Projects. These projects are supported by the European Commission 5th and 6th Framework Programmes. To a large extent they form the European contribution to the Generation-IV International Forum.

NRG is also performing a Materials Test Reactor project to support British Energy in preparing extended operation of their Advanced Gas-cooled Reactors (AGR).

Irradiations of commercial and developmental graphite grades for HTR core structures are undertaken in the range of 650 to 950°C, with a view to get data on physical and mechanical properties that enable engineering design. Various C- and SiC-based composite materials are considered for support structures or specific components like control rods. Irradiation test matrices are chosen to cover commercial materials, and to provide insight on the behaviour of various fibre and matrix types, and the effects of architecture and manufacturing process. The programme is connected with modelling activities to support data trending, and improve understanding of the material behaviour and micro-structural evolution. The irradiation programme involves products from a large variety of industrial and research partners, and there is strong interaction with other high technology areas with extreme environments like space, electronics and fusion.

The project on AGR core structures graphite focuses on the effects of high dose neutron irradiation and simultaneous radiolytic oxidation in a range of 350 to 450°C. It is aimed to provide data on graphite properties into the parameter space for extended operational life of the AGR fleet. To this aim specimens taken from actual cores of the leading stations as well as virgin material will be irradiated in both oxidising and inert environment. It requires the design and operation of a carbon dioxide purge and gas handling system for the irradiation stages, allowing on-line gas composition monitoring and control. Furthermore the high weight losses anticipated require a targeted verification of the validity range of existing test methods, and potentially their extension, or even development of new tests.

The presentation is an overview of the irradiation and post-irradiation testing projects for present and future gas cooled reactors, and will highlight results and expectancies.

Acknowledgements

Work on (V)HTR graphite technologies is financially supported by the European Commission and the Netherlands Ministry of Economic Affairs. Work on AGR graphites is fully supported by British Energy Ltd.

* *Session II*

MECHANICAL PERFORMANCE OF HTR TURBINE MATERIALS AFTER PRE-EXPOSURE TO CORROSIVE ENVIRONMENTS*

P. Hähner, M. Musella, K. Mathis

European Commission, JRC – Institute for Energy
P.O. Box 2, NL-1755 ZG Petten, The Netherlands

R. Couturier

CEA-Grenoble, DRT LITEN
17 Rue des Martyrs, F-38054 Grenoble Cedex 9, France

Abstract

Materials performance and possible strength deterioration due to corrosion are of particular concern in the design of HTR turbine components. In the present work, the creep behaviours of IN792 DS and CM247 LC DS blade materials have been investigated at 850°C after the following pre-treatments: (i) ageing heat treated, (ii) fully decarburised, and (iii) heavily carburised. As to a candidate disc material, the creep performance of Udimet720 has been studied at 750°C in a heavily carburised state. Furthermore, LCF tests have been carried out at 650°C on Udimet720 fully decarburised and heavily carburised. In all cases, results are compared to those of the as-received materials. Strength properties are observed to be deteriorated by the corrosive pre-treatments. Optical microscopy of transverse and longitudinal sections of the pre-exposed and mechanically tested specimens has been carried out to characterise the corrosive attack and creep damage. Failure modes have been identified by means of scanning electron microscopy of the fracture surfaces.

* *Session II*

MATERIAL REQUIREMENTS FOR THE VERY HIGH TEMPERATURE REACTOR – RESULTS AND PROGRESS WITHIN THE RAPHAEL-IP*

Derek Buckthorpe

AMEC NNC Limited

Booths Park, Knutsford, UK

Tel: 0044 1565 684840; Fax: 0044 1565 684870

derek.buckthorpe@amecnnc.com

Plus contributions from

M. Davies¹, J. Baker¹, I Hugon², Y. Lejeail², J. Hegeman³, J. van der Laan³, A. Vreeling³,

O Gelineau⁴, R Hurst⁵, B Schogl⁶, D de Lorenzo⁷, B-C. Friedrich⁸, M. Blatt⁹,

M Marek¹⁰, J Chen¹¹, K Hingst¹², Bernard Tahon¹², P. Homerin¹³, G. Hall¹⁴

¹AMECNNC Ltd., Knutsford, UK

²Commissariat à l'Énergie Atomique (CEA.), France

³Nuclear Research and Consultancy Group (NRG), Petten, Netherlands

⁴AREVA–NP-SAS, Lyon, France

⁵European Commission, Joint Research Centre (JRC), Institute for Energy, Petten, Netherlands

⁶Forschungszentrum Jülich GmbH (FZJ..ISR), Germany

⁷Empresarios Agrupados Internacional S A (EASA.MD), Spain

⁸AREVA-NP (GmbH), Erlangen, Germany

⁹Électricité de France (EdF), France

¹⁰NRI Rez, Czech Republic

¹¹Paul Sherer Institute (PSI), Switzerland

¹²SGL Carbon Group, Germany

¹³Graphtech Intern Ltd, France

¹⁴University of Manchester, UK

Abstract

The modular VHTR is one of six advanced fission systems of interest for meeting the Generation IV goals of attaining highly economic, safe, reliable, sustainable, proliferation-resistant systems. The VHTR offers significant advantages for long-term development of sustainable energy and in particular for heat applications and hydrogen generation. This system can operate with either a direct or indirect cycle and makes use of the high efficiency Brayton cycle. Work on materials investigations for the HTR within Europe recommenced with the EU 5th Framework Programme (5FP) projects HTR-M and M1 [1] and together with other 5FP projects (fuel, reactor physics, components, safety,..) and the establishment of the European High Temperature Reactor Technology Network HTR-TN, served as the main European platform for the co-ordination and development of VHTR issues.

* Session II

The HTR-M & M1 projects addressed material requirements for the key components of the direct cycle HTR. The work especially focused on the materials development for the pressure vessel, high temperature components (including turbine), and the graphite core. Alongside this, developments were undertaken on key component issues (HTR-E) associated with the gas turbine, the recuperator and other system developments (e.g. tribology, corrosion, bearings, seals, etc.) concerned the operation and performance of the power circuit components. Within this paper the main highlights from the results of the 5FP programmes affecting material issues are reviewed and examined.

For the 6th Framework Programme activities the main European research focus on VHTR is through the RAPHAEL Integrated Project (IP). The project started in 2005 and addresses a range of issues (materials, components, fuel, code qualification, etc.), which are structured in a similar way to the corresponding GIF VHTR projects. The materials issues are addressed within one of the RAPHAEL sub-projects with a focus on outstanding issues. The main emphasis on materials is for graphite development, materials for the heat exchangers, continuation of vessel qualification and work on design code requirements. The progress of the materials issues within the RAPHAEL-IP, which has reached its mid-term stage will be reviewed and the expected future orientations of the programme described.

The main materials issues addressed in the paper are as follows:

- *reactor pressure vessel:*
 - review and database actions covering existing and new vessel material options;
 - tests on Mod 9Cr 1Mo steel welded joints under irradiated and non-irradiated conditions to determine suitability for vessel application.
- *High temperature materials:*
 - review and database actions for the control rod and turbine;
 - review and database actions for the heat exchangers;
 - tests on selected materials (carbon/carbon (C/C) composites, high alloy steels) at temperature and under short and intermediate times in air, and simulated carburising and de-carburising environments.
- *Graphite core:*
 - review of experience plus data base actions for new graphites;
 - oxidation tests on graphites and C composites;
 - graphite selection and irradiation testing at 750°C and 950°C;
 - micro-structural modelling and development of guidelines.

REFERENCE

- [1] Buckthorpe, D., M. Davies, R. Couturier, J. van der Laan, H. Hegeman, A. Vreeling, B. Riou, H. Rantala, P. Ennis, G. Haag, K. Kuhn, A. Buenaventura, B-C. Friedrich, “High Temperature Reactor Materials: Progress of HTR-M Projects”, 3rd NEA/OECD Information Exchange Meeting on Basic Studies in the Field of High Temperature Engineering, Japan (2003).

DEVELOPMENT OF STRUCTURAL MATERIALS FOR JAPANESE DEMONSTRATION FAST BREEDER REACTOR*

Tai Asayama, Toshio Nakagiri, Takashi Wakai
Japan Atomic Energy Agency, Japan

Abstract

This paper summarises the activities within the Japan Atomic Energy Agency (JAEA) on the development of new structural materials for the demonstration reactor of Japanese fast breeder reactor, of which operation is presumed to be around 2025. The design of the demonstration reactor has various innovative features to meet the goals of safety, reliability, and cost effectiveness that suppresses future light water reactors. These design features involve a compact reactor vessel without special devices to cool vessel wall that is subject to higher stress, shortened primary coolant piping system made of high chromium steel with a reduced number of elbows, and steam generators with straight heat exchange tubes that are made of high chromium steel as well. The design life of the demonstration reactor is 60 years. To realise the innovative design, 316FR (FBR Grade Type 316 stainless steel) has been developed for reactor vessel and core internals, and high chromium steels are being developed for coolant systems including heat exchangers and steam generators. The paper overviews the current status of the development and also discusses various issues to be addressed in the coming phase of development, such as maintaining long-term stability of microstructures, manoeuvring technologies for mass production of materials with more challenging specifications, quality control in mass production processes, and establishing a material strength standard for 60-year design with technologies for evaluating long-term material properties based on experimentally obtained data and observations.

* *Session III*

FAST REACTOR MATERIALS DEVELOPMENT AND TESTING FOR THE GNEP PROGRAMME*

Stuart A. Maloy

Los Alamos National Laboratory, MS H816, Los Alamos, NM 87545 USA

Mychailo Toloczko

Pacific Northwest National Laboratory, Richland, WA

Abstract

One of the main goals of the Global Nuclear Energy Partnership is to transmute minor actinides from spent fuel to reduce their half-lives. This requires irradiating fuels in fast reactors to high burn-ups (greater than 20%). Thus, the cladding for these fuels must be able to withstand significant radiation damage incurred during irradiation (greater than 200 dpa). Ferritic/martensitic(F/M) steels were developed in the breeder reactor programme to withstand high doses at 400-550°C without significant swelling (less than 2%). Thus, to quantify the effects of irradiation on these materials, F/M steels are being tested after fast reactor irradiation to high doses. Future testing of fast spectrum irradiated materials will include advanced F/M steels irradiated to doses up to 200 dpa in a fast reactor. Also, specimens have been provided for irradiations in progress at the Phénix Reactor in France and the SINQ accelerator in Switzerland. The maximum dose expected is up to 70 dpa at temperatures of 400-500°C. Recent results and plans for future testing will be discussed.

* *Session III*

MATERIALS ISSUES IN ACCELERATOR DRIVEN-SYSTEMS*

A. Al Mazouzi

SCK•CEN, Nuclear Materials Science Department, LHMA
Boeretang 200, B-2400 Mol, Belgium

Abstract

Nuclear energy has to cope with critical topics to resolve the economical question of increasing energy demand and, in particular, the public acceptability demands:

- increasing the absolute safety of the installations;
- managing more efficiently the nuclear waste;

In that respect, the development of a new type of nuclear installation coping with above constraints of technological as well as socio-economical nature may be of high importance for the future of sustainable energy provision. An accelerator-driven system (ADS) – a subcritical core, operated as a waste burner for minor actinides (MAs) and long-lived fission products (LLFPs) or as nuclear amplifier for energy production, fed with primary neutrons by a spallation source – has the potential to cope with above constraints and to pave the way to a more environmentally safe and acceptable nuclear energy production.

Within the framework of EUROTRANS, the European community has launched a broad R&D programme in collaboration with partners from Europe and abroad (USA, Japan), to address the technical, technological and fundamental issues related to the realisation of an experimental machine that is intended to allow:

- continuation, and extension of the present knowledge towards ADS, in the field of reactor materials, fuel and reactor physics research;
- enhancement and triggering of new R&D activities such as nuclear waste transmutation, ADS technology, liquid metal embrittlement;

The present lecture will cover the main aspects of the design of an experimental XT-ADS taking as example the work that has been performed at SCK•CEN within MYRRHA project. The safety aspect of such machine will be addressed on terms of structural material performance, with emphasis on issues related to the interaction between structural materials (austenitic and ferritic martensitic steels) and the liquid metal coolant (lead-alloys). Finally, a discussion will be given on the open issues and future R&D needed to be able to construct such machines in the near future.

* *Session III*

RADIATION-INDUCED SEGREGATION IN ADVANCED REACTOR STRUCTURAL MATERIALS*

Jeremy T. Busby
Materials Science and Technology
Oak Ridge National Laboratory

Abstract

Radiation-induced solute segregation (RIS) refers to the redistribution of elements (solute or interstitial impurities) under irradiation. This redistribution can result in enrichment or depletion at defect sinks such as grain boundaries, dislocations, voids and precipitates. RIS is a well-known form of degradation in light water reactors where stainless steels experience Cr depletion, which can impact corrosion resistance and lead to irradiation-assisted stress corrosion cracking. However, RIS also occurs in other alloy systems and could lead to radiation-induced precipitation and impact mechanical properties or lead to embrittlement. For example, RIS has been observed in ferritic/martensitic steels such as T91. The measurement of Cr enrichment is contrary to what is found in stainless steels and could help explain the observation of radiation-induced alpha-prime phase and subsequent embrittlement. In this paper, the potential influence of RIS on structural materials for various advanced reactor applications will be examined.

* *Session III*

AN OVERVIEW OF MECHANICAL PROPERTIES AND MICROSTRUCTURE OF FERRITIC/MARTENSITIC STEELS AFTER IRRADIATION IN SINQ TARGETS*

Yong Dai

Spallation Neutron Source Division, Paul Scherrer Institut
CH-5232 Villigen PSI, Switzerland

Abstract

Ferritic/martensitic (FM) steels have been used in various nuclear applications such as fission nuclear reactors and spallation neutron targets. In a spallation target, some components in/near the spallation reaction zone may be subject to severe irradiation damage induced by high energy protons and spallation neutrons. As compared to neutrons, high energy protons produce not only displacement damage, but also helium and hydrogen at high rate, which may result in more serious embrittlement in FM steels. Therefore, it is essential to understand the behaviours of FM steels under such an irradiation condition. For this reason, investigations on FM steels irradiated in proton and neutron mixed spectra have been included in various materials R&D programmes for developing high power spallation targets. While the SINQ (the Swiss Spallation Neutron Source) target irradiation programme (STIP) is one of the main sources supplying the irradiated specimens. Since 1998 five large irradiation experiments have been carried out in the targets of SINQ. Thousands of samples of different FM steels such as T91, EM10, F82H, Optifer, Eurofer 97 have been irradiated up to 20 dpa in a wide temperature range. Although only a small part of specimens were examined, some interesting results have been achieved. In this presentation, an overview will be given on the results obtained from mechanical tests and microstructural investigations of the FM steels irradiated in SINQ targets.

Acknowledgements

This work is partially supported by EU FP6 EUROTRANS programme under contract no. FI6W-CT-2004-516529.

* *Session III*

STRUCTURAL MATERIALS CONCEPTS FOR NUCLEAR POWER PLANTS*

E. Roos, K. Maile, A. Klenk, X. Schuler
MPA Universität Stuttgart

Abstract

Materials concepts for light water reactors to ensure safe inclusion of nuclear inventory have been developed and established to a great extent. One example of this is the Basis Safety Concept with the Break Exclusion Concept.

In Germany in the past, within the area of high-temperature application, extensive investigations have been carried out into materials behaviour under HTR conditions.

Similar investigations, also with similar and further developed materials, have been and are still being carried out, currently at temperatures of up to around 700°C for fossil fuel power plant technology.

These studies provide a good basis for the further development of the materials and the safety concepts for Gen IV reactors. This is documented in the contribution by means of examples.

* *Session IV*

SCC TESTS OF AISI 304 AND 316L TYPE STAINLESS STEELS IN SCW CONDITIONS*

Radek Novotny, Dusan Prchal, Luigi Debarberis, Peter Haehner
JRC IE Petten, The Netherlands

Abstract

Super Critical Water Reactors (SCWR) have been pre-selected as a one of the candidate concepts for the new generation of nuclear reactors in frame of Generation IV. Beside the design concept choice of construction materials is the most important question. Despite extensive research due to using various materials either in the conventional supercritical coal power plants or SCWO systems there is still missing knowledge about the properties of the materials in operational conditions of SCWR. That includes influence of irradiation and environment composition on chemistry of water especially process of radiolysis, mechanical properties of the materials and oxide films properties. The process of choice and testing of possible construction and fuel cladding materials are still under R&D (e.g. EU HPLWR project).

Two types of tests were undertaken in SCW environment conditions ($t = 600^{\circ}\text{C}$, $p = 250$ bar): U-bend specimens for constant displacement SCC tests and tensile specimens for SSRT tests. SSRT tests were carried out in SCW environment with different concentration of dissolved O_2 : 1, 10, 100, 20 ppb (± 5 ppb) and with different displacement rates: 0.1, 1, 10 $\mu\text{m}/\text{min}$.

In SCC test with U-bend specimens different time expositions were carried out in two concentrations of dissolved O_2 : 0 and 200 ppb.

Water chemistry was continually monitored by means of pH, conductivity and dissolved O_2 sensors. After the test the specimens were analysed by optical microscopy, SEM and XRD.

* *Session IV*

DEVELOPMENT OF STRUCTURAL DESIGN CRITERIA FOR INTERNALS OF LWR*

G.M. Kalinin, S.V. Evropin, V.M. Filatov
Engineering Center of Nuclear Equipment Strength (ENES)
Moscow 101000, P.O. Box 788. Russia
Phone/Fax: +7 (495) 268 92 37, +7 (495) 264 79 34
E-mail: gmk@nikiet.ru

Abstract

Some operating conditions of LWR (PWR, VVER type) internals, such as irradiation, exposure in water, high temperature, static and cyclic stresses, as well as trends toward extension of the design service life of operating and newly developed NPPs to 60 years, dictate the need for providing relevant regulations for the reactor internals.

Russian regulations PNAEG for NPP equipment and pipelines do not cover VVER internals, wherefore the design, manufacture and operation of the latter are based on the existing experience, which have not been transferred and specified into regulatory terms.

There are not known codes or recommendations for the lifetime and structural integrity assessment of PWR and BWR internals. The existing regulatory rules that can be found in ASME and RCC-M codes refer to the core supports, but leave out the conditions specific to the internals, which give rise to metal degradation mechanisms, such as radiation-induced swelling and creep, fatigue under irradiation, radiation induced loss of work hardening capability, embrittlement effect, vibration, wear, etc.

The rules for accounting of LWR internals working conditions and specific of their design are under development in ENES.

Effect of irradiation on tensile behaviour, fracture toughness, fatigue and swelling were analysed on the bases of available data of solution annealed austenitic steels, mainly of 316, 304 and 321 types (the last one is the AISI designation of Russian grade X18H10T used for VVER internals). Equations for the best fit of available experimental data were generated for the mentioned above properties that allow to specify design allowables for irradiated austenitic steels used for PRI.

Criteria for assessment of structural integrity of reactor components subjected to irradiation are also discusses in the paper.

* *Session IV*

PREDICTION OF IRRADIATION DAMAGE EFFECTS BY MULTI-SCALE MODELLING: EURATOM 6TH FRAMEWORK INTEGRATED PROJECT PERFECT*

**Jean-Paul Massoud¹, Stéphane Bugat¹, Bernard Marini²,
David Lidbury³, Steven Van Dyck⁴, Luigi Debarberis⁵**
¹EDF R&D, ²CEA DEN, ³SERCO, ⁴SCK•CEN, ⁵EC-JRC

Abstract

In nuclear PWRs, materials undergo degradation due to severe irradiation conditions that may limit their operational life. Utilities operating these reactors must quantify the aging and the potential degradations of reactor pressure vessels and also of internal structures to ensure safe and reliable plant operation.

The EURATOM 6th Framework Integrated Project PERFECT (Prediction of Irradiation Damage Effects in Reactor Components) addresses irradiation damage in RPV materials and components by multi-scale modelling. This state-of-the-art approach offers potential advantages over the conventional empirical methods used in current practice of nuclear plant lifetime management. Launched in January 2004, this 48-month project is focusing on two main components of nuclear power plants which are subject to irradiation damage: the ferritic steel reactor pressure vessel and the austenitic steel internals. This project is also an opportunity to integrate the fragmented research and experience that currently exists within Europe in the field of numerical simulation of radiation damage and creates the links with international organisations involved in similar projects throughout the world.

Continuous progress in the physical understanding of the phenomena involved in irradiation damage and continuous progress in computer sciences make possible the development of multi-scale numerical tools able to simulate the effects of irradiation on materials microstructure. The consequences of irradiation on mechanical and corrosion properties of materials are also tentatively modelled using such multi-scale modelling. But it requires to develop different mechanistic models at different levels of physics and engineering and to extend the state of knowledge in several scientific fields. And the links between these different kinds of models are particularly delicate to deal with and need specific works.

Practically the main objective of PERFECT is to build numerical tools simulating the effect of irradiation respectively on reactor pressure vessel fracture toughness and on internal structure irradiation-assisted stress corrosion cracking with different degrees of accuracy and uncertainty in their application according to the available state of knowledge of involved mechanisms. Specific modules and database complement each of these tools. These resulting numerical tools are being integrated in a software integration platform.

The development, in the different scientific sub-projects, of models and modules, dealing with damage production, microstructure evolution and mechanical phenomena induced by irradiation allowed to build the first prototypes of RPV-2 and toughness modules. Although basic, these prototypes will have their definitive operating schemes. But in a first step they will not account for the whole complexity of the real steels and operating conditions. Nevertheless their modular structure will allow for future improvement when more advanced models will be available.

* *Session V*

DENSITY FUNCTIONAL CALCULATIONS OF STRUCTURES AND DYNAMICS OF DEFECTS IN FE AND NI ALLOYS*

C. Domain^{1,2}, C.S. Becquart², P. Olsson¹

¹EDF R&D, Dept. MMC, Les Renardières, F-77250 Moret-sur-Loing, France

²Laboratoire de Métallurgie Physique et Sciences des Matériaux
UMR CNRS 8517, USTL Bât. C6, F-59655 Villeneuve-d'Ascq Cedex, France

Abstract

Alloys used as nuclear materials are submitted to irradiation which induces the creation of a large amount of point defects (vacancies and interstitials) and in some conditions to He production. These defects interact with each other as well as with the different elements constituting the alloys. These interactions are responsible for the elementary mechanisms governing the kinetics of the system, and they are among the key parameters to model the time evolution of the microstructure, under ageing or irradiation conditions. Indeed the microstructure properties are directly linked to the chemical interactions between the different constituting elements, and these defects. *Ab initio* methods allow determining properties such as defect formation, binding or migration energies.

The data obtained by *ab initio* calculation of point defects (vacancies and self interstitial atoms, foreign interstitial defects (C, N, H and He) in different matrix element with different crystallographic structure (bcc :Fe, fcc: Ni) as well as of some substitutional elements (Cu, Ni, Mn, Si, Cr, and P...) in bcc Fe will be presented and discussed. When possible, the results will be compared with experimental data in order to assess the validity of the method. The consequences of the results obtained will be discussed.

* Session V

**SIMULATION OF THE MICROSTRUCTURAL EVOLUTION
UNDER IRRADIATION OF DILUTE Fe-CuNiMnSi ALLOYS BY ATOMIC
KINETIC MONTE CARLO MODEL BASED ON *AB INITIO* DATA***

E. Vincent^{1,2}, C.S. Becquart¹, C. Domain^{1,2}

¹Laboratoire de Métallurgie Physique et Génie des Matériaux
UMR 8517, Université de Lille 1, F-59655 Villeneuve-d'Ascq Cedex, France

²EDF-R&D Département MMC
Les Renardières, F-77818 Moret-sur-Loing Cedex, France

Abstract

The embrittlement and the hardening of pressure vessel steels under radiation has been correlated with the presence solutes such as Cu, Ni, Mn and Si. Indeed it has been observed that under irradiation, these solutes tend to gather to form more or less dilute clusters. The interactions of these solutes with radiation induced point defects thus need to be characterised properly in order to understand the elementary mechanisms behind the formation of these clusters.

Ab initio calculations based on the density functional theory have been performed to determine the interactions of point defects (vacancies as well as interstitials) with solute atoms in dilute FeX alloys (X = Cu, Mn, Ni or Si) in order to build a database used to parameterise an atomic kinetic Monte Carlo model. The model has been applied to simulate thermal ageing as well as irradiation conditions in dilute Fe-CuNiMnSi alloys. Results obtained with this model will be presented.

* *Session V*

FUNDAMENTAL INVESTIGATION OF POINT DEFECT INTERACTIONS IN FE-CR ALLOYS*

Brian D. Wirth, Hyon-Jee Lee, J.H. Shim¹, Kevin Wong

Nuclear Engineering Department, University of California, Berkeley

¹Materials Science and Technology Division, Korea Institute of Science and Technology

Abstract

Fe-Cr alloys are a leading candidate material for structural applications in Generation IV and fusion reactors, and there is a relatively large database on their irradiation performance. However, complete understanding of the response of Fe-Cr alloys to intermediate-to-high temperature irradiation, including the radiation induced segregation of Cr, requires knowledge of point defect and point defect cluster interactions with Cr solute atoms and impurities. We present results from a hierarchical multi-scale modelling approach of defect cluster behaviour in Fe-Cr alloys. The modelling includes *ab initio* electronic structure calculations performed using the VASP code with projector-augmented electron wave functions using PBE pseudo-potentials and a collinear treatment of magnetic spins, molecular dynamics using semi-empirical Finnis-Sinclair type potentials, and kinetic Monte Carlo simulations of coupled defect and Cr transport responsible for microstructural evolution. The modelling results are compared to experimental observations in both binary Fe-Cr and more complex ferritic-martensitic alloys, and provide a basis for understanding a<100> dislocation loop evolution and the observations of Cr enrichment and depletion at grain boundaries in various irradiation experiments.

* Session V

THERMODYNAMICAL ANALYSES OF MOLECULAR SIMULATIONS OF DISLOCATION-DEFECT INTERACTIONS: SIMULATIONS AT 0 K*

G. Monnet

EDF – R&D, Department MMC, avenue des Renardières, F-77818 Moret-sur-Loing, France

Abstract

Static molecular (SM) simulations of dislocation-defect interaction are analysed through a framework of different interaction regimes, in which the applied work has different roles. In most regimes, the applied work is transformed into elastic energy, a dissipative energy resulting from the lattice friction and a large quantity of energy needed to enable the dislocation to bow out when it is pinned by the defect. While the dissipative work is entirely evacuated in SM simulations, the elastic and curvature energies contribute to a large increase of the internal energy of the system. A method is presented in this work to evaluate the curvature energy and the result is compared to prediction of the line tension model. These analyses allow the determination of the dislocation-defect interaction energy.

* *Session V*

ATOMIC-SCALE EFFECTS IN STRENGTHENING DUE TO VOIDS AND COHERENT PRECIPITATES IN METALS*

Yu.N. Osetsky¹, R.E. Stoller¹ and D.J. Bacon²

¹Oak Ridge National Laboratory

P. O. Box 2008, Oak Ridge, TN 37831-6138 USA

²Materials Science and Engineering, Department of Engineering, The University of Liverpool
Liverpool L69 3GH, UK

Abstract

Strengthening due to voids and secondary phase precipitates is a significant radiation effect in metals. Treatment of this by elasticity theory of dislocations is difficult when specific details atomic structure of the obstacle and dislocation are influential. In this paper we report results of extensive large-scale atomic-level modelling of a gliding edge dislocation overcoming spherical voids in fcc copper and bcc iron and also Cu-precipitates in iron of up to 6 nm diameter. We demonstrate that atomistic modelling is able to reveal important effects which are beyond the continuum approach. Some arise from features of the dislocation core and crystal structure, others involve dislocation climb and phase transformation effects. Large obstacles of ≥ 5 nm obey the equation for strengthening by the Orowan mechanism and can be estimated within the continuum approach with a high accuracy.

* *Session V*

EFFECT OF NEUTRON FLUX AND IRRADIATION TEMPERATURE ON RADIATION SWELLING OF AUSTENITIC STEELS AT HIGH NEUTRON DOSES OF FAST REACTOR BN-350 OPERATIONS*

A.I. Ryazanov¹, V.A. Egorov¹, O.G. Romanenko²

¹Russian Research Center “Kurchatov Institute”, 123182 Moscow, Russia

²Nuclear Technology Safety Center, Almaty, Kazakhstan

Abstract

The investigations of changes of physical-mechanical properties of structural materials in fast reactor BN-350 give very important information about physical mechanisms of radiation resistance of these materials at high doses of fast neutrons (up to 100 dpa) in the dependence on irradiation temperature and dose rate. One of the important problems which determines both radiation resistance and degradation of mechanical properties of structural materials is a radiation swelling.

In the present report the effect of dose rate at different temperatures on radiation swelling of austenitic steel is investigated at high neutron doses experimentally and theoretically. Under neutron irradiation of austenitic steels in the atomic reactor helium atoms are produced due to (n,α) nuclear reaction. Therefore it is very important to understand the effect of helium atoms on radiation swelling of these materials. For this aim based on the obtained experimental data in reactor BN-350 a new theoretical model is suggested for the explanation of the effect of helium atoms on the nucleation and growth of helium bubbles and radiation swelling in irradiated metallic materials. The suggested theoretical model is based on the kinetic consideration of point defect cluster formation and growth of helium bubbles in the matrix of irradiated material taking into account on this process the effect of irradiation temperature and neutron flux. In this theoretical model vacancies and small helium-vacancy clusters are considered as additional traps for helium atoms. The developed model allows determining the concentration, average radius of helium bubbles and radiation swelling as a function of irradiation temperature and generation rate of point defects.

It is shown that the radiation swelling of austenitic steel at low temperature ($T \leq 480^\circ\text{C}$) and low generation rates of point defects (10^{-8} dpa/sec) is higher comparing with irradiation conditions at same temperature and higher generation rates of point defects (10^{-7} dpa/sec) at the same total neutron doses. At higher temperatures ($T > 550^\circ\text{C}$) the situation is changed and the radiation swelling of austenitic steel at the same total neutron fluence is increased with the increasing of neutron flux and generation rate of point defects. The obtained theoretical results are compared with the existed experimental data obtained under neutron irradiation in reactor BN-350 in austenitic steels: 12X18H10T and 08X16H11M3 at high doses of neutron irradiation in the dependence on irradiation temperature and neutron flux. It is found that the suggested model is able to describe the main features of the experimentally observed radiation swelling behaviour in austenitic steel in the dependence of neutron flux and irradiation temperature.

The theoretical model developed here can be used for better understanding of swelling behaviour in the structural materials of different atomic reactors, which is an important issue related to life time of reactor operation and its safety.

* Session V

IRRADIATION CREEPS AND MICROSTRUCTURAL CHANGES IN AN ODS FERRITIC STEEL WITH HELIUM IMPLANTATION UNDER STRESS*

J. Chen¹, P. Jung², M.A. Pouchon¹, W. Hoffelner¹

¹Department of Nuclear Energy and Safety, Paul Scherrer Institut, CH-5232 Villigen PSI, Switzerland

²Institut für Festkörperforschung, Forschungszentrum Jülich, D-52425 Jülich, Germany

Abstract

Oxide dispersion strengthened (ODS) ferritic steel, PM2000, has been homogeneously implanted with helium under uniaxial tensile stresses from 20 to 250 MPa to a maximum dose of about 0.75 dpa (3 000 appm-He) with displacement damage rates of 5.5×10^{-6} dpa/s at temperatures of 573, 673 and 773 K. Straining of miniaturised dog-bone specimen under helium implantation was monitored and meanwhile their resistance also measured. The values of the creep compliance were almost constant of 5.7×10^{-6} dpa⁻¹MPa⁻¹ at temperature below 673 K but increased to 18×10^{-6} dpa⁻¹MPa⁻¹ at 773 K. The resistivity of PM2000 samples decreased with dose and showed a tendency to saturation. Subsequent transmission electron microscopy observations indicated the formation of ordered Fe_{3-x}Cr_xAl precipitates during implantation. Correlations between the microstructure and resistivity are discussed. Furthermore, evolutions of dislocation loops and bubbles were also studied in detail by means of TEM observations. Two sets of dislocation loops were identified, both interstitial in nature, with Burgers vector $\mathbf{b} = \langle 100 \rangle$ and $\mathbf{b} = \frac{1}{2}\langle 111 \rangle$, and habit planes of (100) and (111), respectively. No stress effects on loop growth could be detected during irradiation creep tests. TEM investigation also showed formation of bubbles already during implantation at 573 K, of bubble-loop complexes at 673 K, and Y₂O₃ particle changing their shape by the attachment of bubbles at 773 K.

* Session V

MICROSTRUCTURE AND MECHANICAL PROPERTIES OF INCONEL 617 DEGRADED AT HIGH TEMPERATURE WITH ATMOSPHERE*

Tae Sun Jo, Gil-Su Kim, Se-Hoon Kim Woo-Seog Ryu¹, Young Do Kim²
Division of Advanced Materials Science and Engineering, Hanyang University
Seoul 133-791, Korea

¹Nuclear Materials Technology R&D Team, Korea Atomic Energy Research Institute
Daejeon 305-301, Korea

²ydkim1@hanyang.ac.kr

Abstract

Inconel 617 is a candidate tube material of intermediate heat-exchanger and hot gas duct for high temperature gas-cooled reactors (HTGR) for hydrogen production. The microstructure and mechanical properties of Inconel 617 were investigated after exposure at 1 050°C in air and helium. Oxide layers were observed by cross-section image. The de-lamination of oxide layer occurs because of the difference of thermal expansion coefficient between oxide layer and matrix. The depth of Cr-depleted zone and internal oxide increased with exposure time. It was observed that the carbide phase was changed on grain boundary during exposure. These carbides were coarsened increasing exposure time. High temperature compression test and hardness test were carried out after aging at 1 050°C. The changes of yield strength and hardness were observed with increasing aging time.

* *Poster session*

EXPERIMENTAL VALIDATION OF THE MULTI-SCALE APPROACH TO MODEL THE IRRADIATION DAMAGE IN REACTOR PRESSURE VESSEL STEELS*

A. Al Mazouzi

SCK•CEN, Nuclear Materials Science Department, LHMA, Boeretang 200, B-2400 Mol, Belgium

Abstract

Today's reactors are experiencing a high degree of safety and their technology should be the basis for the development of more efficient, safer and more proliferation resistant nuclear power plants. One of the necessary pre-requisite to build and safely operate these reactors is the existence and/or the development of the proper material for each component.

The design of materials with properties adequate for their use in nuclear reactor environment requires an in-depth understanding of the irradiation effects on their physical and mechanical properties. During the last few years, progress has been made in identifying and understanding of the response to irradiation of some structural materials, especially those that are widely used in the existing power plants. Nonetheless, open fundamental questions regarding the characterisation of the microstructure evolution induced by irradiation and the consequent mechanical property changes, particularly in the technical alloys, remain.

This paper will provide an insight on the experimental programme within PERFECT project to provide a quantitative characterisation of the microstructure of irradiated steels to validate simulation results. It consists of two main tasks:

- collect available experimental data for validation of the proposed tools and models;
- perform complementary quantitative micro-structural characterisations on a selected set of model alloys with increasing complexity and steels, western and VVER type, irradiated by neutrons or charged particles to get a precise description of the irradiation-induced hardening defects.

The results are then used to benchmark the models of simulations of irradiation-induced damage against experimental data

* *Poster session*

LIMETS 2: A HOT-CELL TEST SET-UP FOR LIQUID METAL EMBRITTLEMENT (LME) STUDIES IN LIQUID LEAD ALLOYS*

J. Van den Bosch, R.W. Bosch, A. Al Mazouzi
SCK•CEN (Belgian Nuclear Research Centre)
Boeretang 200, B-2400 Mol, Belgium
jvdbosch@sckcen.be

Abstract

In the nuclear energy sector one of the main candidate designs for the accelerator driven system (ADS) uses liquid lead or lead bismuth eutectic both as a coolant and as spallation target. In the fusion community liquid lead lithium eutectic is considered as a possible coolant for the blanket and as a tritium source. Therefore the candidate materials for such structural components should not only comply with the operating conditions but in addition need to guarantee chemical and physical integrity when coming into contact with the lead alloys. The latter phenomena can be manifested in terms of erosion/corrosion and/or of the so called liquid metal embrittlement (LME).

Thus the susceptibility to LME of the structural materials under consideration to be used in such applications should be investigated in contact with the various lead alloys.

LME, if occurring in any solid metal/liquid metal couple, is likely to increase with irradiation hardening as localised stresses and crack initiations can promote it. To investigate the mechanical response of irradiated materials in contact with a liquid metal under representative conditions, a dedicated testing facility has recently been developed and built at our centre. It consists of an instrumented hot cell equipped with a testing machine that allows mechanical testing of active materials in contact with active liquid lead lithium and liquid lead bismuth under well controlled chemistry conditions. The specificity of the installation is to handle highly activated and contaminated samples. Also a dedicated dismantling set-up has been developed that allows to retrieve the samples from the irradiation rig without any supplementary damage.

In this presentation we will focus on the technical design of this new installation, its special features that have been developed to allow testing in a hot environment and the modifications and actions that have been taken to allow testing in liquid lead-lithium and subsequently lead-bismuth environment.

* *Poster session*

INVESTIGATION OF RADIATION DAMAGE RATES IN A LWR VESSEL USING RESULTS OF MOLECULAR DYNAMICS SIMULATIONS*

C.H.M. Broeders, A.Yu. Konobeyev

Institut für Reaktorsicherheit, Forschungszentrum Karlsruhe GmbH, Germany

Abstract

Data for neutron displacement cross-sections were prepared using results of molecular dynamics simulation [Stoller R. (2000), Malerba L. (2006)] and results of calculations with the help of the binary collision approximation model. These data are used to obtain radiation damage rates in stainless steel of a LWR vessel.

A comparison of the new results with the standard NRT approach for the determination of radiation damage rates is discussed. The damage rates determined with the improved data are considerably lower than those from standard NRT calculations.

* *Poster session*

THE RF NUCLEAR DATABASE AND ITS APPLICATION TO THE STRUCTURAL MATERIALS IN NEUTRON SPECTRA OF FISSION AND FUSION POWER REACTORS*

A.I. Blokhin^{1,*}, V.M. Chernov², B.I. Fursov¹, V.N. Manokhin¹

¹A.I. Leypunsky Institute, Obninsk, Russia

²A.A. Bochvar Institute, Moscow, Russia

*Tel: +7-484-399-89-86 • Fax +7-484-396-82-25 • E-mail: blokhin@ippe.ru

Abstract

General requirements in nuclear data for calculations of activation, transmutation and radiation damage in fission and fusion reactor materials are formulated in many works and reported at the IAEA special meetings. These requirements take into account the nuclear data for main structural materials and for their alloys and reaction products. The list of neutron reactions important for fission and fusion power plant technology was prepared. To meet the nuclear data needs the several large neutron data libraries were created, mainly by theoretical calculations. On the basis of national and regional data libraries the current new data library ACDAM for activation/damage calculations in structural reactor materials was formed. The present report describes the results of comparison and analysis of available experimental data and evaluated cross-sections and predictions of systematic received in the Russian Nuclear Data Center (SSC RF IPPE). The recommendations are given for selection of reliable nuclear data and improving their quality. The current new data library ACDAM allows to estimate many activation/radiation damage characteristics of structural materials and alloys for any type of neutron fission/fusion spectra in neutron energy range up to 20 MeV.

* *Poster session*

ACTIVATION AND RADIATION DAMAGE OF THE RF CORE STRUCTURAL MATERIALS IN THE FISSION AND FUSION REACTORS*

V.M. Chernov^{1,*}, A.I. Blokhin², N.A. Demin², M.V. Leont'eva-Smirnova¹, M.M. Potapenko¹

¹A.A. Bochvar Institute, Moscow, Russia

²A.I. Leypunsky Institute, Obninsk, Russia

*Tel +(499)190-3605 • Fax +(495)196-4168 • E-mail: chernovV@bochvar.ru

Abstract

Various structural materials have been proposed as a candidate for the cores of the fission and fusion innovation power reactors. One of the main problems connected with using these materials: to minimise the production of long-lived radionuclides from nuclear transmutations and to provide with good technological and functional properties. The selection of materials and their metallurgical and fabrication technologies for innovation power nuclear reactor core components is influenced by this factor. Low activated V-Ti-Cr alloys, reduced activated ferritic-martensitic steels Fe-12Cr and Zr-alloys are a leading the RF candidate materials for fission (fast and thermal) and fusion reactor applications. Materials “were irradiated” by fission (BN-600, BOR-60, VVER-1000) and fusion (the RF fusion reactor project DEMO-RF, ITER, IFMIF, GDT-NS) typical neutron spectra with neutron fluency up to 10^{22} n/cm² and the cooling time up to 1 000 years. For these materials manufactured in Russia the analysis of radiation damage and induced activity, hydrogen and helium-production as well as the accumulation of such elements as C, N, O, P, S, Zn and Sn as a function of irradiation time was performed and discussed.

* *Poster session*

AB INITIO* STUDY OF Cr INTERACTIONS WITH POINT DEFECTS IN bcc Fe

Pär Olsson¹, Christophe Domain¹, Janne Wallenius²

¹ Department Matériaux et Mécanique des Composants, EDF-R&D
Les Renardières, F-77250 Moret sur Loing, France

² Department of Nuclear and Reactor Physics, Royal Institute of Technology
Stockholm, Sweden

Abstract

Ferritic martensitic steels are candidate structural materials for fast neutron reactors, and in particular high-Cr reduced-activation steels. In Fe-Cr alloys, Cr plays a major role in the radiation-induced evolution of the mechanical properties. Using *ab initio* calculations based on density functional theory, the properties of Cr in α -Fe have been investigated. The intrinsic point defect formation energies were found to be larger in model bcc Cr as compared to those in ferromagnetic bcc Fe. The interactions of Cr with point defects (vacancy and self interstitials) have been characterised. Single Cr atoms interact weakly with vacancies but significantly with self-interstitial atoms. Mixed interstitials of any interstitial symmetry are bound. Configurations where two Cr atoms are in nearest neighbour position are generally unfavourable in bcc Fe except when they are a part of a $\langle 111 \rangle$ interstitial complex. Mixed $\langle 110 \rangle$ interstitials do not have as strong directional stability as pure Fe interstitials have. The effects on the results using the atom description scheme of either the ultrasoft pseudo-potential (USPP) or the projector augmented wave (PAW) formalisms are connected to the differences in local magnetic moments that the two methods predict. As expected for the Fe-Cr system, the results obtained using the PAW method are more reliable than the ones obtained with USPP.

* *Poster session*

ATOMISTICALLY-INFORMED DISLOCATION DYNAMICS IN FCC CRYSTALS*

E. Martínez^{1,2}, J. Marian¹, A. Arsenlis¹, M. Victoria^{2,1}, J.M. Perlado²

¹Chemistry and Materials Science Directorate, Lawrence Livermore National Laboratory
Livermore, CA 94550

²Instituto de Fusión Nuclear, Universidad Politécnica de Madrid
E-28006 Madrid, Spain

Abstract

We will present a nodal dislocation dynamics (DD) model to simulate plastic processes in fcc crystals. The model explicitly accounts for all slip systems and Burgers vectors observed in fcc systems, including stacking faults and partial dislocations. We derive simple conservation rules that describe all partial dislocation interactions rigorously and allow us to model and quantify cross-slip processes, the structure and strength of dislocation junctions, and the formation of fcc-specific structures such as stacking fault tetrahedra. The DD framework is built upon isotropic non-singular linear elasticity, and supports itself on information transmitted from the atomistic scale. In this fashion, connection between the meso and micro scales is attained self-consistently with core parameters fitted to atomistic data. We perform a series of targeted simulations to demonstrate the capabilities of the model, including dislocation reactions and dissociations and dislocation junction strength. Additionally we map the four-dimensional stress space relevant for cross-slip and relate our findings to the plastic behaviour of monocrystalline fcc metals.

* *Poster session*

A FIRST PRINCIPLES STUDY OF PALLADIUM IN SILICON CARBIDE*

G. Roma

Service de Recherches de Métallurgie Physique, CEA Saclay
F-91191 Gif-sur-Yvette, France

Abstract

Silicon carbide has been used in nuclear industry and is still considered as a coating material for nuclear fuel. Its main role should be to retain fission products. It has been observed, however, that some fission products, like palladium and silver, attack the SiC layer and are supposed to be responsible for corrosion of the material, which could facilitate fission products release. We used first principles calculations based on Density Functional Theory (DFT) in order to investigate the energetic, structural, and kinetic properties of Pd impurities inside beta-SiC; we obtained solution and migration energies in pure SiC and discuss some basic thermodynamical issues of the corrosion process. Moreover we consider some possible effects of the disorder, which is known to be induced by irradiation in the form of amorphised regions, on Pd kinetics, and we will mention some issues related to the recombination of intrinsic defects created by irradiation.

* *Poster session*

MODELLING OF RADIATION SWELLING IN GRAPHITE AND SiC MATERIALS*

A.I. Ryazanov, S.V. Kovalenko, A. B. Ustinova, V.A. Egorov

Russian Research Center “Kurchatov Institute”, 123182, Moscow, Kurchatov Sq. 1, Russia

Abstract

Radiation resistance of fission structural materials is determined by many physical phenomena and radiation swelling is the one of more important from them. Graphite and ceramic materials produced on the basis of graphite technology, SiC and SiC/SiC composites are considered due to their high-temperature strength, pseudo-ductile fracture behaviour and low-induced radioactivity as candidate materials for operating gas cooled, HTR, VHTR reactors. One of the main difficulties in the radiation damage studies of graphite and SiC materials lies in the absence of theoretical models and interpretation of many physical mechanisms of radiation phenomena including the radiation swelling and creep of graphite and ceramic materials. The degradation of mechanical properties such as dynamic strength like creep and radiation swelling of these materials under neutron irradiation is determined by the kinetics of point defect accumulation and point defect cluster (dislocation loops, voids) growth in matrix and on grain boundaries. The point defects in ceramic materials are characterised by the charge state and they can have an effective charge. This physical mechanism should be considered in the description of radiation swelling of SiC.

In the present report the general physical mechanisms of radiation swelling of graphite and ceramic materials are investigated. New theoretical models are suggested here for the investigation of radiation swelling in graphite and ceramic materials (SiC). The theoretical models in SiC are based on kinetic consideration of point defect accumulation and kinetic growth of point defect clusters (dislocation loops and voids) in the matrix taking into account the charge state of point defects and the effect of internal electric field formed under irradiation in the matrix on diffusion processes of point defects. The obtained theoretical results allow studying the nucleation and growth of point defect clusters (dislocation loops, voids) in supersaturated system of charged point defects and radiation swelling in ceramic materials (SiC). The physical mechanisms of temperature dependence of radiation swelling at low and high temperatures are proposed here on the basis of suggested theoretical models. Such processes as swelling increase with the increasing of displacement damage level until amorphisation and saturation of swelling without amorphisation at high temperatures are discussed for SiC in the frame of proposed theoretical model. The influence of helium on radiation swelling of SiC is considered here too. The theoretical model for graphite takes into account the nucleation and growth of dislocation loops in anisotropic graphite and the effect of grain size on radiation swelling. The numerical modelling of radiation swelling in polycrystalline graphite has been performed in the dependence on grain size and concentration of impurity atoms.

The recent experimental results concerning the effect of neutron and ion irradiation on radiation swelling of graphite and SiC materials behaviour are presented here too. The obtained theoretical results for radiation swelling are compared with the existed experimental data for irradiated graphite and SiC materials.

* *Poster session*

INVESTIGATION OF Ni-Cr BASED ALLOYS BY MEANS OF MEASUREMENT OF THE ANGULAR CORRELATION OF POSITRON ANNIHILATION PHOTONS*

V.I. Grafutin¹, Zin Min Oo², V.P. Kolotushkin³, V.Yu. Miloserdin²,
A.Yu. Mischenko², V.N. Rechitsky³, V.T. Samossadny², Yu.V. Funtikov¹

¹State Scientific Centre – Institute of Theoretical and Experimental Physics

²State Educational Establishment of High Education – Moscow Engineering Physics Institute

³Federal State Unitary Enterprise – All-Russian Research Institute of Non-organic Materials

Abstract

Ni-Cr alloys with different Cr abundance were investigated by means of measurement of the angular correlation of positron annihilation photons. The results obtained gave the possibility to estimate defects' concentration, their type and allowed to predict the region of short range ordering of these alloys.

This paper is devoted to Ni-Cr alloys investigation. These alloys are known to be ordered at some concentrations of Cr, the last depending on doping of the alloy. This ordering is correlated with increase of the radiation stability of these alloys. The properties of the samples used for the experiment are shown in Table 1.

The results of the experiments processed with the help of the ACARFIT program are shown in Table 2. The basic assumption used for fitting was that there were two values of the conduction electrons densities and Fermi energy (corresponding to parabolic curves) as well as one or two values of the core ionisation energy (corresponding to Gaussians). These assumptions correspond to different types of positions, in which the positron may be trapped.

Here *the.* and *exp.* correspond to values obtained from theoretical calculations and experiments, θ_{p1} and θ_{p2} – are the angles at which the first and second parabolic curve cross the abscissa axis θ , θ_{g1} and θ_{g2} is the dispersion of the first and second Gaussian, I_{p1} , I_{p2} , I_{g1} and I_{g2} are the parts of positron annihilation in the corresponding regions.

It may be concluded from the experimental data that the alloys with Cr abundance less than 38% show no tendency to the second phase generation. This corresponds to absence of the second Gaussian. The alloy with 32% of Cr is characterised by the highest concentration of defects, the I_{p2} value being the highest among all alloys under investigation. The concentration of the second phase has a maximum at 39% Cr concentration and is generated at 38%, when the alloy contained 1% Mo. There are no cores except the main one for the alloy containing no Mo. This phase is growing only provided the concentration of Cr was 42%. This behaviour may be explained by the second phase (Ni_2Cr) generation and growth. The simultaneous growth of the second parabolic curve dependence at 38-39% of Cr and its behaviour during annealing may be explained by the short range ordering, which is followed by defects concentration growth at the boundaries of the phases.

* *Poster session*

Table 1. The properties of the samples used for the experiment

Samples	Heat treatment	Ni	Cr	Mo	C	Si	Ce
1	Quenching at 450°C, 40 000 h	Base.	32.11	1.28	0.027	0.006	0.06
2	~	Base.	37.85	1.3	0.027	0.006	0.06
3	~	Base.	38.9	1.3	0.022	0.005	0.06
4	~	Base.	41.2	–	0.03	0.005	0.06
5	~	Base.	41.35	1.3	0.028	0.005	0.06
6	~	Base.	44.48	1.3	0.026	0.005	0.06
7	Tempering at 1 050°C	Base.	38	–	–	–	–
8	Quenching at 500°C, 10 h	Base.	38	–	–	–	–
9	Quenching at 500°C, 90 h	Base.	38	–	–	–	–
10	Tempering at 1050°C	Base.	42	–	–	–	–
11	Quenching at 500°C, 10 h	Base.	42	–	–	–	–
12	Quenching at 500°C, 90 h	Base.	42	–	–	–	–

Table 2. Results of the experiments processed with the help of the ACARFIT program

Samples	No. of components	θ_p , mrad			θ_g , mrad			I_p , %		I_g , %	
		$\theta_p^{the.}$	$\theta_{p1}^{exp.}$	$\theta_{p2}^{exp.}$	$\theta_g^{the.}$	$\theta_{g1}^{exp.}$	$\theta_{g2}^{exp.}$	I_{p1}	I_{p2}	I_{g1}	I_{g2}
1	2P+G	6.68	6.57 ±0.14	4.2 ±0.27	12.6	12.95 ±0.17	–	16.67 ±1.75	4.33 ±1.05	78.98 ±1.7	–
	2P+2G	–	6.52 ±0.2	4.23 ±0.54	–	13.1 ±0.1	7.52 ±0.73	14.9 ±2.7	2.9 ±1.3	76.83 ±1.25	5.37 ±4.86
2	2P+G	6.67	6.33 ±0.27	4.51 ±0.67	12.8	12.56 ±0.2	–	10.8 ±2.38	2.45 ±1.8	86.73 ±2.14	–
	2P+2G	–	6.52 0.17	4.31 ±0.46	–	13.13 ±0.24	9.65 ±1.45	8.88 ±2.37	1.63 ±0.66	71.01 ±3.37	18.46 ±5.8
3	2P+G	6.66	6.0 ±0.16	3.03 ±0.41	13.1	13.2 ±0.15	–	12.4 ±1.4	1.6 ±0.55	86.0 ±1.44	–
	2P+2G	–	6.27 ±0.14	3.22 ±0.24	–	13.74 ±0.21	10.04 ±1.21	10.77 ±1.83	1.85 ±0.33	72.93 ±2.71	14.43 ±4.42
4	2P+G	6.2	6.22 ±0.20	3.23 ±0.40	13.0	13.16 ±0.22	–	15 ±2.0	3 ±1.0	81 ±2.0	–
	2P+2G	–	6.23 ±0.2	3.2 ±0.4	–	13.7 ±0.1	8.03 ±1.0	14 ±3.0	2 ±0.7	75 ±2.0	7 ±6.0
5	2P+G	6.2	6.44 ±0.08	4.1 ±0.2	14.4	14.5 ±0.11	–	17.6 ±1.0	3.88 ±0.7	78.52 ±0.84	–
	2P+2G	–	6.37 ±0.12	4.26 ±0.36	–	14.65 ±0.08	7.61 ±0.46	13.25 ±1.67	1.91 ±0.73	75.95 ±0.74	8.87 ±2.83

Table 2. Results of the experiments processed with the help of the ACARFIT program (cont.)

Samples	No. of components	θ_p , mrad			θ_g , mrad			I_p , %		I_g , %	
		$\theta_p^{\text{the.}}$	$\theta_{p1}^{\text{exp.}}$	$\theta_{p2}^{\text{exp.}}$	$\theta_g^{\text{the.}}$	$\theta_{g1}^{\text{exp.}}$	$\theta_{g2}^{\text{exp.}}$	I_{p1}	I_{p2}	I_{g1}	I_{g2}
6	2P+G	6.21	6.6 ± 0.17	4.22 ± 0.16	12.8	12.8 ± 0.11	–	10.46 ± 1.37	5.36 ± 0.8	84.16 ± 1.35	–
	2P+2G	–	6.4 ± 0.1	3.42 ± 0.2	–	13.4 ± 0.1	8.6 ± 0.6	7.2 ± 1.8	1.75 ± 0.3	73.2 ± 1.3	17.8 ± 3.2
7	2P+G	6.66	6.41 ± 0.12	4.35 ± 0.2	14.1	14.15 ± 0.1	–	13.66 ± 1.15	4.84 ± 1.0	81.5 ± 0.82	–
	2P+2G	–	6.45 ± 0.13	4.5 ± 0.27	–	14.31 ± 0.1	4.34 ± 9.77	13.87 ± 2.3	4.43 ± 3.24	80.95 ± 0.82	0.74 ± 5.15
8	2P+G	–	6.93 ± 0.24	5.17 ± 0.16	–	14.43 ± 0.1	–	8.61 ± 1.47	7.94 ± 1.38	83.44 ± 0.82	–
	2P+2G	–	6.95 ± 0.25	5.24 ± 0.17	–	14.44 ± 0.1	0.83 ± 0.43	8.47 ± 1.58	8.02 ± 1.52	83.35 ± 0.83	0.14 ± 0.07
9	2P+G	–	6.5 ± 0.25	4.72 ± 0.25	–	14.1 ± 0.11	–	9.7 ± 1.7	5.44 ± 1.55	84.87 ± 0.96	–
	2P+2G	–	6.77 ± 0.24	4.84 ± 0.25	–	14.32 ± 0.11	3.27 ± 11.7	9.83 ± 1.53	6.34 ± 1.66	83.67 ± 1.0	0.15 ± 1.21
10	2P+G	6.2	6.93 ± 0.1	4.25 ± 0.14	13.88	14.62 ± 0.1	–	15.74 ± 0.9	5.41 ± 0.6	78.84 ± 0.8	–
	2P+2G	–	7.0 ± 0.2	4.6 ± 0.46	–	14.8 ± 0.2	7.4 ± 0.84	10.0 ± 2.57	2.12 ± 1.42	76.2 ± 2.57	11.67 ± 5.46
11	2P+G	–	6.06 ± 0.07	3.01 ± 0.34	–	14.0 ± 0.07	–	13.91 ± 0.61	1.03 ± 0.3	85.05 ± 0.6	–
	2P+2G	–	6.44 ± 0.12	5.02 ± 0.54	–	14.12 ± 0.11	6.4 ± 1.43	9.81 ± 2.5	2	83.57 ± 1.53	4.61 ± 3.76
12	2P+G	–	5.76 ± 0.1	3.66 ± 0.27	–	13.74 ± 0.06	–	9.88 ± 0.7	1.9 ± 0.51	88.22 ± 0.55	–
	2P+2G	–	6.12 ± 0.23	5.08 ± 0.54	–	14.0 ± 0.11	6.54 ± 0.87	5.0 ± 2.17	2	86.01 ± 1.7	7.0 ± 3.6

Acknowledgement

These investigations were funded by Russian Foundation for Basic Research (project #06-08-00819-01).

MOBILITY OF INTERSTITIAL CLUSTERS AND DISLOCATION LOOPS IN Fe-Cr ALLOYS*

Terentyev Dmitry
SCK•CEN, Belgium

Abstract

This work is devoted to the study of the mobility of self interstitial atom (SIA) clusters and small SIA dislocation loops (of size up to few nanometers) in Fe-Cr alloys of different concentrations, up to 15% Cr. Static and dynamic atomistic simulations have been performed using recently developed interatomic potential for Fe-Cr system to characterise the migration of interstitial defects and investigate the influence of Cr content on their mobility in diluted and concentrated Fe-Cr alloys. It has been shown that the presence of randomly distributed Cr in Fe matrix leads to the creation of local trapping configurations for the dislocation loops and SIA clusters, the strength (trapping energy) and density of these configurations depend on the Cr content. Whereas coherent Cr-rich precipitates act as strong obstacles preventing the motion of 1D migrating dislocation loops and SIA clusters, thus the mobility of small interstitial loops is expected to be strongly affected during the phase separation or non-equilibrium segregation of Cr occurring during irradiation at elevated temperatures. The obtained results provide quantitative estimates of these effects for different Fe-Cr compositions.

* *Poster session*

MATERIAL CHALLENGES FOR THE VHTR CONCEPT*

S. Teysseyre, D. Kumar, Z. Jiao, R. Zhou, A. Davis, O. Toader, L. Wang, G. Was
University of Michigan

Abstract

Fundamental knowledge about material behaviour is required in order to assess the feasibility of the very high temperature reactor (VHTR). The potential use of pyrolytic carbon (PyC) in the fuel particles raises the question of the creep behaviour of PyC during irradiation and, whereas the helium coolant to be used in the reactor is inert in itself, it inevitably contains gaseous impurities that can interact with the metallic part of the intermediate heat exchanger causing its degradation. To characterise the creep behaviour of PyC under proton irradiation at temperatures up to 1 200°C, a special irradiation stage was designed for creep test of a chemical vapour deposited PyC film. The stage is composed of a high performance pyrolytic boron nitride/pyrolytic graphite heater with operating temperatures up to 1 800°C, a load application assembly and an aperture system for accurate beam alignment. The role of different impurities in the corrosion behaviour of alloy 617, candidate alloy for the intermediate heat exchanger, is being investigated by separating the main impurities in VHTR helium into three simpler helium gas chemistries: (a) (He-CO-CO₂), (b) (He-H₂-H₂O) and (c) (He-CH₄-H₂) for conducting exposure experiments. For both projects, experimental set-ups and preliminarily results will be presented.

* *Poster session*

MATERIAL OPTIMISATION TO MITIGATE IASCC IN SCWR*

S. Teysseyre, G. Gupta, M. Hackett, E. West, G.S. Was
University of Michigan, USA

Abstract

Grain boundary engineering and oversized solute additions were used in an attempt to mitigate stress corrosion cracking (SCC) and irradiation assisted stress corrosion cracking (IASCC) in supercritical water. A method was developed to increase the fraction of special boundaries in austenitic and ferritic alloys. The SCC susceptibility was evaluated in deaerated supercritical water during constant extension rate tensile experiments. Proton irradiation was used to determine if the fraction of special boundaries remains stable after exposure to irradiation at high temperature and if grain boundary engineering can improve the IASCC resistance of irradiated alloys. The role of oversized solute additions in 316L stainless steel was investigated as a way to reduce radiation-induced segregation (RIS) that could impact IGSCC. Experiments with Hf and Zr show that RIS is indeed reduced at low dose, as is IGSCC.

* *Poster session*

NEW INSIGHT ON THE PRODUCTION PROCESS OF RAFM ODS STEELS FOR NUCLEAR APPLICATIONS*

P. Vladimirov¹, A. Möslang¹, R. Lindau¹, M. Klimenkov¹, C. Eiselt¹, V. Borodin²

¹Institute of Material Research-I, Forschungszentrum Karlsruhe, Germany

²Russian Research Center “Kurchatov Institute”, Russia

Abstract

Reduced activation ferritic-martensitic steels reinforced by oxide dispersion strengthened particles possess high strength and creep resistance at elevated temperatures as well as excellent irradiation resistance and are foreseen for the use as structural materials for fusion devices and next generation nuclear power plants. Excellent mechanical properties of ODS materials were achieved by introduction of a homogeneous distribution highly thermally stable nano-scale Y_2O_3 -particles in the steel matrix.

ODS steels are produced by mechanical alloying for several tens of hours followed by hot isostatic pressing at high temperature (1 000-1 200°C) and high pressure (~100 MPa).

According to the contemporary view, oxide particles produced by hipping are the remnants of the initial oxide powder. This view is supported by the fact that hipping temperature is much lower than melting temperature of yttria and therefore any thermal processes of oxide particle transformation are excluded. However, some experimental data obtained by different research groups provide evidence that this picture might be much more complex than it is currently assumed.

The present paper discusses experimental data obtained by X-ray analysis, electron microscopy and 3-D atomic probe indirectly supporting the idea that yttria particles might be formed by dissolution (during mechanical alloying and hipping) and reprecipitation of solute atoms during hipping. Based on this idea a multi-scale modelling program of ODS particle formation is proposed. Preliminary simulation results are also presented.

* *Poster session*

ATOMISTIC SIMULATIONS OF DISLOCATION INTERACTIONS WITH STACKING FAULT TETRAHEDRON*

Brian D. Wirth, Hyon-Jee Lee, Ian M. Robertson¹

Nuclear Engineering Department, University of California, Berkeley

¹Materials Science and Engineering Department, University of Illinois, Urbana-Champaign

Abstract

In the early stages of deformation of irradiated materials, dislocations emitted from grain boundaries and other localised regions of high stress concentration interact with and destroy radiation-induced defects, creating defect-free channels. Although the presence of channels in a wide range of materials is well documented, the atomistic processes responsible for defect annihilation are still subject to debate. In this presentation, we review the results of atomic-scale molecular dynamics (MD) simulations of the interactions between gliding dislocations with either perfect or imperfect stacking fault tetrahedra (SFTs) in face centred cubic (FCC) copper, and compare with dynamic observations from in-situ straining experiments in FCC copper and gold performed in the transmission electron microscopy. The MD simulations have examined the effect of dislocation type (edge, screw and mixed), temperature, SFT size and type (perfect or imperfect), stacking fault energy, dislocation velocity and the interaction geometry. A number of interactions have been characterised, but notably complete annihilation of an SFT has not been observed in the MD simulations. Regardless of the dislocation character, the trailing Shockley partial detaches by an Orowan like mechanism, indicating that the SFT is a very strong obstacle to dislocation motion. The MD simulations also indicate that shearing of the SFT, and not annihilation or absorption, is the most common result of the dislocation interaction with an SFT.

* *Poster session*

LIST OF PARTICIPANTS

AUSTRALIA

HUTCHINGS, Ron	Tel: +43 1 5067 4119
Australian Embassy	Fax: +43 1 504 1178
Permanent Mission to the UN	Eml: ron.hutchings@dfat.gov.au
Mattiellistrasse 2-4, A-1040 Vienna (Austria)	

BELGIUM

AL MAZOUZI, Abderrahim	Tel: +32 14 32 30 96
SCK•CEN	Fax: +32 14 32 12 16
Nuclear Materials Science Institute, LHMA	Eml: aalmazou@sckcen.be
Boeretang 200, B-2400 Mol	
LAMBRECHT, Marlies	Tel: +32 14 33 30 89
SCK•CEN	Fax:
Boeretang 200, B-2400 Mol	Eml: marlies.lambrecht@sckcen.be
MALERBA, Lorenzo	Tel: +32 14 33 30 90
SCK•CEN	Fax: +32 14 32 12 16
Boeretang 200, B-2400 Mol	Eml: lmalerba@sckcen.be
TERENTYEV, Dmitry	Tel:
SCK•CEN	Fax:
Boeretang 200, B-2400 Mol	Eml: dterenty@sckcen.be
VAN DEN BOSCH, Joris	Tel:
SCK•CEN	Fax:
NMS/LHMA	Eml: jvdbosch@sckcen.be
Boeretang 200, B-2400 Mol	

CZECH REPUBLIC

BRUMOVSKY, Milan	Tel: +420 2 2094 1110
Nuclear Research Institute Rez	Fax: +420 2 2094 0519
Vltavska 130, 250 68 Rez	Eml: bru@ujv.cz
HAJEK, Petr	Tel:
UJV Rez a.s.	Fax:
Husinec-Rez 130, 250 68 Husinec-Rez	Eml: hap@ujv.cz

RUZICKOVA, Mariana
UJV Rez a.s.
Husinec-Rez 130, 250 68 Husinec-Rez

Tel:
Fax:
Eml: ruz@ujv.cz

FINLAND

HEIKINHEIMO, Liisa
VTT
Kemistintie 3, POB 1000, 02044 VTT

Tel: +358 0 20 722 5354
Fax: +358 0 20 722 7002
Eml: Liisa.Heikinheimo@vtt.fi

KOHOPAA, Jyrki
Fortum Nuclear Services Ltd
P.O. Box 100, 00048 Fortum

Tel:
Fax:
Eml: jyrki.kohopaa@fortum.com

FRANCE

BALBAUD-CELERIER, Fanny
CEA Saclay
F-91191 Gif-sur-Yvette Cedex

Tel: +33 1 69 08 16 51
Fax: +33 1 69 08 15 86
Eml: fanny.balbaud@cea.fr

BARABASH, Vladimir
ITER Organisation
Bât. 519, CEA Cadarache
F-13108 St. Paul-lez-Durance

Tel:
Fax:
Eml: Vladimir.barabash@iter.org

BECQUART, Charlotte
LMPGM
Bât. C6, Université de Lille I
F-59655 Villeneuve-d'Ascq Cedex

Tel:
Fax:
Eml: charlotte.becquart@univ-lille1.fr

BLAT-YRIEIX, Martine
EDF R&D, Dept. MMC
Les Renardières, Route de Sens
F-77818 Moret-sur-Loing

Tel:
Fax:
Eml: martine.blat@edf.fr

BONNE, Dominique
AREVA NP
10, rue Juliette Récamier
F-69006 Lyon

Tel:
Fax:
Eml: dominique.bonne@areva.fr

BURLET, Hélène
CEA Grenoble
17, rue des Martyrs
F-38054 Grenoble Cedex 9

Tel: +33 4 38 78 94 96
Fax: +33 4 38 78 25 56
Eml: helene.burlet@cea.fr

CABET, Céline
CEA Saclay, DEN/DPC/SCCME
F-91191 Gif-sur-Yvette

Tel:
Fax:
Eml: celine.cabet@cea.fr

DOMAIN, Christophe
EDF R&D
Les Renardières, F-77250 Moret-sur-Loing

Tel:
Fax:
Eml: christophe.domain@edf.fr

GAUDE-FUGAROLAS, Daniel
CEA Saclay, DEN/DMN/SRMA/LA2M
F-91191 Gif-sur-Yvette

Tel:
Fax:
Eml: dgaude@cantab.net

HITTNER, Dominique
AREVA NP
Tour AREVA,
F-92084 Paris-la-Défense Cedex

Tel:
Fax:
Eml: dominique.hittner@areva.com

HOROWITZ, Emmanuel
EDF Generation Nuclear Department
165-173 Av. Pierre Brosolette
BP 900, F-92542 Montrouge Cedex

Tel:
Fax:
Eml: emmanuel.horowitz@edf.fr

MONNET, Ghiath
EDF
Avenue des Renardières
F-77250 Moret-sur-Loing

Tel:
Fax:
Eml: ghiath.monnet@gmail.com

OLSSON, Pär
EDF R&D, Dept. MMC
Avenue des Renardières
F-77250 Moret-sur-Loing

Tel:
Fax:
Eml: olsson.par@gmail.com

ROMA, Guido
CEA Saclay, Service de Recherches
de Métallurgie Physique
F-91191 Gif-sur-Yvette

Tel:
Fax:
Eml: guido.roma@cea.fr

SERRE, Ingrid
CNRS-LMPGM, Université Lille 1
Laboratoire de Métallurgie Physique
Bât. C6, F-59655 Villeneuve-d'Ascq

Tel: +33 (0)3 20 43 66 06
Fax:
Eml: ingrid.serre@univ-lille1.fr

TAVASSOLI, A-A. Farhad
CEA Saclay, DMN/Dir
F-91191 Gif-sur-Yvette

Tel:
Fax:
Eml: tavassoli@cea.fr

YVON, Pascal
CEA Saclay, DDIN
Bât. 121, Saclay

Tel: +33 (0)1 69 08 68 56
Fax: +33 (0)1 69 08 58 92
Eml: pascal.yvon@cea.fr

GERMANY

ALSTADT, Eberhard
FZD Rossendorf
P.O.B. 510119, 01314 Dresden

Tel:
Fax:
Eml: e.altstadt@fzd.de

BERGNER, Frank Forschungszentrum Dresden-Rossendorf P.O. Box 510119, D-01314 Dresden	Tel: Fax: Eml: F.Bergner@fzd.de
BOLT, Harald Max-Planck-Institut für Plasmaphysik Bereich Materialforschung Boltzmannstrasse 2, D-85728 Garching	Tel: Fax: Eml: harald.bolt@ipp.mpg.de
DIETZ, Wolfgang MECS Schoenenborner Weg 15, D-51789 Lindlar	Tel: Fax: Eml: w_dietz@t-online.de
FAZIO, Concetta FZK Hermann-von-Helmholtz-Platz 1 D-76344 Eggenstein-Leopoldshafen	Tel: +49 7247 82 5517 Fax: +49 7247 82 5508 Eml: concetta.fazio@nuklear.fzk.de
FRIEDRICH, Bernd-Christian AREVA NP GmbH Freyeslebenstr. 1, D-91058 Erlangen	Tel: Fax: Eml: Bernd-Christian.Friedrich@AREVA.com
HEINTZE, Cornelia Forschungszentrum Dresden-Rossendorf Postfach 510119, D-01314 Dresden	Tel: Fax: Eml: c.heintze@fzd.de
HEINZEL, Annette FZK Hermann-von-Helmholtz-Platz 1 D-76344 Eggenstein-Leopoldshafen	Tel: Fax: Eml: annette.heinzel@ihm.fzk.de
HOFFMANN, Michael MPA Materialprüfungsanstalt Universität Stuttgart Pfaffenwaldring 32, D-70569 Stuttgart	Tel: Fax: Eml: michael.hoffmann@mpa.uni-stuttgart.de
KONOBEEV, Alexander Forschungszentrum Karlsruhe Institut für Reaktorsicherheit Hermann-von-Helmholtz-Platz 1 D-76344 Eggenstein-Leopoldshafen	Tel: Fax: Eml: konobeev@irs.fzk.de
KONYS, Jürgen Forschungszentrum Karlsruhe Hermann-von-Helmholtz-Platz 1 D-76344 Eggenstein-Leopoldshafen	Tel: +49 7247 82 3720 Fax: +49 7247 82 3956 Eml: juergen.konys@imf.fzk.de
LINDAU, Rainer FZK Institute for Materials Research I Hermann-von-Helmholtz-Platz 1 D-76344 Eggenstein-Leopoldshafen	Tel: Fax: Eml: rainer.lindau@imf.fzk.de

MOSLANG, Anton
FZK
Hermann-von-Helmholtz-Platz 1
D-76344 Eggenstein-Leopoldshafen

Tel: +49 72 47 4029
Fax: +49 7247 5678
Eml: Anton.Moeslang@imf.fzk.de

ROOS, Eberhard
MPA Materialprüfungsanstalt
Universität Stuttgart
Pfaffenwaldring 32, D-70569 Stuttgart

Tel:
Fax:
Eml: eberhard.roos@mpa.uni-stuttgart.de

SCHROER, Carsten
Forschungszentrum Karlsruhe
Hermann-von-Helmholtz-Platz 1
D-76344 Eggenstein-Leopoldshafen

Tel:
Fax:
Eml: carsten.schroer@imf.fzk.de

STEINER, Helmut
Forschungszentrum Karlsruhe
Hermann-von-Helmholtz-Platz 1
D-76344 Eggenstein-Leopoldshafen

Tel:
Fax:
Eml: helmut.steiner@imf.fzk.de

TROMM, Walter
Forschungszentrum Karlsruhe
Hermann-von-Helmholtz-Platz 1
D-76344 Eggenstein-Leopoldshafen

Tel: +49 7247 82 5509
Fax: +49 7249 82 5508
Eml: Walter.Tromm@nuklear.fzk.de

VLADIMIROV, Pavel
Forschungszentrum Karlsruhe
Hermann-von-Helmholtz-Platz 1
D-76344 Eggenstein-Leopoldshafen

Tel:
Fax:
Eml: pavel.vladimirov@imf.fzk.de

WEISENBURGER, Alfons
Forschungszentrum Karlsruhe/IHM
Hermann-von-Helmholtz-Platz 1
D-76344 Eggenstein-Leopoldshafen

Tel:
Fax:
Eml: alfons.weisenburger@ihm.fzk.de

HUNGARY

HORVATH, Akos
KFKI Atomic Energy Research Institute
Konkoly Thege u.29-33, Budapest, H1121

Tel: +36 1 392 2222/3628
Fax: +36 1 395 9162
Eml: hakos@sunserv.kfki.hu

KUNSTAR, Mihály
MTA KFKI AEKI
H-1121 Budapest
Konkoly Thege M. út 29-33.

Tel:
Fax:
Eml: kunstar@sunserv.kfki.hu

INDIA

VALSAKUMAR, Mundachali Cheruvalath
IGCAR, Materials Science Division
Kalpakkam 603 102

Tel:
Fax:
Eml: valsa@igcar.gov.in

ITALY

CAMMI, Antonio
Politecnico di Milano
Departement of Nuclear Engineering
via Ponzio, 34/3, I-20133 Milan

Tel:
Fax:
Eml: antonio.cammi@polimi.it

DI MARCELLO, Valentino
Politecnico di Milano
Departement of Nuclear Engineering
via Ponzio, 34/3, I-20133 Milan

Tel:
Fax:
Eml: valentino.dimarcello@gmail.com

LUZZI, Lelio
Politecnico di Milano
Departement of Nuclear Engineering
via Ponzio, 34/3, I-20133 Milan

Tel: +39 02 23 99 63 26
Fax:
Eml: lelio.luzzi@polimi.it

TAGLIONI, Alberto
ENEA
via Anguillarese n. 300, I-00123 Roma

Tel:
Fax:
Eml: alberto.taglioni@casaccia.enea.it

JAPAN

ASAYAMA, Tai
JAEA
4002 Narita, Oarai, Higashi-Ibaraki
Ibaraki 311-1391

Tel:
Fax:
Eml: asayama.tai@jaea.go.jp

KATO, Chiaki
JAEA
Tokai-mura, Shirakata, Naka-gun
Ibaraki-ken 319-1195

Tel: +81 292826482
Fax: +81 292825864
Eml: kato.chiaki16@jaea.go.jp

KIMURA, Akihiko
Kyoto University
IAE, Kytoto University, Gokasho, Uji, Kyoto

Tel:
Fax:
Eml: kimura@iae.kyoto-u.ac.jp

KOBYAMA, Akira
Institute of Advanced Energy
Kyoto University
Gokasho, Uji, Kyoto, 611-0011

Tel:
Fax:
Eml: kohyama@iae.kyoto-u.ac.jp

OBARA, Satoshi
JAEA
Oarai-machi, Higashiibaraki-gun, Ibaraki-ken

Tel:
Fax:
Eml: obara.satoshi@jaea.go.jp

OYAMADA, Osamu
JAEA
Nuclear Science and Energy Directorate
Tokai-mura, Naka-gun, Ibaraki-ken, 319-11

Tel: +81 29 282 6774
Fax: +81 29 282 6122
Eml: ayamada.osamu@jaea.go.jp

SEKIMURA, Naoto
University of Tokyo
7-3-1 Hongo, Binkyo-ku, Tokyo 113-8656

Tel: +81 3 5841 6986
Fax: +81 3 5841 8614
Eml: sekimura@q.t.u-tokyo.ac.jp

TAKAHASHI, Akiyuki
Tokyo University of Science
2641, Yamazaki, Noda-shi, Chiba 278-8510

Tel:
Fax:
Eml: takahash@me.noda.tus.ac.jp

TAKAHASHI, Minoru
Tokyo Institute of Technology
Research Laboratory for Nuclear Reactors
N1-18, 2-12-1, O-okayama, Meguro-ku
Tokyo, 152-8550

Tel:
Fax:
Eml: mtakahas@nr.titech.ac.jp

KOREA (REPUBLIC OF)

JANG, Chanheui
KAIST
373-1 Guseong-dong, Yuseong-gu
Daejeon, 305-701

Tel:
Fax:
Eml: chjang@kaist.ac.kr

JO, Tae Sun
Division of Advanced Materials Science
& Engineering
Hanyang University
17 Haengdang-dong, Seongdong-ku
Seoul 133-79

Tel:
Fax:
Eml: cts0124@hanyang.ac.kr

KIM, Daejong
KAIST
Hanyang University, 17 Haengdang-dong,
Seongdong-ku, Seoul 133-791

Tel:
Fax:
Eml: quneo@kaist.ac.kr

KIM, Weon-Ju
Korea Atomic Energy Research Institute
(150-1 Deokjin-dong), 1045 Daedeokdaero
Yuseong, Daejeon 305-353

Tel:
Fax:
Eml: weonjkim@kaeri.re.kr

SONG, Tae Yung
Korea Atomic Energy Research Institute
P.O. Box 105, Yuseong, Daejeon

Tel:
Fax:
Eml: tysong@kaeri.re.kr

THE NETHERLANDS

VAN DER LAAN, Jaap G.
NRG
P.O. Box 25, NL-1755 ZG Petten

Tel:
Fax:
Eml: vanderlaan@nrg-nl.com

P.R. OF CHINA

CHEN, Jiming
Southwestern Institute of Physics
P.O. Box 432, Chengdu 610041 Sichuan
Tel:
Fax:
Eml: chenjm@swip.ac.cn

RUSSIAN FEDERATION

CHERNOV, Viatcheslav M.
A.A. Bochvar Institute of Inorganic Materials
P.O. Box 369, Moscow, 123060
Tel: +499 190 3605
Fax: +495 196 4168
Eml: chernovv@bochvar.ru

KALININ, Georgy
Engineering Center of Nuclear Equipment
Strength and Materials (ENES)
Moscow, 101000, P.O. Box 788
Tel:
Fax:
Eml: gmk@nikiet.ru

NIKITINA, Anastasia A.
A.A. Bochvar Institute of Inorganic Materials
(VNIINM)
5a Rogova str., P.O. Box 369
Moscow, 123060
Tel:
Fax:
Eml: nikitina-2a@yandex.ru

RYAZANOV, Alexander
Russian Research Center "Kurchatov Institute"
123182 Moscow, Kurchatov Sq. 1
Tel:
Fax:
Eml: ryazanoff@comail.ru

SAMOSSADNY, Valerie T.
Moscow Engineering Physics Institute
115409 Moscow, Kashirskoyes shosse, 31
Tel:
Fax:
Eml: samossadny@atomic.mephi.ru

SHTROMBAKH, Yaroslav
Institute of Reactor Materials
RRC "Kurchatov Institute"
Kurchatov Sq. 1, 123182 Moscow
Tel:
Fax:
Eml: strombach@irtm.kiae.ru

SLOVENIA

KRSJAK, Vladimír
Slovak Technical University
Dept. of Nuclear Physics
Ilkoviova 3, 812 19, Bratislava
Tel:
Fax:
Eml: vladimir.krsjak@stuba.sk

SPAIN

CATURLA, Maria J.
Universitat d'Alacant, Facultat de Ciències
Fase II, Sant Vicent del Raspeig, Alcant
Tel: +34 965903400, ext. 20
Fax: +34 965909726
Eml: mj.caturla@ua.es

GOMEZ-BRICENO, Dolores
CIEMAT
Avenida Complutense 22
E-28040 Madrid

Tel: +34 91 3466605
Fax: +34 91 3466661
Eml: lola.gomezbriceno@ciemat.es

PERLADO, J. Manuel
Instituto Fusion Nuclear
Universidad Politecnica Madrid
ETSII/J. Gutierrez Abascal 2
E-28006 Madrid

Tel: +34 91 336 3108/09
Fax: +34 91 336 3002/41
Eml: mperlado@din.upm.es

SOLER CRESPO, Laura
CIEMAT
Avda. Complutense 22, E-28040 Madrid

Tel: +34 91 346 60 31
Fax: +34 91 346 60 61
Eml: laura.soler@ciemat.es

SWEDEN

WALLENIOUS, Janne
KTH, Reactor Physics
AlbaNova University Centre
S-106 91 Stockholm

Tel: +46 8 5537 8200
Fax: +46 8 5537 8216
Eml: janne@neutron.kth.se

SWITZERLAND

BLANCHET, David
Paul Scherrer Institut
CH-5232 Villigen PSI

Tel: +41 56 310 2352
Fax: +41 56 310 2327
Eml: david.blanchet@psi.ch

CHEN, Jiachao
Paul Scherrer Institut
OHL D 014
CH-5232 Villigen PSI

Tel: +41 56 310 2280
Fax:
Eml: jiachao.chen@psi.ch

DAI, Yong
Paul Scherrer Institut
ODGA/114
CH-5232 Villigen PSI

Tel: +41 56 310 4171
Fax:
Eml: yong.adi@psi.ch

HOFFELNER, Wolfgang
Paul Scherrer Institut
CH-5232 Villigen PSI

Tel: +41 56 310 4461
Fax: +41 56 310 2203
Eml: wolfgang.hoffelner@psi.ch

MIKITYUK, Konstantin
Paul Scherrer Institut
CH-5232 Villigen PSI

Tel: +41 56 310 2385
Fax:
Eml: konstantin.mikityuk@psi.ch

POUCHON, Manuel Alexandre
Paul Scherrer Institut
CH-5232 Villigen PSI

Tel: +41 56 310 2245
Fax:
Eml: manuel.pouchon@psi.ch

UKRAINE

TSISAR, Valentyn
Physico-Mechanical Institute of National
Academy of Sciences of Ukraine
5, Naukova St., Lviv 79601

Tel:
Fax:
Eml: valentyn_tsisar@ipm.lviv.ua

YELISEYEVA, Olga
Physico-Mechanical Institute of National
Academy of Sciences of Ukraine
5, Naukova St., Lviv 79601

Tel:
Fax:
Eml: olgayeliseyeva@ipm.lviv.ua

UNITED KINGDOM

BERRE, Christophe
University of Manchester
Nuclear Graphite Research Group
Pariser Bldg., Sackville Street
Manchester M60 1QD

Tel:
Fax:
Eml: Christophe.Berre@postgrad.manchester.ac.uk

BUCKTHORPE, Derek Edward
AMECNC Limited
Booths Park, Chelford Road,
Knutsford, Cheshire

Tel:
Fax:
Eml: derek.buckthorpe@amecnc.com

HEGGIE, Malcolm
University of Sussex, Dept. of Chemistry
Falmer, Brighton, BN1 9QJ

Tel:
Fax:
Eml: M.I.Heggie@sussex.ac.uk

MARSDEN, Barry
University of Manchester
P.O. Box 88, Manchester, M60 1QD

Tel: +44 161 275 4399
Fax:
Eml: Barry.J.Marsden@manchester.ac.uk

QUINTA DA FONSECA, Joã
Materials Performance Centre
University of Manchester
Grosvenor Street, Manchester, M17HS

Tel:
Fax:
Eml: joao.fonseca@manchester.ac.uk

UNITED STATES OF AMERICA

ALLEN, Todd
University of Wisconsin
1500 Engineering Dr.
Madison, WI 53706

Tel: +1 608 265 4083
Fax: +1 608 263 7451
Eml: allen@engr.wisc.edu

CHOI, Jor-Shan
Lawrence Livermore National Laboratory
P.O. Box 808, L-632
Livermore, CA 94550

Tel:
Fax:
Eml: choi1@llnl.gov

GHONIEM, Nasr
University of California at Los Angeles
420 Westwood Plaza
Los Angeles, CA 91344

Tel:
Fax:
Eml: ghoniem@ucla.edu

MALLOY, Stuart
Los Alamos National Laboratory
MS H816, Los Alamos, NM 87545

Tel: +1 505 667 9784
Fax: +1 505 667 7443
Eml: maloy@lanl.gov

OSETSKIY, Yury
Oak Ridge National Laboratory
1 Bethel Valley Rd., P.O. Box 2008
MS-6138, Oak Ridge, TN 37931

Tel:
Fax:
Eml: osetskiyy@ornl.gov

SNEAD, Lance
ORNL
1 Bethel Valley Rd.
MS-6140, Oak Ridge, TN 37931

Tel:
Fax:
Eml: sneadll@ornl.gov

TEYSSEYRE, Sébastien
University of Michigan
2355 Bonisteel Blvd.
Ann Arbor, MI 48109

Tel:
Fax:
Eml: teysseyr@umich.edu

WIRTH, Brian
University of California at Berkeley
Nuclear Engineering Department
Berkeley, CA 94720-1730

Tel:
Fax:
Eml: bdwirth@nuc.berkeley.edu

ZINKLE, Steven J.
ORNL
Materials Science & Technology Division
P.O. Box 2008, Oak Ridge, TN 37831-6132

Tel:
Fax:
Eml: zinklesj@ornl.gov

INTERNATIONAL ORGANISATIONS

CLARK, Robert
IAEA
Wagramerstrasse 5, A-1400 Wien

Tel:
Fax:
Eml: r.e.h.clark@iaea.org

COADOU, Jean
European Commission
Bât. Euroforum, EUFO 4384
1, rue Henry M. Schnadt, L-2530
Luxembourg

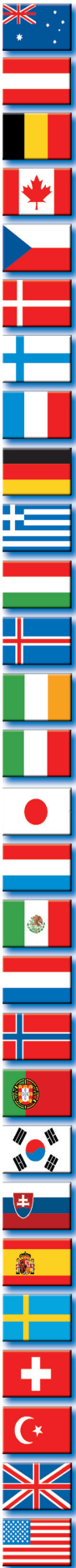
Tel: +352 4301340034
Fax:
Eml: jean.coadou@ec.europa.eu

GRYAZNOV, Denis
EC JRC ITU
Hermon-von-Helmholtz-Platz 1
D-76344 Eggenstein-Leopoldshafen

Tel: +49 7247 951462
Fax:
Eml: denis.gryaznov@ec.europa.eu

HAHNER, Peter EC JRC IE P.O. Box 2, NL-1755 ZB Petten	Tel: Fax: Eml: peter.haehner@jrc.nl
HEIFETS, Eugene EC JRC ITU Hermann-von-Helmholtz-Platz 1 D-76344 Eggenstein-Leopoldshafen	Tel: Fax: Eml: eugene.heifets@ec.europa.eu
INOZEMTSEV, Victor IAEA Wagramer Strasse 5, Vienna, Austria	Tel: +43 1 2600 22760 Fax: Eml: v.inozemtsev@iaea.org
KOTOMIN, Eugene EC JRC ITU Hermann-von-Helmholtz-Platz 1 D-76344 Eggenstein-Leopoldshafen	Tel: Fax: Eml: eugene.kotomin@cec.eu.int
MOMPEAN, Federico J. OECD Nuclear Energy Agency 12, boulevard des Iles F-92130 Issy-les-Moulineaux	Tel: Fax: Eml: federico.mompean@oecd.org
MUSELLA, Manuela EC JRC Institute for Energy P.O. Box 2, NL-1755 ZG, Petten	Tel: Fax: Eml: manuela.musella@jrc.nl
NOVOTNY, Radek EC JRC IE Petten Westerduinweg 3, Petten	Tel: Fax: Eml: Radek.Novotny@jrc.nl
OVER, Hans-Helmut EC JRC IE P.O. Box 2, NL-1755ZG Petten	Tel: +31 224565256 Fax: Eml: hans-helmut.over@jrc.nl
PRCHAL, Dusan EC JRC Petten Westerduinweg 3, NL-1755 Petten	Tel: Fax: Eml: Dusan.prchal@jrc.nl
VAN GOETHEM, Georges EC/DG Research, EC CDMA Building 01/47, B-1049 Brussels	Tel: +32 2 295 1424 Fax: +32 2 295 4991 Eml: Georges.van-goethem@ec.europa.eu
VAN UFFELEN, Paul EC JRC ITU Hermann-von-Helmholtz-Platz 1 D-67344 Eggenstein-Leopoldshafen	Tel: +49 7247 95 1384 Fax: Eml: paul.van-uffelen@ec.europa.eu

OECD PUBLICATIONS, 2, rue André-Pascal, 75775 PARIS CEDEX 16
PRINTED IN FRANCE
(66 2008 04 1 P) ISBN 978-92-64-04806-5 - No. 56303 2008



Structural Materials for Innovative Nuclear Systems (SMINS)

Structural materials research is a field of growing relevance in the nuclear sector, especially for the different innovative reactor systems being developed within the Generation IV International Forum (GIF), for critical and subcritical transmutation systems, and of interest to the Global Nuclear Energy Partnership (GNEP). Under the auspices of the NEA Nuclear Science Committee (NSC) the Workshop on Structural Materials for Innovative Nuclear Systems (SMINS) was organised in collaboration with the *Forschungszentrum Karlsruhe* in Germany. The objectives of the workshop were to exchange information on structural materials research issues and to discuss ongoing programmes, both experimental and in the field of advanced modelling. These proceedings include the papers and the poster session materials presented at the workshop, representing the international state of the art in this domain.



(66 2008 04 1 P) € 110
ISBN 978-92-64-04806-5

www.oecd.org

